TECHNICAL QUARTERLY PROGRESS REPORT

Prepared By

Advanced Gas Turbine Systems Research
Clemson University Research Foundation

For

U. S. Department of Energy
National Energy Technology Laboratory

Contract No. DE-FC21-92MC29061

Reporting Period: October 1, 2001 – December 31, 2001

Advanced Gas Turbine Systems Research
South Carolina Institute for Energy Studies
Clemson, South Carolina

Technical Quarterly Progress Report

Advanced Gas Turbine Systems Research

Cooperative Agreement DE-FC21MC29061

October 1, 2001 to December 31, 2001

SUMMARY

The activities of the Advanced Gas Turbine Systems Research (AGTSR) program for this reporting period are described in this quarterly report. The report is divided into discussions of Membership, Administration, Technology Transfer (Workshop/Education), Research and Miscellaneous Related Activity. Items worthy of note are presented in extended bullet format following the appropriate heading.

MEMBERSHIP

- At the close of the reporting period, the AGTSR Perfoming Membership held firm at 100 universities represented in 38 states. No new inquiries were received this reporting period.
- The following IRB Membership fees have been received for CY2001:

Full Member	Associate Member
General Electric	Parker Hannifin
Pratt & Whitney	RAMGEN
Rolls Royce	Southern Company Services
Siemens Westinghouse	Woodward FST
Solar Turbines	

- The Associate membership of EPRI has not been completely resolved. Early in the year EPRI advised SCIES they would drop membership. Just prior to the Materials Workshop, SCIES was advised that EPRI would maintain Associate membership. In December, EPRI confirmed to SCIES they would continue membership but has yet provided their associate membership fee for 2001.
- No other membership activities occurred during this reporting period.
- Dr. Robert Delaney replaced Dr. Sy Ali as the AGTSR Focal Point for Rolls Royce.

ADMINISTRATION

- The AGTSR Quarterly Report for the reporting period, July to September 2001 was submitted to NETL on October 31, 2001. The report was submitted via hard copy and disk.
- SCIES submitted a request for an 18 month no-cost time extension from January 1, 2002 through June 30, 2003 for the existing AGTSR program. The DOE approved the request in December.
- SCIES submitted a request to the DOE for an award for a new university research program. The DOE budget for the program first budget period is $ 3.269 million for 2002. A cost share of $150,000 in 2002 from Industrial Review Board membership fees was also proposed.
- The DOE and the Industrial Review Board (IRB) have expressed interest in a number of new activities for SCIES related to the proposed University program. A list of these items follows. They represent a major expansion over the past AGTSR activities of RFP, workshops, and internships. While some of these new activities could be accommodated with existing personnel, others would require significant additional personnel and administration expenses to implement. Implementation of these activities will occur throughout CY2002. Some of the new activities, indicated in the following list, have already started as indicated by *:

  Additional Reporting
  - Yearly Program Plan
  - Outreach Plan
  - Expanded monthly reports *
  - Publish an annual public technical report
  - Power point presentation for overall AGTSR program
  - Power point presentation for each individual university project
  - AGTSR Fact Sheet revised semi-annually
  - Development of style guideline for university semi-annual and final reports
  - Fact Sheets for each university project revised every two years *

  Additional Efforts
  - Coordination/Cooperation with the EU *
  - Additional publication and dissemination of university Success Stories
  - Cost share tracking and reporting
  - SCIES participation in selling proposed university projects to state energy offices
  - Regional University Centers under SCIES
  - SCIES Assistance for obtaining support for DOE programs *
  - University presentation style guide
  - Seminar series
  - Course on energy systems/gas turbines
  - Major By-Law changes *
  - University Program Web Page *
  - Link DOE web page to SCIES web page to access university final reports
  - RFP definition/project coordination with DOE Roadmaps and EU university research *
  - Development and enforcement of conformity to metrics for university contract performance

- Coordination of university research teams
- Development and implementation of additional methods to promote early acceptance of university research
- Development and enforcing university conformity to benefits reporting guideline
- Congressional notifications on new awards for university projects
- Recruit more performing member universities *
- Recruit more IRB member organizations *
- Improve Faculty Fellowships
- Expanding unplanned activities requested by the DOE *

- SCIES asked principal investigators of AGTSR projects for comments on the possibility that DOE might require a minimum of 20 % cost share for projects under the proposed new award. None of the eighteen responders considered cost sharing to be desirable and a number considered cost sharing to be highly objectionable. For the most part, the more prestigious universities with the professors having the greatest reputations tend to be least likely to cost share.
- The IRB voting members were asked for input regarding changing the By-Laws to eliminate the requirement that an IRB voting member company perform "at least 50% of its gas turbine related R&D engineering in the US." Four of the five voting members recommended that this by-law should not be changed.
- At DOE request, SCIES provided Fact Sheet text for each active university project. These Fact Sheets give contract information and describe project goals, activities, and benefits. Figures are needed for some Fact Sheets, which will be provided after they are received from principal investigators for the university projects.
- Normal administrative functions continued throughout the reporting period.

TECHNOLOGY TRANSFER (Workshops and Education)

- Proceedings were distributed for the AGTSR Combustion Workshop VIII which was conducted in Charleston, SC, on July 31, August 1 and 2, 2001.
- The AGTSR Materials Workshop II was co-hosted with Prof. Maurice Gell of the University of Connecticut and conducted in Greenville, SC on October 8-10, 2001. This workshop included discussion of the DOE Materials Roadmap for the NGT Program, presentations by representatives of the turbine industry on needed gas turbine materials research, and presentations by university representatives on results of AGTSR sponsored gas turbine materials research projects. About 47 participants from the government, gas turbine industry, national labs, and academia attended the workshop. Attendance was less than expected due to company travel restrictions resulting from the economic turndown and cancellations resulting from the tragic events of September 11. Proceeding for the workshop are in progress but have been delayed by a lack of speaker response in submitting presentation materials.
- Hotel and meeting room arrangements have been completed for the October 14-16 Materials Workshop III at the University of Connecticut with Professor Maurice Gell.
- Professor Domenic Santavicca at Penn State University has agreed to August 26-28 dates for a Combustion Workshop IX. Four candidate sets of dates in November and early December of 2002 have been suggested to Professor Sumanta Acharya concerning a possible Aero-Heat Transfer workshop at Louisiana State University.

He is out of the country until after mid January but indicated that will respond with preferred dates after he returns.

- An abstract and paper titled “Gas Turbine Research in the AGTSR Program” was prepared and submitted for the ASME Turbo Expo in 2002. This paper describes a number of the turbine technology advances from the AGTSR program.
- The technical semi-annual progress reports received in the third quarter 2001 from the AGTSR university projects were distributed on CD to the DOE and IRB organizations.
- Principal investigators for all active AGTSR projects were requested to prepare posters for presentation on February 26 at the Turbine Power Systems Conference and Condition Monitoring Workshop in Galveston, sponsored by the DOE and other organizations.
- Mr. Irwin Stambler, an editor of Gas Turbine World, requested abstracts from the AGTSR materials workshop on October 8-10, 2001 for a possible article in that publication. Abstracts from the workshop were sent to him. Also sent for his information were the final agenda for the workshop and a booklet of "Success Stories" for many of the AGTSR university projects.
- The Success Stories submitted to NETL during this reporting period are contained in **Attachment I**.

RESEARCH

- **Table I** contains a list of the AGTSR research reports issued this reporting period. Copies of all Table I reports are included in this electronic report and can be accessed by following the links in Table I.
- The top ten of the thirty-five (35) proposals received were previously ranked in order by the Industrial Review Board. The budget requirements for the ten ranked proposals are likely beyond the available funding and the cutoff for awards to the top ranked projects will depend on the available budget for 2002. Consequently, the university principal investigators of the ten short listed proposals were contacted in October and asked to examine their budgets for possible reductions of 5 to 10 % to potentially enable more awards. Eight of the ten short listed proposals have decreased their budgets for a total reduction of $ 241,608.
- At SCIES request, Geo Richards of the DOE provided input concerning year 2002 university RFP research combustion topics related to the DOE materials roadmap. Udaya Rao also responded with materials topic input. Work progressed in December to incorporate the DOE input with input from the Industrial Review Board (IRB) companies to produce a list of research topics for IRB ranking.

RELATED MISCELLANEOUS ACTIVITY

- SCIES met with representatives of Colorado State University to discuss the formation of a reciprocating engine program modeled after AGTSR. The meeting took place at SCIES 18 December 2001.

- At DOE request, information was provided to the 100 AGTSR Performing Universities on a Memorandum of Understanding between the DOE and the European Union (EU) concerning possible collaborations on gas turbine research. A description of ten European university projects was also provided as background information for possible university involvement in response to the EU Framework V call for proposals, due no later than December 14, 2001.
- A request was sent to AGTSR IRB Focal Point persons for their comments and ideas on how collaborations of the AGTSR with the EU might be organized to benefit the US turbine program. All responders favored a suggestion by Bill Day that a US university and a European university might conduct research on different but complementary parts of a project of benefit to both the IRB and the EU. More university funding would thereby be directed to areas of interest to the IRB and less duplication of effort would be expected.
- With DOE concurrence, SCIES has been interacting with a consulting organization, Global Tech Inc (GTI), to facilitate collaboration with the European Union (EU). Discussions with GTI have identified two possible initial activities:
  - Series of workshops or a larger US/EU Gas Turbine Conference involving gas turbine research result presentations by AGTSR funded university projects and European Union (EU) funded university projects
  - Coordination of the next AGTSR RFP with the next EU RFP for university research

  The IRB was contacted for comments on these two areas of possible collaboration, and no objections were raised. Consequently, collaboration in these two areas will be explored further.

- At DOE request, SCIES contacted all AGTSR Performing Member universities in November concerning their input for planning technology development for future gas turbine systems. Instructions and data collection sheets were provided for university input. This survey was not highly successful as only one professor (Scott Sanders of the University of Wisconsin) responded to this request. He recommended development of spectroscopic absorption/emission sensors for monitoring and controlling fuel evaporation and mixing, gas temperature profiles, and pollutant emissions. The indication here is the industry is more knowledgeable of research needs.
- At DOE request (Kate Lessing), write-ups were provided on five AGTSR university projects for the congressional report on the HEET Program.
- At DOE request, SCIES contacted AGTSR universities to write a letter of support for the DOE-FE turbines program called High Efficiency Engines and Turbines (HEET) to be included in a DOE report to Congress on the Office of Fossil Energy Turbines Program. Fourteen responses were received from the universities. Responders ranged from a university president (Purdue) to graduate students.
- In response to a request from the DOE, SCIES prepared a list of 12 detailed candidate subjects and criteria for success for an international university contest to be hosted under FE Power Programs.

ATTACHMENT-I

University of California, Santa Barbara (UCSB) Advances TBC Life-Prediction And Non-Destructive Inspection

Under the Advanced Gas Turbine Systems Research (AGTSR) program, the University of California, Santa Barbara (UCSB) has been developing a mechanism-based strategy to assess the damage evolution and failure of thermal barrier coatings (TBC) in addition to a life-prediction methodology and non-destructive evaluation (NDE) testing protocol using the mechanism-based strategy. Elements of the mechanism-based strategy for life prediction have been put into place. A finite element framework has been developed to integrate several of the various mechanisms that contribute to coating spallation and failure. UCSB has also advanced the use of Photo-Stimulated Luminescence Spectroscopy (PSLS) as a practical NDE tool for TBCs. The project has demonstrated that PSLS can identify different types of coating internal damage, quantify the thermally grown oxide (TGO) stresses around flaws and other coating internal features, identify transient phases in the TGO, and explore the kinetics of TGO transformations. Since PSLS can identify and quantify sources of TGO transformations which produce the stresses that result in TBC spallation and failures, PSLS has been shown to be a promising tool for determining the quality and reproducibility of coatings as they emerge from the manufacturing process.

University of Connecticut Identifies Promising New Compositions for TBCs

Under the Advanced Gas Turbine Systems Research (AGTSR) program, the University of Connecticut (UCONN) has been exploring new materials for thermal barrier coatings (TBCs). A new composition with decreased thermal conductivity compared to conventional TBC materials would better insulate turbine alloy surfaces and enable higher turbine operating temperatures, with resulting improvements in engine power and efficiency. UCONN has screened candidate materials with respect to nine physical and chemical properties pertinent to TBC performance and life. The most promising candidates were determined to be a variety of rare-earth zirconates and lanthanum phosphate. Measurements for hot-pressed compacts of gadolium zirconate have shown a 33% lower thermal conductivity compared to the conventional TBC material used in turbines. Compositional modifications of the zirconates are being evaluated to reduce susceptibility to hot corrosion and reactivity with the thermally grown alumina layer that forms under TBCs in turbine operating environments.

University of Connecticut Determines Effects of Turbine Cycles on TBC Life

There is no accurate measurement technique to predict the expected remaining coating life on turbine parts. Consequently, the great variability of TBC coating lifetimes has resulted in turbine coating failures in the field or parts prematurely taken out of service if removed based on a conservative lower bound of expected coating lifetime.

Under the Advanced Gas Turbine Systems Research (AGTSR) program, the University of Connecticut (UCONN) has been evaluating the use of laser fluorescence (LF) to measure average internal stresses for non-destructive evaluation (NDE) of thermal barrier coatings (TBCs). Experiments in the project subjected TBC coated specimens to thermal cycles up to a temperature of 1121 C (2050 F). The LF technique was able to predict remaining life of coatings to within 5% for specimens that had been exposed to 1 hour thermal cycles and to within 7% for specimens that had been exposed to 24 hour thermal cycles. Useful engineering predictions of remaining TBC lifetimes were consequently shown for 1 hour and 24 hour thermal cycles. However, except for LF measurements taken near the end of coating life, the correlation of LF data with remaining TBC life differed for the two different cycle times. Additional work using LF measurements at times closer to end of life will evaluate whether the prediction method can be used without requiring knowledge of cycle times.

AGTSR Progress Reports Received 10/1/01-12/31/01

Aero-Heat Transfer	University of Pittsburgh FINAL REPORT Subcontract #98-01-SR088 Paper Version Only	"Experimental And Computational Studies Of The Nozzle Endwall Region Of Advanced Gas Turbines" PI – Minking Chyu
Aero-Heat Transfer	University of North Dakota Semi-Annual Report Ending 11/1/01 Subcontract #00-01-SR086 **LINK TO REPORT**	"Characterization Of Catalytic Combustor Turbulence And Its Influence On Vane And Endwall Heat Transfer And Endwall Film Cooling" PI – Forrest Ames
Aero-Heat Transfer	University of Texas-Austin Semi-Annual Report 3/1/01-9/1/01 Subcontract #01-01-SR092 **LINK TO REPORT**	"Attenuation Of Hot Streaks And Interaction Of Hot Streaks With The Nozzle Guide Vane And Endwall" PI – Dave Bogard/Karen Thole
Aero-Heat Transfer	University of Central Florida Annual Report 8/1/00-8/1/01 Subcontract #99-01-SR080 **LINK TO REPORT**	"Tip Clearance Heat Transfer And Desensitization in High Pressure Turbines" PI – Jay Kapat
Combustion	Purdue University Semi-Annual Report 3/1/01-8/31/01 Subcontract #00-01-SR085cs **LINK TO REPORT**	"Measurements For Improved Understanding Of Combustion Dynamics In Lean Premixed Gas Turbine Combustor Flames" PI – Jay Gore
Combustion	California Institute of Technology FINAL REPORT Subcontract #98-01-SR063 **LINK TO REPORT**	"Nonuniformities Of Mixture Ratio As A Mechanism Of Combustion Instabilities In Lean Pre-Mixed Combustors" PI – Fred Culick
Combustion	University of Washington Semi-Annual Report 6/1/01-11/30/01 Subcontract #00-01-SR087 **LINK TO REPORT**	"The Staged Prevaporizing-Premixing Injector: High Pressure Evaluation" PI – Philip Malte
Combustion	University of California, Irvine Semi-Annual Report 4/1/01-10/31/01 Subcontract #00-01-SR084cs Paper Version Only	"Correlation Of Ignition Delay With Fuel Composition And State For Application To Gas Turbine Combustion" PI – Scott Samuelsen
Combustion	Georgia Institute of Technology Semi-Annual Report 2/1/01-7/31/01 Subcontract #99-01-SR075 **LINK TO REPORT**	"Extending The Lean Blowout Limits Of Low NOx Gas Turbines By Control Of Combustion Instabilities" PI – Ben Zinn
Combustion	Pennsylvania State University Semi-Annual Report 2/1/01-8/1/01 Subcontract #99-01-SR078 Paper Version Only	"Dual Fuel Issues Related To Performance, Emissions And Combustion Instability In Gas Turbine Systems" PI – R. J. Santoro
Materials -TBC	University of Connecticut Semi-Annual Report 2/1/01-8/1/01 Subcontract #00-01-SR081 Paper Version Only	"Advanced Thermal Barrier Coatings For Industrial Gas Turbines" PI – Nitin P. Padture/Maurice Gell
Materials -TBC	University of Connecticut Semi-Annual Report 2/1/01-8/1/01 Subcontract #01-01-SR091 **LINK TO REPORT**	"Thermal Barrier And Metallic Coatings With Improved Durability" PI – Maurice Gell/Eric Jordan
Materials -TBC	University of California, Santa Barbara FINAL REPORT Subcontract #98-01-SR068 **LINK TO REPORT**	"A Mechanism-Based Approach To Life Prediction And Non-Destructive Evaluation For Thermal Barrier Coatings" PI – Anthony Evans
Materials -TBC	University of Connecticut Semi-Annual Report 3/1/01-8/31/01 Subcontract #99-01-SR073 **LINK TO REPORT**	"Development Of Laser Fluorescence As A Non-Destructive Inspection Technique For Thermal Barrier Coatings" PI – Eric Jordan

Characterization of Catalytic Combustor Turbulence and its Influence on Vane and Endwall Heat Transfer and Endwall Film Cooling

Executive Summary

The current combined experimental and computational investigation is designed to reduce the risk associated with developing vane and endwall cooling schemes for new low NOx combustion systems. The program is in the middle of the second year of a two year program. The experimental study uses the large-scale low speed linear cascade facility of the University of North Dakota to acquire full surface vane and endwall heat transfer data as well as endwall film cooling data. The heat transfer and film cooling data are being acquired over chord exit Reynolds numbers ranging from 500,000 to 2,000,000 using up to five different turbulence inlet conditions tested over two separate cascade geometries.

The complimentary computational predictions are being conducted using ADPAC, an industry developed 3D RANS method, which uses a multiblock method to speed computation convergence time. The ADPAC predictions are being made by the Aerothermal Methods Group at Rolls Royce (Allison) for both vane and endwall heat transfer as well as endwall film cooling. Selected results will be transferred to engine relevant conditions using the code.

Experimental Effort. The experimental effort has acquired full surface heat transfer data on the endwall of the conventionally loaded cascade for four turbulence generator geometries at Reynolds numbers ranging from 500,000 to 2,000,000. Inlet boundary layer profiles and turbulence spectra have been acquired for all test conditions. Midline measurements have been acquired for six turbulence conditions taken over the full range of Reynolds numbers. These data have are viewed as an excellent test case for grounding predictive methods for vane heat transfer. The two draft papers covering the vane and endwall heat transfer measurements are attached to this report. These two papers have been submitted to IGTI for possible presentation at the 2002 IGTI Conference in Amsterdam. We are interested in obtaining the approval of the AGTSR consortium to allow for these presentations. A third experimental paper is planned to document heat transfer levels for the mock catalytic and dry low NOx combustor turbulence generators. This work has already been completed.

Work continues on the current cascade to obtain endwall film cooling distributions for both two rows of film cooling holes and for a slot. The film cooling supply system has recently been completed and we expect to install the film cooling plenums in the conventional cascade shortly. The contoured endwall cascade is nearing completion and we should be ready to acquire endwall heat transfer data as soon as we have completed film-cooling measurements in the conventional cascade.

Currently, the project is behind schedule due to some difficulties with the initial heat transfer vane and due the development of the film cooling supply system. However, we plan to ask for a no cost extension and continue the heat transfer and film cooling measurements with the contoured endwall cascade. The University of North Dakota will be supporting a new master's level student on a ½ time basis starting January 2002 in support of this project. The new master's student will be responsible for completing the new contoured endwall cascade and acquiring the heat transfer and film cooling data in that test section. This work is expected to be completed under a no-cost extension of this project.

Contoured Endwall Cascade. The new contoured inlet cascade includes a new aft loaded vane, which has been designed to inhibit transition of the suction surface of the vane. A symmetrical inlet contraction is designed to accelerate the flow strongly into the leading edge of

the vane to reduce the strength of the horseshoe vortex and the resulting secondary flows. We expect to complete the fabrication of the contoured endwall cascade by the time the film cooling measurements are completed in the conventional cascade.

Analytical Effort. Rolls Royce has made aerodynamic and heat transfer predictions for the vane and endwall for the four turbulence conditions and across. We have offered a paper on the endwall heat transfer predictions for the 38th AIAA/ASME/SAE/ASEE Joint Propulsion Conference in Indianapolis in July.

The ADPAC code is currently using the Spalart Allmarus one-equation eddy diffusivity transport turbulence model. Current vane heat transfer predictions show fully turbulent behavior on the vane. We are expecting to move to the k-R turbulence model to produce better heat transfer predictions. The abstract for the computational paper is attached to this package.

Attachements

Ames, F. E., Wang, C., and Barbot, P. A., "Measurement and Prediction of the Influence of Catalytic and Dry Low NOx Combustor Turbulence on Vane Surface Heat Transfer," offered for presentation at the 2002 IGTI Conference in Amsterdam.

Ames, F. E., Barbot, P. A., and Wang, C. "Effects of Aeroderivative Combustor Turbulence on Endwall Heat Transfer Distributions Acquired in a Linear Vane Cascade," offered for presentation at the 2002 IGTI Conference in Amsterdam.

Hall, E. J., and Bermingham, E., "Assessment of Endwall Flow and Heat Transfer by CFD Analysis," offered for presentation at the 38th AIAA/ASME/SAE/ASEE Joint Propulsion Conference in Indianapolis.

Effects of Aeroderivative Combustor Turbulence on Endwall Heat Transfer Distributions Acquired in a Linear Vane Cascade

By F.E. Ames, P.A. Barbot, and C. Wang

Abstract

Vane endwall heat transfer distributions are documented for a mock aeroderivative combustion system and for a low turbulence condition in a large-scale low speed linear cascade facility. Inlet turbulence levels range from below 0.7 percent for the low turbulence condition to 14 percent for the mock combustor system. Stanton number contours are presented for both conditions for chord length Reynolds based on exit conditions ranging from 500,000 to 2,000,000. Low turbulence endwall heat transfer shows the influence of the complex three-dimensional flow field, while the effects of individual vortex systems are less evident for the high turbulence cases. Turbulent scale has been documented for the high turbulence case. Inlet boundary layers are relatively thin for the low turbulence case while inlet flow approximates a nonequilibrium channel flow for the mock combustor case. Inlet boundary layer parameters are presented across the inlet passage for the three Reynolds numbers and both the low and mock combustor inlet cases. Both midspan and 95 percent span pressure contours are included. This research provides a well-documented database taken across a range of Reynolds numbers and turbulence conditions for assessment of endwall heat transfer predictive capabilities.

Nomenclature

C	vane chord length, m
Cf/2	skin friction coefficient, $Cf/2 = \tau_w/\rho U_\infty^2$
Cp	specific heat at constant pressure, J/kg K
h	heat transfer coefficient, $W/m^2/K$, based on T_{green} and T_∞
H	Shape factor, $H = \delta_1/\delta_2$
Lu	energy scale, $Lu = 1.5\ |u'|^3/\varepsilon$
Lx	longitudinal integral scale of u' fluctuation
P	Pressure, Pa
q"	surface heat flux
Re_C	Chord Reynolds number, based on exit conditions
$Re_{\delta 2}$	momentum thickness Reynolds number, $Re_{\delta 2} = U_\infty \delta_2/\nu$
St	Stanton number, $St = h/(\rho Cp U_\infty)$
T	temperature, K
Tu	turbulence level, $Tu = |u'|/U_\infty$
U_∞	freestream velocity, m/s
U+	velocity nondimensionalized on inner variables, $U+ = U(y)/[U_\infty \bullet (Cf/2)^{1/2}]$
u', |u'|	streamwise component rms fluctuation velocity, m/s
Y	normal distance from test surface, m
Y+	wall normal distance nondimensionalized on inner variables, $Y+ = y \bullet [U_\infty \bullet (Cf/2)^{1/2}]/\nu$

Greek letter symbols

δ_1	displacement thickness, Eqn. (6.5) Kays and Crawford [1]
δ_2	momentum thickness, Eqn. (6.6) Kays and Crawford [1]
ε	emissivity
ε	turbulent dissipation rate, m^2/s^3
ν	kinematic viscosity, m^2/s
ρ	fluid density, mass per unit of volume, kg/m^3
σ	Stefan-Boltzman's constant
τ	shear stress, N/m^2

Subscripts

green	refers to peak in green intensity condition
rad	refers to radiative mode of heat transfer
s	refers to static condition
t	refers to total or stagnation condition
∞	evaluated in the free stream

Introduction

New low emission combustion systems are designed to have limited peak temperatures using lean combustion mixtures to produce low levels of NOx. A consequence of these lower peak temperatures is flatter temperature profiles leaving the combustion system. Another consequence of low NOx strategies is that any cooling air added after the combustion system reduces average rotor inlet temperature and the resulting performance of the engine. Older systems often burned fuel/air mixtures at higher equivalence ratios for better operability ranges producing higher peak temperatures. Endwall surfaces were often insulated from higher peak gas temperatures by supplying plentiful supplies of colder air near these surfaces. Consequently, new combustion strategies have the effect of reducing midspan heat loads to vanes and significantly increasing endwall heat loads. Cooling engineers no longer have the option of adding more cooling air and compensating by increasing the combustion temperature. Designers must provide reliable component cooling using a minimum amount of air. As a result, they need better tools to predict endwall heat transfer.

The present research has been designed to develop of comprehensive database of endwall heat transfer measurements across a range of relevant turbulence conditions. This current paper presents results taken at a low level of turbulence and at a high level of turbulence generated with a mock aeroderivative combustor. These heat transfer measurements have been taken at chord exit Reynolds numbers ranging from 500,000 to 2,000,000 and inlet turbulence characteristics and inlet boundary layer integral parameters have been comprehensively documented for all cases. A complementary analytical effort is being conducted jointly with Rolls Royce of Indianapolis with a goal of grounding and improving predictive methods for endwall heat transfer.

Background

Secondary Flows. Sieverding [2] presented a noteworthy review of secondary flows in turbine blade passages collecting information from various sources and presenting models of secondary flows from Klein [3] and Langston [4]. Sieverding gives Klein credit for first recognizing the complex secondary flows developing on the endwall of a blade row. He indicates that the importance of work on secondary flows became evident as heat transfer and aerodynamic loss investigations began to show the impact of these secondary flows on heat transfer rates and secondary losses. Langston's model denotes the main vortex systems including the suction and pressure side leg of the horseshoe vortex as well as the passage vortex. Additionally, Langston indicates the existence of corner vortices in the stagnation region and along the pressure and suction surfaces of the blade. Marchal and Sieverding [5] suggest that secondary losses grow more rapidly in the region of the flow downstream from the maximum velocity. Unpublished work by Ames, Hylton, and York [6] at Allison Gas Turbine Division of General Motors showed that secondary losses increased with increasing thickness of the endwall inlet boundary layer and the position of the passage vortex core rose above the endwall in the exit region of the vane cascade. Recent vane cascade investigations show that leading edge fillets (Zess and Thole [7]) and inlet endwall contouring (Burd and Simon [8]) can reduce the impact of secondary flows.

Endwall Heat Transfer. Experimental studies on vane endwall heat transfer include studies by York et al. [9], Harasgama and Wedlake [10], and Arts and Heider [11]. Experimental studies on blade endwall heat transfer include studies by Goldstein and Spores [12] and Giel et al. [13]. Generally, similar results are achieved showing increased heat transfer in the stagnation region of the airfoil and downstream of or adjacent to the pressure surface of the airfoil. Location of the hotspot off the pressure surface seems to depend on cascade geometry, Reynolds number, and Mach number. Harasgama and Wedlake conducted heat transfer tests in a compressible annular cascade and found that heat transfer in the hub differed somewhat from heat transfer in the tip region. CFD computations can at times produce reasonable predictions of endwall heat transfer cases but can also produce inaccurate results. Boyle and Lucci [14] found that endwall heat transfer predictions are dependent on the turbulence model and agreement between predictions and experiment can vary from case to case for a given model. This suggests that shroud endwall heat transfer data taken over a relevant range of parameters is needed to adequately test the relevancy of turbulence models.

Experimental Approach

This heat transfer research has been conducted in the University of North Dakota's large-scale low speed cascade facility. This facility is configured in a steady state blow down arrangement and is documented to a further extent in 999-GT-2002. The wind tunnel is powered by a 45 kW blower capable of providing 6.6 m^3/s of air at a static pressure rise of 5000 Pa. The blower outlet flow is directed through a two stage multivane diffuser section to distribute and diffuse the flow prior to entering a heat exchanger. The heat exchanger system, which uses a cooling water recirculation system, helps to provide a steady and controllable inlet air temperature. The flow is further conditioned downstream of the heat exchanger in a four section screen box. The low turbulence baseline configuration uses a 3.6 to one two-dimensional nozzle to further accelerate the air prior to entrance into the linear vane cascade test section.

The cascade test section used in this study is based on an eleven times scale mid span vane profile representative of a modern mid-sized industrial gas turbine and is shown schematically in figure 1. The vane profile was designed for incompressible flow and has a velocity distribution, which is consistent with current conventionally or fully loaded vanes in industrial engines. The cascade test section is designed to produce accurate two-dimensional aerodynamics with a four-vane three-passage configuration. The cascade has inlet bleeds and exit tailboards to allow inlet flow uniformity and exit flow periodicity. The inlet bleed flows were designed along two-dimensional streamlines predicted by FLUENT [15] and the flexible exit tailboards can be shaped to account for streamline curvature. The cascade has a row of inlet static taps one-quarter axial chord upstream from the vane leading edge and a row of exit taps one-quarter axial chord downstream to monitor the cascade setup. Ten probe access ports are provided along the row of inlet static pressure taps to measure inlet temperature and total pressure and to survey inlet turbulence characteristics.

The vane has a true chord of 47.8 cm and an axial chord of 25.0 cm. The vanes have a 38.4 cm spacing and a height of 25.4 cm. The diameter of the leading edge is 5.59 cm and the diameter of the trailing edge is 0.98 cm. The stagger angle of the vane is 55.1 degrees and the calculated air exit angle is 73.4 degrees.

The cascade was run at nominal exit chord Reynolds numbers of 500,000, 1,000,000, and 2,000,000 for this study. This range of first vane chord exit Reynolds numbers is consistent with a range of small to medium industrial or propulsion gas turbine engines.

Turbulence Generator. This study was designed to investigate turbulence characteristics representative of modern combustion systems and their influence on endwall heat transfer. A mock aeroderivative combustion system was developed to provide turbulence with characteristics, which are representative of with many current engines and has been documented in the literature. The combustor liner and nozzle configuration is shown schematically in figure 2. This liner geometry replaces the 3.6 to one contraction nozzle for the high turbulence test case.

Vane Pressure Distribution. The third vane from the bottom was used to acquire the heat transfer and pressure distributions. This "instrumented" vane can be inserted through a machined hole in the acrylic endwall where it is held in place using a flange. The pressure vane was cast out of epoxy with 82 pressure tubes incrementally spaced along and cast adjacent to its surface. Static pressure taps were fabricated by drilling through the epoxy surface into the brass tube with a 0.8 mm diameter drill bit. The baseline pressure distribution for the low turbulence case is shown in figure 3 where it is compared to a prediction using FLUENT. On this figure negative surface distance is taken from the calculated stagnation point (0 cm) along the pressure surface toward the trailing edge and positive surface distance is determined along the suction surface. The viscous prediction calculates the data with precision. Overall, the comparison is excellent and demonstrates the quality of the two-dimensional aerodynamics produced by the cascade. Developing accurate aerodynamics is critical to producing a heat transfer database, which is valuable for understanding the impact of new combustion systems and for grounding predictive methods.

Endwall Heat Transfer Measurements. Endwall surface heat transfer measurements have been acquired using a combination of a constant heat flux boundary condition generated by a 0.001" Inconel foil and narrow band thermochromic liquid crystal thermometry. On the third vane from the bottom, a commercially fabricated foil was wrapped from the suction surface trailing edge around the leading edge to the pressure surface trailing edge to generate a constant

surface heat flux. Two foils were applied to the endwall to develop a constant surface heat flux in that region. All three foils were heated to incrementally at consistent heat flux levels to incrementally paint isotherms over the endwall. Backup instrumentation for the vane heat transfer test was fabricated by casting fine wire thermocouples along the surface of an epoxy vane to determine the midline surface temperatures. These temperatures measurements served to check the narrow band liquid crystal paint temperatures.

Application of narrow band microencapsulated thermochromic liquid crystal (TLC) paints have resulted in uncertainty bands for driving temperature difference of +/- 1 percent for a 25° C temperature difference (Hippensteele, Russell, and Torres, [16]; Hippensteele, Russell, and Torres, [17]; Hippensteele and Russell, [18]; Jones and Hippensteele, [19]. Camci et al. [20] report the ability to resolve surface temperature using narrow band liquid crystal paints to within +/- 0.1° C when using a single color such as green. Giel et al. [13] indicate microencapsulated liquid crystals are less sensitive to viewing and illumination angles. The narrow band liquid crystal selected for the present experiment was a narrow band liquid crystal with a 1° C bandwidth with a 37° C start. The microencapsulated liquid crystal paint was calibrated using an aluminum test surface, which was first heated then allowed to cool. Temperatures were recorded as a function of time during the cooling process while digital photos of the test surface were acquired periodically. The camera was set to a fully manual mode to allow the highest reproducibility of color and intensity. The results show a sensitivity of 229°/°C around 37° C. This sensitivity of hue angle to temperature for the highest green intensity is very high and accuracy of the 37° C color change was estimated to be within 0.2° C over the span of the tests.

A constant heat flux boundary condition was generated on one of the endwall using a rectangular constant heat flux foil. The foil was adhered to a thin epoxy board, which in turn was secured to a one-inch layer of polyisocyanurate foam insulation. Under the footprint of the vane, an aluminum vane shaped heat exchanger was placed to conduct away the thermal energy generated in this region by the foil. In this way, both the endwall and the vane could be run at a constant heat flux that was matched. Many full surface vane and endwall heat transfer experiments do not have matched boundary conditions between at the vane and endwall interface. This condition produces an unheated starting length condition when flow approaches from an inactive surface.

The surface Stanton number data were acquired by first increasing the heat flux rate on all the plates until the first green color appeared on the surface. At that point, the surface heat flux was increased until the next incremental Stanton number was achieved based on exit conditions and surface to total temperature difference.

$$St = \frac{\left(q'' - q''_{rad}\right)}{\left(T_{green} - T_{T,IN}\right) \rho U_{\infty} Cp}$$

The radiative heat loss was estimated to be:

$$q''_{rad} = \varepsilon \sigma \left(T_{green}^{\ 4} - T_{T,IN}^{\ 4}\right)$$

The conduction loss was ignored because the radiative loss estimate was expected to be slightly over-estimated and the conduction loss was within the uncertainty band of that estimate. When the test surface had reached steady state, pictures were acquired using a digital camera in the

manual mode for all endwall locations where color appeared. The heat flux rate of the foils surface was then adjusted to produce the next incremental iso-Stanton number. The procedure to change the heat flux, wait for steady state, and then acquire digital images was repeated until the last incremental iso-Stanton number was achieved. Uncertainties were highest for the lowest Stanton numbers at the lowest Reynolds number where the overall uncertainty was estimated to be +/- 10 percent at 20 to 1 odds. At the highest Reynolds number the maximum uncertainty in Stanton number was estimated to be +/- 5 percent at 20 to 1 odds. The largest source of error was due to the uncertainty in the radiative loss.

Data Acquisition. Pressures were acquired using two Rosemount Smart Pressure Transmitters scaled to ranges of 250 and 5000 Pa full scale with 0.1 percent of scale accuracy. Voltage outputs for both the pressure transmitters and for the chromel-alumel thermocouples were scanned and read using an HP 3497A data acquisition system. The data acquisition unit has an integral voltmeter with 1 μV sensitivity. Thermocouples were all connected through a passive constant temperature junction and were referenced using an ice bath junction. Hot wires were powered, low pass filtered, bucked and gained using a two channel TSI ISA 300 hot wire anemometry bridge. Raw signals were read with a PC based high-speed data acquisition card with 12 bits of resolution. Mean velocities were acquired at a data acquisition rate equivalent to about three integral time scales. Velocity time records for spectral analysis were acquired in 40 sets of 8192 samples and post processed.

Data Uncertainties. Estimates for the uncertainty in heat transfer, pressure, velocity, and turbulence measurements were determined using the root sum square method described by Moffat [21]. Uncertainty in the local vane surface static pressure was estimated at a maximum of 2.5 percent. Exit velocity was determined at a precision of 2 percent. The uncertainty in turbulence level for the single wire was estimated to be 3 percent of the reported value. The experimental error in turbulent scale is estimated to be 11 percent. All uncertainty estimates are quoted for a 95 percent confidence interval.

Inlet Conditions and Turbulence Characteristics. Two turbulence conditions are reported in this endwall heat transfer paper. Both heat transfer data, inlet velocity profiles, and turbulence measurements were taken for both turbulence conditions and all three Reynolds numbers. Span average turbulence data (Tu, Lx, Lu, and ε) are reported in the initial section of the tables while parameters for the inlet velocity profiles are reported for five circumferential positions in the remainder of the tables. These measurements were acquired 7 cm upstream from the leading edge plane of the vanes. Midspan or peak velocity (U_∞), integral thicknesses (δ_2 & δ_1), shape factor (H) skin friction coefficient (Cf/2), turbulence level (Tu), and momentum thickness Reynolds number ($Re_{\delta 2}$) were determined for each condition and are presented in Tables 1a and 1b.

Experimental Results

The experimental results documented in this paper include comprehensive inlet boundary layer parameters and turbulence conditions, 95% span pressure distributions for the six conditions, and endwall heat transfer distributions for the six conditions. The inlet boundary layers have been documented using a single-wire probe for all six conditions at five inlet locations. These inlet locations are equally spaced at $1/5^{th}$ of the vane circumferential spacing. For the low turbulence inlet conditions the boundary layers are very thin and the lower Reynolds number inlet boundary layers show laminar behavior. The six 95% span pressure distributions provide an indication of the pressure gradients present on the endwall surface, which are drivers

for secondary flows. The six endwall surface heat transfer distributions provide a well resolved picture of influence of turbulence level and Reynolds number on the Stanton number distribution and are expected to useful for grounding computational models.

Inlet Boundary Layer Parameters and Turbulence Conditions. Inlet boundary layer measurements were taken at the inlet to the cascade at 5 circumferential positions and are documented in Table 1a and 1b for both turbulence conditions and all Reynolds numbers. The circumferential position (Y) is taken from the bottom most position of the vane. For the low turbulence condition at the low Reynolds number, the inlet boundary layers are all laminar as indicated by the skin friction coefficient, Cf/2, and the shape factor. The entering boundary layer is very thin due to the entrance contraction just upstream of the cascade test section. At the 1,000,000 chord Reynolds number, the boundary layers at the top three positions are turbulent, while the lower two stations show transitional flow. Inlet boundary layers for the low turbulence, high Reynolds number condition, are all turbulent. Determining the skin friction coefficients for the laminar and transitional boundary layers was quite uncertain, perhaps as much as 20 percent or more due to the lack of near wall velocity measurements.

Inlet boundary layer measurements for the aero-combustor simulator are presented in Table 1b for three Reynolds numbers. Generally, peak velocities occurred at the midspan of the channel so perhaps the term nonequilibrium channel flow would be a better term. These profiles are nonequilibrium in the sense they are strongly influenced by the freestream turbulence, which is convected downstream from the turbulence generator. The profiles exhibit no wake due to the turbulence interaction but are affected by the pressure gradients at the inlet plane of the cascade. Momentum thickness at a given position scales inversely with the local peak velocity. Velocity profiles suggest that the large-scale high intensity turbulence is very effective at redistributing low momentum flow. Figure 4 shows the measured velocity distribution at the highest measuring station for the highest Reynolds number compared with a nonequilibrium channel flow calculation assuming a linear shear stress distribution [$\tau/\tau_w = 1-(2y)/H$] and the ATM model of Ames, Kwon and Moffat [22].

Ninety-Five Percent Span Pressure Distributions. Ninety-five percent span pressure profiles for the low and aero-combustor turbulence cases are shown in figures 5 through 7 compared with midspan profiles. The profiles are plotted in terms of Ps/Pt versus surface arc for the low through high Reynolds numbers respectively. The 95% span profiles show a reduction in minimum pressure on the near suction surface (positive surface distance) due to the secondary flows, which first move away from the suction surface and then are pushed toward and up onto the surface. The high turbulence case with the largest momentum thickness shows the biggest variation between the midspan and 95% span distributions. However, the difference in the pressure distributions is not large. Generally similar trends appear at the three Reynolds numbers but influence of the secondary flows on the highest Reynolds number is the most significant.

Endwall Flow Visualization. A lampblack and oil endwall flow visualization is presented in figure 8 taken from Ames, Hylton, and York [6]. This figure shows the separation saddle point upstream from the vane along with the pressure surface and suction surface separation lines. The pressure side of the horseshoe vortex and the passage vortex form above the separation saddle point and are sweep upward toward the adjacent vane suction surface. The suction side of the horseshoe vortex move downward around the suction surface and are swept up onto the surface. These flow visualization measurements were taken in a five vane cascade at an exit Reynolds number based on chord length of 2,000,000. The geometry of the cascade used

by Ames, Hylton, and York has similarities to the present cascade and the flow visualization provides some insight for the heat transfer patterns seen on the present endwall.

Endwall Stanton Number Distributions. Endwall Stanton number contours are shown in figures 9 through 14 for Reynolds numbers ranging from 500,000 to 2,000,000 with low and high turbulence levels. All Stanton numbers are based on exit conditions. Comparisons between the low freestream Stanton numbers and the mock aerocombustor Stanton number distributions have been shown on one page at a single Reynolds number. In the first comparison, Stanton number contours are shown for an exit chord Reynolds number of 500,000 for the low turbulence condition in figure 9 and for the aerocombustor in figure 10. In these figures, the middle vane has a consistent heat flux boundary condition with the black endwall surface, while the upper and lower vanes have no heating. Around the leading edge of the middle vane, Stanton number levels decrease as the thermal boundary layer thickens and then increase as the stagnation region is approached. The high heat transfer rates in this region are consistent with the horseshoe vortex with forms in this region and Stanton number levels in this regions are as high as any shown on the surface. The favorable static pressure gradient, which moves away from the stagnation region and the pressure surface tends to drive the separation line for the inlet boundary layer toward the suction surface of the adjacent vane. The results of this separation line can be seen in the jagged contour lines for the 0.0013 Stanton number and the low heat transfer island shown for the 0.0011 Stanton number. This lowest heat transfer region is consistent with the convergence of the separation streamline from the suction surface leg of the horseshoe vortex and the separation streamline due to the roll up of the pressure surface leg of the horseshoe vortex by the passage vortex. The influence of the convergence of these vortices and their lift off onto the suction surface can be seen in the Stanton number contours along the suction surfaces of the upper and middle vanes. Heat transfer levels are generally highest downstream from the trailing edge region of the vanes due to the intense generation of turbulence, which occurs in the wakes due to the velocity gradient present. The trajectory of this high heat transfer island curves toward the circumferential direction. This path is consistent with the characteristic over turning near the endwall, which is typically present due the combination of endwall pressure gradients and an accumulation of low momentum fluid in the endwall region. Additionally, the presence of corner vortices along the suction surface appears to affect heat transfer in the aft region of the surface. The combination of high convective velocity and pressure gradient off the pressure surface produces a relatively high Stanton number (0.0015) in the region downstream from that surface. However, this Stanton number is significantly lower than levels in the same region for the highest Reynolds number flow. For the 500,000 Reynolds number this level of Stanton number is more consistent with laminar or transitional flow than turbulent flow for this high velocity region. The presence of the heated vane does not appear to have a strong influence for this condition. However, some significant differences are apparent down stream from the trailing edges of the vane.

The Stanton number patterns on figure 10 for the high turbulence case appear to be less affected by the secondary flows than the lower turbulence case. Other than outside of the stagnation region and downstream from the trailing edge, few patterns can be correlated with the expected secondary flow structures. This difference is likely due to the large-scale turbulence. Large-scale turbulence is very effective at mixing away gradients in the flow. Mixing is not only enhanced in the wall normal direction, but the large scale motions present in the streamwise and lateral components of turbulence are effective at both moving around flow structures and to a lesser extent mixing them away. Generally, the heat transfer appears to be about 10 to 20

percent higher in most locations for the higher turbulence case and the isotherm area seem to have a pattern which is smoother and more aligned with the geometry of the passage. High heat transfer rates are still present in the stagnation region and downstream from the trailing edge of the vane but the effect of the separation streamline is not apparent. In this high turbulence case the heated middle vane appears to affect the level of heat transfer in the middle of the passage. This is evident by the appearance of a 0.0012 iso-Stanton number in the upper passage with no similar feature in the lower passage. Additionally, the heat transfer level in the heated vane wake is lower than the unheated vane wake.

Figure 11 presents the Stanton number patterns for the 1,000,000 exit chord Reynolds number case for the low free-stream turbulence case. The patterns show many similarities to the 500,000 Reynolds number case for the low turbulence condition. However, in this higher Reynolds number case the effect of the leading edge corner vortex appears to be much more evident. A low heat transfer region adjacent to mid arc on the pressure surface (St = 0.001) appears to be due to the downwash of laminar flow from the pressure surface. Again the convergence and lift off of the suction leg of the horseshoe vortex with the passage/pressure leg of the horseshoe vortex shows a noticeable influence on heat transfer at mid arc along the suction surface. Downstream from the trailing edge of the vanes we see the influence of the wake on endwall heat transfer. In addition, the highest velocities occur just downstream from the trailing edge and cause a high heat transfer location in between the lower wake and upper suction surface.

Figure 12 shows a psuedo picture of iso-Stanton numbers for the high turbulence, 1,000,000 Reynolds number case. The overall level of heat transfer is similar to the level for the low turbulence case. However, similar to the lower Reynolds number comparison the iso-Stanton numbers have a pattern, which is smoother and has a weaker connection to typical secondary flow patterns. Again, the leading edge and wake footprint are regions of high heat transfer. The footprint of the wake is much wider than compared to the low turbulence case. This spreading is consistent with effects of turbulence on wake development documented by Ames and Plesniak [23]. However, this widening of the wake footprint may also be associated with the high heat transfer area seen for the low turbulence case.

Figure 13 shows the endwall Stanton number contours for the 2,000,000 exit chord Reynolds number case for the low turbulence condition. Patterns for this condition show the influence of the vortex system in the leading edge region, downstream from the trailing edge and off the suction surface where the two vortex systems merge and are swept off the endwall. The high heat transfer, which was evident off the trailing edge of the pressure surface and between the wakes, has now expanded. The endwall region just off the pressure surface shows a region of low heat transfer likely due to laminar fluid sweeping down off the surface due the the cross passage pressure gradient. Downstream of this region, steep Stanton number contours correspond to significant changes in velocity occurring on the endwall in a region where the boundary layer is expected to be thin, leading to the high heat transfer region between the wake of the lower airfoil and the suction surface of the upper one. Heat transfer off the heated vane pressure surface is noticeably lower in this figure suggesting that the consistent thermal boundary condition in this case has a significant effect.

Figure 14 presents the Stanton number contours for the higher turbulence condition at a chord exit Reynolds number of 2,000,000. The patterns are much smoother than the low turbulence condition at a 2,000,000 Reynolds number but the overall level does not appear to be significantly higher. Stanton number contours through the passage seem to be tied to the local

convective velocity indicating turbulence flow on the surface. The high heat transfer footprint downstream from the pressure surface trailing edge has expanded. However, unlike the low turbulence case, which shows two distinct regions, one wake generated, and one likely generated by high velocities and thin boundary layers, the high turbulence condition shows only one high heat transfer region.

Conclusions

The present endwall heat transfer data document surface heat transfer for a low inlet turbulence with relatively thin boundary layers and for a turbulence condition generated using a mock combustor, which produces peak velocities at mid channel. The data were taken at exit chord Reynolds numbers of 500,000, 1,000,000, and 2,000,000. The data have well documented inlet boundary layers and turbulence conditions and are expected to have significant merit for use in predictive comparisons.

The low turbulence heat transfer contours show strong evidence of the impact of secondary flows on heat transfer patterns. Not only do the leading edge horseshoe vortex and trailing edge wake show the impact of these secondary flows on raising surface heat transfer but the impact of the passage vortex and suction surface leg of the horseshoe vortex can be seen as well.

The inlet laminar boundary layers, which occurred at the lowest Reynolds number and turbulence condition, generally produced a lower average passage Stanton number by 10 to 20 percent. The overall influence of turbulence on endwall heat transfer was less dramatic for the higher Reynolds number cases. This small difference is likely due to the thin inlet boundary layers developed for the low turbulence case.

The high turbulence heat transfer contours show weaker evidence of the impact of secondary flows on heat transfer patterns due to the enhanced turbulent mixing and because the larger scales tend to push around the flow structures. High heat transfer rates in the leading edge and wake regions are still present due to the influence of the horseshoe vortex and wake.

The heated constant heat flux boundary condition on the vane generally had a significant influence on the heat transfer level in the passage and downstream in the wake region. However, the influence of the active vane surface was not shown to be dramatic.

Acknowledgements

The authors gratefully acknowledge the support from the Advanced Gas Turbine System Research consortium, which funded this research and to Rolls Royce of Indianapolis for providing the vane geometry used in this study. Additionally, the authors would like to acknowledge the seed grant from the North Dakota EPSCoR program, which supported the development of the large-scale low speed cascade facility used in this study. In addition, the authors are indebted to the University of North Dakota for providing additional support and laboratory space and to Jay Evenstad for machine shop support. Finally, the authors would like to acknowledge the work of Dan Pelarski, Robert Stengel, Scott Ciocetto, Jeremy Stocke, and Bobby Shimpa who helped design and fabricate the original test section as a senior design project and to Troy Lassle, Mark Hettwer, Brad Wall, and Scott Lindfors who worked as summer research assistants on this project.

References

1. Kays, W.M., and Crawford, M.E., 1993, *Convective Heat and Mass Transfer*, 3rd Edition, McGraw-Hill, New York.
2. Sieverding, C.H., 1985, "Recent progress in the understanding of basic aspects of secondary flow in turbine blade passages," ASME Journal of Engineering for Gas Turbines and Power, Vol. 107, pp. 248-257.
3. Klein, A., 1966, "Investigation of the entry boundary layer on the secondary flows in the blading of axial turbines, BHRA T 1004.
4. Langston, L.S., Nice, M.L., and Hooper, R.M., 1977, "Three-dimensional flow within a turbine cascade passage," ASME Journal of Engineering for Power, January, 1977, pp. 21-28.
5. Marchal, P., and Sieverding, C.H., 1977, "Secondary flows within turbomachinery bladings," Secondary Flows in Turbomachines, AGARD CP 214.
6. Ames, F.E., Hylton, L.D. and York, R.E., 1986, Unpublished work on the impact of the inlet endwall boundary layer on secondary losses and velocity vectors in a compressible turbine cascade, Allison Gas Turbine Division of General Motors.
7. Zess, G.A. and Thole, K.A., 2001, "Computational design and experimental evaluation of using an inlet fillet on a gas turbine vane," ASME Paper No. 2001-GT-404.
8. Burd, S.W., and Simon, T.W., "Flow measurements in a nozzle guide vane passage with a low aspect ratio and endwall contouring," ASME Journal of Turbomachinery, Vol. 122, pp. 659-666.
9. York, R.E., Hylton, L.D, and Milelc, M.S, 1984, "An experimental investigation of endwall heat transfer and aerodynamics in a linear vane cascade," ASME Journal of Engineering for Gas Turbines and Power, Vol 106., p. 159.
10. Harasgama, S.P., and Wedlake, E.T., 1989, "Heat transfer and aerodynamics of a high rim speed turbine nozzle guide vane tested in the RAE isentropic light piston cascade," Journal of Turbomachinery, Vol. 113, pp. 384-391.
11. Arts, T. and Heider, R., 1994, "Aerodynamic and thermal performance of a three dimensional annular transonic nozzle guide vane, Part-I experimental investigation," Paper No. 1994-31, 30th AIAA/ASME/SAE/ASEE Joint propulsion conference.
12. Goldstein, R.J., and Spores, R.A., 1988, "Turbulent transport on the endwall in the region between adjacent turbine blades," Journal of Heat Transfer, Vol. 110, pp. 862-869.
13. Giel, P.W., Thurman, D.R., Van Fossen, G.J., Hippensteele, A.A., and Boyle, R.J., 1996, "Endwall heat transfer measurements in a transonic turbine cascade," ASME Paper No. 96-GT-180.
14. Boyle, R. J., and Lucci, B.L., 1996, "Predicted turbine heat transfer for a range of test conditions," ASME Paper No. 96-GT-304.
15. FLUENT 5.5, 2000, FLUENT 5.5 User's Guide, Fluent, Inc., Lebanon, N.H.
16. Hippensteele, S.A., Russell, L.M., and Torres, F.J., 1985, "Local heat-transfer measurements on a large, scale-model turbine blade airfoil using a composite of a heater element and liquid crystals," MASA Technical Memo. 86900.
17. Hippensteele, S.A., Russell, L.M., and Torres, F.J., 1986, "Use of a liquid-crystal, heater-element composite for quantitative, high-resolution heat transfer coefficients on a turbine airfoil, including turbulence and surface roughness effects, NASA Technical Memo. 87355.

18. Hippensteele, and S.A., Russell, 1988, High-resolution liquid-crystal heat-transfer measurements on the end wall of a turbine passage with variations in Reynolds number," NASA Technical Memo. 100827.
19. Jones, T.V., and Hippensteele, S.A., 1988, "High-resolution heat-transfer-coefficient maps applicable to compound-curve surface using liquid crystals in a transient wind tunnel," NASA Technical Memo. 89855.
20. Camci, C., Glezer, B., Owen, J.M., Pilbrow, and R.G., Syson, B.J., 1998, "Application of thermochromic liquid crystal to rotating surfaces," ASME Journal of Turbomachinery, Vol. 120, pp. 100-103.
21. Moffat, R.J., 1988, "Describing the uncertainties in experimental results," Experimental Thermal and Fluid Science, Vol. 1., pp. 3-17.
22. Ames, F.E., Kwon, O., and Moffat, R.J., 1999, "An algebraic model for high intensity large scale turbulence," ASME Paper No. 99-GT-160.
23. Ames, F.E. and Plesniak, M.W., "The Influence of Large Scale, High Intensity Turbulence on Vane Aerodynamic Losses, Wake Growth, and Exit Turbulence Parameters," ASME J. Turbomachinery, Vol. 119, pp. 182.

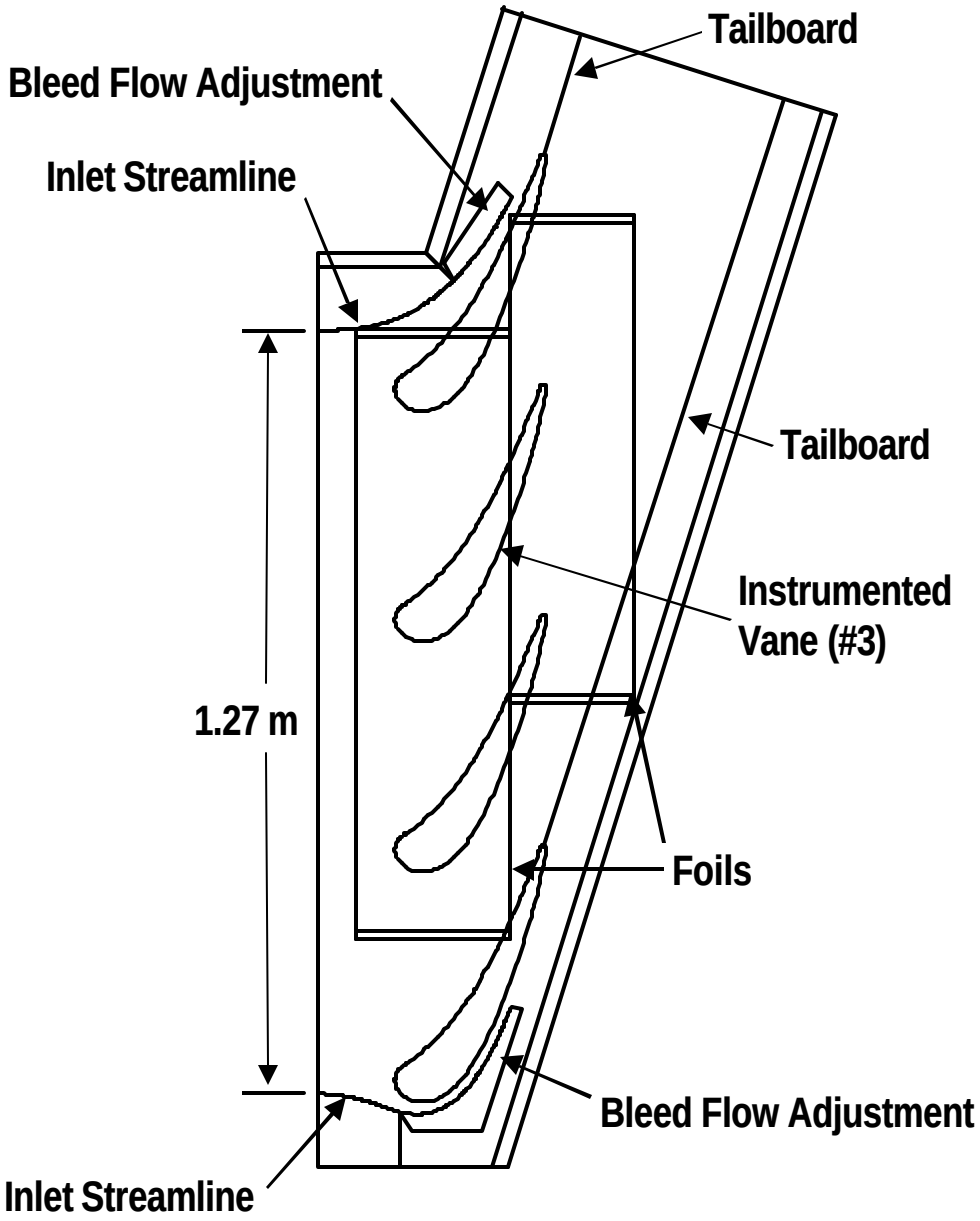

Figure 1. Schematic of the UND linear cascade test section.

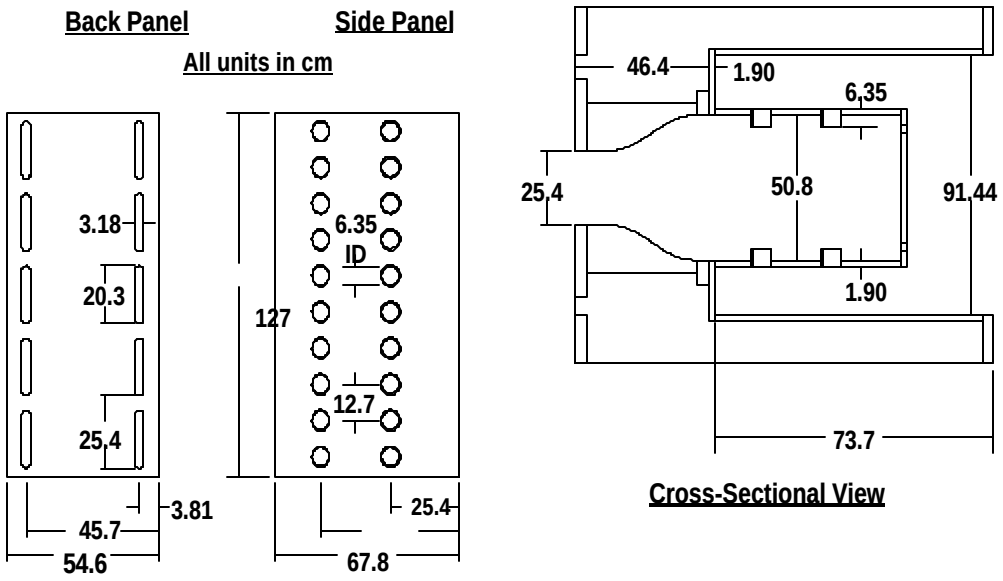

Figure 2. Schematic of mock aeroderivative combustor turbulence generator

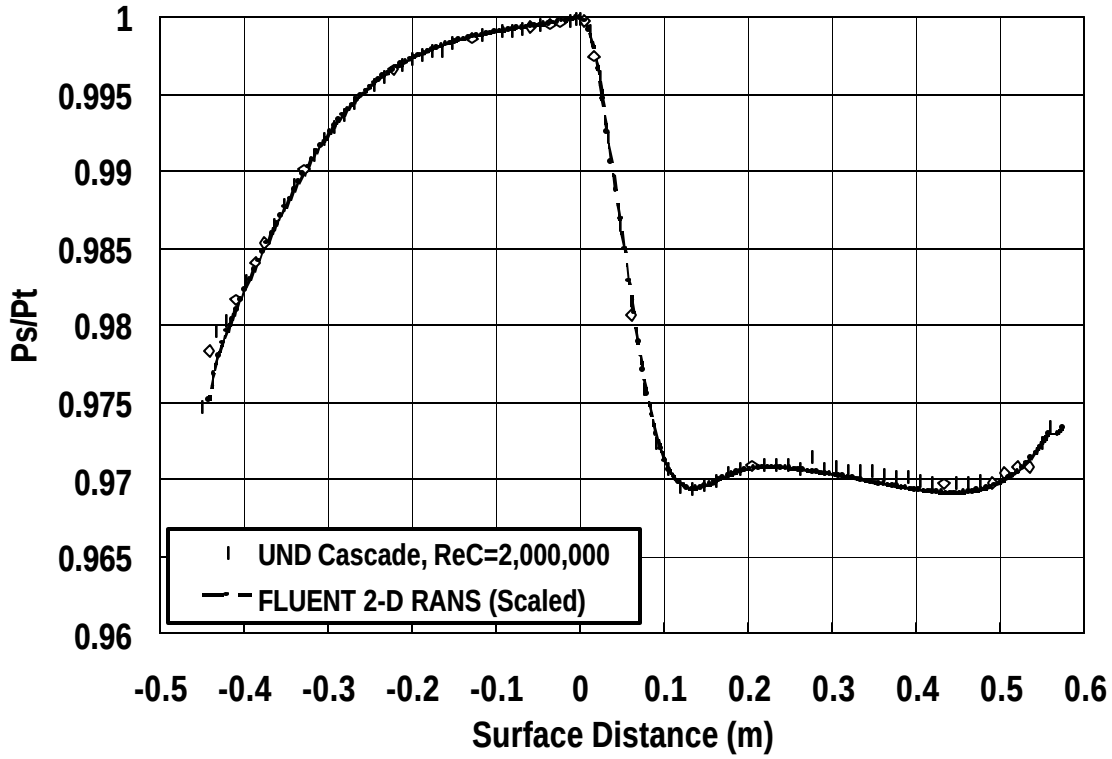

Figure 3. Comparison between measured and predicted vane midspan pressure distribution

Low Turbulence

Reynolds	Tu	U (m/s)	Lx (cm)	Lu (cm)	e (m^2/s^3)
500,000	0.0069	4.96	8.12	127.0	0.00005
1,000,000	0.0076	10.43	5.02	154.5	0.00035
2,000,000	0.0060	18.71	3.58	15.5	0.0144

Low Turbulence (LT) Re_C = 500,000

Y (cm)	U_∞ (m/s)	δ_2 (cm)	δ_1 (cm)	H	Cf/2	Tu_∞	$Re\delta_2$
16.90	4.55	0.076	0.195	2.560	0.00099	0.0081	222
9.22	4.09	0.094	0.223	2.370	0.00097	0.0086	247
1.54	4.63	0.102	0.243	2.390	0.00087	0.0070	301
-6.14	5.82	0.098	0.228	2.320	0.00080	0.0067	362
-13.82	5.26	0.091	0.235	2.580	0.00075	0.0076	300

Low Turbulence (LT) Re_C = 1,000,000

Y (cm)	U_∞ (m/s)	δ_2 (cm)	δ_1 (cm)	H	Cf/2	Tu_∞	$Re\delta_2$
16.90	8.63	0.054	0.095	1.770	0.00270	0.0079	297
9.22	7.59	0.062	0.105	1.700	0.00280	0.0087	302
1.54	9.80	0.058	0.093	1.590	0.00297	0.0043	370
-6.14	11.83	0.064	0.122	1.930	0.00165	0.0036	486
-13.82	10.65	0.070	0.148	2.110	0.00130	0.0050	484

Low Turbulence (LT) Re_C = 2,000,000

Y (cm)	U_∞ (m/s)	δ_2 (cm)	δ_1 (cm)	H	Cf/2	Tu_∞	$Re\delta_2$
16.90	16.03	0.063	0.095	1.520	0.00245	0.0080	647
9.22	15.70	0.074	0.127	1.530	0.00230	0.0087	743
1.54	19.52	0.071	0.102	1.440	0.00243	0.0057	874
-6.14	22.92	0.057	0.081	1.430	0.00253	0.0046	821
-13.82	19.94	0.053	0.082	1.530	0.00234	0.0050	671

Table 1a. Endwall inlet boundary layer parameters, low turbulence condition

Aero-Combustor

Reynolds	Tu	U (m/s)	Lx (cm)	Lu (cm)	e (m^2/s^3)
500,000	0.1313	5.24	3.68	7.24	6.67
1,000,000	0.1402	9.32	3.52	6.36	51.5
2,000,000	0.1339	18.39	3.58	7.35	302.0

Aero-Combustor (AC) Re_C = 500,000

Y (cm)	U_∞ (m/s)	δ_2 (cm)	δ_1 (cm)	H	Cf/2	Tu_∞	$Re\delta_2$
16.90	4.83	0.726	0.889	1.226	0.00250	0.1567	2238
9.22	4.41	0.786	0.988	1.261	0.00220	0.1732	2184
1.54	5.40	0.411	0.500	1.217	0.00275	0.1321	1409
-6.14	6.09	0.360	0.428	1.189	0.00298	0.1097	1408
-13.82	5.48	0.456	0.544	1.195	0.00280	0.1270	1599

Aero-Combustor (AC) Re_C = 1,000,000

Y (cm)	U_∞ (m/s)	δ_2 (cm)	δ_1 (cm)	H	Cf/2	Tu_∞	$Re\delta_2$
16.90	8.43	0.706	0.860	1.217	0.00225	0.1625	3774
9.22	7.88	0.806	0.997	1.245	0.00191	0.1720	3890
1.54	9.51	0.382	0.456	1.201	0.00248	0.1350	2235
-6.14	11.10	0.278	0.322	1.160	0.00295	0.1073	1928
-13.82	9.90	0.311	0.368	1.181	0.00278	0.1255	1953

Aero-Combustor (AC) Re_C = 2,000,000

Y (cm)	U_∞ (m/s)	δ_2 (cm)	δ_1 (cm)	H	Cf/2	Tu_∞	$Re\delta_2$
16.90	16.96	0.575	0.860	1.193	0.00190	0.1557	6217
9.22	15.33	0.627	0.767	1.223	0.00151	0.1741	6121
1.54	18.60	0.306	0.359	1.178	0.00221	0.1287	3557
-6.14	21.47	0.237	0.269	1.136	0.00265	0.1034	3247
-13.82	19.37	0.268	0.312	1.165	0.00232	0.1197	3311

Table 1b. Endwall inlet boundary layer parameters, aero-combustor condition

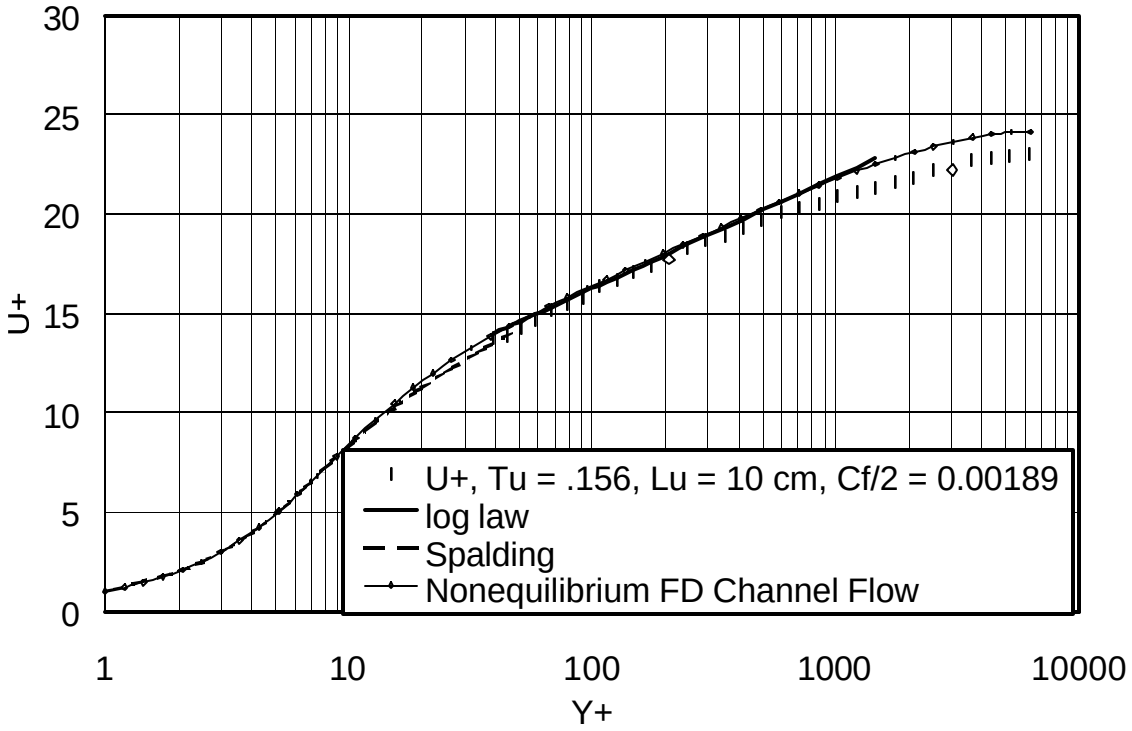

Figure 4. Cascade Inlet Velocity Profile Compared with Nonequilibrium FD Channel Flow, ATM

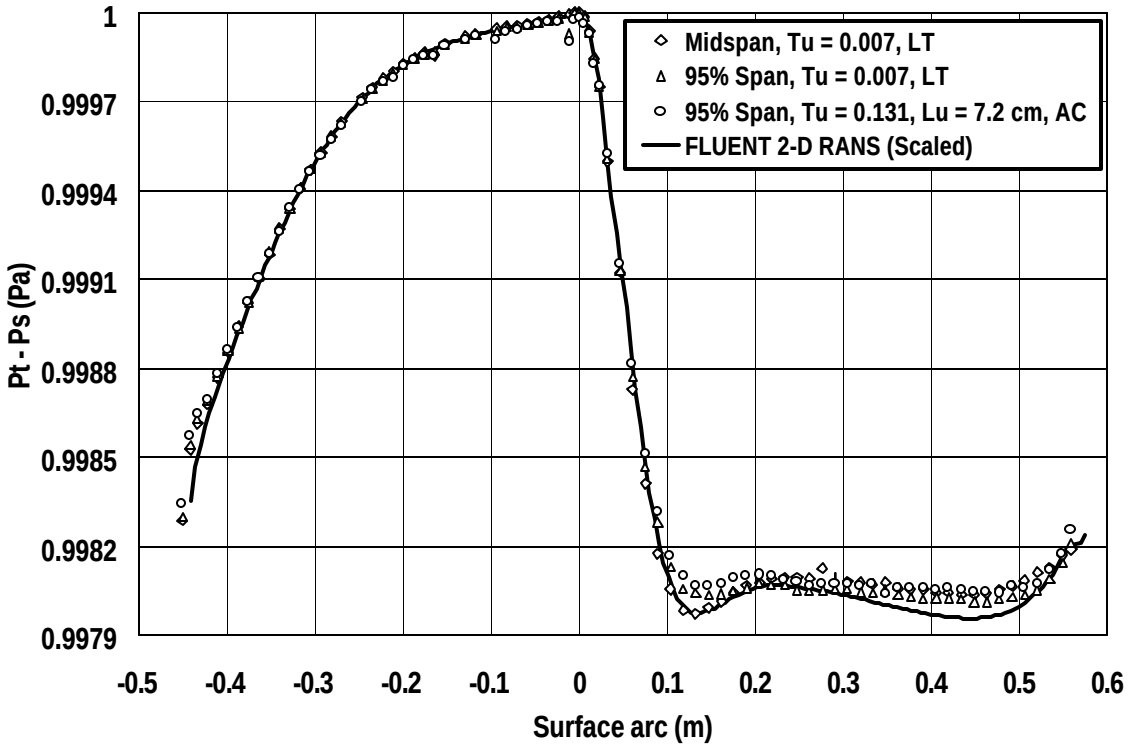

Figure 5. Comparison of 95% span pressure distributions with midspan values, Re_C = 500,000

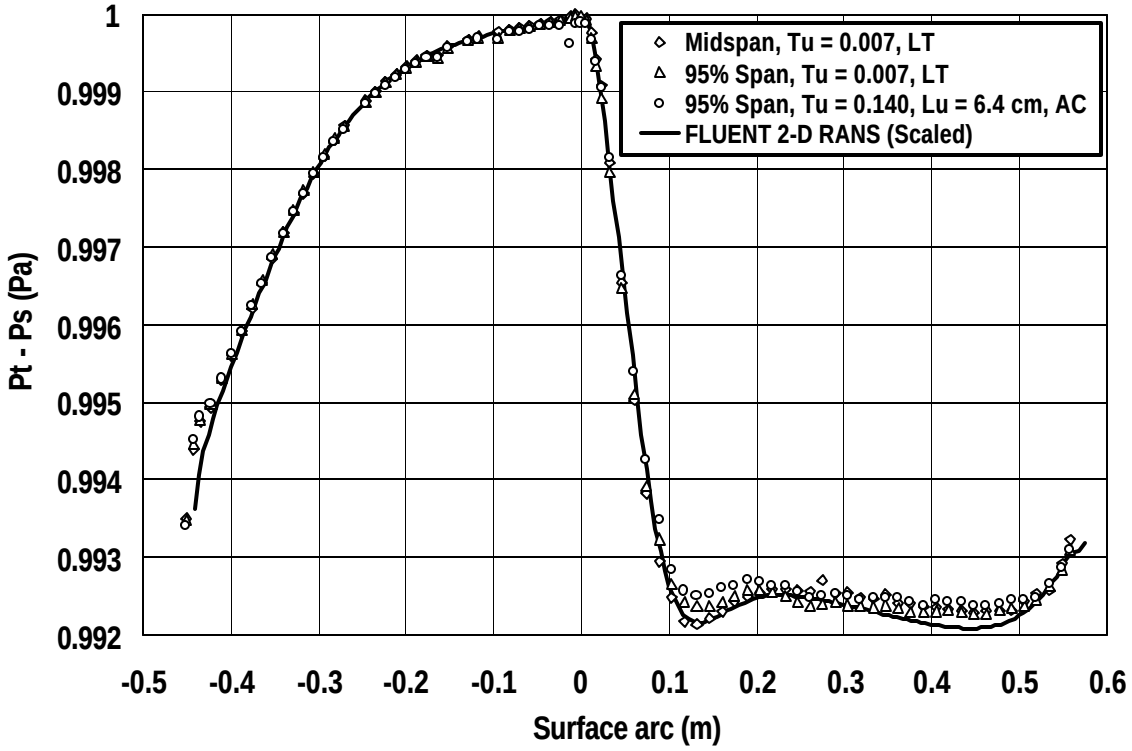

Figure 6. Comparison of 95% span pressure distributions with midspan values, Re_C = 1,000,000

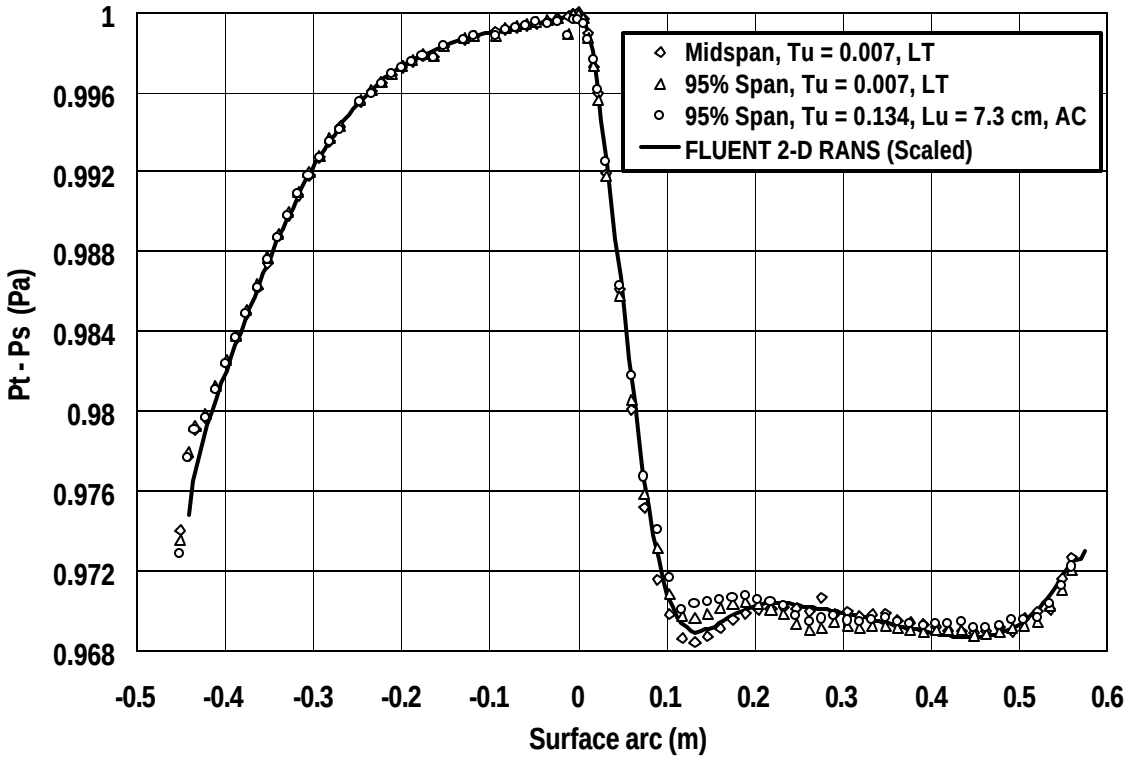

Figure 7. Comparison of 95% span pressure distributions with midspan values, Re_C = 2,000,000

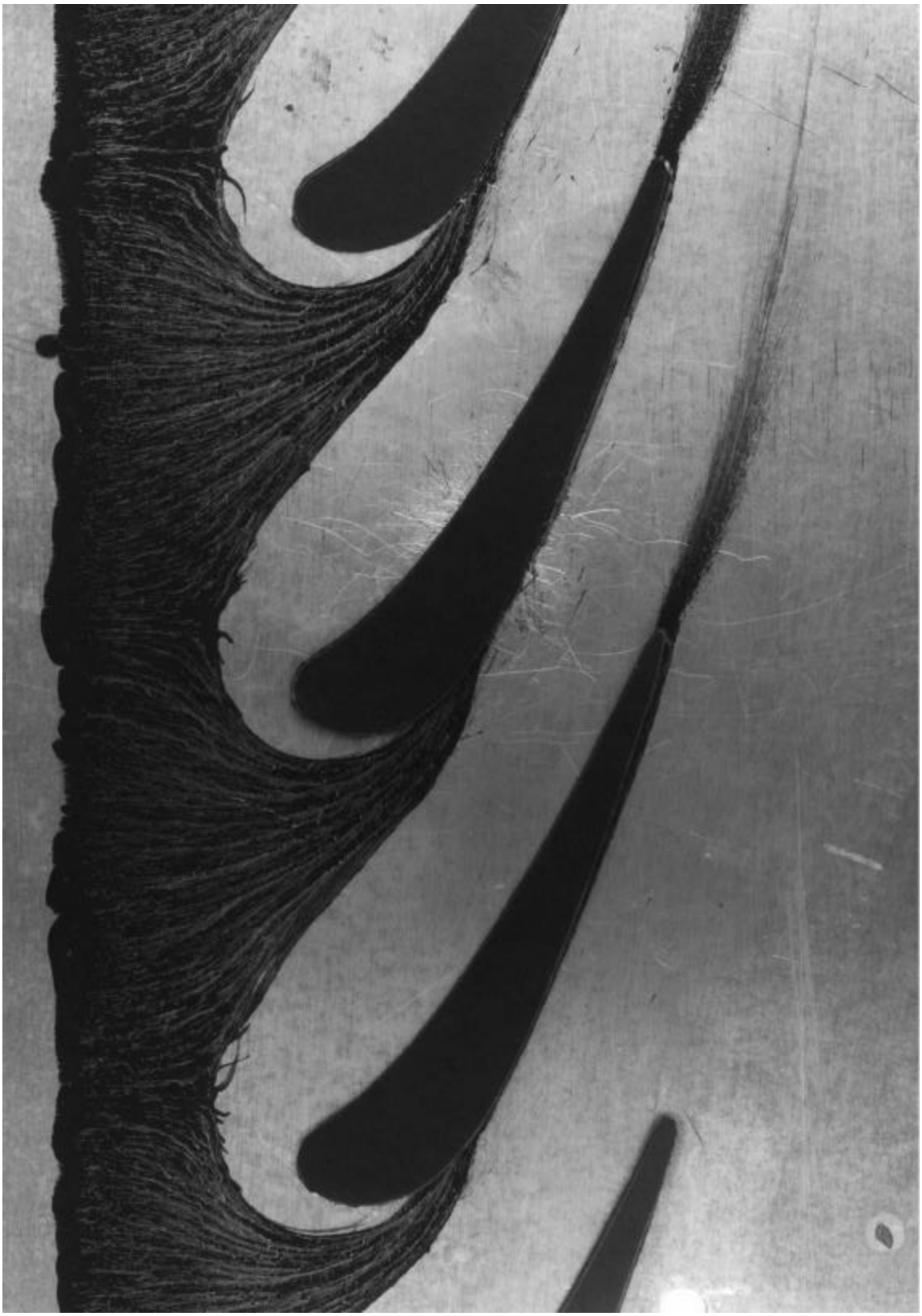

Figure 8. Endwall flow visualization using lampblack and oil showing the separation saddle point and pressure and suction surface separation lines. (Ames, Hylton, and York

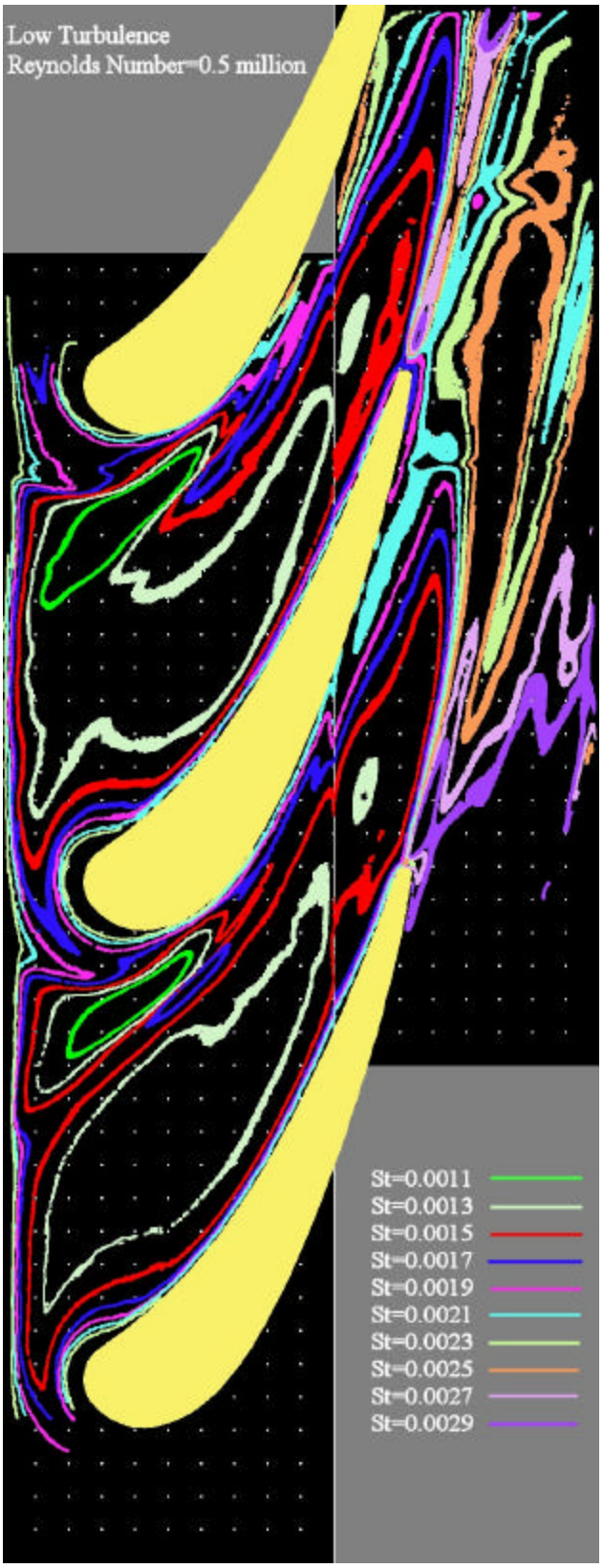

Figure 9. Endwall Stanton number contours, LT, Tu = 0.007, Re_C = 500,000

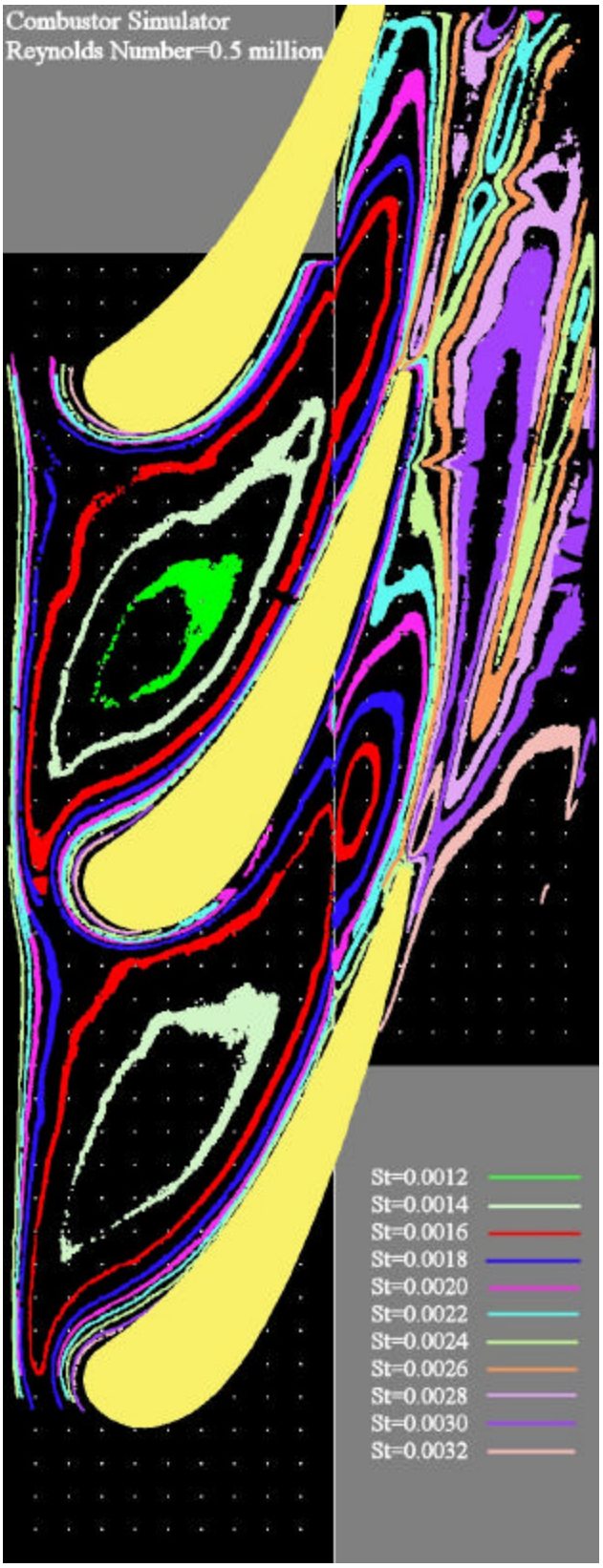

Figure 10. Endwall Stanton number contours, AC, Tu = 0.131, Lu = 7.2 cm, Re_C = 500,000

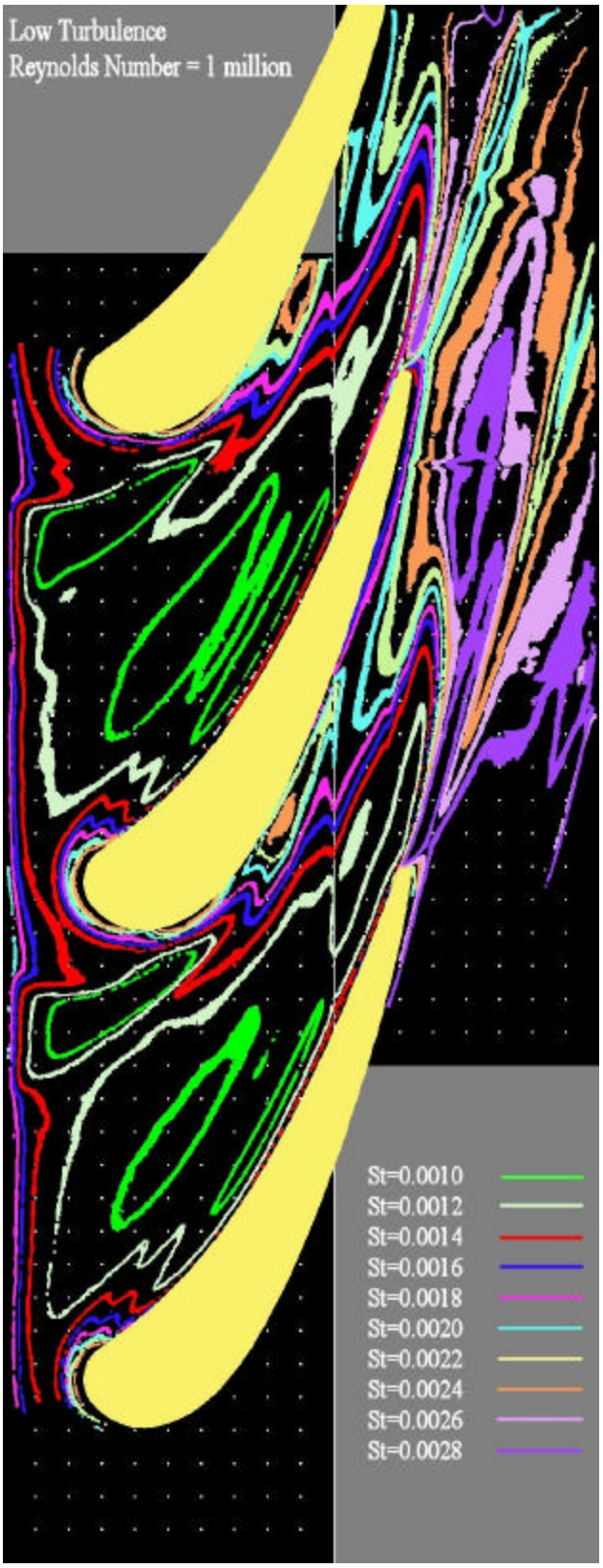

Figure 11. Endwall Stanton number contours, LT, Tu = 0.007, Re_C = 1,000,000

Figure 12. Endwall Stanton number contours, AC, Tu = 0.140, Lu = 6.4 cm, Re_C = 1,000,000

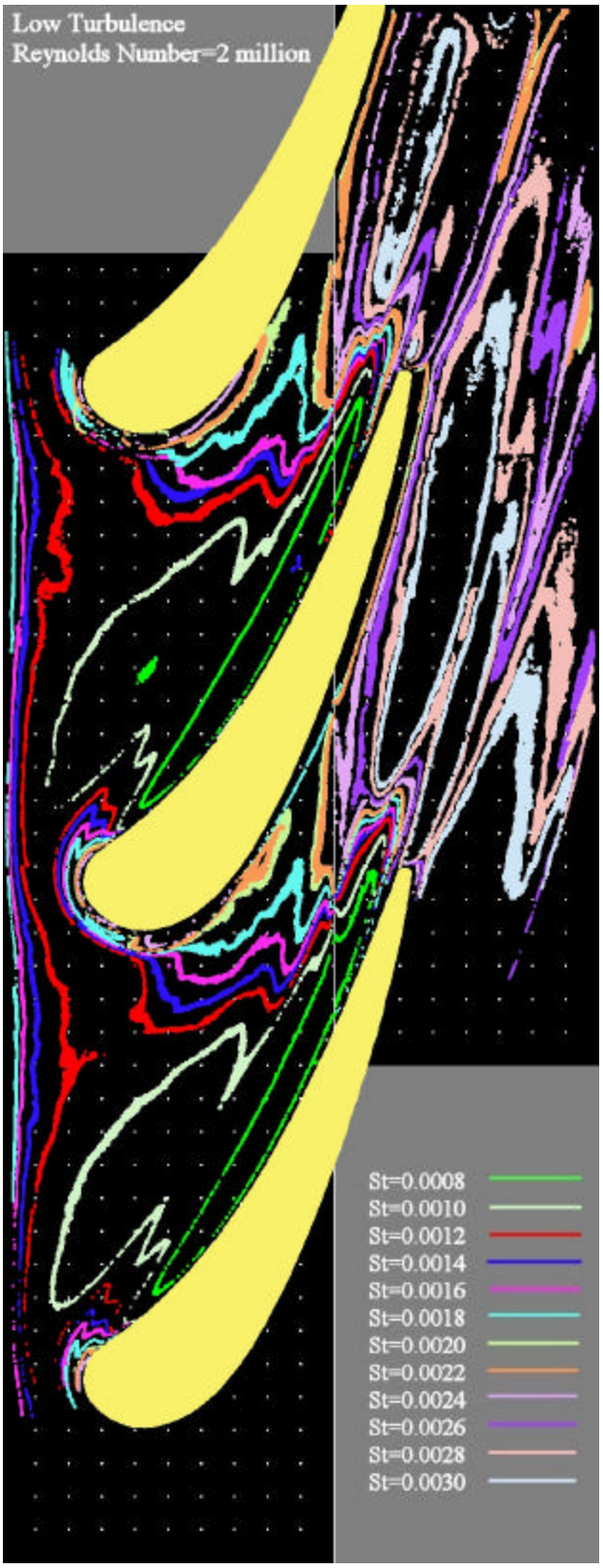

Figure 13. Endwall Stanton number contours, LT, Tu = 0.007, Re_C = 2,000,000

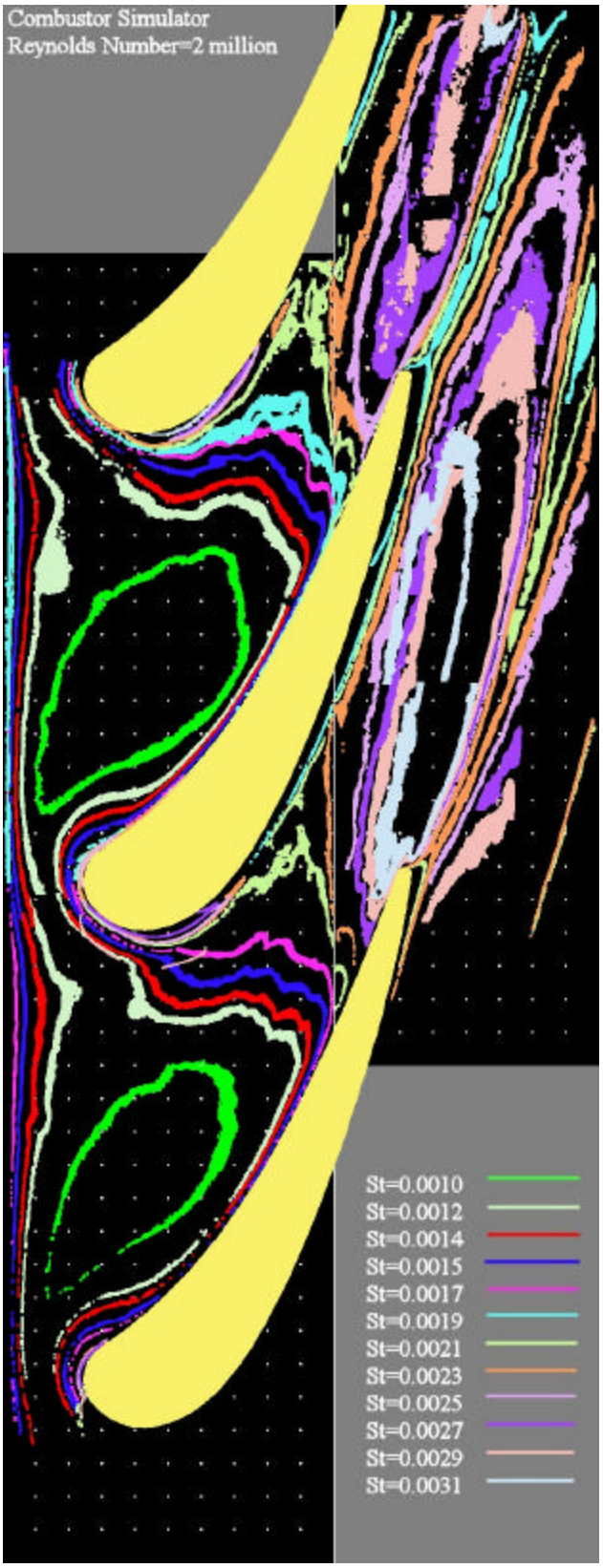

Figure 14. Endwall Stanton number contours, AC, Tu = 0.134, Lu = 7.3 cm, Re_C = 2,000,000

Measurement and Prediction of the Influence of Catalytic and Dry Low NOx Combustor Turbulence on Vane Surface Heat Transfer

By F.E. Ames, C. Wang, and P.A. Barbot

Abstract

New combustion systems developed for low emissions have produced substantial changes to the characteristics of inlet turbulence entering nozzle guide vanes. This paper documents the characteristics of turbulence generated by mock combustion system configurations representative of recently developed catalytic and dry low NOx combustors. Additionally, heat transfer rates are determined on the surface of a vane subjected to inlet turbulence generated by these mock combustor configurations. Six different inlet turbulence conditions with levels ranging up to 14 percent are documented in this study and vane heat transfer rates are acquired at vane exit chord Reynolds numbers ranging from 500,000 to 2,000,000. Heat transfer distributions show the influence of turbulence level and scale on heat transfer augmentation and on transition. Cascade aerodynamics are well documented and match pressure distributions predicted by a commercial CFD code for this large scale low speed facility. The vane pressure distribution could be characterized as a conventional or fully loaded distribution. This comprehensive data set on vane heat transfer is expected to represent an excellent test case for vane heat transfer predictive methods. Predictive comparisons are shown based on a two-dimensional boundary layer code using an algebraic turbulence model for augmentation as well as a transition model.

Nomenclature

C	vane chord length, m
Cp	specific heat at constant pressure, J/kg K
C_μ	A k – ε model constant, $C_\mu = 0.09$
D	vane leading edge diameter or effective diameter based on $D = 3.62\ U_\infty/(dU_\infty/dx)$
D_ν	A near wall viscous damping function
$E_1(f)$	one dimensional spectrum as a function of frequency, f, of the streamwise fluctuation velocity, u’
$E_1(k_1)$	one dimensional energy spectrum function, $E_1(k_1) = U\ E_1(f)/2/\pi$
f	frequency, 1/s
h	heat transfer coefficient, $W/m^2/K$, based on T_r and T_w
k	thermal conductivity, W/m/K
K	free stream acceleration parameter, $K = \nu/U_\infty^2 \bullet (dU_\infty/dx)$
k_1	wavenumber, $k_1 = 2\pi f/U$
Lu	energy scale, $Lu = 1.5\ |u'|^3/\varepsilon$
Lx	longitudinal integral scale of u’ fluctuation
Nu	Nusselt number, hD/k
P	Pressure, Pa
Pr	Prandtl number, $Pr = \rho Cp\nu/k$
Pr_t	turbulent Prandtl number, see Eqn. (13)
Re_C	Chord Reynolds number, based on exit conditions

St	Stanton number, $St = h/(\rho C_p U_\infty)$
Tu	turbulence level, $Tu = \|u'\|/U_\infty$
TRL	turbulence, Reynolds number, length scale parameter for correlating stagnation region heat transfer, $TRL = Tu \bullet Re_D^{5/12} \bullet (D/Lu)^{1/3}$
u', |u'|	streamwise component rms fluctuation velocity, m/s
Y	normal distance from test surface, m

Greek letter symbols

ε	turbulent dissipation rate, m^2/s^3
η	the Kolmogoroff micro length scale, $\eta = (\nu^3/\varepsilon)^{1/4}$
ν	kinematic viscosity, m^2/s
ν_M	eddy diffusivity for momentum, m^2/s
ρ	fluid density, mass per unit of volume, kg/m^3

Subscripts

0	refers to value at same position for low turbulence condition
i	refers to "inner region" of the boundary layer
o	refers to "outer region" of the boundary layer
s	refers to static condition
t	refers to total or stagnation condition
∞	evaluated in the free stream

Introduction

Turbulence from combustion systems has a very large influence on heat transfer distributions of first stage vanes. New strategies for achieving very low NOx levels have produced a variety of new combustor technologies, which have a significant influence on the turbulence levels at the entrance of high-pressure turbines. Consequently, gas turbine engineers are being challenged with developing component cooling systems, which match the heat load requirements of these new systems. In order to achieve reliable yet efficient cooling schemes for first vanes, gas turbine engineers must be equipped with knowledge of the turbulence characteristics produced by these new low NOx combustion systems. They also need an understanding of the impact that turbulence with these characteristics has on heat transfer distributions.

The objective of this research has been to investigate the characteristics of turbulence generated by new low NOx combustion systems and acquire heat transfer distributions on the surface of a vane and endwall in a linear cascade facility. Consequently, a mock dry low NOx (DLN) combustion system was designed and fabricated based on two industrial representative configurations. A mock catalytic combustion system was also developed based on an industry representative catalytic surface. In addition, for comparison purposes turbulence was generated with a low turbulence configuration, a mock aero-derivative combustion system in two upstream positions, and a biplanar square-mesh square bar grid. Turbulence levels and scales have been comprehensively documented for the six turbulence configurations. Vane heat transfer distributions were taken over a four to one range of chord exit Reynolds numbers and provide a comprehensive test case to ground heat transfer predictive capabilities.

Background

Heat transfer on central portion of a turbine vane is predominately two-dimensional. Consequently, heat transfer on a vane surface can be discussed in terms of the different regimes of flow. In addition to the specific velocity distribution on the surface of a vane, inlet turbulence boundary conditions are the major driver of heat transfer augmentation and transition on smooth airfoils. Therefore, this background section will discuss typical inlet turbulence conditions from combustion systems, stagnation region heat transfer augmentation, heat transfer augmentation to the laminar region on the pressure surface, transition, and augmentation to the turbulence boundary layer.

Combustor Turbulence. Values of turbulence intensity at the exit of gas turbine combustion systems reported in the literature have ranged from about 7 percent to nearly 30 percent (see Dils and Follansbee [1], Zimmerman [2], Bicen and Jones [3], Ames and Moffat [4], Moss and Oldfield [5], Goebel et al. [6], Zhang and Glezer [7], Ames [8], and Van Fossen and Bunker [9]. Ames [8] measured turbulence downstream from a mock aero-derivative combustor and suggested that turbulence scale, Lu, was typically 1/3 to ½ of the inlet passage. For most conventional combustion systems, which depend on large-scale recirculation to stabilize flames, turbulence level seems to depend on length to height ratio of the combustor and on the main flow to turbine inlet contraction ratio. For example in this present paper, the turbulence intensity downstream from the mock dry low NOx (DLN) combustor is about 14.3 percent for the two to one combustor area to inlet flow contraction ratio. Van Fossen and Bunker [9] report turbulence levels of 27 percent downstream from their DLN combustion system with its 1 to 0.9 combustor flow to inlet area contraction. Since the local fluctuation velocity and scale are the main drivers for heat transfer augmentation and transition, understanding turbulence conditions in turbine passages is critical for accurate predictions.

Stagnation Region Heat Transfer Augmentation. Stagnation regions often have the highest heat transfer rates on a turbine airfoil. Relative heat transfer rates in stagnation regions tend to increase with lower chord Reynolds numbers and higher inlet to exit velocity ratios. Inlet turbulence can produce augmentation levels more than 50 percent greater than the low turbulence baseline level. Recent research (Ames and Moffat [4] and Van Fossen, Simoneau, and Ching [10]) has shown that both scale and turbulence intensity have a significant impact on stagnation region heat transfer. Hunt [11] predicted that relatively small-scale turbulence is amplified by vortex stretching resulting from the strain field applied by a stagnation region flow. Britter, Hunt, and Mumford [12] later corroborated this theory. Ames and Moffat applied Hunt's work to the development of an algebraic eddy viscosity model and a correlating parameter, which are used to predict and correlate the results of this experimental investigation.

Laminar Region Heat Transfer Augmentation. In spite of significant disturbances due to free-stream turbulence, the pressure surface of a vane is typically laminar when exit chord Reynolds numbers are below one million due to the high flow field acceleration. However, a significant level of heat transfer augmentation can take place due to mixing caused by the external turbulence. For example, Arts, et al. [13] found augmentation levels of up to 100 percent on the laminar portion of a vane subjected to 6 percent grid turbulence. Ames [8] found laminar augmentation scaled on turbulence intensity, chord to length-scale ratio to the $1/3^{rd}$ power, and Reynolds number to the $1/3^{rd}$ power. He suggested that this $1/3^{rd}$ power Reynolds number scaling was consistent with no noticeable amplification of turbulence occurring. However, his Reynolds numbers range was limited. Wang, Goldstein, and Olson [14] looked at

the effect of high turbulence levels with large scale on turbine blade mass transfer. The suction surface of their blade accelerated to mid chord and they found increasing mass transfer augmentation and earlier transition with increasing turbulence level and Reynolds number. The pressure surface of their blade had an overspeed region, which made comparative assessment of parametric affects more difficult.

Transition. Mayle [15] presented a relatively comprehensive account of transition on the surface of a turbine airfoil. He suggests onset of transition is largely affected by the momentum thickness Reynolds number and turbulence level. However, he indicates that turbulent scale likely impacts transition onset as well. In addition, transition is suppressed on surfaces with high acceleration rates, where K is greater than 3E-6, even at high levels of turbulence. Zhang and Han [16] looked at the effect of grid generated turbulence on heat transfer augmentation and transition on a turbine blade. There results showed that at roughly equivalent turbulence levels, their finer grid produced earlier transition on the suction surface. In addition, Boyle and Simon [17] suggest that Mach number significantly influences transition length.

Turbulent Boundary Layer Augmentation. Ames and Moffat [4] and Thole and Bogard [18] have shown that relatively large-scale turbulence has a reduced influence on turbulent boundary layer heat transfer augmentation. Consequently, thin turbulent boundary layers on first vane suction surfaces are typically not strongly influenced by the relatively large-scale turbulence produced by combustion systems.

Experimental Approach

This heat transfer research has been conducted in the University of North Dakota's large-scale low speed cascade facility. This facility is configured in a steady state blow down arrangement and is shown schematically in figure 1. Air enters the facility through a large inlet filter, which protects the hot wires from fouling. The wind tunnel is powered by a 45 kW blower capable of providing 6.6 m^3/s of air at a static pressure rise of 5000 Pa. The blower outlet flow is directed through a two stage multivane diffuser section to distribute and diffuse the flow prior to entering a heat exchanger. The heat exchanger system, which uses a cooling water recirculation system, helps to provide a steady and controllable inlet air temperature. The flow is further conditioned downstream of the heat exchanger in a four section screen box. The low turbulence baseline configuration uses a 3.6 to one two-dimensional nozzle to further accelerate the air prior to entrance into the linear vane cascade test section.

The cascade test section used in this study is based on an eleven times scale mid span vane profile representative of a modern mid-sized industrial gas turbine and is displayed in figure 2. The vane profile was designed specifically for incompressible flow and has a velocity distribution, which is consistent with current conventionally or fully loaded vanes in industrial engines. The cascade test section was designed to produce accurate two-dimensional aerodynamics with a four-vane three-passage configuration. The cascade has inlet bleeds and exit tailboards to allow inlet flow uniformity and exit flow periodicity. The inlet bleed flows were designed along two-dimensional streamlines predicted by FLUENT [19] and the flexible exit tailboards can be shaped to account for streamline curvature. The cascade has a row of inlet static taps one-quarter axial chord upstream from the vane leading edge and a row of exit taps one-quarter axial chord downstream to monitor the cascade setup. Ten probe access ports are provided along the row of inlet static pressure taps to measure inlet temperature and total pressure and to survey inlet turbulence characteristics.

The coordinates of the eleven times scale vane are provided in the Appendix to allow for predictive comparisons. The vane has a true chord of 47.8 cm and an axial chord of 25.0 cm. The vanes have a 38.4 cm spacing and a height of 25.4 cm. The diameter of the leading edge is 5.59 cm and the diameter of the trailing edge is 0.98 cm. The stagger angle of the vane is 55.1 degrees and the calculated air exit angle is 73.4 degrees.

The cascade was run at nominal exit chord Reynolds numbers of 500,000, 1,000,000, and 2,000,000 for this study. This range of first vane chord exit Reynolds numbers is consistent with a range of small to medium industrial or propulsion gas turbine engines.

Turbulence Generators. This study was designed to investigate turbulence characteristics representative of modern low NOx combustion systems and their influence on vane heat transfer. Two separate low NOx configurations were developed. One configuration represented a conventional dry low NOx combustion system and the other a catalytic combustion system. In addition, an aeroderivative combustion system was developed to provide turbulence with characteristics, which are representative of with many current engines and has been documented in the literature. All three mock combustion systems used the same combustor liner and nozzle configuration, which is shown with the aero-derivative geometry in figure 3. This liner geometry replaces the 3.6 to one contraction nozzle for the high turbulence test cases. For the low NOx combustor configurations the side panels of the mock combustor system are replaced with solid panels and either the swirler arrangement or the catalytic surface are attached at the back panel position. The swirler arrangement for the conventional DLN is shown in figure 4 while the mock catalytic surface is shown in figure 5.

The back panel for the mock DLN combustor consists of 10 swirlers. Each swirler is fabricated from a 20.3 cm schedule 40 PVC pipe and has a 5.1 cm centerbody. Each swirler has 12 vanes, which are essentially a 36 degree projection of a 45 degree slice through the pipe. The design of the low NOx combustion system is more a less a compromise between the model dry low NOx system published by Van Fossen and Bunker [9] and a green thumb combustor system of Rolls Royce [19]. The Van Fossen mock combustor had a swirler flow to combustor liner flow area ratio of 33 percent and a vane inlet flow to combustor liner flow area ratio of 90 percent. The swirlers used by Van Fossen had 45 degree vanes. The Rolls Royce green thumb combustor has a swirler to combustor flow area ratio of 40 percent and a vane inlet area to combustor flow area ratio of 33 percent. The swirler vane angles range from 45 to 60 degrees. The current design has a swirler flow to combustor flow ratio of 46 percent and an inlet to liner flow ratio of 50 percent.

The mock catalytic combustion system was crafted after the system used by Catalytica. Catalyica's foil has a serpentine groves running across it. These grooves are spaced at 2.2 mm apart. As the foils are folded back across each other and rolled together to form a round porous structure, grooves from one side of the foil cross with grooves from the adjacent foil helping to promote mixing. UND's mock catalytic combustor is made from evaporative cooling pads, which contain the same type of crossing grooved channels. The evaporative cooling pads are 12 times the size of the actual catalytic combustor surface. This scaling is very similar to the vane scaling, which is 11 times the actual size.

Turbulence was also generated using a square bar square mesh biplanar grid. The grid used 1.27 cm square bars, which were spaced on 6.35 cm centers producing a 64 percent open area grid. The grid was held 63.5 cm or 10 mesh lengths upstream of the vane leading edges for the heat transfer tests. The grid was held in a 25.4 cm by 127 cm flow area spool section, which

was 91.5 cm long and attached between the 3.6 to one contraction nozzle and the cascade test section.

In addition, a second level of turbulence was generated with the mock aero-combustor turbulence generator using the 91.5 cm long spool section. For this condition the spool section was placed between the mock combustor and the cascade test section to allow the mock combustor turbulence to decay.

Vane Pressure Distribution. The third vane from the bottom was used to acquire the heat transfer and pressure distributions. This "instrumented" vane can be inserted through a machined hole in the acrylic endwall where it is held in place using a flange. The pressure vane was cast out of epoxy with 82 pressure tubes incrementally spaced along and cast adjacent to its surface. Static pressure taps were fabricated by drilling through the epoxy surface into the brass tube with a 0.8 mm diameter drill bit. The baseline pressure distribution for the low turbulence case is shown in figure 6 where it is compared to a prediction using FLUENT. On this figure negative surface distance is taken from the calculated stagnation point (0 cm) along the pressure surface toward the trailing edge and positive surface distance is determined along the suction surface. The viscous prediction calculates the data with precision. Overall, the comparison is excellent and demonstrates the quality of the two-dimensional aerodynamics produced by the cascade. Developing accurate aerodynamics is critical to producing a heat transfer database, which is valuable for understanding the impact of new combustion systems and for grounding predictive methods.

Heat Transfer Vane Description. The heat transfer vane has a polyurethane foam core with a 1.6 mm epoxy shell cast around it. The present heat transfer data were acquired using the 52 fine wire chromel-alumel thermocouples cast around the surface. The vane was covered with a 0.023 mm Inconel foil bonded to a 0.127 mm sheet of Kapton and backed with 0.05 mm of high temperature acrylic adhesive. The 101.6 cm by 25.4 cm foil has 6.35 mm by 0.5 mm copper bus bar soft soldered to the end of the foil to evenly distribute the large DC current, which is used to produce the surface heat flux. These copper bus bars are recessed into the surface of the epoxy near the trailing edge on both the pressure and suction surfaces. The resulting Inconel foil, as adhered to the epoxy surface, produces an aerodynamically smooth visually attractive heat transfer surface. The heating starts and ends 1.3 cm from the trailing edge on the pressure and suction surfaces.

Heat transfer baselining tests were conducted for the low turbulence condition over the four to one range in Reynolds numbers. Prior to heating the foil, the recovery temperature distribution was acquired. Subsequently, the midline surface temperature distribution was acquired at the desired surface heat flux condition. Surface heat flux was determined by measuring the voltage across the heater and the current through. The heater current was determined using a precision shunt resistor. Only radiation losses were accounted for. Due to the relatively thick and very low conductivity polyurethane core, conduction through the vane was ignored. Conduction along the surface of the foil was also ignored due to the thin Inconel foil. Radiation losses were estimated using the local surface temperature radiating to the inlet total temperature using a foil emissivity of 0.21 and assuming a blackbody background. As a consistency check heat transfer data were acquired at one-half and full power. The resulting root mean square difference was only 0.5 percent with a maximum variation of 1.7 percent.

A comparison between the experimentally determined Stanton number distribution and a finite difference boundary layer calculation (STAN7 Kays [21]) using the predicted pressure distribution is shown in figure 7 for the three low turbulence cases. Notice that all three

distributions are laminar. The comparisons between the predicted and experimental Stanton number distributions are generally better than 10 percent and give confidence to the experimental technique.

Data Acquisition. Pressures were acquired using two Rosemount Smart Pressure Transmitters scaled to ranges of 250 and 5000 Pa full scale with 0.1 percent of scale accuracy. Both transmitters were read for each pressure and the most sensitive reading was kept. Pressures were scanned using a homemade miniature solenoid valve system and were referenced to the inlet total pressure. Transmitters were zeroed at the beginning of each use to minimize uncertainties due to drift. Voltage outputs for both the pressure transmitters and for the chromel-alumel thermocouples were scanned and read using an HP 3497A data acquisition system. The data acquisition unit has an integral voltmeter with 1 μV sensitivity. Thermocouples were all connected through a passive constant temperature junction and were referenced using an ice bath junction. Hot wires were powered, low pass filtered, bucked and gained using a two channel TSI ISA 300 hot wire anemometry bridge. Raw signals were read with a PC based high-speed data acquisition card with 12 bits of resolution. Mean velocities were acquired at a data acquisition rate equivalent to about three integral time scales. Velocity time records for spectral analysis were acquired in 40 sets of 8192 samples and post processed.

Data Uncertainties. Estimates for the uncertainty in heat transfer, pressure, velocity, and turbulence measurements were determined using the root sum square method described by Moffat [22]. Based on a data reduction program perturbation method, Nth order uncertainty in reported local Stanton number ranged to plus or minus 5 percent at a 95 percent confidence interval. The uncertainty estimate for run-to-run comparisons was estimated at plus or minus 3 percent. Uncertainty in the local vane surface static pressure was estimated at a maximum of 2.5 percent. Exit velocity was determined at a precision of 2 percent. The uncertainty in turbulence level for the single wire was estimated to be 3 percent of the reported value. The experimental error in turbulent scale is estimated to be 11 percent. All uncertainty estimates are quoted for a 95 percent confidence interval.

Inlet Conditions and Turbulence Characteristics. A total of six different turbulence conditions were developed for this midspan heat transfer investigation. Both heat transfer data and turbulence measurements were taken for all turbulence conditions and Reynolds numbers. Velocity and turbulence data were acquired at the midspan of the inlet at five positions distributed evenly across one passage. These measurements were acquired 7 cm upstream from the leading edge plane of the vanes. The turbulence level (Tu), average midspan velocity (U), integral scale (Lx), energy scale (Lu), and dissipation (ε) were determined for each condition and are presented in Table 1. Mean velocity and turbulence intensity were determined from 8192 data samples acquired at a time increment equal to about two or three integral time scales. Turbulent scales and dissipation rates were determined from 40 records of 8192 points taken at 10 to 35 kHz depending on the cascade inlet velocity. This allows for better statistical resolution of the power spectrum for the lower wavenumbers. The longitudinal integral scale was determined using Taylor's hypothesis by multiplying the integral time scale by the local convective velocity. The integral time scale was determined by integrating the autocorrelation in time to the first zero crossing. The autocorrelation was calculated using an inverse FFT of the average power spectral density function of the velocity time records.

The energy scale (or dissipation scale of Hancock and Bradshaw [23]), Lu is a macro scale of turbulence estimated from 1.5 times the cube of the rms value of u' divided by the dissipation rate.

$$Lu = 1.5 |u'|^3/\varepsilon \quad (1)$$

The dissipation rate is determined from the inertial subrange of the u' power spectrum. Hinze [24] suggests that in the inertial subrange of a turbulent spectrum for u' the spectrum function can be related to the dissipation rate and the wavenumber.

$$E_1(k_1) = 18/55\ A\ \varepsilon^{2/3}\ k_1^{-5/3} \quad (2)$$

Ames and Moffat [25] suggest that the constant A be taken as 1.62. The energy scale is quite useful because as Hinze [24] suggests, the inertial subrange of a spectrum to the end of the dissipation range can be determined by the dissipation rate along. Also, since the integral of the one-dimensional spectrum of u' is equal to u'^2, the turbulence intensity, local velocity, and energy scale provides a quantitative description of an energy spectrum. A typical one-dimensional spectrum of u' is shown in figure 8 as taken downstream from the mock aero-derivative turbulence generator.

Heat Transfer Results

This section examines the vane surface heat transfer results both qualitatively and quantitatively for the influence of turbulence, scale, and Reynolds number on heat transfer augmentation and location of transition. First, the qualitative effects of the turbulence on augmentation and location of transition will be observed. Next, the level of augmentation in the laminar regions of the flow will be examined quantitatively in terms of turbulence level, scale and Reynolds number. Finally, heat transfer predictions will be made using STAN7 [21], the augmentation model of Ames, Moffat, and Kwon [25], and the transition model of Mayle [15].

Stanton number results. Stanton number distributions are presented in figures 9 through 11 for all six turbulence conditions for exit chord Reynolds numbers of 500,000, 1,000,000, and 2,000,000. The figures plot Stanton number versus surface distance with negative surface distance taken over the pressure surface and positive surface distance taken over the suction surface. The turbulence intensities quoted in the figures have been adjusted to account for the decay, where $Tu(x) = 1/[1/Tu(0) + x/(2\ Lu)]$. Figure 9 presents the distributions of the six turbulence conditions for the 500,000 Reynolds number case. Here the low turbulence (LT) case with a turbulence level of 0.7 percent is given by the round solid symbols and shows laminar flow over the entire surface. The catalytic combustor produces a turbulence level of only 1.0 percent with about a 2 cm energy scale (Lu) and shows little effect from the turbulence. This low turbulence level produced by the catalytic combustor has important significance for design as flow over the majority of the vane surface will be laminar. Turbulence produced by the grid and the aero-combustor with spool (ACS) significantly augments laminar heat transfer on the pressure surface and stagnation region and leads to transition on the suction surface. Notice that the grid condition transitions earlier than the aero-combustor with spool in spite of the latter's higher turbulence level. This slightly earlier transition is likely the result of the grid turbulence's smaller scale and occurs at all three Reynolds numbers. This observation is consistent with the expectations of Mayle [15]. Results for the mock dry low NOx (DLN) and aero-combustor (AC) show similar trends but higher heat transfer augmentation in the laminar flow regions and earlier transition the suction surface. Notice that the smaller scale turbulence of

the mock AC compensates for the slightly higher turbulence level of the mock DLN combustor in terms of laminar augmentation and transition location.

Figure 10 presents Stanton number distributions for six turbulence conditions for the 1,000,000 chord Reynolds number case. Qualitatively the trends for the six turbulence cases are very similar to the lower Reynolds number data. However, laminar region augmentation levels are higher, suction surface transition occurs at an earlier location, and the AC and DLN cases show signs of the initiation of transition at a surface distance of about –0.3 m. Additionally, at this higher Reynolds number the turbulent boundary layer Stanton numbers on the suction surface now approach the level of heat transfer in the stagnation region. Figure 11 presents Stanton number distributions for the 2,000,000 chord Reynolds number case. Again the trends are qualitatively similar but laminar augmentation levels are higher and suction surface transition occurs even earlier. Also, the four higher turbulence cases (DLN, AC, ACS, and Grid) show signs of transition on the pressure surface at a surface location of about –0.22 m. For this higher Reynolds number case the catalytic combustor now shows some laminar augmentation on the pressure surface and the start of transition on the suction surface at a surface arc of 0.31 m. Now the turbulent boundary layer Stanton numbers on the suction surface exceed those of the stagnation region.

Pressure surface heat transfer augmentation. Heat transfer augmentation to the pressure surface is presented as $(St-St_0)/St_0$ versus surface distance in figures 12 through 14. Figure 12 shows the fractional increase in Stanton number for the 500,000 chord Reynolds number case. The pressure surface or negative surface arc shows a rising increase past the stagnation region and a relatively steady value further downstream past a surface arc of –0.1 m. This behavior is representative of laminar augmentation on the pressure surface. The augmentation levels at –0.2 m are about 6 percent for the mock catalytic system, 36 percent for the grid and aerocombustor with spool, and about 58 percent for the aerocombustor and DLN combustor. The increase on the suction surface is of course due to transition. Figure 13 shows the fractional increase in Stanton number for the 1,000,000 Reynolds number case. The majority of the pressure surface shows laminar behavior. However, these augmentation curves show a change in behavior toward the aft end of the surface with upturn in augmentation rate. This behavior is consistent with the start of transition on the pressure surface and it occurs for the four highest turbulence levels. The laminar augmentation levels at –0.2 m are about 14 percent for the mock catalytic combustor, 46 percent for the grid and aero-combustor with spool, and 75 percent for the aero and DLN combustors. Figure 14 shows Stanton number augmentation for the 2,000,000 Reynolds number case. The augmentation curves suggest transition starts at about –0.3 m for the grid and aero-combustor with spool and at after –0.2 m for the aero and DLN combustors. Since the onset of transition is similar for the grid and aero-combustor with spool, while the scale and turbulence level is somewhat different, these heat transfer data set may be useful for testing transition models. Further the laminar augmentation level at –0.2 m are about 22 percent for the catalytic combustor, 64 percent for the grid and aero-combustor with spool and about 98 percent for the aero and DLN combustors. Augmentation noticeably increases with Reynolds number and turbulence intensity, while the comparisons between the grid and aero-combustor with spool suggest that given similar turbulence levels and Reynolds number augmentation increases with decreasing scale.

Ames [8] suggested that heat transfer augmentation to a laminar boundary layer should scale on turbulence intensity (Tu), Reynolds number to the 1/3rd power and energy scale (Lu) to the negative 1/3rd power. That is $(St-St_0)/St_0 \propto Tu\ Re_C^{1/3}\ (C/Lu)^{1/3}$. This implies that the

dissipation of the turbulence adjacent to a pressure surface boundary layer is unaltered by the boundary layer velocity gradient or the streamwise acceleration. Further it implies that the relatively larger turbulent eddies in the v' spectrum are blocked by the presence of the wall leaving only the smaller eddies to penetrate into the thin pressure surface boundary layer and augment mixing. Ames [8] studied heat transfer on a vane pressure surface at chord Reynolds numbers of 800,000 and 500,000. He concluded that the data supported a Reynolds number dependence of a 1/3rd power for laminar heat transfer augmentation of the pressure surface boundary layer. He suggested that this dependence was also supported by a simple asymptotic analysis of a laminar boundary after Ames and Moffat [4]. The present data represent an opportunity to test this physical model across a much wider (4 to 1) range in Reynolds numbers. Figure 15 presents augmentation levels $(St-St_0)/St_0$ on the pressure surface versus the heat transfer dependence parameter, $Tu\ (C/Lu)^{1/3}\ Re_C^{1/3}$ for average augmentation levels at –0.162 m and –0.199 m. A best-fit line through the data is shown along with plus and minus 5% error bands with very good results. These data provide clear support of the above augmentation dependence.

Stagnation region augmentation. At lower chord Reynolds numbers heat transfer levels in the stagnation region of a vane or blade are often higher than any other location as shown in figures 9 and 10. Consequently, predicting heat transfer accurately in this region is critical to designing cooling methods, which are reliable and efficient. Heat transfer through the laminar boundary layer in a stagnation region is different than on a pressure surface due to the rate of strain, which is present there. Hunt [11] first predicted the response of small and large scale turbulent eddies to the straining, which occurs in the stagnation region of a cylinder using rapid distortion theory. He concluded that the relatively small scale eddies are amplified as they are stretched around the stagnation region of a cylinder by the approaching flow and the large scale eddies are largely blocked by the cylinders presence. Britter, Hunt, and Mumford [12] later experimentally verified this conclusion. Ames and Moffat [4] used the results of Hunt to develop a simple model spectrum for turbulence approaching a cylinder stagnation point. They used the spectrum model in a simple asymptotic analysis to develop a correlating parameter for stagnation region heat transfer, which included the effect of scale. Based on this analysis heat transfer augmentation $[(Nu-Nu_0)/Nu_0]$ in a stagnation region is expected to increase as a function of turbulence intensity, Reynolds number to the 5/12th power, and diameter to energy scale to the 1/3rd power. That is $(Nu-Nu_0)/Nu_0 \propto Tu\ Re_D^{5/12}\ (D/Lu)^{1/3}$. The different Reynolds number dependence compared to the pressure surface is due to the amplification of the turbulence from to the straining effect. Since the present data represents a relatively wide range of turbulence levels and Reynolds numbers, it provides a good test to this correlation. Ames [8] suggests a good engineering approximation for this correlation is $(Nu-Nu_0)/Nu_0 = 0.04\ Tu\ Re_D^{5/12}\ (D/Lu)^{1/3}$. Figure 16 presents stagnation region heat transfer augmentation data in terms of (St-St0)/St0 versus the $Tu\ Re_D^{5/12}\ (D/Lu)^{1/3}$ for the two data points on either side of the predicted stagnation point (-.01 m and +0.0088 m). The solid line represents the above correlation, while data for the three Reynolds numbers are presented for each of the five higher turbulence conditions. The data are well correlated by this turbulence parameter and all data fall within +/- 7.4 percent of the line. Considering the collective uncertainty of the turbulence parameter is +/- 5 percent and the repeatability of the heat transfer data is +/- 3 percent, the correlation fits the data with very good accuracy.

Finite difference boundary layer predictions. These data provide an excellent test for vane heat transfer predictive capabilities due to the range of turbulence conditions and Reynolds

numbers present as well as the relevant fully loaded vane design. Two-dimensional finite difference boundary layer predictions were made for this complete data set using the algebraic turbulence model [ATM] of Ames, Kwon, and Moffat [25], the transition model of Mayle [15], and STAN7, a finite difference boundary layer code. The ATM is a simple spectral model of v' turbulence accounting for the attenuation of large eddies in the proximity of the wall due to the wall's blocking effect. It was originally developed to predict the augmentation to a turbulent boundary layer (Ames and Moffat [4]) and was shown to produce the correct near wall eddy viscosity distributions in a laminar boundary layer developing on the pressure surface of a vane by Ames, Kwon, and Moffat []. The basic model is given below:

$$\nu_{M,o} = 1.5\, C_\mu\, Tu_\infty\, U_\infty\, Lu_\infty\, [1 - \exp(-2.9\, Y/Lu_\infty)]^{4/3}\, D_\nu \qquad (3)$$

The near wall damping function, D_ν, accounts for the effect of viscous action on the turbulent spectrum and is presented below:

$$D_\nu = (1 - \exp(-y/[\eta C_\eta])) \qquad (4)$$

η is the Kolmogorov length scale and C_η is a constant set equal to 6.7. Note that the constant, C_η was erroneously given in the numerator rather than the denominator of the exponential in Ames, Kwon, and Moffat [25]. For these heat transfer predictions, the turbulent Prandtl number is taken as 0.85. This value is an estimate and data are needed to determine the actual turbulent Prandtl number across an accelerating laminar boundary layer subjected to high levels of flow field turbulence.

Heat transfer predictions are shown for the three Reynolds numbers in figures 17, 18, and 19. Largely, the level of augmentation predicted by the ATM matches the experimental augmentation on the laminar region of the pressure surface well. On the pressure surface for the lower Reynolds number shown in figure 17, the data are as much as 12 percent below the predictions midway along the pressure surface but improve toward the trailing edge. This represents the largest discrepancy found in the laminar region of the pressure surface for all data sets. On the suction surface near the stagnation region, the calculations underpredict the level of augmentation because the ATM does not account for the action the rapid strain has on the turbulence in the stagnation region. This underprediction for the stagnation region is consistent across all three Reynolds numbers. The pressure surface data of figures 18 and 19 for chord exit Reynolds numbers of one and two million show the start of transition. Mayle's [15] transition model begins to predict transition when the acceleration parameter, K, drops below 3E-6 on the pressure surface at a surface arc of –0.35 m. Augmentation data in figure 13 suggest that this location is appropriate for the grid, aero-combustor with spool, and aero-combustor. However, the data for the DLN combustor indicate that transition may start before –0.3 meters. For the highest Reynolds number the acceleration constraint allows transition to proceed after a surface arc of –0.25 m. However, the DLN combustor data indicate transition starts at around –0.2 m. In spite of slight discrepancies in the location of transition, Mayle's transition model performs very well on the pressure surface for these data.

The transition model is shown to predict transition early on the suction surface for all Reynolds numbers at the higher levels of turbulence. For the lowest Reynolds number case, figure 17, transition is predicted to proceed after the adverse pressure gradient on the suction surface begins. However, after a favorable pressure gradient commences, the spot production rate model drops rapidly producing the wiggle in the prediction.

Stagnation region prediction. The ATM given in equation (3) underpredicts the stagnation region heat transfer data as shown in figures 17 through 19. However, stagnation region heat transfer correlates well on the TRL parameter of Ames and Moffat [4] as shown in figure 16. This suggests that the ATM model could be improved if we could account for the effect of the rapid strain in the stagnation region of an airfoil by predicting this turbulence amplification similar to the TRL correlation. Hunt [11] used rapid distortion theory to account for the amplification of small-scale turbulence in the presence of a cylindrical stagnation region. The spectrum function in the inertial subrange can be related to the dissipation rate. By applying Hunt's results to the edge of the stagnation region boundary layer, the increase in the dissipation rate can be correlated by the stagnation region's diameter Reynolds number.

$$\varepsilon/\varepsilon_0 = (Re_D/4)^{1/4} \tag{5}$$

The stagnation region diameter Reynolds number can be estimated using the local streamwise velocity gradient at the stagnation region.

$$Re_D \cong \rho_\infty U_\infty^2 \, 3.62/(dU_\infty(X=0)/dx)/\mu_\infty \tag{6}$$

The change in the dissipation can be related to an increase in the near wall eddy viscosity through the length scale term, Lu_∞ in equation (3). This turbulence amplification is observed to be present around the stagnation region where high strain rates occur but is not noticeably present on the pressure surface as shown the by Reynolds number dependence in the present data as well as by the eddy diffusivity data of Ames, Kwon, and Moffat [25]. Other turbulence models have previously been tied to the local strain rates. For example, Forest [26] used the Pohlhausen parameter to correlate a constant in his eddy viscosity model. In the calculations shown in figure 20 the following function was used "turn on" and "turn off" the amplification of turbulence:

$$f_{amp} = [1 - \exp\{-2.5\,[(dU_\infty(X)/dx)/(dU_\infty(X=0)/dx)]^2\} \tag{7}$$

The increase in eddy viscosity can be estimated as shown below:

$$\nu_M/\nu_{M,o} = 1 + [(Re_D/4)^{1/12} - 1] * f_{amp} \tag{8}$$

This function works well in the stagnation region, where the function f_{amp} is close to 1.0. The accuracy of these predictions in the stagnation region support the appropriateness of the Ames and Moffat [4] stagnation region turbulence model. The function also works well over the pressure surface where the f_{amp} is close to zero. However, the accuracy of the function in estimating the amplification of turbulence as the acceleration changes from the high levels found in the stagnation region to more moderate levels found on the pressure surface has not been determined.

SUMMARY AND CONCLUSIONS

The present vane heat transfer data document the influence of mock DLN and catalytic combustion systems on a conventionally loaded vane over a four to one range in Reynolds numbers. These data should help reduce the risk of integrating these new technology combustors

into industrial gas turbine systems. Additionally, heat transfer data have been acquired for low turbulence, grid turbulence, and two levels of aero-derivative combustor turbulence over the same Reynolds number range. These data offer turbine designers heat transfer comparisons between known and new inlet configurations providing information on the likely response of turbine heat transfer to these new systems.

These data provide quantitative information on turbulence characteristics developed in DLN and catalytic combustion systems, which previously have had little documentation in the open literature. Additionally, these data suggest that in clean environments laminar flow is predominately present on first vanes in small to medium sized gas turbine systems with catalytic combustion systems. This knowledge has significant potential for simplifying gas turbine systems with catalytic combustion.

These data help demonstrate the impact of flow field straining on the turbulence in the stagnation region of a vane and the corresponding impact on heat transfer. The resulting difference in the effect of Reynolds number scaling was shown for the pressure surface and the stagnation region. Further, a simple method to account for this leading edge effect has been added to the ATM of Ames, Moffat, and Kwon [25] based on eddy viscosity scaling ideas developed by Ames and Moffat [4].

Comparative predictions have been made using the STAN7 [21] finite difference boundary layer code with the ATM model of Ames, Moffat, and Kwon [25] and the Mayle [15] transition model. Results showing laminar augmentation in the stagnation region and pressure surface were very good. The location and length of transition were captured well on the pressure surface but appeared slightly conservative on the suction surface. These present midline heat transfer data are expected provide a useful database for the grounding of vane heat transfer predictive methods.

ACKNOWLEDGEMENTS

The authors would like to gratefully acknowledge support for this work from the Advanced Gas Turbine System Research program, which is funded by a consortium including the Department of Energy and participating industrial members. Additionally, this project was also initially funded through a seed grant from the North Dakota EPSCoR program, the University of North Dakota, and the Mechanical Engineering Laboratory endowment fund. The authors would like to acknowledge the turbine aero group at Rolls Royce of Indianapolis for developing a special incompressible vane design in a conventionally loaded configuration for this project. Additionally, the authors would like to thank UND student's Dan Pelarski, Troy Lassle, and Mark Hettwer as well as the senior design team, which helped with this project.

REFERENCES

1. Dils, R. R., and Follansbee, P. S., 1977, "Heat transfer coefficients around cylinders in crossflow in combustor exhaust gases," J. Engr. Power, Vol. 99, pp. 497.
2. Zimmerman, D. R., 1979, "Laser anemometer measurements at the exit of a T63-C20 combustor," NASA CR-159623.
3. Bicen, A. F., and Jones, W.P., 1986, "Velocity characteristics of isothermal and combusting flows in a model combustor," Combust. Sci. and Tech., Vol. 49, pp. 1.
4. Ames, F.E., and Moffat, R.J., 1990, "Heat Transfer with High Intensity, Large Scale Turbulence: The Flat Plate Turbulent Boundary Layer and the Cylindrical Stagnation Point,"

Report No. HMT-44, Thermosciences Division of Mechanical Engineering, Stanford University.
5. Moss, R.W., and Oldfield, M.L.G., 1991, "Measurements of Hot Combustor Turbulence Spectra," ASME Paper No. 91-GT-351.
6. Goebel, S. B., Abuaf, W., Lovette, T. A., and Lee, C.-P., "Measurement of Combustor Velocity and Turbulence Profiles," ASME Paper 93-GT-228.
7. Zhang, L.J., and Gleazer, B., 1995, "Indirect turbulence measurement in gas turbine stages using heat flux probe," ASME Paper No. 95-GT-153.
8. Ames, F.E., 1997, "The Influence of Large-Scale High-Intensity Turbulence on Vane Heat Transfer," Journal of Turbomachinery, Vol. 199, pp. 23-30.
9. Van Fossen, G. J., Bunker, R. S., "Augmentation of stagnation heat transfer due to turbulence from a DLN can combustor," ASME Paper No. 2000-GT-215.
10. Van Fossen, G.J., Simoneau, R.J., and Ching, C.Y., 1995, "The influence of turbulence parameters, Reynolds number, and body shape on stagnation region heat transfer," ASME Journal of Heat Transfer, Vol. 117. pp. 597-603.
11. Hunt, J.C.R., 1973, "A Theory of Turbulent Flow Round Two-Dimensional Bluff Bodies," J. Fluid Mech., Vol. 61, Part 4, p. 625.
12. Britter, R. E., Hunt, J.C.R., and Mumford, J.C., 1979, "The distortion of turbulence by a circular cylinder," Journal of Fluid Mechanics, Vol. 92.
13. Arts, T., Lambert de Rouvroit, M., and Rutherford, A.W., 1990, "Aero-thermal Investigation of a Highly Loaded Transonic Linear Turbine Guide Vane Cascade," Technical Note 174, von Karman Institute for Fluid dynamics, Belgium.
14. Wang, H. P., Goldstein, R. J., and Olson, S. J., 'Effect of free-stream turbulence with large length scale on blade heat/mass transfer," Journal of Turbomachinery, Vol. 121, pp. 217-224.
15. Mayle, R.E., 1991, "The Role of Laminar-Turbulent Transition in Gas Turbine Engines," ASME Journal of Turbomachinery, Vol. 113, pp. 509-537.
16. Zhang, L, and Han, J.-C., 1994, "Influence of mainstream turbulence on heat transfer coefficients from a gas turbine blade," ASME Journal of Heat Transfer, Vol. 116, pp. 896-903.
17. Boyle, R.J., and Simon, F.F., 1999, "Mach number effects on turbine blade transition length prediction," ASME Journal of Turbomachinery, Vol. 121. pp. 694-701.
18. Thole, K.A. and Bogard, D.G. 1995, "Enhanced Heat Transfer and Skin Friction due to High Freestream Turbulence," ASME Journal of Turbomachinery, Vol. 117, pp. 418.
19. FLUENT 5.3, 1999, FLUENT 5.3 User's Guide, Fluent, Inc., Lebanon, N.H.
20. Smith, D., 2000, "Private communication," Rolls-Royce, Indianapolis.
21. Kays, W.M., 1987, "STAN7, a finite difference boundary layer code."
22. Moffat, R.J., 1988, "Describing the uncertainties in experimental results," Experimental Thermal and Fluid Science, Vol. 1., pp. 3-17.
23. Hancock, P.E., and Bradshaw, P., 1983, "The effect of free stream turbulence on turbulent boundary layers," J. Fluids Engr., Vol. 105, pp. 284.
24. Hinze, J., 1975, Turbulence, 2nd ed. McGraw-Hill, New York.
25. Ames, F.E., Moffat, R.J., and Kwon, K, 1999, "An algebraic model for high intensity large scale turbulence," Offered for presentation at the 1999 IGTI conference in Indianapolis, IN.
26. Forest, A.E., 1977, "Engineering Predictions of Transitional Boundary Layers," AGARD-CP-224.

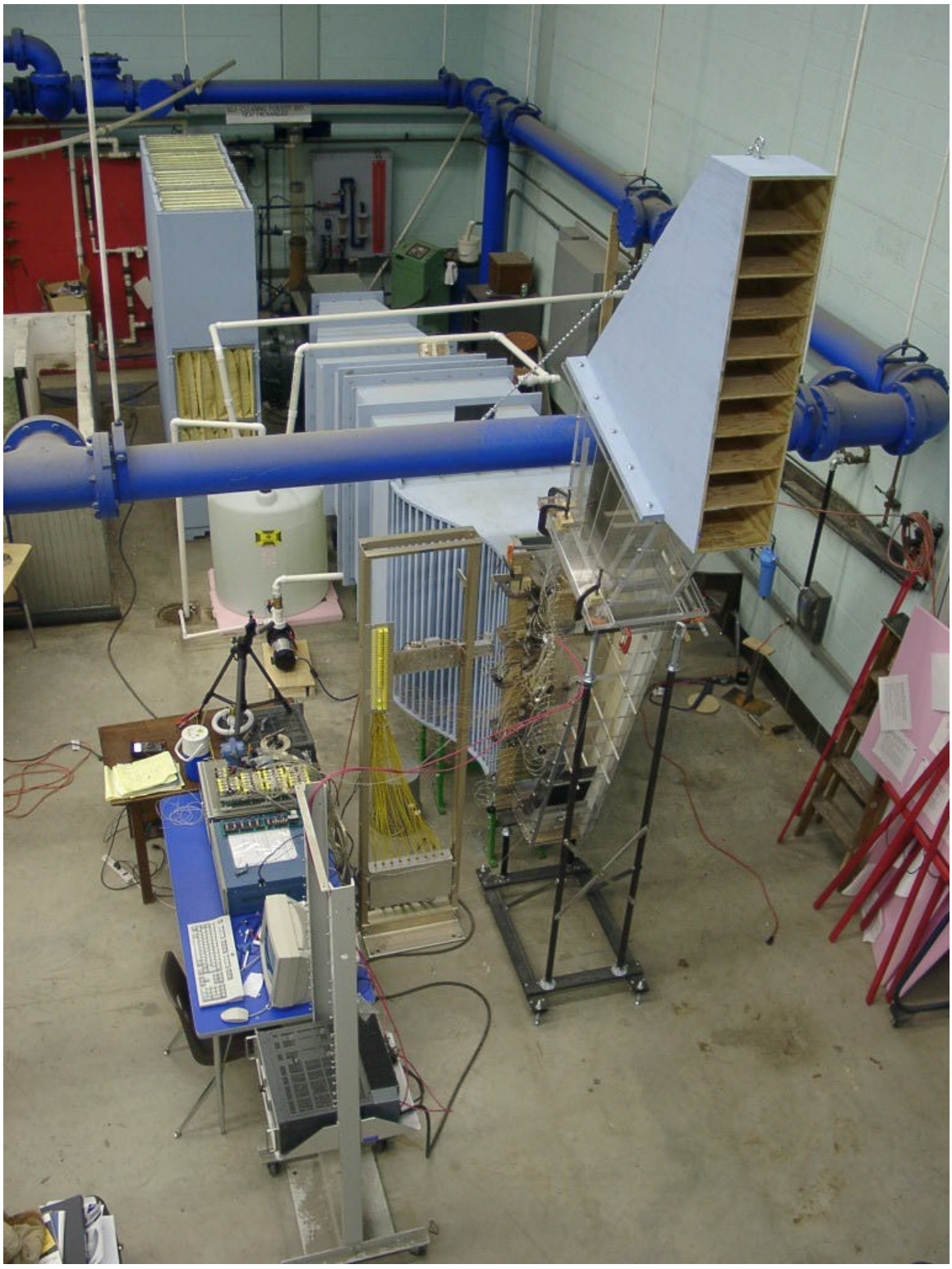

Figure 1. Digital photo of blow down wind tunnel with large-scale low speed linear vane cascade.

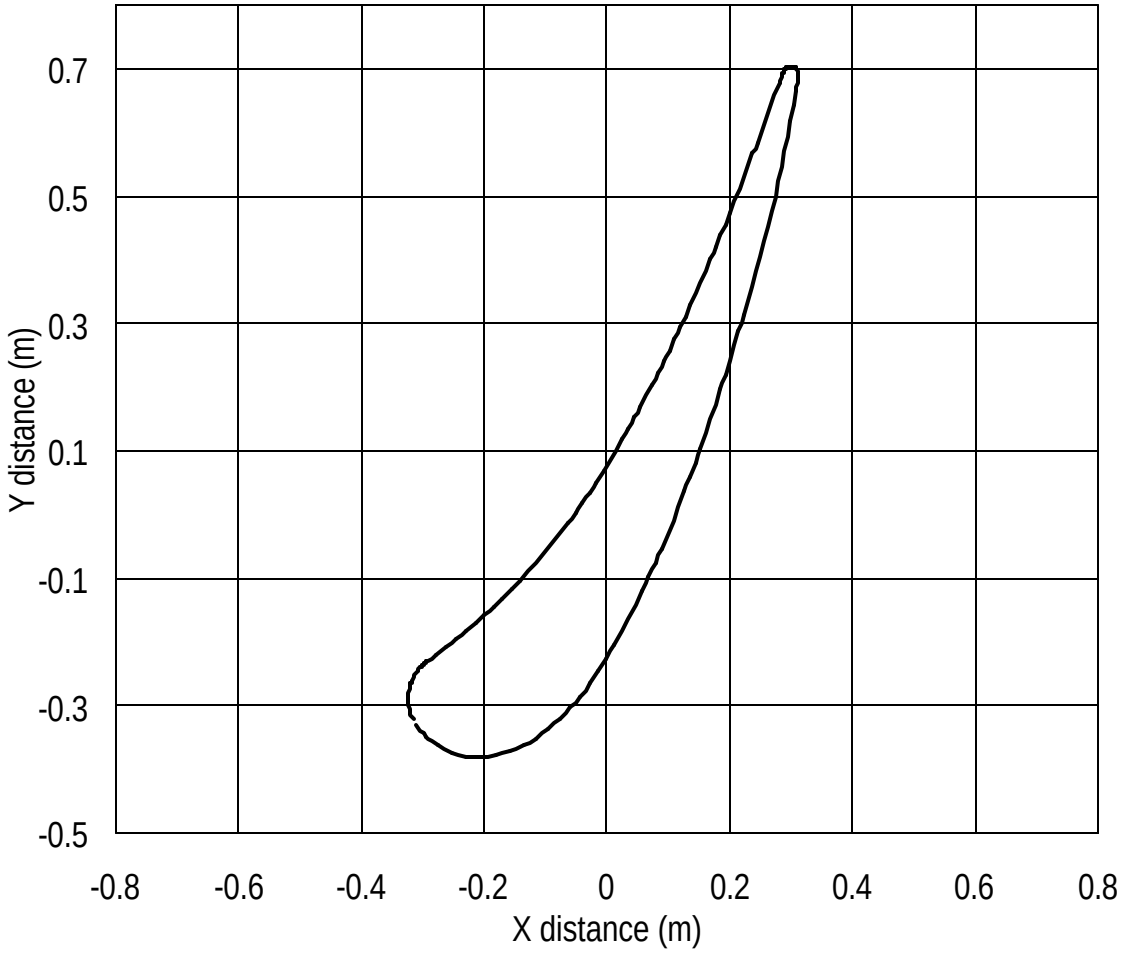

Figure 2. Cross-sectional view of large scale conventionally loaded vane used in this study.

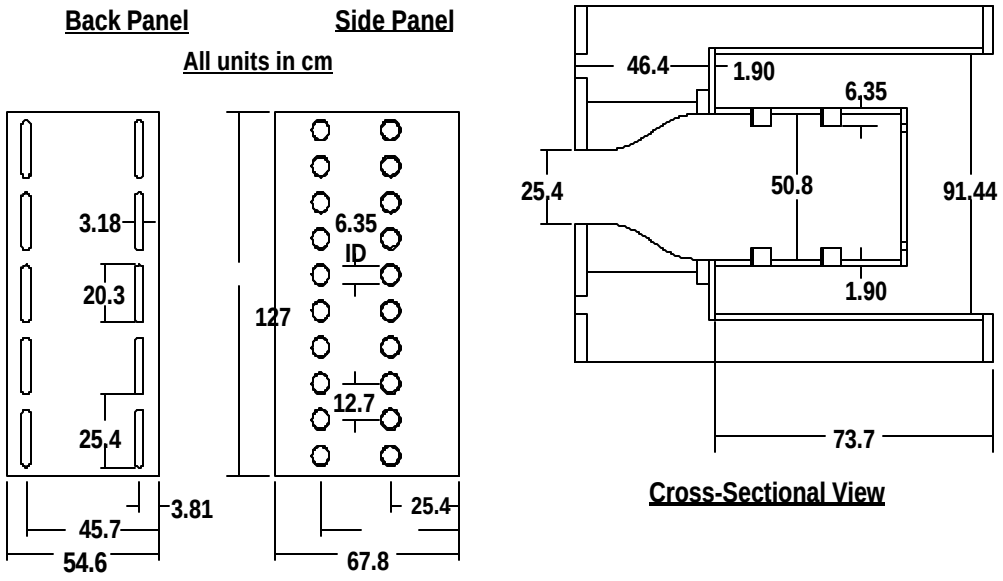

Figure 3. Schematic of mock aeroderivative combustor turbulence generator

Figure 4. Digital photo of dry low NOx swirlers installed in mock combustor liner

Figure 5. Digital photo of catalytic combustor surface installed in mock combustor liner

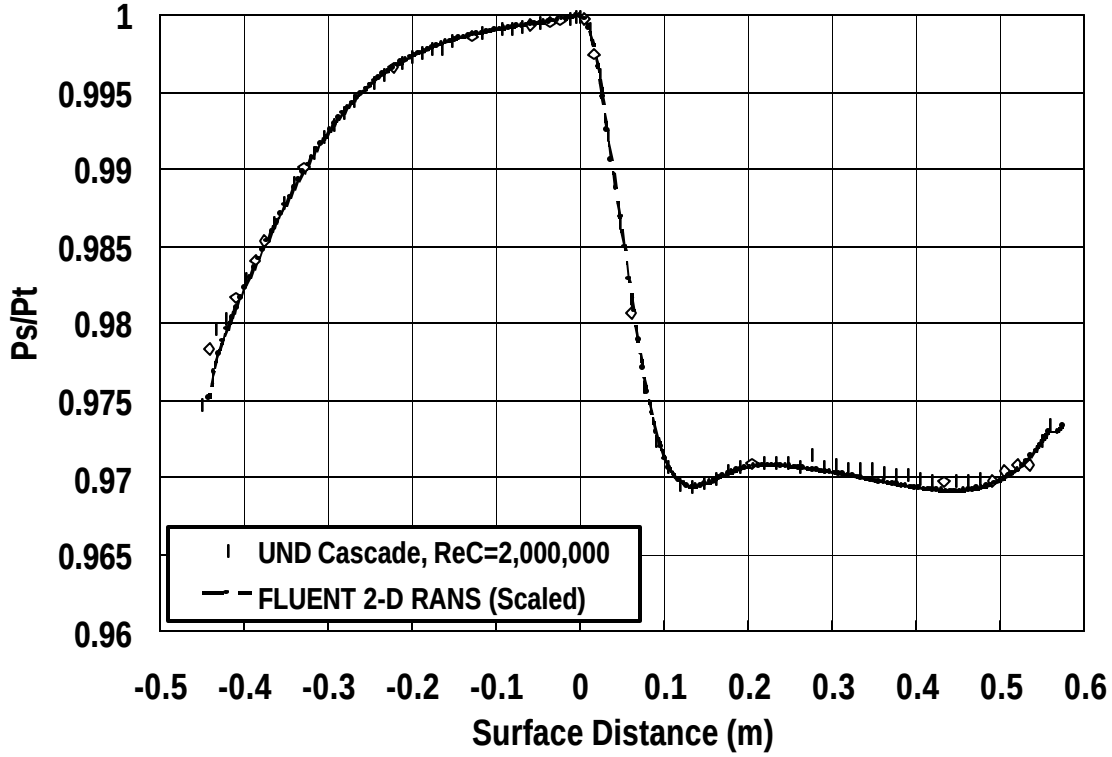

Figure 6. Comparison between measured and predicted vane midspan pressure distribution

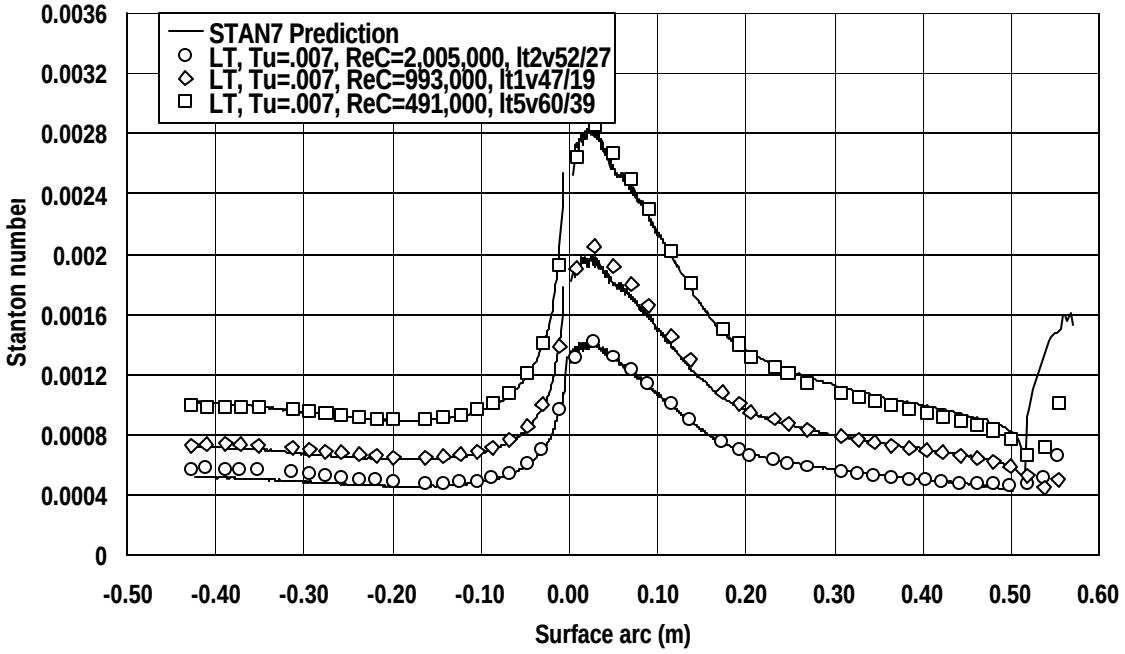

Figure 7. Low turbulence vane Stanton number distributions with STAN7 predictions

	Reynolds	Tu	U (m/s)	Lx (cm)	Lu (cm)	e (m^2/s^3)
Low turbulence	500,000	0.0069	4.96	8.12	127.0	0.00005
	1,000,000	0.0076	10.43	5.02	154.5	0.00035
	2,000,000	0.0060	18.71	3.58	15.5	0.0144
combustor	500,000	0.1313	5.24	3.68	7.24	6.67
	1,000,000	0.1402	9.32	3.52	6.36	51.5
	2,000,000	0.1339	18.39	3.58	7.35	302.0
grid	500,000	0.0821	4.77	2.00	3.27	2.70
	1,000,000	0.0861	10.19	2.04	3.35	29.8
	2,000,000	0.0884	19.27	2.35	3.53	206.8
catalytic comb	500,000	0.0103	4.95	5.26	3.83	0.0052
	1,000,000	0.0153	9.46	0.62	5.15	0.093
	2,000,000	0.0102	19.63	0.89	1.75	0.680
spool	500,000	0.0915	5.11	5.08	9.03	1.67
	1,000,000	0.0950	9.74	4.61	8.81	13.23
	2,000,000	0.0928	18.19	4.44	9.49	75.17
swirler	500,000	0.1342	5.17	4.57	8.78	5.60
	1,000,000	0.1433	9.65	4.34	8.95	43.73
	2,000,000	0.1417	19.11	4.47	10.77	274.5

Table 1. Characteristics of inlet velocities, turbulence level and scale, and dissipation for various turbulence generators

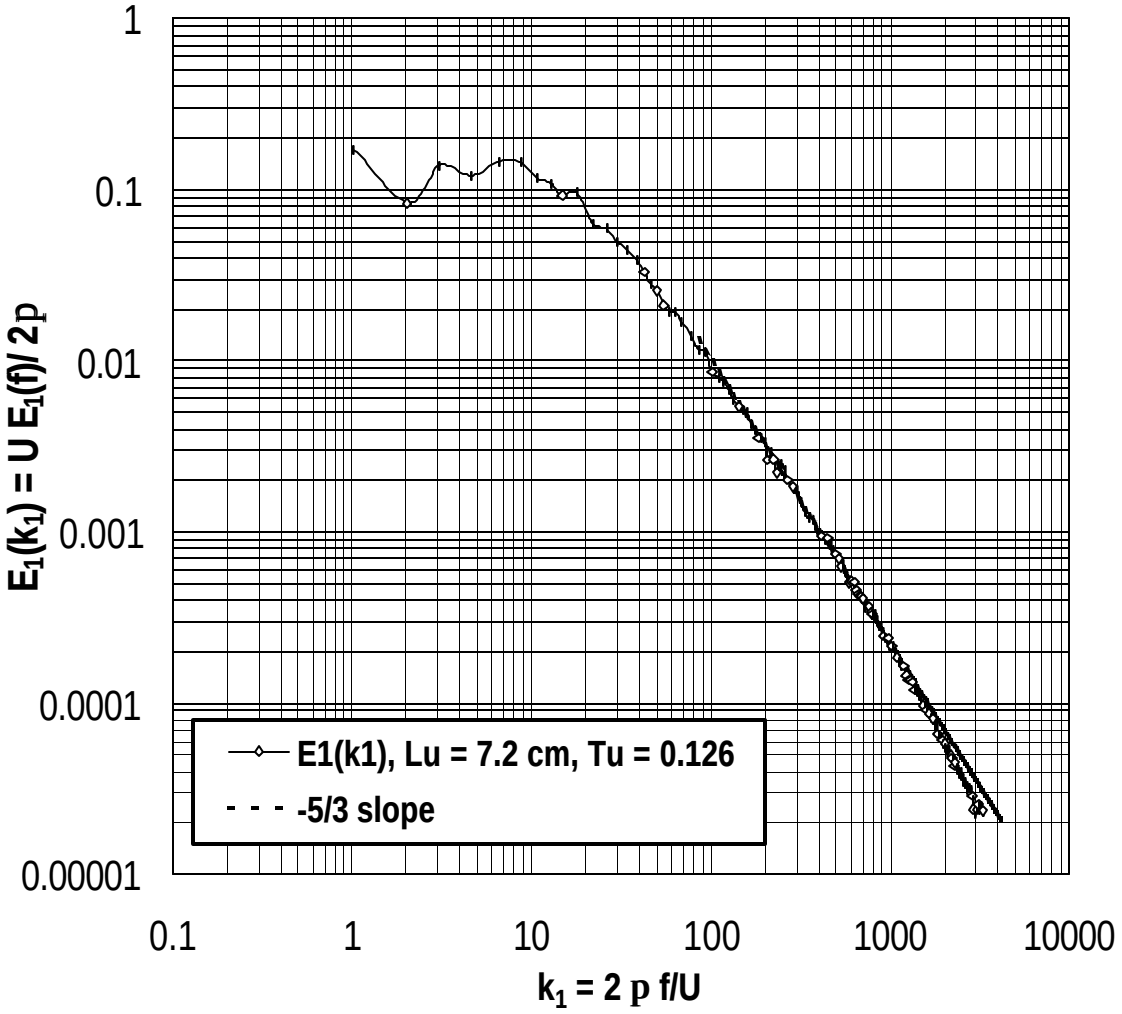

Figure 8. One-dimensional spectra of u' for aero-derivative combustor

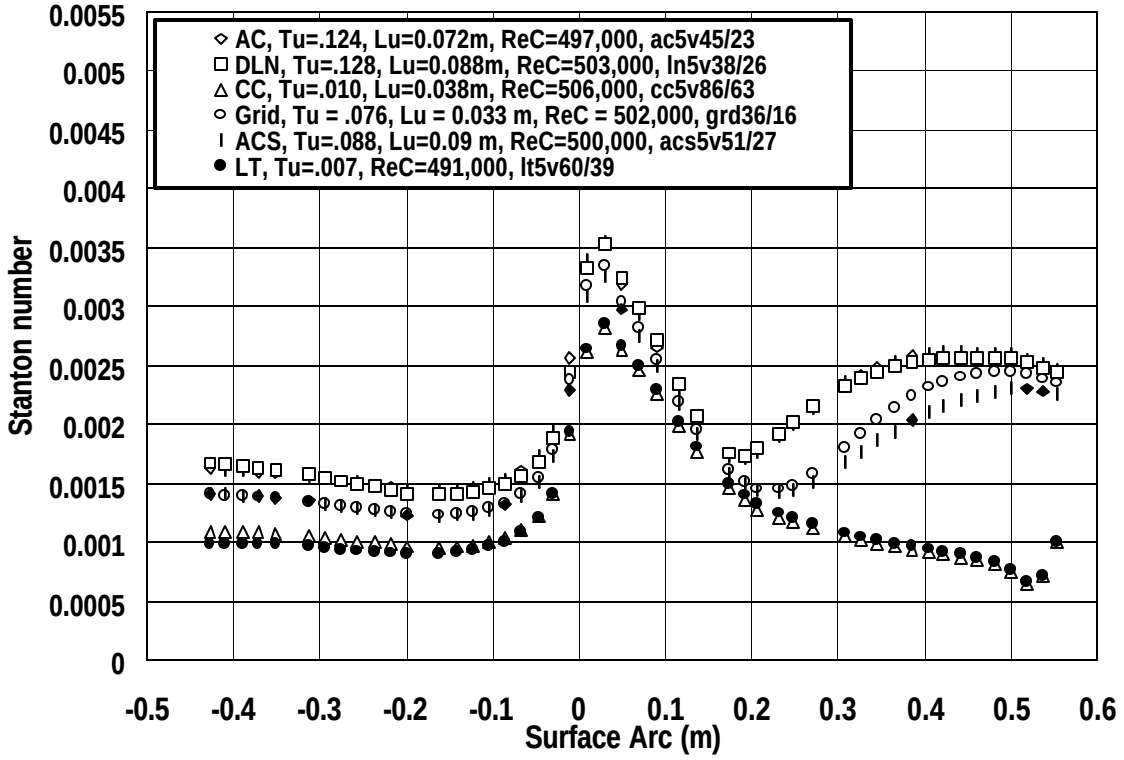

Figure 9. Effects of mock combustor turbulence characteristics on vane Stanton number distributions, Re_C = 500,000

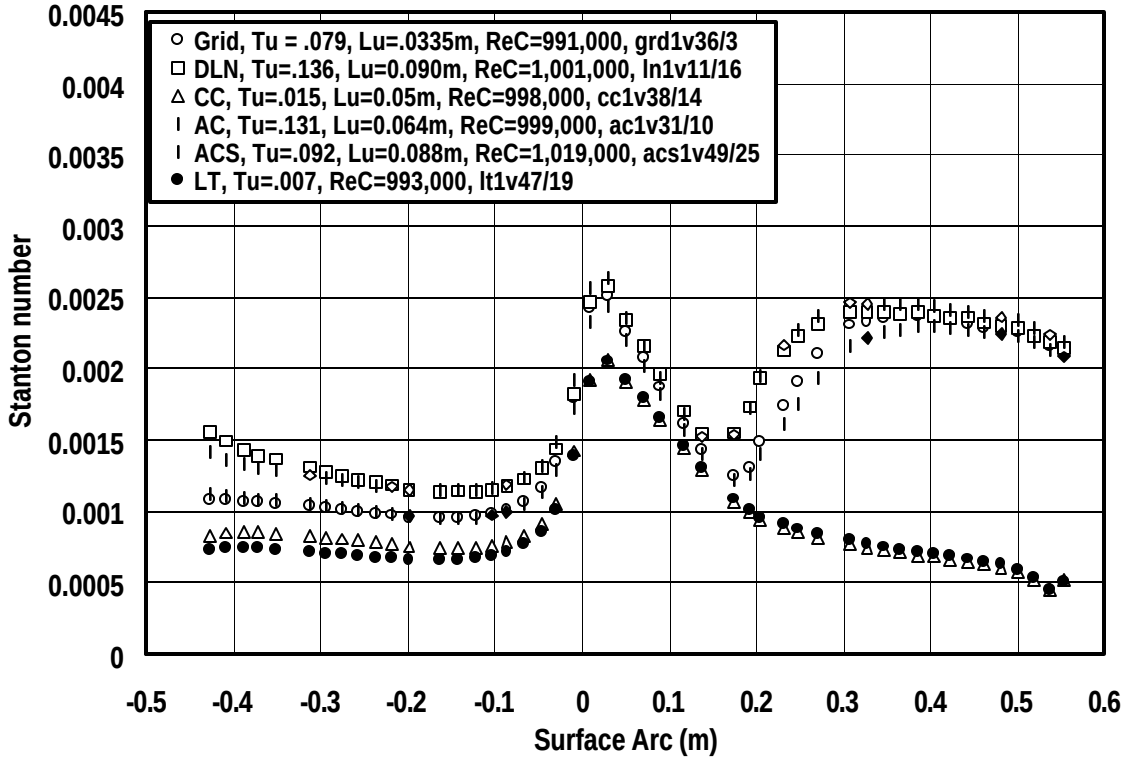

Figure 10. Effects of mock combustor turbulence characteristics on vane Stanton number distributions, Re_C = 1,000,000

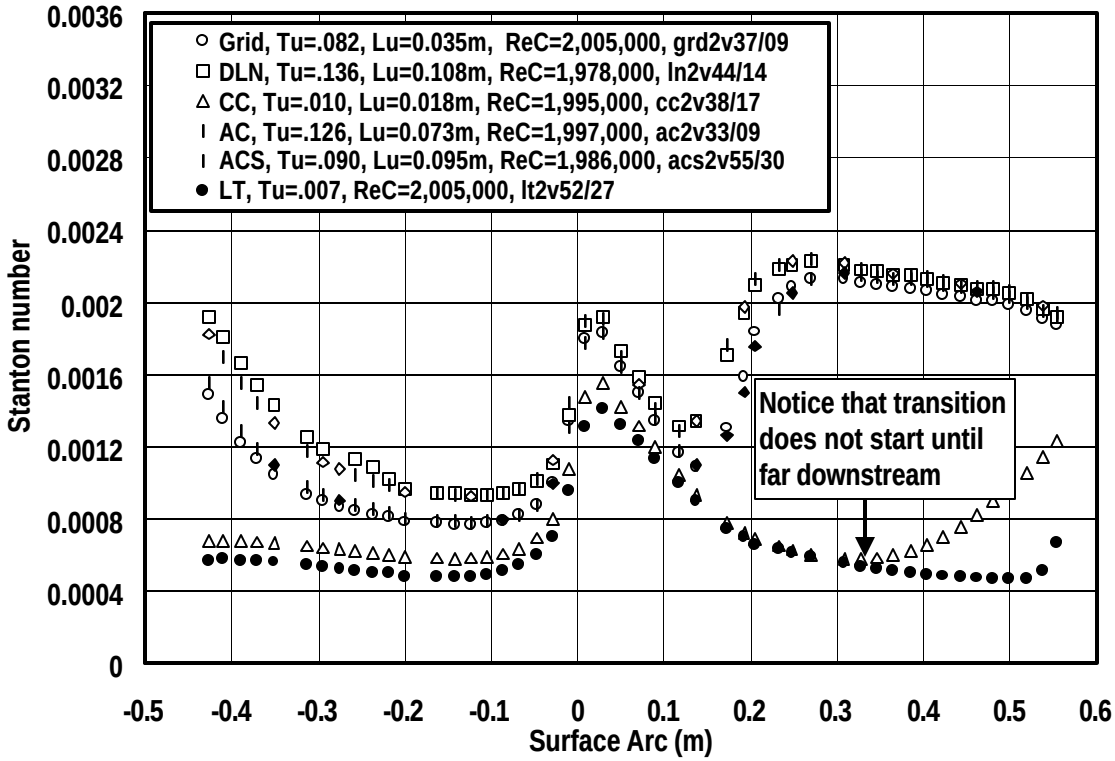

Figure 11. Effects of mock combustor turbulence characteristics on vane Stanton number distributions, Re_C = 2,000,000

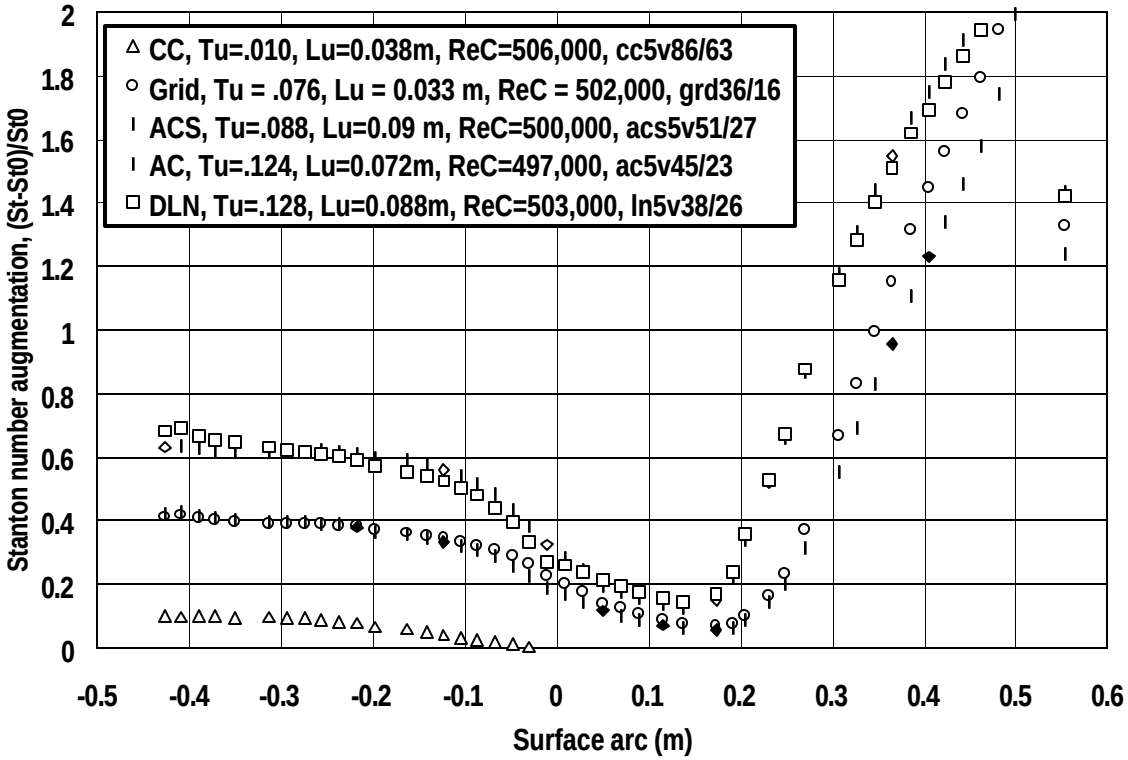

Figure 12. Effects of mock combustor turbulence characteristics on Stanton number augmentation and location of transition, Re_C = 500,000

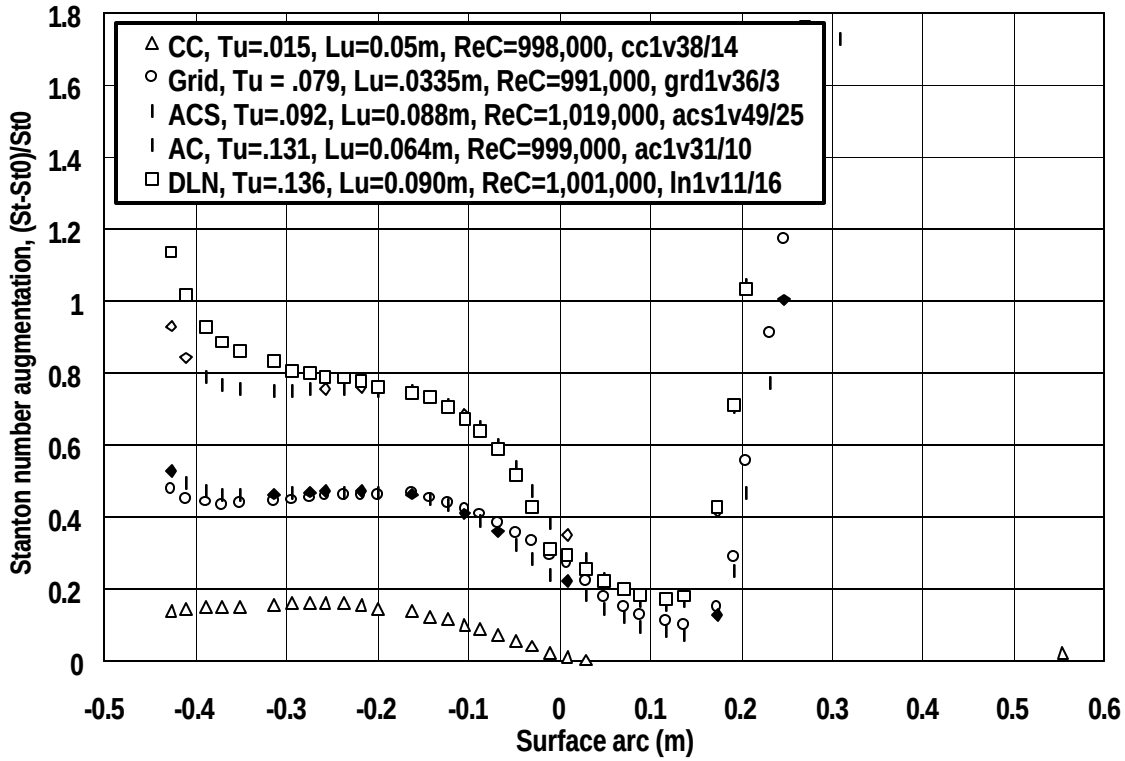

Figure 13. Effects of mock combustor turbulence characteristics on Stanton number augmentation and location of transition, Re_C = 1,000,000

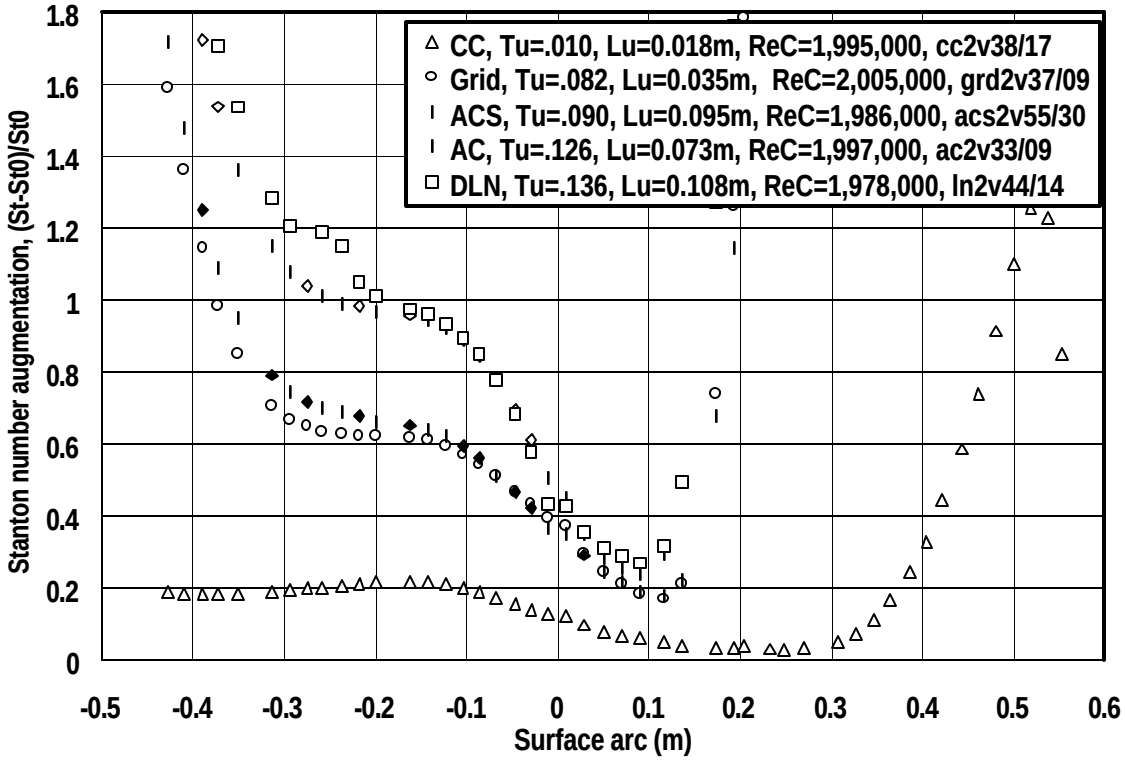

Figure 14. Effects of mock combustor turbulence characteristics on Stanton number augmentation and location of transition, Re_C = 2,000,000

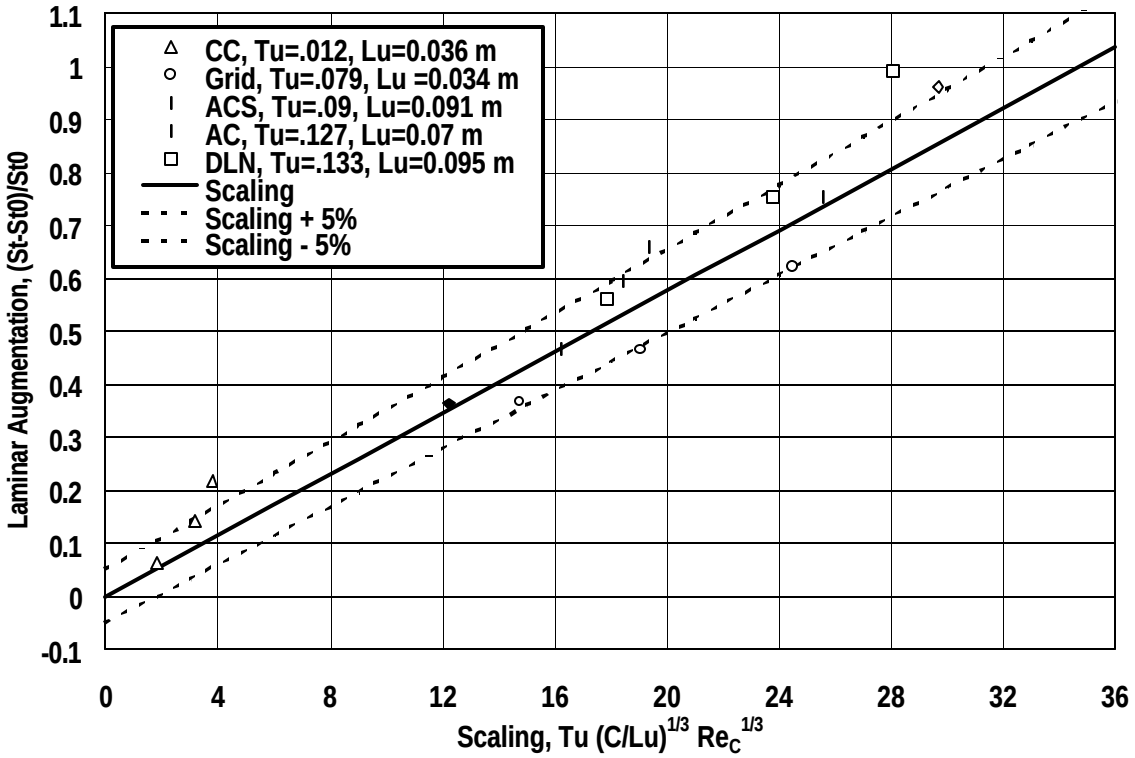

Figure 15. Correlation of turbulence on pressure surface Stanton number augmentation

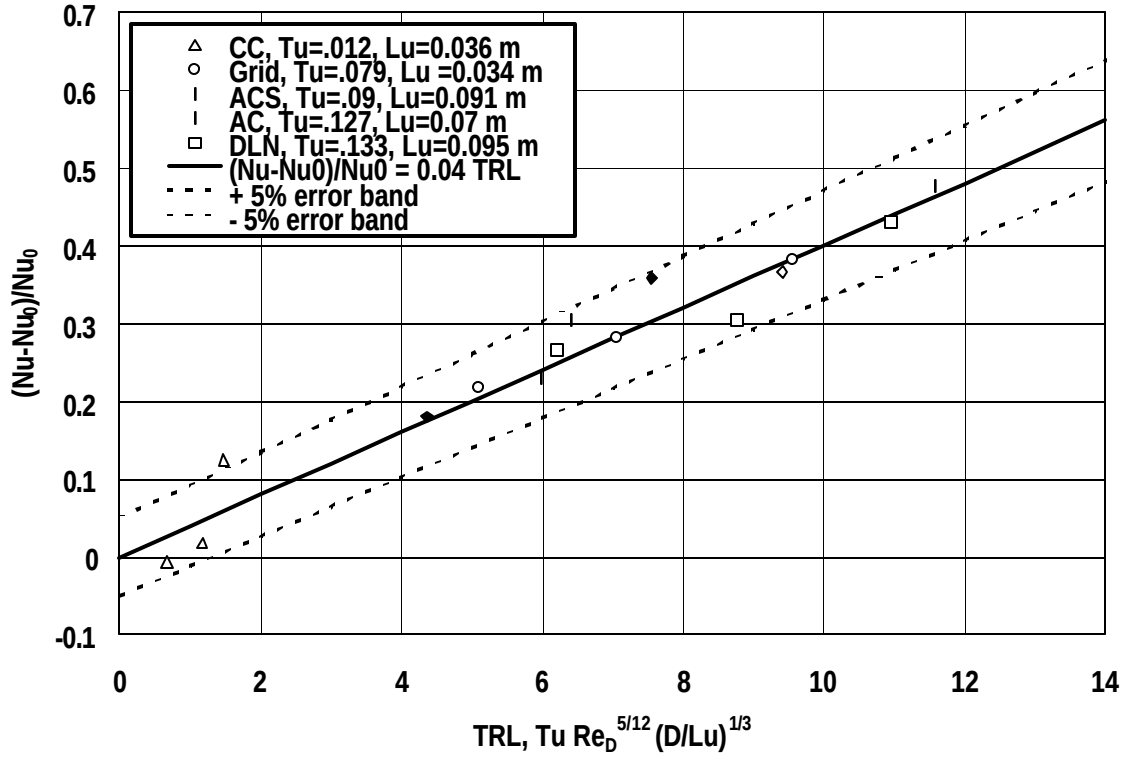

Figure 16. Correlation of turbulence on stagnation region Stanton number augmentation

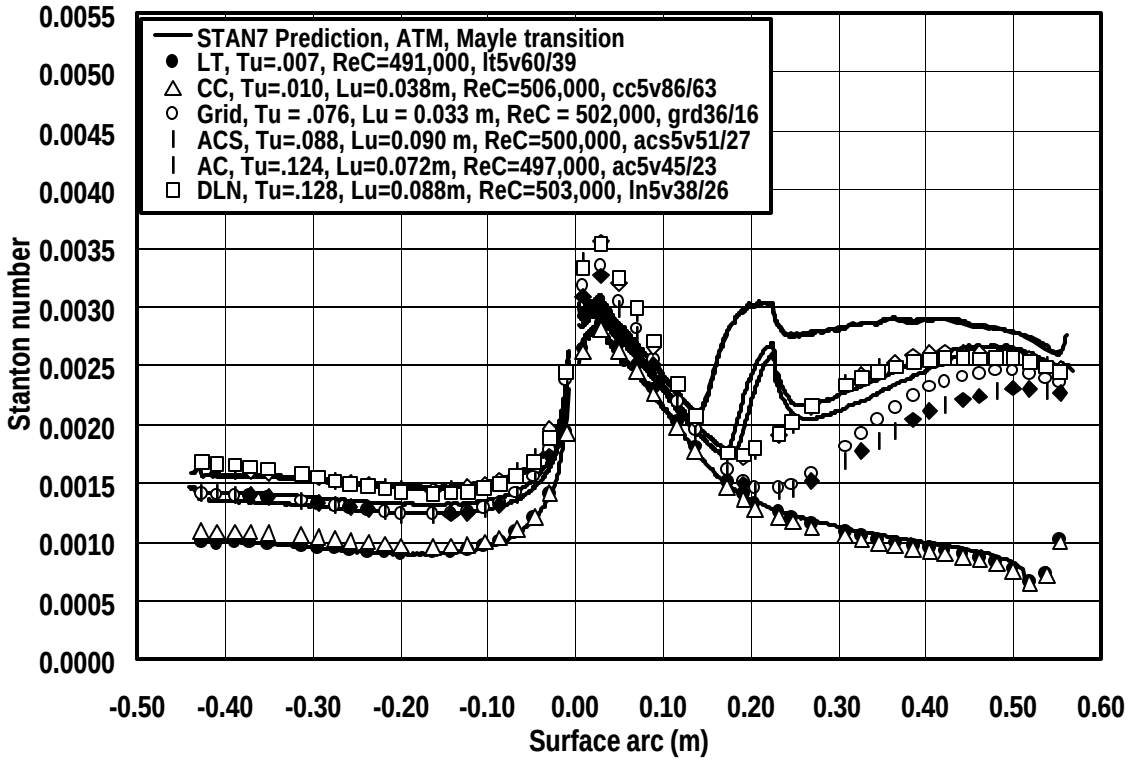

Figure 17. Prediction of turbulence effects on vane Stanton number distributions using STAN7 with ATM and Mayle (1991), Re_C = 500,000

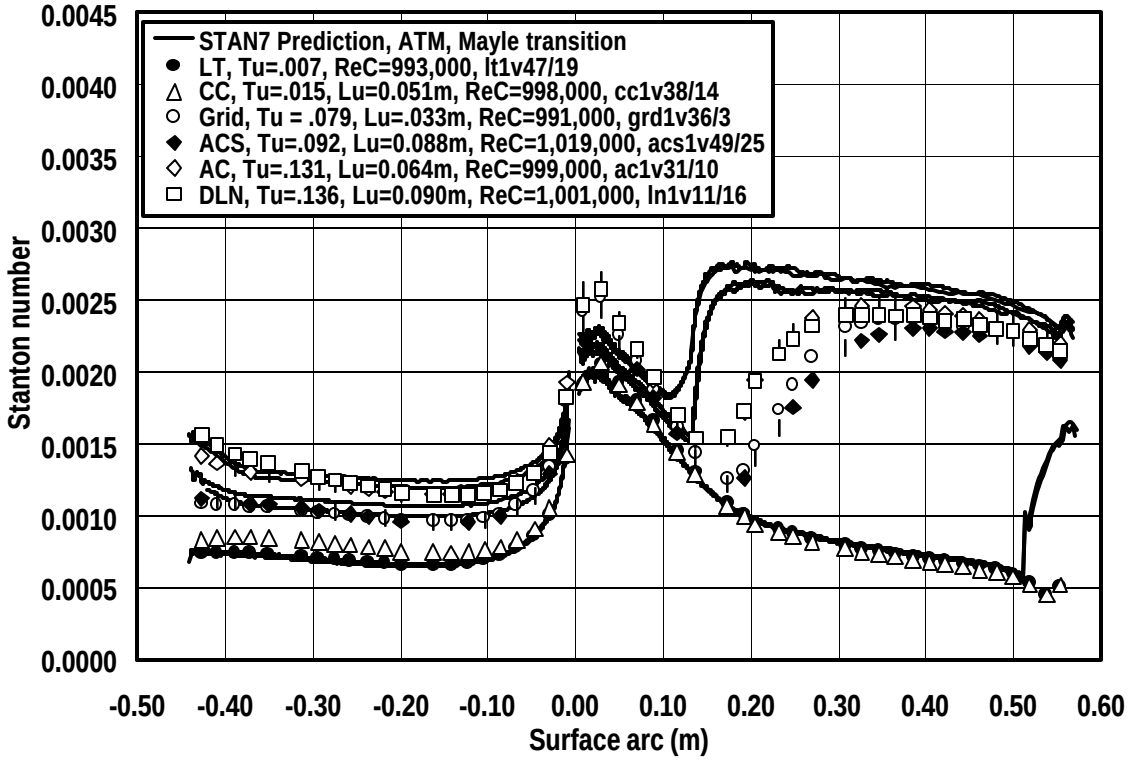

Figure 18. Prediction of turbulence effects on vane Stanton number distributions using STAN7 with ATM and Mayle (1991), Re_C = 1,000,000

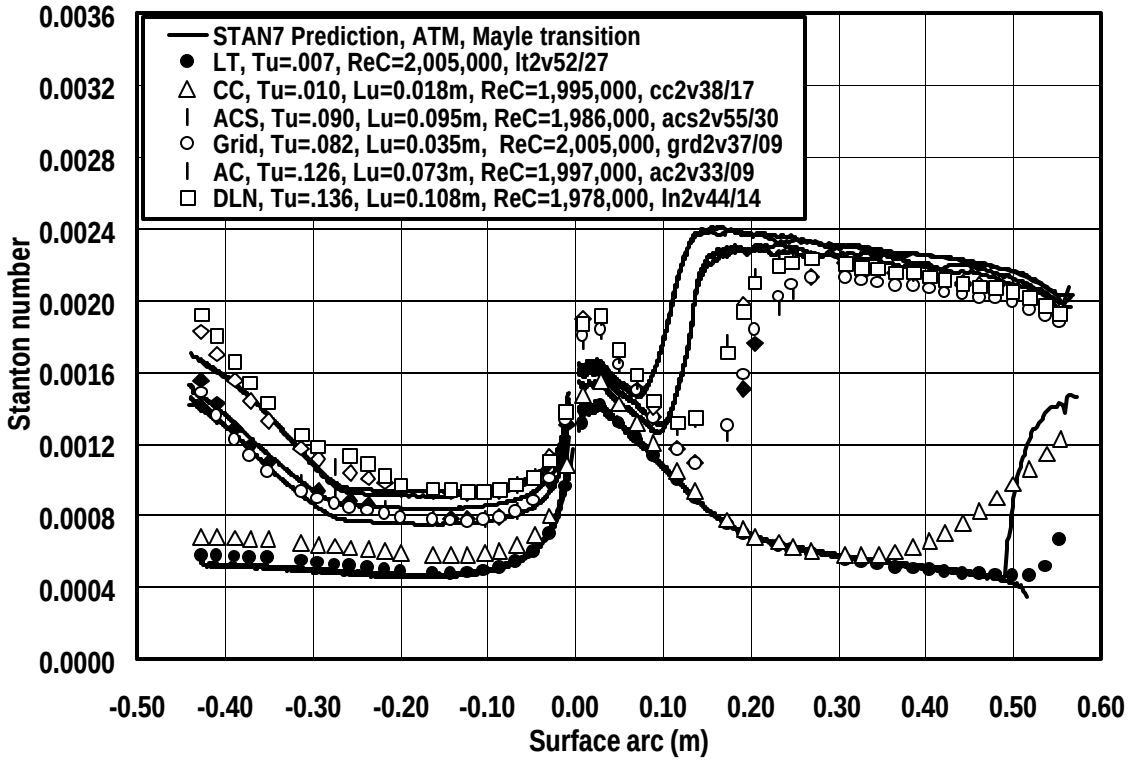

Figure 19. Prediction of turbulence effects on vane Stanton number distributions using STAN7 with ATM and Mayle (1991), Re_C = 2,000,000

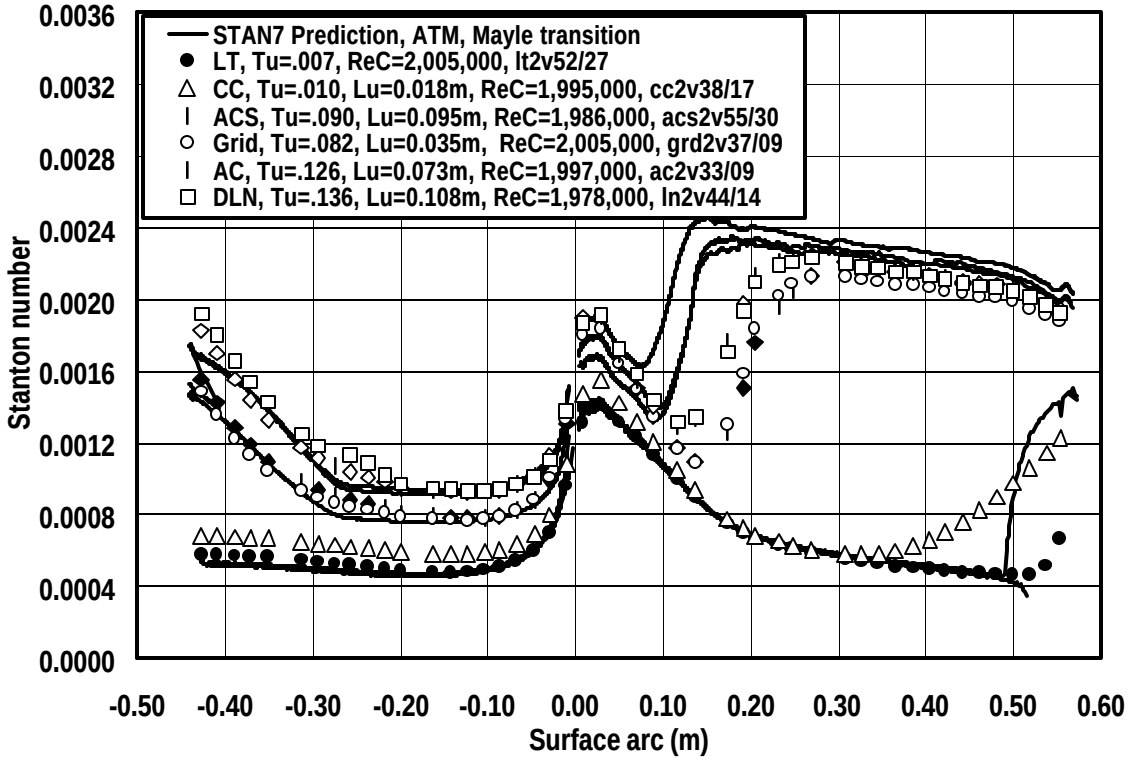

Figure 20. Prediction of turbulence effects on vane Stanton number distributions with stagnation region model, Re_C = 2,000,000

Abstract

Assessment of Endwall Flow and Heat Transfer by CFD Analysis

Edward J. Hall Eric Bermingham
Rolls-Royce
Indianapolis, IN

This paper represents the computational portion of a combined experimental and computational investigation designed to reduce the risk associated with developing vane and endwall cooling schemes for new low NOx gas turbine combustion systems. The flatter temperature profiles generated by current and future generation low NOx combustion systems offer some relief to the vane midspan cooling design of nozzle systems. However, the temperatures experienced along the endwall surface will be significantly higher and represent an area of increased risk. Consequently, cooling designers will need better methods to predict endwall heat transfer and film cooling. In addition, the pressure gradients along endwall surfaces can affect secondary and film cooling flows and sweep away film cooling coverage.

A computational analysis was performed on the University of North Dakota large scale low speed linear turbine cascade using ADPAC, a 3-D Reynolds Averaged Navier Stokes (RANS) code. Values of Stanton number and heat transfer coefficient were calculated on the vane and endwall for comparison to experimental results. The effect of grid size, turbulence model, and Reynolds number was investigated. Large scale simulations involving CFD models as great as 9 million mesh points were employed to sort out issues related to the accurate prediction of endwall heat transfer in high Reynolds number flow. After grounding the computational results to the experiment, the code will be used to study heat transfer on actual engine geometries and operating conditions.

The complete paper includes results for the cascade contributed from variations in simulation mesh size, turbulence model, Reynolds number, and freestream turbulence level. Qualitative and quantitative comparisons with the test data are included to validate the simulation methodology.

Example Mesh System

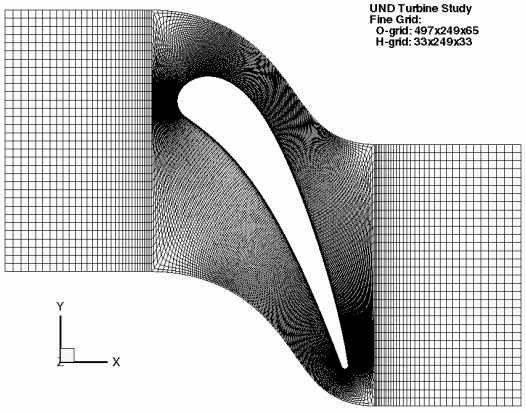

Endwall Heat Transfer Prediction

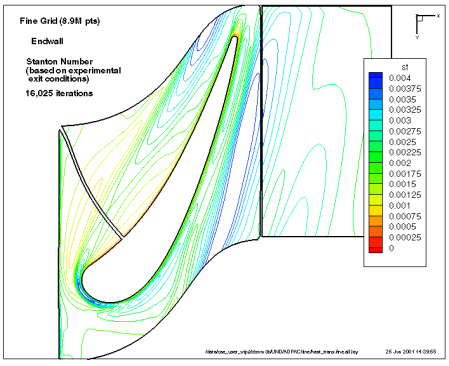

Attenuation of Hot Streaks and Interaction of Hot Streaks with the Nozzle Guide Vane and Endwall

1 March 2001 to 1 September 2001
Semi-Annual Report

Contract Number 01-01-SR092

D. G. Bogard, PI
Mechanical Engineering Department
University of Texas
Austin, TX 78712

K. A. Thole, Co-PI
Mechanical Engineering Department
Virginia Tech
Blacksburg, VA 24061

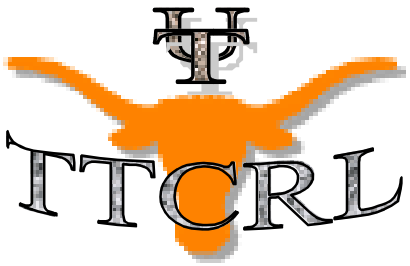

Attenuation of Hot Streaks and Interaction of

Hot Streaks with the Nozzle Guide Vane and Endwall

Semi-Annual Report

David G. Bogard, University of Texas-Austin, Principal Investigator;
Karen A. Thole, Virginia Tech, Co-principal Investigator;
Sean Jenkins and Krishnakumar Varadarajan, University of Texas, Student Researchers
Severin G. Kempf and Daniel G. Knost, Virginia Tech, Student Researchers; and

Contract Number 01-01-SR092
Clemson University Research Foundation
South Carolina Energy Research and Development Center
Clemson University
Clemson, SC 29634-5702

Dec. 3rd, 2001

This report was prepared with the support of the US Department of Energy,

Morgantown Energy Technology Center,

Executive Summary

AGTSR ANNUAL REPORT

Turbulence and Turbine
Cooling Research Lab
Department of Mechanical Engineering
University of Texas
Austin, TX 78712
Phone: (512)471-3128
Fax: (512)471-8727

VT Experimental and Computational
Convection Lab (VTExCCL)
Mechanical Engineering Department
Virginia Tech
Blacksburg, VA 24061
(540)231-7192
(540)231-9100

Project Title:	Attenuation of Hot Streaks and Interaction of Hot Streaks with the Nozzle Guide Vane and Endwall
AGTSR Subcontract No.:	Contract Number 01-01-SR092
Principal Investigator:	David G. Bogard, University of Texas-Austin
Co-Principal Investigator:	Karen A. Thole, Virginia Polytechnic Institute and State University
UT Research Students:	Sean Jenkins and Krishnakumar Varadarajan
VT Research Students:	Severin G. Kempf and Daniel G. Knost
Subcontract Information:	
	First Year Start Date: March 1, 2001
	AGTSR First year contract value: $160,495

STATUS AND RESULTS FOR THE REPORTING PERIOD

Task 1 **Initial Planning meeting with industrial partners**

Although we could not organize an initial planning meeting that could be attended by all industrial partners, industrial partners were consulted about the design of film cooling configurations and rough surface simulations to be used in this study.

Task 2 **Benchmark hot streak measurements**

No work has been done on these tasks during this reporting period.

Specific Tasks at Virginia Tech

Task 3 **Interaction of a hot streak / temperature gradient with the endwall**

Preliminary testing is in progress at Virginia Tech to generate the desired hot streaks / temperature profiles to study. Work has centered on verifying the flow field entering the turbine section and determining the required heater settings to generate a range of two-dimensional temperature profiles. Flow measurements at the vane inlet or endwall heat transfer effects have not been conducted during this reporting period.

Task 4 **Modify endwall test surface to include film cooling holes**

During this period an endwall film-cooling pattern has been designed. The design is a result of input given by industrial partners participating in the project (Pratt & Whitney, GE, and Rolls-Royce). Arrangements are being made to have the proposed endwall manufactured.

Task 5 **Endwall film cooling performance tests – with isothermal conditions**

No work was done on this task during this reporting period

Task 6 **Endwall film cooling performance tests – with a steep temperature gradient**

No work was done on this task during this reporting period

Task 7 **CFD simulation of baseline hot streak/vane interaction**

A model of the test section without either the slot or the film-cooling holes has been developed using commercial software by FLUENT Inc. The focus of these calculations has been to achieve an understanding of the thermal field passing through the turbine vane passage. The model will next be modified to include a leakage slot and film-cooling holes.

Specific Tasks at the University of Texas at Austin

Task 8 **Installation of a hot streak generator and baseline tests**

Design of hot streak generator and purchase of the required components has been accomplished. Further work will be required to install the generator in a wind tunnel section.

Task 9 **Effects of the vane on the hot streak attenuation**

No work was done on this task during this reporting period

Task 10 **Effects of the hot streak on vane film cooling performance**

No work was done on this task during this reporting period

Task 11 **Roughness effects on film cooling performance**

A rough surface was designed to appropriately simulate the roughness on a turbine airfoil in a ground based gas turbine engine. Simulated rough surfaces were constructed.

Task 12a **Interaction of the hot streak with a film cooled rough surface**

No work was done on this task during this reporting period

Task 12b Improved hot streak dispersion with modified coolant injection

No work was done on this task during this reporting period

Industrial Contact

Direct industrial interaction has taken place during this reporting period in several modes. The University of Texas has interacted with Pratt & Whitney in their rough surface design. There have been a number of exchanges between Virginia Tech and the industrial partners including Pratt & Whitney, GE, and Rolls-Royce on the design of the endwall film-cooling hole pattern. In early October, Pratt & Whitney visited Virginia Tech to discuss their current contract as well as the DOE work.

Introduction

This research program has a focus on how the non-uniform temperature profiles and hot streaks exiting the combustor interact with the first nozzle guide vane and endwall in a turbine. There have been numerous previous studies of hot streaks, but most of these studies have been directed at the effects of the hot streak on the first stage rotor. These studies generally assumed that the hot streak is undisturbed as it passes through the nozzle guide vane passage. None of these studies have addressed the effects of the interaction of a hot streak with a highly film cooled vane, or the interaction with the endwall. This is of concern for a number of reasons. First, as the hot streak interacts with a highly cooled vane, mixing between the coolant and hot streak will significantly attenuate the maximum hot streak temperature, with obvious advantages. The interaction of a hot streak with flow near the endwall is of concern because of the potential of very hot fluid being drawn to the wall by secondary flows. There have been no previous studies that demonstrate the mechanisms by which this occurs, and quantifies the severity of the effects on the wall. Furthermore, high mainstream turbulence would be expected to significantly increase the dispersal of hot streak fluid as passes through the vane passage. Finally, surface roughness due to extended operation of a turbine is expected to significantly affect the film cooling performance on the vane, and hence affect the ability of the film cooled vane to withstand the impact of a hot streak. These high mainstream turbulence and surface roughness effects will also be investigated in this research program.

Project Overview

This report describes progress during the first six month period in this project. However, because of delays in contract negotiations, the contract for this work was not finalized at the University of Texas until June 2001, and a month later at Virginia Tech University. Consequently, progress over the first six months was limited.

The primary concern at the start of this project was the design, construction, and testing of facilities specific to this project. Generation of simulated hot streaks was first priority at both the UT and VT facilities. At Virginia Tech the generation of two-dimensional hot streaks located at the at the centerline and close to the endwall was tested using the simulated combustor facility. At the University of Texas the heater hardware and installation technique for generating a simulated hot streak was designed. Further tasks that were addressed was the design of the film cooling configuration to be used on the endwall at Virginia Tech and the design of the rough surface configuration to be used on the vane at the University of Texas. CFD simulation of the two-dimensional hot streak was completed at Virginia Tech. Review of progress in specific Tasks follows.

Task 1 Initial Planning meeting with industrial partners.

We tried to arrange an initial planning meeting with representatives from GE, Pratt & Whitney, and Rolls-Royce at Virginia Tech University in early October, but the companies were not able to send representatives to Virginia Tech as the same time. In lieu of this common meeting, we have discussed designs for this project with company representatives with phone conversations. Specifically, film cooling configurations to be used in the Virginia Tech facility for endwall cooling were discussed with representatives from GE, Pratt & Whitney, and Rolls-

Royce. The rough surface design to be used on the vane tests at the University of Texas was discussed with representatives Pratt & Whitney.

Specific Tasks at Virginia Tech

Task 3 Interaction of a hot streak / temperature gradient with the endwall

Preliminary work is being conducted on hot streak and temperature profile generation at the Virginia Tech ExCCL laboratory. Work has been conducted preparing the wind tunnel and data acquisition systems; surveying the capability of the current wind tunnel configuration, and making the needed adjustments. Preliminary thermal field profiles have also been produced. The following discussion is a description of the wind tunnel facility and the needed modifications for this study.

VT ExCCL Wind Tunnel Facility and Instrumentation

The VTExCCL wind tunnel arrangement can be seen in Figure 1. The wind tunnel is a 9X scale, closed loop system with a combustor simulator and a linear cascade first stage vane section. After flowing through the primary heat exchanger, the flow is split into a top and bottom bypass flow and a main channel flow. A perforated plate provides the needed pressure drop to ensure the correct mass flow split to the coolant and main channel. This project uses bypass flow only for slot and endwall film-cooling injection at the vane inlet plane. Progress on the endwall cooling hole design and correlation with the industrial partners is further discussed in Task 4.

The VTExCCL wind tunnel contains 18 heater elements in the main channel (representing the main gas path) flow. There is a total power output of 55kW. To obtain adequate control over the profiles, the heaters were re-wired into a delta-configuration, giving three separately controlled banks of six heater elements. Each bank can provide 18.3 kW of heat input to the flow.

To further the capabilities of the thermal conditioning for the endwall-film-cooling and slot flows, a 15-ton chiller was purchased (with funds outside of this DOE contract) and installed into the VTExCCL wind tunnel. This chiller can provide a coolant temperature as low as 5°C while the mainstream temperature is nominally 45°C. The chiller capability will provide the needed temperature differential to insure accurate effectiveness measurements.

The experiments conducted for the DOE work will use only the slot ejection in the bypass loop, accounting for 2% of the total mass flow and endwall film-cooling. Only the bottom plenum will provide the endwall film-cooling, which requires an additional 1.5% of the total mass flow. A new design for the perforated plate was required to insure the needed pressure drop required to give the proper mass flow splits between the primary and coolant channels. An analytical flow model was generated to aid in the design of a new perforated plate. The new perforated plate has been constructed, installed, and benchmarked. Flow field measurements have verified the correct mass flow split and flow uniformity in the pitch and span direction.

The wind tunnel was instrumented with thermocouples before the primary heat exchanger and before the heater elements. A number of new thermocouple probes were built to aid in the thermal field measurements. A more sophisticated program was also written to speed up the data

acquisition process. A new module and block were added to the current data acquisition chassis to allow for simultaneous pressure and temperature measurements. This will allow for a real time monitor inside the cooling hole plenums and of the pressure distribution around the vane section, ensuring matched engine conditions.

Previous studies for the VTExCCL wind tunnel facility have involved film-cooled combustor liner walls as shown in Figure 2. There are four panels providing coolant flow. Since this is not the focus for the DOE study, panel covers are being designed and will be installed to guarantee no coolant leakage into the main flow. These covers will be fastened to the existing panels on both the top and bottom bypass loops.

Preliminary Temperature Profiles

A number of different temperature profiles were generated using the heater banks with various control settings. Measurements of the thermal field at the entrance to the turbine were taken using a thermocouple rake. At the time this data was taken, the chiller was not yet installed and, as such, the heaters alone were used to generate these profiles. To ensure comparisons can be made for different conditions, the measured temperature was normalized in the following manner:

$$\theta = \frac{\left(T - T_{in}\right)}{q_t \Big/ \dot{m} c_p} \tag{1}$$

In this equation, T_{in} is the temperature upstream of the heater and q_t is the total heat provided by the heater elements.

Figure 3 shows three two-dimensional profiles generated to date. Note that the profiles were uniform across the pitch (circumferential in the turbine) direction. The flat profile shows a baseline case. Two peaked profiles are also depicted. One profile is near midspan and one is near the endwall. These profiles illustrate the ability to move the peak to a desired location between the midspan and endwall.

Task 4 Modify endwall test surface to include film cooling holes.

Design of Film-Cooling Pattern

A film-cooling pattern has been designed for the endwall. Input from participating industrial partners, which includes Pratt & Whitney, GE, and Rolls-Royce, was solicited and these ideas were combined into one final design. The proposed design can be seen in Figures 4-7 with a summary of relevant parameters given in Tables 1 and 2. The design consists of an upstream slot, a leading row of holes, and a unique film-cooling pattern in each of the two passages. Two unique passages were designed to account for the presence of a "gutter" in one of the passages. The gutter represents the region in which the mating of two turbine vane platforms occurs. For the DOE studies, no flow will exit this gutter. Holes were placed outside of a manufacturing fillet. This fillet will not, however, be used in the experiment.

Traditional, round holes are being used because this is the preliminary endwall film-cooling study being performed at Virginia Tech. This will provide data for a baseline study in the event that shaped holes are studied in the future. All film-cooling holes eject at an angle of 30 degrees with respect to the surface as is shown in Figure 6.

The leading row of film-cooling holes is designed to provide cooling to the forward part of the endwall. The holes between the vanes inject in the same direction as the flow turning of the vanes. The holes in front of the vanes serve as leading edge blockers and inject in the direction with the main flow.

The passage without the *gutter* will be referred to as passage one and the passage containing the gutter will be referred to as passage two. The holes in passage one are designed to lie along and inject normal to the iso-velocity lines. In the interest of simplifying the manufacturing process, the holes were placed along straight lines, which approximate these iso-velocity lines. This approximation was developed by drawing straight lines between the points where the iso-velocity contours intersect the separation lines. As can be seen in Figure 5, this method provides a reasonably good approximation of the iso-velocity contours. The first hole (closest to vane) in each row ejects parallel to the vane. The subsequent holes in each row eject with the main flow and in a direction normal to the lines approximating the iso-velocity contours.

The gutter is designed to model the separation between plates carrying the vanes. Under normal circumstances, one would expect leakage flow through the gutter. However, in this study no flow will be injected from the gutter. Once again, the decision not to allow flow through the gutter was made in the interest of performing a baseline study. In passage two the holes nearest to the pressure side of the vane lie on the iso-velocity contours. The holes then extend toward the front of the passage at a spacing of three hole diameters. All holes in this passage, with the exception of hole 78, eject at a compound angle of zero degrees.

The slot is flush with the endwall. The slot was incorporated into the design to simulate leakage flow between the combustor and the turbine. As can be seen in Figure 6, the slot injects at a surface angle of 45 degrees.

General Plastics, of Tacoma, Washington, has agreed to provide us with samples of the foam that the test endwall will be cut from. Huffman Corporation, in Clover, South Carolina, has been identified as a vendor capable of reproducing the proposed cooling design. Huffman is in the process of making test cuts and will then provide us with an estimate for cutting the pattern.

The combustor simulator in our wind tunnel is currently configured for a particular test case different than that needed for this DOE project. These tests should conclude within the next month. The tunnel will then be partially disassembled and the first case, consisting of the slot but no endwall film-cooling holes, will be installed. The case without film cooling will then be conducted. Simultaneously, plenums used to feed the endwall film-cooling holes will be designed. Once, the testing phase without film-cooling is completed, the film-cooling endwall and the new plenums will be installed.

Task 7 CFD simulation of hot streak/vane interaction.

A computational model of the test section without either the slot or the film-cooling holes has been developed using commercial software by FLUENT Inc. The solution domain may be seen in Figure 8. The passage was modeled to midspan and a symmetry condition was applied at midspan. Also, periodic conditions were applied in the stagnation plane and in the trailing plane.

The focus of these computations has been to achieve proper grid spacing to accurately model boundary layer turbulence and achieve convergence. A temperature profile that was generated in the test facility by Severin Kempf was used as an inlet boundary condition. This profile may be seen in Figure 9. A uniform velocity field was also specified at the inlet of the domain.

Results from the simulation are shown in Figures 10-12. The thermal fields in the stagnation plane and midway through the passage are shown, as well as the surface temperature distribution on the vane and on the endwall. The velocity field in the near-wall region of the stagnation plane is also shown.

As can be seen, there is very little distortion of the temperature field in the near-wall region. A distortion of the temperature field down towards the endwall and up towards midspan is visible in Figure 10, but the thermal field remains relatively stratified. This is because the velocity profile is relatively uniform near the endwall. As a result, there is not a large total pressure gradient near the wall. The incoming total pressure gradient dictates the secondary flow field, which ultimately dictates the thermal field distortion.

The other factor contributing to low thermal transport in the nearwall region is the fact that the maximum temperature is at midspan. This is well out of the region of influence of the horseshoe vortex. The horseshoe vortex can be seen in Figure 12. It is expected that if the maximum temperature is shifted closer to the endwall, a more pronounced distortion of the thermal field will occur. These results are expected to change with the introduction of the upstream slot flow.

Specific Tasks at the University of Texas at Austin

Task 8 Installation of a hot streak generator and baseline tests.

The hot streak will be introduced into the test facility using an electric coil heater. The hot streak will have a diameter of approximately 0.35 pitch, and will be heated to a temperature ratio of $T_{hs}/T_{\infty} = 1.1$, and will be introduced so that the stagnation pressure profile is uniform. Although this is a small temperature ratio, it is more than sufficient to provide an accurate marker of the hot streak fluid, and is arguably more representative of ground based gas turbines. A hot streak diameter of 0.35 pitch was chosen to reduce the amount of overall heat input into the wind tunnel, thus reducing the load on the heat exchangers required to maintain overall room temperature conditions in the tunnel. We believe that a hot streak of this size is a good representation of the hot streak found in the actual engines.

The hot streak will be produced by an electric coil heater situated in the wind tunnel flow approximately 0.5 m upstream of the simulated vane, shown schematically in Figure 13. The electric coil heater is a nominally 200 x 200 mm square duct heater with a heating capacity of 7kW, which may be run at full and half power. This allows a temperature ratio of 1.1 or 1.05 where the reference temperature is approximately 300 K, or a ΔT of 30° C or 15° C respectively. The square heater section contains 80/20 nichrome heating elements, spaced to heat the flow uniformly. This heating element will be contained within a square duct section with a transition section leading to an 200 mm diameter round section. The apparatus will be suspended within the wind tunnel using steel rods and electrical conduit to supply the appropriate current to the heater. The circuit, control and breaker boxes will be mounted on the exterior of the tunnel. The pitch position of the hot streak will be adjustable with three hot streak positions to be tested: aligned with the stagnation line, and ± 0.25 pitch from the stagnation line. Maintaining a

uniform mean flow and low turbulence are highly important factors in this study. Honeycomb material followed by screening will be used to remove the larger scale eddies allowing viscous effects to dampen smaller turbulence scales.

Task 11 Roughness effects on film cooling performance.

The rough surface to be used in this study was designed based on information from two papers that surveyed typical turbine airfoil roughness characteristics: Bogard et al. (1998) and Bons et al. (2001). Both these papers point out that there are a number of different measures for characterization of surface roughness. Most theoretical correlations for the effects of surface roughness on wall shear or heat transfer are based on the "equivalent sand grain roughness". This is not a direct geometrical measure of the roughness, but rather a measure based on the effect of the roughness on the flow in terms of the sand grain size that would have the same effect on the flow. Consequently, sand grain roughness can not be determined directly from a measurement of the geometry of the roughness. However, ultimately the surface roughness used in the laboratory simulation should have an equivalent sand grain roughness (k_s) that is matched to the k_s for the actual turbine airfoil to ensure similar flow and heat transfer effects.

As noted by Bons et al. (2001), there are a number of different geometric measures of surface roughness magnitude. A commonly used geometric measure of surface roughness is the "centerline average roughness," (R_a) defined as:

$$R_a = \frac{1}{N}\sum_{i=1}^{N}|y_i|$$

where y_I is the distance from the local surface height to the mean height.

From their survey of operational turbine airfoils, Bons et al. (2001) found that the centerline average roughness ranged from R_a = 3 μm to 40 μm. This was consistent with the sample of relatively rough turbine airfoils studied by Bogard et al. (1998) who found a range of R_a = 10 μm to 40 μm. Both studies found that the roughness not only varied according to the operating history of the engine, but on a given airfoil it varied significantly with position on the airfoil. We elected to simulate an airfoil with a roughness level of R_a = 20 μm, i.e. not the maximum level measured on actual airfoils, but a large level.

The effect of surface roughness on flow and heat transfer is not determined solely by R_a , but is also strongly dependent on the shape and spatial distribution of the roughness elements. For example, a shallow angled cone is not expect to have the same effect as a cylindrical element even though they have the same roughness height. To account for this, Sigal and Danberg (1990) developed a roughness shape and density parameter, Λ_s, that can be used to predict the equivalent sand grain roughness, k_s, for roughness elements with height k. Although the Λ_s correlation was developed for geometrically regular roughness elements, Bogard et al. (1998) showed that it could be applied to the irregular roughness elements on an operational turbine airfoil. Bogard et al. found the average peak to valley roughness height was $R_z \approx 5R_a$. Note, R_z is a measure of the average roughness height, i.e. $R_z \approx k$. Bons et al. (2001) obtained a similar result, i.e. $R_z \approx 4R_a$ to $8R_a$. Consequently, we elected to use a value of $k/R_a = 5$ for the design of the rough surface.

The shape and density parameter representative of roughness on an operational turbine airfoil was found to be $\Lambda_s \approx 60$ by Bogard et al. (1998). However, Bons et al. (2001) surveyed a much wider range of airfoils, and found that Λ_s ranged from 20 to 1000. A large number of the

samples tested by Bons et al. had a value of $\Lambda_s \approx 150$. Based on the correlation from Sigal and Danberg (1990), the range of $\Lambda_s = 60$ to 150 corresponds to $k_s/k = 0.7$ to 0.2. Consequently we elected to base our rough surface design on a ratio of $k_s/k = 0.5$ which corresponds to $k_s/R_a = 2.5$. Hence the equivalent sand grain roughness for the operational turbine airfoil that corresponds to $R_a = 20$ μm is $k_s = 50$ μm.

The geometric scale factor for the simulated vane is x 9, so the desired equivalent sand grain roughness for the simulated airfoil is $k_s = 50$ μm x 9 or $k_s \approx 0.5$ mm. Based on estimates of the local wall shear at the first row of holes on the suction side of the simulated vane, the roughness Reynolds number for this roughness surface is $Re_k = 60$. This represents a "fully rough" condition, i.e. the flow is dominated by resistance due to roughness rather vane viscous shear.

The actual geometry of the simulated rough surface can be somewhat arbitrary as long as it has the correct equivalent sand grain roughness. We chose to use an array of cones due to the simplicity of constructing this surface and due to previous experience with this surface. The cone surface was designed so that it would have the same k_s/k ratio as for the actual turbine airfoil, i.e. $k_s/k = 0.5$. So the height of the cone elements was set to be $k = 1$ mm. To obtain the appropriate k_s/k ratio, Figure 4 from Bogard et al. (1998) shows that the shape density parameter can have two possible values: $\Lambda_s = 3$ or 70. A value of $\Lambda_s = 3$ corresponds to very closely spaced roughness elements, and as indicated previously, does not correspond to typical turbine airfoil roughness. So the cone array was designed to have $\Lambda_s = 70$.

As derived by Sigal and Danberg (1990), the shape and density parameter is defined as follows:

$$\Lambda_s = \left(\frac{S}{S_f}\right)\left(\frac{A_s}{A_f}\right)^{1.6}$$

where: S = total surface area

S_f = frontal surface area of roughness elements (total)

A_s = wetted frontal surface area for roughness elements

A_f = projected frontal area of roughness elements

For cones with a height to base diameter ratio of $k/d = 4$ (similar to past designs used in our laboratory), the cone area ratio is $A_s / A_f = 3.5$. The ratio S/S_f is dependent on the spacing between roughness elements, p. Assuming a square arrangement of roughness elements, i.e. equal lateral and streamwise spacing between roughness elements, this ratio is:

$$\frac{S}{S_f} = \frac{2p}{d \cdot k}$$

For $\Lambda_s = 70$ the required spacing between roughness elements is $p/d = 1.08$. Hence the roughness configuration has the following dimensions: $k = 1$ mm, $d = 4$ mm, and $p = 4.3$ mm. A schematic of this configuration is given below.

Goals for Next Reporting Period

The goals for the work being done at Virginia Tech for the next reporting period are the following: install the slot configuration into the wind tunnel, define the inlet temperature profiles that will be studied, and construct the endwall film-cooling hole plate. Several temperature profiles will be generated, which will include a flat profile, mid-span peaked, a peak at nominally 30% of the span, and a peak near the wall. The newly installed chiller will be used to generate a large range for the temperature profiles. The chiller provides a cooler inlet temperature to the heater bank thereby allowing more peaked profiles to occur. After these profiles are characterized, endwall heat transfer measurements will begin. Regarding the computational work of this project, the CFD model will be made to include the slot alone and slot/endwall film-cooling configurations. Simulations for the slot flow alone will be run to gain a comparison for tests examining the interaction of the hot streak with the endwall.

At the University of Texas the heater section for the simulated hot streak generation will be installed, and temperature field measurements will be made of the hot streak approaching the vane and through the vane passage. Film cooling tests will be done, with coolant injection from the showerhead alone, and from showerhead combined with downstream holes. The attenuation of the hot streak will be quantified. Film cooling adiabatic effectiveness will be measured for smooth and rough wall conditions.

References

Bogard, D.G., Schmidt, D.L., and Tabbita, M., "Characterization and Laboratory Simulation of Turbine Airfoil Surface Roughness and Associated Heat Transfer," *ASME Journal of Turbomachinery*, Vol. 120, pp. 337-342, 1998.

Bons, J. P., McClain, S. T., Taylor, R. P., and Rivir, R. B., "The Many Faces of Turbine Surface Roughness," ASME Paper 2001-GT-0163, 2001

Ethridge, M. I., Cutbirth, J. M., and Bogard, D. G., "Scaling of Performance for Varying Density Ratio Coolants on an Airfoil with Strong Curvature and Pressure Gradients," *ASME Journal of Turbomachinery,* Vol. 123, pp. 231-237, 2001.

Sigel, A. and Danberg, J. E., "New Correlation of Roughness Density Effects on the Turbulent Boundary Layer," *AIAA Journal,* Vol. 28, pp. 554-556, 1990.

Table 1. Comparison of Engine and Wind Tunnel Endwall Film Cooling Parameters

Feature	WindTunnel (9X)	Engine
Hole Diameter (in)	0.162	0.018
L/D	9.26	10
Gutter Width (in)	0.450	0.050
Slot Width (in)	0.585	

Table 2. Endwall Film-Cooling Parameters for the Wind Tunnel Study

Parameter	Value
Film Hole Surface Ejection Angle (deg)	30
Hole -to- Hole Spacing (diams)	3
p/d - Lead Holes with Main Flow	3
p/d - Lead Holes with Turning	4
Gutter Angle (deg)	45
Slot Location (true chords)	-0.16*C
Slot Surface Ejection Angle (deg)	45
Coolant Flow Rate (% m_{tot}) I.D. or O.D	1.5 (3% total)
Slot Leakage Rate (% m_{tot}) I.D. or O.D.	1 (2% total)

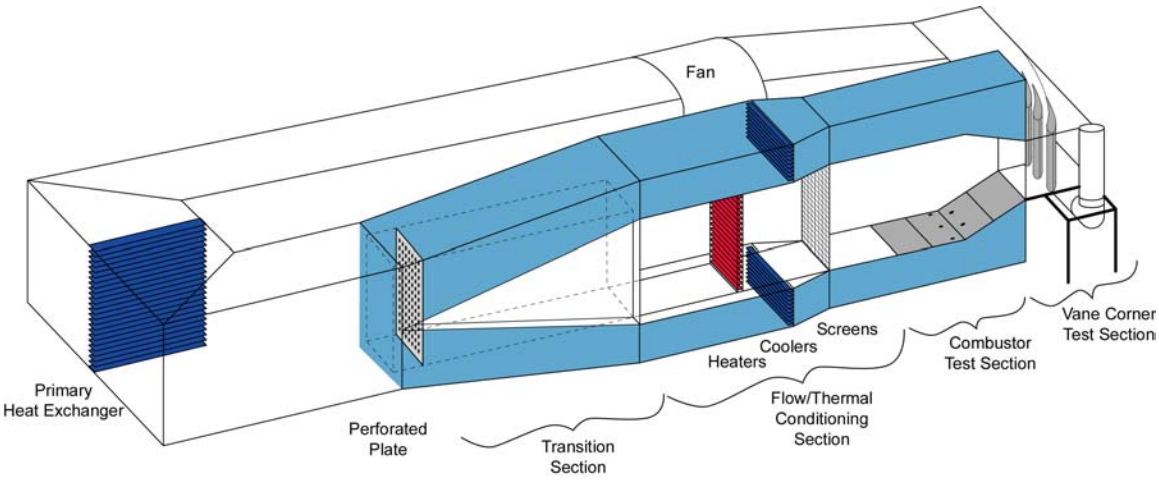

Figure 1. Overview of VTExCCL Wind Tunnel Facility showing complete loop.

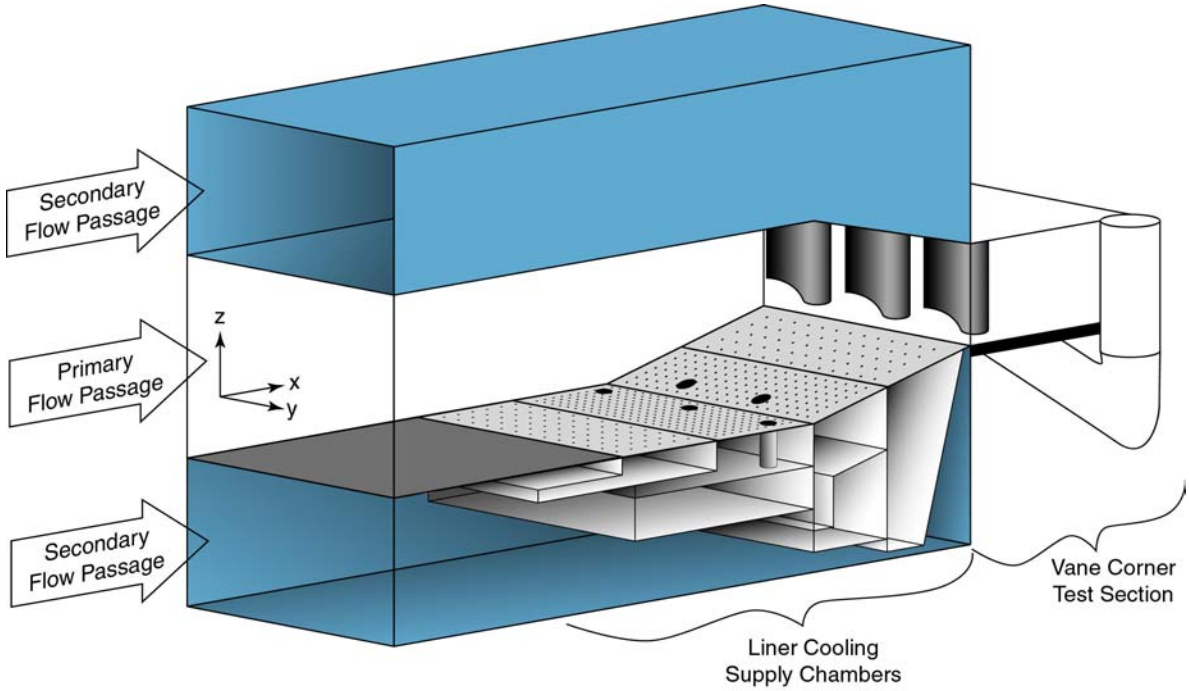

Figure 2. Enlarged combustor simulator section of wind tunnel.

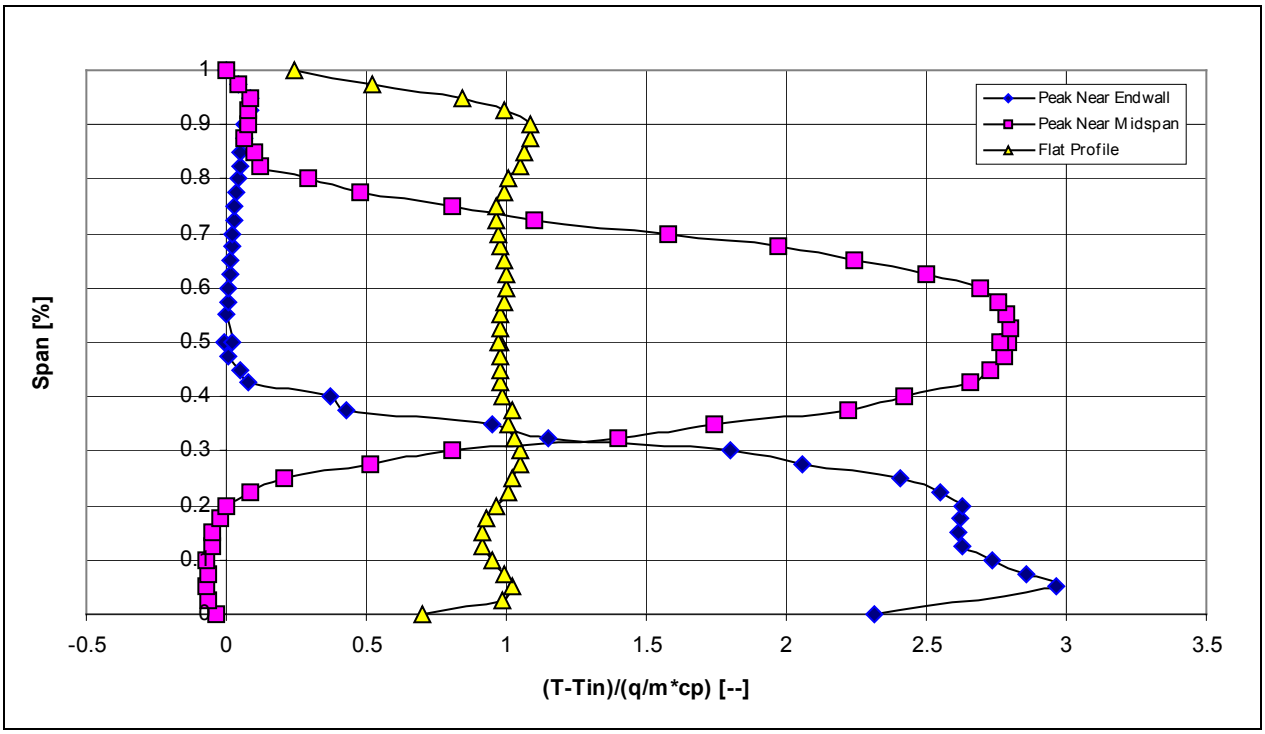

Figure 3. Span (radial) temperature profiles measured at midpitch vane inlet in the Virginia Tech ExCCL wind tunnel.

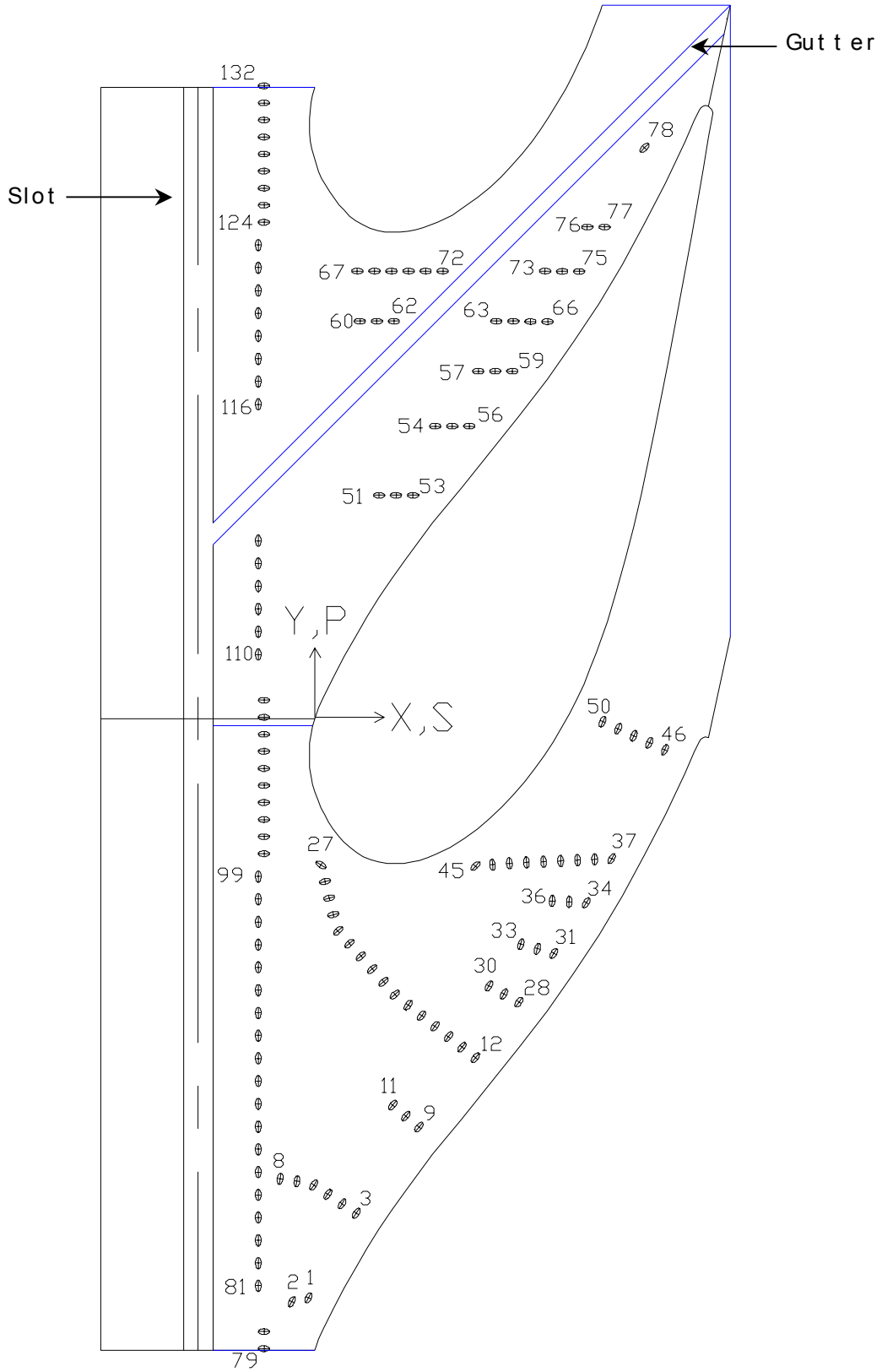

Figure 4. Film cooling pattern that will be installed into the VTExCCL wind tunnel.

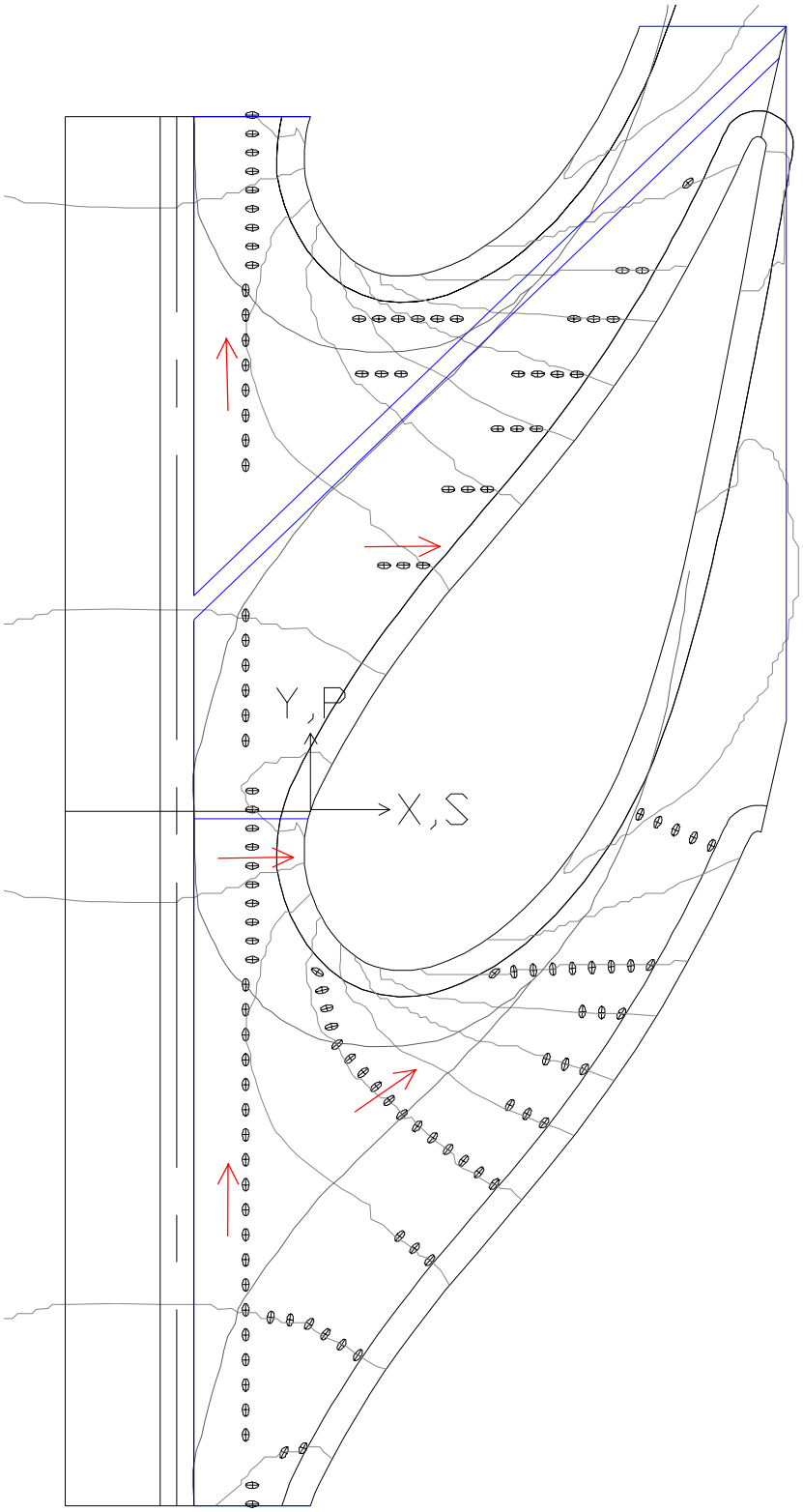

Figure 5. Film-cooling holes shown with iso-velocity contours and separation lines. Red arrows indicate coolant ejection direction. A manufacturing fillet was included to show the location relative to the nearest film-cooling hole.

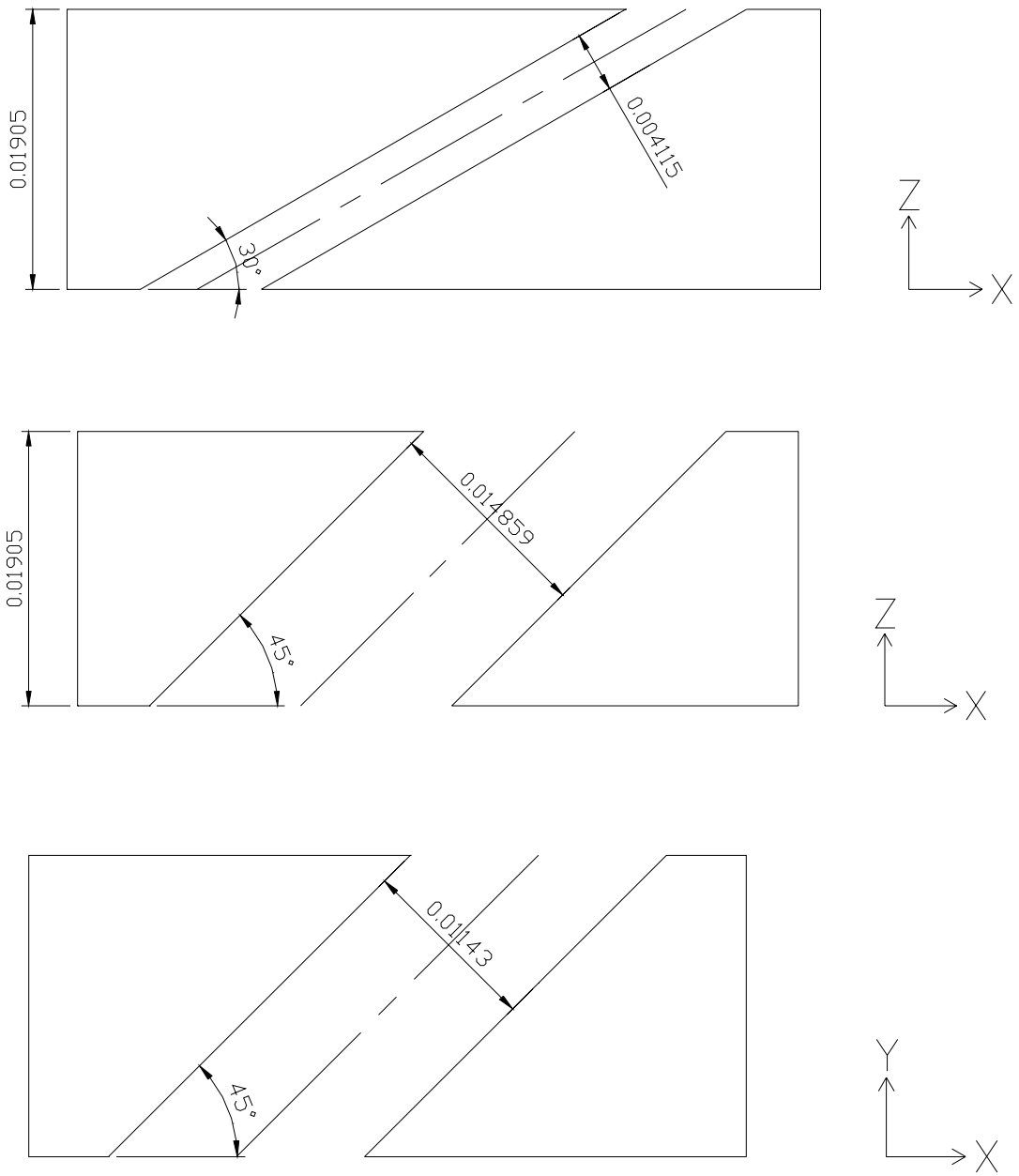

Figure 6. Cross-sectional view of a film-cooling hole (top) slot (middle) and gutter (bottom). Dimensions are given in meters for the scaled-up dimensions of the wind tunnel model.

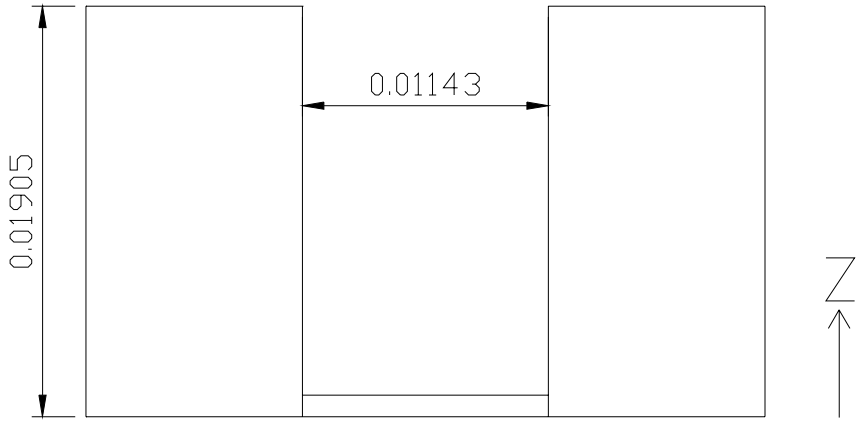

Figure 7. Cross-sectional view of "gutter". Dimensions are given in meters. Note that the gutter will be blocked off (no flow) for the film-cooling experiment.

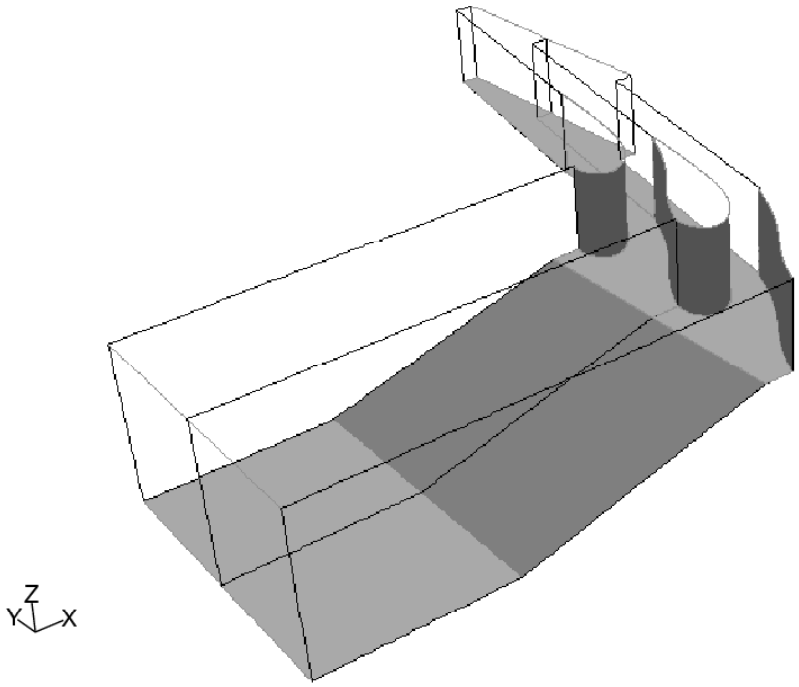

Figure 8. Solution domain for CFD simulations of the inlet thermal field.

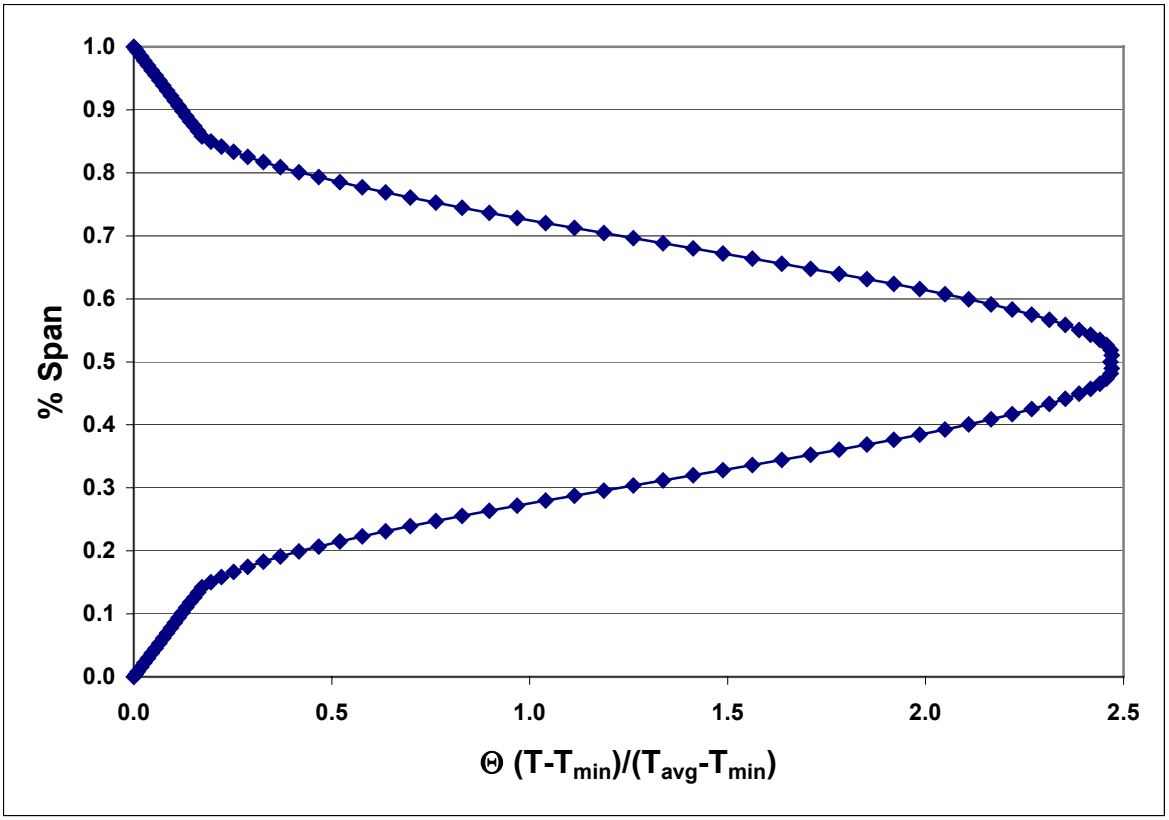

Figure 9. Temperature profile specified at CFD domain inlet. The profile used was similar to that measured in the wind tunnel.

$$\Theta = \frac{T - T_{\min}}{T_{ave} - T_{\min}}$$

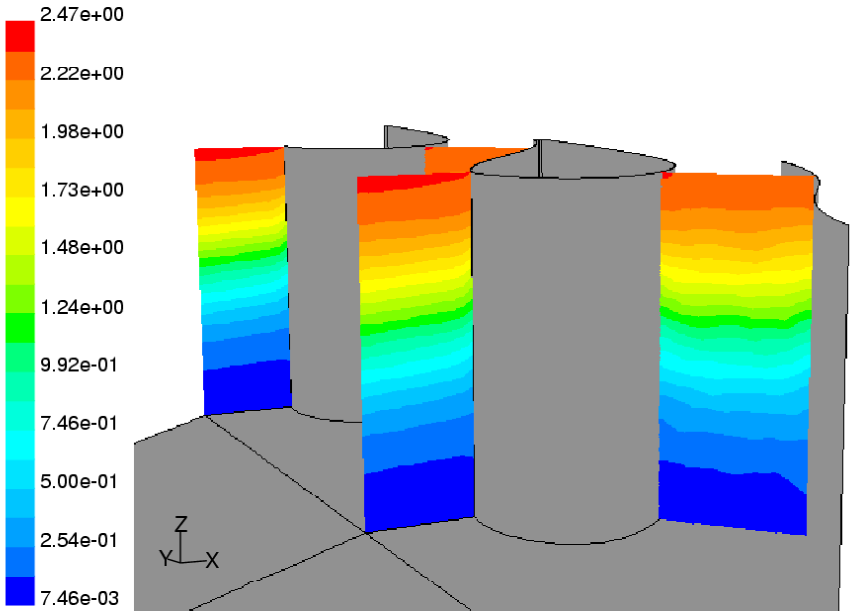

Figure 10. Temperature distribution in the stagnation plane and SS2 plane.

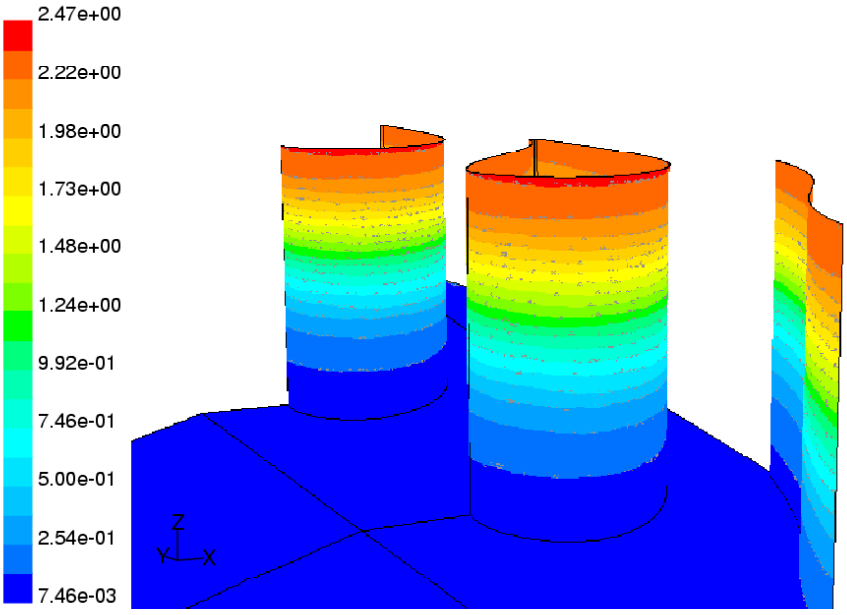

Figure 11. Non-dimensional adiabatic wall temperatures on the vane and endwall.

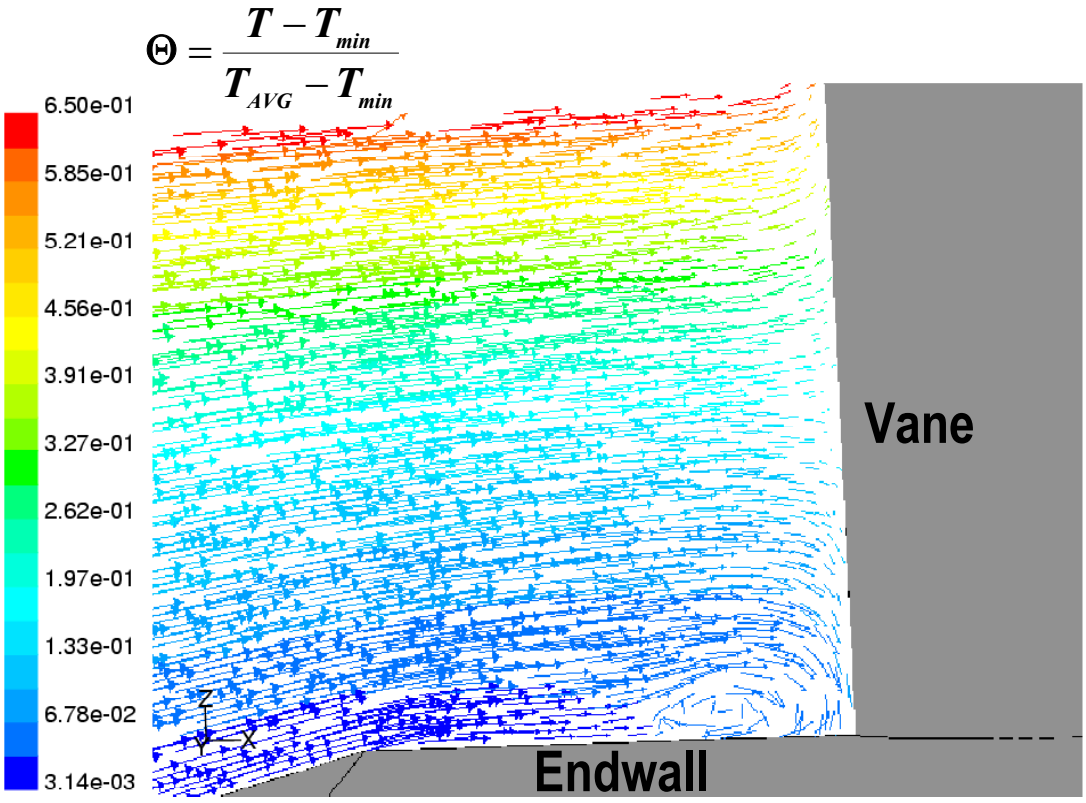

Figure 12. Flow field in the stagnation plane colored by non-dimensional temperature.

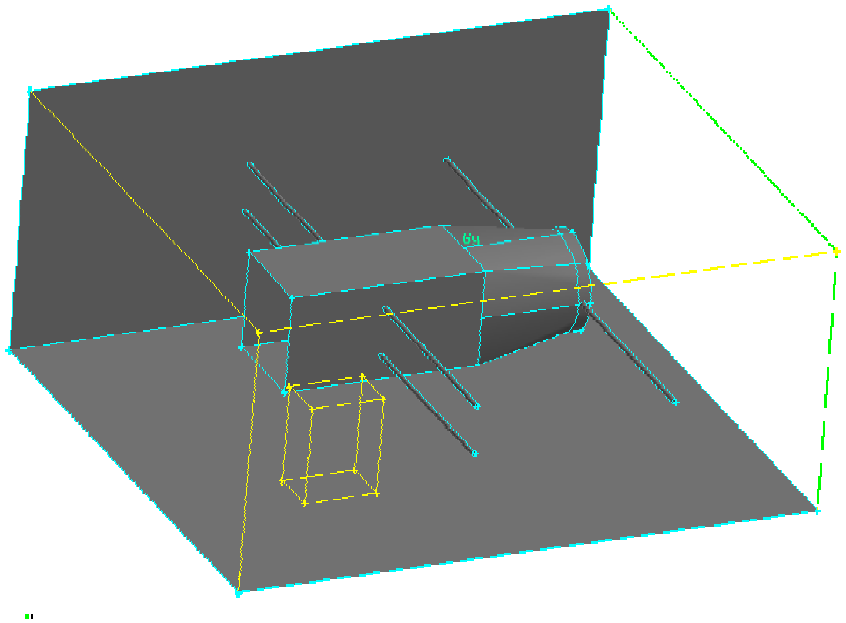

Figure 13. Schematic of heater section for hot streak generation in the University of Texas facility.

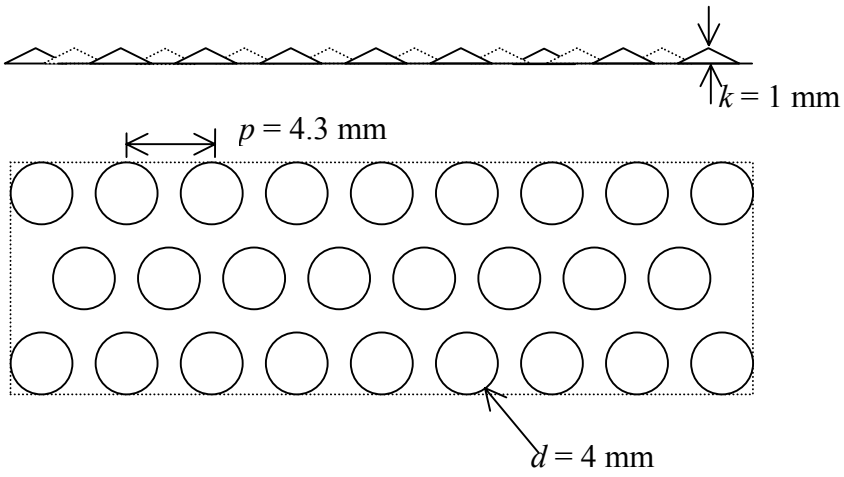

Figure 14: Scale drawing of the proposed rough surface.

Annual Report

For

"Tip Clearance Heat Transfer and Desensitization in High Pressure Turbines"

AGTSR Project # 99-01-SR080

Dr. Jay Kapat and Dr. Alain Kassab
Department of Mechanical, Materials & Aerospace Engineering
University of Central Florida, Orlando, FL 32816-2450
Phone: (407) 823-2179; e-mail: jkapat@pegasus.cc.ucf.edu

Reporting Period: August 1, 2000 – July 31, 2001

This short report is to update the status of this project, which is currently on hold. Since the last reporting, no ***direct*** technical progress has been done.

1. As has been reported informally and discussed in the Minneapolis meeting, the Turbine Research Facility (TRF) at Air Force Research Laboratory has not been available for this project because of the changed priorities at TRF, in spite of an agreement to the contrary in the beginning. Even otherwise, TRF would not have been available for this project as it has been down for component failures. No other appropriate facility could be found for use of this project as either the facility was unavailable for heavy usage and commitment for other projects or the necessary instrumentation was not available.

2. The P/TSP (pressure and temperature sensitive paints) related equipment was already available in TRF for usage as stated in the original proposal. Since TRF is now unavailable, we have to procure the equipment in order to continue this and/or similar projects in the future. Accordingly, through other external grants, an imaging type P/TSP set up has been procured at a cost of about $25,000[1] over the past nine months. The set up has been fully calibrated for imaging application with TSP and the results have been quite encouraging[2]. Most importantly, it has been found that TSP does not suffer from the severe dependence on viewing and lighting angles that is common for TLC (thermo-chromic liquid crystal) technique. This feature is particularly important for study of vane/blade heat transfer. Even in a non-rotating case, the curvature of an aerofoil can cause uncertainties in measurements with TLC. In contrast, TSP technique would provide more accurate results under realistic conditions, as established from the calibration results.

3. Because of unavailability of suitable test facility, decision was taken to have an in-house test facility, and the concept is strongly supported by Siemens Westinghouse and the State of Florida. A rough concept paper has been prepared through discussion with all parties involved over a time period of more than a year, and the final version would be submitted by December 1, 2001. In brief, the plan calls for a facility in excess of 20,000 sqf where heat transfer, aerodynamics, combustion and materials aspects can be studied together in a true multi-disciplinary form, and which would include a high temperature, high pressure and high flow rate combustion system. The plan draws strength from all the AGTSR awards that have been made in the past to the University of Central Florida in different disciplines. Even though complete plan is still under preparation, portions of it have been already approved. One such component is discussed next.

4. With funds from Siemens Westinghouse Power Corporation and the State of Florida, a suction-type wind tunnel with 20,000 SCFM air-flow and 40 inches of water head is being installed. This set up is designed to support 3 to 8 flow passages for study of endwall/airfoil film cooling and tip leakage flow and associated heat transfer. The set up is scheduled to be completed in February 2002 and the testing and calibration would be completed in May 2002.

5. The experimental setup for the scanning method (requiring another $20,000) for P/TSP, along with necessary testing and calibration, is scheduled to be completed in June 2002.

---

[1] It should be noted that the AGTSR funds were not used for this purpose as facility building cannot be supported with AGTSR contracts. Also, AGTSR funds are frozen since July 31, 2000 because of the on-hold status of the project.

[2] The details are given in Appendix.

6. Subject to the condition that the above work gets completed on schedule, a request will be submitted to AGTSR in this month to consider the continuation of this project with the following two objectives.

   (a) Measurement of tip heat transfer in a linear cascade (with 5 or more passages), with focus on the effect of inter-passage aerodynamic interaction and the effect of wakes and approaching velocity profiles.

   (b) Identification of limitations of scanning TSP thermography and the BEM/IP[3] method for possible future use in a high-speed rotating blow-down facility, with focus on the effect of speed of rotation on the accuracy and spatial resolution of the method.

[3] Boundary element method with inverse problem formulation is a technique developed and tested under this project for the retrieval of surface heat flux distribution from measured surface temperature distribution.

Appendix: Development and Calibration of the Imaging Method for TSP Thermography

1. Imaging method of TSP thermography requires three main components: excitation or light source, test surface or the painted surface, and the receiving optics. In our test set up, blue LED array from ISSI (Dayton, OH) was used as the light source. The receiving optics consist of a long pass filter (to cut off all light coming from the light source and only allowing light that are emitted by the paint), and a CCD camera (from Pixelvision, OR) that is connected to a computer for data acquisition. The TSP paint is stored in an aerosol can (as supplied by ISSI, OH) and is applied like any other paint. A minimum of 3 coatings was found to be necessary to produce repeatable results. Since the paint gets degraded in light, the painted surface should be covered up in black cloth to minimize photo-degradation.
2. An isothermal chamber was built for calibration of the TSP paint, which was heated by a thermo-electric module (TCM), as shown in the following figure. The paint was calibrated against an E-type thermocouple, which itself was calibrated against a NIST traceable standard to within 0.2 ^{o}C (at 95 % confidence). The calibration results are shown in Figure 2. [Note: The air jet on the cold side of the TCM is to remove heat and provide a heat sink so that TCM can maintain the desired temperature.

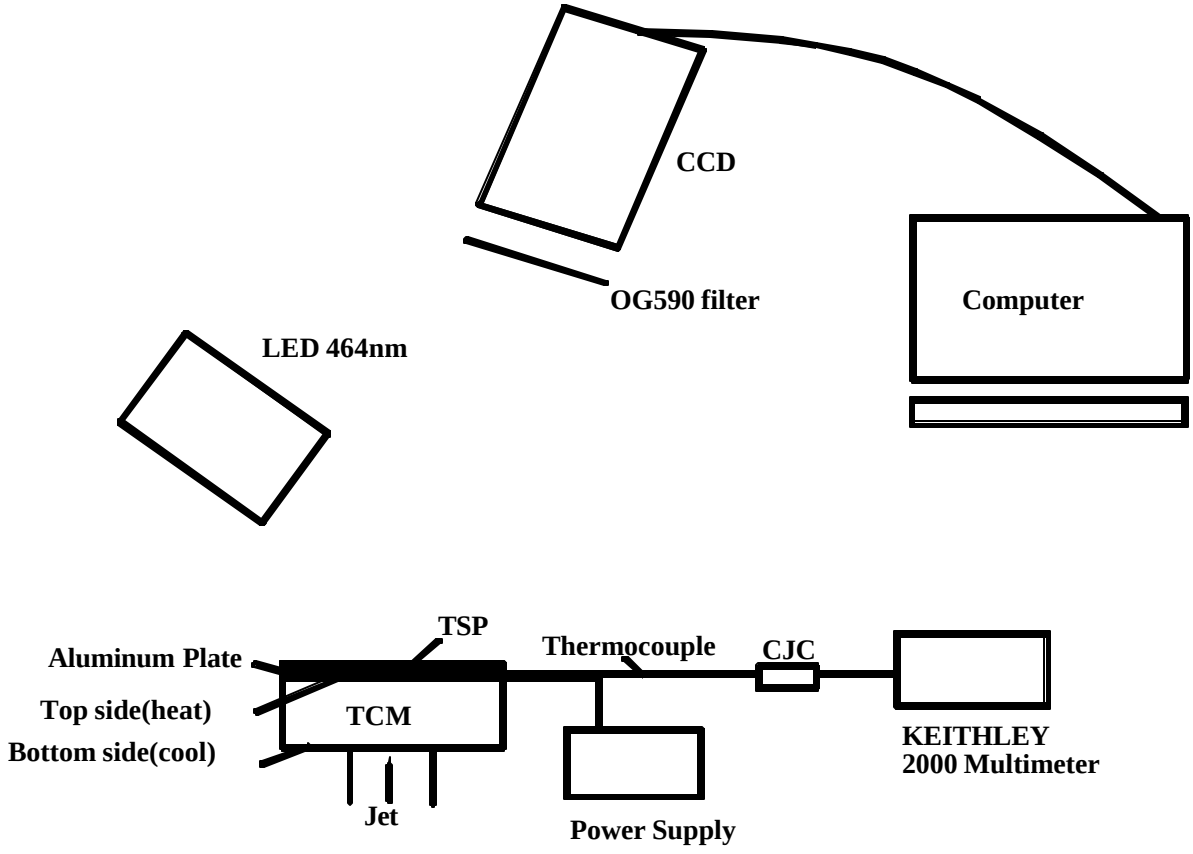

Figure 1. Experimental Setup for TSP Calibration

3. Since lighting and camera angles seriously affect the measurements in the competing methods using thermo-chromic liquid crystals, dependence of TSP calibration on lighting and viewing angles was tested during calibration.

Table 1. Variation in Position of Excitation Light and CCD Camera

	LED position			Camera position		
	X	Y	Z	X	Y	Z
20-Sep	0	2.9"	12.0"	2.6"	21.3"	55.2"
21-Sep	0	2.9"	12.0"	0	1.0"	16.6"
23-Sep	0	2.9"	12.7"	0	1.0"	16.6"
24-Sep	0	2.9"	9.4"	0	1.0"	16.6"
27-Sep	0	2.9"	12.0"	2.6"	21.3"	52.7"
1-Oct	0	2.9"	12.0"	2.6"	21.3"	55.2"

Note: Coordinate origin is on the center of the sample plate and Z-axis is perpendicular to the test plate.

The resulting calibration curves are shown in Figure 2. The calibration is found to be insensitive to lighting and viewing angles and positions. The scatter at 95% confidence level was found to be 0.3^{o}C, most of which is perhaps due to the thermocouple itself.

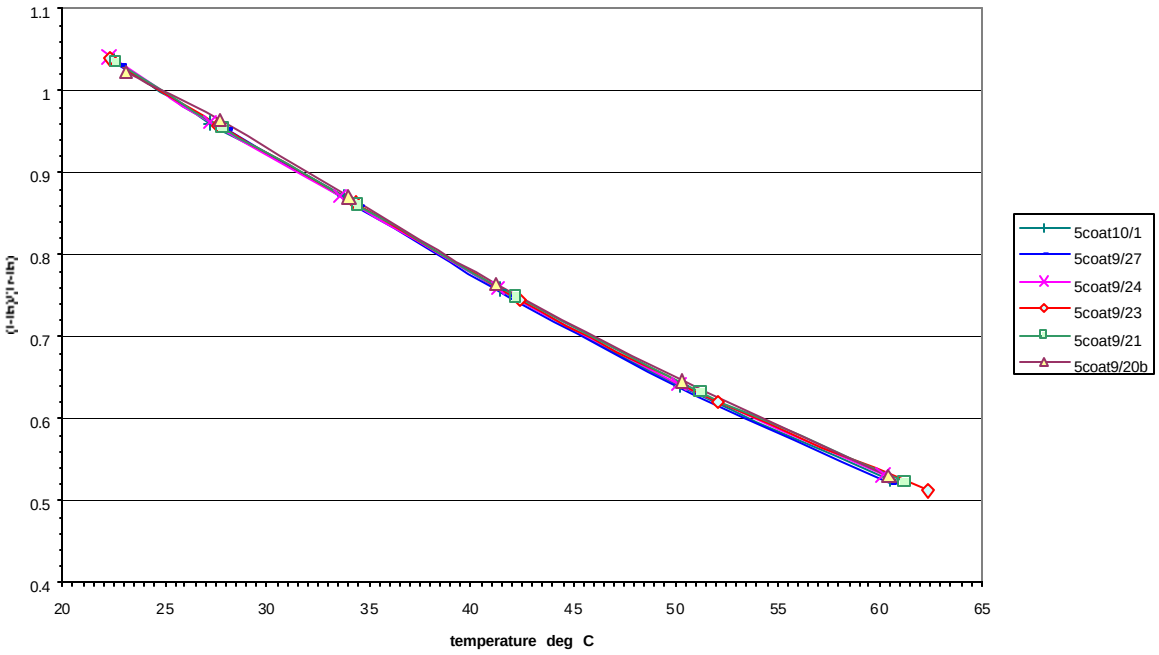

Figure 2. Effect of Camera and LED Positions on TSP Calibration (5coat)

4. In order to apply the technique to a benchmark experiment, a transient heated jet impingement experiment was set up, as shown in Figure 3. Here the plate indicated as the TSP plate is an acrylic plate with the paint coated on the impingement surface.

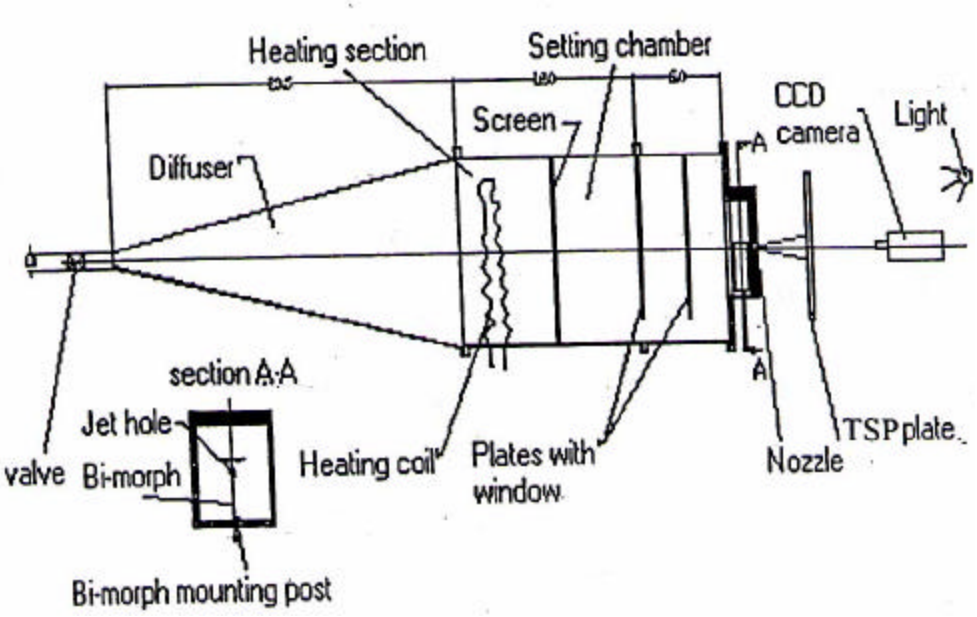

Figure 3. Schematic of the Jet Impingement Set Up
(This set up was originally built to study the effect of hydrodynamic jet instability on impingement heat transfer, and for that reason the bi-morph assembly was used. In the current experiment, the bi-morph was not excited and hence the impingement jet was un-perturbed.)

In this experiment, the heated jet was originally blocked and the TSP plate was initially at the ambient temperature. Then, the blockage was impulsively removed at an instant that was designated $t = 0s$. Camera was started subsequently and all frames were taken at an interval of 30 seconds.

Data has not been completely analyzed. Preliminary data reduction shows good agreement with results available in the literature. As an example, one of the instantaneous temperature distributions for a certain test (one of our first attempts) is shown in Figure 4 and radial variations of temperature at different instants for the same test is shown in Figure 5. [Note: As indicated in the caption for Figure 4, the CCD camera also captured the reflected image of a surrounding object, that shows up in the third and partially in the second and the fourth quadrants. In obtaining the radial profiles, the temperature at each radial position is obtained by averaging temperatures over angles around the center (not including the affected portion of the image) and over +/- 2 pixels in the radial direction, to reduce the effect of image noise.]

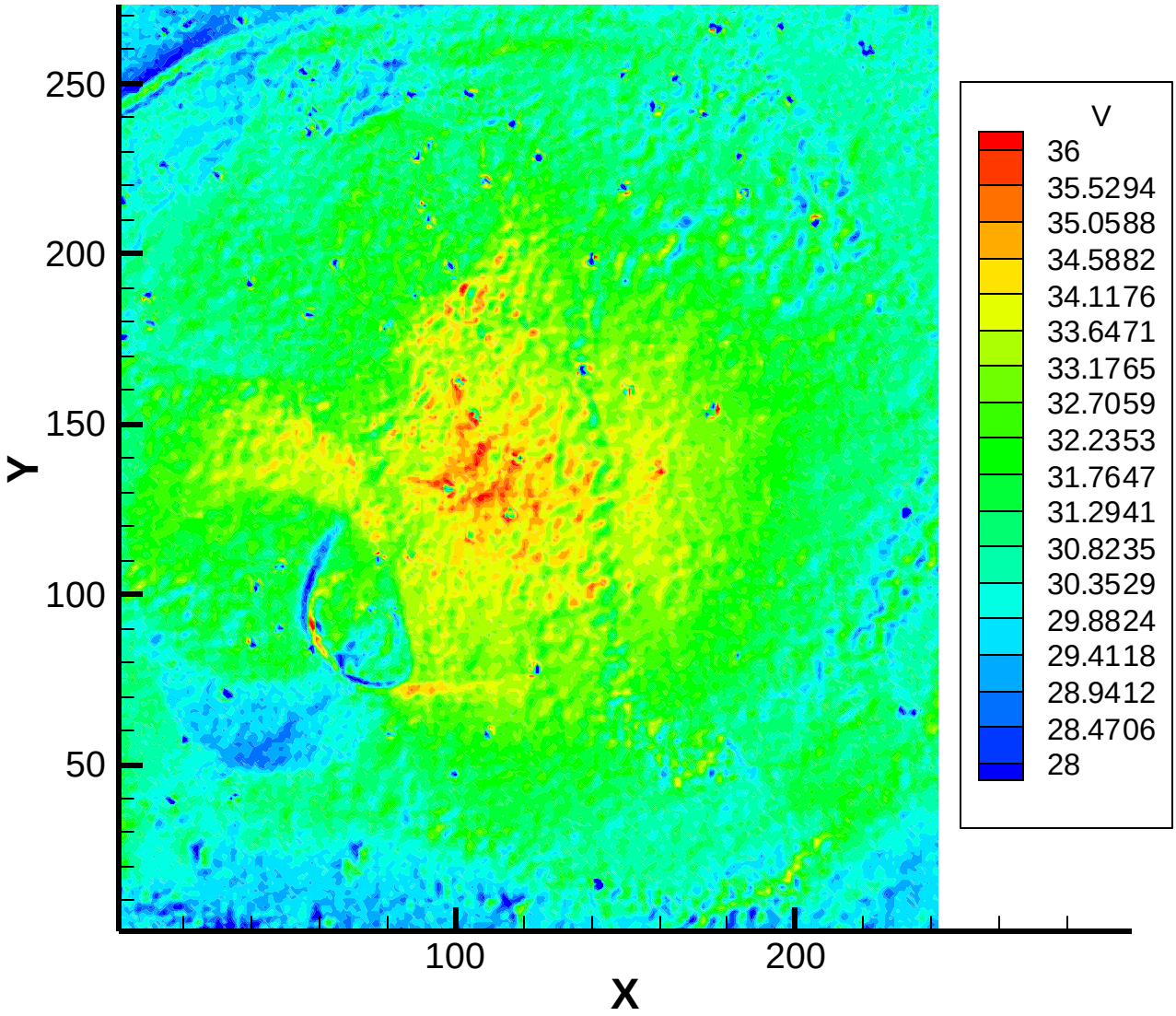

Figure 4. Instantaneous Surface Temperature Distribution (Frame #10)
[Note: The CCD camera also captured the reflected image of a surrounding object that shows up in the third and partially in the second and the fourth quadrants. In analysis, this portion of the image was not considered.]

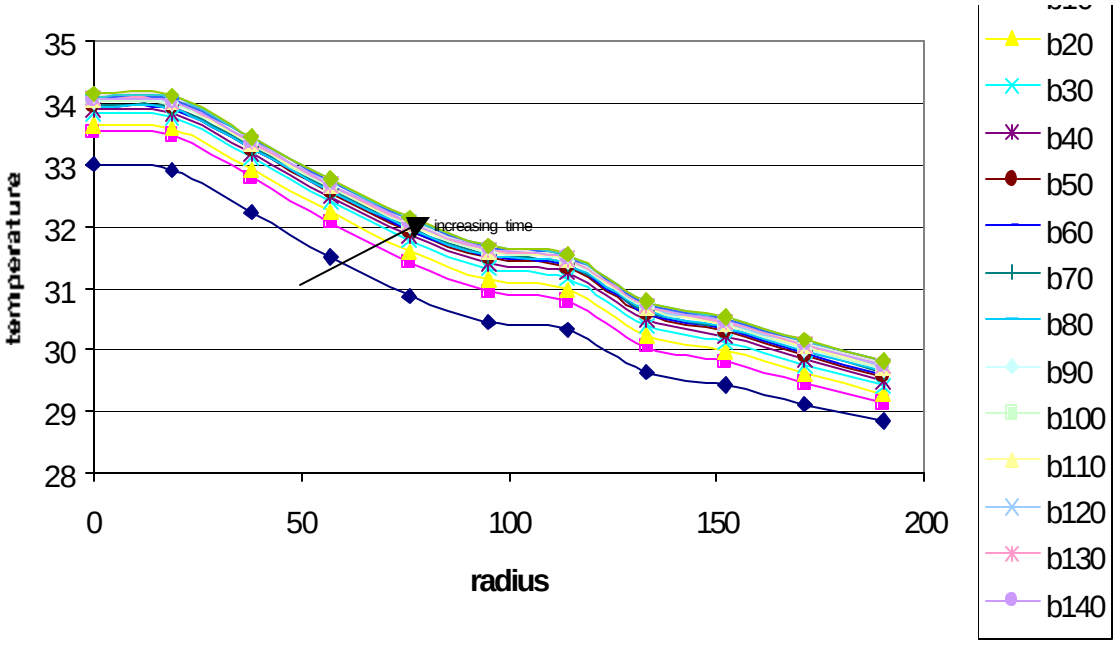

Figure 5. Instantaneous Radial Variation of Temperature

MEASUREMENTS FOR IMPORVED UNDERSTANDING OF COMBUSITON DYNAMICS IN LEAN PREMIXED GAS TURBINE COMBUSTOR FLAMES

March 1, 2001 to August 31, 2001

AGTSR Semi-Annual Report

Jay Gore, Principal Investigator,
Jun Ji, Research Associate

Maurice J. Zucrow Laboratories
(Formerly Thermal Sciences and Propulsion Center)
School of Mechanical Engineering
Purdue University
West Lafayette, IN 47907-1003

Contract No. 00-01-SR085CS
Advanced Gas Turbine Systems Research
South Carolina Institute for Energy Studies
386-2 COLLEGE AVENUE
Clemson, South Carolina 29634-5180

September 20, 2001

This report was prepared with the support of the US Department of Energy, Morgantown Energy Technology Center, Contract Number DE-FC21-92MC29061.

EXECUTIVE SUMMARY

AGTSR SEMI-ANNUAL REPORT

Maurice J. Zucrow Laboratories
Purdue University
West Lafayette, IN 47907-1003
Ph: (765)-494-1452 Fax: (765)-494-0530

Project Title:

MEASUREMENTS FOR IMPORVED UNDERSTANDING OF COMBUSITON DYNAMICS IN LEAN PREMIXED GAS TURBINE COMBUSTOR FLAMES

AGTSR Subcontract No: 00-01-SR085CS
Principal Investigator: Jay Gore
Research Associate: Jun Ji

Start Date: 3/1/2001, End Date: 2/28/2002
AGTSR Second Year Contract Value: $176,247

RESULTS FOR THE REPORTING PERIOD

The overall objective of the present project is to study the effects of interacting swirler generated flows on combustion dynamics. Double swirler configurations consisting of both axial and radial swirlers are being considered. The work of designing and constructing generic radial swirling premixers and evaluating the feasibility of using an existing PIV system in our laboratory for measuring the two dimensional velocity fields was completed during the first year of the project. It was determined that an upgrade of the PIV system was necessary. In this period, the swirling flow characteristics and swirling combustion characteristics were studied, using an upgraded PIV system and a high-frequency piezoelectric pressure transducer. Preliminary velocity measurements were also completed for premixers supplied by two industrial partners of the ATS program. These data will be described in the next report. During the next report period, measurements will be extended to premixers involving axial swirlers and further industrial interactions will continue.

1. Upgrading to the Cross-Correlation PIV system

The generic swirling premixers made in the first year of the current project and industrial swirling premixers from our industrial partners create very strong three dimensional flow fields with multiple high velocity components. The auto-correlation PIV system previously used in our lab and state of the art a few years back was found to be incapable of capturing the details of the instantaneous flow structure for the strong swirling flow fields. Therefore, during this period, we upgraded our auto-correlation PIV system to a cross-correlation PIV system, which was described in the last report. PIV software was also upgraded from INSIGHT^{TM} v. 1.0 to INSIGHT^{TM} ULTRA v. 3.3 (TSI Inc.) with a built-in parallel processing engine. The spatial

resolution of the velocity measurements was improved significantly with the cross-correlation PIV system and the new version of the PIV software.

2. Studies of the Generic Radial Swirling Premixers

A generic radial swirling premixer was studied first. The generic swirling premixer is composed of two radial swirlers. Use of two vane angles of 21º and 31º combined with changing the orientation of the blades formed a total of ten combinations of the swirling premixer. Designs resulting from these combinations are used in the industry and are characterized as co-rotating and counter-rotating combinations. Instantaneous and mean velocities in the flow fields were measured with the PIV and the corresponding pressure fluctuations were measured with a high-frequency piezoelectric pressure transducer. The global characteristics of the lean premixed swirling combustion were also noted in this period using flame photography.

From the test results, the mean velocity fields of the swirling flows clearly shows an internal recirculation zone, which helps to stabilize the combustion process. The instantaneous flow patterns display much different characteristics, which help our understanding of the instabilities in the swirling flows. Stronger swirling flows form larger internal recirculation zones. Co-rotating swirlers enhance the swirling flows, and always form internal recirculation zones under the present operating conditions. Counter-rotating swirlers promote high flow rates through the premixer, but have smaller internal recirculation zones. Under some configurations, internal recirculation zones are not observed for the counter-rotating swirlers. The vane angle of the upper swirler is significant in determining pressure fluctuation levels because most of the airflow goes through the upper swirler for the present design. For an upper swirler with a vane angle of 21°, the pressure fluctuation levels were almost doubled when the lower swirler was used in a co-rotating orientation. For an upper swirler with a vane angle of 31°, the pressure fluctuations have similar levels under all swirler configurations. The PDF and the PSD curves of the pressure fluctuations also depend on the vane angle of the upper swirler.

The combustion process interferes with the flow instabilities. With nearly identical gas flow rate in the single swirler premixer, the velocity scale in the flow field is doubled, and the pressure fluctuation level is almost doubled because of combustion under the present operating conditions. The combustion process in the swirling flows also shifts the energy of pressure fluctuations to frequencies different than those observed in corresponding cold flows.

TABLE OF CONTENTS

LIST OF FIGURES

LIST OF TABLES

1. INTRODUCTION

In the first year of the project, the work of designing and constructing two types of generic swirling premixers with radial swirlers had been done as reported in the last two project reports. The swirlers are designed to create swirling flow with three different swirl numbers, and the swirlers can be assembled in counter-rotating or in co-rotating orientation. The swirlers have been fabricated using Stereolithography (SLA), a rapid prototyping process, due to their complex structure.

The performance of swirling premixers is mostly affected by the flow patterns inside and outside of the premixers, and flame stabilization process outside these premixer occurs by means of recirculating hot combustion products into flammable reactants. The Particle Imaging Velocimetry (PIV) is capable of capturing the instantaneous two- or three-dimensional flow patterns with a high spatial resolution. Flow properties such as vorticity and strain rates can be obtained for the entire region based on the PIV instantaneous velocity measurements. Mean velocities, turbulence intensities and other higher order flow statistics can also be obtained from the measurements.

In this period, swirling flow characteristics and swirling combustion characteristics were studied using PIV velocity measurements and a high-frequency piezoelectric pressure transducer. The generic swirling premixers and the industrial swirling premixers create very strong three dimensional flow fields with high velocity components. Auto-correlation PIV system we have used previously in our lab is not capable of capturing the detailed instantaneous flow structure for these flow fields. Therefore, during this period, we upgraded our auto-correlation PIV system to a state of the art cross-correlation PIV system, which was described in the last report. The PIV software was also upgraded from INSIGHT^{TM} v. 1.0 to INSIGHT^{TM} ULTRA v. 3.3 with a built-in parallel processing engine. The spatial resolution of the velocity measurements was improved with the cross-correlation PIV system and the new version of the PIV software. First, a generic radial swirling premixer was studied during this period. The generic swirling premixer is composed of two radial swirlers. Using two vane angles of 21º and 31º and changing the orientation of the two parts of the generic swirlers, a total of ten combinations of premixers can be formed. Instantaneous and mean velocities in the flow fields were measured with the PIV and the corresponding pressure fluctuations were measured with a high-frequency piezoelectric pressure transducer. The global characteristics of the lean premixed swirling combustion were also noted in this period using flame photography.

2. MEASUREMENTS OF VELOCITY AND PRESSURE FLUCTUATION FOR GENERIC RADIAL SWIRLER PREMIXERS

2.1. Experimental Methods

The experiments were conducted in an enclosure with dimensions of 1.3 m (L) X 1.2 m (W) X 3.0 m (H) with an exhaust fan at the top. The premixer with swirlers was assembled on a plenum, which supplies air and fuel. The plenum is mounted on a three-dimensional traverse system. A buffer plate is installed inside the plenum to create a uniform upstream airflow. Fig. 1 shows a schematic drawing of the plenum and measurement locations for the pressure fluctuations and the velocity measurements (PIV measuring window).

The pressure inside the plenum was measured using a miniature piezoelectric ICP pressure transducer, Model 112A22. The pressure transducer has a resolution of 6.9 Pa. Its resonant frequency is 250 kHz, and its low frequency response is 0.50 Hz. The rise time is 2 microseconds. The pressure transducer is mounted on the sidewall of the air plenum chamber to measure the pressure variations. The signals from the pressure transducer are passed through a signal conditioner, Model 482B11, which is calibrated with the pressure transducer by the manufacturer. The frequency response of the Signal Conditioner is 200 kHz for gains of x1 and x10, and is 100 kHz for a gain of x100. The linearity of the calibration of the pressure transducer system is within 1 % (zero based best straight line).

An UltraPIV system from TSI Inc. was used for the velocity measurements. The cross-correlation CCD camera possesses frame-straddling capabilities, allowing the time between two successive frames to be as short as 200 nanoseconds, and offering an 8-bit digital output at a frame rate of 30 Hz, which translates to 15 frame-straddled pairs per second. A Spectra-Physics PIV 400 Nd:YAG laser, which has two independent cavities allowing a wide range of time separation between the two light pulses, was used with this UltraPIV system. Limited by the laser repetition rate, the pairs of particle image frames were acquired at a rate of 10 Hz. The PIV computer with a 512 MB RAM has the capability to capture 200 pairs of image frames continuously in 20 seconds. Each frame covers a flow area of 99 mm (W) X 100 mm (H), and the spatial resolution is 3 mm X 3 mm

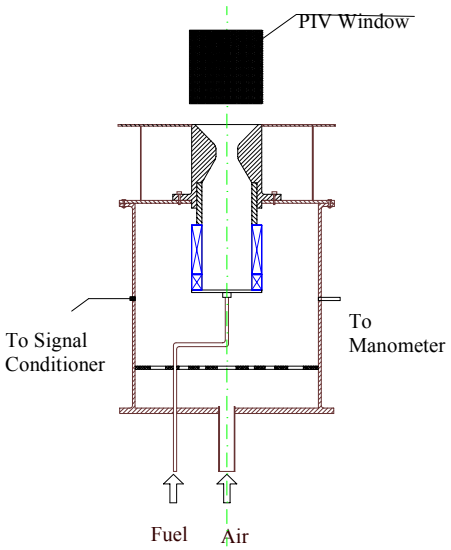

Fig. 1. A schematic of testing plenum and location of PIV window

2.2. Swirling Premixer

The swirling premixers used in the present study consist of four parts: a nozzle head, an upper swirler, a lower swirler and a base plate. A three-dimensional solid model of the swirling premixer is shown in Fig. 2. The vane length ratio of the upper swirler and the lower swirler is about 3.8. The lower swirler can be oriented in different directions to form counter-rotating or co-rotating double swirlers. If the lower swirler is removed, the upper swirler forms a single swirler premixer. In the present study, flat-vaned swirlers with vane angles of 21° and 31° were used. A total of ten combinations of the two swirlers can form the different premixers (Table 1).

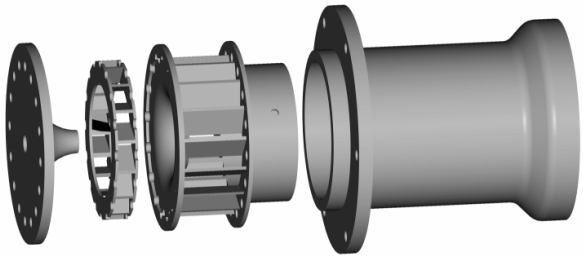

Fig. 2. Three Dimensional Solid Model of the Premixer Assembly

2.3. Experimental Conditons

A manometer was connected to the sidewall of the plenum and used to control the pressure drop across the swirling premixers. In the present study, the pressure drop across the swirling premixer was set at 2.5 % of atmospheric pressure. The airflow rates for the different combinations of the swirlers are listed in Table 1. For identical vane angles of the upper swirler and lower swirler, co-rotating swirlers generate a higher air flow rate than the single swirler because of the larger air entry area, but the counter-rotating swirlers generate even higher air flow rate than the co-rotating swirlers since the lower counter-rotating swirling flow decreases the effective swirl, which enhances the flow in the premixer. The swirlers with a vane angle of 31° generate higher flow rates than those with the vane angle of 21°.

Flow Rate (m^3/min)		Upper Swirler (28.8 mm)	
		21°	**31°**
Lower Swirler (7.6 mm)	None	1.85	2.82
	Co-Rotating **21°**	2.10	3.21
	Counter-Rotating **21°**	2.59	4.17
	Co-Rotating **31°**	2.46	3.37
	Counter-Rotating **31°**	3.21	4.21

Table 1. Airflow rates under cold flow operating condition

Measurements of swirling combustion were conducted under the lowest airflow rate in Table 1, which has a single swirler with a vane angle of 21°. The lean premixed equivalence ratio that made stable swirling combustion possible with this arrangement is 0.94.

2.4. Cold Swirling Flows

In the present study, the PIV was used to measure the instantaneous flow pattern. Maximum instantaneous velocities in each PIV frame of the swirling flows are listed in Table 2.

Maximum Instantaneous Velocity (m/s)		Upper Swirler (28.8 mm)	
		21°	**31°**
Lower Swirler (7.6 mm)	None	20.1	17.5
	Co-Rotating **21°**	23.6	23.1
	Counter-Rotating **21°**	29.8	18.1
	Co-Rotating **31°**	24.6	20.8
	Counter-Rotating **31°**	24.0	37.6

Table 2. Maximum instantaneous velocities in cold flow for generic swirling premixers

Mean velocity fields generated by the single swirler premixer are illustrated in Fig. 3. The internal recirculation zone is clearly observed in Fig. 3 similar to that shown in previous work using LDV. Internal recirculation zone generated by the swirler with 21° vane angle is larger than that generated by the swirler with the 31° vane angle. The swirler with a vane angle of 21° generates much stronger swirling flow compared to that with a vane angle of 31°, and forms a larger internal circulation zone.

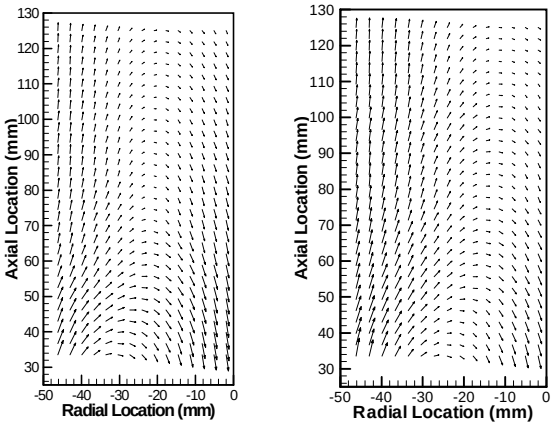

(a) 21° (b) 31°

Fig. 3. Mean velocity fields generated by a single swirler premixer

Mean velocity fields generated by the co-rotating swirler premixer are shown in Fig. 4. The numbers appearing in the sub-captions in Fig. 4 are the swirler vane angles. The first number is the vane angle of the upper swirler, and the second number is the vane angle of the

lower swirler. This notation is used consistently in all the figures. Similar to the case of the single swirler, an internal recirculation zone is observed in all cases of the co-rotating swirling flows. Swirlers with both vane angles of 21° (Fig. 4a) generated largest internal recirculation zone, and swirlers with both vane angles of 31° (Fig. 4b) generated smallest internal recirculation zone. The internal recirculation zones generated by the mixed swirlers with vane angles of 21° and 31° (Fig.4c and 4d) are of a size between the first two (Fig. 4a and 4b). Fig. 4d showed a stronger recirculation flow than that of Fig. 4c because the total flow rate for Fig. 4d is one third higher than that for Fig. 4c.

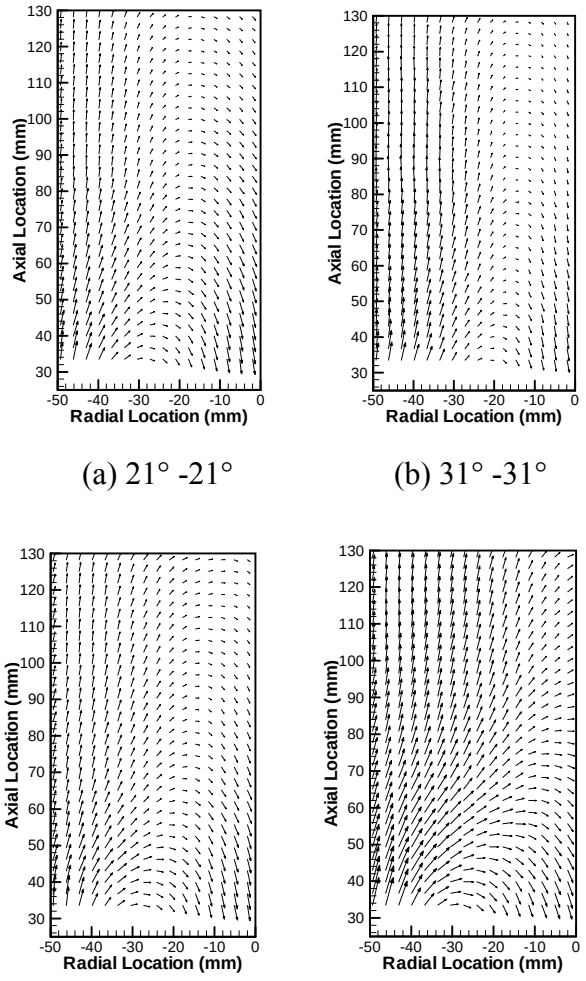

(a) 21° -21° (b) 31° -31°

(c) 21° -31° (d) 31° -21°

Fig. 4. Mean velocity fields generated by co-rotating swirler premixer

Mean velocity fields generated by the counter-rotating swirlers are shown in Fig. 5. The flow patterns are more complicated for this swirler configuration. No internal recirculation zone at the nozzle exit was observed in the case of the counter-rotating swirlers with the vane angles of 31° (Fig. 5b), and the gas flow traveled in the axial direction. Inside the premixer, the two swirling flows generated by the counter-rotating swirlers created a high shear region, which promoted rapid mixing but swirling momentum was consumed greatly. No recirculation zone is formed if swirling flow is not strong, i.e., swirl number is less than 0.6. The internal recirculation zones were observed in other three cases of the counter-rotating swirling flows.

The internal recirculation zone generated by swirlers with vane angles of 21° (Fig. 5a) became smaller because some swirling momentum was consumed inside the premixer. It was interesting that the internal recirculation zone was broadened in the case of the vane angle combination of 21°-31°. The internal recirculation zone in the case of the vane angle combination of 31°-21° was smaller than that of the vane angle combination of 21°-21° even though the total gas flow rate in the case of the vane angle combination of 31°-21° was 60 % higher.

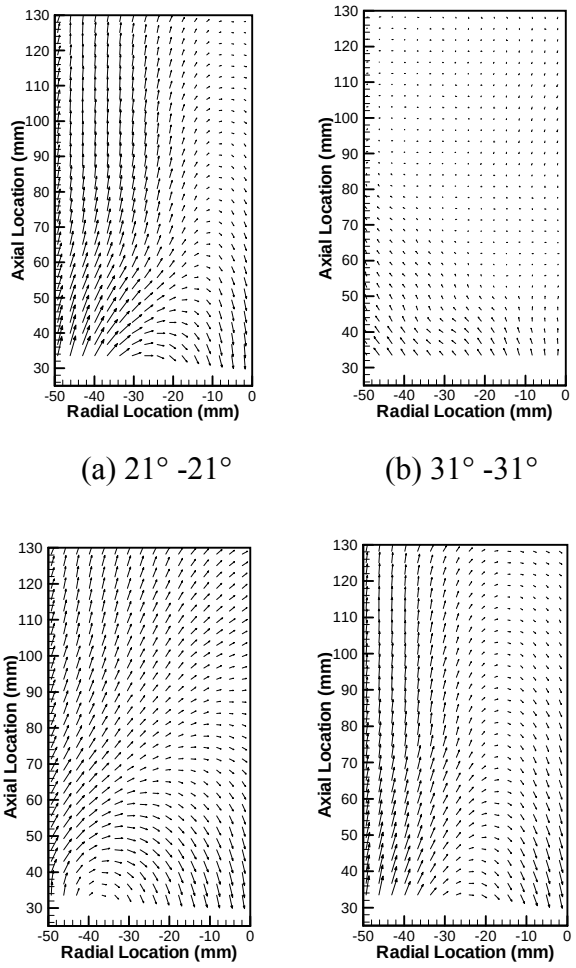

(a) 21° -21° (b) 31° -31°

(c) 21° -31° (d) 31° -21°

Fig. 5. Mean velocity fields generated by counter-rotating swirler premixers

The mean velocity fields of the swirling flows show obvious internal recirculation zone, which helps to stabilize the combustion process. However, the instantaneous flow patterns display much different characteristics of the swirling flows, which help to understand the instabilities.

Samples of the instantaneous flow patterns generated by the different swirlers are shown in Figs. 6 - 8. In the instantaneous velocity fields, there are no obvious boundaries dividing the recirculation zone and the main flows. Small (relative to the mean recirculation zone) vortical structures could be observed virtually at any point in the swirling flow field, and orientation of the vortex could be in either directions. Swirling flow is a three-dimensional phenomenon. The PIV system used in the present study only measures two-dimensional flow patterns. Since the

actual flow is three dimensional, the velocity vectors do not obey two-dimensional mass-conservation laws. Therefore, abrupt changes in velocities can be occasionally observed.

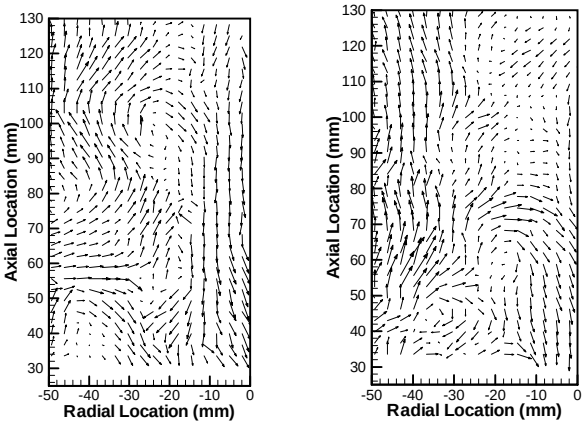

(a) 21° (b) 31°

Fig. 6. Instantaneous flow patterns generated by a single swirler premixer

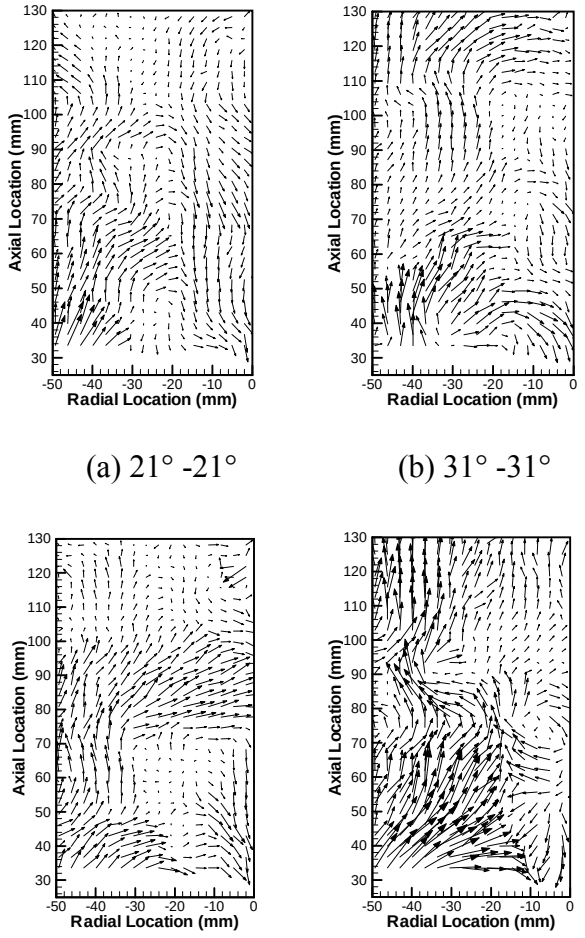

(a) 21° -21° (b) 31° -31°

(c) 21° -31° (d) 31° -21°

Fig. 7. Instantaneous flow patterns generated by co-rotating swirler premixers

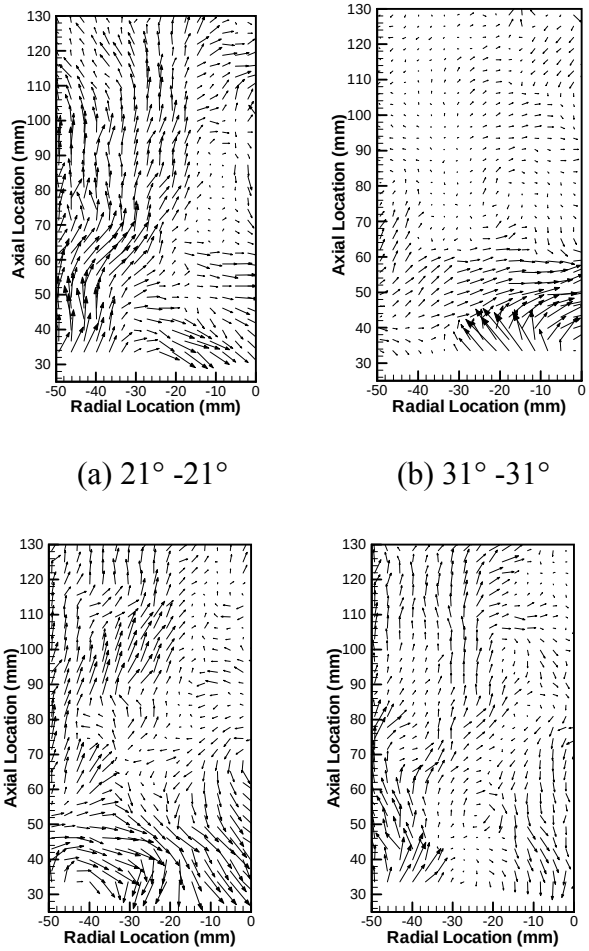

Fig. 8. Instantaneous flow patterns generated by counter-rotating swirler premixers

Instabilities in the swirling flows are related to the pressure fluctuations inside the plenum. The total air flow rate changes significantly for the different configurations of the swirlers (refer to Table 1) under an operating condition of 2.5 % pressure drop across the swirling premixer. The higher flow rate itself introduces some level of pressure oscillation changes in addition to those generated by the swirler geometry. Therefore, the pressure fluctuations are normalized by the total flow rate through the swirling premixer, and a dimensionless parameter is proposed for the evaluation of the pressure fluctuation levels. The dimensionless parameter is defined as

$$\Lambda = \frac{\sqrt{\overline{p'^2}} \bullet A^2}{\rho \bullet \dot{V}^2} \tag{1}$$

where p' is the instantaneous pressure fluctuation, A is the throat area of the nozzle head, ρ is the gas density, and V is the total volumetric gas flow rate.

Pressure fluctuation data were normalized using Eq. (1) and results are tabulated in Table 3. The vane angle of the upper swirler influences pressure fluctuation levels significantly

because a large portion of the airflow goes through the upper swirler (The vane length ratio of the upper swirler and the lower swirler is about 3.8). For the upper swirler with a vane angle of 21°, in comparison with the single swirler, the pressure fluctuation levels were almost doubled when a lower swirler was used in the co-rotating orientation. The pressure fluctuations decrease to the same level as of the single swirler if the lower swirler is set in a counter-rotating orientation. For the upper swirler with a vane angle of 31°, the pressure fluctuations remain almost constant out of the lower swirler usage and orientation except in the case of a lower swirler with a vane angle of 21° in the counter-rotating orientation. This combination leads to a 50 % decrease in the pressure oscillation levels.

Dimensionless Pressure Fluctuations Λ		Upper Swirler (28.8 mm)	
		21°	**31°**
Lower Swirler (7.6 mm)	None	0.073	0.055
	Co-Rotating **21°**	0.154	0.065
	Counter-Rotating **21°**	0.089	0.031
	Co-Rotating **31°**	0.134	0.053
	Counter-Rotating **31°**	0.067	0.047

Table 3. Pressure fluctuations for cold flow with general swirling premixer

The Probability Density Functions (PDF) of the pressure fluctuations in the plenum for different swirler combinations are plotted in Figs. 9 - 11. A Gaussian distribution is plotted in the figures for reference. The single swirlers with vane angles of 21° and 31° generated similar PDF profiles with a single peak. For the double swirler premixers, PDF curves depend on the vane angle of the lower swirler independent of the orientation. If lower swirlers of the premixer have a vane angle of 31°, the PDFs are similar those of the single swirlers. If the lower swirlers have a vane angle of 21°, the PDFs show multiple peaks, which need further investigation.

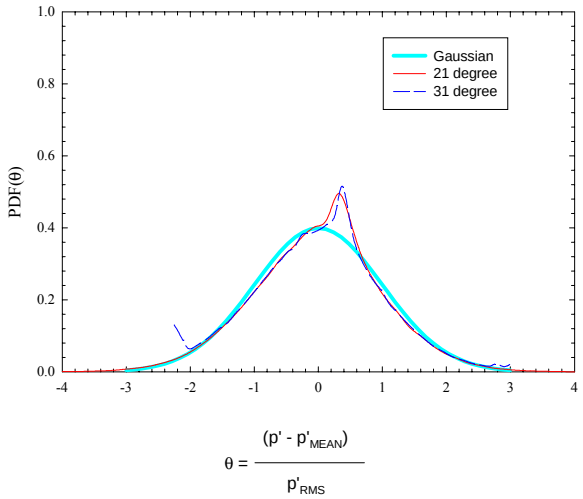

Fig. 9. Probability density functions of pressure fluctuations in single swirler premixers

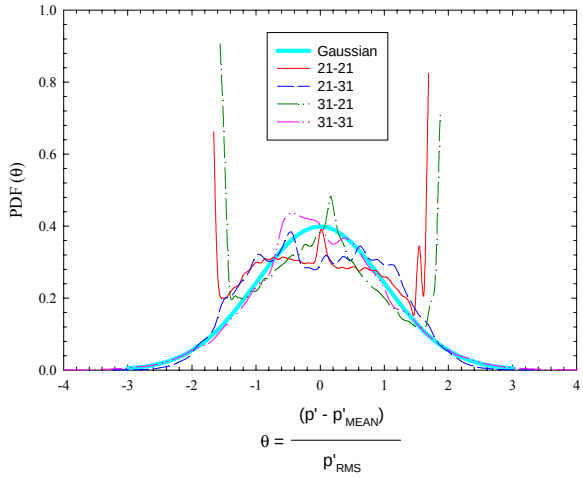

Fig. 10. Probability density functions of pressure fluctuations in co-rotating swirler premixers

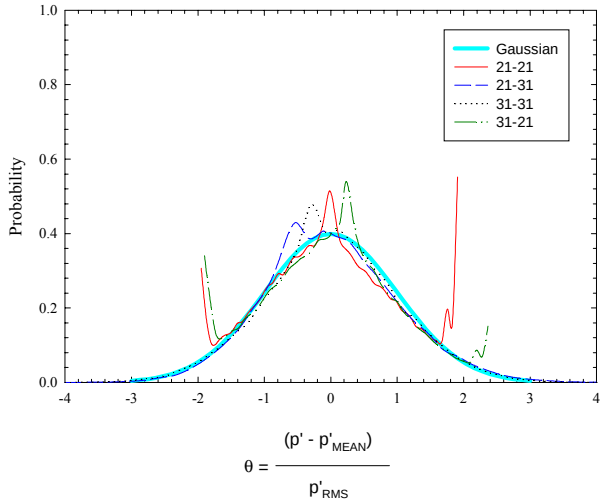

Fig. 11. Probability density functions of pressure fluctuations in counter-rotating swirler premixers

Dominant frequencies of pressure fluctuations could be found from the power spectral density (PSD) using a Fast Fourier Transform (FFT) of the pressure fluctuations. Figures 12 - 14 show power spectral densities of pressure fluctuations in the plenum. The single swirler combinations have similar PSD profiles: high-energy peaks at 150 Hz and 1000 Hz are observed. Like the PDF profiles of the pressure fluctuations, PSD profiles were strongly influenced by the vane angle of the upper swirler. In the case of co-rotating orientation, the upper swirler with a vane angle of 21° produces a dominant frequency at 130 Hz, but the upper swirler with a vane angle of 31° produces peaks at higher frequencies of 1000 Hz, 1400 Hz, 1650 Hz and 1750 Hz. In case of the counter-rotating orientation, the dominant frequency shifts to 100 Hz for the upper swirlers with a vane angle of 21°, but some energy also appears in the high frequencies at 1000 Hz, 1650 Hz and 1750 Hz. The upper swirlers with a vane angle of 31° have more energy at the higher frequencies of 1000, 1400, 1650 and 1750 Hz.

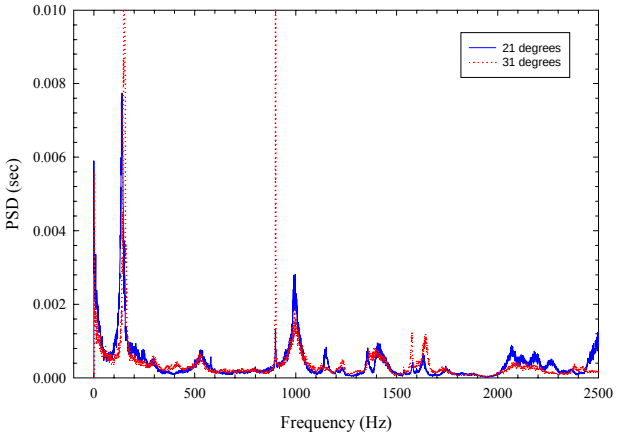

Fig. 12. Power spectral density functions of pressure fluctuations in single swirler premixers

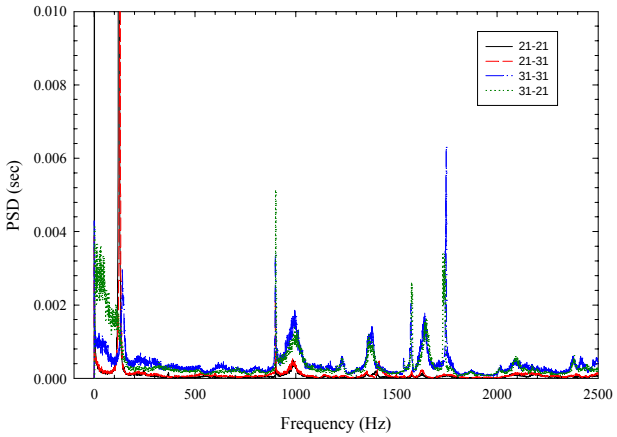

Fig. 13. Power spectral density functions of pressure fluctuations in co-rotating swirler premixers

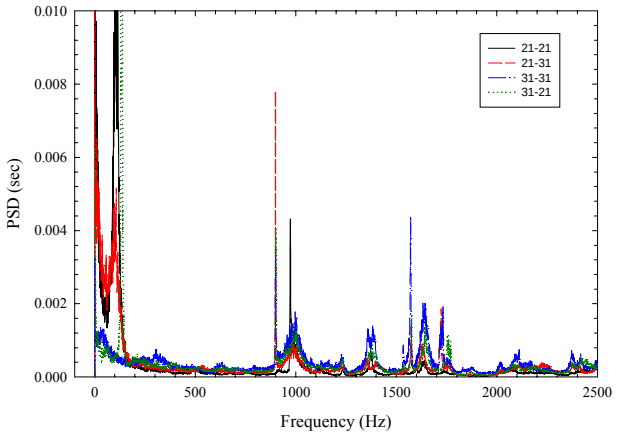

Fig. 14. Power spectral density functions of pressure fluctuations in counter-rotating swirler premixers

2.5. Swirling Combustion

A swirling flame was established on a single swirler premixer with a vane angle of 21°. The equivalence ratio of the premixed gas mixture is about 0.94. Considering the internal recirculation and the strong external recirculation and entrainment, the local equivalence ratio in the combustion zone could be much less than 0.94. The maximum instantaneous velocity in the PIV window is about 41 m/s in the swirling combustion flow field, compared with the 20 m/s in the cold airflow generated with the same swirler premixer.

The mean velocity field in the swirling combustion zone is shown in Fig. 15 along with the mean velocity filed in the non-reacting gas flow. The magnitude of the velocity is almost doubled because of the stronger entrainment and thermal expansion. The internal recirculation zone is enlarged in both axial and radial directions. The internal recirculation flow is also very strong in the downward direction. Instantaneous flow pattern in the swirling combustion is shown in Fig. 16. Very strong vortex structures appear in the flow field.

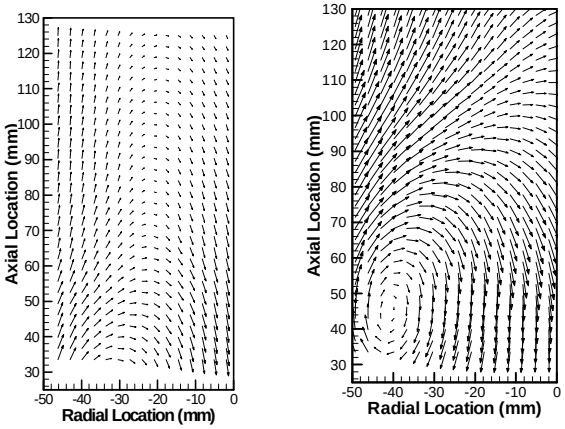

(a) Cold Flow (b) With Flame

Fig. 15. Mean velocity fields created by a single swirler premixer

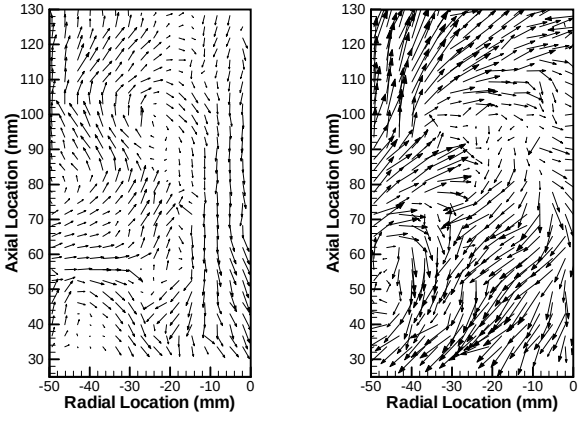

(a) Cold Flow (b) With Flame

Fig. 16. Instantaneous flow patterns created by a single swirler premixer

The dimensionless pressure fluctuations in the plenum with the swirling combustion along with other measured quantities are tabulated in Table 4. With a nearly identical gas flow rate, the velocity scale in the flow field of swirling combustion is doubled, and the pressure fluctuation level is almost doubled. The combustion process interferes with the flow instabilities and enhances these in the case of single swirler premixer under the present operating conditions.

	Cold Flow	With Flame
Flow Rate (m^3/min)	1.85	2.02
Maximum Velocity (m/s)	20	41
Dimensionless Pressure Fluctuation, Λ	0.073	0.138

Table 4. Pressure fluctuations for swirling combustion with general swirling premixer

Probability density function of the pressure fluctuations with swirling combustion is non-symmetric (Fig. 17), like those in the non-reacting swirling flows.

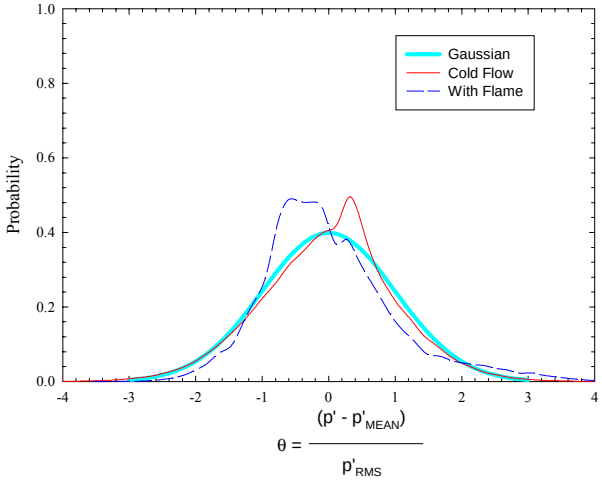

Fig. 17. Probability density functions of pressure fluctuations in a single swirler premixer

Fig. 18 shows the power spectral density (PSD) of the pressure fluctuations inside the plenum with swirling combustion. Combustion dampens the pressure fluctuations at 150 Hz, but enhances the pressure fluctuations at frequencies of 1000 Hz, 1200 Hz, and 1400 Hz. The energy of pressure fluctuations is shifted to the higher frequencies by the combustion process under the present operating conditions.

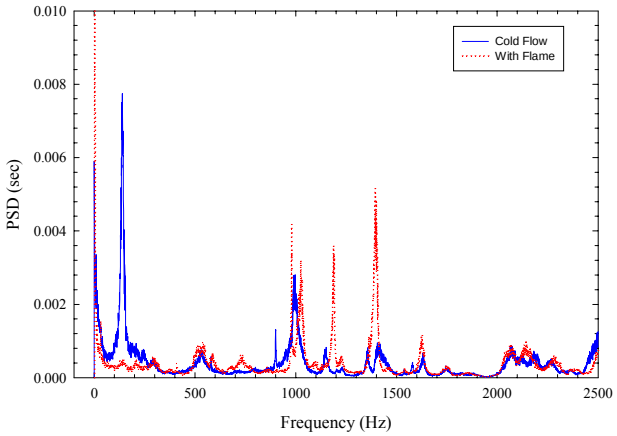

Fig. 18. Power spectral density functions of pressure fluctuations in a single swirler premixer

2.6. Summary

Instabilities in the swirling flows with or without flame were experimentally studied using two-dimensional particle imaging velocimetry and a piezoelectric pressure transducer.

Mean velocity fields of the swirling flows clearly show internal recirculation zones, which help to stabilize the combustion process. The instantaneous flow patterns display much different characteristics, which help understanding of the instabilities in the swirling flows. Stronger swirling flows form larger internal recirculation zones. Co-rotating swirlers enhance the swirling flows, and always form internal recirculation zones under the present operating conditions. Counter-rotating swirlers promote high flow rates going through the premixer, but have smaller internal recirculation zones. Under some configurations, internal recirculation zones are not observed for the counter-rotating swirlers.

A dimensionless parameter is proposed to evaluate the pressure fluctuations levels. The vane angle of the upper swirler is significant in determining pressure fluctuation levels because most of the airflow goes through the upper swirler. For an upper swirler with a vane angle of 21°, the pressure fluctuation level was almost doubled when the lower swirler was used in a co-rotating orientation. For an upper swirler with a vane angle of 31°, the pressure fluctuations have similar levels under all swirler configurations. The PDF and the PSD curves of the pressure fluctuations also depend on the vane angle of the upper swirler.

The combustion process interferes with the flow instabilities. With nearly identical gas flow rate in the single swirler premixer, the velocity scale in the flow field is doubled, and the pressure fluctuation level is almost doubled because of combustion under the present operating conditions. The combustion process in the swirling flows also shifts the energy of pressure fluctuations from low frequencies (150 Hz) to high frequencies (1000 Hz to 1400 Hz).

3. WORK PLANNED FOR THE NEXT PERIOD

During the next six months, measurements of velocities and broadband chemiluminescence phase locked with the pressure oscillation signals will be obtained for the radial swirler combination premixers the axial swirler combination premixers, and the resulting data will be converted to a set of design rules for minimization of combustion dynamics. We will also report on the measurements on the premixers supplied by the ATS industrial participants.

ACKNOWLEDGEMENT

This research was sponsored by the South Carolina Energy Research Development Center under the ATS program (Contract No. 00-01-SR085CS) with the support of the US Department of Energy, Morgantown Energy Technology Center Contract Number DE-FC21-92MC29061.

Nonuniformities of Mixture Ratio as a Mechanism of Combustion Instabilities in Lean Pre-Mixed Combustors

1 March 1998 to 30 June 2001
Final Report

Fred E. C. Culick, Principal Investigator;
Albert Ratner, Postdoctoral Scholar;
Giorgio Isella, Konstantin Matveev, Steve Palm, Winston Pun,
Claude Seywert, Grant Swenson, Student Researchers

Jet Propulsion Center

California Institute of Technology
Pasadena, CA 91125

Subcontract No. 98-01-SR063
Clemson University Research Foundation
Under DOE Cooperative Agreement DE-FC21-92MC29061

September 28, 2001

Table of Contents

List of Figures & Tables

AGTSR Annual Report

Jet Propulsion Center
California Institute of Technology
Pasadena, CA 91125

Phone: (626) 395-4783 FAX: (626) 395-8469

Project Title: Nonuniformities of Mixture Ratio as a Mechanism of Combustion Instabilities in Lean Pre-Mixed Combustors
AGTSR Subcontract No. 98-01-SR063
Principal Investigator: Fred E. C. Culick
Postdoctoral Scholar: Albert Ratner
Research Students: Giorgio Isella, Konstantin Matveev, Steve Palm, Winston Pun, Claude Seywert, Grant Swenson, Kevin Shand (UG)
Contract information:
Start Date: March 1, 1998 Completion Date: June 30, 2001
AGTSR Total Contract Value ($390,200)

Executive Summary

Objectives

The primary objective of this program is to establish the role of upstream fluctuations of fuel/air ratio on the stability and dynamical behavior of unsteady motions in a premixing gas turbine combustor; and to develop and make available to the technical community analytical methods for predicting the effects of this behavior in practical combustors.

Our technical objectives include:

1) Developing a general procedure for analyzing the influences of fluctuations of mixture ratio by close coordination of numerical simulations and an analytical framework based on a form of spatial averaging applied to the nonlinear equations for unsteady motion;
2) Working out a procedure for constructing reduced-order models from the results of 1) and for incorporating the general principles of active feedback control in realistic analyses of gas turbines combustors;
3) Confirming experimentally in realistic premixed and combustor configurations the presence and consequences of fluctuations of mixture ratio.

Final Status

The tasks for this program included a combination of numerical, theoretical and experimental work.

Task 1 – Numerical Simulations

During this program, we worked with Analytical & Computational Research, Inc. (ACRi) to adapt their commercial code ANSWER to simulations of unsteady motions in gas turbine combustors. The results have been mixed and we have not reached the level we had planned. However, we have found (fairly good) qualitative comparison with some experimental data. Our purpose has been to use numerical simulation as an aid to investigating the mechanisms of instabilities and *not* to develop computer programs. Particular aspects to be emphasized in this work are acoustics and sufficiently detailed chemistry to allow assessment of the production of NO_x under unsteady conditions. Ultimately our goal is to be able to extract sufficient information from the simulations to allow modeling the local dynamical response of a reacting flow in the form required for the analytical framework used in Task 2. The results of this task have been published in a Ph.D. thesis (G. Swenson) at the end of the second year of this program (February 2000).

Task 2 – Analysis of Combustor Dynamics

The essentials of our analytical framework for studying combustor dynamics remain unchanged. During the last year of this program, the Principal Investigator prepared notes on this subject for lectures given as part of the short course "Control of Engine Dynamics" held 14–18 May, 2001 at the Von Karman Institute in Brussels, Belgium. The results are also included in a short course cited at the end of this program.

During this program we also investigated work on possible influences of noise in combustors, particularly when active feedback control is used. A significant advantage of our analytical framework is that we are able rigorously to incorporate formal representations of noise generated within the flow. As a result we find both additive and multiplicative sources, in contrast to purely additive sources conventionally treated in the field of stochastic control. Multiplicative sources contain explicit coupling to the acoustic field, and hence provide a different channel for control.

Task 3 – Reduced Order Modeling and Methods of Feedback Control

During the final year of the program we continued our effort to develop a unified analysis of feedback control of combustor dynamics. We have several purposes. First, we want to show that essentially all published analyses of linear feedback control of combustor dynamics can be covered as specializations of one general analysis. Second, by doing so, we will be able objectively to compare the performances of the various control laws unobscured by any differences in the physical problems being treated. Most of the problems treated compare three control laws (PID, LQG and H∞) with noise, parametric uncertainties and time delays; we continue to investigate all three.

Task 4 – Experimental Work

When this program began, we intended to carry out experiments relating to the influences of fluctuations of mixture ratio and feedback control, in a new combustor test rig. The diagnostics would be primarily pressure measurements, pulsed laser induced velocimetry (PLIF), and a probe developed by Professor Dibble at UCB to monitor the mixture ratio CH_4/air. Economic problems

at the company, Alturdyne, Inc., who was fabricating the rig as a donation, have set our schedule way back. We have assembled an atmospheric pressure rig with which we have obtained spatially resolved, time accurate measurements of a flame. To date, data have been obtained at relatively low frequencies, but the characteristics of the system should allow tests to 1 kHz. The Dibble probe is operating but has been used only for preliminary tests with new optical components intended to improve the signal/noise ratio.

Virtually all of our work in the year of the program has been devoted to tests of acoustically driven flames using our new PLIF system. We have successfully carried out tests in the frequency range 22–55 Hz. Simultaneous measurements of CH concentration and unsteady pressure allow evaluation of Rayleigh's criterion, both globally and locally (with a spatial resolution of $0.05mm^3$. We have been able to detect the dynamical consequences of a small change in the geometry of a single burner operating at atmospheric pressure. This application is related to a problem of oscillations in a full-scale flare at a solid-waste landfill in Los Angeles.

We believe that our results for the flame dynamics are the first obtained using PLIF applied to a forced system operating over a range of frequencies. Several groups have previously used chemiluminescence to obtain values of the Rayleigh index, the most immediately useful measure of combustion dynamics. The chief advantage of PLIF is the much superior spatial resolution. Thus if the method is successful, the potential exists for obtaining data for a few species concentrations (presently CH, OH and NO) accurate in time and on a very fine spatial scale. Such results will be most obviously useful for comparison with those obtained with numerical simulations. An eventual practical application is determination of influences of geometry in local production of NO.

In related experimental work as part of this program, two students (Pun and Matveev) have expended much effort acquiring accurate date for the performance of an electrically driven Rijke tube. The reason for this project is to provide a solid and comprehensive database for this simple system, which is probably the most widely used example for applying active control of combustion dynamics. Yet no complete set of data exists as the basis for checking theory applied to the uncontrolled system.

Short Course — Dynamics of Combustion Systems: Fundamentals, Acoustics and Control

Several months after this program began, the PI received a small grant to give the subject short course at the United Technologies Research Center. By mutual agreement of the PI and UTRC, the course comprises four visits with six hours of lecture during each visit. Much of the PI's time during the first fifteen months of this program was spent preparing the material and accompanying viewgraphs. The course will be given again at the NASA Glenn Research Center in September 2001. The outline of the current version of the course is included as Appendix A of this report.

1. Introduction

This research program was designed to be one of the first to investigate in depth the influences of fuel/oxidizer fluctuations and nonuniformities on the unsteady behavior of gas turbine combustors. The reason for this focused emphasis is the hypothesis that fluctuations of the mixture ratio in the flow generated in the premixer are a dominant contribution to the mechanism causing combustion instabilities in gas turbine combustors. Convection of temporal and spatial nonuniformities of mixture ratio into the combustion zone will produce fluctuations of reaction rate and hence of the energy release rate. The consequent coupling with the pressure field and the development of pressure waves may then develop into the global unsteady behavior observed with pressure transducers. This proposed mechanism is particularly attractive because it is conceivably present in any combustor, independent of geometry and, if true, immediately suggests possible strategies to reduce the severity of instabilities in operational systems.

The program at Caltech has been designed to examine the above behavior with all of the available tools. Numerical simulations will be used to provide more flexibility in the design of the combustor configuration as well as better time accurate details about the interaction between the heat release and the flow field. A theoretical analysis will also be used based mainly on a spatial averaging technique which has been used in the past to study combustion instabilities in solid propellant rockets. Along with the theoretical analysis, reduced order models will be developed which will reflect the true behavior in a combustor. These reduced order models will be used to examine various methods for feedback control of the instabilities, including the use of secondary fuel source that has shown promising results in a dump combustor. Experimental work will also play a significant role in this program. We intend to use various combustor and fuel injector designs to examine the interaction of fuel/oxidizer nonuniformities with the pressure field in an oscillating environment.

However, it is unlikely that one mechanism will explain the behavior of instabilities even in a particular combustor. The dynamics of combustion, as is even seen in simple flames, must always play a role. Thus, our work involves examining other mechanisms as well as fluctuations of mixture ratio.

2. Project Overview

As stated previously, the primary objective of this program was to establish the role of upstream fluctuations of fuel/oxidizer ratio on the stability and dynamical behavior of unsteady motions in a premixing gas turbine combustor; and to develop and make available to the technical community analytical methods for predicting the effects of this behavior in practical combustors.

Our technical objectives included: the development of a general procedure for analyzing the influences of fluctuations on mixture ratio by close coordination of numerical simulations and an analytical framework based on a form of spatial averaging; a procedure for constructing reduced order models and incorporating the general principles for active feedback control; and an experimental confirmation in a realistic premixer and combustor of the presence and consequence of fluctuations of mixture ratio. The primary diagnostics for the experimental work is our PLIF

system designed to give high spatial resolution and temporal accuracy for frequencies up to 1000 Hz.

Task 1 – Numerical Simulations

The numerical simulations were included as a part of this research program to be used in conjunction with the experimental results in Task 4 to better understand the mechanisms behind the development of instabilities in premixed combustors. Numerical simulations provide more flexibility in evaluating the designs of both the premixer and the combustor. This information can be valuable in the development of a wide range of experimental configurations. Time-resolved simulations can also provide more details about the flow field that might not be attainable experimentally. This information can be useful for the development of low-order heat release models, which can be valuable for use in Tasks 2 and 3 of this program. Finally, the experimental results can be used to fine-tune the numerical code in order to provide more accurate predictive capabilities for future gas-turbine combustor designs.

Since the focus of this work was not the construction of a numerical method, but the use of such a method in the further exploration of other issues, a commercially available code ANSWER, developed by ACRi, has been used. The code has a full Navier-Stokes solver that makes use of a fully implicit central and fully implicit upwind finite difference method to solve for the flow field variables. Past testing by ACRi has demonstrated the stability and accuracy of the steady state solver. Determining the steady state is useful as al beginning point for time-resolved simulations of the transient behavior of a given system. These time-resolved simulations of various combustor designs have shown progress in past efforts and are expected to provide more complete details about the flow field in the combustor designs used as a part of this program.

The key issues we are dealing with as a part of the time-resolved simulations are the chemical reaction rates, the turbulence, the acoustic wave speed, the boundary conditions and the added numerical dissipation and dispersion (due to a finite difference truncation of the spatial and temporal gradients). In order to reduce the computational time, the chemistry rates were simplified to a 3-step methane reaction:

$$CH_4 + 1\tfrac{1}{2}O_2 \rightarrow CO + 2H_2O$$
$$CO + \tfrac{1}{2}O_2 \leftrightarrow CO_2$$

A 5-step reaction rate that includes NO_x can be added to the above system to provide, at the very least, a qualitative examination of how the NO_x production varies. A standard k-ε model is used to determine the turbulence. In simulations where the turbulence has an influence on the mixing properties, a standard eddy breakup model was used to relate the reaction rate to the turbulence. The code has been modified to make use of the local temperature and chemical properties to determine the local acoustic speed for the pressure wave propagation. The issue of excess numerical dissipation and dispersion is due to finite difference truncation of the gradients (Runchal, 1977). If the dissipation is too great, then the system becomes overly damped and any oscillations may quickly diminish. In order to decrease the effects of numerical dissipation and more accurately simulate the real flow behavior, the non-numerical viscosity can be reduced,

leading to an overall viscosity more comparable with the real flow. During the course of this work, the greatest concern was with the modeling of the wave interactions at the numerical boundaries. The default boundary conditions for answer are configured such that the inlet behaves like an acoustically closed boundary (pressure gradient is zero) and the outlet behaves like an acoustically open boundary (pressure is fixed). For the dump combustor simulations, this default configuration was acceptable. However, these boundary conditions were not ideal for a Rijke tube simulation in which it was desired to have both boundaries acoustically open. Other methods for improving the modeling of the boundary conditions are being explored, but these methods have other deficiencies that need to be understood before the methods can be applied to generic problems.

Currently, there are four heat release configurations that are being simulated numerically. The first is an electrically heated Rijke tube. The second is a dump combustor. Both of these configurations have been tested experimentally at Caltech and provide a good comparison for the examination of the accuracy of the numerical simulations. The third is a full-scale gas turbine combustor with both a premixed and diffusion flame. This configuration is being studied as part of another program. The fourth is a reacting flow over a triangular wedge. This fourth configuration has been designed as the first experimental configuration for use in the combustor described in Task 4.

Because of the simple design and the well-defined acoustic modes, the Rijke or Sona Hauss tube provides a good starting point for examining how well the numerical techniques simulate transient behavior of pressure instabilities. Results were obtained for both a simulation acoustically open at both ends and acoustically closed at both ends.

As shown experimentally and theoretically, the strength of the excited harmonics is dependent on the location and strength of the heat source. Rayleigh's criterion states that when the pressure and heat release fluctuations are in phase, the system will be driven at that frequency. This is described by the equation:

$$R = \oint_V \int_t^{t+\tau} \frac{p'}{\bar{p}} \frac{Q'}{\bar{p}} dt dV$$

where p is the pressure, Q is the heat release and τ is the period of the mode. If R is positive the system is driven and if R is negative the system is damped. Theory indicates that p' lags u' by 90° and predicts that Q' lags u' by about 60° (Raun et al., 1993). Therefore, for an acoustically open-often tube, the fundamental mode will be excited if the heat source is located between $0 < x < \frac{1}{2}$, where L is the length of the tube.

Figure 1 shows a sketch of the experimental Rijke tubes studied at Caltech and the numerical domain. The numerical simulations assure a 2-D flow structure and no turbulence. The reference pressure is 1.013×10^5 Pa and the inlet temperature is 300 K. All results are presented based on the tube length, L.

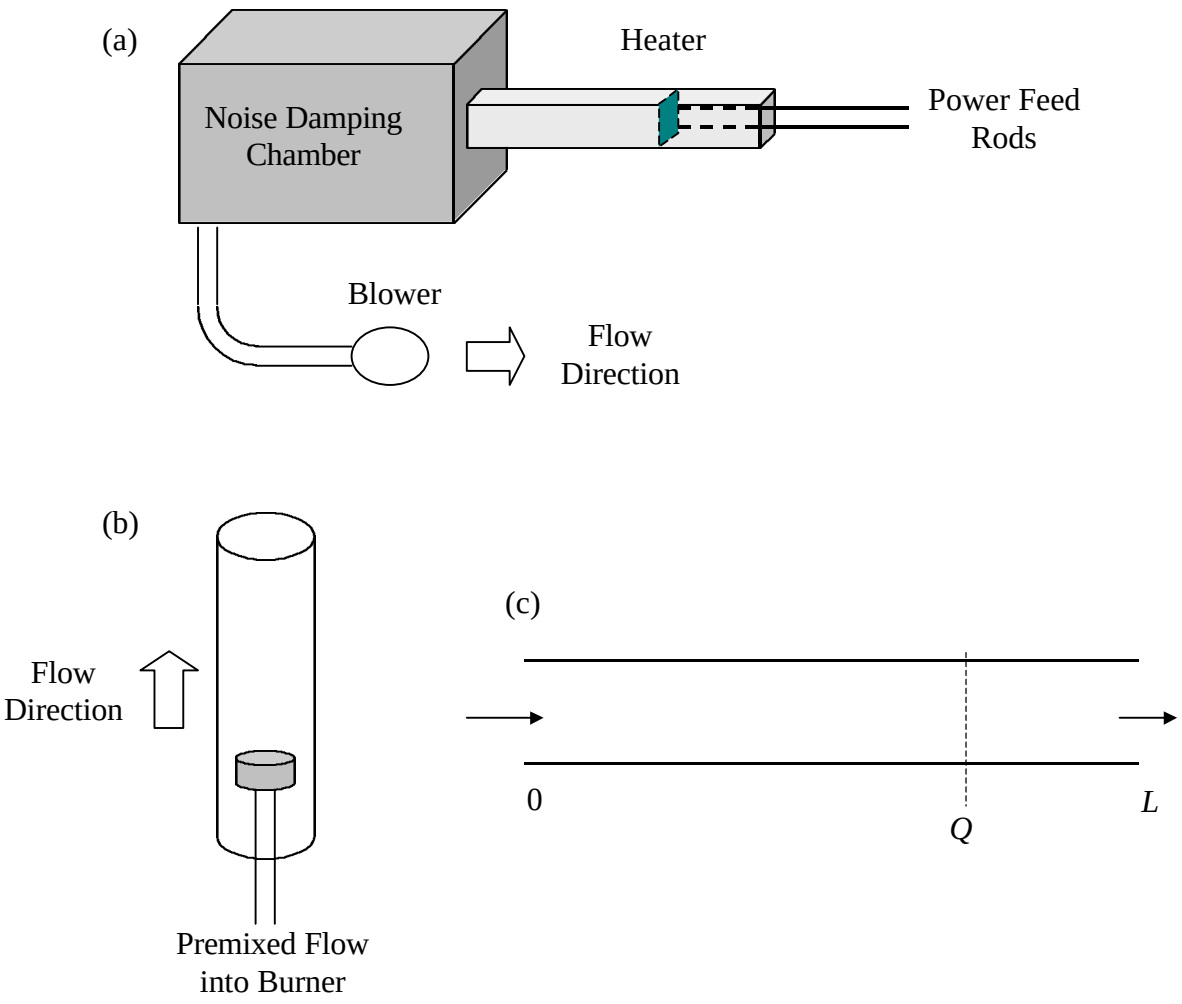

Figure 1. (a) Sketch of Experimental Rijke Tube with Planar Heat Source; (b) Sketch of Rijke Tube with Premixed Flame; (c) Sketch of Numerical Domain

Figure 2 shows the results for a simulation which is acoustically closed at both ends. A power source of 40,000 w/m^2 was placed at two locations in the tube. Theory and experiments match the numerical results, which show that the fundamental mode is excited with the heat source at 3*L*/4 and is damped with the heat source at *L*/4. Figure 3 shows the pressure and velocity mode shapes for the 3*L*/4 case. Figure 4 shows the time dependence of the fluctuating velocity, pressure and heat release. Averaging over the period of the fundamental frequency shows that the heat release and pressure are in phase when the heat source is at 3*L*/4. Rayleigh's criterion is positive and the system is driven as is seen in Figure 2. These results indicate that we could possibly use a simple *n*-*x* model to describe the heat release oscillations in a Rijke tube.

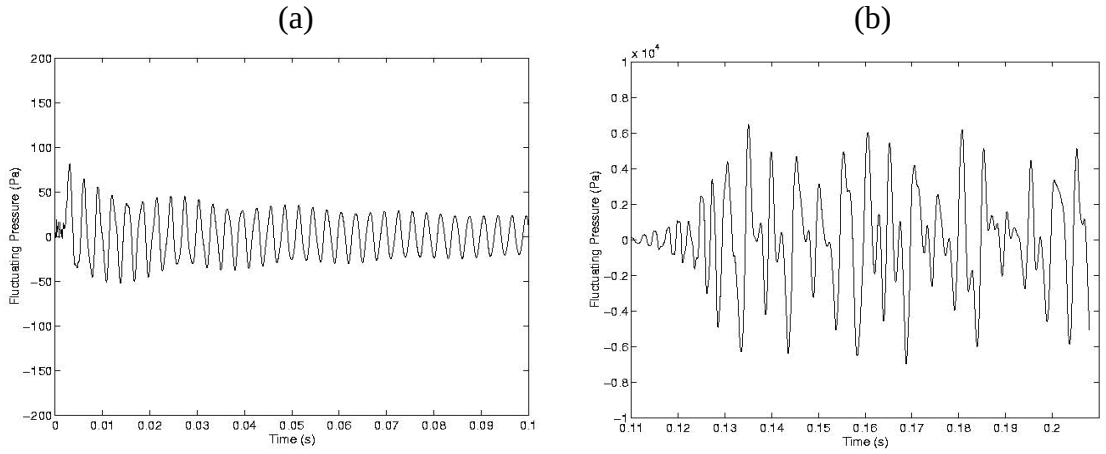

Figure 2. Results for Heat Source in Tube Acoustically Closed at Both Ends (a) Heat Source at *L*/4; (b) Heat Source at 3*L*/4

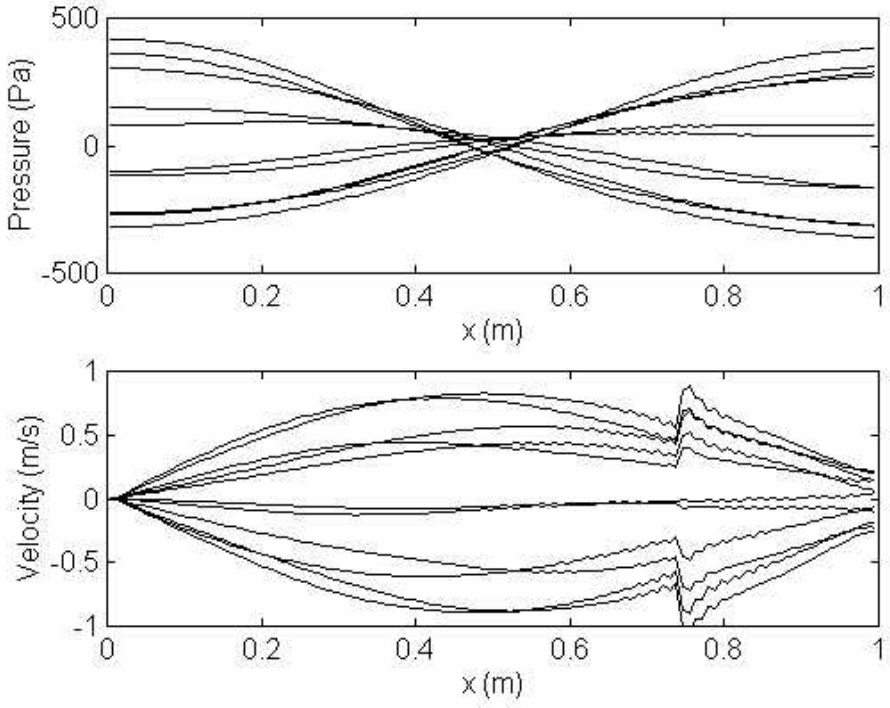

Figure 3. Pressure and Velocity Mode Shapes with Heat Source at 3*L*/4

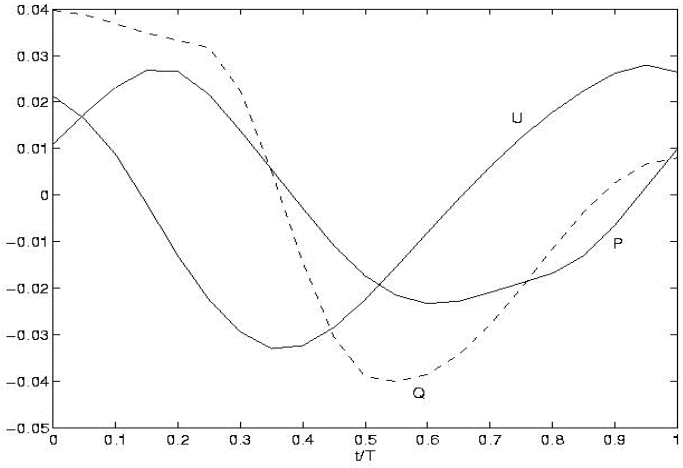

Figure 4. Fluctuating Flow Variables During Cycle of Oscillation with Heat Release at 3*L*/4

For the dump combustor, we add the increased complexity of a turbulent, reacting fluid. A sketch of the dump combustor is shown in Figure 5. For the inlet section, x_s is 0.43m and H_s is 0.0254m. The step ramps up to a 75% blockage at the dump plane. The height at the dump plane, D, is 0.00635m and will be used as the reference length scale. The total length, X_l, is 1.29m and the expansion ratio, H_s:D, is 12:1 for the simulations.

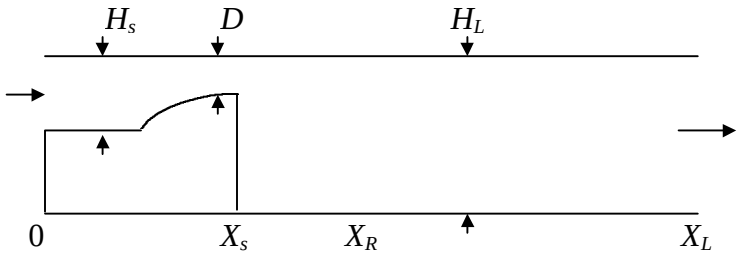

Figure 5. Sketch of Dump Combustor Configuration

The main configuration designated as Case A matches the experimental results of Zsak (1993) with a methane-air mixture at an equivalence ratio of 1.3. The mean flow velocity at the dump plane, U_{step}, is 21 m/s. For the steady state results, the recirculation length, X_R, is reduced for a reacting case as compared to a non-reacting simulation. Based on Step Height, $S = 11D$, $X_{R/s}$ = 5.47 for a non-reacting flow and 2.24 for a reacting case.

The transient results for Case A are shown in Figure 6. The primary unstable acoustic modes are 226 Hz and 165 Hz, which compare well with theoretical and experimental modes determined by Zsak (1993) (235 and 187 Hz). Figure 7 shows the axial velocity during a period of the cycle for Case A. There is a clear vortex shed from the step.

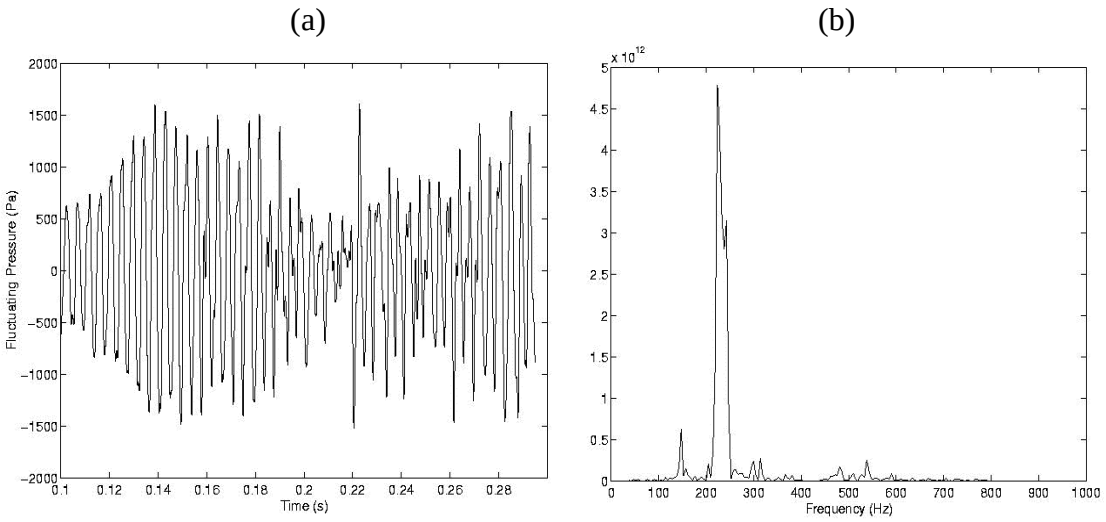

Figure 6. (a) Case A Transient Simulation; (b) FFT of Pressure Record

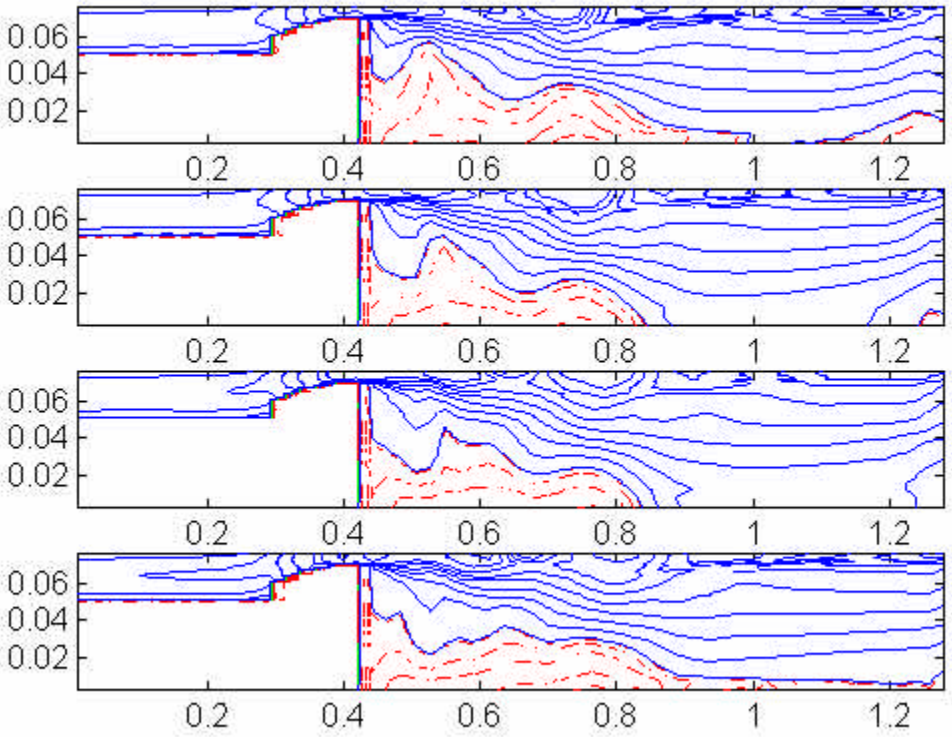

Figure 7. Axial Velocity During a Period of the Cycle for Case A

Four additional cases were examined to determine the impact of flow velocity and equivalence ratio on the stability. Figure 8 shows a mapping of the results, which matches closely the experimental results at Caltech for the dump combustor.

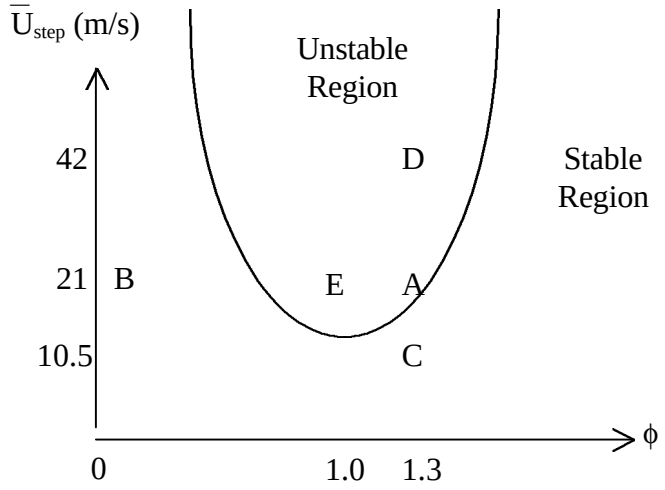

Figure 8. Stability Map for 12:1 Dump Combustor Simulation

A basic passing control method using a Helmholtz resonator was tested with the numerical simulations. Helmholtz resonators have been used as sound filters and noise suppressors since the late nineteenth century (Harrje, 1972). Figure 9 shows the two configurations tested. Figure 10 and Figure 11 show the pressure traces compared with Case A. Both configurations seemed to show damping of the oscillation. More work needs to be undertaken to better study the possible impact of using Helmholtz resonators as passive control devices.

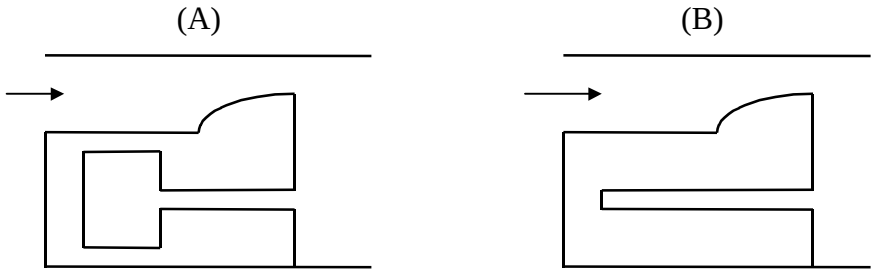

Figure 9. Helmholtz Resonator Configurations

At this point, we have only examined the triangular wedge configuration in steady state. We have been trying to work out the deficiencies in the numerical code with the Rijke tube and dump combustor configurations before attempting a proper simulation of the other flow configurations.

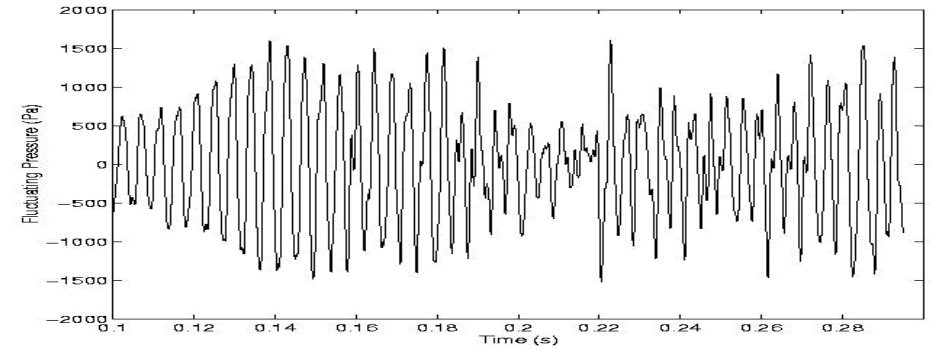

(a)

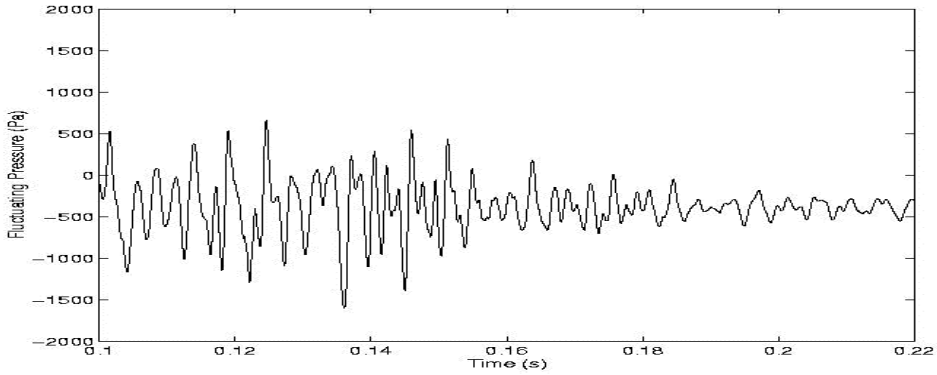

(b)

Figure 10. (a) Case A without Resonator; (b) Case A with Resonator (A)

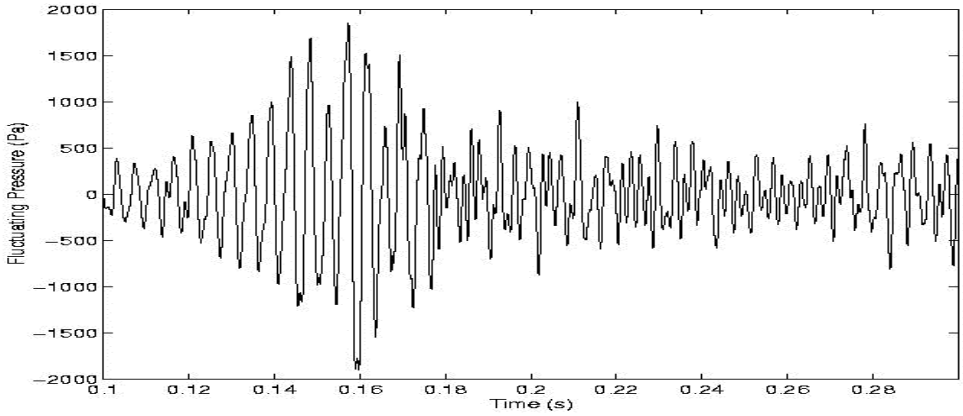

Figure 11. Case A with Resonator (B)

These simulations have shown promising results. It is possible to properly simulate unsteady combustion with numerical methods. The major concern that still needs to be worked out for future efforts is proper simulation at the boundaries. Once the boundary conditions have been worked out, numerical simulations will become a useful tool for the study of instabilities.

Task 2 – Analysis of Combustor Dynamics

The framework we use for our analysis begins with a suitable expansion of the general equations of motion in two small parameters, Mach numbers characterizing the steady and unsteady flows. Several classes of problems can be defined, differing in the orders of terms retained. After expansion of the unsteady field in the normal acoustic modes of the chamber, with time-varying amplitudes, the equations are spatially averaged. The result is a set of coupled ordinary nonlinear equations for the amplitudes of the modes. The forcing functions of the oscillators contain formal representations of all the relevant physical processes. At this stage the analysis is quite generally applicable but cannot produce quantitative results because the values of various parameters and coefficients are not known.

Only the representation of the unsteady gas dynamics is completely known. All other processes must be modeled. Those matters are the business of Task 2. However, apart from continuing modest effort with some theoretical aspects not reported here, during the past year we have mainly been concerned with using this analysis to investigate various aspects of feedback control of combustion dynamics with noise and time delays included.

Much of the work accomplished in this task has been included in Professor Culick's notes forming part of the short course "Control of Engine Dynamics" given at the Von Karman Institute, Brussels, Belgium, May 14–18, 2001; and in the short course "Dynamics of Combustion Systems: Fundamentals, Acoustics, and Control" given at the NASA Glenn Research Center in September 2001. A previous version was given at the United Technologies Research Center, 1998–99 under AGTSR sponsorship. **Without AGTSR support, it is highly unlikely that this short course would have been formed.**

Task 3 – Reduced Order Modeling and Methods of Feedback Control

All of our work in this Task is set within the analytical framework developed at Caltech and being continued in Task 2. One of our purposes is to investigate varying methods of control within a common analytical structure that has been proven successful for studying combustor dynamics generally.

The typical characteristics of combustors make designing a controller a challenging task. The model used in the design is a considerably reduced representation of the real system; this causes large uncertainties in the parameters. In addition to that, there are very intense internal noise sources due to gas dynamics and combustion and significant time delays that reduce the stability margin. Scaling is also an issue: most of the experiments are conducted in laboratory-scale combustors. Nonlinear processes, especially in the flame models, are not completely understood, and the models normally include a limited representation of those processes. In the case of laboratory combustors, it is possible to ignore the nonlinearities and design a controller on the system linearized around the 'unstable' equilibrium point that the control aims to reach. In the case of classical controllers, they scale linearly with dimensions, but, at this point, it is not clear how the nonlinear processes in the combustor scale: they could become a major issue in large combustors. Moreover, a clearer understanding of nonlinearities is required for the design of

nonlinear controllers, that have the potential of being much more efficient in terms of the ratio of the energy going into the control effort versus the total energy released into the system.

Instabilities in combustion chambers typically manifest themselves as pressure oscillations growing to limit cycles. Experiments (Isella et al., 1997) show that in some combustors there is a subcritical bifurcation leading to the instability: in this case nonlinear control might be more appropriate, and results from linear simulations could be misleading, especially in the vicinity of the bifurcation point.

While several of the studies cited include sensor noise and/or parameter variations as part of the system, none of them makes a clear distinction between those uncertainties, the intrinsic noise sources of the system (additive and multiplicative), and the unmodeled dynamics. In the following we will describe how each one of these effects can be included in the control design process. Time-delay, often overlooked in the consideration of combustion systems, can be introduced in the control design as a further uncertainty by using the same framework. A different method, based on an external compensation network, is also presented.

The controller is designed and tested on the model of a small cylindrical combustor with an instability in the first longitudinal mode. The model, based on an approximate finite-dimensional representation of the flowfield (Culick 1989), has been widely used in literature as a test case for the analysis (Culick and Yang, 1992, Yang et al. 1992, Haddad et al. 1997); even if this might not be realistic in the specific value of the parameters, the model presents a dynamical behavior representative of a combustion chamber, and serves well as a test case. The methods described are obviously not limited to this specific case, and can be applied in general.

Noise sources arise from nonlinear fluid mechanics and as such form an integral part of the system; previous studies have only taken into account external noise sources (such as noisy sensors/actuators). Recently we have shown how these intrinsic noise sources affect the system response and how they can be used to identify the linear parameters of a stable system (Seywert and Culick, 2000).

Task 3 (a) Combustion Instability Model

The fluid dynamical equations (continuity, momentum and energy) governing the flow in the combustion chamber can be combined to yield a nonlinear wave equation for the pressure which in turn, after applying ‘spatial averaging’ leads to a system of coupled oscillator equations. This system can be truncated to a finite number of modes to get a low order representation of the combustion chamber. This procedure has been described elsewhere in full detail (Culick, 1976, Culick and Yang, 1992) and is not repeated here.

The central idea motivating the structure of the analysis is that combustion instabilities are dominated by acoustic waves. Hence the pressure field has been represented by an expansion in terms of the acoustic modes of the chamber. However, following a principle discussed by (Chu and Kovaznay, 1956), small disturbances are in general made up of three kinds of waves: acoustic, entropy and vorticity waves. Unlike previous analyses in which only the organized

oscillatory acoustic field was accounted for, all three wave types were retained here. The extra waves give rise to stochastic terms in the equation (Burnley, 1996).

The resulting system of acoustic equations is similar to the one used in previous work (Culick and Yang, 1992) with the additional source terms representing stochastic or noise sources:

$$\ddot{\eta}_n + w_n^2 \eta_n = \underbrace{-\sum_{i=1}^{\infty} \left(D_{ni} \dot{\eta}_i + E_{ni} \eta_i \right)}_{\text{Linear gasdynamics}} + \underbrace{\sum_{i=1}^{\infty} \left[x_{ni}^{u}(t) \dot{\eta}_i + x_{ni}(t) \eta_i \right] + \Xi_n(t)}_{\text{Noise source terms}} \tag{1}$$

We have retained only the linear terms in the acoustic amplitudes. Since we are going to design a controller to eliminate the pressure oscillations (i.e. drive all acoustic amplitudes to zero) this is equivalent to linearizing the nonlinear system around the unstable equilibrium point. Note that the linear terms include all linear processes, including linear combustion dynamics. The linear combustion part has in this formulation been lumped together with the linear fluid dynamics into the coefficients E_{ni} and D_{ni}; in fact it is the linear combustion that makes the system unstable to begin with. Note also that while the higher order acoustic terms have been neglected the nonlinear dynamics due to the vorticity and entropy waves are included in the noise terms. The combustor is linearly stable if and only if all modes are linearly stable.

For control applications it is advantageous to reformulate this set of equations in state-space form:

$$\dot{x} = Ax + Bu$$
$$y = Cx + Du$$

where the matrices A, B, C, D are formed appropriately.

Task 3 (b) Control Theory

General Considerations

Even before the development of models including combustor dynamics and feedback control, experimental application of feedback control of combustion instabilities was successfully tested on small systems (mainly using loudspeakers as actuators). Those laboratory demonstrations report examples in which the amplitudes of limit cycles in linearly unstable combustors have been significantly reduced, sometimes even to vanishingly small values (for example Poinsot et al. 1987, Gulati and Mani, 1992). In most cases, the 'practical' controller was a simple proportional feedback or a variation of a PID controller. One might wonder why that simple approach works or, conversely, ask why we need more sophisticated control methods.

From a general viewpoint, experiments show that an unstable combustion chamber is a system exhibiting a linear instability (rapidly) growing to a limit cycle (defined by the nonlinearities) that typically shows a marked predominant frequency. In terms of dynamical systems, the combustor is characterized by two unstable complex-conjugate poles and a series of stable poles with relatively large damping. Provided that the combustor is observable and controllable, for this kind of system, a proportional feedback or a PID controller can be successfully tuned to obtain a stable feedback loop. Regarding the issue of controllability (and observability) of the system, for the

purpose of this argument, we will say that controllability has been proved in practice by the success of the experiments cited.

The need for more sophisticated control methods derives mainly from two aspects: first one might want to impose performance specifications on the controller, for example on the maximum control action, or on the noise or disturbance rejection. Second, combustion systems show a high degree of uncertainty and variability (Lieuwen and Zinn), and a controller 'tuned' on a particular operating point does not guarantee a reliable performance. Modern control design methods allow for the introduction of this kind of consideration during the synthesis of the controller.

All the considerations above and the design method presented in the following section are based on a linear model of the combustor. On the other hand, the real system is manifestly nonlinear: the main indication of that is the fact that the pressure oscillations in the combustion chamber rapidly reach a limit cycle. A complete understanding of the dynamics of the combustor would allow tracing the source of the nonlinear behavior observed in the experiments (limit cycles, hysteresis, as in, for example, Isella et al. 1997 and Lieuwen and Zinn 2000) to its origin: nonlinear fluid dynamics or nonlinear combustion. In that case nonlinearities in the system could be exploited by an *ad hoc* form of (nonlinear) control to overcome the main limitations of linear control: requirement of a relatively high control effort and actuation frequency at the same frequency of the instability.

Since such a complete model is not yet available, we decided to limit the analysis to the linear case. Note that the linear model of the combustion chamber presented in the previous section is actually a linearization of the full model around the operating point. Given that the main purpose here is to keep the system 'stable', i.e. as close as possible to the linearized equilibrium point, the linear model and simulation is a valid approximation to the real case, provided that the nonlinearities do not give rise to a subcritical bifurcation. Note that nonlinearities have the effect of limiting the amplitude of the oscillations: hence the linear model is in this sense a 'conservative' approach to the problem (for example, in terms of required control action, we will find an upper limit).

In short, within the present approach, nonlinearities can actually be neglected, except as a formal vehicle for rigorously introducing noise sources. As a consequence, we will not be able to capture the effects of any instability mechanism different from the linear growth and phase shifting included in the model presented above. On the other hand, the present approach allows for a clear distinction of the effects of uncertainties, intrinsic noise sources, external noise sources, unmodeled dynamics and time-delay.

Robustness

As mentioned above, any controller should be able to accommodate changes in operating conditions and various disturbances (e.g. varying fuel/air ratio) and at the same time be easy to implement. The strategy we propose allows for the presence of parameter uncertainty (due to uncertainties in the modeling or system identification process), multiplicative noise (in this case intrinsic to the system, arising from vorticity and entropy waves) and residual dynamics. The system is split into two parts: the controlled dynamics that will be used in the design of the controller and the residual modes that are neglected in this design. The reasoning behind this

splitting is that we want to achieve a controller that is as simple as possible. This desire leads to a need for a low order model of the system. The controlled dynamics describe that low order system (which at the minimum needs to include all unstable modes) whereas the residual modes describe those parts of the original system that the designer chooses to disregard (the higher acoustic modes which are strongly attenuated in the combustion chamber).

The coefficients representing the multiplicative and additive noise, lacking precise information about their nature (as in many practical applications), are assumed to be described by Gaussian white noise processes with a mean of zero (a nonvanishing mean value can be included in the nominal system parameters).

The various parameters of the system are characterized by their nominal value and an uncertainty range which can be different for each parameter – e.g. while the frequencies of each mode might be well defined and invariant with operating conditions the growth rates might depend substantially on flame location or fuel/air composition.

The controller (for the nominal low order system) can be designed following standard methods; in our case we use an LQG design. LQG is advantageous here because it allows for the inclusion of additive system noise. The stability of the closed-loop system in the presence of noise, uncertainties and neglected dynamics can then be checked using an algebraic relation that we have derived from the results of Chou et al. (1998) and Biswas (1998).

Time Delay

Time delays often arise in combustion systems: for example, even when no control is present, there is delay between injection of the fuel mixture and fully developed combustion for the case of liquid or gas combustors. When feedback control is present, there are delays intrinsic to the controller due to finite rates of actuators and sensors, time spent for signal acquisition and processing, and clock time in case a digital computer is used. Also fluctuations of the air/fuel ratio at the injection point propagate with finite speed to the flame zone, giving rise to a possible mechanism for instability. Even for the typical laboratory-scale combustor, when a loudspeaker is used as an actuator, time delays play an important role: suppose the first unstable acoustic mode has a frequency of 1kHz. Assuming that the controller, implemented on a digital computer, can be much faster than that, the bottleneck for this case is the time it takes for the pressure input (from the loudspeaker) to influence the chamber acoustic response. This time, for a 50cm chamber, is of the order of 1–2ms, just the same order of the instability. In the case of industrial scale combustors, or when using secondary fuel injection as control actuation, the necessity of considering time delays becomes even more compelling, since in these cases the time delay can easily be larger than the characteristic time scale of the instability.

Time delays always reduce the stability of a system; hence, it is very important to take them into consideration when simulating a realistic combustor and when designing a suitable controller. Regarding the controller design phase, three general approaches are possible.

- *Classical Control*. The time delay is approximated with a rational function that increases the effective order of the plant, making the control design problematic. In the present work we

do not take this method into consideration, since we focus our attention on control design methods capable of incorporating robustness requirements.

- *Modern Control*. In this case, time delay can be viewed as an uncertainty in the system and incorporated in the design as a multiplicative perturbation to the original plant. In general performance is degraded and, if τ is large enough, it might be impossible to design a stabilizing controller for the delayed system. On the other hand, when a solution exists, stability and performance are guaranteed according to the design. Uncertainty in the numerical value of the time delay, as it is typical in combustion systems, is automatically taken into consideration by the design method.

- *Delay Compensation*. In the example presented later, we will examine a method based on the idea of *predictive control*: the time delay is compensated by a predictor that acts on the measured or estimated state and feeds the controller with the appropriate "forecast" signal to perform the feedback action at the correct time. A discussion of predictive control can be found in Furukawa and Shimemura (1983). The time delay is compensated in a secondary predictor-loop; application of this scheme allows inclusion of significant time delays in the system without compromising performance in the design of the controller. On the other hand, the use of a second loop reduces the robustness of the system to uncertainties in the value of the parameters.

Task 3 (c) Examples

In the following we will briefly demonstrate the described design procedures on a particular example. The example has been chosen solely because it has been used previously in the literature. The methods used are obviously much more general and can be applied to any linearized (combustion) system—as mentioned previously, *all* processes, including combustion, have been linearized and are embedded in the model parameters.

The numerical example used is the same one as given in Haddad et al. (1997) and used previously by Culick and Yang, (1992) and Yang et al. (1992). The combustion chamber is assumed to be cylindrical of length L and only longitudinal modes are considered. The chamber is closed on the upstream end and has a nozzle at the downstream end that acts as an acoustically closed boundary. The sensor detecting the instability is a microphone located at x_s whereas the actuator used to control the pressure oscillations is a loudspeaker located at x_a. The internal dynamics of the loudspeaker are modeled as a second order system and included in the state-space formulation through augmentation of the state. In this way the actuator dynamics are accounted for in the design of the controller. In this example the actuator (and sensor) are treated as perfectly known systems; within the framework described here it is straightforward to include uncertainties or noise in those systems too.

Note that the model of the actuator as a `loudspeaker', a second order system with a high gain, is actually more general than it seems. If we wanted to represent an injector, the same model would still apply, with a longer time delay, and some difference in the numerical value of the parameters, but substantially the same structure, i.e. second order dynamics and very high gain; see Neumeier et al. (1997) for an example.

In this design study we consider uncertainty in the acoustic parameters and noise in those terms given in equation (1). In other words there is no noise or uncertainty in the sensing or actuation process and the stochastic sources act (as described by the model) as random perturbations of acoustics. Furthermore we assume that all stochastic sources (due to the vorticity and entropy modes in the chamber) are uncorrelated and have the same variance σ^2. Finally we assume that the parameter uncertainties can all be described by a single variable ε. These assumptions are only made to simplify the expressions and do not introduce any loss of generality.

A controller was designed using an LQG technique by taking only *one* mode (the unstable first mode) into consideration. It is assumed that the complete system is given by four modes and thus the remaining three modes are considered to give the residual dynamics. Basing the controller on a minimal set of modes is desired as it reduces the order of the controller and thus allows for easier implementation. Figure 12 shows the response of the reduced and complete system to the controller (turned on at $\tilde{t} = 100$). As expected, the presence of the extra modes (not considered in the design) in the full system reduces the performance of the controller (slower decay).

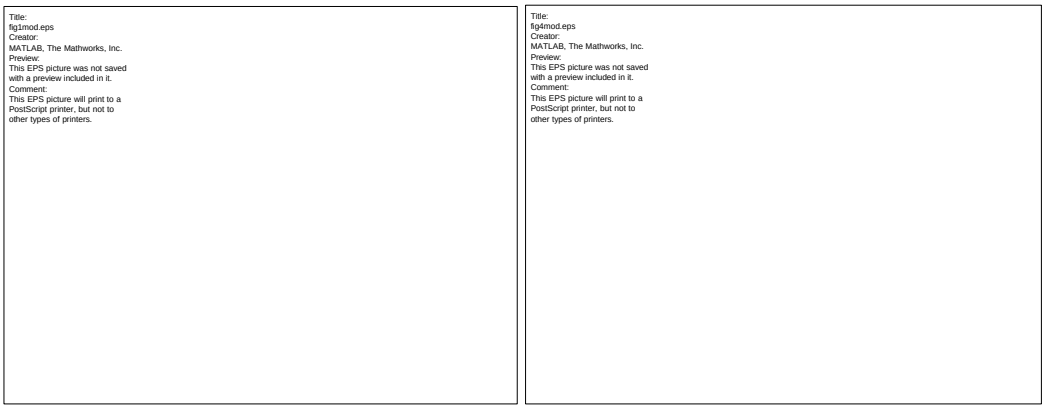

Figure 12. Left: Nominal system (only 1 mode) response to control. Right: Response of complete system (all 4 modes) to the same controller

Figure 13 shows the guaranteed stability limits (in terms ε and σ) of the controller. The solid line is the predicted stability limit for the truncated system where only *one* mode is used in the simulation. The other lines describe the stability region as more modes are added in the simulation, i.e. as the system approaches the 'complete' system. The region shrinks as additional modes are introduced into the simulation while the same controller (based on one mode) is retained. In this extreme case (where we considered only one mode to base the controller on) the changes are drastic, but as the neglected modes become more heavily damped their influence grows smaller (as can be seen by the lines moving closer together).

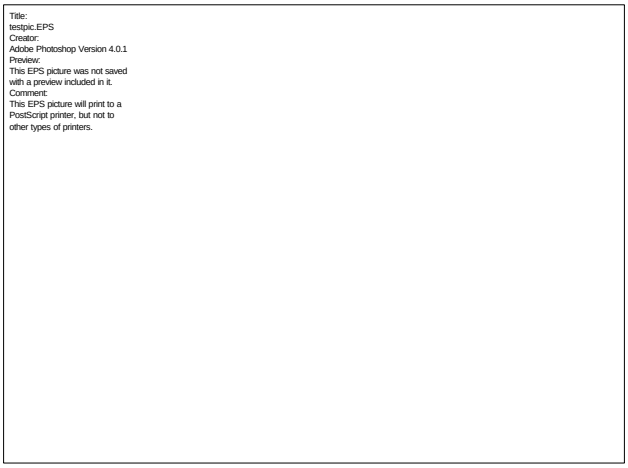

Figure 13. Guaranteed stability limits for closed-loop system in σ-ε plane (noise variance and uncertainty) depending on number of residual modes considered

Figure 14 illustrates the effect the (stable) residual system can have in the presence of noise. The same controller (based only on the unstable first mode) is used in all three cases. In case A (low noise) the controller is able to stabilize the full system (all four modes included in the simulation); however, at a higher noise level (case B) the pressure oscillations do not decay to zero. Note that this noise level is well within the stability limits as predicted with the truncated (one mode) system and thus underlines the importance of the neglected dynamics. If the simulation is performed with the reduced system, the instability does indeed decay as anticipated (case C).

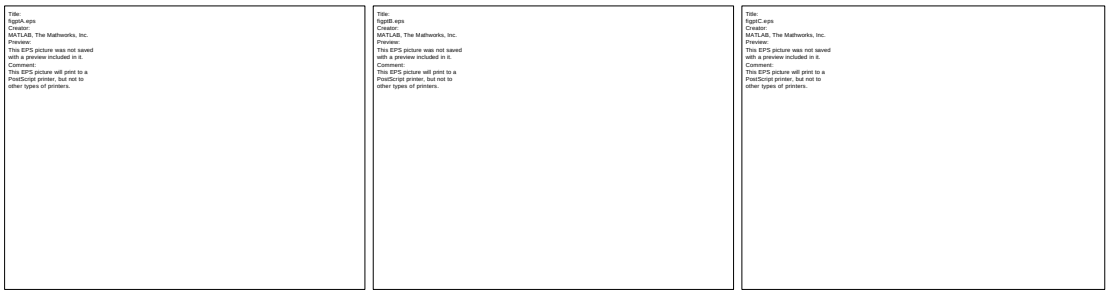

Figure 14. From left to right: time simulations of cases A, B (complete system), and C (reduced system) as defined in Figure 13.

Example with Time Delay Compensation

The delay compensation approach allows separating the control problem from compensation of the time delay. Figure 15 presents the results of the application of the method to our model combustor. The non-dimensional time delay is chosen to be $\tau=10$, which corresponds to a delay of about 10ms, i.e. five periods of an oscillation at 500Hz and constitutes a reasonable upper limit to the delay that can be expected in a real combustor controlled by modulating the injection of a secondary fuel. Note how the predictor works: the controller (control action is plotted in the bottom half of Figure 15) starts sending commands immediately when it is activated. The control is computed on a prediction of the future state of the system, i.e. the state of the system when the control signal will effectively reach the plant. The system response, plotted in the top half of Figure 15, shows that the system effectively starts reacting to the control at a non-dimensional time of 40 when the controller is put online at a non-dimensional time of 30.

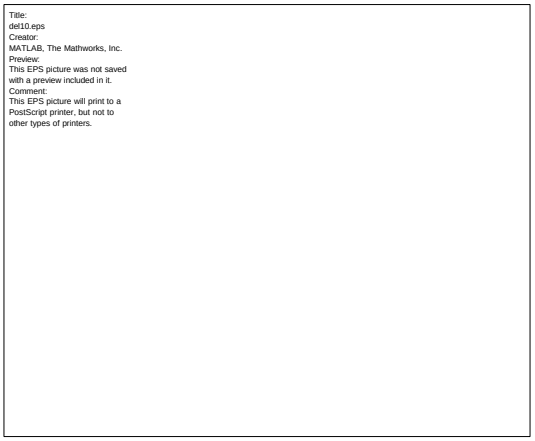

Figure 15. Control with time-delay, (τ=10). Top half: system response. Bottom half: control action.

Task 3 (d) Concluding Remarks

This recent work shows how uncertainties, noise, unmodeled dynamics and time-delay can be included in the controller design for combustion instabilities.

A clear distinction has been made between the uncertainty and the noise. This is necessary as the parameter uncertainty can be bounded; e.g. in practical applications we might know that in the operating range of interest or for all applicable fuel/air ratios the various parameters are located within certain numerical bands. In contrast, true noise sources can in general not be bounded, and thus do not fit in the common control frameworks; they are characterized by their mean values, which we include in the system parameters and by their variation.

Explicit consideration of the neglected modes allows studying their influence on the controller robustness. This is especially important since in most experimental implementations to date the controller has been designed by taking only the unstable mode(s) into account. In the example given here only the first mode is unstable and it is in fact possible to stabilize the system by solely controlling this one mode. Note that the controller is designed to accommodate large uncertainties (or noise) since we anticipate that the residual modes will affect the dominant first mode. This is the way unmodeled dynamics are traditionally handled: by including them in the uncertainties of the system. The framework presented here shows how much of that uncertainty can be attributed to the neglected modes. In the example given, the damping of the ignored modes (notably the second one) is rather small and thus we see that the actual parameter uncertainty ε (or noise intensity σ) that the controller can tolerate declines dramatically as additional modes are considered. Therefore we conclude that the residual dynamics dominate the uncertainty unless the neglected modes are highly damped.

Inclusion of a time-delay in the modern-design framework as an uncertainty is adequate when the time-delay is of the same order of the characteristic time of the instability, defined as the inverse of the frequency of the unstable mode. Cases with longer time delays, as it might be the case in full-scale combustors, can be treated by adding a second loop to compensate for the delay: simulation shows very good performance, but issues about robustness to uncertainty and

perturbations need to be addressed carefully. An adaptive observer might be needed for application to real systems.

Future work in this area should include testing of the concepts on an experimental combustor; and system identification to define better models of real actuators, in particular injectors and fuel flow modulators. More analysis is also needed to characterize (and eventually take advantage of) nonlinearities naturally present in combustion chambers.

Task 4 – Experimental Work

Task 4(a) The Caltech Combustor Rig

Progress continues slowly to be made on a combustor test rig. Business troubles at Alturdyne, Inc. (the principal contractor for the rig) have slowed production of the unit and made the delivery date uncertain. Our plans have changed. The test rig will be located in a new Alturdyne laboratory off-campus. That decision solves potential problems of noise and safety that we feared we would encounter with the rig on campus.

Task 4(b) Optical Probe for Mixedness Studies

Nonuniformities in the mixture ratio can have a dramatic effect on the pollutant production in the combustion chamber of a gas turbine engine. Under lean conditions, it is desirable to be completely mixed; minimizing "hot" pockets which will increase the overall production of NO_x. Studies using a hydrogen-piloted lean premixed burner (Mongia, et. al, 1996) have shown that an unmixedness level of $U = 0.0085$ can result in a fourfold increase in NO_x concentrations over the perfectly mixed case. The degree of unmixedness, U, is given by:

$$U = c'_{rms}{}^2 / (c_m (1 - c_m))$$

where c'_{rms} is the rms fluctuation of the fuel concentration, and c_m is the mean fuel concentration. $U = 0$ corresponds to the perfectly mixed case, while $U = 1$ indicates perfect unmixedness.

An infrared (IR) optical probe is being employed to measure the degree of unmixedness in the premixer sections of various combustion arrangements. Technical experience regarding this probe is provided courtesy of Prof. R. W. Dibble of U.C. Berkeley, where practical application of the probe has been successfully demonstrated on simpler combustor designs. Details of the probe have been discussed in the Semi-Annual Report, 1 March 2000 to 31 August 2000. Our version is working and has been calibrated. It is currently being improved as part of an undergraduate student's summer research.

Task 4(c) PLIF Laser Diagnostics for Unsteady Motions[1]

Introduction

As emissions regulations continue to drive the gas turbine industry towards lean premixed operation, combustion instabilities have caused increased concern. Operating in the lean regime has the advantage of suppressing flame temperatures and lowering the production of thermal NO_x. The drawback is that combustors in the lean limit tend to exhibit unstable behavior more readily, and are highly sensitive to fluctuations in mixture ratio.

The mechanisms causing combustion instabilities in gas turbine combustors are not well understood. Although similar in principle to a Rijke tube (Raun et al. 1993) (a heat-driven acoustic oscillation), the added geometric complexities and injector configurations of a practical combustor make their dynamical behavior unpredictable. Current industry design techniques are largely empirical and not clearly defined in respect to combustion instabilities. Ultimately, industrial combustor designs are finalized without a clear measure of the stability margins of the system. A method for predicting and evaluating the stability characteristics for a given combustor configuration is required as part of the basis for more robust design. A central objective of our work is to develop such a method that if successful would avoid the costs of troublesome designs after fabrication.

In order to study the unsteady dynamics of a combustion chamber, a reliable technique to visualize the combustion processes and their response to an oscillating pressure field would be extremely useful. Two important techniques used to perform these measurements are chemiluminescence and planar laser-induced fluorescence (PLIF).

Chemiluminescence of the CH radical, an excellent marker for the reaction zone, has been used by a number of researchers to study heat release in an unsteady flame. They can be categorized into two groups; measurements using a PMT with a slit obscuring a portion of the flame to obtain some spatial (typically axial) resolution (Sterling and Zukoski 1991; Chen et al. 1993; Kappei et al. 2000), and fully two-dimensional imaging using a CCD based camera (Broda et al. 1998; Kendrick et al. 1999; Venkataraman et al. 1999). Of these works, one involved an acoustically forced flame (Chen et al. 1993), but used a PMT with a slit configuration which obtained only integrated one-dimensional information.

The first demonstration of 2-D (planar) LIF of the hydroxyl radical in a flame was apparently performed by Dyer and Crosley (1982). This technique has been used to measure a variety of chemical species in unsteady reacting flows, including OH as a measure of the heat release (Cadou et al. 1991; Shih et al. 1996), and fuel-seeded NO to measure the temperature field (Cadou et al. 1998). A summary of these various works involving both chemiluminescence and PLIF is provided in Table 1, including the acoustic frequencies used in the studies.

[1] This section contains an adaptation of work presented at the July 2000 AIAA Joint Propulsion Conference held in Huntsville, AL, paper AIAA-2000-3123, subsequently accepted as a paper to be published in *Combustion Science and Technology*.

	Chemiluminescence	PLIF
Naturally Unsteady	• Sterling and Zukoski (1991) (188 Hz) • Broda et. al. (1998) (1750 Hz) • Kendrick et. al. (1999) (235 Hz, 355 Hz) • Venkataraman et. al. (1999) (490 Hz) • Kappei et. al. (2000) (370-460 Hz)	• Cadou et. al. (1991) (43 Hz) • Shih et. al. (1996) (400 Hz) • Cadou et. al. (1998) (328 Hz)
Acoustic Forcing	• Chen et. al. (1993) (300 Hz, 400 Hz)	• Cadou et. al. (1998) (360 Hz, 420 Hz)

Table 1. Previous Work in Oscillating Flames

While chemiluminescence measurements are much more convenient to apply since they do not require a costly laser pump source, they have several disadvantages. Chemiluminesence measurements cannot capture fine structures in the flame, since the signal is integrated through the depth of the flame. PLIF images are taken on a very specific plane where the laser sheet illuminates the flame. Another disadvantage of chemiluminescence is that the signal strength is several orders of magnitude lower than PLIF. This will decrease the temporal resolution of measurements, since longer integration times are required to obtain sufficient signal strength. A typical integration time for a single shot using chemiluminescence is approximately 250μs, versus 200ns when performing PLIF.

Most experimental work to characterize various combustor configurations has been done on naturally unstable systems. However, the results are specific to the combustors tested, and provide little insight to how a particular injector or burner design will behave in a different combustor. A study of the acoustic coupling between fuel injectors and an applied acoustic field has been carried out by Anderson (1998), but only includes cold flow experiments. Work by Chen (1993) with premixed flames was specifically designed to simulate solid rocket propellants, contains only one-dimensional spatial results, and used only two forcing frequencies. The study by Cadou (1998) was based on a specific 2-D dump combustor configuration, and showed little response to non-resonant forcing. A more generalized body of work is required to provide industry with guidelines that will be useful in designing stable combustion systems.

Towards this end, a test section was constructed, consisting of a jet-mixed flame inside an acoustically forced chamber. The reaction zone of the flame is visualized by probing OH radicals, an intermediary in the combustion chemical reaction, with a planar laser-induced fluorescence (PLIF) system. This non-intrusive technique has been well known to be an excellent analytical tool for flame environments (Battles and Hanson, 1995; Hanson et al. 1990). The PLIF images are then processed and phase-resolved by various post-processing codes.

Although OH radicals have been used by other researchers (Yip et al. 1994) as a marker of the reaction zone, there is some question as to its the validity, since OH is known to persist in high temperature product gas regions (Allen et al. 1993; Barlow et al. 1990). However, in non-premixed flames, the OH radical quickly vanishes on both sides of the reaction zone Cessou and Stepowski 1996). Since the burner configuration is only partially premixed in this study, we

assume OH to be sufficient as an indicator for fuel burning. Work is in progress to apply PLIF to CH radicals and chemiluminescence for both OH and CH, all with the experimental configuration used here.

Objectives

The purpose of this study is to demonstrate a technique that can be used as part of a method to assess stability margins over a range of frequencies for various burner designs. An important difference between this work and previous studies is that this technique provides sufficient temporal and spatial resolution that can be used to improve predictive capabilities and correlate experimental results with numerical simulations. A burner using a mixture of methane and CO_2 is operated in two configurations: aerodynamically stabilized; and stabilized with a bluff-body. The burner is subjected to a forced acoustic field, with frequencies ranging from 22 Hz to 55 Hz. The configuration discussed here has been chosen to simulate a practical application. It serves as a relatively simple device for which the new diagnostics can be tested with minimal difficulties arising with the test apparatus.

Experimental Setup

The test section, shown in Figure 16, consists of three major components: the acoustic driving system; the acoustic cavity; and the burner section.

The acoustic driving system is mounted above the acoustic cavity on the outer quartz tube. It consists of a large tubular stainless steel section in the shape of a cross, approximately 12″ in diameter. The exhaust section is open to the atmosphere, providing an acoustically open exit condition. A pair of acoustic drivers are sealed to a pair of air jet film cooling rings (to prevent failure of the drivers), which are in turn sealed to opposite sides of the steel structure. The acoustic drivers are 12″ subwoofers (Cerwin-Vega model Vega 124), with a sensitivity (1 W @ 1 m) of 94 dB, and a continuous power handling capability of 400 W. They are driven by a 1000 W power amplifier (Mackie M1400i) and a function generator (Wavetek 171). Significant power is required to provide reasonable amplitude pressure oscillations. The amplitude of the fundamental driving mode is actively controlled by measuring the pressure in the acoustic chamber at the burner with a pressure transducer (PCB 106B50), and appropriately scaling the power output of the speakers.

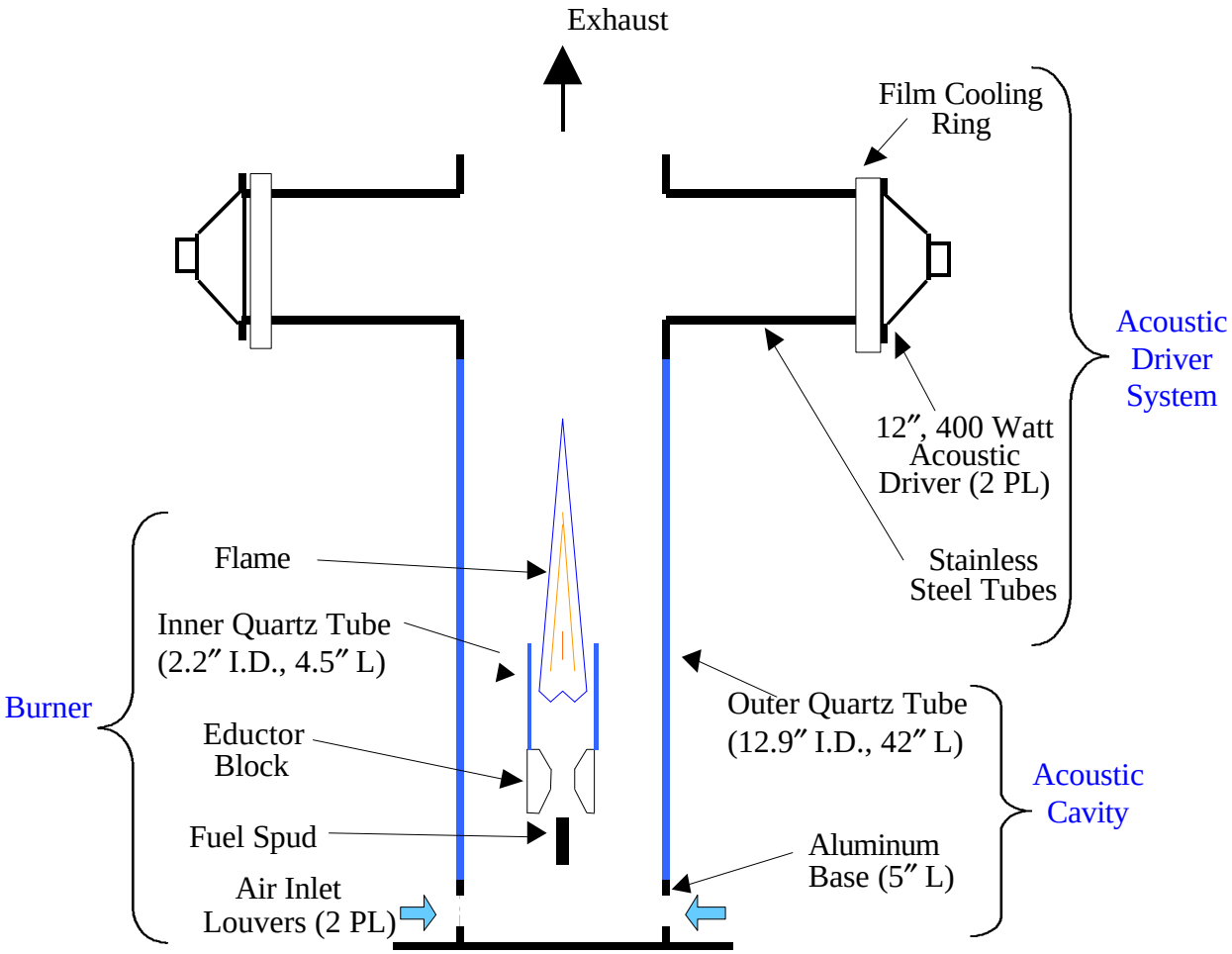

Figure 16. Schematic of Test Section

The acoustic cavity consists of an aluminum ring, closed at the bottom end. It has two sets of inlet louvers cut on opposing sides to allow air to flow into the tube, while providing an acoustically closed end condition. A large diameter-matched quartz tube rests in a thin register on the aluminum ring, and extends for an additional 42″. Quartz was used in order to withstand high flame temperatures, as well as to allow transmission of the ultraviolet laser sheet and fluorescence signal. The tube also has several laser-drilled holes at various locations to provide instrumentation entry ports.

Planar Laser-Induced Fluorescence of OH

The PLIF system is based on an Nd:YAG laser (Continuum Powerlite 9010) operating at 10 Hz, pumping a tunable dye laser (Continuum ND6000), which in turn drives a mixer/doubler system (U-Oplaz) as in Figure 2. Use of Rhodamine 590 in the dye laser optimizes conversion efficiency near 564nm, which is then doubled to approximately 282nm to excite the (1,0) band (Dieke and Crosswhite 1962) of OH. Energy in excess of 30 mJ/pulse is easily provided by this system in the measurement volume. Laser energy is measured for each pulse by using a beam-splitter with an energy meter (Molectron J9LP). The detector for the fluorescence signal is an intensified CCD

camera (Princeton Instruments ICCD-MAX), using a 512x512 CCD (Thomson) array, operated with a gate width of 200ns. Attached to the camera is a catadioptric UV lens, with a focal length of 105mm and an f/# of 1.2. This results in a spatial resolution of 215µm x 215µm per pixel. The fluorescence signal is filtered by 2mm thick UG5 and WG305 Schott glass filters. A digital delay/pulse generator (Stanford Research Systems DG-535) controlled camera timing, which was synchronized to the laser pulse.

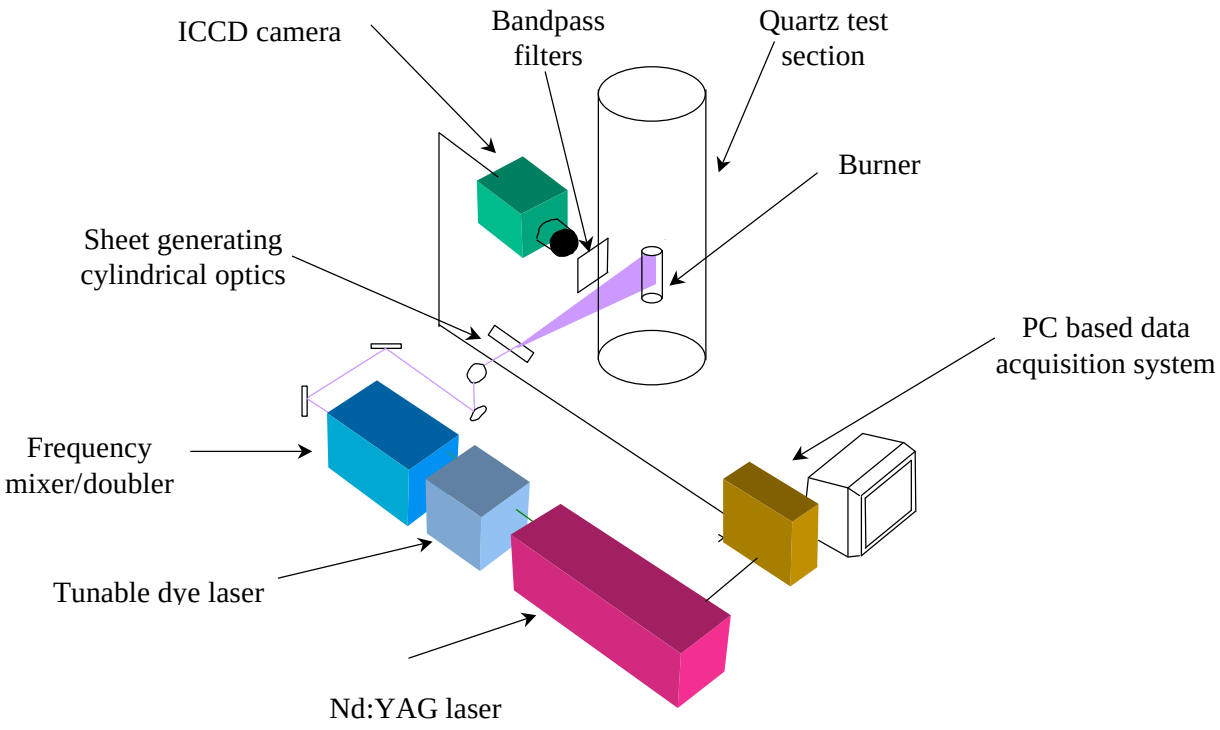

Figure 17. PLIF System

Data Analysis

By taking advantage of the periodic forcing of the chamber, and assuming that the flame responds accordingly in a periodic fashion, the PLIF images can be phase-locked and averaged together, to generate the periodic response of the OH fluorescence in the flame. The oscillating pressure used to phase-lock the images is acquired by a pressure transducer located 8 cm above the fuel spud, in the zone where the flame is stabilized. Since the hydroxyl molecule is an intermediary of combustion, and thus an indicator for the reaction zone in the flame, this procedure yields a proportional measurement of the heat release over a period of the acoustic driving cycle.

Due to the distributed nature of the flame under study and limitations on the ICCD camera's field of view, two sets of images were taken at each test condition at different heights. Each case contains a total of over 5000 images, phase-averaged into 36 equally spaced bins. Statistics indicate an even distribution among the bins, with well over 100 images per bin. The background is subtracted in each bin to eliminate scattering effects from the laser; and corrections are made for variations in spatial and shot-to-shot beam intensity. Images at the same phase but different

heights are then matched geometrically, and their intensities adjusted to match in the overlap region using a least-squares minimization routine.

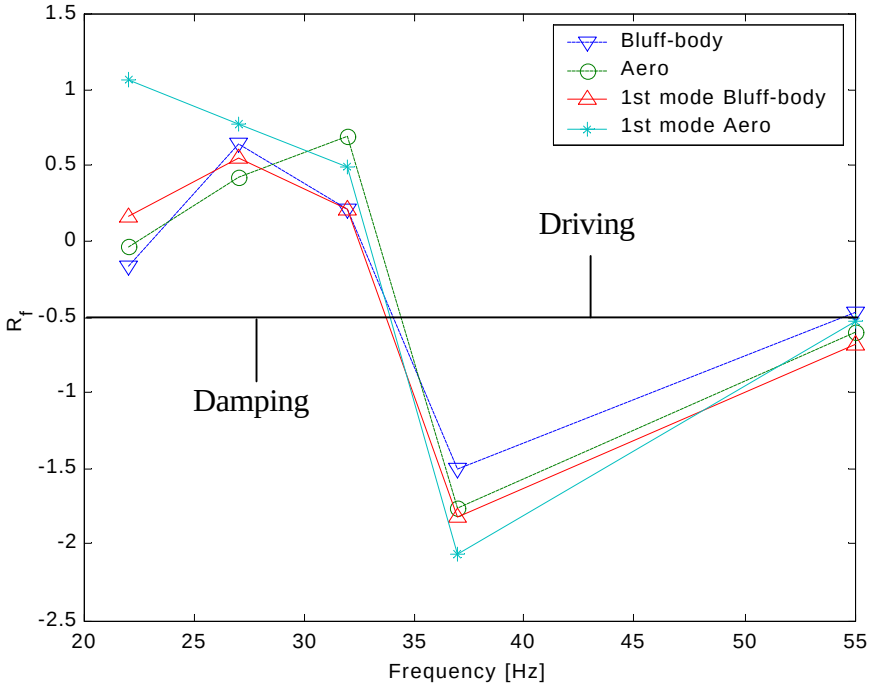

Figure 18. Frequency-Driven Global Rayleigh Index for Aerodynamically and Bluff-Body Configurations, with and without filtering of the 1st Mode of Pressure.

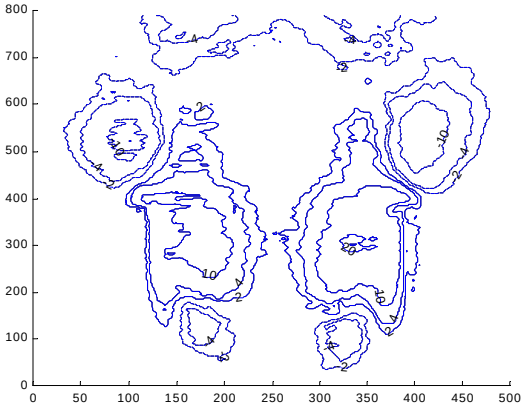

Figure 19. Contour Plot of R_f: Aerodynamically Stabilized Burner at a driving frequency of 32 Hz.

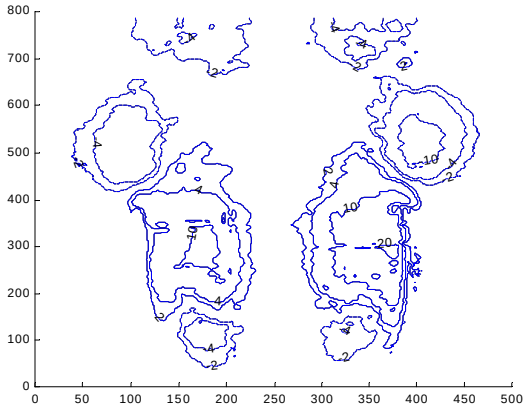

Figure 20. Contour Plot of R_f: Bluff-Body Stabilized Burner at a driving frequency of 32 Hz

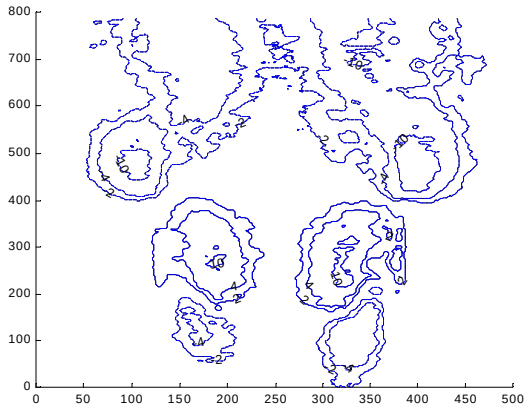

Figure 21. Contour Plot of R_f: Aerodynamically Stabilized Burner at a driving frequency of 37 Hz.

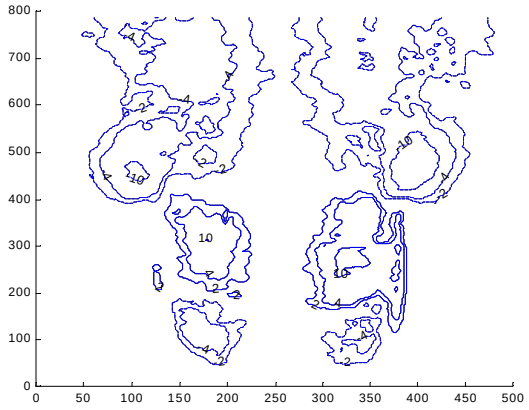

Figure 22. Contour Plot of R_f: Bluff-Body Stabilized Burner at a driving frequency of 37 Hz.

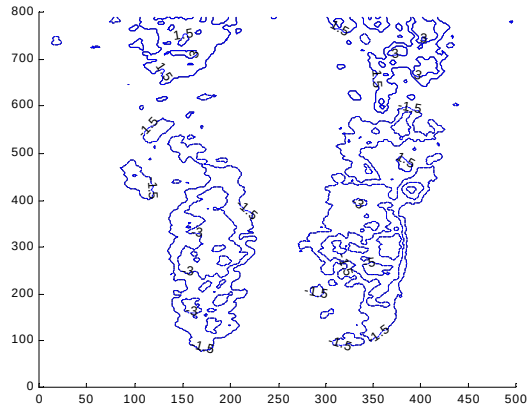

Figure 23. Contour Plot of R_f: Aerodynamically Stabilized Burner at a driving frequency of 55 Hz.

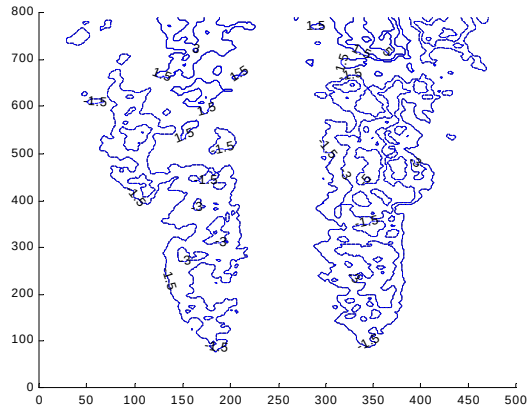

Figure 24. Contour Plot of R_f: Bluff-Body Stabilized Burner at a driving frequency of 55 Hz.

Results

Extensive results were discussed in the Semi-Annual Report, 1 March 2000 to 31 August 2000. Improved data have been obtained during the last six months of the program by using rewritten software intended to take more accurate account of background optical noise. Previously we concentrated on inferring the Rayleigh Index, a measure of the driving of acoustic waves by the fluctuating energy release. Figure 3 shows the main results for the index as a function of frequency.

During the period we began processing the data to give values of the dynamical combustion response, the ratio of the fluctuation of energy release to the fluctuation of pressure. That work is in progress and will be reported in the Final Report.

3. Concluding Remarks and Plans for Subsequent Work

During the past four years especially we have assembled numerical, analytical and experimental methods in an integrated program of basic research in the dynamics and control of combustion chambers. We have proven the methods in relatively elementary situations and we are prepared to move on to applications closer to practical requirements.

In parallel with our program addressed here and directed to gas turbine combustors, we have a small project involving application in a large flare used to burn off waste gases at a solid-waste landfill (see Task 4(c)). That work has enabled us to develop the diagnostics for a realistic and important application at atmospheric pressure.

When our high-pressure, high flow rate combustor is operational, we will begin investigating problems and configurations directly of interest to gas turbine designers. Our group has been strengthened considerably by the addition of a new Postdoctoral Scholar (Dr. Albert Ratner) whose Ph.D. work was concerned with PLIF and PIV (particle imaging velocimetry) applied to turbulent flames. He will continue and extend his work within our program for understanding the fundamentals of combustion dynamics.

We therefore have considerable reason to be optimistic about bringing together at last our theoretical, numerical and experimental methods for understanding the dynamics and control (both active and passive) of combustion instabilities in combustors intended for use in gas turbines.

In particular, our long-range plan includes the ambitious goal of developing methods to measure the dynamical combustion response, spatially resolved and time accurate, as a function of local fluctuations of velocity, pressure and mixture ratio. Those methods will have significant applications to all types of combustion systems.

4. Personnel

Principal Investigator:	F. E. C. Culick
Postdoctoral Scholar:	A. Ratner
Students:	Giorgio Isella (G) Konstantin Matveev (G) Steven Palm (G) Winston Pun (G) Claude Seywert (G) Grant Swenson (G)
Degrees Awarded:	Grant Swenson (Ph.D., June 2000) Giorgio Isella (Ph.D., June 2001) Winston Pun (Ph.D., June 2001) Claude Seywert (Ph.D., June 2001)

5. References

Allen, M.G., et. al., (1993) "Fluorescence Imaging of OH and NO in a Model Supersonic *AIAA Journal*, Vol. 31, No. 3.

Anderson, T.J., Kendrick, D.W., and Cohen, J.M., (1998) "Measurement of Spray/Acoustic Coupling in Gas Turbine Fuel Injectors", presented at the *36th Aerospace Sciences Meeting & Exhibit*, Reno, NV, AIAA 98-0718.

Barlow, R.S., Dibble, R.W., Chen, J.-Y., and Lucht, R.P., (1990) "Effect of Damkohler Number on Superequilibrium OH Concentration in Turbulent Nonpremixed Jet Flames", *Combustion and Flame*, Vol. 82, pp. 235-251.

Battles, B.E., and Hanson, R.K., (1995) "Laser-Induced Fluorescence Measurements of NO and OH Mole Fraction in Fuel-Lean, High-Pressure (1-10 atm) Methane Flames: Fluorescence Modeling and Experimental Validation", *J. Quant. Spectrosc. Radiat. Transfer*, Vol. 54, No. 3, pp. 521-537.

Biswas, S., (1998) "Robust Stabilization of Linear Systems in the Presence of Gaussian *Optimal Control Applications and Methods* 19: 271-286.

Broda, J.C., Seo, S., Santoro, R.J., Shirhattikar, and Yang, V., (1998) "An Experimental Study of Combustion Dynamics of a Premixed Swirl Injector", *Twenty-Seventh Symposium (International) on Combustion*, The Combustion Institute.

Burnley, V. (1996) "Nonlinear Combustion Instabilities and Stochastic Sources", Ph.D Thesis, California Institute of Technology.

Cadou, C.P., Logan, P., Karagozian, A.R., and Smith, O.I., (1991) "Laser diagnostic techniques *Environ. Sensing Combust. Diagn., SPIE*, Vol. 1434, pp. 67-77.

Cadou, C.P., Smith, O.I., and Karagozian, A.R., (1998) "Transport Enhancement in Acoustically Excited Cavity Flows, Part 2: Reactive Flow Diagnostics", *AIAA Journal*, Vol. 36, No. 9, pp. 1568-1574.

Cessou, A., and Stepowski, D., (1996) "Planar Laser Induced Fluorescence Measurement of [OH] in the Stabilization Stage of a Spray Jet Flame", *Combust. Sci. and Tech.*, Vol. 118, pp. 361-381.

Chen, T.Y., Hegde, U.G., Daniel, B.R., and Zinn, B.T., (1993) "Flame Radiation and Acoustic Intensity Measurements in Acoustically Excited Diffusion Flames", *J. Propul. Power*, Vol. 9, No. 2.

Chou, J., Chen, S., Chao, C, (1998) "Robust Stabilization of Flexible Mechanical Systems Under Noise Uncertainties and Time-varying Parameter Perturbations", *Journal of Vibration and Control* 4: 167-185.

Chu, B.-T., Kovasznay, L., (1956) "Nonlinear Interactions in a Viscous Heat-Conducting *Journal of Fluid Mechanics* 3(5): 494-514.

Culick, F.E.C and Yang V., (1992) "Prediction of the Stability of Unsteady Motions in Solid Propellant Rocket Motors, Nonsteady Burning and Combustion Stability of Solid Propellants", *Progress in Astronautics and Aeronautics* 143: 719-779.

Culick, F.E.C, (1976) "Nonlinear Behavior of Acoustic Waves in Combustion Chambers, parts I *Astronautica Acta* 3: 714-757.

Culick, F.E.C, (1989) "Combustion Instabilities in Liquid-Fueled Propulsion Systems – An Overview", AGARD CP-450 pp. 1-73.

Culick, F.E.C., (1987) “A Note on Rayleigh’s Criterion”, *Combust. Sci. and Tech.*, Vol. 56, pp. 159-166.

Culick, F.E.C., (1999) “Dynamics of Combustion Systems: Fundamentals, Acoustics and Control,” A Short Course of Lectures sponsored by AGTSR and given at the United Technologies Research Center.

Dieke, G.H., and Crosswhite, H.M., (1962) “The Ultraviolet Bands of OH”, *J. Quant. Spectrosc. Radiat. Transfer*, Vol. 2, pp. 97-199.

Dyer, M.J., and Crosley, D.R., (1982) “Two-dimensional imaging of OH laser-induced *Optics Letters*, Vol. 7, No. 8.

Eckbreth, R.C., (1988) *Laser Diagnostics for Combustion Temperature and Species*, Abacus Press, Cambridge.

Furukawa, T., Shimemura, E., (1983) “Predictive Control for Systems with Time Delay”, *Int. Journal of Control* 37: 399-412.

Gulati, A., Mani, R., (1992) “Active Control of Unsteady Combustion-Induced Oscillations”, *Journal of Propulsion and Power* 8(5): 1109-1115.

Haddad, W. M., Leonessa, A., Corrado, J. R., Kapila, V., (1997) “Robust Reduced-Order Control of Combustion Instabilities”, *1997 IEEE International Conference on Control Applications*, Hartford, CT, October.

Hanson, R.K., Seitzman, J.M., and Paul. P.H., (1990) “Planar Laser-Fluorescence Imaging of *Applied Physics B*, Vol. 50, pp. 441-454.

Harrje, D. T. (ed.) 1992, “Liquid Propellant Rocket Combustion Instability”, NASA SP-194.

Isella, G., Seywert C., Culick, F., Zukoski, E., (1997) “A Further Note on Active Control of Combustion Instabilities Based on Hysteresis”, *Combustion Science and Technology*.

Kappei, F., Lee, J.Y., Johnson, C.E., Lubarsky, E., Neumeier, Y., and Zinn, B.T., (2000) “Investigation of Oscillatory Combustion Processes In Actively Controlled Liquid Fuel *36th Joint Prop. Conf.*, Huntsville, Al, AIAA 2000-3348.

Kendrick, D.W., Anderson, T.J., Sowa, W.A., and Snyder, T.S., (1999) “Acoustic Sensitivities of Lean-Premixed Fuel Injectors in a Single Nozzle Rig”, *J. Eng. Gas Turbines and Power*, Vol. 121, Iss. 3, pp. 429-436.

Lieuwen, T., Zinn, B., (2000) “Experimental Investigation of Limit Cycle Oscillations in an Unstable Gas Turbine Combustor”, *38th Aerospace Sciences Meeting & Exhibit*, AIAA paper No. 2000-0707.

Neumeier, Y., Nabi, A., Arbel, A., Vertzberger, M., Zinn, B., (1997) “Open-loop Performance of a Fast-response, Actively Controlled Fuel Injector Actuator”, *Journal of Propulsion and Power*.

Paul, P.H., and Dec, J.E., (1994) “Imaging of reaction zones in hydrocarbon-air flames by use of *Optics Letters*, Vol. 19, No. 13.

Poinsot, T., Bourienne, F., Candel, S., Esposito, E., (1987) “Suppression of Combustion Instabilities by Active Control”, *Journal of Propulsion* 5: 14-20.

Raun, R. L., Beckstead, M. W., Finlinson, J. C., and Brooks, K. P., (1993) “A Review of Rijke Tubes, Rijke Burners and Related Devices”, *Prog. Energy Combust. Sci.* 19: 313-364.

Raun, R. L., Beckstead, M.W., Finlinson, J.C., and Brooks, K.P., (1993) “A Review of Rijke Tube Burners and Related Devices”, *Prog. Energy Combust. Sci.*, Vol. 19, pp. 313-364.

Rayleigh, J.W.S., (1945) *The Theory of Sound Vol. II*, Dover Publications.

Combust. Sci. and Tech., Vol. 77, pp. 225-238.

Venkataraman, K.K., Preston, L.H., Simons, D.W., Lee, B.J., Lee, J.G., and Santavicca, D.A., (1999) "Mechanism of Combustion Instability in a Lean Premixed Dump Combustor", *J. Propul. Power*, Vol 15, Iss. 6, pp. 909-918.

Yang, V., Sinha, A., Fung, Y., (1992) "State-feedback Control of Longitudinal Combustion *Journal of Propulsion and Power* 8(1): 66-73.

Yip, B., Miller, M.F., Lozano, A., and Hanson, R.K., (1994) "A combined OH/acetone planar laser-induced fluorescence imaging technique for visualizing combusting flows", *Experiments in Fluids*, Vol. 17, pp.330-336.

Zsak, T. W., (1993) "An Investigation of the Reacting Vortex Structures Associated with Pulse Combustion", Ph.D. Thesis, Daniel and Florence Guggenheim Jet Propulsion Center, California Institute of Technology, Pasadena, CA.

APPENDIX A

Short Course
DYNAMICS OF COMBUSTION SYSTEMS:
FUNDAMENTALS, ACOUSTICS, AND CONTROL

The first version of this short course funded by a different contract under the AGTSR Program, was completed in June 1999. It was the intention of the course to provide in 24 hours of lectures as much as possible of the fundamentals of combustion, acoustics, linear and nonlinear dynamics of combustion chambers and controls. Hence, although a brief survey of methods of feedback control is included (current as of September 1998) the course is not a survey of practical methods, but rather a fairly detailed exposition of basic material.

In revised form, the course was given in September 2001 at the NASA Glenn Research Center. The outline of the second version of this course is included here. Access to the viewgraphs posted on the web can be had upon request: fecfly@caltech.edu.

A SHORT COURSE OF LECTURES ON
DYNAMICS OF COMBUSTION SYSTEMS:
FUNDAMENTALS, ACOUSTICS, AND CONTROL

I INTRODUCTION & HISTORICAL BACKGROUND

1.1 Historical Background and Case Histories of Combustion Instabilities
1.2 Mechanisms of Combustion Instabilities in Various Devices
1.3 Elementary Interpretation of Combustion Instabilities
1.4 The NO_x Problem: Power Generation and Combustion Instabilities
1.5 Elementary Active and Passive Control of Combustion Instabilities
1.6 A Brief Survey of Laboratory Results for Active Control of Combustor Dynamics
- 1.6.1 Cambridge University
- 1.6.2 Ecole Central
- 1.6.3 GE Corporate Research and Development
- 1.6.4 Technische Universitat Munchen
- 1.6.5 Georgia Institute of Technology

1.7 The Simplest Example of Thermo-Acoustic Instabilities with Rijke Tube
- 1.7.1 Mean Flow in a Rijke Tube
- 1.7.2 Acoustic Field in a Rijke Tube
- 1.7.3 Linear Stability and Transient Growth of Oscillations in an Electrically Driven Rijke Tube
- 1.7.4 Nonlinear Behavior due to Rectification
- 1.7.5 Elementary Active Control of the Rijke Tube

1.8 A Simple Method of the Flame-driven Rijke Tube
- 1.8.1 Conditions for Instability: Application of Spatial Averaging
- 1.8.2 Conditions for Instability: Application of Wave Modeling

1.9 Elementary Active Control of the Flame-driven Rijke Tube
- 1.9.1 Linear Control by Acoustic Sources at the Boundary

1.10 General Scheme of the Course: Dynamics of Combustion Systems: Fundamentals, Acoustics, and Control
- 1.10.1 The General Scheme
- 1.10.2 Application of Feedback Control to Combustor Dynamics

II PRINCIPLES AND METHODS OF CLASSICAL CONTROL IN THE FREQUENCY DOMAIN

2.1 Introduction
2.2 General Scheme of Classical and Modern Control Theory
2.3 Feedback Control of Second-Order Systems
- 2.3.1 The Mass/Spring/Dashpot System
- 2.3.2 Frequency Response of the Linear Second-Order System

2.4 The Laplace Transform; Elementary Transient Responses
- 2.4.1 Some Results for Laplace Transforms
- 2.4.2 Poles and Zeros
- 2.4.3 Transient and Forced Responses for a Second-Order System
- 2.4.4 Effects of Added Poles and Zeros

2.5 PID Feedback Control of a Second-Order System
2.6 Bode Plots: The 'Frequency Response Method'
2.7 Remarks on Expected (Desired) Forms of Bode Plots ("Loop Shaping")
2.8 Polar Plots
- 2.8.1 Examples of Polar Plots
- 2.8.2 Properties of Polar Plots

2.9 Dynamical Stability; Routh and Hurwitz Criteria

V FUNDAMENTALS OF COMBUSTION PROCESSES

5.1 Governing Equations for One-Dimensional Laminar Reacting Flows
- 5.1.1 Global Conservation of Mass
- 5.1.2 Equations for Conservation of Species
- 5.1.3 Momentum Equation
- 5.1.4 Energy Equation

5.2 Equations for Modeling Low-Speed Deflagrations (Flames)
- 5.2.1 A Gallery of Flames

5.3 Steady One-Dimensional Flows with Finite Heat Addition
- 5.3.1 Steady Flow in a Uniform Duct with Heat Addition
- 5.3.2 Changes of State for Steady Flow with Finite Heat Addition
- 5.3.3 The Rankine-Hugoniot Diagram

5.4 Elementary Examples of Laminar Pre-Mixed Flames
- 5.4.1 An Elementary Laminar Pre-Mixed Flame
- 5.4.2 Thermal Theory of Laminar Pre-Mixed Flames
  - 5.4.2.1 Infinitesimally Thin Flame Front
  - 5.4.2.2 Finite Flame Front, Uniform Combustion

5.5 Equations of Motion for a Reacting Two-Phase Mixture

5.6 Laminar Diffusion — Controlled Non-Premixed Flames
- 5.6.1 Matching Conditions at a Reacting Interface
- 5.6.2 Diffusion Flames Between Parallel Plates
- 5.6.3 The Burke-Schumann Problem
- 5.6.4 Time-Dependent One-Dimensional Diffusion Flame ($\beta \rightarrow \infty$)

5.7 Strained Laminar Flames
- 5.7.1 The Kinematics of Strained Flows
- 5.7.2 Strained Diffusion Flame in Stagnation Point Flow

5.8 Ignition and Combustion in a Laminar Mixing Region
- 5.8.1 Early Stage : Ignition
- 5.8.2 Development of the Laminar Flame

5.9 Combustion of Fuel Strips
- 5.9.1 Combustion of an Unstrained Fuel Strip
- 5.9.2 Strained Fuel Strip

5.10 Some Basic Mechanisms for Instabilities in Combustors Operating with Gaseous Reactants
- 5.10.1 General Remarks on the Context
- 5.10.2 Some Classes of Possible Mechanisms
- 5.10.3 Present Status of the Dynamics of these Processes

5.11 Combustion in a Vortex
- 5.11.1 Kinematics of the Vortex – Flame Interaction

5.12 Modeling a Turbulent Combustor Field as a Distribution of Flamelets (Coherent Flames)
- 5.12.1 Summary of the Procedure

VI FUNDAMENTALS OF ACOUSTICS

6.1 Linearization of the Equations of Motion; The Wave Equation and the Velocity Potential

6.2 Elementary Solutions to the Wave Equation: Plane, Spherical, and Cylindrical Waves
- 6.2.1 Plane Waves
- 6.2.2 Spherical Waves
- 6.2.3 Cylindrical Waves

6.3 An Estimate of the Influence of Heat Conduction

6.4 Energy and Intensity Associated with Acoustic Waves
- 6.4.1 Results for Sinusoidal Plane Waves
- 6.4.2 The Decay or Growth Constant
- 6.4.3 The Decibel and the Response of the Human Ear

Semi-Annual Report #3

1 June 2001 to 30 November 2001

"The Staged Prevaporizing-Premixing Injector: High Pressure Evaluation"

AGTSR Subaward No. 00-01-SR087
University of Washington
Seattle, Washington

Executive Summary

This report covers the third period of performance for this AGTSR project on the staged prevaporizing premixing (SPP) injector. Work performed over the six-month period from 1 June to 30 November 2001 is reported herein.

There are three major parts to this project:

1. High-pressure testing and evaluation of the SPP injector on diesel fuel.

2. CFD modeling of the SPP injector to aid in the evaluation and in design upgrades.

3. Extension of the one-atmosphere tests of the pre-AGTSR research on the SPP injector.

During the third period of performance, effort was focused on the following activities:

1. Equipment and services were ordered for setting up the high-pressure testing of the industrial-scale SPP at Solar Turbines in San Diego.

2. Preliminary CFD computations of the lab-scale SPP operating at high pressure and short residence time were undertaken. These also served to train a new graduate student Research Assistant on the CFD modeling.

3. Atmospheric pressure, short residence time testing of the lab-scale SPP was undertaken. These tests showed the need for some repairs to the lab-scale SPP. Arrangements were made for the repairs.

These three activities are discussed in the sections that follow.

Introduction

In our last report (#2), we discussed the need to arrange for a new site for the high-pressure testing of the industrial-scale SPP. In May, we reached agreement with Solar Turbines for the high-pressure testing. Following this, in June, we submitted our revised testing plan to AGTSR for approval. This plan carried no additional cost to AGTSR. In early September we received official authorization from AGTSR to continue with the research with the high-pressure testing to be conducted at Solar Turbines. In early September we restarted spending on the project, after the three-month period required for AGTSR approval.

High-Pressure Testing

During the autumn, the vendor quotes were obtained for the equipment and services required to modify the test rig at Solar Turbines for testing of the industrial-scale SPP. Rig modification is required because of the two stages of air temperature used by the SPP. In November the equipment and services were ordered. The major items are as follows:

- Air flow measuring unit.
- Air flow shut off valve.
- Test cell modification, involving new air flow piping and test cell remodeling to accommodate the new piping, and including pipe stress analysis.

Additionally during the autumn, Parker Hannifin began the design modifications and fabrication of the industrial-scale SPP to be tested.

The test cell modification is scheduled to begin over the end-of-December holiday break. Completion of the modification and the installation of the equipment are expected to take place over the first half of the first quarter of 2002. The high-pressure testing should commence in the second half of the quarter. The pressure range scheduled is 10 to 16 atm, and the maximum stage #2 temperature scheduled is about 850 K.

Schematic drawings of the experimental equipment will be available once the test cell modifications have been completed and the industrial-scale SPP and combustor to be fired have been installed.

CFD Modeling

Previous CFD modeling of the SPP, as shown in our first report, was restricted to atmospheric pressure, long residence time running of the lab-scale SPP. During the present reporting period, new CFD computations of the lab-scale SPP were

begun. These new computations are centered on high pressure and short residence time running of the SPP. They have also served to provide training of the new graduate student RA involved in the research, MSME/PhD student Igor Novosselov.

Preliminary results for a very demanding case are shown in Table 1. In this case, the pressure is near the maximum used in power generation gas turbines (30 atm), and the residence time in the hot stage #2 of the SPP is very short (1.6 ms). The estimated diesel droplet size resulting from injection of the fuel into the SPP is 15 microns. The overall fuel-air equivalence of the SPP is about 0.5. The vaporization in the SPP is complete. The stage #2 air admission holes are enlarged so that the overall air pressure drop for the SPP is 5%. The enlargement of the holes causes a small spatial non-uniformity of the diesel vapor mass fraction at the SPP outlet: the standard deviation divided by the mean of the diesel vapor mass fraction at the outlet is about 0.05.

Table 1. CFD Modeling of the SPP at 30 atm

	STAGE #1	STAGE #2
Air Inlet Temperature	746 K	823 K
Mean Temperature at Outlet of the Stage	700 K	800 K (outlet SPP condition)
Mean Velocity at Outlet of the Stage	30 m/s	80 m/s (outlet SPP condition)
Mean Residence Time	4.16 ms	1.63 ms

CFD plots and final results will be presented in report #4, due in six months.

Atmospheric Pressure Testing

During this past summer, atmospheric pressure testing of lab-scale SPP was conducted. This testing was done on UW funds, since AGTSR spending authorization for this project was unavailable from June 1 to early September 2001. Newly calibrated mass flow controllers permitted the air flow rate to be increased three-fold over the pre-AGTSR testing of the SPP. The geometry of the SPP was not modified. Thus, the three-fold increase in air flow rate lead to an increased pressure within the SPP and an increased pressure loss across the SPP. The outlet velocity of the SPP (at actual temperature) was about 275 m/s.

Light naphtha was vaporized and mixed in the SPP and injected and burned in the lab atmospheric pressure jet-stirred reactor. The reactor was highly loaded, with a mean residence of slightly less than 1 ms. The reactor ran stably, and exhibited NOx formation as a function of temperature similar to that measured in

the pre-AGTSR research – about 10 ppm (15% O_2, dry) at 1800 K – indicating the highly loaded SPP continued to vaporize and mix the fuel well.

At the conclusion of the first phase of the atmospheric pressure testing, air leaks in the SPP were noted. (The 1 ms residence time quoted above has been corrected for these leaks.) Upon inspection some of the flanges of the SPP were found to be slightly warped. While this did not lead to significant loss of air for the design point, pre-AGTSR running of the SPP, it did impact the running at high flow rate and increased SPP pressure. Attempts to seal the flanges proved unsuccessful. Thus, it was decided to repair the SPP. Additionally, it was decided to enlarge the air admission holes of stage #2 in order to maintain an overall pressure loss in the 5% range.

Currently, the rebuilding of the lab-scale SPP is being conducted by Parker Hannifin. This includes machining of the new parts and brazing. Parker Hannifin is not charging the project for this cost.

Restart of the atmospheric pressure testing is scheduled for February 2002, and completion is scheduled for May 2002. The atmospheric pressure testing is conducted by MSME student Ryan Edmonds.

Set up of the laser diagnostic system for measuring the degree of mixedness of the outlet stream of the atmospheric pressure lab-scale SPP has been underway during the autumn. This setup has been conducted by MSME student Andrew Campbell Lee. A 1 watt continuous argon ion laser is used, with the laser Rayleigh scattering method used to distinguish lean from rich fluid particles of mixture. The laser has been provided to this project by one of the materials research teams in the UW-ME Department. At the end of November, the laser system, with collection optics and signal acquisition, had been set up. Check-out testing on a helium jet mixing in air is scheduled for the first part of the first quarter of 2002. Application of the laser to the SPP outlet stream is scheduled for the second quarter of 2002.

Project Budget

All project funds have been expended or encumbered. The encumbrances cover the following:

- The equipment and services for the setup of the high-pressure tests at Solar Turbines. (Site hourly testing costs are covered through an agreement with Solar Turbines.)
- Graduate student RA support (in the first quarter of 2002) for the remaining CFD modeling. (Graduate student RA support for the atmospheric pressure experiments is covered from other funding sources.)

- Supplies and materials for the atmospheric pressure experiments.

Cost sharing by the UW covers the time of the Principal Investigator to analyze the high-pressure test results and provide the reporting.

AGTSR SEMI-ANNUAL TECHNICAL REPORT
01 February 2001 to 31 July 2001

Laboratory for Control of Energetic Processes
School of Aerospace Engineering
Georgia Institute of Technology
Atlanta, Georgia 30332-0150

Ph: (404) 894-3033 **FAX: (404) 894-2760**

Project Title

EXTENDING THE LEAN BLOWOUT LIMITS OF LOW NOx GAS TURBINES BY CONTROL OF COMBUSTION INSTABILITIES

AGTSR Subcontract No.: 99-01-SR075

Principal Investigator: Ben T. Zinn
Co-Investigators: Yedidia Neumeier, and Timothy C. Lieuwen

Research Students: Ben Bellows

1. EXECUTIVE SUMMARY

The objective of this program is to investigate the causes and active control of detrimental combustion instabilities in low NO_X gas turbines (**LNGT**) that burn natural gas in a lean premixed mode to reduce NO_X emissions. In an effort to eliminate these instabilities, this program is studying (1) the processes that control the linear and nonlinear characteristics of the unstable combustor and (2) active and passive methods for suppressing these instabilities. This report describes the progress made under this program in these areas.

During this reporting period, studies of the interactions between acoustic waves and turbulent flames were preformed. These studies found that coherent plane waves incident upon turbulent flames generate reflected coherent and incoherent waves. The excitation of the incoherent waves is due to the random flame front movement, and serves as a source of damping of coherent acoustic energy. The key parameters affecting these interactions are the statistical characteristics of the flame front position, the relative angle between the flame front and the acoustic wave, and the temperature ratio across the flame.

Additional analysis of data, originally presented in the last report, was performed. These studies were performed to improve understanding of the nonlinear oscillatory characteristics of the combustion process. These studies determined the transfer function between pressure and heat release oscillations over a range of amplitudes. It was found that the amplitude relationship between the pressure and heat release oscillations saturates at oscillatory amplitudes on the order of 0.5-1% of the mean. The phase between the pressure and heat release was also found to also depend on amplitude.

Contacts were also maintained with several major gas turbine manufacturers that kept us informed of problems that were of concern to industry and enabled us to inform industry about our progress in the understanding and control of LNGT instabilities.

2. Introduction

Increasingly stringent emissions legislation has increased the demand for low NO_x gas turbines (LNGT) that operate at low temperatures. However, LNGT are often prone to detrimental combustion instability. To develop rational approaches for preventing or controlling these instabilities, an understanding of the controlling mechanism(s) and capabilities for predicting the conditions under which they occur must be developed.

The following sections describe experimental and theoretical work performed to understand the nonlinear dynamics of unstable combustors and the interactions between acoustic waves and turbulent flames.

3. Experimental Investigation of the Nonlinear Flame Response to Flow Disturbances

During this reporting period, we performed an experimental study of the linear and nonlinear response of the gas turbine combustion process to imposed pressure oscillations. These data were obtained to improve current understanding of the nonlinear phenomenon in unstable combustors that play an important role in its limit cycle behavior. They were obtained by forcing oscillations in the combustor at discrete frequencies and measuring the resulting pressure and global CH* radical chemiluminescence oscillations.

Introduction

Effective implementation and optimization of either passive or active methods of eliminating these oscillations requires a thorough understanding of the fundamental processes that affect the combustor's dynamics[1,2,3,45]. These dynamics are controlled by a complex interplay of linear, nonlinear, and stochastic processes that affect the conditions under which instabilities occur, the amplitude of the oscillations, and the effectiveness of passive and active control approaches.

Linear combustor processes generally control the balance between driving and damping processes at low levels of oscillation and, thus, determine whether inherent disturbances in the combustor grow in time. Much of the early instability modeling work developed the basic linear analysis

techniques used today[6], and attempted to determine the conditions under which a combustor would spontaneously become unstable. Although by its very nature such linear analysis could not determine the amplitude of the instabilities, they could often predict the frequency of the oscillations and, in some cases, the conditions under which instabilities occurred. As a result of this work, capabilities for modeling the acoustics of the combustor system are reasonably well developed (e.g., see [7]). Also, capabilities for modeling the interactions of flow and mixture disturbances with flames, needed to predict the conditions under which instabilities occur, is improving rapidly[8,9,10]. Much of this work is being transitioned to industry and is being incorporated into dynamics predictions codes. In fact, most of the gas turbine manufacturers have reported some efforts and progress in development of models to predict instability frequencies, mode shapes, and conditions of occurrence[4,9,11,12,13].

The understanding of the combustor's linear dynamics is only part of the overall problem. For example, a linear analysis cannot predict the limit cycle amplitude of a combustion instability. Such information is needed to assess whether a potentially unstable operating condition will result in oscillations with sufficient amplitude to be destructive, or to understand the dynamics of actively controlled combustors[14]. The need to predict the instability amplitude and observation of "triggered" instabilities in rockets that were linearly stable[15], motivated past workers to consider these nonlinear effects. Extensive work by Crocco and Cheng[6], Zinn and co-workers (e.g., see [16]), Culick and co-workers (e.g., see [17]), and others resulted in significant improvements in the understanding of such phenomena. This work allowed for the systematic development and study of model equations describing nonlinear combustor dynamics. Most of this older work focused on the role of nonlinear gas dynamics in combustors, however. As such, it is likely more relevant to instabilities in combustion systems where fluctuating pressure amplitudes can achieve significant percentages of the mean (e.g., p'/p_o ~20-50%, such as is observed in rockets), than lean premixed gas turbine combustors where reported instability amplitudes are typically well under 10% of the mean value[1,2,5,18]

Recent studies[18,19,20] have suggested that acoustic (i.e., gas dynamic) processes *essentially remain in the linear regime, even under limit cycle operation*, and that it is the nonlinear relationship between flow and heat release oscillations that causes saturation of the instability amplitude. For example, Dowling[20] suggested a linear acoustics/nonlinear heat release model of oscillations in a combustor. The heat release was assumed to linearly depend upon the flow velocity for small amplitude

oscillations, but saturated as the unsteady flow velocity achieved values larger than the mean. Similarly, others[18,19] have suggested that the nonlinear relationship between flow oscillations at the fuel injection point and the resulting equivalence ratio oscillation could play an important role in limit cycle oscillations. At this point, however, this work has not been subjected to experimental examination.

In order to better understand the relationship between acoustic and heat release oscillations, suggested by the above studies to play a dominant role in limit cycle behavior, we obtained measurements of their amplitude and phase relationships over a range of driving amplitudes. These results were obtained by externally driving oscillations in the combustor with varying amplitude. In agreement with the above discussed studies, it was found that the amplitude relationship between the pressure and heat release saturates at sufficiently high forcing levels. The following section describes the experimental setup and data analysis procedure. Then, we present typical results that illustrate the nonlinear transfer function between pressure and heat release oscillations and briefly discuss the phenomenon of frequency locking.

Experimental Setup

The data presented in this paper were measured in a lean, premixed gas turbine combustor simulator, see Figure 1, which has been described in Ref. [21]. These tests were performed at an equivalence ratio and mean pressure of approximately 0.85 and 1.3 atmospheres, respectively.

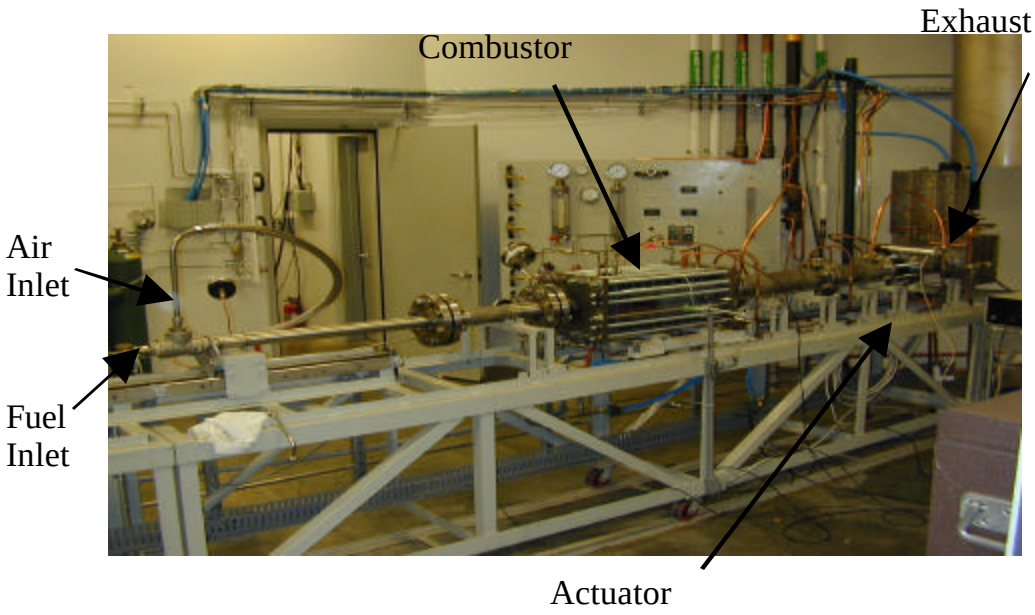

Figure 1 Photograph of the Georgia Tech's lean, premixed combustor.

The developed setup consists of inlet, combustor and exhaust sections. Air enters the circular 4.75cm diameter, 60cm long inlet section through a choked injector plate at its upstream end. The length of the inlet section can be changed be moving the air injector plate axially. Fuel is supplied through a fuel injection tube that protrudes into the inlet section through the center of the air injector and can be moved axially to vary the fuel injection location. The fuel and air mix in the inlet section and then pass through a swirler prior to entering the combustor. Combustion occurs in the 5x5x51cm square combustor downstream of the conical flame holder, and the combustion products then flow through a circular 7.6cm diameter, 195cm long exhaust section before leaving the system. A separate high-pressure air stream cools the combustor walls, and is then injected through a tube into the exhaust section where it mixes with the combustion products. The "combined" flow leaves the setup through an exhaust nozzle and an adjustable bypass valve.

Pressure oscillations were measured with Model 211B5 Kistler pressure transducers mounted along the inlet section and combustor. The pressure data presented in this paper were obtained from a water-cooled transducer located 5.1 cm downstream of the flame holder in the combustion chamber. The relative magnitude of the combustion heat release oscillations was obtained by measuring the global

CH* chemiluminescence with a photomultiplier tube (PMT) fitted with a 10 nm bandwidth filter centered at 430 nm. The PMT was installed downstream of a window at the rear end of the setup in a manner that permitted it to "view" the entire combustion zone. The linearity of the PMT over the range of light intensities encountered in this study was also verified in off-line tests.

Data was recorded with a National Instruments DAQ controlled by Labview software at a sampling rate of 4 KHz. A total of 8192 data points were taken during each test.

Oscillations were driven in the combustor with an actuator developed at Georgia Tech for active combustion control applications[22]. The actuator is capable of driving oscillations over a frequency range of approximately 0-1500Hz. The actuator modulates a secondary supply of air that is introduced near the combustor exit by periodically varying the degree of constriction of a reed valve. Maximum amplitude of driving occurs when the flow passage is completely blocked for a portion of the cycle, and thus the actuator modulates 100% of the mean flow of air through the valve. The amplitude of forcing can be controlled via the supply pressure of air to the actuator.

Figure 2 illustrates fourier transforms of the combustor pressure and chemiluminescence obtained while driving oscillations at 157 Hz. The amplitude of the driven pressure and heat release oscillations were p'/p_o=0.87% and E'/E_o=40%, where E denotes the CH* chemiluminescence level. Harmonics of the driving frequency can also be observed at 314, 471, and 628 Hz. It should be noted that these harmonics are introduced by both nonlinear processes in the combustion chamber and saturation of the actuator.

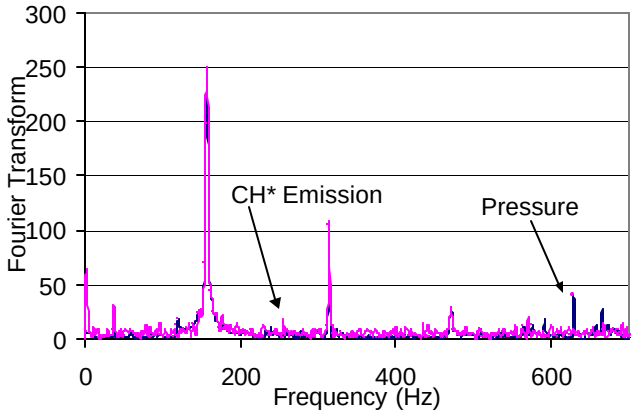

Figure 2 Fourier transform of the combustor pressure and CH* emission.

In order to obtain meaningful transfer function data, it is important that there is a high degree of coherence between the pressure and CH* oscillations at the driving frequency. The coherence ranges in value between zero and unity and is defined by the relation[23]:

$$\gamma_{pE}(f) = \frac{|F_{pE}(f)|}{\sqrt{F_{pp}(f)F_{EE}(f)}} \qquad [1]$$

where F_{pE} , F_{EE}, and F_{pp} denote the pressure-CH* cross spectrum, the pressure power spectrum and the CH* power spectrum. Figure 3 plots the dependence of γ_{pE} upon frequency for a driving frequency of 235 Hz.

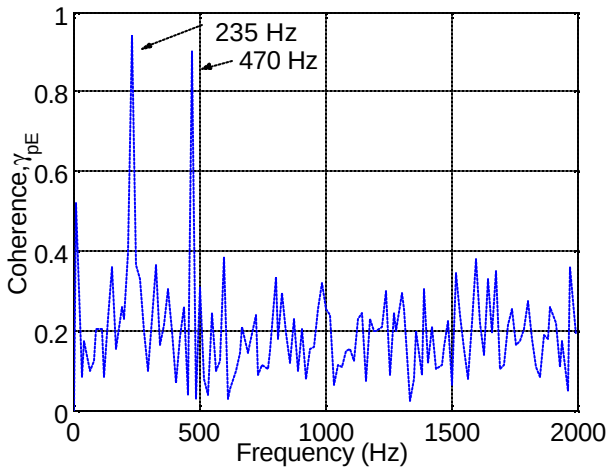

Figure 3 Dependence of pressure-CH* coherence upon frequency at a drive frequency and normalized pressure amplitude of 235 Hz and 1.5%, respectively.

The figure shows that the coherence has a value of roughly 0.95 at the driving frequency and its first harmonic, 470 Hz. Figure 4 plots the dependence of the coherence at the driving frequency, in this case f=235 Hz, upon the amplitude of imposed pressure oscillations.

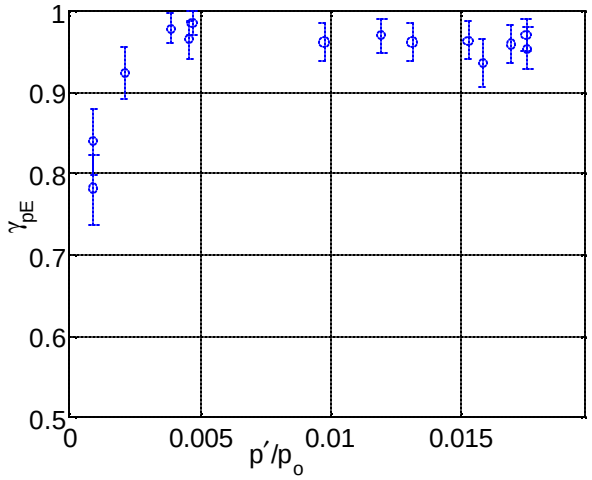

Figure 4 Dependence of pressure-CH* coherence upon amplitude of driven pressure oscillations at a 235 Hz driving frequency.

The figure shows that its lowest value is around 0.8 at the lowest drive amplitudes, but for most results has a value of around 0.95. The uncertainty in our coherence estimates are indicated by the errorbars in Figure 4 and were obtained from the expression[23]:

$$\mathrm{Var}(\gamma_{pE}) = \frac{\gamma_{pE}\sqrt{2(1-\gamma_{pE)}^2}}{n} \qquad [2]$$

where n denotes the number of ensembles that were averaged (we used a value of n=16 in these coherence calculations). These near unity coherence values at the driving frequency shows that the use of these data to determine the pressure-heat release transfer function is appropriate.

Results

We now present typical results illustrating the amplitude and phase characteristics of the pressure and radical chemiluminescence. The amplitudes of the driven oscillations were determined by integrating the area under the power spectrum over a bandwidth of approximately 3 Hz centered at the driving frequency. The RMS level of the oscillations were determined from this value via Parseval's relation. The RMS level was then multiplied by $\sqrt{2}$ to obtain a fluctuating amplitude. This procedure is equivalent to determining the fluctuating amplitude after bandpass filtering the signal about the driving

frequency. The phase of the fluctuating pressure and CH* level was determined from their Fourier transforms at the driving frequency. The uncertainty in phase was estimated from the relation[23]:

$$\mathrm{Var}(\theta_{pE}) = \frac{\sqrt{1-\gamma_{pE}^2}}{\gamma_{pE}\sqrt{2n}} \qquad [3]$$

Figure 5 and Figure 6 present the dependence of these characteristics upon the driven pressure amplitude for a case where oscillations were driven at 157 Hz. Figure 5 shows a linear relationship between the pressure and radical emissions fluctuations up to amplitudes of $p'/p_o \sim 0.5\%$. At higher drive levels, the CH* fluctuations begin to saturate. The departure of this transfer function from linearity are illustrated by comparing the data with the drawn in straight line that goes through the data in the linear regime. It is noteworthy to compare the normalized amplitudes of the pressure and heat release oscillations at the point where nonlinear effects become obvious; the normalized pressure amplitude is roughly 0.5% while the normalized chemiluminescence is 30%, a difference of a factor of 60. These relatively low pressure fluctuations and significant chemiluminescence oscillations lend credibility to speculations that heat release nonlinearities, as opposed to gas-dynamic ones, control the amplitude of limit cycles in these combustion systems. Turning next to the phase relationship, Figure 6 shows that the phase exhibits very little dependence upon the driving amplitude. Rather, the pressure and heat release remain nearly in phase over the driving amplitude range.

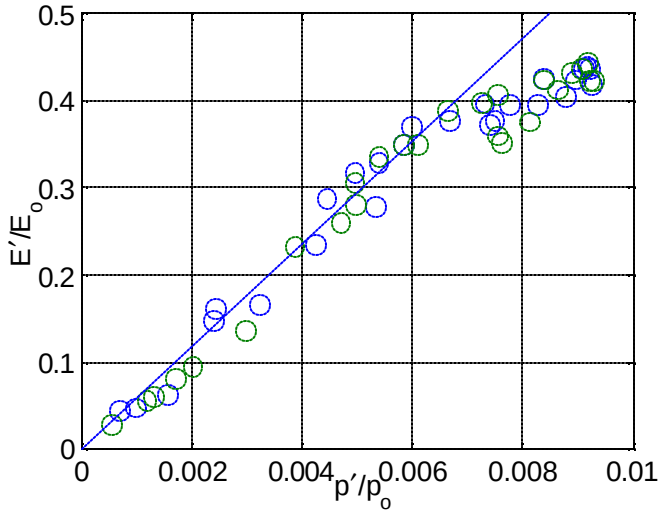

Figure 5 Dependence of the normalized fluctuating CH* level (denoted by E) upon the normalized fluctuating pressure amplitude (157 Hz driving).

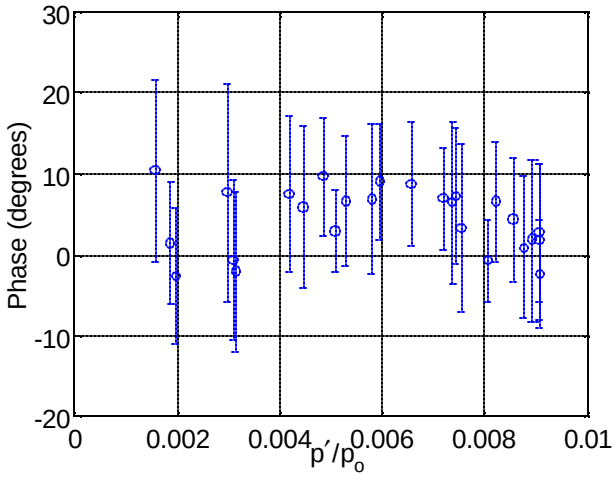

Figure 6 Dependence of the pressure-CH* phase upon the normalized fluctuating pressure amplitude (157 Hz driving).

Figure 7 and Figure 8 illustrate the pressure-CH* amplitude and phase relationships at a 235 Hz driving frequency. The dependence of the fluctuating CH* levels upon p' shown in Figure 7 is similar to that in Figure 5, except that the pressure-radical emissions relation remains nearly linear for larger values of driving pressure; i.e., up to $p'/p_o \sim 1\%$. Note that the normalized CH* fluctuations at the point where nonlinearity is evident has a similar value, in this case about 25%, as in the 157 Hz driving case. The

slope of the nondimensional pressure-CH* relationship in the linear regime has a value of approximately 25, which is less than half that measured in the 157 Hz driving case. These results suggest that nonlinearity becomes important when the normalized CH* fluctuations attain values on the order of 25-30%, with the resultant value of the unsteady pressure controlled by the pressure-CH* transfer function in the linear regime. This conjecture is supported by an additional data set taken at a driving frequency of 190 Hz, where nonlinearity in the pressure-CH* transfer function also occurred at a normalized CH* value of about 25%. It should be pointed out that these pressure amplitudes where nonlinearities in the p'-CH* relationship are observed (p' ~0.5-1%) are of very similar magnitude as typical instability amplitudes (p'~0.5-2%) which we measured in other tests on this combustor (e.g., see data in Refs. [18, 21]).

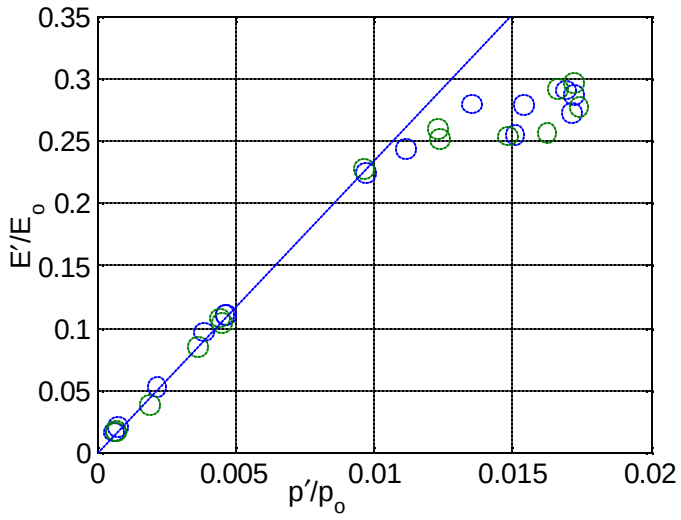

Figure 7 Dependence of the normalized fluctuating CH* level (denoted by E) upon the normalized fluctuating pressure amplitude (235 Hz driving).

Figure 8 shows that the fluctuating pressure-CH* phase difference exhibits some amplitude dependence, in contrast to the 157 Hz results shown in Figure 6. The phase between the oscillations has a value of approximately 100 degrees for low driving amplitudes, but appears to monotonically decrease with increasing drive amplitudes to a value of about 75 degrees. Similar results were observed

in the 190 Hz driving case, where the phase decreased from a value of approximately 70 to 50 degrees with increasing drive amplitude.

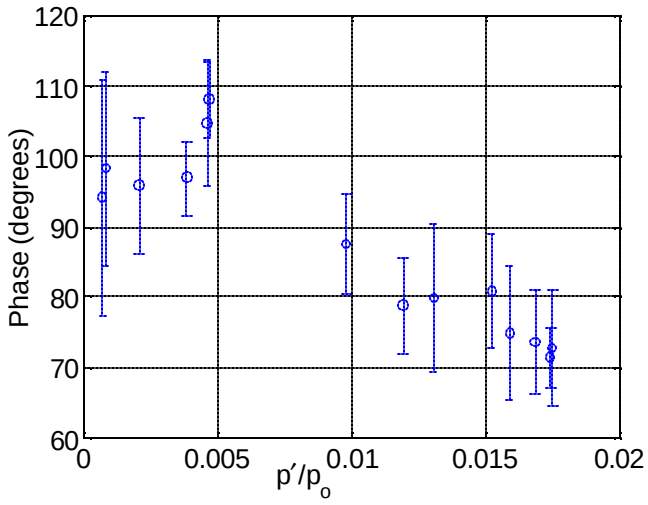

Figure 8 Dependence of the pressure-CH* phase upon the normalized fluctuating pressure amplitude (235 Hz driving).

4. Theoretical Analysis of Acoustic Wave-Turbulent Flame Interactions

This section describes an analysis of the characteristics of acoustic waves scattered by turbulent flames. These waves are scattered because of the abrupt change in sound speed and density at the flame front. The characteristics of the scattered waves are likely complex, due to the fact that they are interacting with a dynamic flame surface that is convoluted over a broad range of length and time scales that interacts with the waves. Due to the complex nature of these interactions, their current understanding is quite incomplete. Several analyses are in the literature, however, that have made important contributions to their current understanding. These analyses are briefly summarized below.

Chu appears to have first studied the response of a thin flame front to an acoustic disturbance[24]. His one-dimensional analysis considered the response of an infinitely long flat flame to normally impinging acoustic waves. The resultant acoustic field was determined from conservation and kinematical matching conditions applied across the flame. He calculated the amplitude of the reflected and transmitted waves that are excited by an incident wave impinging normal to the flame, as well as the

time varying position of the flame front. A significant result of the study was its demonstration that acoustic waves could be excited or amplified by flames.

Chu's work was generalized to account for the interactions between a planar flame and two dimensional acoustic fields by Lieuwen [25]. This study showed that phenomenon not present in 1-D interactions, such as flame wrinkling and vorticity production, introduced qualitatively new and significant effects, such as introducing a mechanism of acoustic damping.

Such models of flame-acoustic wave interactions in simplified geometries were incorporated into more realistic geometries by Marble and Candel[26], Yang and Culick[27], Dowling[28] and Fleifel *et al.*[29]. These investigations analyzed the interactions between acoustic waves and flames stabilized in combustors with two dimensional mean flow fields. A significant result of these studies was their demonstration that maximum amplification of acoustic waves by the flame occurred at certain values of the flame Strouhal number, $St = fL_{flame}/\bar{u}$.

All of these studies considered the reflection, transmission, and excitation of acoustic waves by ***laminar*** flames with ***smooth fronts***. No study has analyzed these interactions, however, for turbulent flames with rough, convoluted, and moving surfaces. As such, a number of fundamental issues related to interactions between acoustic waves and turbulent flames are unclear or unexplored. Since almost all practical systems operate in turbulent regimes, it is likely that clarification of these issues could contribute to improved understanding of turbulent flame processes in practical systems.

The objective of this work is to perform such an analysis in an idealized geometry in order to clarify the fundamental processes controlling these interactions.

Problem Statement and Basic Assumptions

The geometry under consideration is shown in Fig. 2. It generalizes the geometry considered by Chu [24] and Lieuwen and Zinn [25], and consists of a time varying, wrinkled flame surface whose average position is flat. The following basic assumptions are made in the analysis: (1) the flame has a thickness, δ, which is much smaller than an acoustic wavelength and, thus, can be treated as a surface of discontinuity, (2) outside of the flame itself, the flow field is isothermal, has a low Mach number, M, and is composed of a perfect gas; as such, mean flow affects (such as wave scattering by turbulent flow fluctuations) on acoustic wave propagation are neglected, (3) the acoustic field can be approximately

described with the single scattering Kirchhoff approximation (explained below), (4) the time scales over which flame surface properties and movement occurs is long relative to that of the acoustic period (discussed below), and (5) flame displacement due to the incident wave disturbance is small relative to that in the absence of the incident wave (discussed below).

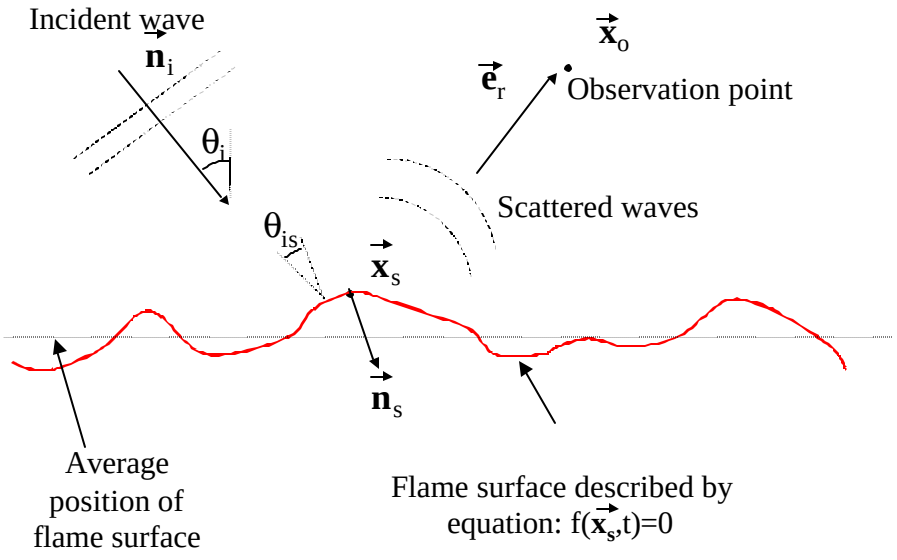

Figure 9. Schematic illustrating flame surface and acoustic field quantities.

With these basic assumptions, the acoustic field in the "cold", unreacted gases upstream of the flame is described by the classical wave equation [30]:

$$\frac{1}{\bar{c}_1^2}\frac{\partial^2 p'}{\partial t^2} - \nabla^2 p' = 0 \qquad [4]$$

where p' is the acoustic pressure and $\bar{c}_1$ is the speed of sound. In the same way, the acoustic field in the "hot", reacted gases downstream of the flame is described by a similar equation, but with the speed of sound replaced by its value in the reacted gases, $\bar{c}_2$. These wave equations describe the acoustic field up and downstream of the flame. These unsteady flow fields are coupled across the flame front by the following matching conditions that can be derived from the mass, momentum, and energy equations [31]:

Mass: $\rho_1 S_1 = \rho_2 S_2$ [5]

Normal Momentum: $p_1 + \rho_1 S_1^2 = p_2 + \rho_2 S_2^2$ [6]

Tangential Momentum: $(\vec{u}_1 - \vec{u}_2)\,x\,\nabla f = 0$ [7]

Energy: $\rho_1 S_1 (h_1 + \frac{\vec{u}_1 \cdot \vec{u}_1}{2}) = \rho_2 S_2 (h_2 + \frac{\vec{u}_2 \cdot \vec{u}_2}{2})$ [8]

where ρ, S, $\vec{u}$, and h denote density, flame speed relative to the gases, velocity, and enthalpy, respectively. The flame surface is described by the parametric equation $f(\vec{x}_s, t) = 0$, see Figure 9.

These matching conditions are applied at the flame surface whose time varying position is described by the kinematical relations [31]:

$$\frac{\partial f}{\partial t} + \vec{u}_1 \cdot \nabla f - S_1 |\nabla f| = 0, \qquad \frac{\partial f}{\partial t} + \vec{u}_2 \cdot \nabla f - S_2 |\nabla f| = 0 \qquad [9]$$

For this moving, convoluted boundary problem, it is difficult to calculate the acoustic field using the formulation of the wave equation in Eq. (1). Rather, it is more convenient to solve an integral equation formulation, known as the Kirchhoff – Helmholtz integral (KHI) equation, that is equivalent to Eq. (1) [30]. This equation can be written as:

$$p'(\vec{x}_o, t) = p_i'(\vec{x}_o, t) + \frac{1}{4\pi} \iint_{S_s} (\bar{\rho}_1 \frac{\frac{\partial}{\partial t}(\vec{n}_s \cdot \vec{u}'(\vec{x}_s, t - R/\bar{c}_1))}{R} + \frac{\vec{e}_r \cdot \vec{n}_s}{R} (\frac{1}{\bar{c}_1} \frac{\partial}{\partial t} + \frac{1}{R}) p'(\vec{x}_s, t - R/\bar{c}_1)) dS_s \qquad [10]$$

where p_i', $\vec{n}_s$, $\vec{x}_o$, $\vec{x}_s$, and $\bar{\rho}_1$ denote the incident wave, instantaneous flame surface normal vector, observation point, flame surface point, and the average gas density of the unburned gas, respectively. In addition, the vector $\vec{e}_r$ points from the surface point, $\vec{x}_s$, to the observation point, $\vec{x}_o$, and R denotes the distance between the source and observation point, $R = |\vec{x}_s - \vec{x}_o|$. The surface integral is carried out over the surface of integration; i.e., over the flame, $\vec{x}_s$, and other boundaries. These quantities are illustrated in Figure 9. An analogous equation can be written for the pressure in Region 2, with the values of the density and speed of sound replaced by their appropriate values.

Two assumptions that have been made in writing Eq. (7) should be emphasized. Strictly speaking, Eq. (7) is valid for a stationary surface. A development of an integral equations for sound generation by rigid moving surfaces by Ffowcs-Williams and Hawkings[32] shows that, first, an additional surface movement correction term occurs of the form $1/|1-M_r|$, where M_r is the Mach number of the

surface in the observer direction. This correction has been neglected, see Assumption (2) above. Second, because the surface characteristics change in time, the time derivatives in Eq. (7) should actually be placed outside of the integral. Consistent with Approximation (4), however, we have neglected temporal differentiation of flame surface characteristics.

We next divide the pressure field into the incident wave field, p', the field scattered by this wave, p'_{sc}, and the field that is excited by the flame in the absence of the incident wave, p'_{exc}; i.e.,:

$$p'(\vec{x}_o, t) = p_i'(\vec{x}_o, t) + p_{sc}'(\vec{x}_o, t) + p_{exc}'(\vec{x}_o, t) \qquad [11]$$

It can be shown that the following integral equations describe the scattered and excited waves.[12]

$$p_{sc}'(\vec{x}_o, t) = \frac{1}{4\pi}\iint_{S_s} (\bar{\rho}_1 \frac{\frac{\partial}{\partial t}(\vec{n}_s \cdot \vec{u}_{sc}'(\vec{x}_s, t - R/\bar{c}_1))}{R} + \frac{\vec{e}_r \cdot \vec{n}_s}{R}(\frac{1}{\bar{c}_1}\frac{\partial}{\partial t} + \frac{1}{R})p_{sc}'(\vec{x}_s, t - R/\bar{c}_1))dS_s \qquad [12]$$

$$p_{exc}'(\vec{x}_o, t) = \frac{1}{4\pi}\iint_{S_s} (\bar{\rho}_1 \frac{\frac{\partial}{\partial t}(\vec{n}_s \cdot \vec{u}_{exc}'(\vec{x}_s, t - R/\bar{c}_1))}{R} + \frac{\vec{e}_r \cdot \vec{n}_s}{R}(\frac{1}{\bar{c}_1}\frac{\partial}{\partial t} + \frac{1}{R})p_{exc}'(\vec{x}_s, t - R/\bar{c}_1))dS_s \qquad [13]$$

The equation for the excited field describes the sound generation by flames (i.e., combustion noise) which is not the subject of this paper.

Equation (9) shows that the scattered acoustic field is determined by the value of the acoustic velocity and pressure at the surface of the flame. These quantities are not independent of each other; thus solving Eq. (9) for the scattered pressure requires first solving for the pressure and velocity on the flame surface. Since the pressure appears both on the left side of the equation and inside the integral, its solution requires solving an integral equation that is obtained by taking the limit as the observation point tends toward the surface. The resulting integral equation is essentially the same as Eq. (9), except the pressure on the left side becomes the pressure at the surface, $p'(\vec{x}_s, t)$ and the numerical factor in front of the surface integral is replaced by $1/8\pi$. Analytical solutions of this integral equation cannot be obtained for general situations and numerical methods must be employed. For example, the author has solved the problem of wave scattering by laminar flames in complex geometries numerically using boundary element methods [33].

In certain limiting cases, approximate analytical solutions to the Kirchhoff-Helmholtz integral equation can be obtained; e.g., using the Born, Rytov, or Kirchhoff approximations[34]. In this paper, we use the single scattering Kirchhoff approximation to provide an approximate relationship between the acoustic pressure and velocity at the flame, see Assumption (3).

The basic Kirchhoff approximation assumes that the acoustic field on the scattering surface is approximately equal to its value when the surface is flat. The single scattering approximation assumes that the scattered waves do not re-interact with the flame and, thus, neglects multiple scattering. The theory is exact for an infinitely long, smooth, plane scattering surface. As discussed in the literature[10] it is approximately true when the radii of curvature of the surface, Ra_s, is significantly larger than the wavelength of the disturbance, λ; i.e., the theory applies to disturbances with short wavelengths and, thus, at high frequencies. In this case, the scattering surface "looks" plane to the incident acoustic wave.

Denoting the surface reflection coefficient of the smooth scattering surface as $V(\vec{x}_s, t)$, the surface pressure and velocity are given in the single scattering Kirchhoff approximation as:

$$p'(\vec{x}_s, t) = p_i'(\vec{x}_s, t)(1 + V(\vec{x}_s, t))$$

$$\vec{n}_s \cdot \vec{u}'(\vec{x}_s, t) = \vec{n}_s \cdot \vec{v}_i'(\vec{x}_s, t)(1 - V(\vec{x}_s, t)) \qquad [14]$$

In general, the flame surface moves as a result of turbulent flow fluctuations and the flow fluctuations from the incident wave. In this study, we assume that the flame surface position is prescribed and, thus, assume that the effects of the incident acoustic fluctuations upon its position are small, see Assumption (5). This allows us to solve Eq. (9) independent of Eq. (6). Such an approximation is reasonable in that the developed theory is appropriate at high frequencies (i.e., short wavelengths so that $\lambda << Ra_s$). Since the flame displacement from an incident wave with frequency ω scales as $1/\omega$, its effect becomes small as the frequency is increased. It is likely that the flame motion due to the incident disturbance will play an important role in low frequency interactions, however. In such a case, however, the Kirchhoff theory developed here will not apply.

Analysis

Given the assumptions in the prior section, the scattered field can be explicitly written as an integral over the rough surface, rather than an integral equation in the more general case. Substituting Eq. (11) into Eq. (9) yields:

$$p_{sc}'(x_o,t)=\frac{1}{4\pi}\iint_{S_s}(\bar{\rho}_1\frac{\frac{\partial}{\partial t}(-V(\vec{x}_s,t)\vec{n}_s\cdot\vec{u}_i'(\vec{x}_s,t-R/\bar{c}_1))}{R}+\frac{\vec{e}_r\cdot\vec{n}_s}{R}(\frac{1}{\bar{c}_1}\frac{\partial}{\partial t}+\frac{1}{R})V(\vec{x}_s,t)p_i'(\vec{x}_s,t-R/\bar{c}_1))dS_s \quad [15]$$

Assuming that the incident disturbance is a plane wave, the pressure and velocity of the incident wave are related by:

$$\vec{n}_s\cdot\vec{u}_i'(\vec{x}_s,t)=\frac{p_i'(\vec{x}_s,t)}{\bar{\rho}_1\bar{c}_1}\vec{n}_i\cdot\vec{n}_s \quad [16]$$

Substituting Eq. (15) into (14) and ignoring the farfield $1/R^2$ term yields:

$$p_{sc}'(x_o,t)=\frac{1}{4\pi\bar{c}_1}\iint_{S_s}(\frac{V(\vec{x}_s,t)\vec{n}_s\cdot(\vec{e}_r-\vec{n}_i)}{R}\frac{\partial}{\partial t}p_{inc}'(\vec{x}_s,t-R/\bar{c}_1)dS_s \quad [17]$$

Consistent with Approximation (4), time derivatives of flame surface properties are neglected. Equation (16) is a general expression for the farfield scattered pressure within the single scattering Kirchhoff approximation. Its dependence upon the characteristics of the flame surface can be seen more explicitly by noting the relationships:

$$dS_s=dx_s dy_s\sqrt{1+(\frac{\partial\zeta}{\partial x_s})^2+(\frac{\partial\zeta}{\partial y_s})^2},\quad \vec{n}_s=\frac{\frac{\partial\zeta}{\partial x_s}\vec{e}_x+\frac{\partial\zeta}{\partial y_s}\vec{e}_y-\vec{e}_z}{\sqrt{1+(\frac{\partial\zeta}{\partial x_s})^2+(\frac{\partial\zeta}{\partial y_s})^2}} \quad [18]$$

where the flame surface is assumed to be a single valued function of x_s and y_s and can be written as:

$$f(\vec{x}_s,t)=z-\varsigma(x_s,y_s,t)=0 \quad [19]$$

Assume that the incident disturbance is harmonically oscillating:

$$\frac{\partial}{\partial t} p_{inc}'(\vec{x}_s, t - R/\bar{c}_1) = -i\omega P_I e^{-i\omega_o t} e^{ikR(t)} e^{ik\vec{n}_i \cdot \vec{x}_s} \qquad [20]$$

where, consistent with Approximation (4), it is assumed that the time scale of the acoustic disturbance is small relative to that over which the flame moves. Introduce the notation:

$$()_i - ()_o = ()_\Delta \qquad [21]$$

For example, $k(\vec{n}_i - \vec{n}_o) = \vec{k}_\Delta$. Utilizing the farfield approximation [30]:

$$R \approx |\vec{x}_o| - \vec{x}_s \cdot \frac{\vec{x}_o}{|\vec{x}_o|} = |\vec{x}_o| - \vec{x}_s \cdot \vec{n}_o \qquad [22]$$

leads to the following expression for the scattered pressure:

$$\frac{p_{sc}'(\vec{x}_o, t)}{P_I} = \frac{ie^{-i\omega_o t} e^{ikR_o}}{4\pi R_o} \Phi(\vec{x}_o, t) \qquad [23]$$

where: $\Phi = \int_{x_s} \int_{y_s} V(\vec{x}_s, t)(\vec{n}_s \cdot \vec{k}_\Delta) e^{i\vec{k}_\Delta \cdot \vec{x}_s} \sqrt{1 + (\frac{\partial \zeta}{\partial x_s})^2 + (\frac{\partial \zeta}{\partial y_s})^2}\, dx_s dy_s \qquad [24]$

Further progress in analyzing Eq. (23) requires specifying the surface reflection coefficient, V. In general, V depends upon the density and sound speed ratio across the flame, the flame speed, and the flame speed sensitivity to flow and pressure disturbances. Based upon the analysis in Ref. [25], it is assumed that flame speed corrections to the surface reflection coefficient are of the order of the flame speed Mach number, and thus, neglected in this study. As such, the resulting expression for the reflection coefficient is equivalent to that from an interface separating two media at different temperatures and densities. Manipulating Eqs. (2-5), it can be shown to equal [25, 30]:

$$V(\vec{x}_s, t) = \frac{\frac{\bar{\rho}_2 \bar{c}_2}{\bar{\rho}_1 \bar{c}_1} \cos\theta_{is} - \sqrt{1 - (\frac{\bar{c}_2}{\bar{c}_1} \sin\theta_{is})^2}}{\frac{\bar{\rho}_2 \bar{c}_2}{\bar{\rho}_1 \bar{c}_1} \cos\theta_{is} + \sqrt{1 - (\frac{\bar{c}_2}{\bar{c}_1} \sin\theta_{is})^2}} = \frac{\frac{\bar{\rho}_2 \bar{c}_2}{\bar{\rho}_1 \bar{c}_1} (\vec{n}_i \cdot \vec{n}_s) - \sqrt{1 - (\frac{\bar{c}_2}{\bar{c}_1})^2 (1 - (\vec{n}_i \cdot \vec{n}_s)^2)}}{\frac{\bar{\rho}_2 \bar{c}_2}{\bar{\rho}_1 \bar{c}_1} (\vec{n}_i \cdot \vec{n}_s) + \sqrt{1 - (\frac{\bar{c}_2}{\bar{c}_1})^2 (1 - (\vec{n}_i \cdot \vec{n}_s)^2)}} \qquad [25]$$

where θ_{is} denotes the angle between the incident wave and instantaneous flame location, see Fig. 2. In another study [35], the author presents numerical results for the scattered coherent field using Eq. (24). To retain analytical tractability, in this paper we restrict attention to cases where $\frac{\bar{c}_2}{\bar{c}_1}\sin\theta_{is} \ll 1$. Thus, this analysis applies to cases where the incident wave is nearly normal to the flame, or when the sound speed ratio is small. Note then that this theory applies over a wider range of incident angles, θ_i, when the disturbance is incident from downstream (where $\bar{c}_2 < \bar{c}_1$) than upstream. As such, we use the following approximate expression for V.

$$V(\vec{x}_s, t) = \frac{Z(\vec{n}_i \cdot \vec{n}_s) - 1}{Z(\vec{n}_i \cdot \vec{n}_s) + 1} \qquad [26]$$

where Z denotes the ratio of the impedance of the gases on either side of the interface, $Z = \bar{\rho}_2 \bar{c}_2 / \bar{\rho}_1 \bar{c}_1$. Substituting Eq. (25) into Eq. (23) yields:

$$\Phi = \int_{x_s} \int_{y_s} \frac{Z(\frac{\partial \zeta}{\partial x_s} n_{i,x} + \frac{\partial \zeta}{\partial y_s} n_{i,y} - n_{i,z}) - 1}{Z(\frac{\partial \zeta}{\partial x_s} n_{i,x} + \frac{\partial \zeta}{\partial y_s} n_{i,y} - n_{i,z}) + 1} (\frac{\partial \zeta}{\partial x_s} k_{\Delta,x} + \frac{\partial \zeta}{\partial y_s} k_{\Delta,y} - k_{\Delta,z}) e^{i\vec{k}_\Delta \cdot \vec{x}_s} dx_s dy_s \qquad [27]$$

Because of the strong nonlinear dependence of the solution upon the flame position and its derivative, this equation generally requires numerical evaluation. We will next make additional approximations that allow for its analytical evaluation.

First, we expand V in a power series using $Z(\vec{n}_i \cdot \vec{n}_s)$ as the expansion parameter. Thus, the analysis considers the case where the nondimensional surface impedance, Z, is either large or small (note that in cases of grazing incidence, the term $(\vec{n}_i \cdot \vec{n}_s)$ is generally small regardless of the value of Z; in this case, however, the starting equation (14) that only accounts for single scattering is not accurate). This limit is marginally satisfied for most flames. For example, an equilibrium calculation for a stoichiometric propane-air flame shows that Z = 0.35 or 3, depending upon whether the incident wave is up or downstream of the flame. In the same way, Z = 4 or 0.25 in a stoichiometric propane-oxygen flame. The following approximations for V are then obtained:

$$\text{if } Z(\vec{n}_i \cdot \vec{n}_s) << 1\text{: } V = -1 + 2Z(\vec{n}_i \cdot \vec{n}_s) = -1 + 2Z\frac{\frac{\partial \zeta}{\partial x_s} n_{i,x} + \frac{\partial \zeta}{\partial y_s} n_{i,y} - n_{i,z}}{\sqrt{1 + (\frac{\partial \zeta}{\partial x_s})^2 + (\frac{\partial \zeta}{\partial y_s})^2}} \qquad [28]$$

$$\text{if } Z(\vec{n}_i \cdot \vec{n}_s) >> 1\text{: } V = 1 - \frac{2}{Z(\vec{n}_i \cdot \vec{n}_s)} = 1 - \frac{2\sqrt{1 + (\frac{\partial \zeta}{\partial x_s})^2 + (\frac{\partial \zeta}{\partial y_s})^2}}{Z(\frac{\partial \zeta}{\partial x_s} n_{i,x} + \frac{\partial \zeta}{\partial y_s} n_{i,y} - n_{i,z})} \qquad [29]$$

Because of the strong nonlinear dependence of V upon the surface derivatives, we will consider cases where the surface slopes are small in order to make further analytical progress. The conditions under which such an approximation are true can be determined by noting that $\left\langle (\frac{\partial \zeta}{\partial x})^2 \right\rangle = \sigma^2 \frac{\partial^2 C(a)}{\partial a}\Big|_{a=0}$, where $\sigma^2 = \left\langle \zeta^2 \right\rangle$, C(a) is the correlation function defined as $C(a) = \left\langle \zeta(\vec{x}_{s,1}, t)\zeta(\vec{x}_{s,2}, t) \right\rangle$ and $a = \left| \vec{x}_{s,1} - \vec{x}_{s,2} \right|$ [36]. Note that it has been assumed that ζ is stationary. The second derivative of the correlation function at the origin can be interpreted as a correlation length scale, Λ, implying that $\left\langle (\frac{\partial \zeta}{\partial x})^2 \right\rangle \propto \sigma^2 / \Lambda^2$. Thus, this "small slope" approximation assumes that the standard deviation of the surface location, σ, is small relative to the length over which the flame surface is well correlated. In this analysis, we will retain only linear terms in surface derivatives, implying that the analysis is accurate to $O(\sigma/\Lambda)$. In this case, we can linearize Eqs. (27-28) to obtain:

$$\text{if } Z(\vec{n}_i \cdot \vec{n}_s) << 1$$

$$V(\vec{n}_s \cdot \vec{k}_\Delta) = k_{\Delta,z}(1 + 2Zn_{i,z}) -$$
$$\frac{\partial \zeta}{\partial x_s}(2Zn_{i,x}k_{\Delta,z} + k_{\Delta,x}(1 + 2Zn_{i,z})) - \frac{\partial \zeta}{\partial y_s}(2Zn_{i,y}k_{\Delta,z} + k_{\Delta,y}(1 + 2Zn_{i,z})) \qquad [30]$$

if $Z(\vec{n}_i \cdot \vec{n}_s) >> 1$

$$V(\vec{n}_s \cdot \vec{k}_\Delta) = -k_{\Delta,z}(1+\frac{2}{Zn_{i,z}}) + \frac{\partial\zeta}{\partial x_s}(-\frac{2n_{i,x}k_{\Delta,z}}{Zn_{i,z}^2} + k_{\Delta,x}(1+\frac{2}{Zn_{i,z}})) + \frac{\partial\zeta}{\partial y_s}(-\frac{2n_{i,y}k_{\Delta,z}}{Zn_{i,z}^2} + k_{\Delta,y}(1+\frac{2}{Zn_{i,z}})) \quad [31]$$

For brevity, in the subsequent analysis we will in either case write $V(\vec{n}_s \cdot \vec{k}_\Delta)$ as $V(\vec{n}_s \cdot \vec{k}_\Delta) = A + B\frac{\partial\zeta}{\partial x_s} + C\frac{\partial\zeta}{\partial y_s}$; i.e.,

$$\Phi = \int_{x_s}\int_{y_s}(A + B\frac{\partial\zeta}{\partial x_s} + C\frac{\partial\zeta}{\partial y_s})e^{i\vec{k}_{\Delta,x}x_s}e^{i\vec{k}_{\Delta,y}y_s}e^{i\vec{k}_{\Delta,z}\zeta}dx_s dy_s \quad [32]$$

We now seek a description of the statistical characteristics of the scattered pressure in terms of the flame surface characteristics. Turning attention first to calculation of the coherent scattered wave (the mean field) leads to consideration of the equation:

$$\langle\Phi\rangle = \int_{x_s}\int_{y_s}\langle(A + B\frac{\partial\zeta}{\partial x_s} + C\frac{\partial\zeta}{\partial y_s})e^{i\vec{k}_{\Delta,x}x_s}e^{i\vec{k}_{\Delta,y}y_s}e^{i\vec{k}_{\Delta,z}\zeta}\rangle dx_s dy_s \quad [33]$$

where $< >$ denotes the expected value operator. Assuming that the statistical characteristics of the surface position are stationary, Eq. (32) equals:

$$\langle\Phi\rangle = \int_{x_s}\int_{y_s}Ae^{i\vec{k}_{\Delta,x}x_s}e^{i\vec{k}_{\Delta,y}y_s}\left\langle e^{i\vec{k}_{\Delta,z}\zeta}\right\rangle dx_s dy_s = \int_{x_s}\int_{y_s}Ae^{i\vec{k}_{\Delta,x}x_s}e^{i\vec{k}_{\Delta,y}y_s}f(k_{\Delta,z})dx_s dy_s = \Phi_{sm}\tilde{f}(k_{\Delta,z}) \quad [34]$$

where $\tilde{f}(k_{\Delta,z})$ is the characteristic function of $e^{i\vec{k}_{\Delta,z}\zeta}$ and Φ_{sm} is the value of Φ were the surface smooth..[22] Equation (33) is analogous to that obtained in other studies of scattering from rough surfaces,[10,11,12] and shows that the effect of the rough, turbulent flame surface upon waves scattered at the incident frequency is equivalent to a reflection coefficient that is reduced by the factor $\tilde{f}(k_{\Delta,z})$.

We next consider the diffuse wave field (i.e., the field that is not coherent with the incident wave). As opposed to the coherent field, which only oscillates at the incident disturbance frequency, the diffuse field has other spectral components because of the flame's movement. Thus, it is useful to

examine the spectral characteristics of the scattered wave field. Define the Fourier transform of the temporal component of the scattered field:

$$F(\vec{x}_o,\omega)=\int_t(\Phi(\vec{x}_o,t)e^{-i\omega_o t})e^{i\omega t}dt \qquad [35]$$

Its mean squared value then equals:

$$\left\langle|F(\omega)|^2\right\rangle=\int_t\int_{t'}e^{i(\omega-\omega_o)(t-t')}\int_{x_s}\int_{y_s}\int_{x_s'}\int_{y_s'}e^{ik_{\Delta,x}(x_s-x_s')}e^{ik_{\Delta,y}(y_s-y_s')}\left[A^2e^{ik_{\Delta,z}(\zeta(x_s,y_s,t)-\zeta(x_s',y_s',t'))}+\right.$$
$$\frac{AB}{ik_{\Delta,z}}\left(\frac{\partial}{\partial x_s}\left(e^{ik_{\Delta,z}(\zeta(x_s,y_s,t)-\zeta(x_s',y_s',t'))}\right)-\frac{\partial}{\partial x_s'}\left(e^{ik_{\Delta,z}(\zeta(x_s,y_s,t)-\zeta(x_s',y_s',t'))}\right)+\right.$$
$$\left.\left.\frac{AC}{ik_{\Delta,z}}\left(\frac{\partial}{\partial y_s}\left(e^{ik_{\Delta,z}(\zeta(x_s,y_s,t)-\zeta(x_s',y_s',t'))}\right)-\frac{\partial}{\partial y_s'}\left(e^{ik_{\Delta,z}(\zeta(x_s,y_s,t)-\zeta(x_s',y_s',t'))}\right)dx_s dy_s dx_s' dy_s' dt dt'\right.\right. \qquad [36]$$

Defining the two dimensional characteristic function:

$$\left\langle e^{ik_{\Delta,z}(\zeta(x_s,y_s,t)-\zeta(x_s',y_s',t'))}\right\rangle=g(x_s,y_s,x_s',y_s',t,t') \qquad [37]$$

Consistent with the prior assumptions of stationary flame surface statistics, it will be assumed that g depends only upon the distance between (x_s,y_s) and (x_s',y_s'). Then Eq. (35) can be simplified by the following manipulation of the terms in the second and third lines:

$$\int_{x_s}\int_{y_s}\int_{x_s'}\int_{y_s'}e^{ik_{\Delta,x}(x_s-x_s')}e^{ik_{\Delta,y}(y_s-y_s')}\left[\frac{\partial}{\partial x_s}g(x_s,y_s,x_s',y_s',t,t')-\frac{\partial}{\partial x_s'}g(x_s,y_s,x_s',y_s',t,t')\right]dx_s dy_s dx_s' dy_s'=$$
$$\int_{x_s}\int_{y_s}\int_{x_s'}\int_{y_s'}e^{ik_{\Delta,x}(x_s-x_s')}e^{ik_{\Delta,y}(y_s-y_s')}\frac{\partial}{\partial x_s}g(x_s,y_s,x_s',y_s',t,t')-$$
$$e^{ik_{\Delta,x}(x_s'-x_s)}e^{ik_{\Delta,y}(y_s'-y_s)}\frac{\partial}{\partial x_s}g(x_s',y_s',x_s,y_s)dx_s dy_s dx_s' dy_s'=$$
$$\int_{x_s}\int_{y_s}\int_{x_s'}\int_{y_s'}2i\sin(k_{\Delta,x}(x_s-x_s')+k_{\Delta,y}(y_s-y_s'))\frac{\partial}{\partial x_s}g(x_s,y_s,x_s',y_s',t,t')dx_s dy_s dx_s' dy_s' \qquad [38]$$

Assuming that the surface statistics are isotropic, it is convenient to convert to an (a,θ) polar coordinate system:

$$x_s-x_s'=a\cos\theta \qquad y_s-y_s'=a\sin\theta \qquad t-t'=\tau \qquad [39]$$

Substituting Eqs. (37-38) into Eq. (35) yields:

$$\left\langle |F(\omega)|^2 \right\rangle = \int_t \int_\tau e^{i(\omega-\omega_o)\tau} \int_{x'_s} \int_{y'_s} \int_a \int_{\theta=0}^{2\pi} A^2 g(a,\tau) e^{ik_{\Delta,x} a\cos\theta} e^{ik_{\Delta,y} a\sin\theta} + \frac{2A(B\cos\theta + C\sin\theta)}{k_{\Delta,z}} \sin(k_{\Delta,x} a\cos\theta + k_{\Delta,y} a\sin\theta) a \frac{\partial g(a,\tau)}{\partial a} da\, d\theta\, dx_s'\, dy_s'\, dt\, d\tau \quad [40]$$

The angular integrals can be evaluated by noting the following relationships obtained from manipulation of formulas in Section 3.715 in Gradshteyn and Ryzhik [37]:

$$\int_{\theta=0}^{2\pi} e^{ik_{\Delta,x} a\cos\theta} e^{ik_{\Delta,y} a\sin\theta} d\theta = 2\pi J_o\left(a\sqrt{k_{\Delta,x}^2 + k_{\Delta,y}^2}\right) \quad [41]$$

$$\int_{\theta=0}^{2\pi} \cos\theta \sin(k_{\Delta,x} a\cos\theta + k_{\Delta,y} a\sin\theta) d\theta = \frac{2\pi k_{\Delta,x}}{\sqrt{k_{\Delta,x}^2 + k_{\Delta,y}^2}} J_1\left(a\sqrt{k_{\Delta,x}^2 + k_{\Delta,y}^2}\right) \quad [42]$$

$$\int_{\theta=0}^{2\pi} \sin\theta \sin(k_{\Delta,x} a\cos\theta + k_{\Delta,y} a\sin\theta) d\theta = \frac{2\pi k_{\Delta,y}}{\sqrt{k_{\Delta,x}^2 + k_{\Delta,y}^2}} J_1\left(a\sqrt{k_{\Delta,x}^2 + k_{\Delta,y}^2}\right) \quad [43]$$

Substituting these expressions into Eq. (39) yields:

$$\frac{\left\langle |F(\omega)|^2 \right\rangle}{2\pi A_m T_i} = \int_a \int_\tau e^{i(\omega-\omega_o)\tau} \left[A^2 g(a,\tau) J_o\left(a\sqrt{k_{\Delta,x}^2 + k_{\Delta,y}^2}\right) + \frac{2A(Bk_{\Delta,x} + Ck_{\Delta,y})}{k_{\Delta,z}\sqrt{k_{\Delta,x}^2 + k_{\Delta,y}^2}} J_1\left(a\sqrt{k_{\Delta,x}^2 + k_{\Delta,y}^2}\right) \frac{\partial g(a,\tau)}{\partial a} \right] a\, da\, d\tau \quad [44]$$

where A_m and T_i are the intervals/areas over which the spatial and temporal integration is performed. Note in the limit as $T_i \to \infty$, that $\left\langle |F(\omega)|^2 \right\rangle / 2\pi T_i$ is simply the power spectral density of $\Phi(\vec{x}_o, t) e^{-i\omega_o t}$. Equation (43) can be evaluated for a given characteristic function, g(a,τ).

Equations (33) and (43) are the principle results of this analysis. They describe the characteristics of the scattered field in terms of the statistical characteristics of the flame surface. Further progress in analyzing the scattered field requires specifying more information about these statistics. In the following section, we present results for surfaces with Gaussian statistics.

Results for Flame Surfaces with Gaussian Statistics

Turning first to the coherent field, it can be shown that if the flame surface position, $\varsigma(\vec{x}_s, t)$, is Gaussian, then the characteristic function, $\tilde{f}(k_\Delta, z)$, equals[12]

$$\tilde{f}(k_\Delta, z) = e^{-(k\sigma(\cos\theta_i + \cos\theta_r))^2/2} \qquad [45]$$

Figure 11 illustrates the dependence of $\tilde{f}(k_\Delta, z)$ upon $k\sigma$ and θ_i for the case of specular reflection (i.e., when $\theta_i=\theta_r$; note that when the size of the scatterer is very large relative to a wavelength, the scattered wave amplitude becomes very small in all other directions.) The figure illustrates that the amplitude of the reflected wave inversely depends upon $k\sigma$, implying that the scattered field that is coherent with the incident disturbance is smaller for flames with larger scales of wrinkling relative to a wavelength. Presumably, the rest of the energy in the incident wave is transmitted or scattered incoherently in other directions. This result suggests that a turbulent flame front can act as a source of damping to incident coherent waves by scattering them incoherently.

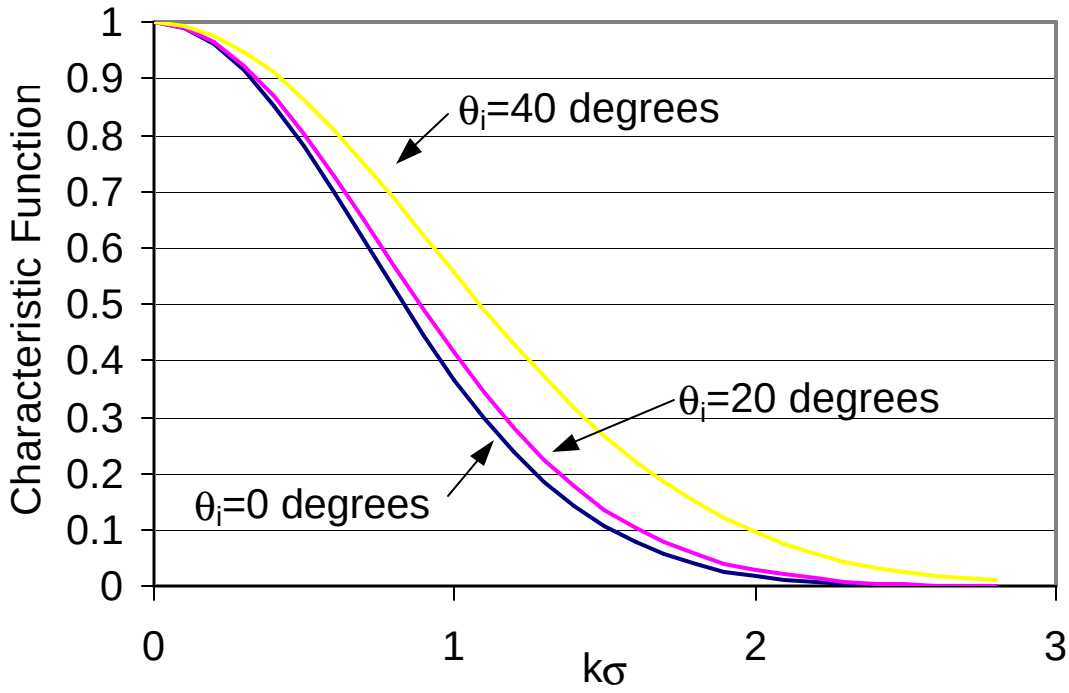

Figure 10. Dependence of the characteristic function amplitude upon k_s and the incident wave angle.

We next consider the characteristics of the diffuse field. For a Gaussian surface, its characteristics depend upon the two point correlation function, $C(a,\tau)$, as it and the two dimensional characteristic function $g(a,\tau)$ are related by[12]:

$$g(a,\tau) = e^{-(k_{\Delta,z}\sigma)^2(1-C(a,\tau))} \qquad [46]$$

This expression for $g(a,\tau)$ can be inserted into Eqs. (43) and evaluated analytically in the limiting cases where $(k_{\Delta,z}\sigma)^2$ is either large or small.

We will first consider the case where $(k_{\Delta,z}\sigma)^2 >> 1$. Equation (50) shows that $g(a,\tau)$ is exponentially small except where $C(a,\tau)\approx 1$. As such, the integral in Eq. (43) is dominated by the characteristics of $C(a,\tau)$ around $a=0$ and $\tau=0$. Expanding $C(a,\tau)$ in a Taylor series:

$$C(a,\tau) = C(0,0) + a\frac{\partial C}{\partial a}\Big|_{a,\tau=0} + \tau\frac{\partial C}{\partial \tau}\Big|_{a,\tau=0} + \frac{1}{2}a^2\frac{\partial^2 C}{\partial a^2}\Big|_{a,\tau=0} + \frac{1}{2}\tau^2\frac{\partial^2 C}{\partial \tau^2}\Big|_{a,\tau=0} + a\tau\frac{\partial^2 C}{\partial a\partial \tau}\Big|_{a,\tau=0} + \ldots \qquad [47]$$

The constraint that surface derivatives (e.g., $\partial\varsigma/\partial y_s$) remain finite implies that all first derivatives are zero; e.g., $\partial C/\partial\tau|_{a,\tau=0} = 0$ [36]. Thus, Eq. (51) can be written as:

$$C(a,\tau) = 1 + \frac{1}{2}\left(\frac{a}{\Lambda_f}\right)^2 + \frac{1}{2}\left(\frac{\tau}{\tau_f}\right)^2 + \ldots \qquad [48]$$

where the integral length and time scales, Λ_f and τ_f are defined by:

$$\left(\frac{1}{\Lambda_f}\right)^2 \equiv -\frac{\partial^2 C}{\partial a^2}\Big|_{a,\tau=0}, \qquad \left(\frac{1}{\tau_f}\right)^2 \equiv -\frac{\partial^2 C}{\partial \tau^2}\Big|_{a,\tau=0} \qquad [49]$$

Substituting Eq. (52) into Eq. (50) yields:

$(k_{\Delta,z}\sigma)^2 >> 1$: $$g(a,\tau) \approx e^{-(k_{\Delta,z}\sigma)^2(a/\Lambda)^2} e^{-(k_{\Delta,z}\sigma)^2(\tau/\tau_f)^2} \qquad [50]$$

Equation (54) is substituted into Eq. (43), which can be explicitly evaluated if $a_{max} \to \infty$, which in practice will hold true for finite a as long as $a_{max} >> \Lambda$. Noting the following relationships (determined from formulas in Section 13.31 in Watson [13]):

$$\int_{a=0}^{\infty} e^{-\Xi a^2} J_o\left(a\sqrt{k_{\Delta,x}^2 + k_{\Delta,y}^2}\right) a\,da = \frac{1}{2\Xi} e^{-(k_{\Delta,x}^2 + k_{\Delta,y}^2)/4\Xi} \qquad [51]$$

$$\int_{a=0}^{\infty} e^{-\Xi a^2} J_1(a\sqrt{k_{\Delta,x}^2 + k_{\Delta,y}^2}) a^2 da = \frac{(k_{\Delta,x}^2 + k_{\Delta,y}^2)}{4\Xi^2} e^{-(k_{\Delta,x}^2 + k_{\Delta,y}^2)/4\Xi} \qquad [52]$$

leads to the final result for the spectral density of the scattered wave:

Case where $(k_{\Delta,z}\sigma)^2 >> 1$: $$\frac{\left\langle |F(\omega)|^2 \right\rangle}{2\pi A_m T_i} = \frac{\Omega(\vec{n})}{(n_{\Delta,z})^2} (\frac{\Lambda}{\sigma})^2 e^{-\frac{(n_{\Delta,x}^2 + n_{\Delta,y}^2)}{2(n_{\Delta,z})^2}(\frac{\Lambda}{\sigma})^2} e^{-\frac{(\omega-\omega_o)^2 \tau_f^2}{2(k_{\Delta,z}\sigma)^2}} \qquad [53]$$

where the function $\Omega(\vec{n})$ is given by:

$$Z(\vec{n}_i \cdot \vec{n}_s) << 1: \qquad \Omega(\vec{n}) = (1 + 4Z|n_{i,z}|)(\frac{n_{\Delta,z}^2}{2} + n_{\Delta,y}^2 + n_{\Delta,x}^2) + 2Z n_{\Delta,x} n_{\Delta,z} n_{i,x} \qquad [54]$$

$$Z(\vec{n}_i \cdot \vec{n}_s) >> 1: \qquad \Omega(\vec{n}) = (1 + \frac{4}{Z|n_{i,z}|})(\frac{n_{\Delta,z}^2}{2} + n_{\Delta,y}^2 + n_{\Delta,x}^2) - \frac{2 n_{\Delta,x} n_{\Delta,z} n_{i,x}}{Z n_{i,z}^2} \qquad [55]$$

Equation (57) shows that the frequency dependence of the scattered field remains the same at all positions, and consists of an exponential decay about the incident wave frequency, ω_o. This result shows that flame surface movement causes the spectral characteristics of the scattered wave to be "smeared" about the incident wave frequency. This is analogous to the Doppler broadening observed in other applications. These characteristics are plotted in Figure 11, which plots the frequency dependence of the scattered field for the case $\omega_o \tau_f = 50$.

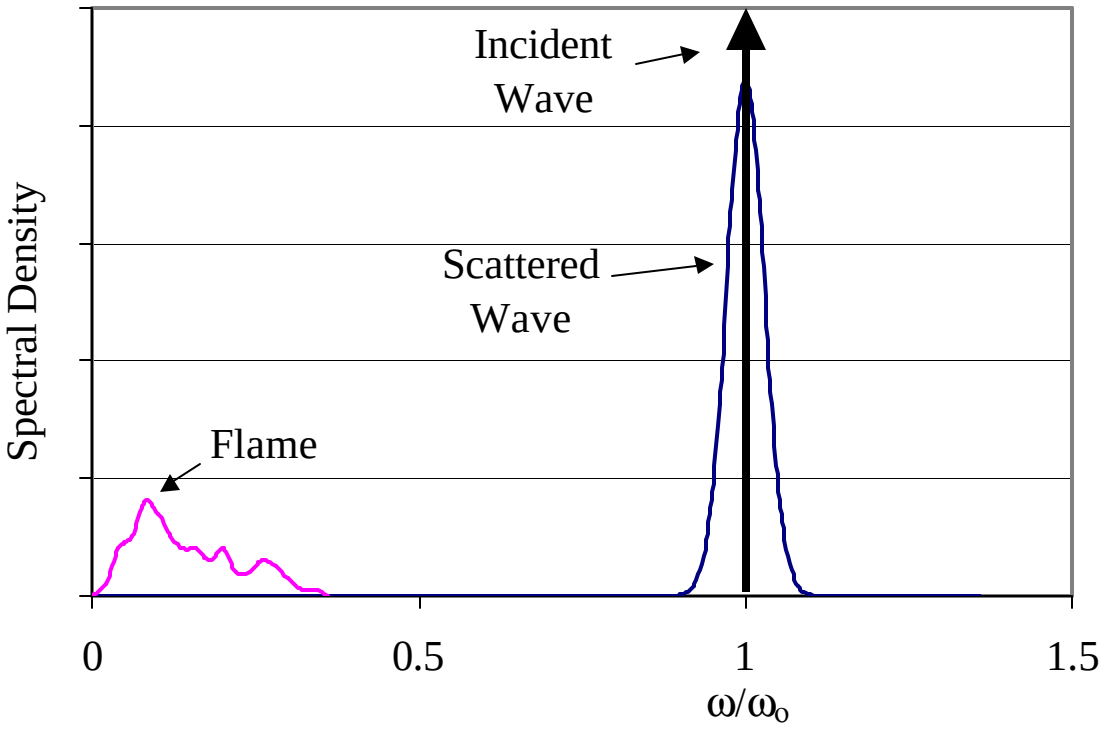

Figure 11. Example of spectral characteristics of incident wave, flame position and scattered field when $(k_{D,z}s)^2 >> 1$ (calculated with $w_o t_f$=50).

Note that the spectral characteristics of the scattered wave depend only upon an integral time scale of the flame surface and, thus, contain very little information about the temporal characteristics of the flame surface.

We next consider the characteristics of the diffuse field when $(k_{\Delta,z}\sigma)^2$ is small. In this case, the exponential in Eq. (50) can be expanded as:

$$g(a,\tau) = e^{-(k_{\Delta,z}\sigma)^2} \sum_{n=0}^{\infty} \frac{(k_{\Delta,z}\sigma)^{2n} C^n(a,\tau)}{n!} \qquad [56]$$

For the subsequent analysis, we will assume that C(a,τ)=C(a)C(τ) (note that such an assumption is *not* necessary in the $(k_{\Delta,z}\sigma)^2$ >>1 case) . Inserting Eq. (61) into Eq. (43) yields:

$$\frac{\left\langle |F(\omega)|^2 \right\rangle - \left\langle F(\omega) \right\rangle \left\langle F(\omega) \right\rangle^*}{2\pi A_m T_i} = e^{-(k_{\Delta,z}\sigma)^2} \sum_{n=1}^{\infty} \frac{(k_{\Delta,z}\sigma)^{2n}}{n!} \hat{\xi}_n(\omega) \Omega_n(\vec{k}_\Delta) \qquad [57]$$

where the contribution of the coherent field has been subtracted out and:

$$\hat{\xi}_n(\omega) = \int_\tau C^n(\tau) e^{i(\omega-\omega_o)\tau} d\tau \qquad [58]$$

$$\Omega_n(\vec{k}_\Delta) = \int_a \left[A^2 C^n(a) J_o\left(a\sqrt{k_{\Delta,x}^2 + k_{\Delta,y}^2}\right) + \frac{2A(Bk_{\Delta,x} + Ck_{\Delta,y})}{k_{\Delta,z}\sqrt{k_{\Delta,x}^2 + k_{\Delta,y}^2}} J_1\left(a\sqrt{k_{\Delta,x}^2 + k_{\Delta,y}^2}\right) \frac{dC^n(a)}{da} \right] ada \qquad [59]$$

Examining the frequency dependence of the diffuse field, it can be seen that the first order approximation (i.e., truncating the series in Eq. (62) after one term) to the spectrum of the diffuse field, $\hat{\xi}_1(\omega)$, is equal to the Fourier transform of the correlation function shifted by the incident wave frequency, ω_o. The correlation function and the power spectral density can be related with the Wiener-Khinchin theorem, showing that the *spectral characteristics of the incident frequency shifted scattered field are equal to that of the flame surface* when $(k_{\Delta,z}\sigma)^2 << 1$; i.e.,

$$\hat{\xi}_1(\omega) = \frac{\tilde{\xi}(\omega - \omega_o)}{4\pi^2} \qquad [60]$$

An example illustrating this result is shown in Figure 12. As opposed to the $(k_{\Delta,z}\sigma)^2 >> 1$ case, this result shows that the scattered field spectrum is directly related to the temporal spectral characteristics of the flame surface. This result suggests a potential diagnostic for elucidating the spectral characteristics of the flame surface movement.

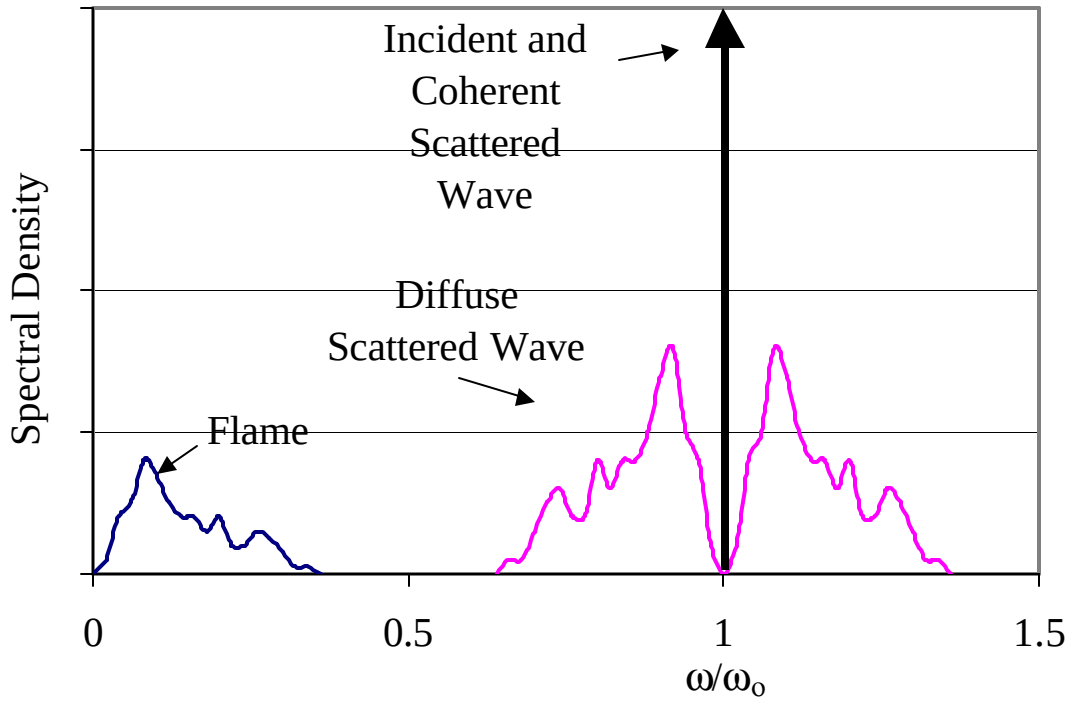

Figure 12. Example of spectral characteristics of incident wave, flame position and scattered field (series truncated at n=1) when $(k_{D,z}s)^2 << 1$.

With increasing $k_{\Delta,z}\sigma$, however, the spectrum of the scattered field becomes more and more distorted relative to the flame's. For example, using Eq. (62), the second order correction to the scattered field, $\hat{\varsigma}_2(\omega)$, can be shown to equal:

$$\hat{\varsigma}_2(\omega+\omega_o) = \int_{\omega_2} \tilde{\varsigma}(\omega+\omega')\tilde{\varsigma}(\omega')d\omega' \qquad [61]$$

Equation (66) shows that the spectral characteristics of the flame are smeared over the spectrum of the second order correction to the diffuse field. Similar observations apply to higher order corrections so that the temporal spectrum of the scattered field exhibits progressively less resemblance to that of the flame with increasing $k_{\Delta,z}\sigma$.

Consider next the spatial characteristics of the scattered field in Eq. (62). As opposed to the $(k_{\Delta,z}\sigma)^2 >> 1$ case where only the second derivative of the correlation function at the origin (i.e., a=0) is required, evaluation of $\Omega_n(\vec{k}_\Delta)$ requires explicitly specifying the spatial correlation function C(a). For

example, if it is assumed that the correlation function is exponential, i.e., $C(a) = e^{-(a/\tilde{\Lambda})^2}$, then the function $\Omega_n(\vec{k}_\Delta)$ equals:

$$\text{if } C(a) = e^{-(a/\tilde{\Lambda})^2}: \quad \Omega_n(\vec{k}_\Delta) = \frac{(k\tilde{\Lambda})^2 \Omega(\vec{n}_\Delta) e^{-(k_{\Delta,x}^2 + k_{\Delta,y}^2)\tilde{\Lambda}^2/4n}}{n} \qquad [62]$$

Equations (62) and (67) show that the spatial characteristics of the scattered field depend upon the same parameters as in the $(k_{\Delta,z}\sigma)^2 >> 1$ case, as well as the frequency through the dimensionless parameter $k\tilde{\Lambda}$. The amplitude of the diffusely scattered waves depends upon both $k\tilde{\Lambda}$ and $k\sigma$, while Eq. (62) shows that, to first order in $k\sigma$, the range of angles over which significant scattering occurs depends primarily upon $k\tilde{\Lambda}$.

Equation (64) can also be evaluated for other specified correlation functions. For example, Eq. (67) can be readily generalized to a surface with *k* length scales whose correlation function is given as

$$C(a) = \sum_{i=1}^{k} J_n e^{-(a/\tilde{\Lambda}_i)^2} \qquad \text{where} \quad \sum_{i=1}^{k} J_n = 1 \qquad [63]$$

5. Industrial Interactions

Contacts were maintained with several major gas turbine manufacturers that kept us informed of problems that were of concern to industry and enabled us to inform industry about our progress in the understanding and control of LNGT instabilities. In related work that leveraged off the work performed under this program, active control studies were performed with Siemens-Westinghouse in Germany on full scale hardware.

6. Goals for Next Reporting Period

The goals of the program for the next reporting periods are:

1. Continue studies of the nonlinear combustion response to imposed oscillations over a range of operating conditions.

2. Continue the development and optimization of a real time, adaptive active control system to rapidly attenuate combustion driven oscillations.

7. References

[1] Cohen, Jeffrey, Anderson, Torger, *AIAA paper # 96-0819*, 1996.

[2] Straub, D.L., Richards, G.A., *ASME paper # 98-GT-492*, 1998.

[3] Paschereit, C.O., Gutmark, E., Weisenstein, W., *27th Int'l Symp. on Combustion (The Combustion Institute)*, Pittsburgh, PA, 1998.

[4] Hsiao, George C., Pandalai, Raghavan P., Hura, Harjit S., Mongia, Hukam C., *AIAA paper # 98-3380*.

[5] Broda, J.C., Seo, S., Santoro, R.J., Shirhattikar, G., Yang, V., *Twenty Seventh Symposium (International) on Combustion*, The Combustion Institute, Pittsburgh, PA, 1998.

[6] Crocco, L., Cheng, S., *Theory of Combustion Instability in Liquid Propellant Rocket Motors*, Butterworths Scientific Publications, London, 1956.

[7] Munjal, M., *Acoustics of ducts and mufflers*, John Wiley: New York, 1987.

[8] Fleifil, M., Annaswamy, A.M., Ghoniem, Z.A., Ghoniem, A.F., *Comb. and Flame*, Vol. 106, 1996, pp. 487-510.

[9] Lee, D.H., Lieuwen, T., *AIAA Paper #2001-3851*, 2001.

[10] Ducruix, S., Durox, D., Candel, S., *28thInternational Symposium on Combustion*, The Combustion Institute, Pittsburgh, PA, 2000.

[11] Kruger, Uwe *et al*., *ASME Paper #99-GT-111*, 1999.

[12] Walz, G. *et al*, *ASME Paper #99-GT-113*.

[13] Schuermans, B. *et al*, *ASME Paper #99-GT-132*.

[14] Lieuwen T. and Lee, D.H., *AIAA Paper # 2000-3464*.

[15] Culick, F.E.C., Burnley, V., Swenson, G., *J. Prop. Power*, Vol. 11(4), 1995.

[16] Zinn, B.T., Powell, E.A., *Thirteenth Symposium (International) on Combustion*, The Combustion Institutute, 1970, pp. 491-503.

[17] Culick, F.E.C., *Comb. Sci. Tech*., Vol. 3(1), 1971.

[18] Lieuwen, T., , To appear in *J. Prop. Power*, 2001.

[19] Peracchio, A.A., Proscia, W.M., *ASME paper # 98-GT-269*, 1998.

[20] Dowling, A.P., *J. Fluid Mech*. Vol. 346, pp. 271-290, 1997.

[21] Torres, H., Lieuwen, T., Johnson, C., Daniel, B.R., Zinn, B.T., *AIAA paper # 99-0712*, 1999.

[22] Neumeier, Y., Nabi, A., Zinn, B.T., *AIAA paper # 96-2757*, 1996

[23] Bendat, J., Piersol, A., *Random Data: Analysis and Measurement Procedures*, Joh Wiley and Sons: New York, 1986.

[24] Chu, B.T., On the Generation of Pressure Waves at a Plane Flame Front, *Fourth Symposium (International) on Combustion*, The Combustion Institute, 1953, pp. 603-612.

[25] Lieuwen, T., "Theoretical Investigation of Unsteady Flow Interactions With a Planar Flame", to appear in *J. Fluid Mech., AIAA Paper # 99-0324*.

[26] Marble, F.E., Candel, S. M., An Analytical Study of the Non-Steady Behavior of Large Combustors, *Seventeenth International Symposium on Combustion*, The Combustion Institute, Pittsburgh, 1978, pp. 761-769.

[27] Yang, V., Culick F.E.C., Linear Theory of Pressure Oscillations in Liquid-Fueled Ramjet Engines, *AIAA Paper # 83-0574*.

[28] Dowling, A., Nonlinear Self Excited Oscillations of a Ducted Flame, *J. Fluid Mech.*, Vol. 346, 1997, pp. 271-290.

[29] Fleifel, M., Annaswamy, A.M., Ghoniem, Z.A., Ghoniem, A.F., Response of a Laminar Premixed Flame to Flow Oscillations: A Kinematic Model and Thermoacoustic Instability Results, *Comb. and Flame*, Vol. 106, 1996, pp. 487-510.

[30] Peirce, A., *Acoustics: An Introduction to its Physical Principles and Applications*, Acoustical Society of America: New York, 1991.

[31] Markstein, G.H., Theory of Flame Propagation, in *Nonsteady Flame Propagation*, Markstein, G.H., Ed., Pergamon Press, New York, 1964.

[32] Ffowcs-Williams, J.E., Hawkings, D.L., Sound Generation by Turbulence and Surfaces in Arbitrary Motion, *Phil. Trans. Roy. Soc. London A*, Vol. 264, 1969, pp. 321-342.

[33] Lieuwen, T., "Analysis of Flame-Acoustic Wave Interactions using Boundary Element Methods", *Proceedings of the Technical Meeting of the Central States Section of The Combustion Institute*, 2000.

[34] Morse, P., Ingard, K., *Theoretical Acoustics*, Princeton University Press: Princeton, 1986.

[35] Lieuwen, T., "Coherent Acoustic Wave Scattering by Turbulent, Premixed Flames", *Proceedings of the 2nd Joint Meeting of the U.S. Sections of the Combustion Institute*, Paper # 171, 2001.

[36] Papoulis, A., *Probability, Random Variables, and Stochastic Processes*, McGraw Hill: New York, 1991.

[37] Gradshteyn, I.S., Ryzhik, *Table of Integrals, Series, and Products*, Fifth Edition (Jeffrey, A., Ed.), Academic Press: New York, 1994.

THERMAL BARRIER AND METALLIC COATINGS WITH IMPROVED DURABILITY

AGTSR Subcontract Number 01-01-SR091
First Semi-Annual Report
February 1, 2001 to August 1, 2001

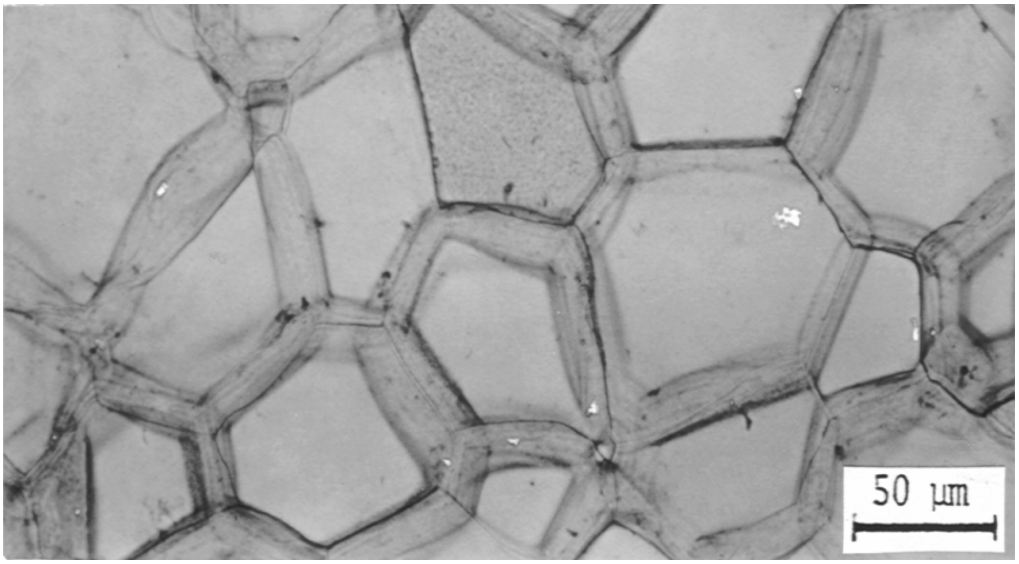

Ridges on the surface of Pt-Al bond coat

Maurice Gell and Eric Jordan, Principal Investigators
School of Engineering
University of Connecticut, Storrs, CT

In collaboration with

Gerry Meier and Fred Pettit
Materials Science & Engineering Department
University of Pittsburgh, Pittsburgh, PA
And
Yongho Sohn
Adv. Materials Processing & Analysis Center
University of Central Florida, Orlando, FL.

1.0 EXECUTIVE SUMMARY

Advanced industrial gas turbine engines require the use of reliable and highly durable thermal barrier coatings (TBCs) and metallic, stand-alone coatings to meet performance and durability goals. Current TBCs and stand-alone metallic coatings lack the necessary durability and reliability. Much progress has been made in understanding the mechanisms of damage initiation and progression in current TBCs and metallic coatings that ultimately leads to spallation. This understanding indicates that significantly improvements in TBC and metallic coating life and reliability can be achieved by focusing on coating composition and processing. The University of Connecticut (UConn), the University of Pittsburgh (UPitt), and the University of Central Florida (UCF) are partnering in this research program that has the potential of improving electron beam physical vapor deposition (EB-PVD) TBC and metallic coating life by more than a factor of 3X.

Research conducted by the UCONN and Pitt, including previous AGTSR programs, indicates that spallation in electron beam physical vapor deposited TBCs depends strongly on (1) the perfection of the initial, thermally grown oxide (TGO), (2) the magnitude of the localized out-of-plane tensile stress at the TGO to bond coat interface, and (3) the adherence of the TGO during thermal cycles. In this proposed program, the salient bond coat composition and processing features will be systematically investigated in order to demonstrate the optimum combination of features that will provide at least a 3X durability improvement compared to current TBCs and stand-alone metallic coatings. The following features will be assessed individually and in combination for platinum aluminide (Pt-Al) and MCrAlY coatings used as both bond coats for TBCs and as stand-alone coatings:

I. **TGO Perfection: (a) presence or absence of metastable/transient oxides versus the desirable stable alpha alumina oxide.**

II. **TGO Stress: (a) surface roughness, (b) presence or absence of bond coat surface defects.**

III. **TGO Adherence: (a) presence or absence of active elements (silicon and hafnium) contributing to improved TGO adherence.**

Most of the first reporting period has been devoted to (1) obtaining coated specimens, (2) evaluating commercially viable surface finishing treatments and (3) conducting initial oxidation trials.

All metallic and TBC coatings are being provided by Howmet's Technology Center and Thermatech Division. Initial Pt-Al bond coated CMSX-4 specimens have been provided and NiCoCrAlY bond coats with and without silicon and hafnium are on order.

The as-coated Pt-Al bond coats contain grain boundary ridges that have been shown to be the source for early damage initiation and progression. Spallation life was shown to be a strong function of the height of the ridges. Ridge height and geometry is being quantitatively assessed for all specimens using laser surface profilometry. Commercial media finishing trials were conducted, with times ranging from 20 to 120 minutes on the as bond coated specimens, to determine the rate of ridge height reduction. As-coated ridge heights of 2.6 microns were reduced to 2.0 and 1.5 microns after 40 and 120 minutes respectively of media finishing.

Initial oxidation trials have been conducted at the University of Pittsburgh on the as-coated Pt-Al bond coats. It is found that, in this as-processed condition, porosity forms during initial high temperature exposure in various environments and leads to early TGO spallation. Heat treatments and processing effects are being investigated to understand and overcome this early oxidation effect.

2.0 INTRODUCTION

Both TBCs and stand-alone metallic coatings, that protect turbine blades and vanes from the hot gas stream, are required to meet the stringent performance, durability, reliability and environmental goals for ATS and Next Generation Gas Turbine industrial engines. This program seeks to develop metallic coatings, to be employed as a stand-alone coating or a bond coat for TBCs, with improved durability and reliability with at least 3X improvement in cyclic oxidation and spallation life. Specifically, the effects of heat treatment, surface finish and alloying for the metallic coatings will be addressed to demonstrate that modified processing techniques and compositions can significantly improve the resistance to thermal cycling damage of metallic coatings. Understanding from this program can be used to develop industrial processing routes and design optimum coating compositions to improve the overall performance of both stand-alone metallic coatings, and bond coats for EB-PVD TBCs.

2.1 Background

TBCs are complex engineering material systems consisting of 4 layers (Figure 1): substrate, bond coat, TGO and ceramic layer.[1-4] The composition and processing of each layer affect the durability of the TBC. A comprehensive review of the state-of-the-art has been carried out in preparation for this program. It has been concluded that significant improvement in TBC reliability and durability can be achieved by focusing on the bond coat and the TGO layers. Significant bond coat and TGO factors that determine TBC reliability and durability include:

- **Bond coat composition[5-7]**
- **Bond coat deposition method[3,4]**
- **Post-bond coat processing[8,9]**
- **Bond coat creep strength[3,10]**
- **Bond coat defects[11,12]**
- **Surface roughness[13,14]**
- **TGO-bond coat residual stress[11,12,15-17]**
- **Composition / crystal structure of TGO[8,17-20]**
- **TGO to bond coat adherence (active elements effects)[21-34]**

Of these bond coat and TGO factors, it is concluded that significant improvements in TGO durability and reliability can be achieved by focusing on (a) TGO perfection, (b) TGO stress and (c) TGO adherence in the program.

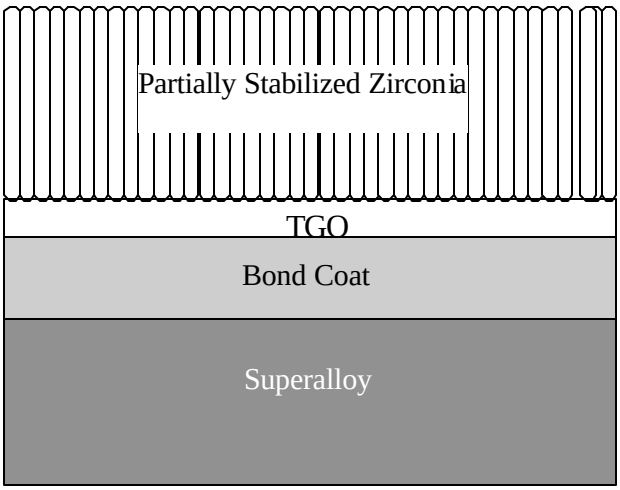

Figure 1. A schematic illustration of the EB-PVD TBC system.

TGO Perfection

Phase constituents of TGO, especially during early stages of oxidation, have been identified as critical factors influencing the adhesion at TGO/coating interface.[8,17-20] Specifically, the formation of the transient θ-Al_2O_3 and its conversion to the stable α-Al_2O_3 in the protective oxide scale has been reported to have a profound effect on the structural integrity of TGO/coating interface during

thermal cycles. An image[19] of a-Al_2O_3 islands nucleated within a q-Al_2O_3 TGO formed by oxidation of NiAl for 1 hour at 1000°C is presented in Figure 2. It has been proposed by Clarke and coworkers[18,19] that the transformation from q-to-a Al_2O_3 is responsible for additional residual stress from the volumetric constraint in the TGO scale and nucleation of sub-critical cracks, eventually leading to the spallation of a-Al_2O_3 TGO scale. Thus, the formation of a "perfect" oxide that consist only of stable a-Al_2O_3 prior to deposition of ceramic layer and thermal cyclic oxidation can lead to improved oxidation resistance, durability and reliability of both stand-alone metallic coatings and TBC bond coats.

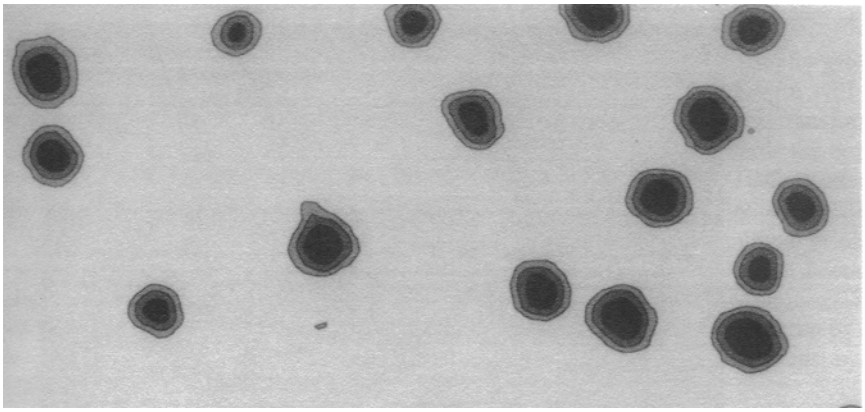

Figure 2. Photoluminescence image of a-Al_2O_3 islands nucleated within a q-Al_2O_3 TGO formed by oxidation of NiAl for 1 hour at 1000°C.[19]

Extensive microstructural examination of TBCs by Gell and co-workers[11,12] has identified bond coat surface features/defects as damage initiation sites. Figure 3 shows these surface features/defects to be: "ridges" associated with platinum aluminide (Pt-Al) coatings and "entrapped" oxides associated with shot-peening of MCrAlY coatings. Also presented in Figure 3 are the oxide cavities and accelerated growth of oxide scale resulting from the cyclic plasticity and oxidation of these features/defects during thermal cycling. It has been demonstrated that the removal of the ridges by fine polishing can improve the TBC lifetime by 3X.[35]

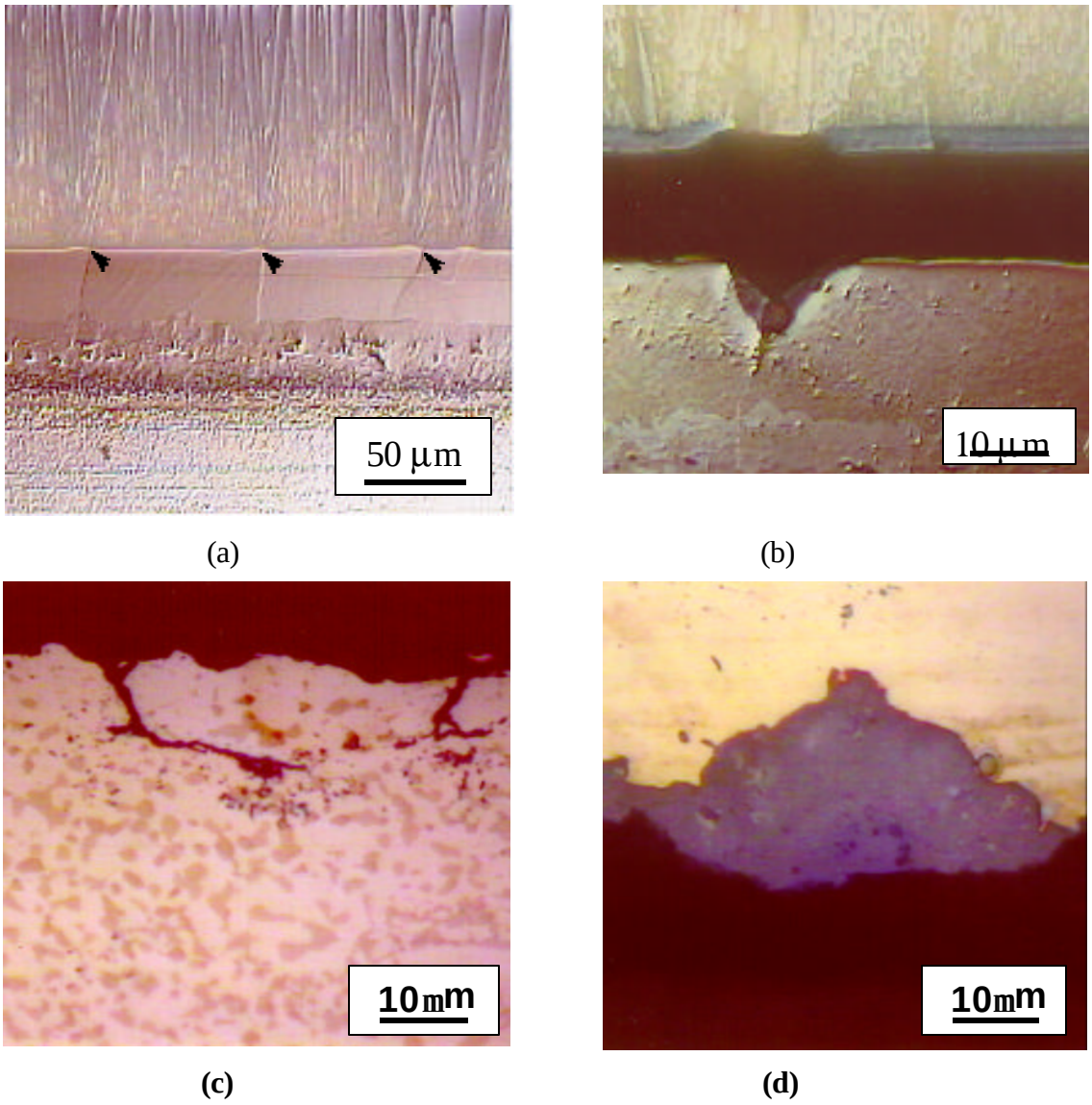

(a) (b)

(c) **(d)**

Figure 3. Surface features/defects: (a) "ridges" and (b) oxide-filled cavities in platinum aluminide (Pt-Al) EB-PVD TBCs; (c) "entrapped" oxides and (d) oxide-filled cavities associated with MCrAlY EB-PVD TBCs. These features/defects are present due to the processing of the coatings before thermal cycling and evolve into oxide-filled cavities during thermal cycling.[11,12]

In addition, surface roughness has a significant effect on the level of in-plane and out-of-plane tensile stress in the TGO[13,14] as illustrated in Figure 4. In-plane tensile stresses crack the TGO, allowing molecular oxygen to reach the bond coat surface, and oxidation is accelerated. Out-of-plane tensile stress eventually leads to TGO and TBC spallation. Thus, a reliable industrial processing technique that ensures optimum surface roughness and consistent removal of the undesirable surface features/defects would provide improved durability and reliability for both stand-alone and TBC bond coats.

Under the current UCONN AGTSR contract, AGTSR 99-01-SR073, residual stress in the TGO is being measured using a laser fluorescence technique as a function of thermal cycles for various commercial TBC systems. This technique, pioneered by Clarke,[11,12,15-19,36] measures the residual stress in the TGO by examining the shifts in wave-number of Cr^{3+} photoluminescence in a-Al_2O_3 TGO scale. The shift in photoluminescence can be translated into a biaxial residual stress in TGO through piezo-spectroscopic coefficients. This technique has been applied successfully for both laboratory scale TBC specimens, and thermal barrier coated engine components.[37]

During this study, researchers at UCONN and UC-SB (subcontractor) have found that the laser fluorescence can readily provide information regarding (1) the formation and transformation of transient phases in TGO, specifically regarding the q-to-a Al_2O_3 transformation[17-19] (2) changes in the TGO stress due to surface roughness/defects and (3) presence of microscopic spallation of TGO from metallic coatings. Figure 5 shows a typical spectrum collected from a TGO that contain both q-Al_2O_3 and a-Al_2O_3. Preliminary results also reveal that the surface preparation of bond coat can significantly influence the residual stress of TGO. In addition, the laser fluorescence technique can conveniently detect the presence of microcracks that are associated with spallation (i.e., relief of residual stress) of TGO scale as shown in Figure 6.

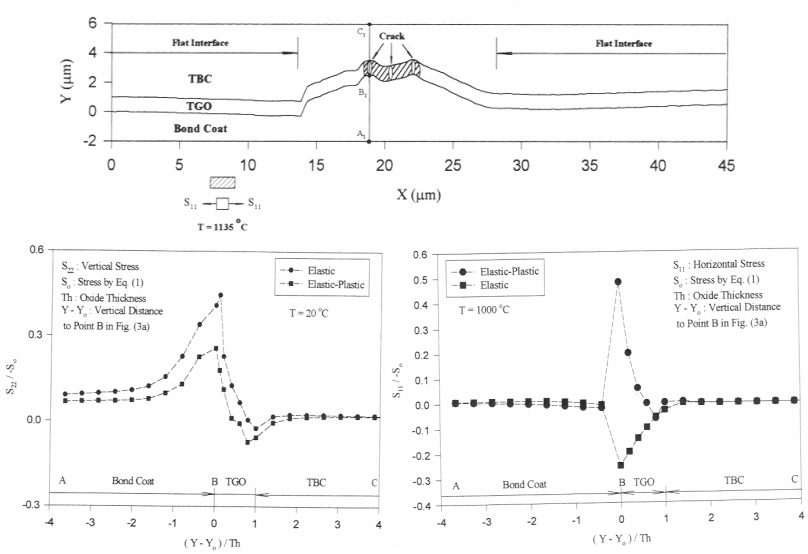

Figure 4. Tensile stress calculated from finite element analysis for out-of-plane (vertical) and in-plane (horizontal) stress in the TGO along the line A-B-C near the ridge of the Pt-Al bond coat surface.[14]

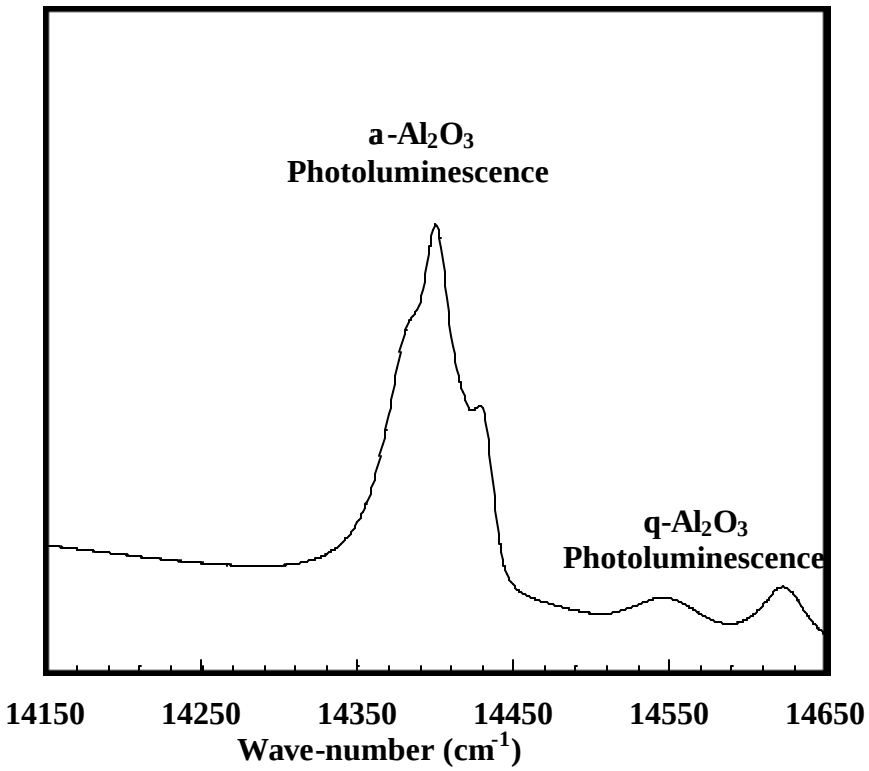

Figure 5. Laser fluorescence spectrum collected from a TGO scale that contains both q-Al_2O_3 and a -Al_2O_3.

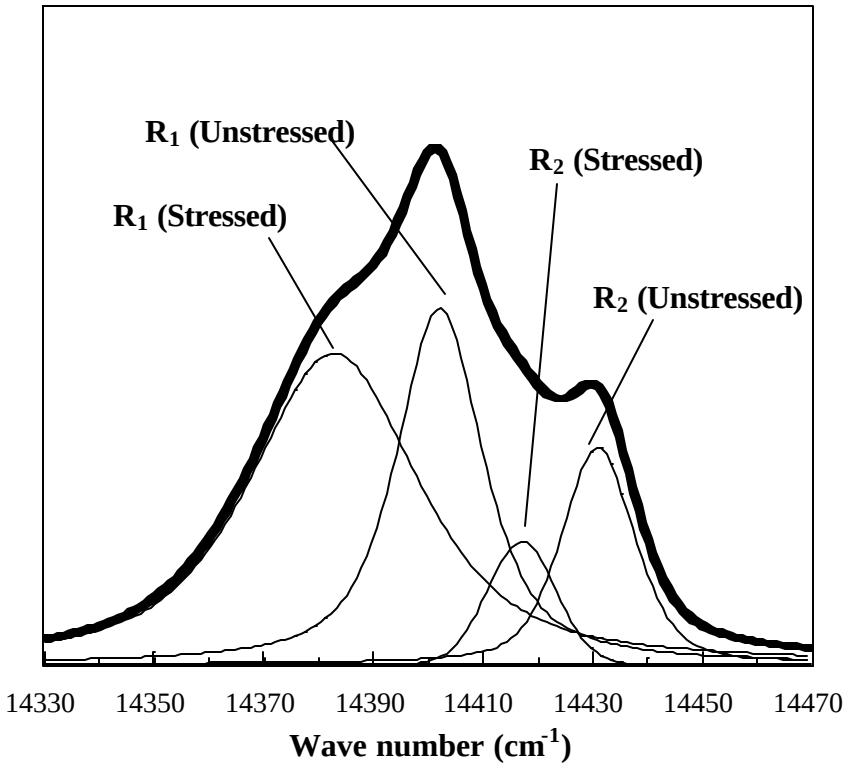

Figure 6. Bi-modal laser fluorescence spectrum containing stressed and unstressed regions.

TGO Adherence

Considerable literature[5,21-33] describes the improved oxidation resistance associated with alloying additions for MCrAlY, nickel aluminide (NiAl) coatings and superalloys. Figure 7 shows the improvement in oxidation and spallation resistance of MCrAlY coated specimens and turbine blades.[21] However, controversy exists concerning the mechanisms associated with the improvement, e.g, pegging, neutralization of sulfur segregation, reduced oxidation rate, microstructural enhancement of TGO, inhibition of interdiffusion. Pint and coworkers[5,24] at Oak Ridge National Laboratory (ORNL) have shown that the addition of Hf improved the oxidation resistance of Pt-Al coatings. Preliminary results indicate that the addition of both Si and Hf can significantly improve oxidation resistance of the Pt-Al coatings.[34] This work will study for the first time the synergistic benefit of Si and Hf to Pt-Al coatings for both stand-alone and TBC coatings.

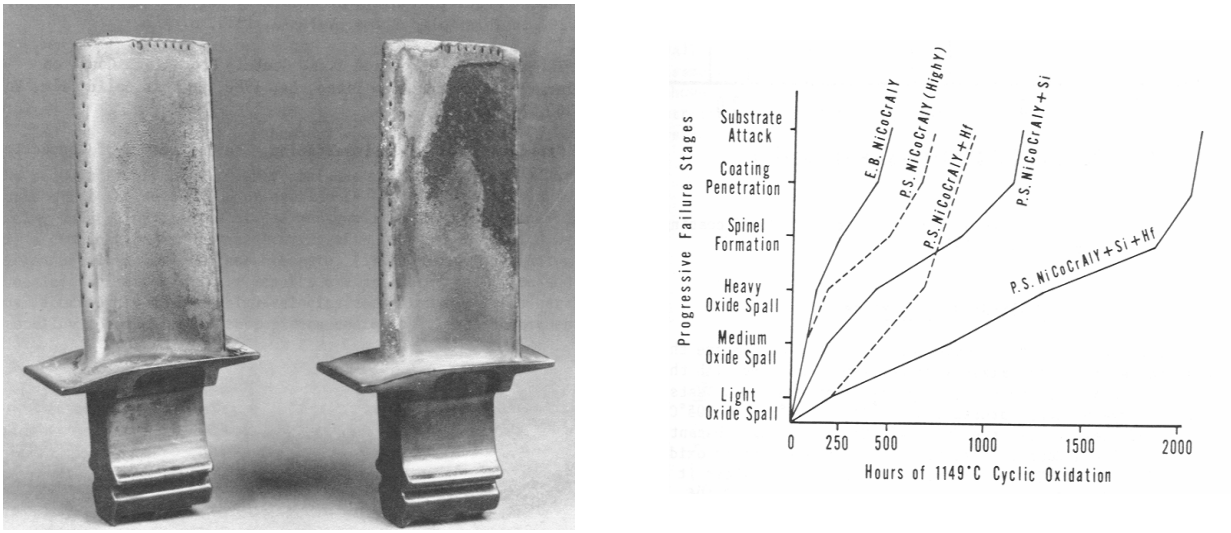

(a) **(b)**

Figure 7. (a) Single crystal turbine blades showing superior coating durability of the Si,Hf added MCrAlY coating (left) vs. the failed MCrAlY coating (right) after 2500 endurance engine cycles. (b) This superiority can be attributed to the synergetic benefits of Si and Hf shown by the progressive failure stages described on the y-axis.[21]

REFERENCES

1. **S.M. Meier, D.M. Nissley and K.D. Sheffler, NASA CR-189111, 1991.**
2. **D.J. Wortman, B.A. Nagaraj and E.C. Duderstadt, Mater. Sci. Eng. A., 1989, vol. A121, pp. 433.**
3. **R.A. Miller, *Surf. Coat. Technol*., 1987, vol. 30, pp. 1.**
4. **R.L. Jones, in Metallurgical and Ceramic Protective Coatings, ed. K.H. Stern, Chapman and Hall, 1996, pp. 194.**

5. B.A. Pint, I.G. Wright, W.Y. Lee, Y. Zhang, K. Pruessner and K.B. Alexander, *Mater. Sci. Eng. A*., 1998 vol. 245A, pp. 201.
6. Y.H. Sohn, E.Y. Lee, R.D. Sisson, Jr., Proc. 1992 Coatings for Advanced Heat Engine Workshop, 1992, pp. II-49.
7. W.J. Brindley and R.A. Miller, Surf. Coat. Technol., 1990, vol. 43/44, pp. 446.
8. W. Lih, E. Chang, C.H. Chao and M.L. Tsai, Oxid. Metals, 1992, vol. 38, pp.99.
9. W. Lih, E. Chang, B.C. Wu and C.H. Chao, Oxid. Metals, 1991, vol. 36, pp. 221.
10. D. Zhu and R.A. Miller, NASA CR-113169, 1997.
11. M. Gell, K. Vaidyanathan, B. Barber, J. Cheng and E. Jordan, *Metall. Mater. Trans. A*, 1999, vol. 30A, pp. 427.
12. M. Gell, E. Jordan, K. Vaidyanathan, K. McCarron, B. Barber, Y.H. Sohn and V.K. Tolpygo, *Surf. Coat. Technol.*, 1999, vol. 120-21, pp. 53.
13. A.G. Evans, M.Y. He and J.W. Hutchinson, Acta Metall., 1997, vol. 45, pp. 3543.
14. J. Cheng, E.H. Jordan, B. Barber and M. Gell, Acta Mater., 1998, vol. 46, pp. 5839.
15. J.R. Christensen, D.M. Lipkin, D.R. Clarke and K. Murphy, *Appl. Phys. Lett.*, 1996, vol. 69, pp. 3745.
16. D.M. Lipkin and D.R. Clarke, *Oxid. Metals*, 1996, vol. 45, pp.267.
17. D.R. Clarke, J.R. Christensen and V. Tolpygo, *Surf. Coat. Technol*., 1997, vol. 94-95, pp. 89.
18. C. Mennicke, D.R. Mumm and D.R. Clarke, *Zeits. Fur Metall*., 1999, vol. 90, pp. 1079.
19. D.R. Clarke, V. Sergo and M.Y. He, Elevated Temperature Coatings: Science and Technology III, ed. J. M. Hampikian and N. B. Dahotre, TMS, Warrendale, PA, 1999, pp. 67.
20. J.C. Schaeffer, NASA Conference Publication, No. 207429, 1998, pp. 99.
21. D.K. Gupta and D.S. Duvall, Superalloy 1982, pp. 711.
22. K.G. Schmitt-Thomas and M. Hertter, *Surf. Coat. Technol*., 1999, vol. 120, pp. 84.
23. J.H.W. de Wit and P.A. van Manen, *Mater. Sci. Forum*, 1994, vol. 154, pp. 109.
24. B.A. Pint, *Oxid. Metals*, 1997, vol. 48, pp. 303.
25. E.J. Felten and F.S. Pettit, *Oxid. Metals*, 1976, vol. 10, pp. 189.
26. R. Streiff, O. Cerclier and D.H. Boone, *Surf. Coat. Technol*., 1987, vol. 32, pp. 111.
27. E. Lang, The Role of Active Elements in the Oxidation Behavior of High Temperature Metals and Alloys, 1988.
28. J.A. Haynes, Y. Zhang, W.Y. Lee, B.A. Pint, I.G. Wright and K.M. Cooley, Elevated Temperature Coatings: Science and Technology III, ed. J. M. Hampikian and N. B. Dahotre, TMS, Warrendale, PA, 1999, pp. 185.
29. T.A. Taylor, D.F. Bettridge, R. C. Tucker, Jr., U.S. Patent 5,455,119, 1995.

30. **B.A. Nagaraj, W.B. Connor, R.W. Jendrix, D.J. Wortman, L.W. Plemmons, U.S. Patent 5,427,866, 1995.**
31. **B.G. McMordie and T.A. Kircher, U.S. Patent 5,65,0,235, 1997.**
32. **W.C. Basta, D.C. Punola and B.M. Warnes, U.S. Patent 5,658,614, 1997.**
33. **C.S. Giggins, Jr. and B.H. Kear, U.S. Patent 4,086,391, 1978.**
34. **K. Murphy, Private Communications, 2000.**
35. **M. Gell, K. Vaidyanathan and E. Jordan, *Surf. Coat. Technol*., in Press.**
36. **Q. Ma and D.R. Clarke, *J. Am. Ceram. Soc*., 1994, vol. 77, pp. 298.**
37. **Y.H. Sohn, K. Schlichting, K. Vaidyanathan, E. Jordan and M. Gell, *Metall. Mater. Trans*., in Press.**

2.2 Objectives

The overall objective of this program is to produce oxidation resistant metallic coatings, with improved durability and reliability, to be employed as both the stand-alone coatings and bond coats for TBCs. Specific objectives include:

1. **Generate a detailed processing sequence to optimize the initial formation of thermally grown oxide (TGO) based on environmental control (e.g., temperature and partial oxygen pressure) of pre-oxidation for surface finished Pt-Al, MCrAlY, and MCRAlY with Si + Hf coatings to be used as both stand-alone coatings and TBC bond coats.**

2. **Demonstrate by testing specimens with various surface finishes, that the presence or absence of surface defects on coatings significantly influence the durability and reliability of coatings and demonstrate a production process to remove defects and provide the optimum surface finish for improved durability and reliability of coatings.**

3. **Demonstrate and define the mechanism(s) for improved oxidation resistance resulting adding Si and Hf to Pt-Al coatings.**

4. **Define cost-effective processing techniques for producing a perfect, initial TGO and an optimum surface finish free of defects for Pt-Al, Pt-Al (Si,Hf) and MCrAlY coatings. The process defined will be applicable to complex shaped engine components such as turbine blades.**

5. **Demonstrate that these TGO optimization techniques provide a 3X improvement in oxidation resistance from stand-alone metallic coatings and a 3X improvement in spallation resistance for 3 TBCs in the program.**

6. **Transfer the attained understanding to industrial partners for the rapid implementation of both the improved stand-alone coatings and TBC bond coats.**

3.0 Program Organization, Plan and Schedule

Figure 8 shows the program organization

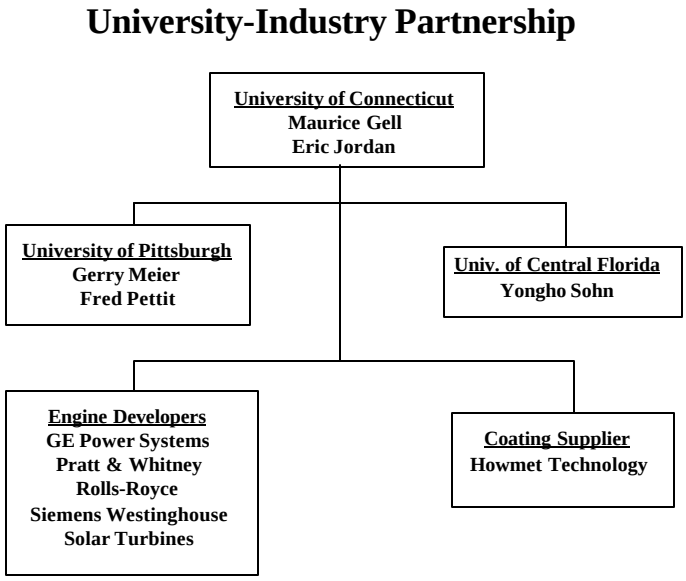

Figure 8 Program Organization

Figure 9 shows a bar-chart schedule with the main tasks.

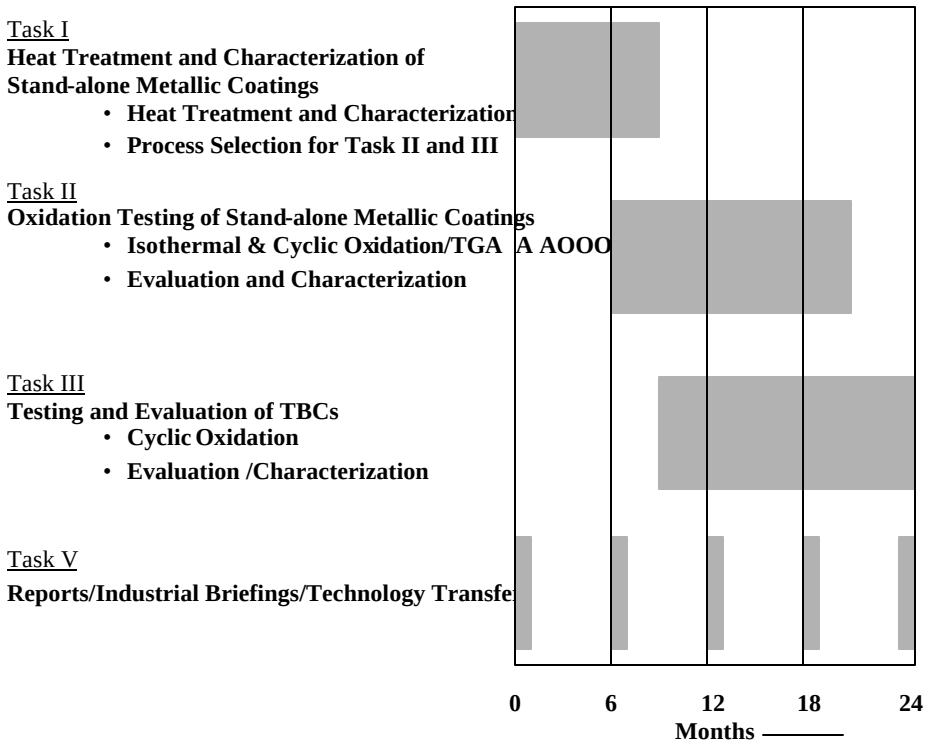

Figure 9: Program Schedule

Figure 10 shows the work flow in the program.

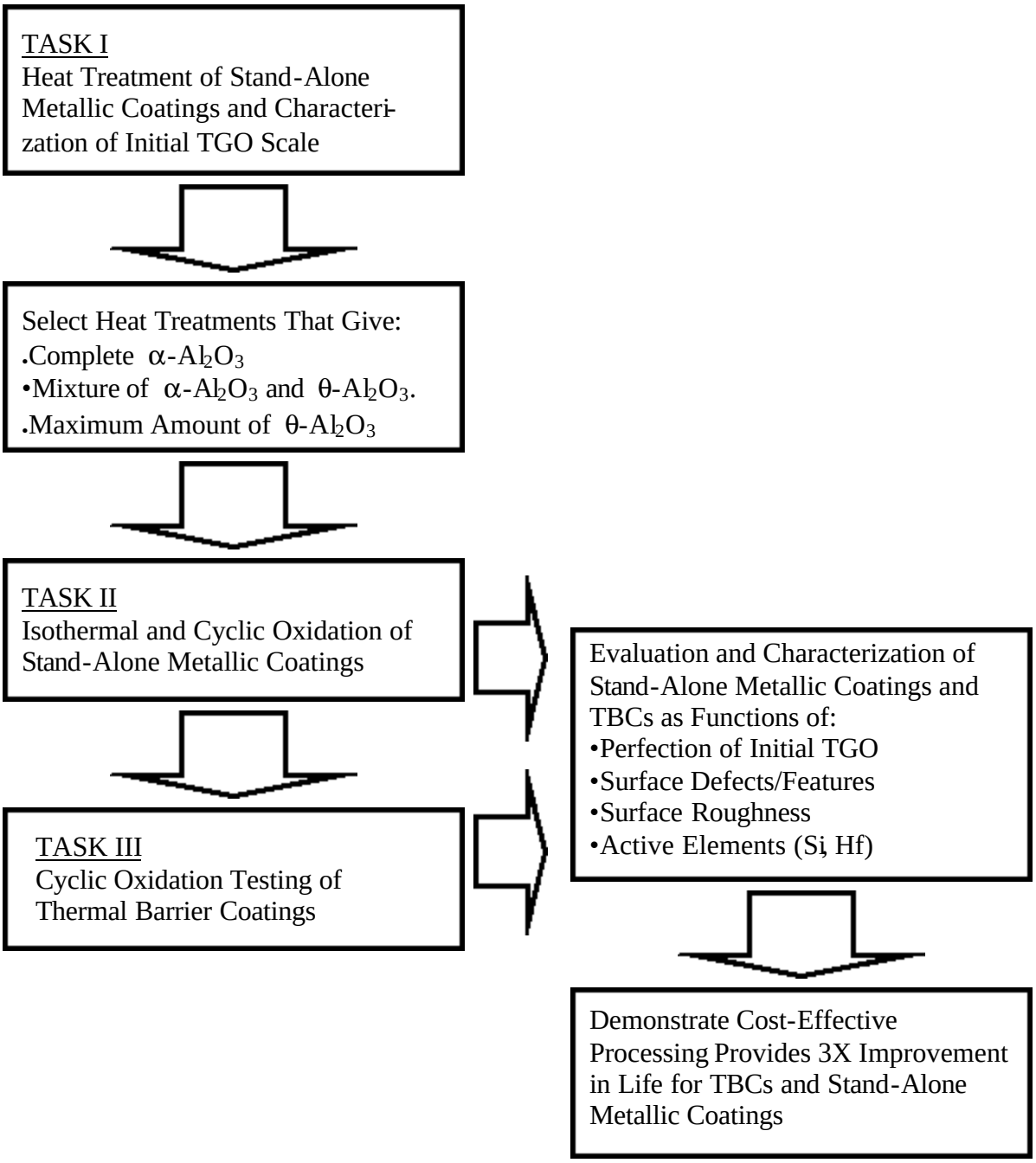

Figure 10: Program Overview

4.0 Experimental Program

Task I: Heat Treatment and Characterization of Stand-alone Metallic Coatings

Objective: To heat treat and subsequently characterize the TGO scale formed on stand-alone metallic coatings as a function of temperature and oxygen partial pressure.

Technical Approach: Specimen (1 inch diameter by 1/8 inch thickness) coated with stand-alone metallic coatings, Pt-Al, Si,Hf modified Pt-Al and MCrAlY on CMSX-4 superalloy substrate will be supplied by Howmet International and other industrial partners in the program and will be fabricated with current commercial processing practices that include various surface finishs: as-coated, grit blasted and media finished. The surface morphology and roughness of the specimens will be analyzed using optical and electron microscopy and ZYGOÔ surface profilometry, capable of measuring roughness in the nano-scale. Emphasis will be given to the relationship between processing technique, surface roughness and the presence of surface defects/features. The specimens will be cut into small pieces and heat treated as a function of temperature (T = 900°, 1000°, 1100°C) and oxygen partial pressure (P_{O2} = 0.01, 0.2, 1.0 atm) for an hour as schematically illustrated in Figure 11. The TGO scale formed during the heat treatment will be characterized with respect to phase constituents, residual stress and morphology by x-ray diffraction, optical and electron microscopy, and by using the laser fluorescence technique. Details of specimen descriptions and heat treatment are presented in Table I.

Based on the characterization of the TGO scale formed on stand-alone metallic coatings that were heat treated, three conditions (3 out of 9 identified in Figure 11) will be selected. These three conditions will be selected so that the specimens will contain three different types of TGO scale: (a) complete a-Al_2O_3, (b) maximum amount of q-Al_2O_3 and (c) mixture of a- and q-Al_2O_3. These three conditions are selected to demonstrate the importance of homogeneous stable a-Al_2O_3 scale compared to other oxide conditions. The selected heat treatments and the corresponding TGO scale formation will be employed for the thermal cycling tests of stand-alone metallic coatings (Task II) and TBCs (Task III).

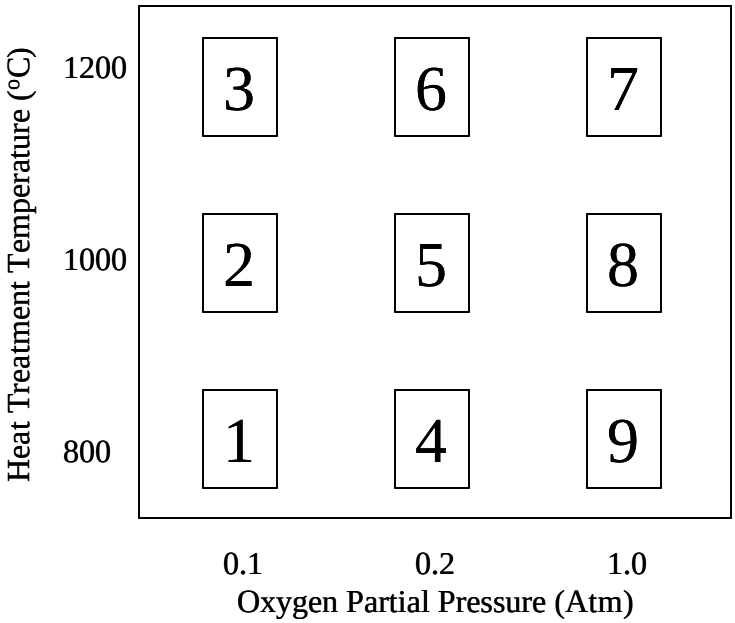

Figure 11. Heat treatment test matrix.

Table I. Specimen Descriptions and Evaluation for Task I and II.

Metallic Coating	Surface Finish	Surface Defect/Features	Heat Treatment	Total Number of Specimen Required
Pt-Al	As-coated	Ridges at full height	As identified in Figure 8	3 for Heat Treatment 3 for Oxidation Testing
	Grit-blasted	Reduced ridge height Rough surface	As identified in Figure 8	3 for Heat Treatment 3 for Oxidation Testing
	Media-finished	No ridges Smooth surface	As identified in Figure 8	3 for Heat Treatment 3 for Oxidation Testing
Pt-Al (Si,Hf)	As-coated	Ridges at full height	As identified in Figure 8	3 for Heat Treatment 3 for Oxidation Testing
	Grit-blasted	Reduced ridge height Rough surface	As identified in Figure 8	3 for Heat Treatment 3 for Oxidation Testing
	Media-finished	No ridges Smooth surface	As identified in Figure 8	3 for Heat Treatment 3 for Oxidation Testing
MCrAlY	Shot-peened	Rough surface	As identified in Figure 8	3 for Heat Treatment 3 for Oxidation Testing
	Media-finished	Smooth surface	As identified in Figure 8	3 for Heat Treatment 3 for Oxidation Testing

Total number of specimen required: 54 stand-alone metallic coatings

Task II: Oxidation Testing of Stand-alone Metallic Coatings

Objective: To test and evaluate selected stand-alone metallic coatings using isothermal and cyclic oxidation testing.

Technical Approach: After the selected heat treatments, the stand-alone coatings will be subjected to isothermal and cyclic oxidation testing. The isothermal oxidation will be carried out at 1100°C with thermal gravimetric analysis (TGA) to examine the oxidation kinetics of the coatings. The cyclic oxidation will be carried out in CM Rapid Temperature Cyclic Furnace. The thermal cycle will consist of a 10-minute heat-up, 40-minute hold at 1100°C and 10-minute cooling. Microstructural evaluation of oxidized coatings will be carried out by x-ray diffraction, optical and electron microscopy as well as by laser fluorescence piezo-spectroscopy. Emphasis will be given to the oxidation kinetics, TGO phases, stress and adherence/spallation as a function of initial oxide phase constituents, surface

roughness, surface defects/features and bond coat compositions. Mechanisms associated with spallation of TGO scale will also be assessed.

Task III: Testing and Evaluation of TBCs

Objective: To procure bond coated TBC specimens with selected heat treatments and to test and evaluate them as a function of thermal cycling.

Technical Approach: In accordance to the specified heat treatment process, bond coated TBCs with CMSX-4 superalloy substrate will be prepared by Howmet International and other industrial partners. Here again, three (3 out of 9 identified in Figure 11) specified heat treatments will include those that form a complete a-Al_2O_3, a maximum amount of q-Al_2O_3 and a mixture of a- and q-Al_2O_3 in the TGO scale. Thermal barrier (ZrO_2-7wt.%Y_2O_3) layer will be deposited on heat-treated bond coats by EB-PVD. The TBC specimens will be subjected to cyclic oxidation testing using a CM Rapid Temperature Cyclic Furnace. The thermal cycle will consist of a 10-minute heat-up, 40-minute hold at 1100°C and 10-minute cooling. During thermal cycling, phase constituents and residual stress of the TGO will be monitored as a function of thermal cycle by laser fluorescence and specimens will be visually inspected frequently for any sign of spallation in order to accurately assess the lifetime of stand-alone metallic coatings and TBCs. Microstructural characterization of TBC specimens will be carried out prior to failure as well as after the failure to address failure mechanisms associated with various heat treatments, surface preparation and bond coat composition. Specimen descriptions and testing plans are presented in Table II.

Table II. Specimen Descriptions and Evaluation for Task III.

Metallic or bond boating	Surface finish	Surface Defect/Features	Heat treatment	Total number of specimen required
Pt-Al	As-coated	Ridges at full height	3 Selected	9 TBCs
	Grit-blasted	Reduced ridge height Rough surface	3 Selected	9 TBCs
	Media-finished	No ridges Smooth surface	3 Selected	9 TBCs
Pt-Al (Si,Hf)	As-coated	Ridges at full height	3 Selected	9 TBCs
	Grit-blasted	Reduced ridge height Rough surface	3 Selected	9 TBCs
	Media-finished	No ridges Smooth surface	3 Selected	9 TBCs
MCrAlY	Shot-peened	Rough surface	3 Selected	9 TBCs
	Media-finished	Smooth surface	3 Selected	9 TBCs

Total number of specimen required : 72 TBCs

5.0 Experimental Results

Task 0: Specimen Procurement

The required specimens described in Task 4.0, in the form of 2.54 cm diameter x 0.32 cm disks are being provided by Howmet Corporation. The disks are bond coated on all surfaces. The original plan was to have 3 metallic/bond coats consisting of a Pt-Al, a Pt-Al with Si+Hf and a NiCoCrAlY coating. Howmet's CVD chamber for the Pt-Al with Si+Hf is not operational, so the decision has been made to study the Hf+Si effect using the NiCoCrAlY coating. Thus the 3 metallic/bond coats will be Pt-Al, NiCoCrAlY, and NiCoCrAlY with Si+Hf.

Of the 3 coating systems, Howmet has delivered 20 specimens with a Pt-Al coating. The remainder of the coatings are on order.

Task IA: Coating Heat Treatments

Introduction

The University of Pittsburgh is collaborating with the University of Connecticut to develop thermal barrier coatings and metallic coatings with superior reliability and durability. As part of this effort platinum aluminide bond coats on the superalloy substrate CMSX-4 have been exposed to a number of different preoxidation treatments. The surfaces of the exposed specimens have been examined by optical and scanning electron microscopy. The results are presented in the following.

Results

The preoxidation exposures which were used to develop oxide scales (TGO) on the platinum aluminide bond coats are described in Table III below.

Table III. Exposure Conditions for Platinum Aluminide Bond Coats

Temperature (°C)	Gas Environments (P_{Total} = 1 atm)/Exposure Times		
900	O_2/2 hrs.	Air/2 hrs.	Ar-H_2 Mixture*/2 hrs.
1000	O_2/2 hrs.	Air/2 hrs.	Ar-H_2 Mixture*/2 hrs. & 15min
1100	O_2/2 hrs.	Air/2 hrs.	Ar-H_2 Mixture*/2 hrs.
1200	O_2/2 hrs.		

* The Ar-H_2 mixture establishes an oxygen partial pressure of 10^{-8} atm.

The surface of the as-processed coating and each exposed specimen have been examined using scanning electron microscopy. The surface of the as-processed platinum aluminide bond coat is shown in Figure 12. The ridged grain boundaries in the bond coat are apparent but there is no evidence of voids or cavities. The surface of this bond coat after exposure for 2 hours at 1000°C in the Ar-H_2 mixture is shown in Figure 13. Numerous voids are evident in the coating beneath the TGO. All other exposures produced morphologies similar to those shown in Figure 13. Voids are evident in Figure 14 along with mounds of oxide on a specimen after 2

hours exposure in pure oxygen at 1100°C. Figure 15 demonstrates the presence of voids after 2 hour air exposures at both 1000 and 1100°C. In some locations the voids were arranged in straight lines (arrows in Fig. 15), however, at the present time, the cause of such arrangements is not understood.

The voids were observed after exposure times of 15 minutes at 1000°C in the Ar-H_2 mixture, Figure 16. The density of voids varied from grain to grain in the coating. For 2 hour exposures in the in the Ar-H_2 mixture at 1100°C, rosette-shaped clumps of oxide developed (arrows in Fig. 15).

X-ray diffraction (XRD) analyses have been performed on each of the specimens exposed at 1100°C. In the case of the oxygen and air exposures diffraction lines for a-Al_2O_3 and the bond coat were detected. In the case of the exposure in the Ar-H_2 mixture, the oxide was so thin that only lines from the bond coat were observed.

Future Work

Future work is being directed at determining the cause of the void development and developing procedures to prevent the void formation. A platinum aluminide bond coat processed by Howmet using a special treatment will be exposed under the following conditions:

a. **2 hours at 1975°F (1079°C)**
b. **16 hours at 1975°F (1079°C)**
c. **16 hours at 2000°F (1093°C)**

The longer time exposures are to ascertain if the initially-formed voids are consumed during subsequent oxide growth since such extensive void formation has not been observed in numerous prior studies of the oxidation of platinum-aluminide coatings.

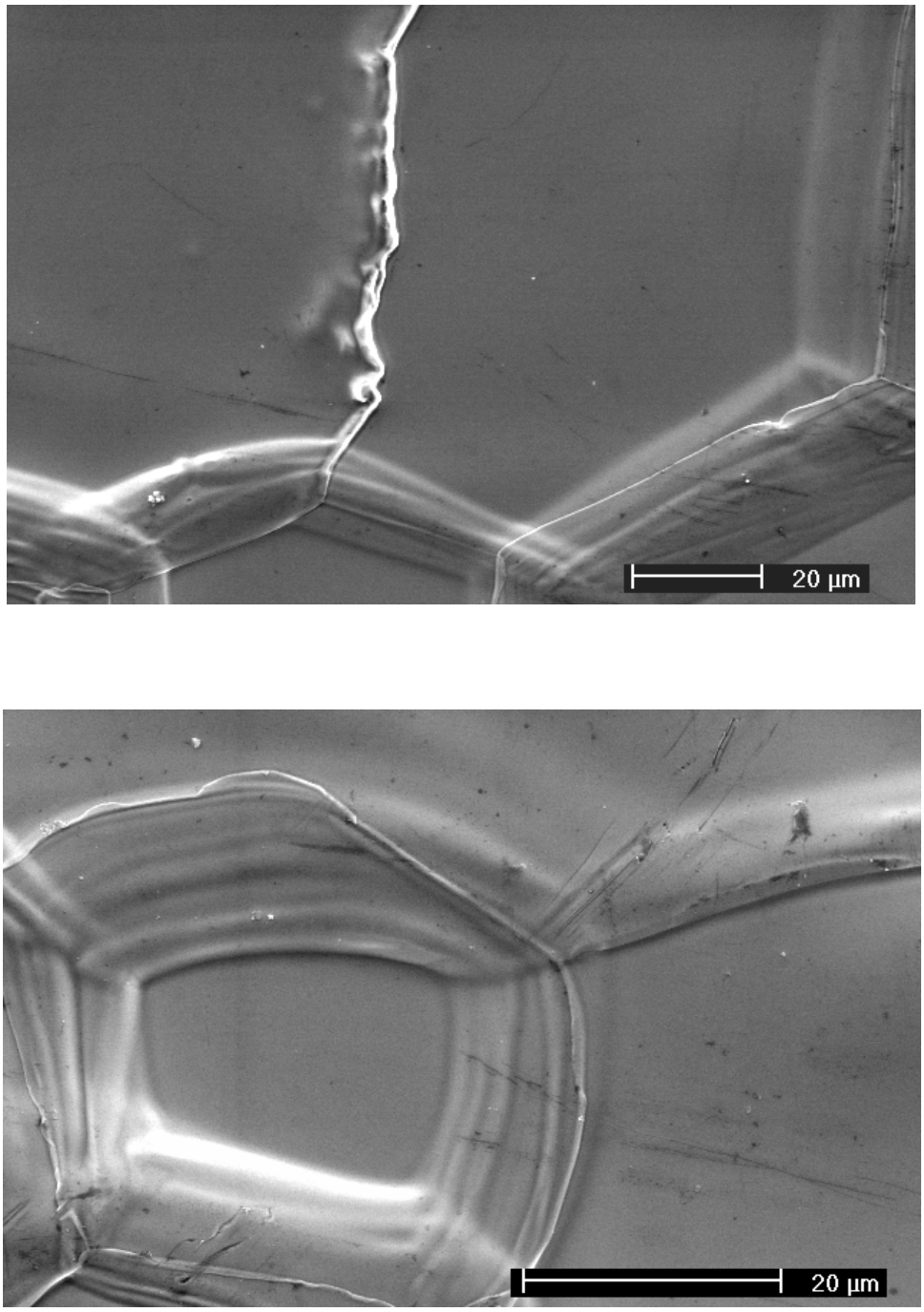

.

Figure 12. Surface of the as-processed platinum aluminide coating showing ridges that grow over grain boundaries in the coating during aluminizing

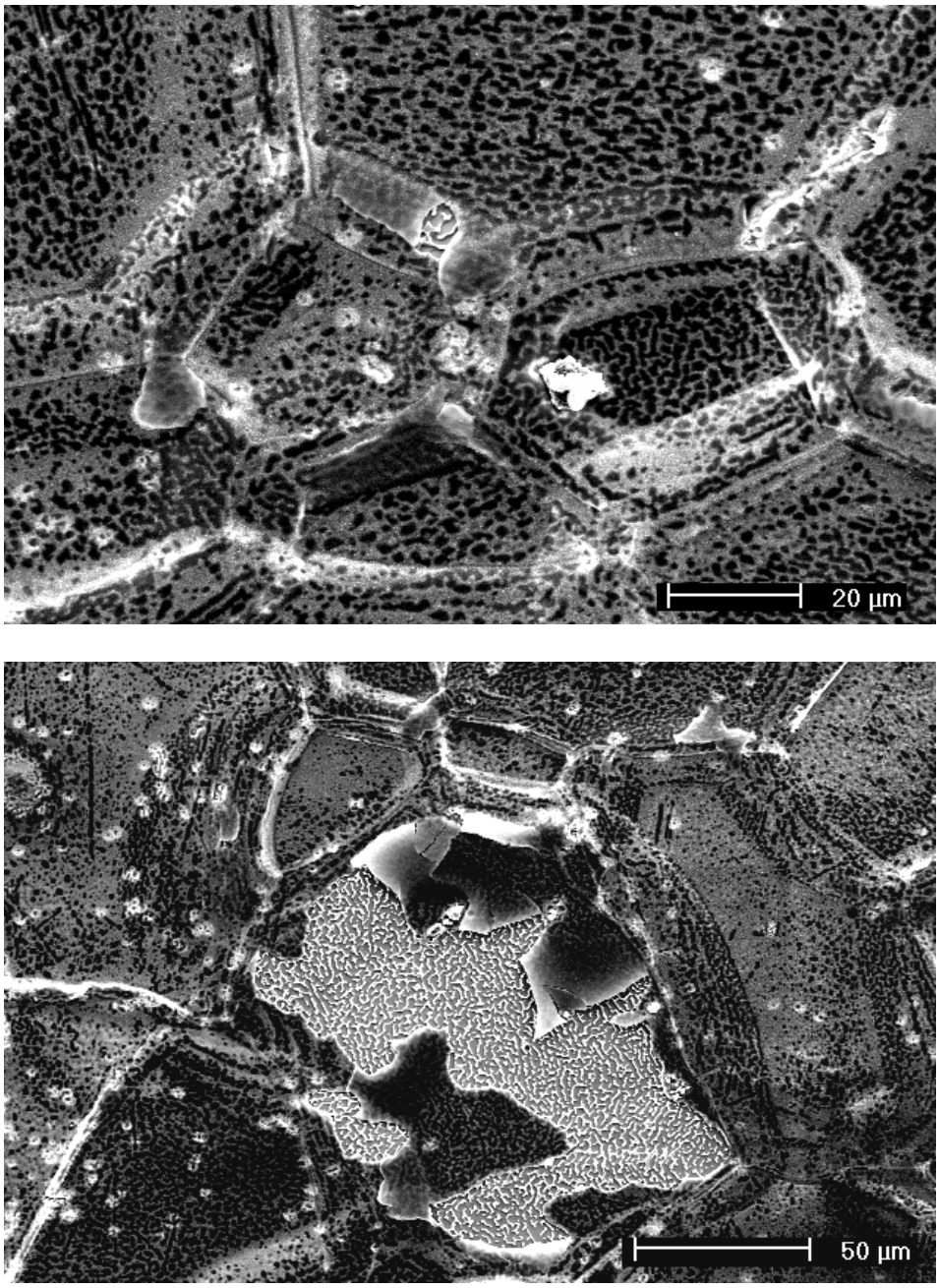

Figure 13. Surface of the coating exposed for 2 hours at 1000°C in the Ar-H_2 mixture showing copious void formation. The right hand micrograph also shows the voids in an area where the oxide spalled during cooling

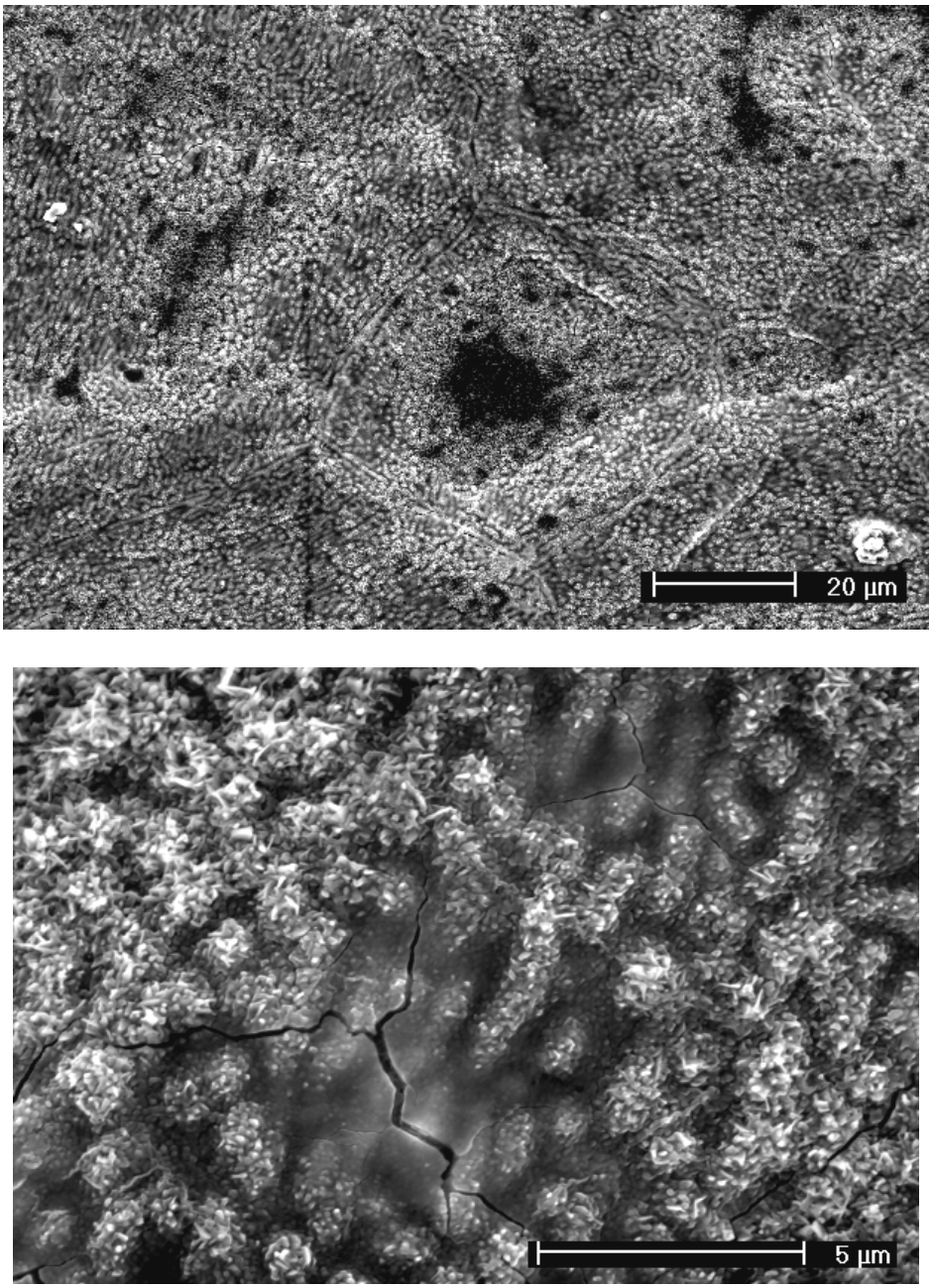

Figure 14. Surface of the coating exposed for 2 hours at 1100°C in O_2 showing void formation and the formation of oxide mounds.

Figure 15. Surface of the coatings exposed for 2 hours in dry air at 1000°C (top) and 1100°C (bottom) showing copious void formation. Preferential alignment of voids is indicated in some locations marked by arrows.

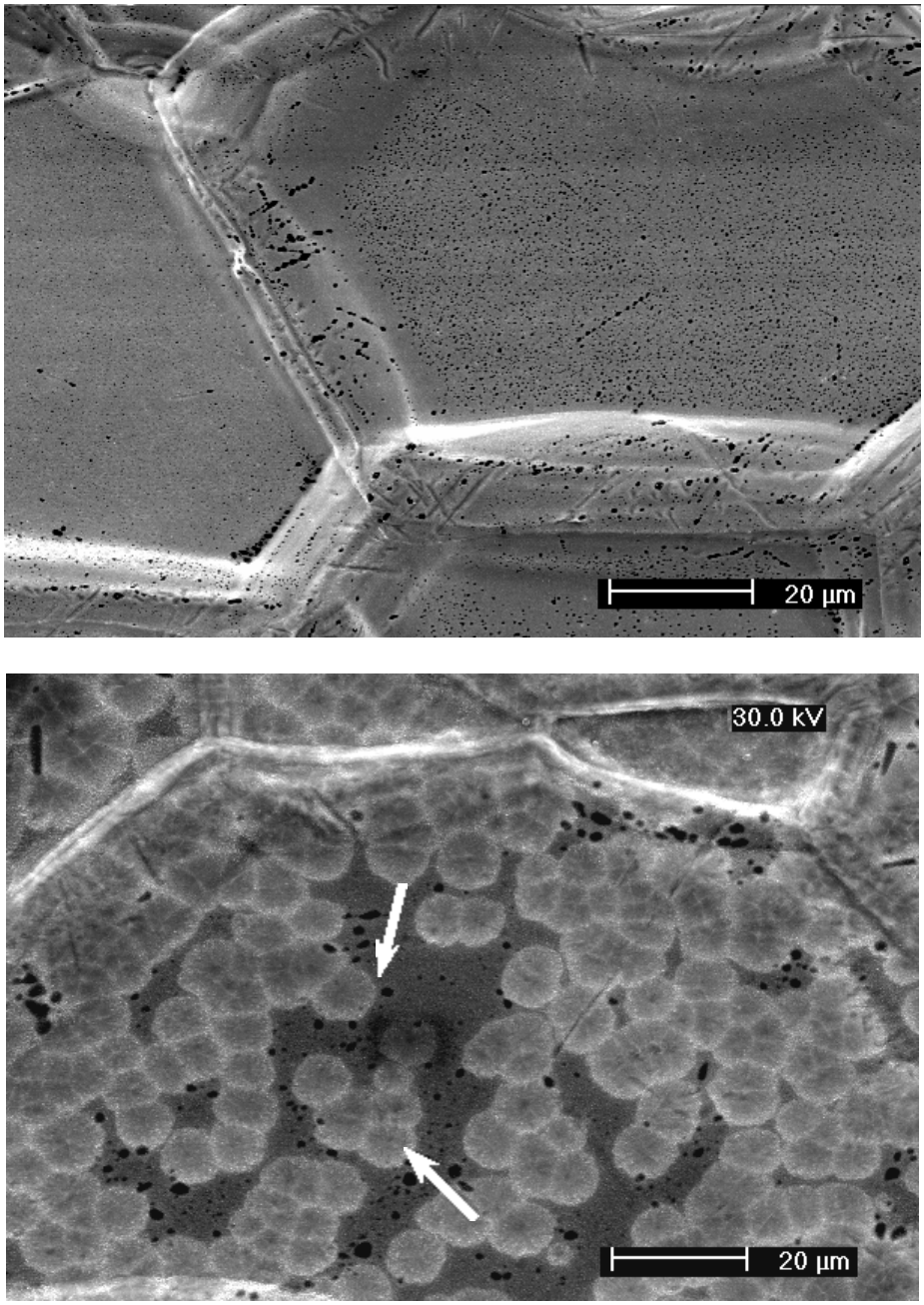

Figure 16. Surface of the coatings exposed in the Ar-H_2 mixture for 15 minutes at 1000°C (top) and for 2 hours at 1100). The void density was found to vary from one coating grain to the next (top). Rosette-shaped oxide formation was observed at 1100°C (bottom).

Task IB: Media Finishing and Surface Roughness

Media finishing trials were carried out on as-coated Pt-Al disk specimens by a media finishing company approved for work on turbine airfoils. Laser surface profilometry was used to quantitatively determine the surface geometry on as-coated samples and the changes that occurred after 20, 40 60 and 120 minutes of media finishing. Data was obtained for changes in (a)ridge height, (b) peak to valley distances, and average roughness.

Introduction

Grain boundary ridges in PtAl bond coats play a prominent role in the initiation and subsequent spallation of TBC's. The large out of plane tensile stress at the crest of these ridges is the primary driving force responsible for crack initiation. Recent experimental evidence, using laboratory polishing techniques, has shown that, in the absence of grain boundary ridges, a 4-fold life improvement was produced (Figure 17). This finding has lead to the present work to determine the magnitude of ridge height reduction and spallation life improvement obtainable from a commercial media finishing method, normally used on turbine blades.

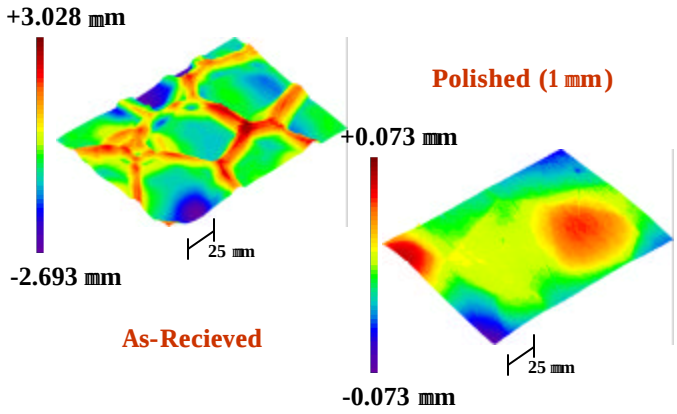

Figure 17: Surface profilometry showing the effects of careful mechanical polishing that lead to 4-fold life improvement

Media finishing

The Media finishing task was initiated by measuring the surface geometry; using laser surface profilometry, of all as-coated Pt-Al bond coated specimens containing ridges. Average roughness (Ra) and Peak to Valley (PV) were the chosen metrics for this study. Two samples were chosen for media finishing for the following times of 20, 40, 60, and 120 minutes and surface profilometry was

repeated and compared. Figures 18 and 19 show the improvement in PV and Ra respectively , with both plots showing absolute values on the y axis. Figure 20 shows the marked reduction in peak height and consequent flattening and broadening of the peaks as a function of finishing time. The large unexpected improvement in PV seen in figure 18. for the 20 minute trials are attributed to random sampling of the surface.

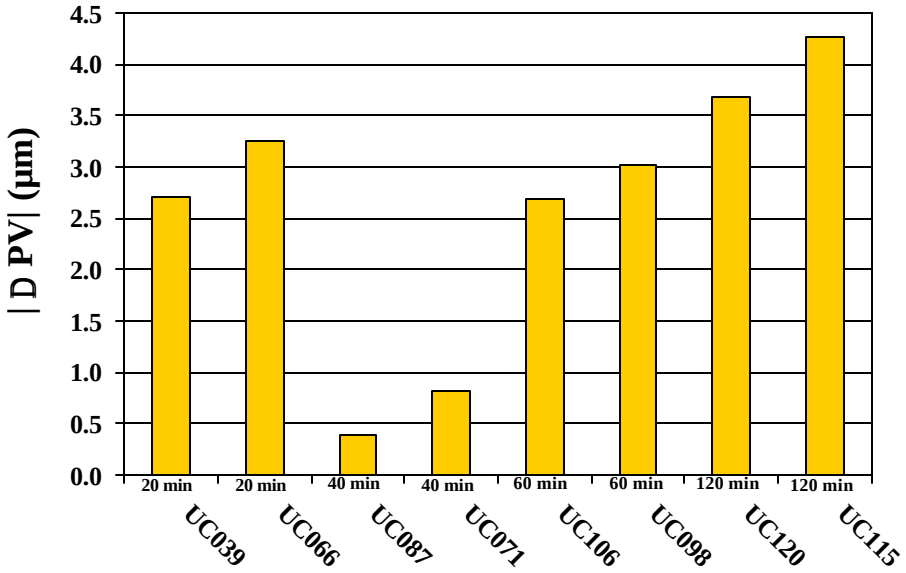

Figure 18: Improvements in PV.

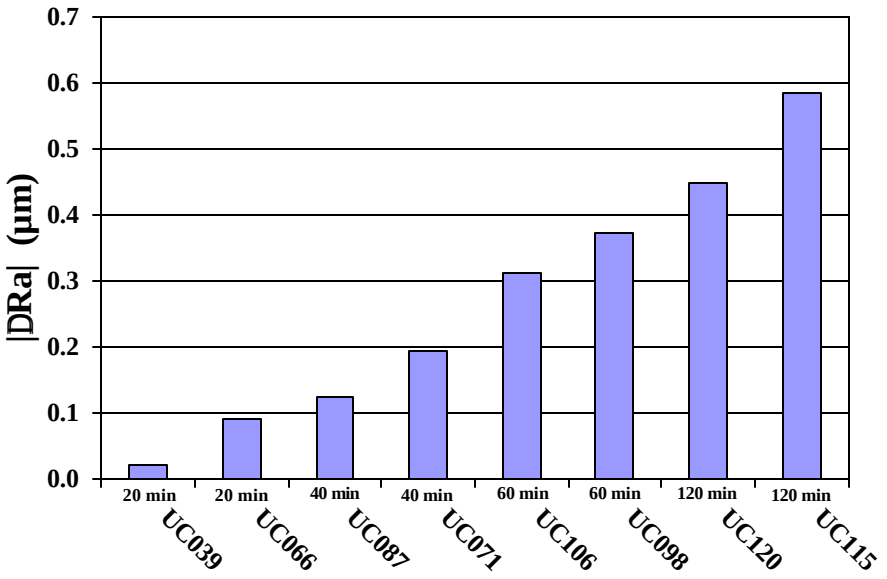

Figure 19: Improvement in Ra.

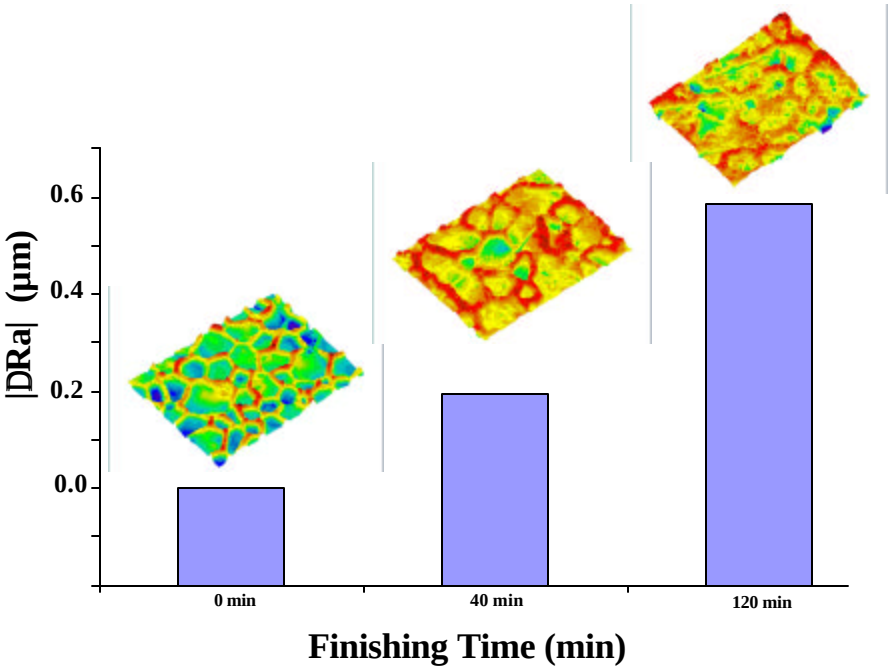

Figure 20: Improvement in Ra and Associated Change In Surface Topography.

On the basis of detailed evaluations, such as those summarized in Figure 20, we have selected media finishing times of 40 and 120 minutes as critical processing times to be carried out in the rest of the program. In addition as-coated and grit blasted specimens will be used as baselines to determine spallation life as a function of surface finish.

Advanced Thermostructural Materials

Materials Department and
Department of Mechanical and Environmental Engineering
University of California
Santa Barbara, CA, 93106-5050

A MECHANISM-BASED APPROACH TO LIFE PREDICTION AND NON-DESTRUCTIVE EVALUATION FOR THERMAL BARRIER COATINGS

ADVANCED GAS TURBINE SYSTEMS RESEARCH PROGRAM

Contract No: 98-01-SR068 (DOE-SCERDC)

South Carolina Institute for Energy Studies

Program Manager: Dr. Richard A. Wenglarz

Final report covering the period

1 February 1998 - 31 January 2001

Principal Investigators:

A.G. Evans, D.R. Clarke, and C.G. Levi

The research described in this report has benefited from the active support and advice of the industrial members of the AGTSR consortium, notably Siemens-Westinghouse, Solar Turbines, General Electric UTRC/Pratt & Whitney, Allied Signal Aerospace, Howmet Chromalloy, Cannon-Muskegon and Rolls-Royce Allison. Additional insight has derived from interactions with the National Institute of Standards and Technology, Argonne NL and NASA-Lewis.

April 30, 2000

AGTSR FINAL REPORT 1998-2001

Materials Department, University of California
Santa Barbara, CA, 93106-5050
Phone: (805) 893-2381 Fax: (805) 893-8486
e-mail: levic@engineering.ucsb.edu

Project Title:

A MECHANISM-BASED APPROACH TO LIFE PREDICTION AND NON-DESTRUCTIVE EVALUATION FOR THERMAL BARRIER COATINGS

AGTSR Subcontract No:	98-01-SR068
Principal Investigators:	Anthony G. Evans, David R. Clarke, and Carlos G. Levi* (* PI to whom correspondence should be addressed)
Graduate Students:	Edward A.G. Shillington (M.Sc.), Jennifer R. Litty (M.Sc.) Noemi Rebollo (Ph.D.)
Undergraduate Interns:	Jennifer B. Pritchard (Junior, Mechanical Engineering, UCSB) Will Gans (Sophomore, Mechanical Engineering, UC Berkeley) Dylan Jones (Junior, Mechanical Engineering, UCSB)
Post-doctoral Associates:	Vladimir Tolpygo and Ming Y. He (part time).
Visiting Scholars:	Xiao Peng and Carsten Menicke (part time, self-supported.)
Extramural Contributors:	J.W. Hutchinson, A. Rabiei (Harvard University) A. Karlsson, D.R. Mumm (Princeton University)
Subcontract Information:	Start date: February 1, 1998
	Completion date: January 31, 2001
	AGTSR total contract value: $600,000

EXECUTIVE SUMMARY

This AGTSR program had two major goals. One was to develop a mechanism-based strategy to assess and understand damage evolution and failure of thermal barrier coatings. A second goal was to develop a lifing methodology and a NDE-assisted testing protocol based on said strategy. The program involved elements of mechanics modeling, testing, characterization and processing aimed at providing insight into the mechanisms that dictate the life of TBCs for advanced turbine systems. Major progress was made during the program although some challenges remain; these are being addressed under a second AGTSR program as well as other related projects.

A menu of failure mechanisms was identified and those considered in greater need of understanding were selected for study. Much of the emphasis was placed in understanding the origin and evolution of interfacial separations that can lead eventually to spallation of the TBC. In general, these separations start at non-planar features in the thermally grown oxide, either in the form of thickness heterogeneities that represent centers of dilatation upon thermal cycling, or in the form

of undulations whose amplitude increases with time. Two competing and possibly complementary mechanisms were suggested for the evolution of interfacial undulations. One is motivated by phase transformations in the bond coat as consequence of the loss of Al by oxidation and interdiffusion. A second mechanism arises from a combination of a finite lateral-growth strain in the TGO and cyclic plasticity in the bond coat induced by repeated thermal excursions. Formation of separations can also be promoted by stresses associated with the constrained transformation of transient aluminas evolving in the early stages of oxidation, or by de-stabilization of the alumina scale owing to Al depletion in the bond coat. In general, all these mechanisms involve a combination of thermochemical and thermomechanical effects that need to be incorporated into suitable quantitative models describing the evolution of the interfacial separations into spallation events. Part of the mechanistic research focused on the behavior of purposely-generated defects, including chemical contamination, topographical features and separations induced by pulsed-laser shock waves. Of these, laser shock showed the most significant promise as a technique to produce interfacial separations of prescribed sizes through suitable control of the irradiation parameters. The mechanistic studies also established the paramount importance of the bond-coat surface characteristics in the durability of the overlaying TBC.

The elements of a mechanism-based strategy for life prediction were put into place. A finite element framework was developed to integrate the various mechanisms that contribute to interfacial separation. The first stage incorporated the roles of cyclic plasticity and the TGO growth strains, with subsequent work aimed at including creep effects as well as phase transformations in the bond coat. Additional tools were developed in the course of the program to assist in identifying failure conditions. These include micro-mechanics models, mechanism maps and scaling laws to provide insight into the relative contributions of the different mechanisms that motivate failure. The advances made under this program have brought the possibility of a full mechanism based model for TBC lifing closer to reality.

A major contribution of the program was the advances made in developing Photo-Stimulated Luminescence Spectroscopy (PSLS) as a practical NDE tool for TBCs. It was demonstrated that PSLS can be used to identify different types of interfacial damage, to quantify the TGO stresses around flaws and morphological features, to identify transient phases in the TGO, and to elucidate the kinetics of TGO transformations. PSLS has thus emerged as a potentially invaluable tool to ascertain the quality and reproducibility of coatings as they emerge from the manufacturing process. Its application as a predictive tool for residual life, however, is more challenging.

Progress in the major components of the program is briefly summarized below. Supporting manuscripts are provided as attachments.[1] Work yet to be published is described in more detail.

---

[1] References to the attachments in the following text are given in brackets.

MATERIALS AND PROCESSES

Emphasis in this program was on TBCs produced by electron-beam, physical vapor deposition (EB-PVD), although significant studies were also performed on plasma-sprayed (PS) coatings. Most of the samples used in the investigation were supplied by the industrial collaborators, notably Solar Turbines, Siemens-Westinghouse, General Electric and Howmet. In addition to as-deposited coupons, some industrial collaborators also provided samples after prescribed exposures in simulated environments, as well as airfoil specimens that had seen actual engine exposure. The latter were used primarily to explore the potential of the PSLS as a tool for field inspection.

Substrate materials without TBC were also provided by the above companies as well as RR-Allison (based on bulk alloy provided by Cannon Muskegon). These coupons were used for baseline oxidation studies, or coated with YSZ in the UCSB EB-PVD facility, some after introducing designed flaws. Specimens with laser-shock debonds were acquired through a collaboration with the EC JRC at Petten.

The close collaboration with industry made it possible to generate especially tailored specimens to study the effect of surface preparation on failure. In one case, specimens coated with (Ni,Pt) Al provided by Howmet were used to study the effect of surface condition on the theta-to-alpha transformation in the TGO [G] and on the evolution of undulations by rumpling [I]. Some of these specimens were also sent back to Howmet to be coated with TBC, and then returned to UCSB for durability studies.

Most recently, a series of EB-PVD coated (Ni, Pt) Al specimens wherein the bond coat surface condition was modified before depositing the TBC were generated in collaboration with General Electric. These specimens are summarized in Table I and briefly described below.

Table I. Specimens used to study bond coat surface condition effects on TBC durability

Series	Substrate	Bond Coat Conditions	Surface Preparation	Remarks
A	N5	1 2	As Processed As Processed	
B	N5	1 2 2 2	Grit Blast (Coarse Grit) Grit Blast (Coarse Grit) Grit Blast (Medium Grit) Grit Blast (Fine Grit)	Baseline Baseline
C	N5	2	Polished	
C	N5	2 2 2	Polished + Grit Blast (Coarse Grit) Polished + Grit Blast (Medium Grit) Polished + Grit Blast (Fine Grit)	
D	N5	2	Grit Blast (Coarse Grit) + Pre-oxidation	
E	R142	2	Grit Blast (Coarse Grit)	

The majority of the specimens comprised N5 substrates, with one additional series based on R142. Two sets of process parameters were used during the application of the bond coat, such that two different surface conditions were generated. In both cases, the bond coat exhibits continuous ridges at the intersections of the grain boundaries with the surface. The resulting samples differ in the bond coat grain size (and, therefore, in the size and separation of the ridges), as well as the initial surface chemistry. The bond coating conditions designated as 1 and 2 in Table 1 correspond to the larger and smaller grain sizes, respectively. In normal practice the samples are given a grit blast treatment to remove the ridges and distort a thin surface layer.

For the purposes of the present investigation, one set of specimens was coated with TBC in the as-manufactured state, i.e. retaining the ridges resulting from the bond coat application (Series A). In Series B, D and E the ridges were removed by conventional grit blasting, using either coarse, medium or fine alumina grit as indicated in Table 1. (The N5 specimens blasted with coarse grit were taken as the baseline for the subsequent comparison.) The effect of pre-oxidation was examined in Series D, where a set of specimens was heat-treated in a controlled atmosphere to form a thin (approximately 0.1-0.3 m) TGO of α-Al_2O_3 before depositing the TBC. Finally, in Series C and C the ridges were first removed by mechanical polishing. One subset (C) was grit blasted after polishing in an effort to assess the relative effect of the surface deformation induced by the particles from that of removing the ridges.

MECHANISMS GOVERNING DURABILITY

Significant progress was made during the program in identifying the sources of failure initiation and elucidating the sequence of events that lead to failure. There were two primary lines of research, one focused on the micro-mechanics of the failure process and the other on the chemical underpinnings of failure. The common link was the evolution of the TGO. At this stage, the efforts in each line are sufficiently advanced that the next steps can focus on elucidating the interactions among mechanisms.

There were two major themes in the investigation of thermochemical effects. The first one was the role of transient alumina phases that evolve in the early stages of oxidation. It was shown that the volume contraction associated with the transformation of these phases into the stable α-Al_2O_3 could give rise to interfacial separations when constrained by the TGO [F]. The identification of a critical TGO thickness below which separations are suppressed suggested the possibility of designing pre-oxidation treatments to minimize this effect. Additional studies yielded insight into the morphological evolution of the TGO and its connection to the growth of transient aluminas [G]. The distinct acicular morphology of θ-Al_2O_3 is clearly preserved upon its transformation to α, with potential implications to the evolution of the intermixed Al_2O_3/ZrO_2 zone often observed in EB-PVD coatings. It was also demonstrated that the $\theta \rightarrow \alpha$ transformation is accelerated by surface roughness, apparently because of an enhancement in the nucleation of α. Through their effect on the transient oxidation behavior, surface preparation and pre-treatment temperature are thus important variables in controlling the morphology of the TGO, and possibly its protective properties, with attendant implications to the durability of the TBC.

A second important theme in the investigation of thermochemical effects was the role of Al depletion in the durability of the TBC. Al depletion results both from oxidation at the bond/top coat interface to form the TGO, as well as from inter-diffusion with the superalloy substrate, which is leaner in Al. The Al loss can amount to a significant change in the total volume of the bond coat, but would not be particularly deleterious if it occurred homogeneously, i.e. if the Al iso-concentrate lines were parallel to a nominally planar interface. One significant effect of this chemical change, however, is the de-stabilization of the β phase, particularly evident in initially single-phase (Ni, Pt)Al bond coats which gradually transform into γ-Ni_3Al as the oxidation proceeds [I]. This transformation occurs in a localized fashion, typically at grain boundaries of the parent β and at the interface with the superalloy. The ensuing local changes in volume can translate into stresses that could deform the bond coat and give rise to surface undulations. In the absence of a top-coat, this can give rise to substantial rumpling of the surface [I]. When a top-coat is involved, the stresses may cause interfacial separations, typically between the TBC and the underlying TGO. The details of the mechanism, however, are not yet fully understood. Notably, rumpling is observed under cyclic oxidation, but not under isothermal oxidation, which typically leads to cavity formation within the bond coat. Conversely, the extent of rumpling for a given number of cycles decreases with the length of the hold time at high temperature, indicating that thermal cycling alone is not sufficient to justify the extent of deformation. In extreme situations, Al depletion can lead to the de-stabilization of the α-Al_2O_3 layer and its replacement with a less adherent oxide. Studies on IN939/ CoNiCrAlY/APS-YSZ clearly demonstrated this effect. TBC adhesion was compromised by the transformation of the TGO from α-Al_2O_3 into a mixture of α-$(Cr,Al)_2O_3$ and a $(Co,Ni)(Cr,Al)_2O_4$ spinel [H]. The system studied is particularly susceptible because the substrate has much lower Al content than advanced airfoil alloys, e.g. CMSX-4.

The thermomechanical studies focused primarily in understanding the role of TGO morphology on the evolution of interfacial separations. This was motivated by an early realization that separations of a scale needed to buckle and spall the TBC from the surface were unlikely to be formed in planar interfaces. The process, however, is much more viable in the presence of imperfections in the TGO [A]. The experimental work was mostly performed under related programs, with the activity under this program focusing on the development of models (see below). A review is presented in [E]. Briefly, the observations suggest that thickness heterogeneities (pegs) in an otherwise planar TGO can act as dilatation centers upon thermal cycling and induce interfacial cracks at their periphery, especially if the interface toughness is concomitantly degraded by impurity segregation. In this mechanism, separations can evolve to cover large portions of the interface. The coating is ultimately held attached by ligaments at the center of the original imperfections (which are under compression) and between the imperfection boundaries, where the critical energy release rate is insufficient [B].

Separations can also arise as pre-existing undulations in the TGO as consequence of thermal cycling. Initial undulations at the bond-coat/top-coat interface are typically the result of surface roughening to enhance adhesion of plasma spray coatings, grit blasting of surfaces in preparation

for EB-PVD, and phase transformations in the bond coat, as discussed above. Studies on PS MCrAlY bond coats [D] revealed cracks into the TBC emanating from the protruding regions of the bond coat as the TGO thickened. These cracks propagated into the TGO and along the BC/TGO interface upon cooling, forming a network of separations held attached by bridging ligaments in the TBC. Final spallation ensued when these ligaments were fractured. Examination of industrial EB-PVD specimens at different stages of cyclic life revealed a substantial increase in the tortuosity of the interface, with concomitant formation of separations at the TGO/TBC interface. The latter typically involve pull-down of pinched-off columns resulting from the evolutionary selection process that occurs during TBC deposition [K]. It is proposed that the amplification of undulations is the result of lateral growth stresses in the TGO which are accommodated by plasticity of the bond coat (and TGO). Thermal cycling leads to reverse plasticity phenomena that considerably enhance the evolution of the initial defect.

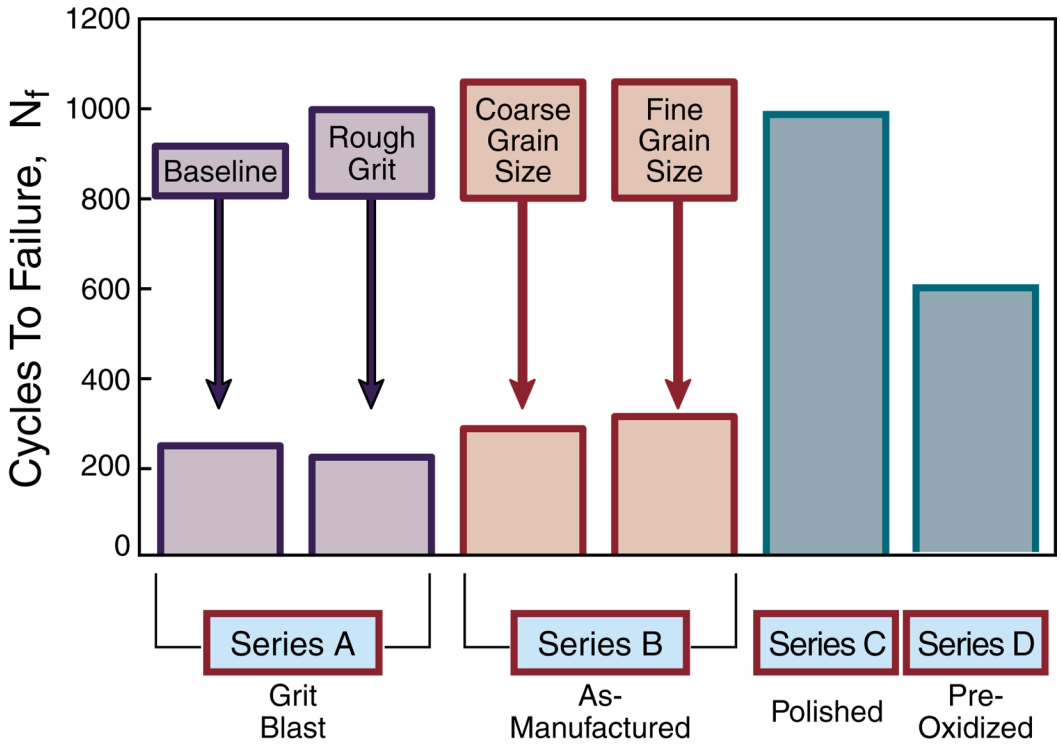

Figure 1. Comparison of cyclic life for the specimens in Table I, highlighting the effect of surface condition on durability.

The previous discussion suggests that surface preparation should play an important role in the morphological evolution of the TGO, and hence on the durability of the system. The results for the different surface conditions outlined in Table I are given in Figure 1.

The study revealed the following surface-related phenomena governing durability.

(i) *Imperfections on the bond coat surface are critical.* Removal of imperfections by polishing suppresses the TGO instability and enhances durability. The failure mechanism changes to edge delamination.

(ii) *The TGO thickening rate is important.* A pre-oxidation heat treatment that diminishes the thickening rate increases the durability, although failure occurs subject to the same TGO instability mechanism, at the same final TGO thickness.

(iii) *The bond coat yield strength is a key factor.* Changing the substrate to an alloy that includes reactive elements results in strengthening of the bond coat. The greater strength suppresses the morphological instability of the TGO, resulting in superior durability.

(iv) *The grain structure of the bond coat correlates with the TGO instability and affects durability.* The correlation has been related to the plastic anisotropy of the β-NiAl, and the grain-boundary dependent formation of γ domains. Both imbue local variations in the bond coat yield characteristics in the vicinity of two/three grain intersections with the TGO.

A complementary set of activities within this program dealt with the introduction of well-characterized flaws or topographical features into specimens and the study of their role in failure. Three types of features were investigated. The first one addressed the role of holes and edges. The emphasis was on the effect of holes on the evolution of damage and residual stresses. Small through-thickness holes of different diameters were drilled into Pt-Al coated CMSX-4 disks, as well as on FeCrAlY strips. Some of these specimens were then coated with EB-PVD YSZ at UCSB whereas others were left non-coated for comparison. The specimens were then subjected to cyclic oxidation. Piezo-spectroscopic measurements of the residual stress in the TGO revealed the stress build-up profile from the edge of the hole into the film. The extent of the buildup zone depends on the diameter of the hole, with the stress distribution fitting a shear-lag type model.

The second activity focused on inducing failure initiation at specific sites, in order to study the subsequent evolution of interfacial damage under cyclic oxidation. The most promising approach was a laser-shock technique under investigation in collaboration with the EC center in Petten. Experiments with chemical contamination of FeCrAl(Y) surfaces using solutions with widely varying concentrations of Na salts yielded a number of interesting surface effects, but no significant interfacial separation even after substantial cyclic oxidation. This was at variance with ample evidence in the literature regarding the deleterious effects of Na on oxide scale adhesion. The presence of Na was verified by SIMS both before and after treatment, so the resistance to spalling could not be ascribed to loss of the contaminant (e.g. by evaporation) during the experiments. Areas in the originally clean surface showed some Na upon SIMS analysis after oxidation, but the amounts were much lower than those detected in the contaminated spots, suggesting that diffusive homogenization of the Na did not occur. Where local spallation was observed it usually occurred at grain boundaries, where the underlying metal experienced relative sliding of the surface grains during thermal cycling. The unusual adherence of the TGO in these alloys, even in the presence of substantial levels of Na contamination, remains to be elucidated.

The third activity addressed the role of surface topography in failure initiation, in an attempt to explore the role of metal plasticity in the absence of phase transformations in either the bond-

coat or the TGO. FeCrAlY coupons (25x25x1mm) properly annealed and polished to an optical quality finish, were selected as model substrates. A series of grooves about 20 m deep, 100 m wide, and 1.25 or 2.5 mm apart, were then cut into the surface using a dicing saw and a precision diamond blade. The surface was planarized by carefully re-polishing, lightly etched and ultrasonically cleaned. Groove profiles at different locations, identified by fiducial marks, were characterized by profilometry. Two specimens were left non-coated and two were coated with YSZ in the EB-PVD facility at UCSB.

One coated and one non-coated specimen prepared in the above manner were subjected to isothermal oxidation in air at 1150¡C for 24 h. A second set of nominally identical specimens was subjected to 24 oxidation cycles in air. Each oxidation cycle comprised a 10 min ramp up to 1150¡C, a 1 h dwell at this temperature, a 10 min ramp down to ambient and a 10 min hold at ambient. After the prescribed oxidation treatments, the specimens were cut along the sections defined by the fiducial marks, polished and examined by scanning electron microscopy.

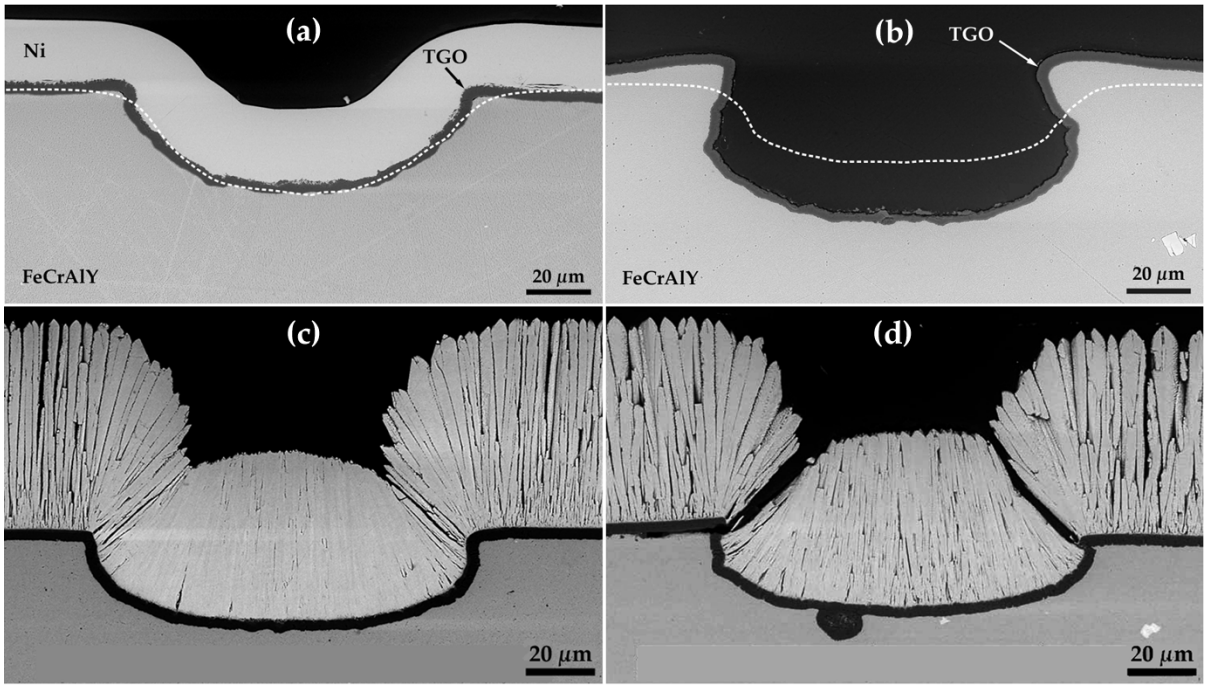

Figure 2. Morphological evolution of shallow grooves in FeCrAlY substrates, without (a, b) and with (c, d) TBC. The specimens on the left (a, c) were subjected to isothermal oxidation for 24 h at 1150°C. The specimens on the right (b, d) were thermally cycled (24 x 1h hold) at the same temperature. The Ni coating in (a) was applied to facilitate sample preparation.

Representative cross sections of the grooves in each specimen are shown in Figure 2. Comparison of the changes in the groove profile for the non-coated specimens vividly demonstrates the effects of thermal cycling on the morphological evolution of the groove. No significant distortion in the profile is observed for the isothermally oxidized specimen (Fig. 2a). In contrast, the thermally cycled specimen (Fig. 2b) exhibits substantial deformation in relation to the original profile. significant pile-up of the alloy at the periphery of the groove. The thermally grown α-Al_2O_3

has a relatively uniform thickness (~2˚ m) at all locations outside and within the groove, albeit somewhat rougher and with more variation at the bottom of the latter. Material pile-up occurred at the edges, the base of the groove displaced downward substantially (the total change in amplitude was ~70% for an initial groove depth of ~32 m). In addition, the groove becomes narrower at the periphery and wider at the bottom. The oxide thickness is essentially the same in both cases, reflecting the similar cumulative time at the maximum temperature.

Deformation near the groove is clearly reduced by the presence of the TBC (Fig. 2c,d), but local damage in the form of TGO and TBC cracks is more abundant than in the non-coated specimens. Two dominant types of damage were observed: one involving shear cracks and delaminations at the TGO/substrate interface, and the other manifested as through-thickness cracks in the TBC along the edges of the grooves. The latter are ascribed to the opening of inter-columnar gaps driven by the upward displacement of the underlying TGO. Numerical simulations are underway with the goal of establishing the TGO growth characteristics that govern these shape changes.

MECHANISM BASED MODELS

Modeling activities within the program focused on developing and integrating the conceptual mechanics models that would form the foundation of the lifing methodology. In general, spalling is envisaged to occur by a sequence of nucleation, propagation and coalescence of microseparations. Early work highlighted the potential role of morphological imperfections in the nucleation stage, leading to the identification of critical imperfection wavelengths and TGO thicknesses. Buckling maps were developed that incorporate the conditions necessary for nucleation as well as stable and unstable propagation of buckles [A]. Analysis of the mechanics of interfacial heterogeneities under residual compression revealed that they play a prominent role. They can serve as potential initiation sites for separation, but also as remnant ligaments that keep the coating attached to the substrate even after most of the TGO/BC interface has separated. Failure then requires that these ligaments be fractured under shear or tensile loads that can overcome the residual compression [B]. Additional modeling revealed that the anisotropic elastic properties of the TBC modify the buckling process and introduce a competitive mechanism of failure by edge delamination [E].

Further work led to the proposition that mechanisms governing durability reside within two basic categories. One of them is representative of operational scenarios with predominant elevated temperature exposure and minimal thermal cycling. The other represents multiple, repetitive cycling. In both cases, durability is affected by misfit strains at imperfections on the interface caused by TGO formation, combined with thermal expansion misfit upon cooling to ambient. The first category is dominated by stresses in the TBC brought about by growth misfit, resulting in cracks that nucleate and extend from the imperfections [D]. These cracks eventually coalesce over a large enough interfacial area to allow large scale buckling and spalling of the TBC. The second involves a synergism between the growth and thermal-expansion-misfit strains that ratchets the TGO into the bond coat through a cyclic plasticity mechanism [C]. Study and analysis of these mechanisms has allowed failure scenarios to be created and some durability models to be developed. However, the models are still under development and need rigorous verification.

Two types of activities were performed with the goal of integrating the mechanistic knowledge base into durability models. The first one was the development of a finite element framework to probe the different conditions that may contribute to the development of surface undulations and interfacial separations. (This is a broad joint effort with related programs.) The software has been used so far to study the problem of cyclic plasticity and the ensuing TGO ratcheting. Important effects of TGO and bond coat creep have yet to be analyzed, and the influence of the in-plane stress on the growth strain tensor for the TGO remains to be addressed. Interdiffusion effects leading to phase transformations in the bond coat, with concomitant volume changes and attendant consequences to the morphological evolution of the TGO are also in need of better understanding.

The second major activity focused on the development of scaling laws to identify the appropriate non-dimensional groups governing key parameters in spallation, notably the stress normal to the TGO and the stress intensity factors for relevant crack configurations. Relationships between these quantities have been developed using first an analytical approach based on spherical imperfections, subsequently refined with numerical analyses. Studies under this program were limited to scenarios involving minimal thermal cycling, where cracks evolve as a result of TGO growth strains combined with thermal expansion misfit upon cooling. The results were used to identify a critical TGO thickness associated with failure, and to express it in terms of material variables.

Ratcheting Simulations

A procedure for incorporating finite TGO thickening within a full numerical simulation has been developed. Simulations using this procedure have been performed for a bond coat having representative thermo-mechanical properties. By introducing features that closely resemble those applicable to actual bond coat systems, the origins of several effects observed in experiments have been distinguished. These include the role of the bond coat mechanical properties as well as the influence of the size of the imperfections present on the bond coat surface, and the effect of TGO growth kinetics (linear relative to parabolic).

TGO growth is simulated by a stress-free strain tensor applied at the maximum temperature. Consistent with experimental findings, this strain has a small lateral component, ε_g, and a larger thickening component, ε_t. The thickening per cycle, Δh, is a variable, initially taken as a fixed fraction, f, of the initial thickness, h_o. Subsequent simulations are performed with the parabolic thickening kinetics found experimentally: whereupon the increment in thickness per cycle, subject to hot time, Δt, becomes:

$$\frac{\Delta h}{h - h_0} = \frac{\Delta t}{2t} \tag{1}$$

where t is the cumulative hot time.

Stress redistribution upon cycling is simulated by imparting the yield characteristics plotted on Figure 3a. At the peak temperature, the TGO yields when the Mises stress reaches –1GPa, imposing a maximum on the growth stress. On cooling and reheating it behaves elastically, because

of the rapid increase in yield strength at lower temperatures. The stress at ambient then equals the sum of that from growth with that from thermal expansion misfit, σ_{amb}^{-}-4.5GPa.

The bond coat is considered next. It is taken to have a temperature dependent yield strength having the form depicted on Fig. 3b. The strength up to temperature T_1 (taken as 300C in all calculations) is 1GPa. At temperatures above T_2, the strength σ_{Ybc}^{min} is allowed to vary in the range 50 to 200MPa. It changes linearly from $T_1 \rightarrow T_2$. Time dependent (creep) effects are not addressed with this representation. They are being examined in a separate study. The bond coat is assigned a thermal expansion misfit with the superalloy substrate. For most calculations, it is taken as: $\Delta\alpha_s^{\circ} = {}^{\circ}\alpha_{sub} - \alpha_{bc}^{\circ} = {}^{\circ}$+3ppm/C.

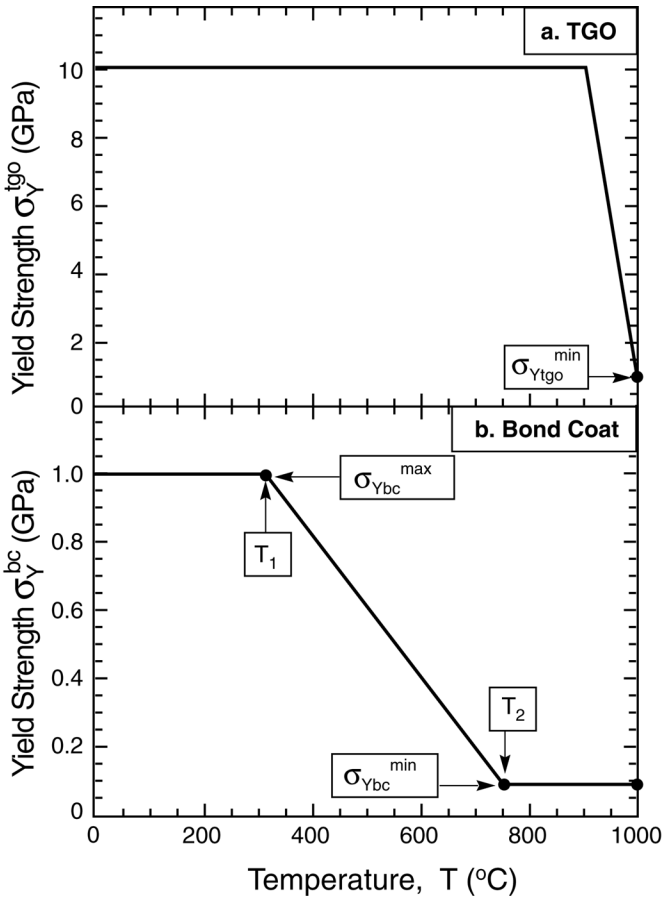

Figure 3. Temperature dependent yield strengths of TGO (a) and bond coat (b) used in the calculations.

One set of results for parabolic thickening (Fig. 4) is typical. It compares the amplitude change rate, *d(ΔA)/dN*, for linear and parabolic growth: all other aspects remaining invariant. Under parabolic conditions, the ratcheting-rate diminishes on a cycle-by-cycle basis (Fig.˚4a), instead of assuming a steady state. Note that the amplitude change per increment in TGO thickness, *ΔA/Δh* (Fig. 4b), is essentially the same for both kinetic representations. This trend mimics that measured experimentally (Fig. 5). Both experiment and simulation reveal that the ratcheting rate decreases by about a factor 3.

To explore size effects, simulations have been performed for ratios of initial TGO thickness to undulation amplitude, h_o/A_o, between 0.1 and 4, all for fixed imperfection aspect ratio, $A_o/L=0.6$, and for linear thickening $(\Delta h/L=0.016)$. The results are plotted on Figure 6. As in all previous simulations, the growth rate, *d(ΔA)/dN*, initially increases and then attains a steady state, $[d(\Delta A)/dN]_{ss}$, after about 5 cycles. Note from Figure 6b that $[d(\Delta A)/dN]_{ss}$ decreases systematically as the imperfection becomes smaller (larger h_o/A_o). There is almost an order of magnitude decrease over the imperfection size range investigated. However, some ratcheting still occurs at the smallest size, $A_o/L=1/4$.

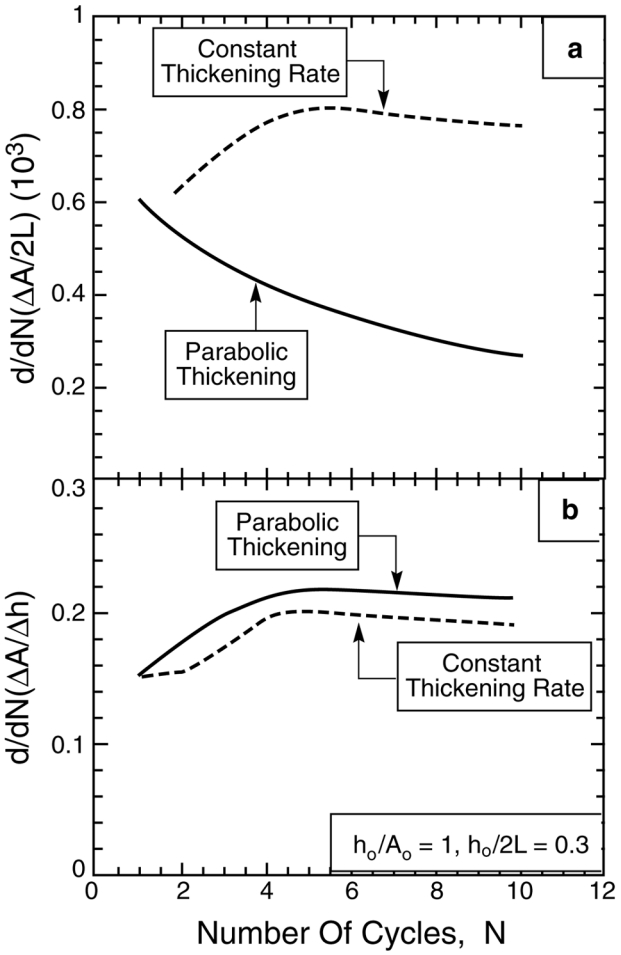

Figure 4 (Left). (a) A comparison of the ratcheting rates for linear and parabolic TGO thickening. (b) The same results plotted as the amplitude change per TGO thickness increment. ($\Delta h_o / L$=0.016, T_2=750C, σ^{min}_{Ybc}=100 MPa).

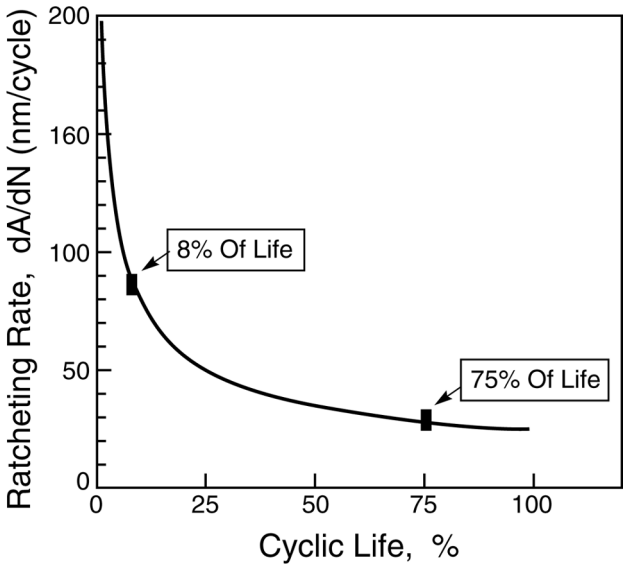

Figure 5. Experimental measurements of the ratcheting rate for a TGO having parabolic growth characteristics.

In summary, four effects have been established.

(i) A lateral growth strain is a necessary condition for continued cycle-by-cycle growth of the instability, because this strain allows the TGO to elongate with the bond coat as the imperfection amplitude increases.

(ii) The ratcheting rate is reduced by elevating the high temperature deformation resistance.

(iii) Substantial reductions in instability growth occur as the imperfection size approaches the thickness of the initial TGO layer, consistent with the effect of surface planarization on instability development.

(iv) The ratcheting rate diminishes on a cycle-by-cycle basis when the TGO exhibits parabolic thickening, in accordance with experimental measurements.

Delamination

In the presence of a sufficient thermal gradient, cracks form and propagate on delamination planes in the TBC parallel to the interface resulting in regions that spall away, leaving a thin layer of zirconia still attached to the substrate. This failure mode does not arise either when the system is subject to furnace cycle or burner rig tests; it is only activated in a high heat-flux environment.

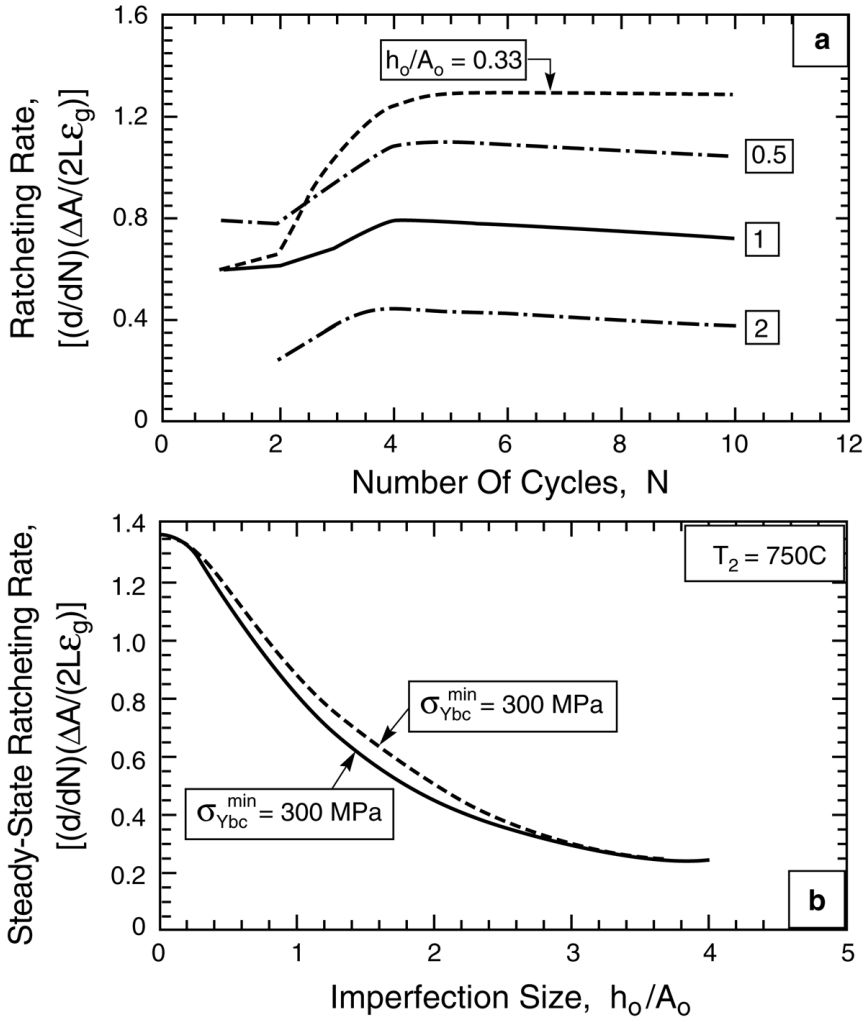

Figure 6. Effects of the relative imperfection amplitude, A_o/h_o, on the ratcheting rate. ε_g=0.001. The other parameters are the same as in Figure 4.

The challenge has been to identify the origins of the stress and hence, the delamination energy release-rate. Two distinct possibilities have been defined, analyzed and compared.

(i) An isolated crack parallel to the interface is envisaged, subject to a thermal gradient, that experiences an energy release rate and exfoliates (Fig. 7a). A similar crack connected to either a free edge (Fig. 7b) or a crack through the thickness of the TBC.

(ii) A shrinkage crack caused by sintering of the top layer of the TBC, which may reorient into a delamination (Fig. 7c).

In all cases, the TBC is assumed to be stress-free at a reference temperature, T_{dep}, assumed equal to the deposition temperature (900-1000C). Deviations from this temperature induce stresses because of the constraint of the superalloy substrate. Additional stresses are created by the presence of a thermal gradient.

The results indicate that only one of the mechanisms appears to be effective: namely, edge delamination subject to energy release rate:

$$G_{ss}^{edge} \approx \frac{1}{2}\left(\overline{E}_{tbc} h \alpha_{tbc}^2\right)\left(T_o + T_i - 2T_{dep}\right)^2 \quad (2)$$

This finding has several implications for conditions likely to activate this failure mode in preference to others (governed by the TGO). The most important parameters are the TBC modulus, $\overline{E}_{tbc}$, as well as the difference between the deposition and surface temperatures, T_{dep}-T_o. The delamination likelihood increases as either of these quantities increase. The modulus is affected primarily by sintering, governed in turn by both to the material and the surface temperature. The temperature difference is associated with manufacturing conditions, T_{dep}, as well as the design of the turbine and the thermal conductivity of the TBC, which affect T_o.

NDE of Residual Stress and Damage

The NDE component of the UCSB program focused primarily on the development and application of photo-stimulated luminescence spectroscopy (PSLS) as a tool in life prediction. PSLS uses the frequency shift of the characteristic luminescence of Cr impurities in alumina to determine the residual stress in the TGO. Additional information can be obtained from monitoring the intensity of the luminescence. Thermal and optical imaging were used as complementary techniques for monitoring damage evolution in TBCs. Salient accomplishments are outlined below.

An initial goal of this research was to assess the potential of PSLS as a novel, non-contact metod of detecting events that signal the im-

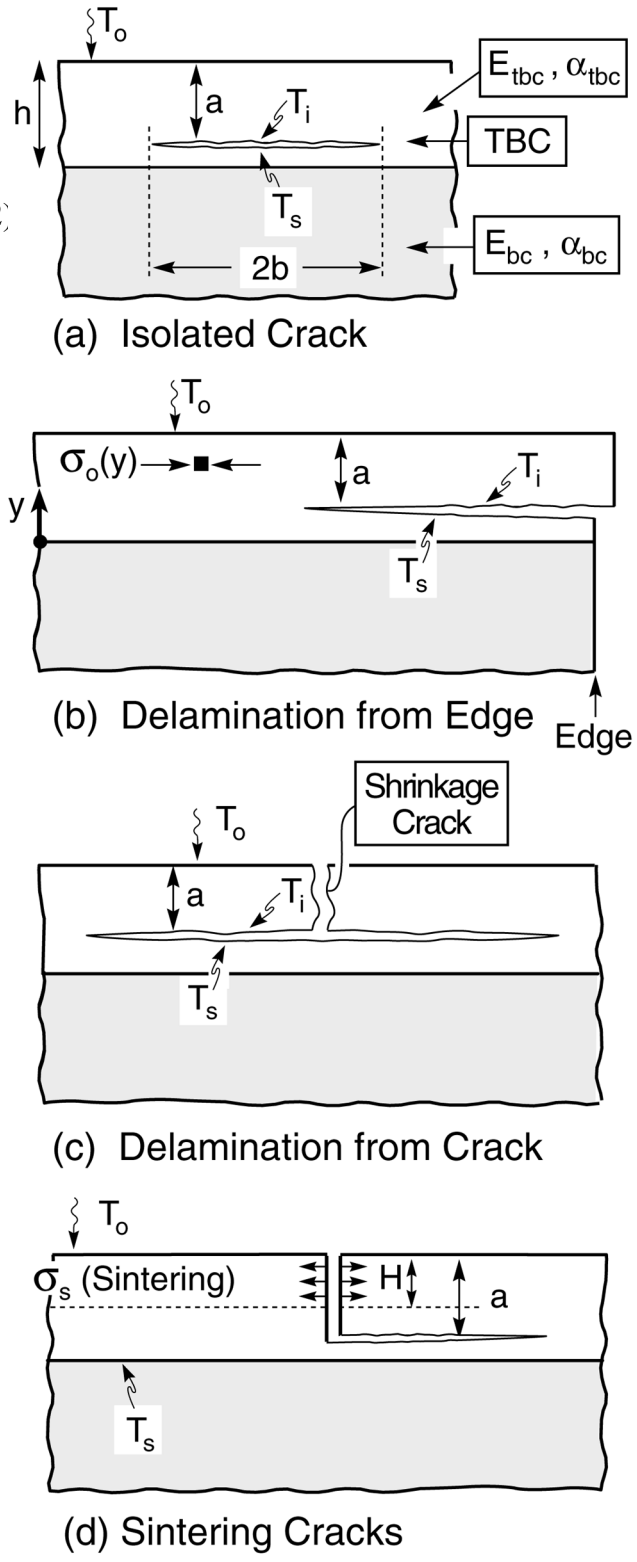

Figure 7. Possible scenarios for the evolution of delamination cracks in the presence of a thermal gradient.

pending failure of the TBC. In one example, it was shown that there is a correlation on oxidation exposure between the luminescence intensity and Al depletion in a CoNiCrAlY (CT-102) bond coat with a plasma-sprayed TBC. Microstructural characterization revealed that the spalling after cyclic oxidation was associated with the conversion of the TGO to α-chromia and spinel, as discussed earlier [H]. The observations suggest that monitoring the luminescence intensity as a function of oxidation time could be used as a nondestructive tool for detecting the onset of failure based on the de-stabilization of α-alumina in the TGO.

The potential of PSLS was further extended by developing a mechanism-based methodology for interpreting the changes in the signals recorded from a TBC as damage evolves in the TGO. The methodology enables the extent of the damage to be quantified by spectral analysis of the luminescence signal and de-convolution into its individual components. The method was successfully demonstrated on a TBC sample in which the damage could be readily verified by optical imaging examination [J]. Bonded and separated areas under an EB-PVD TBC were detected optically and correlated with residual stress measurements**.** Clear differences were established between regions where separation occurred at the bond-coat/TGO interface, and those where the separation occurred between TGO and top-coat.

An extension of the above methodology was applied to quantify the relative proportions of stable and transient aluminas [F, G]. The technique was applied to study the effect of surface preparation on the residual stress in the TGO [G]. Considerably different levels of residual stress were detected in (Ni,Pt)Al surfaces with two different finishes. The different stresses were ascribed to differences in the transformation kinetics of the initial TGO, and the grain size of the resulting alumina. It was established that PSLS affords a quantitative and non-destructive method of monitoring the (stable/transient alumina) phase composition of the TGO and could be developed as a tool for quality control and TBC deposition process control.

A third area of activity focused on ascertaining the stress distributions in the TGO around holes and edges, and their evolution during thermal cycling. This activity sought to establish a database for use in design and to develop analytical expressions that can be used to model stress distributions around features, such as cooling holes. In the long-term, the objective is to obtain information on the *in-situ* mechanical properties of the bond-coat (notably its yield strength and relaxation). The stress distributions in the TGO around holes and edges were determined for a number of alloys and TBC coated samples using PSLS. A complementary study of stress relaxation in oxidized FeCrAl(Y) during thermal cycling was undertaken. This work has identified that stress relaxation in this alloy occurs above 850^{o}C and that the mechanism of stress relaxation depends on the relative alloy/oxide thickness. Surprisingly, it was also shown that there are thermal-cycling conditions under which the TGO goes into tension and can crack in tension at high temperature. This is counter-intuitive because stress relaxation is generally considered a mechanism for reducing failure. However, there are conditions of stress relaxation on cooling that lead to the TGO being driven into tension on subsequent re-heating. This is obvious importance for both the life of the TGO and as a possible mechanism for crack initiation in the BC.

The potential of PSLS as a tool for monitoring damage during service and predicting residual life was also explored. Experiments on a large airfoil provided by Siemens-Westinghouse revealed substantial degradation of the PSLS signal when the TBC is coated with certain types of deposits, notably Fe oxides. The challenges in this application are substantial and will be the subject of further research.

INDUSTRIAL INTERACTIONS

Strong and fruitful collaboratioins with industry were established during the course of the program. These involved primarily Siemens-Westinghouse, Solar Turbines, General Electric (CRD, Aircraft Engines and Power Systems) and Howmet (Termatech). Additional interactions were also established with UTRC/Pratt & Whitney, Praxair, RR-Allison, ABB/Alstom, Chromalloy and Cannon Muskegon. Advice, enthusiastic support and valuable input on the industrial TBC experience resulted from visits of the PI s to these companies. In addition, the industrial collaborators provided different types of materials and specimens in support of the research. Collaborations with NIST, Argonne National Lab, DLR and the European Research Center in Petten were also beneficial to the program. .

A salient point of the outreach activity was the first AGTSR Materials Workshop with the theme Mechanism Based Life Prediction for Thermal Barrier Coatings organized by the PI s and D. Fant, and held at UCSB on January 6-8, 1999. The workshop had approximately 70 participants from 40 different organizations and involved very substantial and insightful discussion of the outstanding issues in the problem of TBC life prediction. A team integrated with participants in the workshop and led by the PI s developed a position paper on Coatings for Advanced Gas Turbines to assist DOE/FETC in the planning of the NGT program This paper included not only an analysis of research needs for TBCs, but also for Environmental Barrier Coatings for ceramics (EBCs).

APPENDICES

A. J. W. Hutchinson, M.Y. He and A.G. Evans: The influence of Imperfections on the Buckling Driven Delamination of Thin Compressed Films, *Journal of the Mechanics and Physics of Solids* **48** (2000) 709-734.

B. A.G. Evans, J.W. Hutchinson and M.Y. He: Micromechanics Model for the Detachment of Residually Compressed Brittle Films and Coatings, *Acta Materialia*, **47** [5] 1513-22 (1999).

C. M. Y. He, A. G. Evans and J. W. Hutchinson: The Ratcheting of Compressed Thin Films on Ductile Substrates, *Acta Materialia* **48** (2000) 2593-2601.

D. A.G. Evans, M.Y. He and J.W. Hutchinson: Mechanics-based scaling laws for the durability of Thermal Barrier Coatings, Progress in Materials Science **46** (2001) 249-271.

E. A.G. Evans, D.R. Mumm, J.W. Hutchinson, G.H. Meier and F.S. Pettit: Mechanisms controlling the durability of thermal barrier coatings, Progress in Materials science **46** (2001) 505-553

F. D.R. Clarke, V. Sergo and M-Y. He: Precursor to TBC Failure Caused by Constrained Phase Transformation in the Thermally Grown Oxide, in *Elevated Temperature Coatings: Science and Technology III*, ed. by J.M. Hampikian and N.B. Dahotre (TMS, Warrendale, PA, 1999), pp. 67-78.

G. V.K. Tolpygo and D.R. Clarke: Microstructural Study of the Theta-to-Alpha Transformation in Alumina Scales Formed on Nickel-Aluminides, *Materials at High Temperatures,* **17** [1] (2000) 59-70.

H. E.A.G. Shillington and D.R. Clarke: Spalling Failure of a Thermal Barrier Coating Associated with Aluminum Depletion in the Bond Coat , *Acta Materialia* **47** [4] 1297-1305 (1999).

I. V.K. Tolpygo and D.R. Clarke: Surface rumpling of a (Ni,Pt)Al Bond Coat Induced by Cyclic Oxidation, Acta Materialia **48** (2000) 3283-3293.

J. X. Peng and D.R. Clarke: Piezospectroscopy Analysis of Interface Debonding in Thermal barrier Coatings , *Journal of the American Ceramic Society*, **83** [5] (2000) 1165-70.

K. S.G. Terry, J.R. Litty and C.G. Levi: Evolution of Porosity and Texture in Thermal Barrier Coatings Grown by EB-PVD, in *Elevated Temperature Coatings: Science and Technology III*, ed. by J.M. Hampikian and N.B. Dahotre (TMS, Warrendale, PA, 1999), pp. 13-26.

Appendix A

PERGAMON

Journal of the Mechanics and Physics of Solids
48 (2000) 709–734

JOURNAL OF THE MECHANICS AND PHYSICS OF SOLIDS

www.elsevier.com/locate/jmps

The influence of imperfections on the nucleation and propagation of buckling driven delaminations

J.W. Hutchinson[a,*], M.Y. He[b], A.G. Evans[a]

[a]*Division of Engineering and Applied Sciences, Harvard University, Cambridge, MA 02138, USA*
[b]*Materials Department, University of California, Santa Barbara, CA 93106, USA*

Received 17 March 1999; received in revised form 5 July 1999

Abstract

The influence of prototypical imperfections on the nucleation and propagation stages of delamination of compressed thin films has been analyzed. Energy release rates for separations that develop from imperfections have been calculated. These demonstrate two characteristic quantities: a peak that governs nucleation and a minimum that controls propagation and failure. These quantities lead to two separate criteria that both need to be satisfied to cause failure. They involve a critical film thickness for nucleation and a critical imperfection wavelength for buckling. Implications for the avoidance of failure are discussed.

Keywords: A. Buckling; Crack propagation and arrest; Fracture toughness; B. Coatings; Films; C. Finite elements; Stability and bifurcation

1. Introduction

Compression in a film on a substrate can arise during the deposition process or due to temperature change when there is thermal expansion mismatch, or due to a combination of the two. Ceramic films or coatings on metal substrates will

* Corresponding author. Tel.: +1-617-495-2848; fax: +1-617-495-9837.
E-mail address: hutchinson@husm.harvard.edu (J.W. Hutchinson).

0022-5096/00/$ - see front matter
PII: S0022-5096(99)00050-2

generally be in compression at room temperature if the film is deposited at high temperature. Oxidation and thermal barrier coatings are important examples receiving attention at the present time. These are multilayer systems consisting of at least one fully dense oxide layer (e.g. Al_2O_3) grown at high temperature on a bond coating applied to the metal alloy substrate. The oxide layer is subject to very large compressive stress when the system is cooled. Various failure modes have been observed, but one of the most common is cracking at the oxide/bond coat interface leading to buckling delamination and spalling.

Two competing failure mechanisms have been documented for compressed thin films (Evans and Hutchinson, 1995; Gioia and Ortiz, 1997; Hutchinson and Suo, 1992; Hutchinson et al., 1992; Nilsson and Giannakopoulos, 1995; Thouless et al., 1994; Wang and Evans, 1998). They comprise edge and buckle driven delamination (Fig. 1). In this paper the emphasis will be on buckling delaminations, but in this Section results for edge-delamination will be cited as background to understand the primary issue of the initial flaw size needed to nucleate failures. Films subject to an equi-biaxial compressive stress state, σ_0, will be considered. When thermal expansion misfit is responsible for the residual compression, with a thick substrate having a higher coefficient of thermal expansion than the film, $\Delta\alpha > 0$, σ_0 is given by

$$\sigma_0 = E\Delta\alpha\Delta T/(1-\nu) \tag{1}$$

when ΔT is drop in temperature from the state where the film is stress-free. Here, and throughout, E and ν are the Young's modulus and Poisson's ratio of the film. The elastic energy per unit area stored in the attached film is $(1-\nu)h\sigma^2/E$, where h is the film thickness. The energy per unit area which becomes available when the film is released from the substrate in a way such that it is still subject to a constraint of in-plane plane strain is

$$G_0 = \frac{(1-\nu^2)h\sigma_0^2}{2E} \tag{2}$$

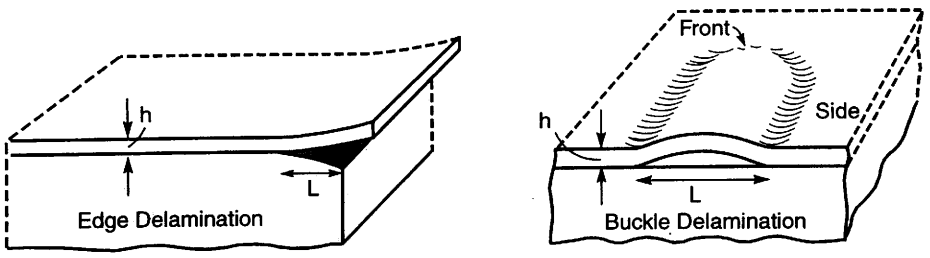

Fig. 1. Two prevalent delamination mechanisms for compressed films and coatings: edge delamination and buckledriven delamination. The buckle delamination is shown spreading from an edge to reveal the separation, but in most instances they initiate in the interior of the film away from any edges.

It will be seen that G_0 figures prominently in the energy release rates for both edge and buckle delaminations.

1.1. Edge delaminations

An initial edge flaw in the interface between film and substrate of sufficient magnitude can serve to nucleate an edge delamination which spreads as a plane strain interface crack (Fig. 1). For a film in compression, the interface crack is in mode II such that the faces remain in contact behind the advancing tip (Hutchinson and Suo, 1992). Under the idealized assumption that frictional sliding plays a negligible role, the steady-state energy release rate of the crack when its length is several times the film thickness is given by Eq. (1): i.e. $G=G_0$. Thus, if the mode II toughness of the interface is Γ_i^{II} (measured in units of energy per unit area), then the critical combination of film stress and thickness at which the edge-delamination can spread without arrest is

$$\sigma_0 = \sqrt{\frac{2E\Gamma_i^{\mathrm{II}}}{(1-\nu^2)h}} \tag{3}$$

Any frictional interaction of the crack faces will consume some of the energy stored in the film, and therefore Eq. (3) is necessarily an underestimate of the critical stress or film thickness.

The size of the interface edge flaws needed to nucleate a propagating edge-delamination are relatively small, generally on the order of several film thicknesses. This point is revisited after the size of flaws needed to initiate buckling delaminations has been discussed.

1.2. Buckling delamination

A buckling index is conveniently defined as

$$\Pi = (1-\nu^2)(\sigma_0/E)(L/h)^2 \tag{4}$$

Throughout the paper both plane strain and axisymmetric delaminations will be considered to show that the behavioral features of interest are common to both. It will be convenient to let L denote both the width of the separation in plane strain and the diameter of a separation for axisymmetric geometries. For buckling to initiate Π must exceed a critical value Π_c. For a plane strain buckle, $\Pi_c=\pi^2/3=3.29$, and for a circular buckle, $\Pi_c=4.89$. The buckling condition may be re-expressed in terms of the width or diameter of the delamination L_b at the *onset* of buckling. This is accomplished upon equating L to L_b and Π to Π_c in Eq. (4), such that

$$L_b/h = 1.81\sqrt{\bar{E}/\sigma_0}\ \text{(plane strain)} = 2.21\sqrt{\bar{E}/\sigma_0}\ \text{(axisymmetric)} \tag{5}$$

where $\bar{E}$ is the plane strain modulus of the film, $\bar{E}=E/(1-\nu^2)$. These lengths represent the smallest interface separations which give rise to buckling delaminations absent any imperfections. For typical moduli and film compression levels, L_b will be about 20 h or more. These relatively large interface flaws motivate the present investigation into the role of imperfections on the nucleation of buckling delaminations.

Energy release rates, G, and mode mixities, $\psi=\tan^{-1}(K_{II}, K_I)$ (where K_I and K_{II} are the mode I and II interface stress intensity factors), have been determined for plane strain and circular buckle delaminations by Hutchinson and Suo (1992) and Hutchinson et al. (1992). Plots of G/G_0 and ψ as a function of L/L_b are presented in Fig. 2 for circular delaminations. The energy release rate increases as the buckle spreads to sizes larger than L_b, while the relative proportion of mode II to mode I increases sharply.

The mode-dependence of the interface toughness $\Gamma_i(\psi)$ plays a critical role in determining the sequence of events in the propagation of the delamination. The following phenomenological interface toughness is adopted to model the dependence (Hutchinson et al., 1992)

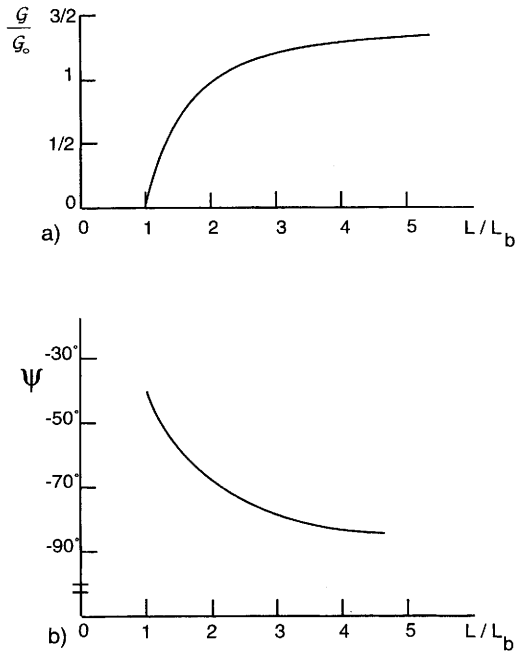

Fig. 2. Normalized energy release rate and mode mixity at the interface crack edge for circular delaminations of diameter L. For a given pre-compression σ_0, L_b defined in Eq. (5) is the smallest diameter for which the film will buckle in the absence of an imperfection. ($\nu=1/3$ and no elastic mismatch between film and substrate in the determination of ψ.)

$$\Gamma_i/\Gamma_i^{\mathrm{I}} = 1 + \tan^2(1-\lambda)\psi \tag{6}$$

where Γ_i^{I} is the mode I toughness and λ is a mixity index lying between 0 and 1. The interface toughness is mode independent in the limit $\lambda = 1$. Representative values of λ for metal–ceramic interfaces generally have $\lambda < 0.3$. The criterion for the buckle delamination to grow is $G = \Gamma_i(\psi)$, which can be implemented using the results for G and ψ from Fig. 2 along with Eq. (6). Curves along which the criterion is satisfied for circular delaminations are plotted in Fig. 3 for four values of λ. The corresponding curves for plane strain delaminations are qualitatively similar. The curves may be interpreted in the following way. Suppose an initial separation of diameter L_0 exists at the interface, and let the compressive stress in the film, σ_0, increase from zero. Two trajectories prior to propagation are illustrated as dashed curves emanating from the origin in Fig. 3, with the one connecting to A having a smaller L_0 than that connecting to B. (Note that on the dashed trajectories, $L/L_b \equiv L_0/L_b$ increases from zero because of the dependence of L_b on σ_0 in Eq. (5).) The condition for propagation is met when the dashed trajectory intersects the solid curve, which in Fig. 3 is illustrated for $\lambda = 0$. If the intersection occurs on a falling portion of the curve, as in the case at A, any perturbed growth of the delamination will result in a state lying above the propagation criterion such that advance will occur dynamically at fixed stress until it arrests at A'. It will then grow stably under increasing stress. For larger initial separations, represented by the intersection at B, the advance is stable from the start with the delamination growing under increasing stress. Experimental observations and measurements have fully confirmed the two types of delamination growth: for a model system of mica bonded to an aluminum

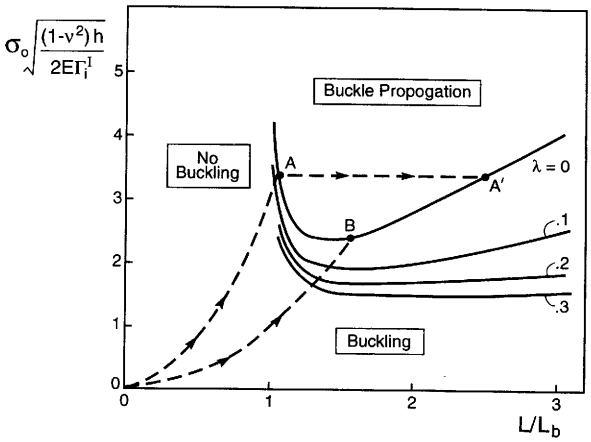

Fig. 3. A buckling map for a compressed film absent imperfections, with an initial separation, diameter L, at the interface. The sequence of steps in the delamination process are described in the text. ($\nu = 1/3$ and no elastic mismatch between film and substrate in the determination of ψ.)

substrate (Hutchinson et al., 1992) and for a thermally grown oxide film (Al_2O_3) on a Ni superalloy substrate with a bond coat (Wang and Evans, 2000).

The limitation at this level of analysis is that the failure process cannot be activated until an interface separation has formed large enough to cause buckling (namely, $L_0 \geq L_b$). As already noted this requires, typically, $L_0 \approx 20\ h$. Mechanisms responsible for creating separations this large have not been addressed, except in a qualitative manner for thermal barrier coating systems (Christensen et al., 1997; Evans et al., 1998; He et al., 1998; Wang and Evans, 1998, 2000). The intent of this article is to establish some of the mechanics relevant to this *nucleation stage of failure*. One consequence will be a modified buckling map that incorporates nucleation and more fully represents the buckling behavior found in practice. At this point it is also instructive to note from Eq. (2) that the energy required to drive a steady-state edge delamination is comparable to that for buckling delamination. Moreover, the size of an initial interface separation at the edge needed to initiate a propagating edge delamination is much smaller than 20 h. The question naturally arises as to why edge delaminations are far less commonly observed as failure modes of compressed films than buckle delaminations. Part of the answer undoubtedly lies in the fact that edge delaminations are controlled by the mode II interface toughness (cf Eq. (3)) and must overcome frictional effects, if present. Although unresolved, the issue highlights the importance of understanding how interface separations much smaller than 20 h must in some way be able to nucleate buckle delaminations.

Two prototypical imperfections responsible for nucleation of interface separations in thermal barrier coatings have been proposed in the references cited above (Fig. 4): undulations and morphological heterogeneities. Both have the underlying feature that they locally redistribute the residual stress such that tensions develop normal to the interface (Evans et al., 1998; He et al., 1998), as illustrated in Fig. 4. These tensions provide the motivation for interface separations to nucleate and propagate. An analogous nucleation mechanism exists at the interface between particles in ceramic matrices driven by thermal expansion mismatch (e.g. Ito et al., 1981).

It has been possible to observe these processes in thermally grown thin films of α-Al_2O_3 (TGO) formed on Ni-based bond coat alloys, because of the translucency of the oxide and the large reflectivity changes where the interface separates (Christensen et al., 1997; Tolpygo and Clarke, 1998; Wang and Evans, 1998, 2000). However, a mechanics analysis of this phenomenon and its implications for buckling delamination have yet to be provided. The intent of this article is to develop such an analysis and to use the results to establish the characteristics of imperfections that nucleate separations large enough to induce buckling and failure. Such results identify a *critical imperfection size* needed to activate the failure process.

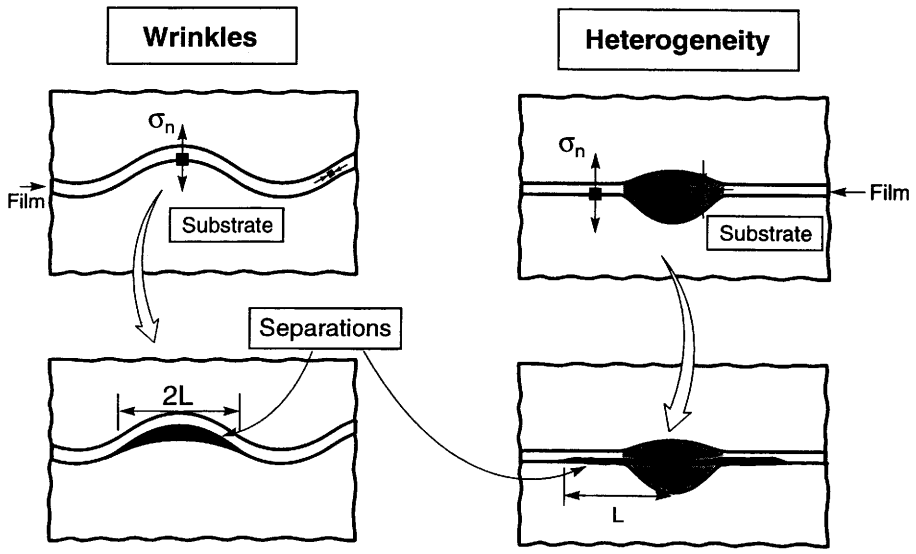

Fig. 4. Two types of imperfections that nucleate interface separations at the interface between the dense ceramic layer (usually a form of Al_2O_3) and the metallic bond coating in multilayer thermal barrier coatings.

2. Basic concepts

2.1. Role of imperfections

Previous analyses of interface separations emanating from imperfections (Evans, 1972; Evans et al., 1998; Rühle et al., 1987; Green, 1982; He et al., 1998; Ito et al., 1981; Shum and Huang, 1990) have revealed that, absent buckling, the energy release rate G exhibits a peak G_{peak} and thereafter asymptotically approaches zero (Fig. 5). Specific results are presented in Section 4. The consequence is that small flaws located near the regions of greatest tension can be activated, resulting in cracks that "pop-in" and arrest. Their size is governed by the declining portion of the energy release rate, with arrest occurring where G becomes coincident with the fracture toughness, Γ_i. This is the behavior identified on Fig. 5 as the *nucleation phase* of film failure.

As the separation becomes longer, it reaches a size large enough to buckle ($L \cong L_b$). When this happens, the energy release rate increases again, and approaches a value on the order of G_0. This is the behavior identified on Fig. 5 as the *propagation phase*. Specific results are presented in Section 4.

The convolution of the opposing trends in G for nucleation and propagation results in a minimum, designated $G_{\min}$. This minimum is one of the predominant

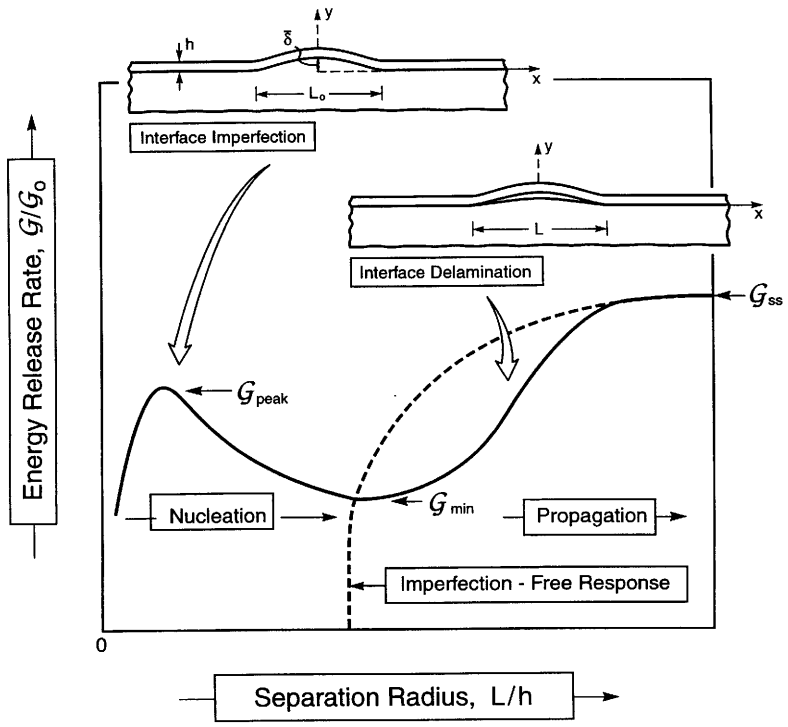

Fig. 5. A schematic of variations in energy release rate with separation width or diameter for the nucleation and propagation phases of failure. The critical quantities $G_{\min}$ and G_{peak} are identified.

features governing film failure. Once $G_{\min}$ attains Γ_i, the buckle propagates and reaches a size readily observable by optical microscopy.[1]

One objective is to characterize G_{min} *and to explore its potential as a failure criterion for compressed thin films. A second is to establish trends in* G_{peak} *relevant to nucleation.*

2.2. Buckling at imperfections

The influence of imperfections on film buckling is addressed at two levels. Analytical results are presented for a two-dimensional geometry, subject to plane strain. The localized imperfections are in the form of undulations having characteristic widths much smaller than the size of a buckled delamination (Fig.

[1] The subsequent approach to failure is dictated by effects of mode mixity and interface friction, discussed elsewhere (e.g. Wang and Evans, 1998).

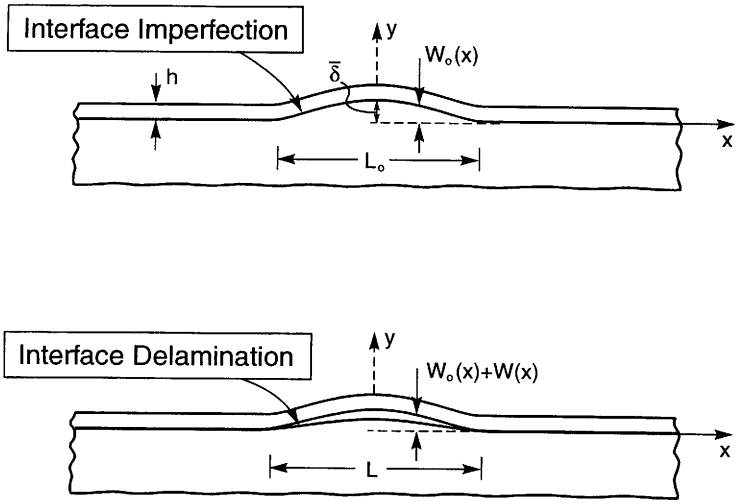

Fig. 6. A schematic of the undulation imperfection considered in the present analysis.

6). Corresponding results for axisymmetric buckles are analyzed numerically, using key insights from the analytical formulae both to establish the scope and to provide scaling relationships.

For the plane strain problem, the undulation, $w_0(x)$, is taken to be symmetric about $x = 0$. The film is otherwise uniform. Under restrictions that the maximum slope of the undulation should not exceed about 20° and that the film thickness is small compared with the delamination width, the von Karman nonlinear plate equations incorporating the imperfection can be used to describe the behavior of the delaminated film. These equations are equivalent to the nonlinear shallow shell equations (Koiter, 1966). They apply both when the delamination is too small to buckle (whereupon propagation is driven by the undulation), as well as when the debonded region is large enough to experience buckling driven delamination. Under the same conditions required for applicability of the Karman equations, the prestress in the attached film due to thermal expansion mismatch can be taken to be uniform and independent of the imperfection amplitude.[2]

The imperfection produces tensile stresses acting across the interface at points where w_0'' is negative. It is these stresses which promote imperfection-driven delamination (Fig. 4). As the delamination spreads into regions where w_0'' is positive, the compressive stress across the interface retards interface crack propagation, diminishing the energy release rate significantly (Fig. 5).

With the width of the delamination as L, the governing equations for $|x| \leq L/2$

[2] Neglecting terms of order $w_0'^2$ compared to unity.

can be reduced to the following system:

$$Dw'' + \sigma h w = -\sigma h w_0 + M^A \tag{7}$$

$$\sigma = \sigma_0 - \frac{\bar{E}}{L}\int_0^{L/2} (w'^2 + 2w_0' w')\mathrm{d}x \tag{8}$$

where $(\,)' = \mathrm{d}(\,)/\mathrm{d}x$, $\bar{\mathrm{E}} = \mathrm{E}/(1-\nu^2)$, $D = \bar{\mathrm{E}}h^3/12$. The term

$$M^A \equiv Dw''(L/2) + \sigma h w_0(L/2) \tag{9}$$

is an unknown quantity to be determined as part of the solution. The average stress in the x-direction in the detached film, σ, is independent of x. It is determined by condition (8) which has been obtained from the requirement that the component of displacement in the x-direction is zero at the end of the delamination. The boundary conditions accompanying Eqs. (7) and (8) are the symmetry condition at $x = 0$ and the clamped condition at $x = L/2$:

$$w'(0) = 0, \quad w(L/2) = 0, \quad w'(L/2) = 0 \tag{10}$$

The imperfection used in most of the numerical studies comprises a single wave having the shape (Fig. 6):

$$w_0 = \frac{\bar{\delta}}{2}\left(1 + \cos\ \frac{2\pi x}{L_0}\right) \quad |\,x\,| \leq \frac{L_0}{2}$$

$$= 0 \quad |\,x\,| \geq \frac{L_0}{2} \tag{11}$$

Application of the von Karman equations requires that the maximum slope of the imperfection not exceed about 1/5, limiting the amplitude of the imperfection to approximately $\delta \leq L_0/10$. A family of extended imperfections (Fig. 7) illustrates barriers to delamination spreading:

$$w_0 = \frac{\bar{\delta}}{2}\left(1 + \cos\ \frac{2\pi x}{L_0}\right)\mathrm{e}^{-(x/L_\mathrm{D})^2} \tag{12}$$

where L_D is a decay length illustrated on Fig. 7.

The two quantities determining the propagation of the interface crack are G and ψ. These are determined from the solution to the governing equations using (Hutchinson and Suo, 1992):

$$G = \frac{h}{2\bar{E}}[(\sigma_0 - \sigma)^2 + 12(M(L/2)/h^2)^2] \tag{13}$$

$$\tan\ \psi = \frac{\sqrt{12}(M(L/2)/h^2) + (\sigma_0 - \sigma)\tan\ \omega}{-\sqrt{12}(M(L/2)/h^2)\tan\ \omega + (\sigma_0 - \sigma)} \tag{14}$$

where $M(L/2) = Dw''(L/2)$ is the moment at the right end of the delamination. Elastic mismatch between the film and substrate has some influence on the mode mixity, through ω. Here, the second Dundurs' mismatch parameter has been taken to be zero. The dependence of ω on the first parameter, $\alpha_D = (\bar{E} - \bar{E}_s)/(\bar{E} + \bar{E}_s)$, is specified in Hutchinson and Suo (1992). When there is no mismatch, $\omega = 52.1°$.

For the single wave imperfection, Eq. (11), Eqs. (7) and (10) can be solved in closed form, with σ as an unknown variable. Then Eq. (8) can be reduced to a single algebraic transcendental equation for σ, completing the solution. The resulting equation for σ must be solved numerically for each set of parameters, except in some special instances. Then, G and ψ are evaluated using Eqs. (13) and (14).

For extended imperfections, Eq. (12), Eq. (7) requires numerical integration in addition to a numerical solution procedure for σ. Further details are given in Appendix A.

In the following Sections, the preceding formulae are used to analyze various effects of imperfections on plane strain buckling and buckle propagation. Corresponding results for axisymmetric buckles are determined numerically. For this purpose, axisymmetric separations are introduced at the interface and the energy release rate, G, as well as mode mixity angle, ψ, calculated as a function of the separation diameter, L, using procedures described elsewhere (Evans et al., 1998; He et al., 1998). The commercial finite element code ABAQUS was

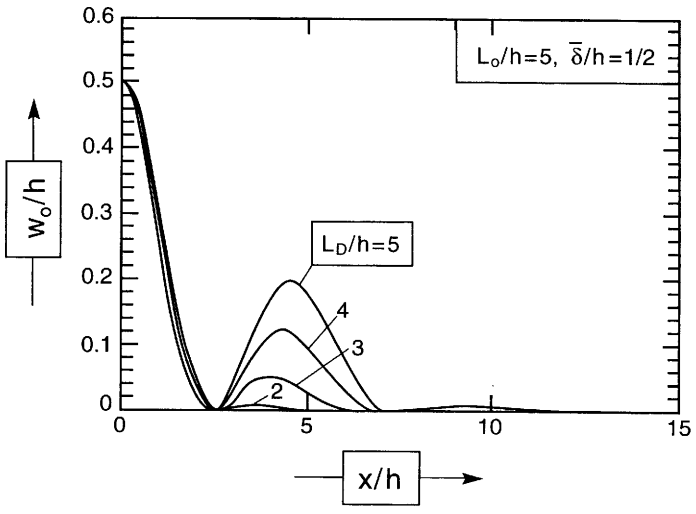

Fig. 7. The shapes of the extended imperfection used in the analysis.

implemented in the nonlinear mode with updated geometry and employing eight-noded axisymmetric elements with five to ten elements through the thickness. For the small imperfection cases, most computations were carried out using a finite element mesh to represent the substrate. For larger detachments, most examples were run taking the attached portions of the film to be rigidly supported along the bottom surface. In general, there was little difference in the predictions obtained from these two ways of supporting the film.

3. Initial buckling

3.1. Asymptotic behavior at small imperfections

The influence of imperfections on initial buckling, expressed in terms of the induced energy release rates, are examined in order to assess the imperfection-sensitivity. This is done by imposing the initial condition that the separations be large enough to satisfy buckling in an imperfection-free film, $L=L_b$. Analytical results are provided for plane strain delaminations as well as numerical results for axisymmetric imperfections. The analytical results are asymptotically valid at small imperfection amplitudes. They are based on Koiter's asymptotic theory of post-buckling and imperfection-sensitivity for elastic structures (Koiter, 1945). A more extensive study of the role of small imperfections on buckling delamination has been conducted by Storåkers and Nilsson (1993), and thus only the outcome of the analysis will be presented here.

For $L=L_b$ the buckling mode from Eq. (4) with $w_0=0$ is

$$w = (b/2)[1+\cos(2\pi x/L)], \quad |x| \le L/2 \tag{15}$$

where b is the buckling deflection amplitude. For sufficiently small imperfections, the deflection of the film above the separation satisfies:

$$\frac{b}{h} = \frac{\sigma}{\sigma_0 - \sigma} k \tag{16}$$

with

$$k = 8\int_0^{L/2} (w_0/h)\cos(2\pi x/L)\mathrm{d}x$$

being a function of δ/h and L_0/L. Moreover, in Eq. (8) the term w'^2 is large compared to $w_0'w'$ when δ/h is small such that

$$1-\sigma/\sigma_0 = 3(b/h)^2/4 \tag{17}$$

The preceding two equations can be solved for b and σ/σ_0 in terms of k. For sufficiently small δ/h, the asymptotic relations are

$$b/h = (4k/3)^{1/3} \quad \text{and} \quad 1 - \sigma/\sigma_0 = (\sqrt{3}k/2)^{2/3} \tag{18}$$

The limiting relation for the energy release rate from Eq. (13) is

$$G/G_0 = 3(4k/3)^{2/3} \tag{19}$$

where G_0 is given by Eq. (2).

Because k is proportional to the imperfection amplitude δ, Eq. (19) dictates that, when the imperfections are sufficiently small, the energy release rate scales as; $G \sim \delta^{2/3}$. The 2/3 power law magnifies the effect of small imperfections, producing an unusually large increase in G. Moreover, in the special case where the imperfection is in the shape of the buckling mode with $L = L_0 = L_b$, $k = \delta/h$, revealing that small imperfections have an exceptionally large influence. It must again be noted that the asymptotic result, Eq. (19), is limited to behavior in the vicinity of the onset of buckling, i.e. $L \cong L_b$.

3.2. Numerical results

The imperfection sensitivity of buckling for "large" imperfections has also been calculated, numerically, for axisymmetric buckles (Fig. 8). These results were determined for axisymmetric undulations in the same form as Eq. (11) with diameter L_0 taken to be equal to the diameter of the delamination L. Again, the notable feature is that appreciable energy release rates develop when the delamination diameter is a fraction of the diameter for the onset of buckling for

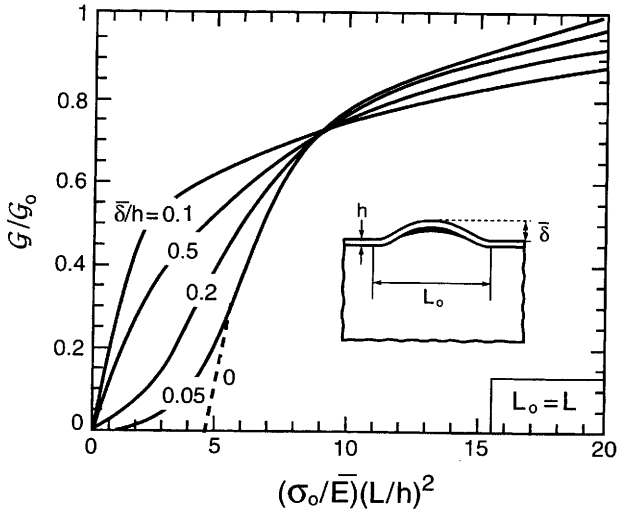

Fig. 8. The imperfection sensitivity of the energy release rate in the presence of an axisymmetric imperfection undulation whose diameter is equal to the diameter of the separation. Note the significant elevation of the energy release rate at separation diameters which are much smaller than onset of buckling for the perfect system (i.e. $(\sigma_0/\bar{E})(L/h)^2 = 4.89$).

the perfectly flat film, as has also been documented by Storåkers and Nilsson (1993). For example, when the imperfection amplitude is only, $\delta/h = 1$, a significant energy release rate develops even at delamination diameters which are only 1/3 the onset value.

4. Buckle propagation

4.1. Single wave imperfections

To highlight the strong nonlinear coupling between relatively small size imperfections and buckling delaminations, results will first be presented for *decoupled imperfection driven and buckle driven delamination* in plane strain. The buckling mode is given by Eq. (15).

An example, presented in Fig. 9, illustrates the behavior. It applies to the following set of parameters:

$$\frac{\sigma_0}{\bar{E}} = 0.005 \left(\frac{L_b}{h} = 25.7\right), \quad \frac{L_0}{h} = 5\left(\frac{L_0}{L_b} = 0.195\right), \quad \bar{E}_s = \bar{E}(\alpha_D = 0)$$

To decouple the two effects, first the imperfection is taken to be zero for buckling delamination, and thereafter, for the imperfection driven delamination, the

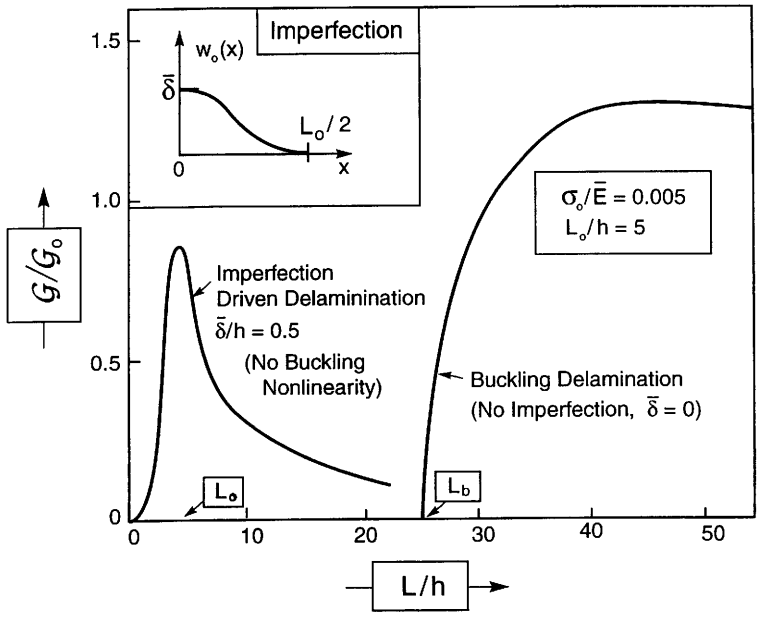

Fig. 9. Decoupled energy release rates associated with nucleation and buckle-driven delamination at plane strain undulations.

nonlinear deflections are deleted. When this is done (Fig. 9), it is found that, when the wavelength of the imperfection, L_0, is small compared with the onset buckling wavelength, $L_b(L_0/L_b=0.195)$, there is little overlap in the energy release, with G dropping to a small value well before the delamination is large enough to be driven by buckling. These decoupled results affirm that there exists a major barrier impeding propagation of the delamination much beyond the width of the imperfection itself.

The coupled results determined with the full nonlinear equations (Fig. 10a and b), indicates a very different picture, similar to that anticipated on Fig. 5. Now, while the energy release rate decreases as the delamination spreads beyond the imperfection, it begins to increase again well before its length attains L_b. As already noted (Section 3), the influence of the imperfection is particularly dramatic for separation widths $L \approx L_b$, even though the imperfection width is less than $L_b/5$.

The mode mixity ψ at the right hand tip of the interface delamination is plotted in Fig. 11. There is significant variation in ψ depending on both imperfection level and delamination width. This variation exerts an important influence on the spread of the delamination. Note that sufficiently wide buckling-driven delaminations always approach mode II conditions (at $L/h \approx 60$ in this example). The relative proportion of mode II is less for delaminations with curved fronts. For this reason, delaminations tend to arrest at a characteristic width and then continue spreading along their front (Hutchinson and Suo, 1992).

The strong interaction of the two types of delamination with disparate wavelengths is a consequence of nonlinear coupling. In Fig. 10a the imperfection width is only about one fifth the width of the onset buckle, yet there is strong coupling, such that G_{min} is well above zero. For a somewhat longer imperfection, but still short compared to L_b (Fig. 10b), the peak is about the same, but the minimum is even larger. Accordingly, nucleation conditions are similar, but propagation is facilitated.

To elaborate on nucleation and the barrier to propagation, plots of G_{peak}/G_0 and G_{min}/G_0 in plane strain are presented in Fig. 12, as a function of L_0/L_b, for two imperfection amplitudes. *Presented this way, the results are independent of* $\sigma_0/\bar{E}$, *as shown in Appendix A*. This feature suggests introduction of another non-dimensional index, referred to as the imperfection size index, $\mathscr{R}$. It is given by:

$$\begin{aligned}\mathscr{R} &= (L_0/L_b)^2 = 0.305(\sigma_0/\bar{E})(L_0/h)^2 \text{ (plane strain)}\\ &= 0.204(\sigma_0/\bar{E})(L_0/h)^2 \text{ (axisymmetric)}\end{aligned} \tag{20}$$

The general form of the minimum is:

$$G_{min}/G_0 = F[L_0/L_b, \bar{\delta}/h] \tag{21}$$

where F is a function which could be obtained by fitting to Fig. 12. Note, however, that the dependence on L_0/L_b is essentially linear and the dependence on

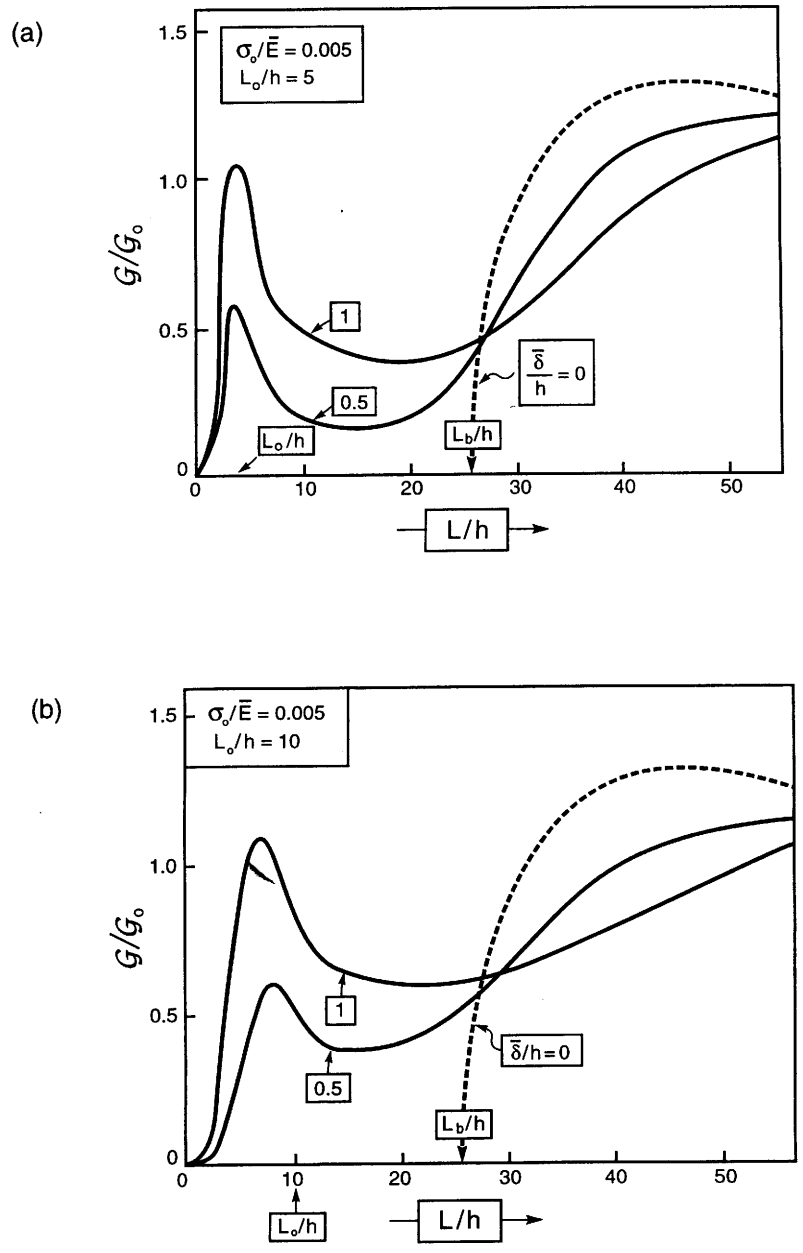

Fig. 10. Energy release rates for plane strain undulations demonstrating the coupling between small imperfections and large buckling deflections: (a) $L_0/L_b=0.195$ (b) $L_0/L_b=0.39$.

δ/h is weak: features also found below for axisymmetric imperfections. Consequently, Eq. (21) can be approximated by:

$$G_{\min}/G_0 \cong c(L_0/L_b) \tag{22}$$

where c is in the range 0.8 to 1.0 (Fig. 12) for imperfections amplitudes in the range $0.5 < \delta/h < 1$. This result and its axisymmetric analog are used in Section 5 to evaluate a critical imperfection wavelength for buckle propagation.

4.2. Extended imperfections

Extended oscillatory interface imperfections can trap a nascent delamination in regions where w_0'' is positive. The family of imperfections plotted in Fig. 7 provides an illustration of this effect. The nominal width of each undulation is taken to be $L_0/h = 5$. Numerical results for the energy release rate are shown in Fig. 13 as a function of the delamination width, for four imperfection shapes. The peak, G_{peak}, is insensitive to the decay length, L_D, but the minimum, $G_{\min}$, is a strong function of L_D. For $L_D/h = 2$, the behavior is similar to that shown in Fig. 10a for the single imperfection having the same amplitude ($\delta/h = 1/2$). However, at larger L_D/h, trapping becomes a dominant feature, resulting in low $G_{\min}$. An imperfection with $L_D/h = 5$ results in $G_{\min}/G_{\text{peak}} \approx 1/10$.

Two-dimensional variations of the surface imperfections may well provide opportunities for the delaminations to spread around such "traps". Nevertheless,

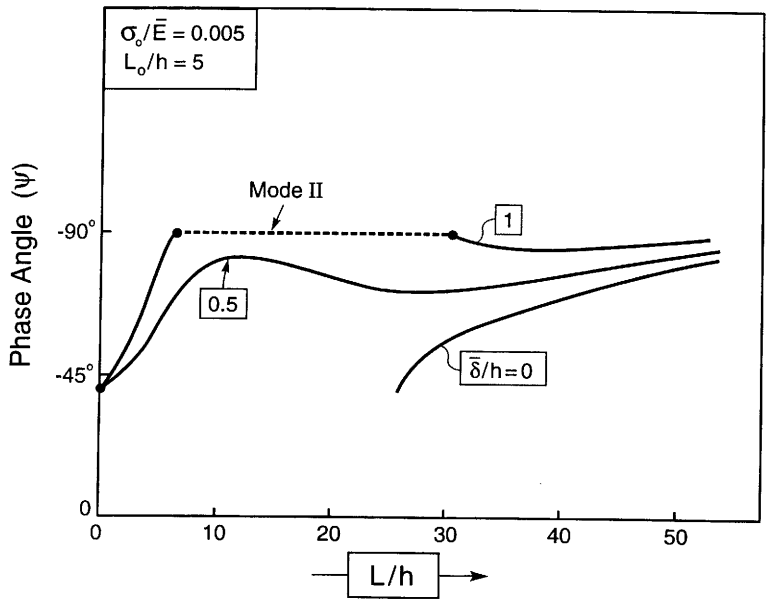

Fig. 11. Variation in mode mixity angle with separation length for a plane strain buckle.

the limited one-dimensional study presented here indicates that the nonlinear coupling between small imperfection-driven delaminations and the larger buckling-driven delaminations depends on details of the imperfection shape. The strong coupling can be defeated by undulations which trap the delaminations while they are still small.

4.3. Axisymmetric imperfections

Energy release rate results for axisymmetric undulations have been obtained numerically for a range of undulation wavelengths and amplitudes. Typical results are presented on Fig. 14 for a range of the imperfection size index, Eq. (20) between 0.12 and 0.6. The features anticipated schematically on Fig. 5 are again apparent.

The analytical results assert that when L_0/L_b is used as the abscissa, G_{min}/G_0 should be independent of the residual strain, $\sigma_0/\bar{E}_f$. This dependence is

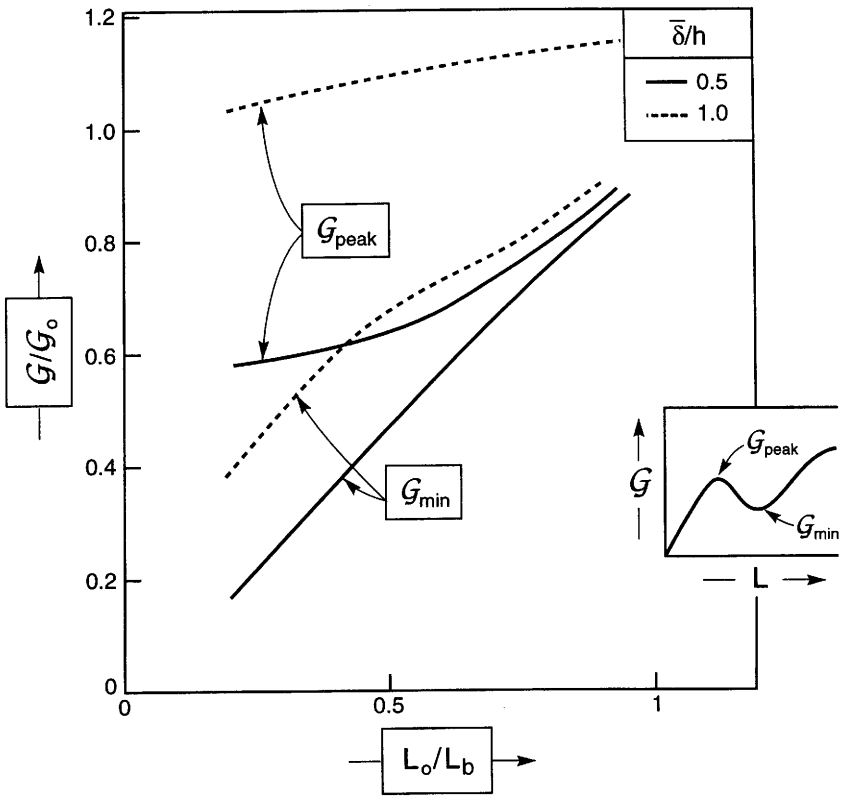

Fig. 12. Non-dimensional plots illustrating the dependence of the peak and minimum energy release rates in plane strain on the relative undulation wavelength L_0/L_b.

demonstrated on Fig. 15a. A fit to these results in the range $0.5 < L_0/L_b < 1$ has the same form found for plane strain delaminations, Eq. (22):

$$G_{\min}/G_0 \cong c(L_0/L_b) \tag{23}$$

where now $c \cong 0.4$. Note that there is minimal effect of the undulation amplitude, even less than that for plane strain delamination (Fig. 12).

5. Critical conditions

5.1. Buckle propagation

Upon equating $G_{\min}$ to the interface fracture toughness at the associated mode mixity, Γ_i, Eqs. (22) and (23) indicate that there is a critical imperfection wavelength, $L_0^c \equiv L_0$, given by:

$$L_0^c = [\Gamma_i L_b/(cG_0)]$$

$$\cong 4\left(\frac{\bar{E}\Gamma_i}{\sigma_0^2}\right)\sqrt{\frac{\bar{E}}{\sigma_0}} \text{ (plane strain)}$$

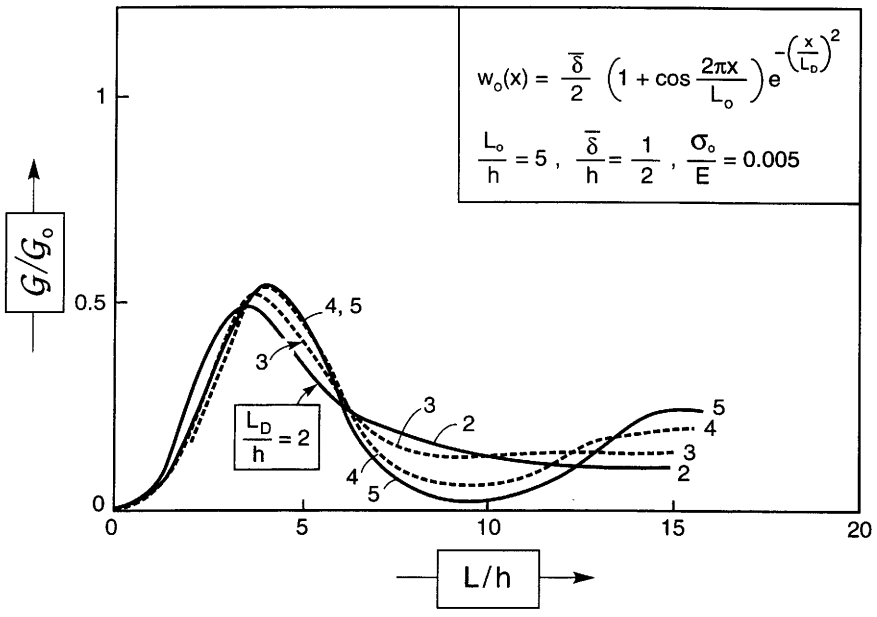

Fig. 13. Influence of extended imperfections on the energy release rate in plane strain.

$$\cong 11\left(\frac{\bar{E}\Gamma_i}{\sigma_0^2}\right)\sqrt{\frac{\bar{E}}{\sigma_0}} \text{ (axisymmetric)} \tag{24}$$

Note that L_0^c is insensitive to the film thickness, h, and imperfection amplitude, δ, for the range $0.5 < \delta/h$.

The significance of this result is as follows. *Imperfections having wavelength* L_0 *smaller than* L_0^c *will not give rise to energy release rates large enough to attain a buckled state.* Accordingly, such imperfections cannot cause failure. Conversely, imperfections having larger wavelength could buckle and cause failure, subject to the presence of a defect large enough to nucleate a separation.

A paradox with Eq. (24) envisaged as a sole failure criterion is that it has no dependence on the film thickness, inconsistent with practical experience (Wright, 1998). The film thickness enters when a nucleation criterion is also imposed, based on G_{peak}, discussed next. Both *criteria* must be satisfied to cause failure.

5.2. Nucleation

In crack nucleation problems in brittle systems (notably those for cracking at indentations and inclusions) (Marshall et al., 1982; Rühle et al., 1987; Shum and Huang, 1990; Green, 1982; Ito et al., 1981; Evans, 1972), the correct scaling is

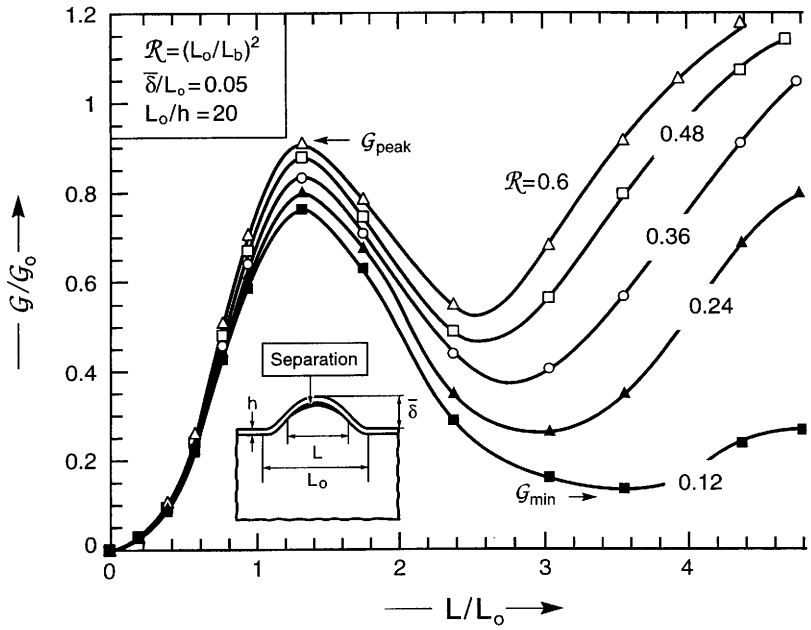

Fig. 14. Energy release rates calculated for axisymmetric undulations over the parameter range indicated on the inset.

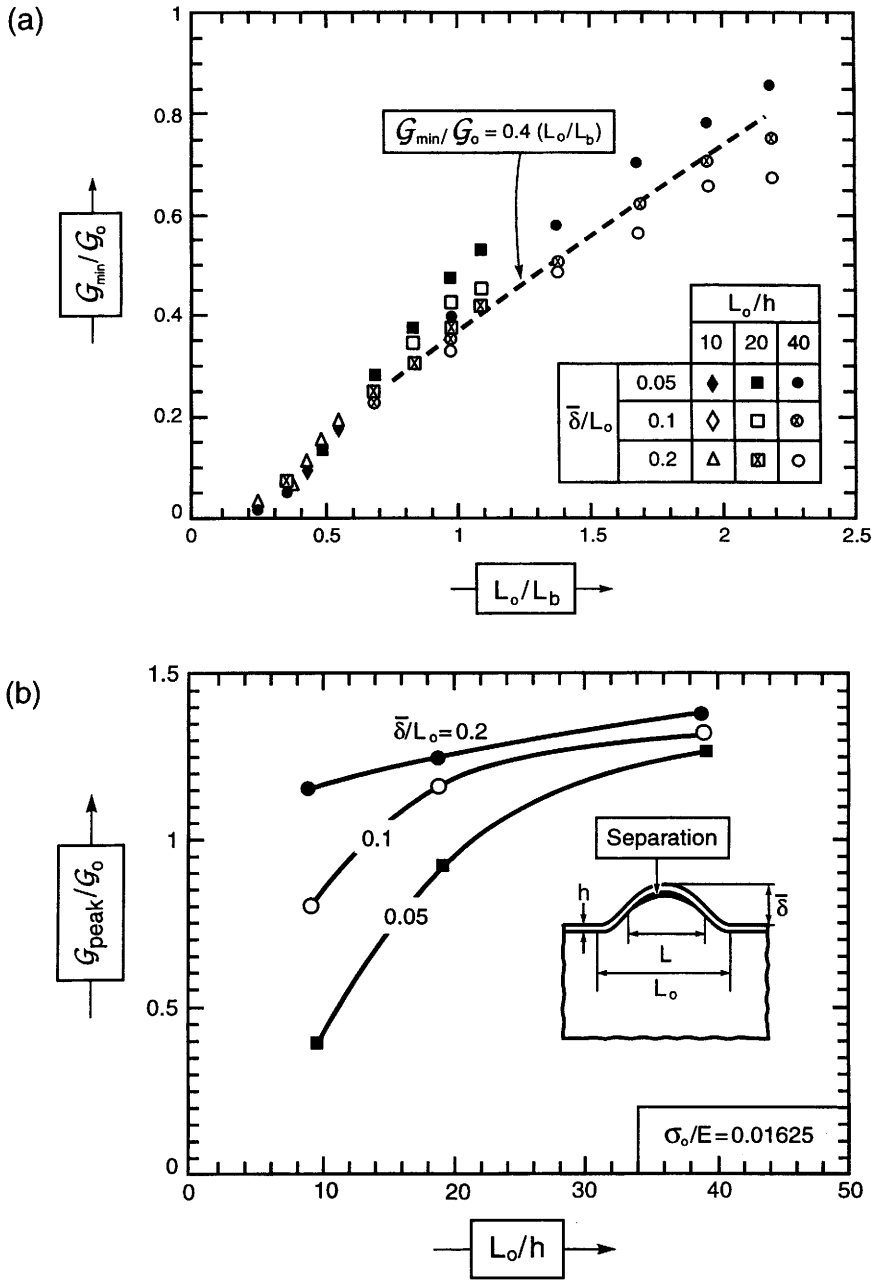

Fig. 15. Non-dimensional minimum and peak energy release rates for axisymmetric undulations, plotted as a function of imperfection index: (a) minimum, (b) peak.

achieved upon equating G_{peak} to the toughness, Γ_i. However, because of the requirement that flaws be present to activate the nucleation process, nucleation conditions must take into account representative initial flaws. This can be done approximately by equating $G_{\text{peak}}/2$ (rather than G_{peak}) with Γ_i (Green, 1982; Ito et al., 1981). In order to implement this approach in the present context, it is noted that G_{peak} for both plane strain (Fig. 12) and axial symmetry (Fig. 15b) are reasonably approximated by G_0 for moderate, but realistic, imperfection amplitudes (e.g. $\delta/h \approx 1$). Recall that G_{peak} has little dependence on the imperfection size, L_0. Imposition of $G_{\text{peak}}/2 = \Gamma_i$ with $G_{\text{peak}} \cong G_0$ gives the critical thickness h_c at which the imperfections nucleate delaminations:

$$h_c \cong 4\bar{E}\Gamma_i/\sigma_0^2 \tag{25}$$

This result depends weakly on L_0/h and only requires modest undulation amplitudes. Note that, from Eq. (24), L_0^c and h_c are inter-related by

$$L_0^c/h_c \cong \sqrt{\bar{E}/\sigma_0} \text{ (plane strain)}$$

$$\cong 2.7\sqrt{\bar{E}/\sigma_0} \text{ (axisymmetric)} \tag{26}$$

For smaller imperfections than those assumed, h_c will be larger than Eq. (25). It can be obtained from the curves presented on Figs. 12 and 15b, with Eq. (26) modified accordingly.

The following interpretation should be given to the two critical lengths. The combined inequalities $h < h_c$ and $L_0 < L_0^c$ *comprise a fail-safe condition.* Film thicknesses less than critical will not nucleate initial delaminations. Moreover, even if initial delaminations develop equal in size to the undulations (L_0), they will arrest before they become unstable. Conversely, if both inequalities are reversed ($h > h_c$ and $L_0 > L_0^c$), delaminations would be expected to nucleate and grow unstably, except that interfaces having high perfection (no defects) would still be capable of resisting failure.

6. Implications

6.1. Revised buckling map

The influence of the imperfections on film failure can be visualized by modifying the buckling map of Fig. 3 to include the energy release rate features found in the nucleation phase. Such a map of $\Sigma \equiv \sigma_0[(1-\nu^2)h/(2E\Gamma_i^I)]^{1/2}$ vs L/L_b is shown schematically in Fig. 16. The consequences for film failure are illustrated by the trajectory superposed on the buckling map. Present an initial interface defect, size L_0, a critical level is reached (position A) at which a separation pops-in to a stable size (position B). As Σ further increases, the separation expands

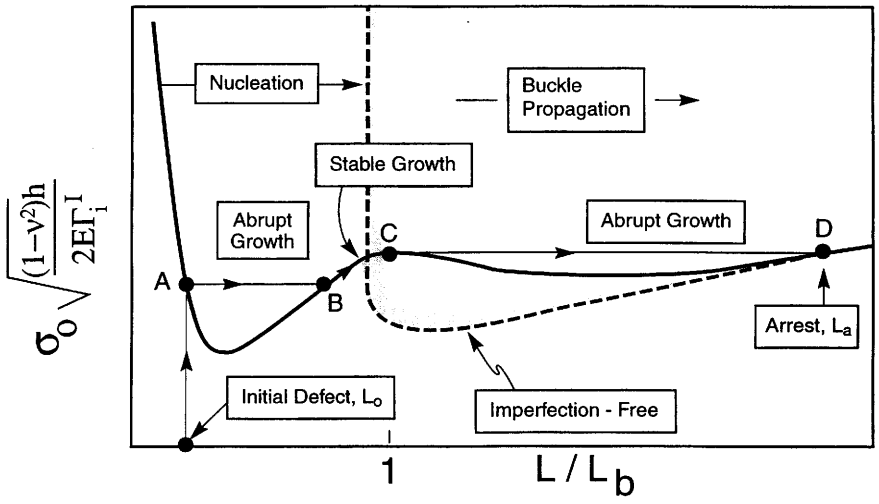

Fig. 16. A modified buckling map that introduces a nucleation condition. The trajectories are described in the text.

stably up to the maximum (point C). Here the separation buckles and abruptly expands to size L_a (point D). At this stage, the buckle may either spall or arrest, depending on conditions relative to the spall criterion (Hutchinson and Suo, 1992; Wang and Evans, 2000). If it arrests, it can again expand stably as Σ increases until spalling conditions are reached. The preceding energy release rate results can be used to plot explicit buckling maps, as a function of imperfection size and shape.

6.2. Critical sizes

Explicit failure conditions are found by determining the critical sizes, L_0^c and h_c. They are illustrated for a thin thermally grown α-Al_2O_3 (TGO) on a superalloy. The film properties are quite well known (Table 1). The residual compression is

Table 1
Properties of α-Al_2O_3 thermally grown on Ni-based bond coats

E (GPa)	380–400
ν	0.2
α ($^\circ C^{-1}$) (ppm)	7–8
α_s ($^\circ C^{-1}$) (ppm)[a]	14–16
h (μm)	1–10
Γ_i^0 (J m^{-2})	5–20
ΔT ($^\circ$C)	1000
λ	0.1–0.3

[a] Ni based superalloy.

about $\sigma_0 \approx 3$ GPa, while Γ_i varies from the low end of the range (5 J m^{-2}) to an upper level given by the TGO itself ($\Gamma_0 \approx 20$ J m^{-2}).

For axisymmetric undulations, neglecting mode mixity effects, the critical imperfection wavelength L_0^c needed to assure propagation and buckling ranges from 20 to 100 μm; while the corresponding critical TGO thickness required for nucleation, h_c, varies from 1/2 to 3 μm. Note that the ratio $L_0^c/h_c \approx 30$ is large enough to allow application of Eq. (26), provided that the amplitude, $\delta/L > 0.05$. Undulations having such magnitude are readily developed by wrinkling, etc. (Tolpygo and Clarke, 1998). Hence, for this thin film system, imperfections comprising locally undulating surfaces provide an effective means for nucleating and propagating failure whenever the TGO thickness exceeds 1/2–3 μm. Further definition is dependent on specifics regarding the interface toughness.

When mode mixity effects are included, h_c increases significantly, dependent on λ, Eq. (6). Upon using the λ measured for TGO (0.3) (Wang and Evans, 1998) in conjunction with ψ calculated on Fig. 11, there is a factor 4 increase: such that L_0^c now ranges from 80 to 400 μm.

7. Summary

Analysis of prototypical imperfections associated with thin compressed films has established criteria for failure by buckle driven delamination. Two basic requirements must be satisfied. One based on the nucleation of interface separations. The other governed by buckling and buckle propagation.

For sufficiently large imperfections, these requirements can be expressed in terms of "critical sizes", manifest as a critical film thickness h_c, and a critical undulation wavelength, L_0^c. Values for these critical sizes determined for a thin thermally grown oxide (TGP), have provided information that can be compared with experimental findings. Analogous results for other imperfections, such as heterogeneities, remain to be determined.

Acknowledgements

The work of JWH was supported in part by the NSF under grant CMS-9634632 and in part by the Division of Engineering and Applied Sciences, Harvard University. The work of MYH was supported in part by the Advanced Gas Turbine Systems Research program of the Department of Energy under grant 98-01-SR068 through the South Carolina Energy Research and Development Center. The work of AGE was supported by the Office of Naval Research.

Appendix A. The plane strain model

Eq. (4) can be put in the following dimensionless form:

$$W'' + (2\pi\xi)^2 W = -(2\pi\xi)^2 W_0 + m \tag{A1}$$

$$\xi^2 = 1 - \frac{3}{\eta\pi^2}\int_0^{\eta/2} [W'^2 + 2W_0' W'] \mathrm{d}X \tag{A2}$$

where

$$\xi^2 = \frac{\sigma}{\sigma_0}, \quad \eta = \frac{L}{L_b}, \quad L_b = \pi\sqrt{\frac{\bar{E}}{3\sigma_0}}h, \quad X = \frac{x}{L_b}, \quad ()' = \frac{\mathrm{d}()}{\mathrm{d}X},$$
$$W = \frac{w}{h}, \quad W_0 = \frac{w_0}{h} \tag{A3}$$

As defined in Eq. (5), L_b is the width of the delamination associated with the onset of buckling in the perfect film. The constant $m = 4\pi^2 M^A/(\sigma_0 h^2)$ is one of the free variables required to meet the two boundary conditions: $W = W' = 0$ at $X = \eta/2$.

Solutions to Eq. (A1) for symmetric imperfections are given by

$$W(X) = A\ \cos(2\pi\xi X) + \frac{m}{(2\pi\xi)^2} - F(X, \xi) \tag{A4}$$

where A is an undetermined coefficient and

$$F(X, \xi) = (2\pi\xi)^2\ \cos(2\pi\xi X)\int_0^X \left[\frac{1}{\cos(2\pi\xi\phi)^2}\int_0^\phi \cos(2\pi\xi X')W_0(X')\mathrm{d}X'\right]\mathrm{d}\phi \tag{A5}$$

Enforcement of the boundary conditions gives

$$m = \frac{2\pi\xi F'(\eta/2, \xi)}{\tan(\pi\xi\eta)} + (2\pi\xi)^2 F(\eta/2, \xi), \quad A = -\frac{F'(\eta/2, \xi)}{2\pi\xi\ \sin(\pi\xi\eta)} \tag{A6}$$

where $F' = \mathrm{d}F/\mathrm{d}X$. By Eq. (A4),

$$W'(X) = -F'(X, \xi) + F'(\eta/2, \xi)\sin(2\pi\xi X)/\sin(\pi\xi\eta) \tag{A7}$$

The use of Eq. (A7) in Eq. (A2) gives a single equation for ξ in terms of η. Note that this relation *depends only on the dimensionless parameters specifying the imperfection*. Generally, ξ must be determined numerically. The solution is then fully determined from Eq. (A7) and the other equations.

For the imperfection shape of Eq. (11), the two integrations defining $F(X,\xi)$ can be carried out explicitly. The dimensionless imperfection parameters are δ/h and L_0/L_b. It is readily established that G/G_0 and ψ depend only on η, δ/h and L_0/L_b.

References

Christensen, R.J., Tolpygo, V.K., Clarke, D.R., 1997. The influence of the reactive element yttrium on the stress in alumina scales formed by oxidation. Acta Mater. 45, 1761–1766.

Evans, A.G., 1972. The strength of brittle materials containing second phase dispersions. Phil. Mag. 26, 1327.

Evans, A.G., Hutchinson, J.W., 1995. The thermomechanical integrity of thin films and multilayers. Acta Metall. Mater. 43, 2507–2530.

Evans, A.G., He, M.Y., Hutchinson, J.W., 1998. Effect of interface undulations on the thermal fatigue of thin films and scales on metal substrates. Acta Mater. 45, 3543–3554.

Gioia, G., Ortiz, M., 1997. Delamination of compressed thin films. Adv. Appl. Mech. 33, 120–192.

Green, D.J., 1982. Critical microstructures for microcracking in Al_2O_3–ZrO_2 composites. J. Am. Ceram. Soc. 65, 610–614.

He, M.Y., Evans, A.G., Hutchinson, J.W., 1998. Effects of morphology on the decohesion of compressed thin films. Mat. Sci. Eng. A245, 168–181.

Hutchinson, J.W., Suo, Z., 1992. Mixed mode cracking in layered materials. Adv. Appl. Mech. 29, 63–191.

Hutchinson, J.W., Thouless, M.D., Liniger, E.G., 1992. Growth and configurational stability of circular, buckling-driven film delaminations. Acta Metall. Mater. 40, 295–308.

Ito, Y.M., Rosenblatt, M., Cheng, L.Y., Lange, F.F., Evans, A.G., 1981. Cracking in particulate composites due to thermalmechanical stress. Intl. J. Frac. 17, 483–491.

Koiter, W.T., 1945. On the stability of elastic equilibrium, thesis Delft (in Dutch with English summary). H. J. Paris, Amsterdam.

Koiter, W.T., 1966. On the nonlinear theory of thin elastic shells. Proc. Kon Ned. Ak. Wet. B69, 1–54.

Marshall, D.B., Lawn, B.R., Evans, A.G., 1982. Elastic/plastic indentation damage in ceramics: the lateral crack system. J. Am. Ceram. Soc. 65, 561–566.

Nilsson, K.F., Giannakopoulos, A.E., 1995. A finite element analysis of configurational stability and finite growth of buckling driven delamination. J. Mech. Phys. Solids 43, 1983–2021.

Rühle, M., Evans, A.G., McMeeking, R.M., Charalambides, P.G., Hutchinson, J.W., 1987. Microcrack toughening in alumina/zirconia. Acta Metall. 35, 2701–2710.

Shum, D.K.M., Huang, Y.Y., 1990. Fundamental solutions for microcracking induced by residual stress. Engnr. Fract. Mech. 37, 107–117.

Storåkers, B., Nilsson, K.F., 1993. Imperfection sensitivity at delamination buckling and growth. Int. J. Solids Structures 30, 1057–1074.

Thouless, M.D., Jensen, H.M., Liniger, E.G., 1994. Delamination from edge flaws. Proc. Royal Soc. London A447, 271–279.

Tolpygo, V.K., Clarke, D.R., 1998. Wrinkling of α-alumina films grown by thermal oxidation — II: oxide separation and failure. Acta Mater. 46, 5167–5174.

Wang, J-S., Evans, A.G., 1998. Measurement and analysis of buckling and buckle propagation in compressed oxide layers on superally substrates. Acta Mater. 46, 4993–5505.

Wang, J.S., Evans, A.G., 2000. Effects of strain cycling on buckling, cracking and spalling of a thermally grown alumina on a nickel-based bond coat. Acta Mater. (in press).

Wright, P.K., 1998. Influence of cyclic strain on life of a PVD TBC. Mat. Sci. Eng. A245, 191–200.

PERGAMON

Appendix B

PII: S1359-6454(99)00023-3

Acta mater. Vol. 47, No. 5, pp. 1513–1522, 1999

Printed in Great Britain
1359-6454/99 $20.00 + 0.00

MICROMECHANICS MODEL FOR THE DETACHMENT OF RESIDUALLY COMPRESSED BRITTLE FILMS AND COATINGS

A. G. EVANS[1], J. W. HUTCHINSON[1]† and M. Y. HE[2]

[1]Division of Engineering and Applied Sciences, Harvard University, Cambridge, MA 02138, U.S.A. and
[2]Materials, University of California, Santa Barbara, CA 93106, U.S.A.

(Received 18 December 1998; accepted 8 January 1999)

Abstract—The durability of residually compressed coatings, particularly thermal barrier coatings (TBCs), is governed by events occurring at the interface with the substrate. In general, failure involves the sequential nucleation growth and coalescence of separations in the presence of imperfections and defects. The growth and coalescence phases are analyzed. Remnant ligaments are expected from the mechanics. These allow the coating to remain attached to the substrate, even when interface separation is profuse. Detachment happens when transverse loads develop. Critical values of these loads are calculated and their implications discussed. © *1999 Acta Metallurgica Inc. Published by Elsevier Science Ltd. All rights reserved.*

1. INTRODUCTION

The integrity of relatively thick, brittle coatings attached to metal substrates has emerged as an increasingly important consideration, as such coatings become more widely implemented. Thermal barrier coatings (TBCs) typify the applications [1–5]. These coating systems often need to retain their integrity when subject to thermal cycling through large temperature ranges, despite significant thermal expansion misfit with the substrate. Accordingly, they are designed to have high in-plane compliance. This is achieved by deliberately incorporating either aligned porosity or microcrack arrays. These methods for incorporating compliance also result in low strength and toughness. Yet, the systems have high durability (often remarkably so). Eventually, the coating spalls away and exposes the substrate. One engineering problem is that the time/cycles to failure exhibits large variability. Understanding and reducing this variability would constitute a major benefit to the expanded and more confident implementation of coatings. This article addresses some aspects of this problem.

A micromechanics approach is taken, based on mechanisms of crack nucleation, growth and coalescence. It is illustrated for TBCs, wherein the energy density needed to induce failure is provided by a thermally grown oxide (referred to as TGO: typically α-alumina) that forms between the TBC and the substrate (usually a Ni- or Pi-based bond coat alloy) [6–9]. The TGO is subject to large compressive stress caused primarily by thermal expansion misfit with the substrate (there are additional growth stresses in some cases). The redistribution of these stresses by morphological imperfections in the TGO, and by other defects [10–22], provides the energy release rate needed to extend and coalesce the separations that cause failure.

Interfacial micro-separations develop from imperfections in the coating (with time/cycles) and become extensive enough to cover an appreciable fraction of the cross-section prior to failure. The coalescence of a domain of such separations into a crack comprises the penultimate phase in the failure sequence. It precedes edge or buckle driven delamination [13, 14]. When large enough, the delamination detaches the coating. This happens when the associated energy release rate exceeds the remnant toughness of the degraded domain.

Solutions to this failure category are provided at several levels of simplification that could lead, ultimately, to a stochastic life prediction model. The most basic model comprises a domain of included imperfections located along a weak plane, subject to a misfit stress in an otherwise isotropic, elastically homogeneous solid [Fig. 1(a)]. Results for this problem can be obtained analytically and provide a basic comprehension of the principles. At a more representative level for coatings, a numerical analysis is performed for an idealized TBC system comprising an electron beam physical vapor deposited (EB-PVD) thermal barrier on a bond coat, with a TGO containing a periodic array of imperfections [Fig. 1(b)]. A single example is used to demonstrate the important issues.

The article is organized as follows. In Section 2, the concepts are outlined. In Section 3, analytical results for the coalescence of separations between heterogeneities are presented. In Sections 4 and 5,

†To whom all correspondence should be addressed.

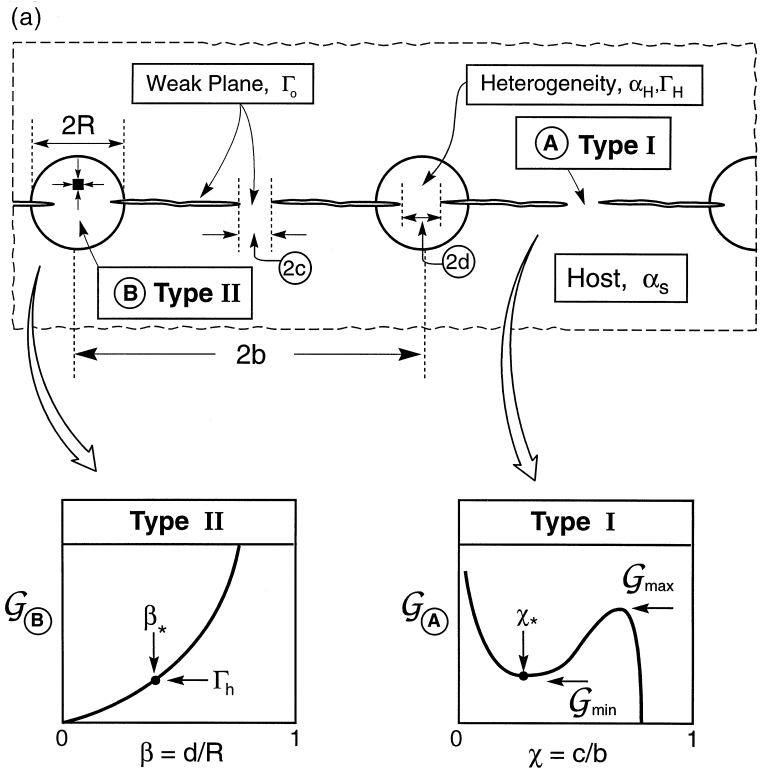

Fig. 1. The two models used to analyze the phases of crack coalescence: (a) inclusion model; (b) film model. The type I and II ligaments are identified, as well as the expected energy release rate trends as the ligaments converge.

remnant ligaments within heterogeneities and their detachment to cause failure are analyzed, analytically. In Section 6, a numerical example for a coating is presented. Finally, in Section 7, the implications for delamination are discussed.

2. THE BASIC CONCEPT

Considerations of crack coalescence from an array of heterogeneities subject to misfit strain (Fig. 1) provide two fundamental mechanics precepts, both associated with the convergence of cracks in residually stressed systems. The concepts are introduced for the case of an elastically homogeneous body containing a periodic co-linear array of cylindrical imperfections having lower thermal expansion coefficient (α_H) than the surrounding host (α_s). The imperfections are connected by a weak plane. Microseparations form on that plane and converge, resulting in intact ligaments (Fig. 1). There are two types of ligament: those *between* imperfections (type I) and those *within* the imperfections (type II). Type I ligaments experience residual tensions. The energy release rate (at location A in Fig. 1) has the form depicted on the inset as G_A. Namely, it becomes unbounded as the separations converge, resulting in a minimum G_{min} at ligament size c_*. Once the ligament diminishes to c_* (by time/cycle dependent growth) the separations abruptly coalesce.

The situation is completely different at type II ligaments within the imperfections (location B in Fig. 1), which experience residual compression. Now, because the residually stressed regions diminish to zero as ligaments coalesce, the energy release rate tends to zero, as indicated by the inset. Accordingly, for a periodic array of imperfections, *small ligaments, length* d_c, *always stay attached*. This is the converging debond situation elaborated elsewhere for films and fiber composites [15–17]. The most vivid visualization has been provided for debonded thin films (Fig. 2).

The remnant ligaments can be detached when other loading situations arise, such as the application of a mechanical load or when moderately large delaminations are present. One illustration is depicted in Fig. 3, comprising attached ligaments ahead of an edge delamination. Now, the displacements associated with the crack faces provide a different loading environment, wherein the energy release rate becomes unbounded as the remnant ligament size tends to zero, $d \longrightarrow 0$. This process is characterized by a strength and a fracture toughness

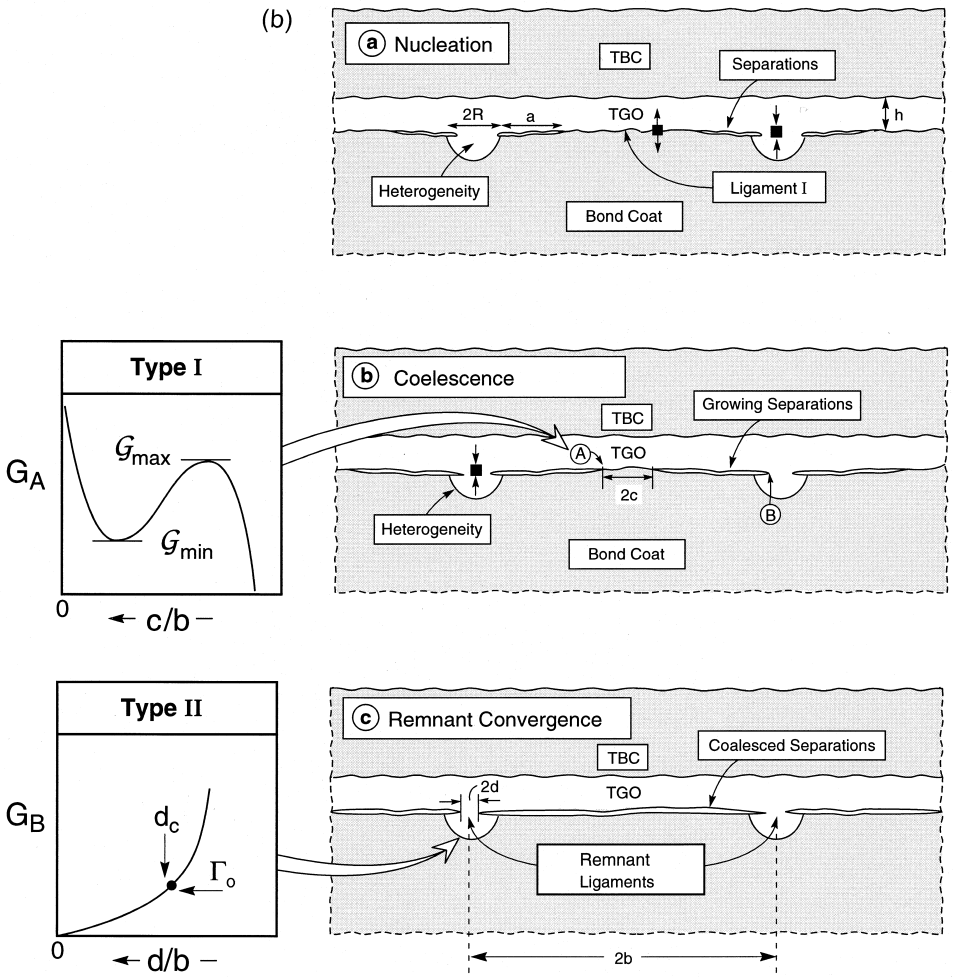

Fig. 1. *continued*

for the plane held together by the ligaments. The criterion that governs failure of attached type II ligaments establishes life. These three phases of the failure sequence are explored below.

The problem has similarities with crack evolution from other centers of dilatation, such as indentations and inclusions [18, 19]. Analytical results that provide useful non-dimensional groups and approximate trends connect with this prior work. The results are presented either in terms of stress intensity factors, K, or energy release rates, G, which can be interrelated in the usual way: $K = \sqrt{\bar{E}G}$, with $\bar{E}$ the bimaterial plane strain modulus (i.e. $\bar{E} = E/(1-\nu^2)$ for the limit of no mismatch).

The presence of remnant ligaments and their detachment upon application of transverse stresses has been experimentally demonstrated in a recent study of failure mechanisms in thermal barrier coatings [20]. The findings of this assessment indicate that inter-heterogeneity coalescence along the TGO/substrate interface occurs with relative facility (Fig. 4). Conversely, the intra-heterogeneity ligaments remain intact until a wedge impression is used to impose transverse stresses. These additional stresses rupture the attached ligaments, which remain embedded in the substrate (Fig. 4).

3. LIGAMENT COALESCENCE

For determination of the qualitative trend in the relationships pertinent to the coalescence of type I ligaments, a two-dimensional plane strain model is employed. The model uses results for an infinite co-linear array of cracks in an infinite homogeneous solid. The cracks are equally spaced a distance $2b$, center-to-center, and separated by ligaments of length $2c$ [cf. Fig. 1(a)]. No attempt is made to replicate the details of the pressure distribution exerted by the imperfection on the crack faces. Instead, an approximation is obtained by taking a

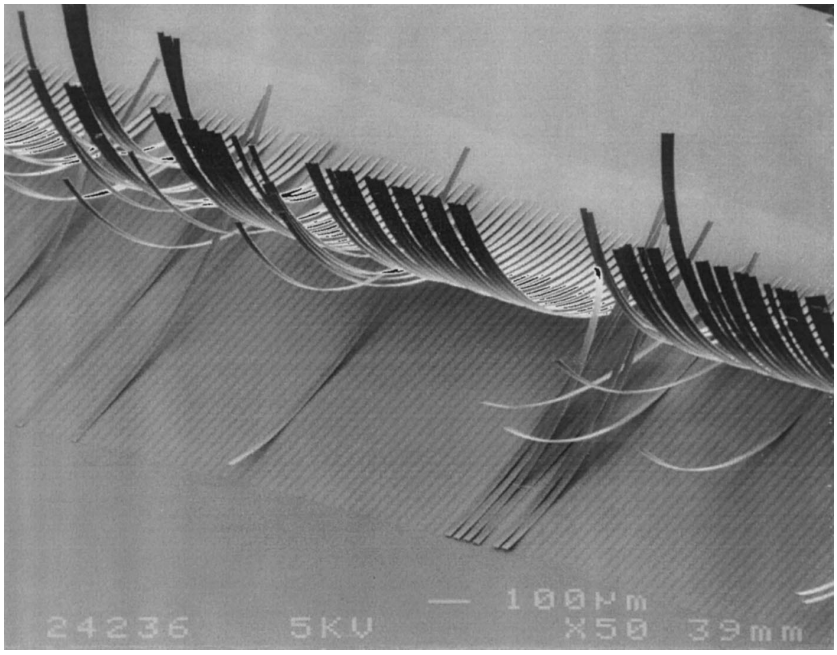

Fig. 2. A vivid illustration of the converging debond phenomenon wherein thin, residually strained strips remain attached to the substrate via small remnant ligaments.

uniform pressure p to act over the entire face area, and then p is chosen such that the opening at the center is consistent with the wedging displacement produced by the imperfection. The stress intensity factor for the cracks at A is [21]

$$K_A = p\sqrt{2b \tan \eta} \tag{1}$$

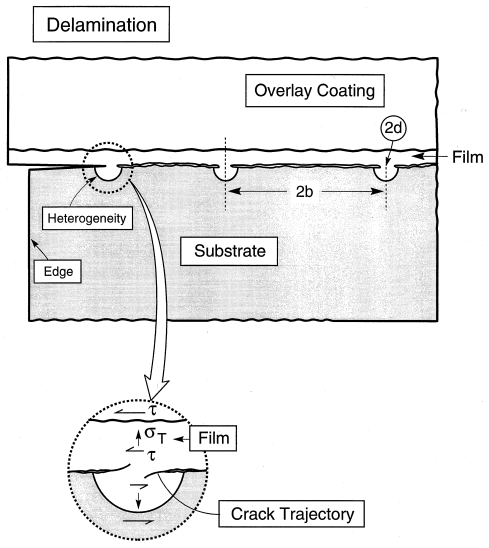

Fig. 3. A schematic showing the displacements that arise when attached ligaments occur in association with edge delamination.

where $\eta = (\pi/2)(b - c)/b$. The associated opening at the center of the cracks is

$$\delta = \frac{8bp}{\pi \bar{E}} \cosh^{-1}[\sec \eta]. \tag{2}$$

The energy release rate at a given opening displacement δ is obtained by eliminating p from equations (1) and (2) as

$$G_A = \frac{\pi^2}{32} \frac{\bar{E}\delta^2}{b} F_A(\eta) \tag{3}$$

with

$$F_A(\eta) = \frac{\tan \eta}{[\cosh^{-1}(\sec \eta)]^2}.$$

The opening displacement at the center of the cracks is governed by the misfit strain, $\Delta\alpha\Delta T$ (where $\Delta\alpha$ is the thermal expansion mismatch and ΔT the temperature drop), and by the imperfection radius, R. It must have the form

$$\delta = gR\Delta\alpha\Delta T \tag{4}$$

where g is a dimensionless coefficient of order unity which, when the ligaments are small compared with the crack spacing, depends very weakly on c/b. When equation (4) is used in equation (3), the dimensionless energy release rate is obtained as

$$\frac{G_A}{\bar{E}R(\Delta\alpha\Delta T)^2} = g^2 \frac{\pi^2}{32} \frac{R}{b} F_A(\eta). \tag{5}$$

The function $F_A(\eta)$ is large when c/b is near unity, decreases to a minimum, of 0.905, at $c/b = 0.18$,

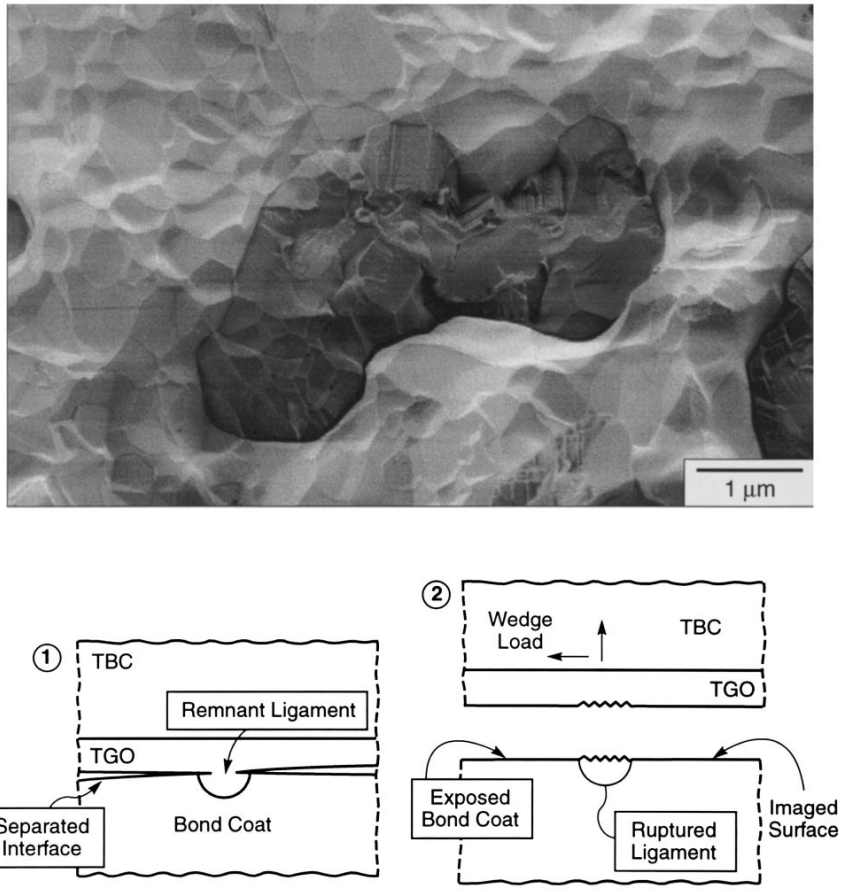

Fig. 4. A schematic showing the detachment of a TGO ligament and a scanning electron microscope image of the ruptured TGO ligament embedded in the substrate [20]. The dark contrast region is the embedded Al_2O_3.

and then increases, becoming unbounded as $c/b \longrightarrow 0$. As a consequence, separations coalesce once the ligaments have been reduced to $c/b = 0.18$. Equating $(G_A)_{\text{minimum}}$ to the fracture toughness along the weak plane, designated Γ_0, yields a criterion for coalescence of the cracks. It requires that the imperfection radius exceed a critical size, R_c, given by

$$\frac{R_c}{b} = (1.89/g)\sqrt{\frac{\Gamma_0}{\bar{E}(\Delta\alpha\Delta T)^2 b}}. \tag{6}$$

The model result [equation (6)] is translated into a form applicable to the coalescence of the type I ligaments in a brittle film by assuming that the imperfections are spherical, radius R, and that there is one per area of interface, radius b. With f_c as the critical area fraction of these imperfections in the weak plane at coalescence, equation (6) provides

$$f_c = \xi \frac{\Gamma_0}{\bar{E}(\Delta\alpha\Delta T)^2 b} \tag{7}$$

where ξ is a non-dimensional coefficient of order unity.

This result may be interpreted as follows. As the heterogeneities increase in size upon film growth, a critical size is reached whereupon type I separations coalesce. This event does not cause failure. Instead, a transition occurs to convergence of type II ligaments, discussed in Section 4.

In order to establish the magnitude of g, some numerical results have been obtained. For this purpose, the finite element method has been used. The method is the same as that discussed elsewhere [10, 11] for determining energy release rates. The results are shown in Fig. 5. Note that the energy release rate minimum increases with increase in R/b, as anticipated by the analytical result (5). Moreover, there is a close correspondence between the numerical and analytical results when R/b is small (≤ 0.05), such that $g \approx 1$. At larger R/b, g becomes a function of R/b. It exceeds unity and increases as R/b increases. Eventually, at $R/b \approx 0.4$, the minimum is eliminated.

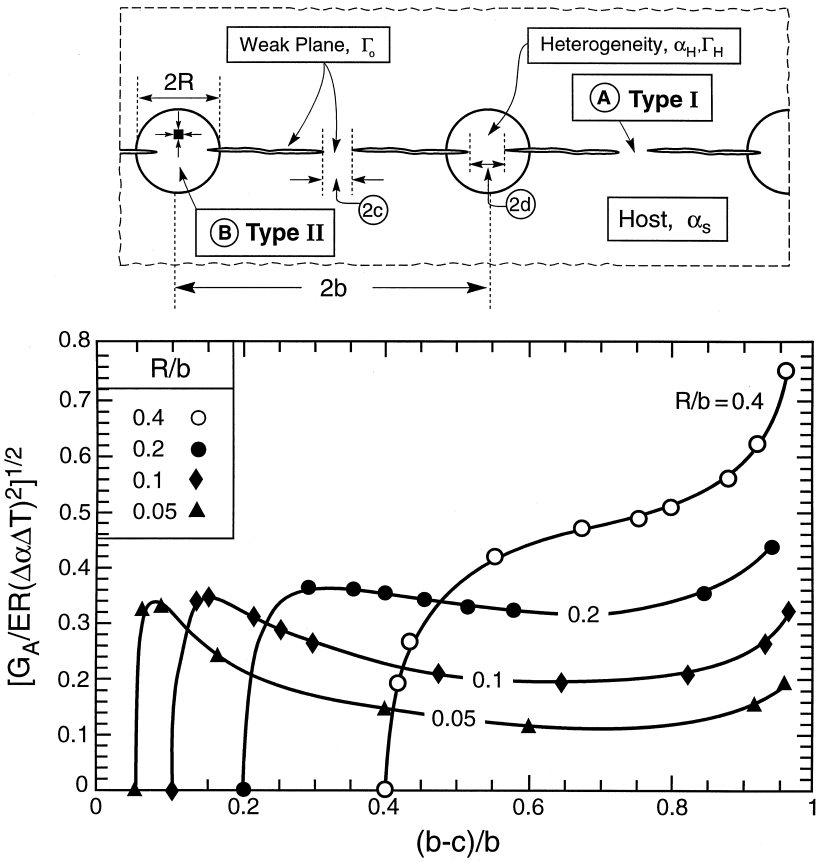

Fig. 5. Numerical results for the energy release rates at coalescing type I ligaments using the model from Fig. 1(a).

4. LIGAMENT CONVERGENCE

After the type I ligaments have failed, the coating remains attached by type II ligaments. Previous analyses of converging debonds [15–17] provide basic concepts. Namely, when the ligament radius d is small compared with the radius of the heterogeneity R, the energy release rate approaches zero as $G_B \approx \sigma_0^2 d/\bar{E}$, where σ_0 is the misfit compression in the heterogeneity, which can be related to the misfit strain $\Delta\alpha\Delta T$ in the usual way. *The residual stress is unable to fail the ligaments and the coating remains attached until some other phenomenon intervenes.* These other phenomena are examined in Section 5.

To obtain explicit results, consider an axisymmetric model of one ligament (Fig. 6), where the heterogeneity is taken to be spherical with radius R and the medium is infinitely thick. Results for the energy release rate can be derived analytically when R is small compared with the spacing ($\approx 2b$) and there is no elastic mismatch between the heterogeneity and the surrounding matrix.

For the model, take the outer radius b in the model to be infinite, and denote the radial coordinate by r. With no crack present, the misfit stress in the heterogeneity is a uniform hydrostatic pressure, $\sigma(r) = -\sigma_0$, where $\sigma_0 \equiv 2E\Delta\alpha\Delta T/[5(1-\nu)]$, while the stress acting on the incipient crack plane outside the heterogeneity ($r > R$) is tensile and given by: $\sigma(r) = \sigma_0(r/R)^{-3}$. The solution for the stress intensity factor at the tip of an external ring crack with radius d is [21]

$$K_B = \frac{2}{\sqrt{\pi d}}\int_d^\infty \sigma(r)\left[\frac{r}{d}\cos^{-1}\left(\frac{r}{d}\right) + \frac{r}{\sqrt{r^2-d^2}}\right]dr. \quad (8)$$

The above integral can be evaluated in closed form as

$$K_B = \sigma_0\sqrt{R}\sqrt{\frac{d}{\pi R}}\left\{2\left(\frac{R}{d}\right)^3 - \left[2\left(\frac{R}{d}\right)^2 + 1\right]\sqrt{\left(\frac{R}{d}\right)^2 - 1}\right\}$$

$$\equiv \sigma_0\sqrt{R}F_B\left(\frac{d}{R}\right). \quad (9)$$

The associated energy release rate can be expressed in the dimensionless form as

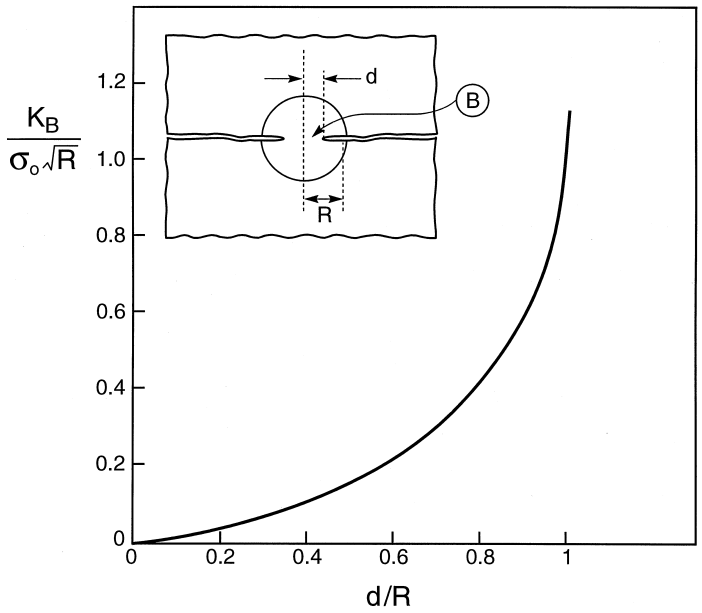

Fig. 6. Stress intensity factor for type II ligaments in the limit that the ligament size $d/b \ll 1$.

$$\frac{G_B}{E(\Delta\alpha\Delta T)^2 R} = \frac{4(1+\nu)}{25(1-\nu)}\left[F_B\left(\frac{d}{R}\right)\right]^2. \quad (10)$$

The stress intensity factor is plotted in Fig. 6. The size of the remnant ligament under the action of σ_0 can be obtained by equating K_B to the heterogeneity toughness K_{Hc}. Inserting typical values for TBCs (Table 1) to evaluate $K_{Hc}/\sigma_0\sqrt{R}$ indicates that the expected remnant ligament size is $d_*/R \approx 0.5$.

5. DETACHMENT

Several means exist whereby extra loads can arise on the attached type II ligaments causing them to fail. These include segments where the substrate has convex curvature and delaminations around edges and holes. The general role of these features is to induce forces normal (or parallel) to the ligaments, causing a change in the character of the energy release rate at the ligament. The behavior is illustrated for the model considered in the previous section when a normal load P acts across the ligament (Fig. 7). The stress intensity factor induced by this load is [21]

$$K_B = \frac{P}{2\sqrt{\pi}d^{3/2}}. \quad (11)$$

This contribution to the stress intensity is unbounded as the ligament radius approaches zero. The combined stress intensity factor from the residual field (9) and the applied load (11) is

$$\frac{K_B}{\sigma_0\sqrt{R}} = F_B\left(\frac{d}{R}\right) + \frac{P}{\sigma_0\pi R^2}\frac{\sqrt{\pi}}{2}\left(\frac{R}{d}\right)^{3/2}. \quad (12)$$

The combined factors have a minimum at $dK_B/d(d/R) = 0$ corresponding to

$$\frac{P}{\pi\sigma_0 R^2} = \frac{2}{3\pi\beta}\left[\frac{\beta(1+2\beta^2)}{\sqrt{\beta^2-1}} + 4\beta\sqrt{\beta^2-1} - 6\beta^2\right] - \frac{1}{3\pi\beta^2}\left[\sqrt{\beta^2-1}(1+2\beta^2) - 2\beta^3\right] \quad (13)$$

where $\beta = R/d$. Upon enforcing $K_B = K_{Hc}$ in equation (12) and then solving equations (12) and (13) simultaneously for the values, P_c and β_c, at the minimum, the results plotted in Fig. 7 are obtained. Because the stress intensity factor associated with P_c is the minimum for all d, attainment of P_c causes the ligament to undergo complete separation.

One limiting result is of interest. When the nondimensional toughness is small,

$$P_c \approx \pi K_{Hc}^3\sqrt{R}/\sigma_0^2. \quad (14)$$

Paradoxically, according to (14), coatings contain-

Table 1. Properties of α-Al_2O_3 thermally grown on Ni-based bond coats

E (GPa)	380–400
ν	0.2
α_H(/°C) (p.p.m.)	7–8
α_s(/°C)[a] (p.p.m.)	14–16
h (μm)	1–10
Γ_0 (J/m^2)	5–20
ΔT (°C)	1000

[a]Ni-based superalloy.

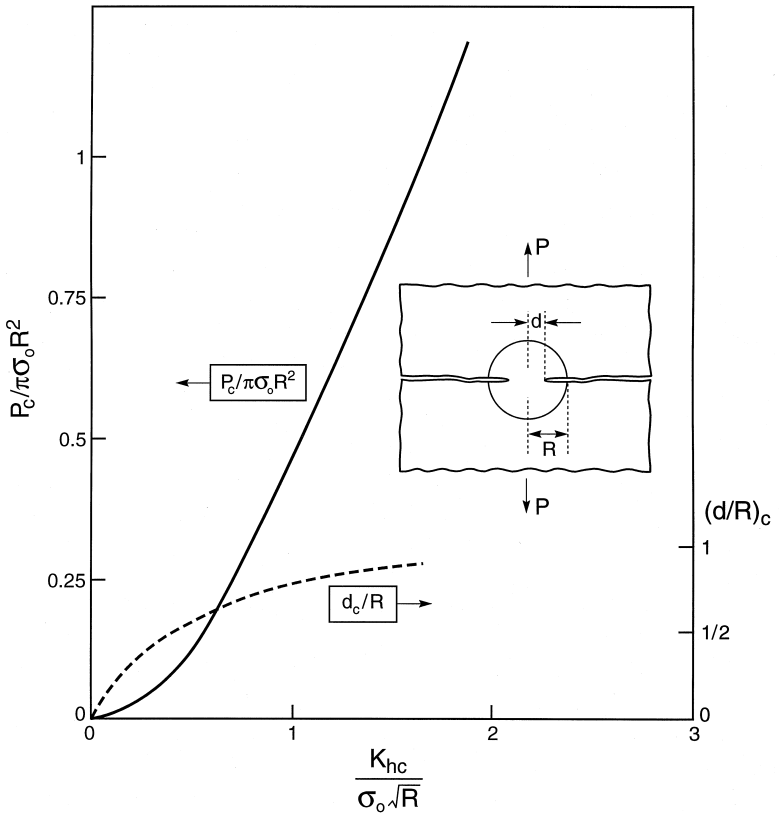

Fig. 7. Influence of the heterogeneity toughness on the transverse strength and critical ligament size at rupture.

ing large imperfections sustain greater loads prior to detachment. Otherwise, consistent with intuition, higher stresses and lower toughnesses are detrimental.

Introducing typical values for TBCs (Table 1), and assuming heterogeneities with $R = 10\ \mu$m and area fraction $f \approx 0.1$ gives $\sigma_T \approx 200$ MPa. The transverse strengths are thus surprisingly large given the extensively cracked character of the system. In practice, non-periodic arrangements of remnant ligaments result in crack-like flaws that weaken the system. This issue is addressed in Section 7.

6. DETACHMENT OF FILMS

Based on the insights gained from the above analyses, numerical results are obtained for the coalescence and convergence stages of the failure of *films/coatings* [Fig. 1(b)]. The intent is to perform calculations for a typical case, primarily to verify that the basic phenomena elucidated for the model system [Fig. 1(a)] also apply to films/coatings. A more complete parametric assessment awaits further calculations. The numerical analysis has been performed for a relative heterogeneity size, $R/b = 0.2$, and for a film thickness equal to the heterogeneity

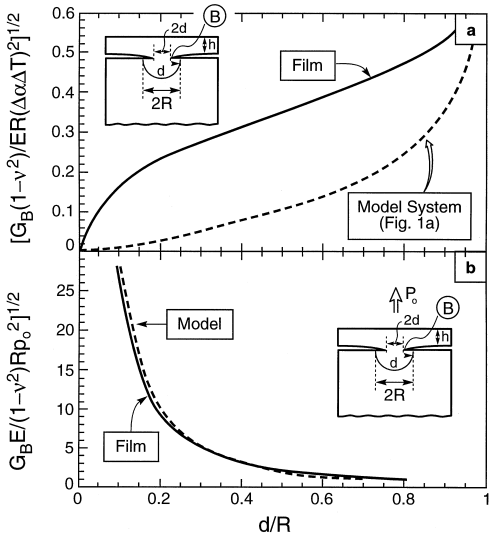

Fig. 8. Numerical results for the model depicted in Fig. 1(b), with $h/R = 1$ and $R/b = 0.2$. (a) Non-dimensional energy release rate for remnant ligament size, compared with the model system [Fig. 1(a) and Fig. 6]. (b) Energy release rate associated with detachment upon application of a transverse stress p_0.

radius, $h/R = 1$ (Fig. 8). The calculations are performed using a cylindrical cell. Two separate computations have been carried out: (i) for loading due to thermal mismatch in Fig. 8(a) and (ii) for a normal tensile stress p_0 applied directly above the inhomogeneity in Fig. 8(b). The elastic moduli are taken to be the same for the film and the substrate. The boundary conditions at the edge of the cell ($r = b$) are taken to mimic a doubly periodic array of heterogeneities. The edge is constrained to remain straight with zero average radial stress and zero shear traction.

Results pertinent to the remnant ligament size are plotted on Fig. 8(a), which represents the rate at which the energy release rate approaches zero $G_B \longrightarrow 0$, as the ligament size, $d/R \longrightarrow 0$. Superposed on the figure is the analytical result from equation (10), previously plotted as the stress intensity factor (Fig. 6). The difference between the model result and that for the film reflects the larger energy density available in the latter, enabled by contributions from both the film and the heterogeneity. The consequence is an appreciably smaller remnant ligament size, d_*/R. For example, based on quantities relevant to a 4 μm thick thermally grown α-Al_2O_3 (Table 1), the energy release rate ordinate of Fig. 8(a) is 0.5, such that $d_*/R \approx 0.8$.

When a transverse stress, p_0, is applied [Fig. 8(b)], the associated energy release rate is almost the same as that for the model, because the free surface does not change the load transmission through the intact heterogeneity.

To assess the critical transverse stress, p_0^c, required to detach the film, denote the ordinate of the function from the numerical calculation in Fig. 8(a) by $F_T(d/r)$ and that in Fig. 8(b) by $F_p(d/r)$. Then, if each contribution to the energy release rate is approximated as mode I, the two results can be superimposed to give

$$\frac{K}{\sqrt{R}\bar{E}(\Delta\alpha\Delta T)} = F_T(d/r) + \frac{p_0}{\bar{E}(\Delta\alpha\Delta T)}F_p(d/r). \quad (15)$$

The relation between K and d/r at fixed p_0 has the same qualitative features described for the model system in Section 5. The critical detachment stress p_0^c is obtained by simultaneously minimizing K with respect to d and equating K to K_{Hc}. The result is plotted on Fig. 9. Note that the stresses are similar to those for the model problem (Fig. 7).

7. DELAMINATION AND FAILURE

If a crack is present at the interface having a radius much larger than the heterogeneity spacing, the fracture toughness controls the transverse strength and the delamination resistance. In mode I loading, wherein the separations converge in a coplanar manner, the toughness is governed simply by the ligament area fraction and the heterogeneity toughness, Γ_H. This must be the case, since the process is strictly elastic and stable [22]. Thus, in

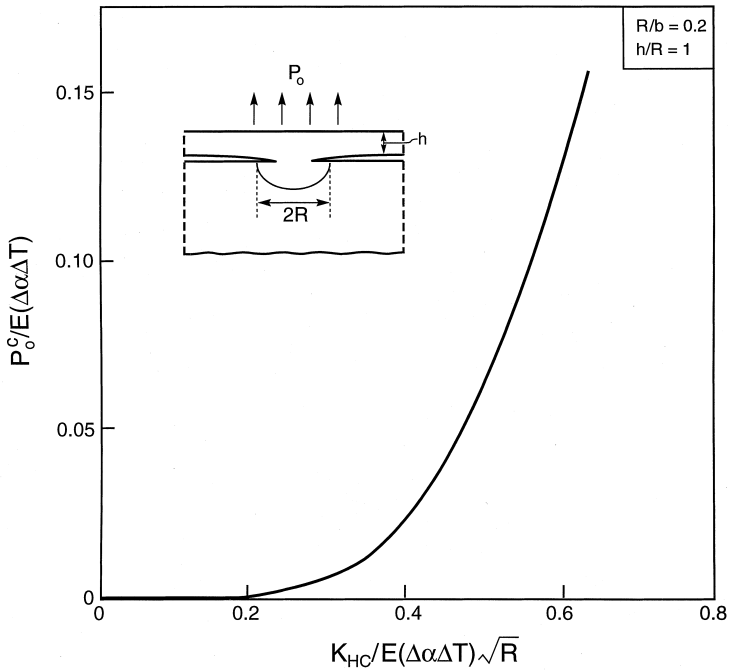

Fig. 9. Critical detachment stress for a film on a substrate [Fig. 1(b)], determined from the numerical results of Fig. 8.

steady-state, the toughness is

$$\Gamma_{ss} = (d_*/b)^2 \Gamma_H \tag{16}$$

where d_* is obtained from equation (10) with $G_B = \Gamma_H$. Inserting typical values for TBCs indicates that $\Gamma_{ss} \approx 0.1\ J/m^2$. Such a low toughness would cause inferior TBC durability, whenever areas subject to mode I loading are present. However, this constitutes a lower bound, since mode I situations are rarely encountered in residually compressed coatings.

More generally, interface cracks experience mixed mode loadings. For example, edge delaminations (Fig. 3) are subject to pure mode II with associated friction [22]. A component of mode II loading changes the ligament detachment mechanism, as sketched on Fig. 3. The key feature is that the mode mixity causes the cracks in the ligament to *diverge* rather than converge. The eventual failure of the ligaments requires a curved coalescence trajectory resulting in frictional contacts. The latter can substantially enhance the toughness, but predictions are not yet tractable.

8. SUMMARY

The major finding of the present analysis is that residually compressed films and coatings can have high durability because of the existence of remnant ligaments that arise as a natural consequence of the mechanics of residually stressed systems. These ligaments are particularly durable when the heterogeneity sites that initiate interface decohesion are distributed periodically along the surface. In this case, detachment of the film/coating requires application of appreciable transverse tensions, of order 100 MPa. Such stresses can arise in regions of high convexity and in situations that induce mechanical loads. When the heterogeneities are stochastically dispersed along the interface and, when well-defined edge delaminations exist (such as at edges or holes), the durability is substantially reduced. While the actual integrity of the coating has yet to be explicitly analyzed, a lower bound has been established by determining the mode I fracture toughness of the remnant ligaments. It is only of order $0.1\ J/m^2$, such that the transverse strength is only a few MPa when flaws of order 50 μm are present. In practice, the durability will be greater, because it is much more difficult to fail the remnant ligament when the loading is predominantly mode II, which it is for edge delaminations. Further measurements and analysis are needed to understand the delamination strength.

REFERENCES

1. Miller, R. A., *J. Thermal Spray Technol.*, 1997, **6**, 35.
2. Cross, L. A., Stewart, S. F. and Ortiz, M., *J. Engng Gas Turbines Pwr*, 1988, **110**, 610.
3. Brindley, W. J. and Miller, R. A., *Surf. Coat. Technol.*, 1990, **43/44**, 446.
4. Taylor, T. A., Appleby, D. L., Weatherill, A. E. and Griffiths, J., *Surf. Coat. Technol.*, 1990, **43/44**, 470.
5. Miller, R. A., *J. Am. Ceram. Soc.*, 1984, **67**, 517.
6. Christensen, R. J., Tolpygo, V. K. and Clarke, D. R., *Acta mater.*, 1997, **45**, 1761.
7. Tolpygo, V. K., Dryden, J. R. and Clarke, D. R., *Acta mater.*, 1998, **46**, 927.
8. Stasik, M. C., Pettit, F. S., Meier, G. H., Ashary, A. and Smialek, J. L., *Scripta metall. mater.*, 1994, **31**, 1645.
9. Scott, F. H. and Atkinson, A., *Mater. High Temp.*, 1994, **12**, 195.
10. He, M. Y., Evans, A. G. and Hutchinson, J. W., *Mater Sci. Engng*, 1998, **A245**, 168.
11. Evans, A. G., He, M. Y. and Hutchinson, J. W., *Acta mater.*, 1997, **45**, 3543.
12. Topylgo, V. K. and Clarke, D. R., *Acta mater.*, 1998, **46**, 5167.
13. Choi, S. R., Hutchinson, J. W. and Evans, A. G., *Mech. Mater.*, submitted.
14. Gioia, G. and Ortiz, M., *Adv. Appl. Mech.*, 1997, **33**, 120.
15. Hutchinson, J. W. and Jensen, H. M., *Mech. Mater.*, 1990, **9**, 139.
16. Zhuk, A., Evans, A. G., Hutchinson, J. W. and Whitesides, G. M., *J. Mater. Res.*, 1998, **13**, 3555.
17. He, M. Y., Evans, A. G. and Hutchinson, J. W., *Acta mater.*, 1997, **45**, 3481.
18. Marshall, D. B., Lawn, B. R. and Evans, A. G., *J. Am. Ceram. Soc.*, 1982, **65**, 561.
19. Evans, A. G., McMeeking, R. M., Charalambides, P. G. and Hutchinson, J. W., *Acta metall.*, 1987, **35**, 2701.
20. Mumm, D. R. and Evans, A. G., to be published.
21. Tada, H., Paris, P. and Irwin, G., *Handbook of Stress Intensity Factors*. Dell Research, 1985.
22. He, M. Y., Wissuchek, D. J. and Evans, A. G., *Acta mater.*, 1997, **45**, 2813.

Appendix C

PERGAMON

Acta mater. 48 (2000) 2593–2601

Acta MATERIALIA

www.elsevier.com/locate/actamat

THE RATCHETING OF COMPRESSED THERMALLY GROWN THIN FILMS ON DUCTILE SUBSTRATES

M. Y. HE[1], A. G. EVANS[2]† and J. W. HUTCHINSON[3]

[1]University of California, Santa Barbara, Santa Barbara, CA 93106, USA, [2]Materials Institute, Princeton University, Princeton, NJ 08540, USA and [3]Division of Engineering and Applied Sciences, Harvard University, Cambridge, MA 02138, USA

(Received 13 December 1999; accepted 8 February 2000)

Abstract—An analysis of the displacements experienced by undulating thermally grown thin films upon thermal cycling has been presented. The film has been assigned a thermal expansion coefficient that causes it to be compressed upon cooling. It has also been allowed to thicken at high temperature by oxidation of the substrate. It is shown that, in some circumstances, ratcheting occurs, wherein the undulation amplitude, a, increases with each thermal cycle. When such a response happens, undesirable cyclic failure modes are induced. The analysis reveals that there is a critical undulation amplitude, a_c, below which ratcheting does not occur. This critical size is related to the expansion misfit, the substrate yield strength and the growth strain in the film per cycle. Connections between these variables and a_c are derived.

Keywords: Physical vapor deposition; Stress/strain theory; Layered materials; Fatigue

1. INTRODUCTION

Thin films on thick, ductile (metal or polymer) substrates when residually compressed by a misfit stress, σ_0, are susceptible to various out-of-plane displacement instabilities [1–9]. The most widely documented examples involve the thin thermally grown oxide (TGO) of α-Al_2O_3 that forms on superalloy components used for propulsion and power generation [1–9]. In this example, a top thermal barrier layer may also be present [Fig. 1(a)]. Related phenomena occur around metal interconnects in semiconductor devices [10]. The displacements occur by distorting the substrate. They reduce in-plane compression, but lead to tensile stresses [8] that, in some cases, initiate the failure sequence.

The starting hypothesis is that pre-existing undulations in the film initiate the instability. The undulations increase in amplitude, with time or cycles [Fig. 1(a)], in accordance with two known manifestations. One occurs isothermally, at elevated temperatures, with the displacements accommodated by substrate creep. This phenomenon is often referred to as "wrinkling" [6]. The other occurs upon thermal cycling [11]. Typically, cycling involves a hold time Δt at the highest temperature with intervening up and down ramps. The film thickens during Δt, because of the kinetics of oxidation. In this manifestation, the undulations are unaffected by time-at-temperature. Instead, they accumulate systematically with each cycle. It will be shown that the displacements are enabled by cyclic yielding of the substrate and require that there be an increment in film thickness in each cycle, governed by its thickening kinetics [4–6]. By analogy with related thermo-mechanical phenomena [12–15], this process is referred to as "ratcheting". This is the mechanism analyzed in the present article.

When ratcheting happens, and a top layer is present, the increase in undulation amplitude upon cycling induces out-of-plane tensile strains, ε_{zz}, in this layer [Fig. 1(a)]. These strains may cause cracks parallel to the interface which, in turn, induce failures, such as those reported for oxide thermal barriers [16]. An example is shown on Fig. 1(b). Moreover, the state of stress in the film changes and becomes tensile at some locations [7, 17]. At these sites, film cracking may occur, despite the overall state of compression.

In general, ratcheting requires the presence of at least two materials having significant differences in thermal expansion coefficient [12, 13]. Then, upon thermal cycling, and in the presence of a strain that provides a directional bias, material displacements occur with each cycle. For any simple thermo-mech-

† To whom all correspondence should be addressed.

1359-6454/00/$20.00
PII: S1359-6454(00)00053-7

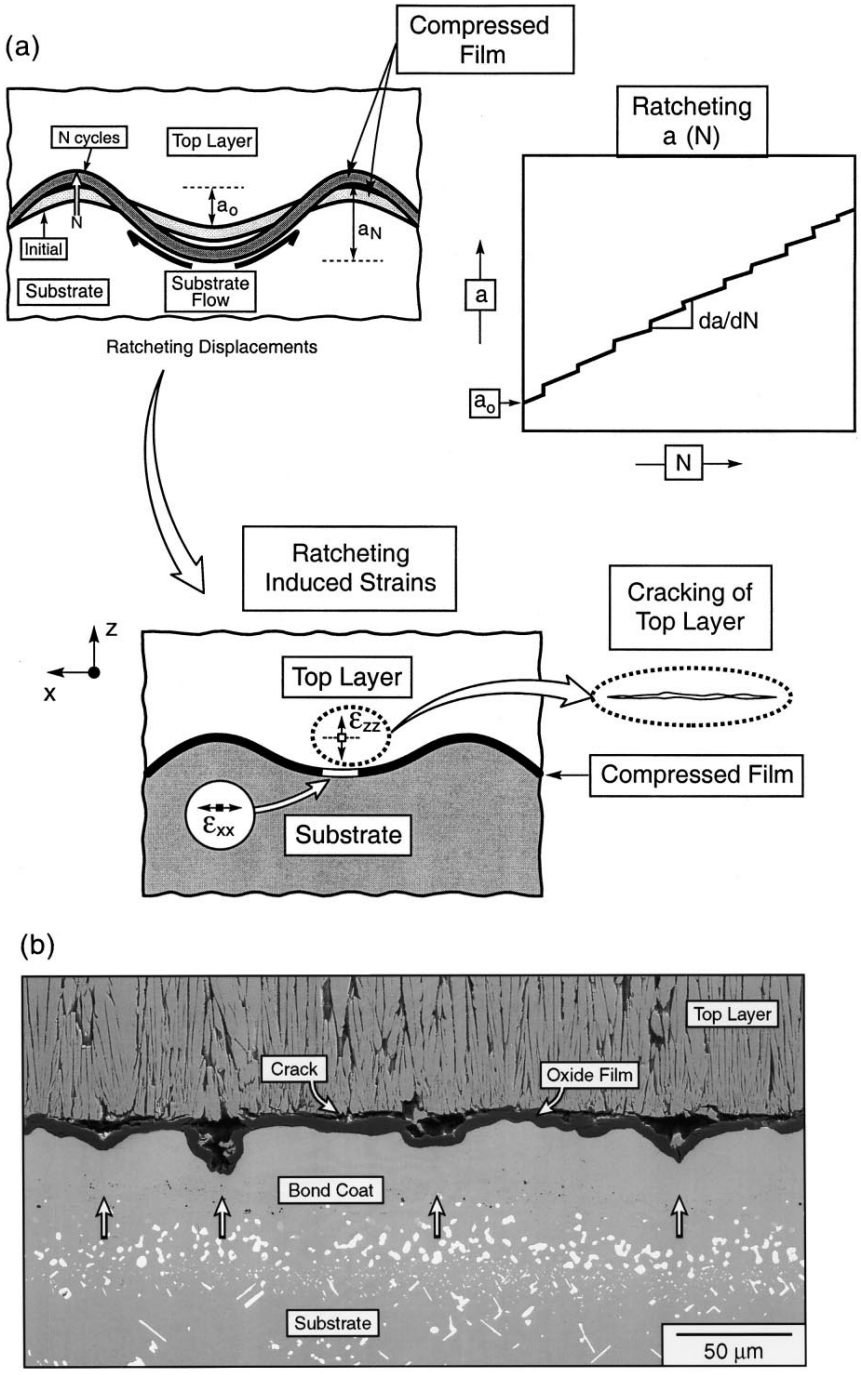

Fig. 1. (a) A schematic indicating the ratcheting phenomenon in thin compressed films and the strain induced in the top layer, which may result in cracking and failure. (b) The undulations in the oxide film, indicated by arrows, grew by ratcheting (they did not exist when the film was deposited). The growth of the undulations caused cracks to initiate in the top layer, in the manner suggested by the schematic (courtesy Dr D. Mumm).

anical loading, the range of responses has been characterized by a Bree diagram (Fig. 2) [14, 15], wherein the regions that experience elastic response, shakedown and ratcheting are identified. The existence of these regions will re-emerge in the present study, albeit with different co-ordinates. A good example is the ratcheting of particle reinforced metals comprising, say, aluminum alloys with SiC reinforcements [12]. These ratchet upon thermal cycling when a small stress is applied.

When the film is perfectly planar, the absence of a shear stress in the substrate (except near free edges) means that there can be no out-of-plane response to thermal cycling [1]. However, shear stresses induced in the substrate by film undulations may exceed its yield strength [1]. When this happens, the undulation amplitude enlarges, through substrate plasticity. The extent to which this continues as the system thermally cycles is examined in this study. It will be shown that the ratcheting is transient when the film thickness remains invariant. However, when a thickening occurs in each thermal cycle (because of a growth mechanism such as oxidation), the ratcheting can attain steady state, wherein the amplitude consistently increases with continued cycling. This is the phenomenon of present concern because of its direct association with failure [Fig. 1(a)].

2. CONCEPTS

While ratcheting is a documented phenomenon [12–15], the conditions that allow it to occur in thin films on thick substrates have not been explicitly identified. Absent isothermal wrinkling at high temperature [11], cyclic plasticity in the substrate affords the only mechanism capable of providing cumulative displacements. Such responses become possible wherever the equivalent stress, σ_e, induced in the substrate exceeds its yield strength, σ_Y. This stress is governed by [1, 3]: the amplitude of the undulations, a_0, relative to their wavelength, $2L$, the film thickness, h, the relative elastic moduli of film, E_f, and substrate, E_s, and the misfit stress, σ_0, defined as

$$\sigma_0 = \Delta\alpha\Delta T E_f/(1-\nu_f) \quad (1)$$

where $\Delta\alpha$ is the difference in thermal expansion coefficient between the substrate, α_s, and the film, α_f, ΔT is the amplitude of the temperature change (with the highest temperature in the cycle as the reference) and ν_f the Poisson ratio for the film. *Note that the misfit stress is that in a perfectly flat film subject to* ΔT (not the stress in the substrate).

It is not sufficient to just yield the substrate on initial cooling. Such yielding only produces an initial displacement, followed by either shakedown or cyclic plastic straining of the substrate [3]. That is, ratcheting effects will damp-out after a few cycles. This assertion is verified by some of the calculations that follow. *An additional phenomenon is needed for continuous ratcheting*. For the particle reinforced metals cited above, this is achieved with an applied stress, which biases the plastic response to the extent needed to induce continuous plastic straining with each thermal cycle [12]. For thin compressed films on thick substrates, the analog is less obvious.

Two high temperature effects operate in thermally grown oxides that might lead to ratcheting. One involves creep in the TGO [18], which would relax the stresses. The other involves the growth strain that occurs upon oxidation [17]. That is, at the highest temperature in the cycle, taken to be 1000°C, the film thickens during the hold time Δt in accordance with oxidation kinetics. The present article demonstrates that ratcheting can arise in situations that involve growth strains (Fig. 3). The philosophy adopted for these calculations is to seek the most basic elements of material behavior that result in ratcheting. Once the principles have been established, explicit determinations of ratcheting rates, with realistic material properties, would follow. The simplest model that can be envisaged comprises a thin film with a smaller thermal expansion coefficient than that for the substrate: with the latter having a temperature independent yield strength, σ_Y. The elastic moduli of the film, E_f, and substrate, E_s, are taken to be different and representative of an oxide film on a metal substrate ($E_f/E_s = 2$).

The calculations are performed by imposing on the film an isotropic growth strain, ε_g, at the highest temperature (Fig. 3), taken to be 1000°C, then cycling to room temperature and back. This is a stress-free strain, analogous to a thermal expansion. For simplicity, ε_g is taken to be the same for each cycle. Later embellishments might allow it to

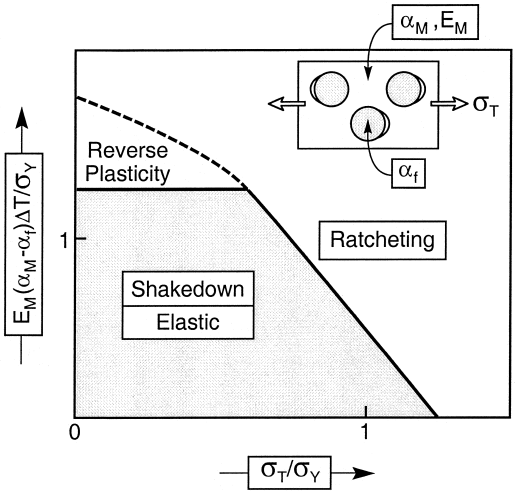

Fig. 2. A Bree diagram developed for transverse loading of a metal matrix composite [12].

change as the film thickens. Also, for tractability, the film is considered to be elastic, with a temperature independent modulus E_f (except for the growth strain). The temperature dependence of E_f and creep in the film will be addressed in a subsequent paper.

The major emphasis concerns the dependence of the ratcheting rate on ε_g, as well as the material properties (especially σ_Y and $\Delta\alpha$) and the film morphology ($a_0/2L$ and h). The authors are unaware of an analytical method that could elucidate this role with appropriate accuracy. The approach taken, therefore, is to use numerical methods to find property domains susceptible to ratcheting.

In the following analysis, the top layer depicted on Fig. 1(a) has been neglected, primarily because the material comprising this layer has low shear modulus [19] (created by incorporating inter-columnar porosity to attain strain tolerance). This low modulus would provide minimal resistance to displacements of the film. In subsequent studies, the explicit (though small) influence of this layer will be examined.

3. RATCHETING ANALYSIS

3.1. Method

The finite element method is employed for the calculations, using the ABAQUS code. The substrate is taken to be 100 times thicker than the film to suppress overall bending of the system. Periodic boundary conditions are used with a unit cell having width, L (Fig. 3). Generalized plane strain conditions account for the bi-axial nature of thermal loading. The growth strain ε_g is introduced at the temperature maximum ($T = 1000°C$) in each cycle. This can be accomplished in several ways, depending on the flexibility and options available within the finite element code. A code that incorporates a transformation strain option enables growth to be introduced as a sequence of transformation steps, giving rise to the accompanying elastic and plastic strain increments. When the properties of the film and substrate are temperature-independent, as in the present case, an equivalent approach based on a fictitious temperature change may be used. Then, the growth strain can be achieved by adding an extra temperature change, ΔT_g, at the temperature maximum in each cycle: where $\varepsilon_g = \Delta\alpha\Delta T_g$.

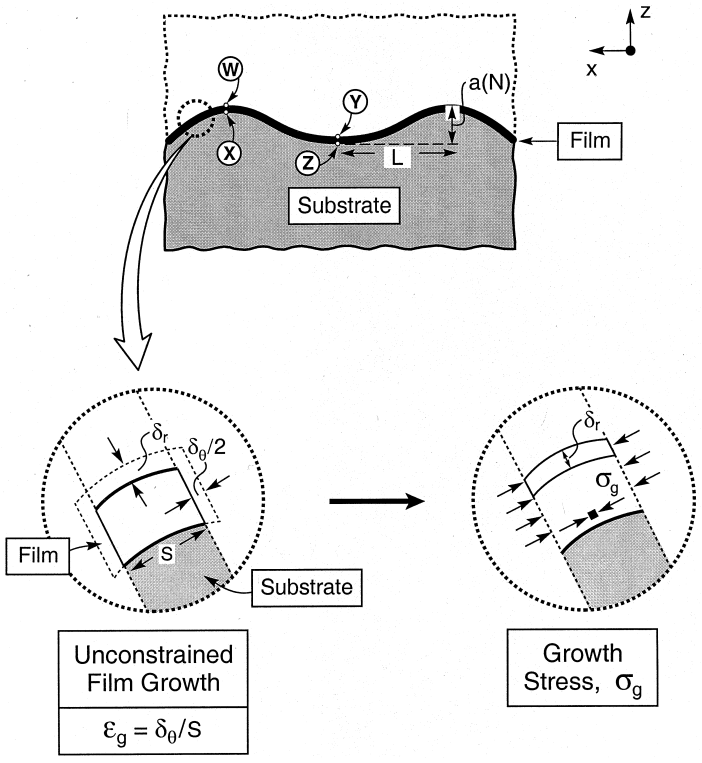

Fig. 3. The geometry subject to analysis and a schematic showing the film growth strain (unconstrained) and the consequent growth stress.

Accordingly, the temperature increase becomes, $\Delta T + \Delta T_g$, while the temperature decrease is still ΔT. In the calculation, ΔT_g is divided into incremental steps and the associated elastic and plastic strains computed.

3.2. General trends

Most of the results have been obtained for a growth strain [17], $\varepsilon_g = 10^{-4}$. A few results have been obtained for smaller and larger values in order to assess the scaling with ε_g. In all cases, the wavelength, L, is assumed to remain constant with only changes in amplitude, Δa, allowed.

The results for various initial undulation amplitudes, $a_0/2L$, are presented using the non-dimensional quantities:

$$\Sigma \equiv \sigma_0/\sigma_Y, \quad \Pi \equiv \Delta a/2L\varepsilon_g$$

where Δa is that part of the amplitude change attributed to ε_g and $\Delta\alpha$, with the contribution arising from uniform $\alpha_s \Delta T$ subtracted. The normalization used for Π does not imply that Δa is proportional to ε_g, as elaborated later. The partitioned amplitude change is a natural choice, since in performing the calculations, it has been convenient to regard α_s of the substrate to be zero and to use, $\Delta\alpha = \alpha_f - \alpha_s$, as the coefficient of thermal

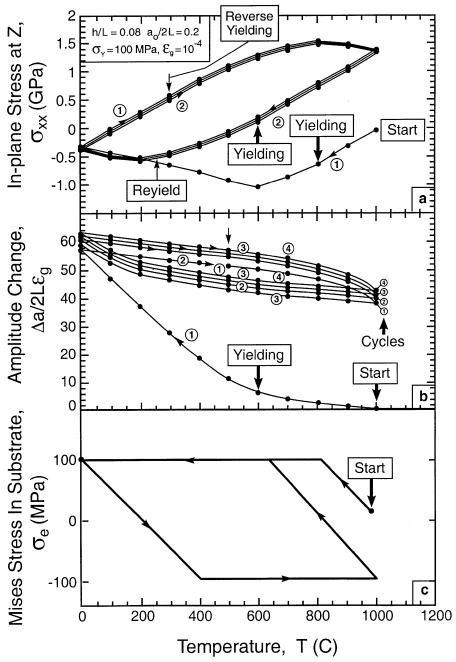

Fig. 4. Numerical calculations performed over four thermal cycles for the parameter set indicated on the inset, with $\sigma_Y = 100$ MPa: (a) in-plane stress, σ_{xx}, at site Z; (b) the change in undulation amplitude, Δa; (c) the effective, Mises, stress in the substrate (which for consistency is always taken to be positive).

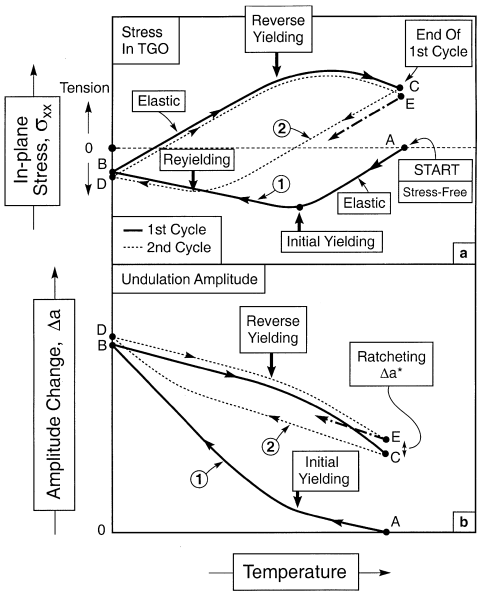

Fig. 5. A schematic of Fig. 4, highlighting the salient features.

expansion of the film. Accordingly, the total amplitude change in the first cool down, $\Delta a_{total} = \Delta a + a_0 \alpha_s \Delta T$, can be larger than that due to ε_g and $\Delta\alpha$: but, since it is completely reversible under temperature cycling, it makes no contribution to ratcheting. All of the calculations have been performed with the following material parameters: $E_s = 200$ GPa, $\nu_s = 0.3$, $E_f = 400$ GPa, $\nu_f = 0.2$ and $\sigma_Y = 100$–500 MPa.

The initial calculations have been conducted for conditions that elicit the greatest likelihood of ratcheting. That is, results are obtained for relatively large values of Σ and $a_0/2L$, subject to an appreciable temperature cycle, $\Delta T = 1000°C$ (Figs 4 and 5). Typical results over four cycles for the in-plane stress in the film, σ_{xx} [Fig. 4(a)], at site

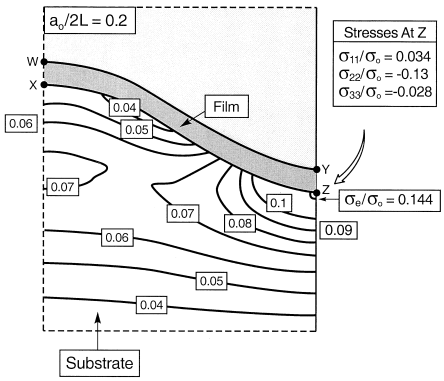

Fig. 6. Contours of equivalent stress σ_e induced in the substrate (normalized by the misfit stress, σ_0) for the same parameter set used to obtain Fig. 4. The stresses have been calculated at ambient after one cycle.

Z (see Fig. 3), and for the change in undulation amplitude, Π [Fig. 4(b)] illustrate the salient characteristics. The corresponding stresses in the substrate, at Z, are plotted on Fig. 4(c). The distribution of stresses in the substrate that lead to yielding are indicated on Fig. 6 for one of the cases used in the study. The magnitudes are those existing at room temperature. Note that the largest stresses are immediately beneath the valley in the film, so that yielding initiates at this site. The consequence for the stresses in the film will be addressed later.

To facilitate visualization and understanding, the key phenomena are shown in schematic form on Fig. 5. The system is stress-free at the beginning, starting at high temperature (coordinate A). Upon cooling, the initial development of σ_{xx} and Δa occur elastically. With further cooling, when the stresses induced in the substrate next to the film attain its yield strength [Figs 4(c) and 6], plastic deformation commences (denoted "initial yield" on Fig. 5). The associated plastic strains allow the film at the valley to displace downward. Upon yielding, the rate of stress development $|\mathrm{d}\sigma_{xx}/\mathrm{d}T|$ decreases: whereas the displacement rate, $|\mathrm{d}\Delta a/\mathrm{d}T|$ increases. For the specific parameters chosen to obtain the results on Fig. 4, even the actual stress level decreases; that is, it becomes less compressive with continued cooling. Upon re-heating (from coordinate B), the initial response is elastic. With further heating, reverse yielding initiates, as indicated on Figs 4 and 5. Thereafter, again, $|\mathrm{d}\sigma_{xx}/\mathrm{d}T|$ decreases and $|\mathrm{d}\Delta a/\mathrm{d}T|$ increases. At the end of the first cycle (coordinate C) the stress is now non-zero (tensile in this case) and there has been an increase, Δa^*, in the undulation amplitude. Before embarking on another cycle, an increment of growth strain, ε_g, is imposed on the film. This is manifest as a small increment in the undulation amplitude. On the second cycle (CDE), the process repeats, but along a slightly different path. The consequence is a somewhat smaller stress and larger displacement at E than at C.

3.3. Ratcheting amplitude

The increase in undulation amplitude during the initial few cycles is not, in itself, particularly significant. The important issue is whether the amplitude change, Δa^*, continues with each cycle and *ratchets*, or whether it damps-out after only a few cycles, resulting in *shakedown*. These alternative responses may be explored by repeating the thermal cycling and monitoring the change in Δa^* that arises with each cycle. Examples are shown on Fig. 7(a) for two cases. One example pertains to a zero growth strain, while the other uses $\varepsilon_g = 10^{-4}$. For the former, the ratcheting rate, $\mathrm{d}\Delta a^*/\mathrm{d}N$, decreases with each cycle and essentially stops after 10 cycles, resulting in shakedown. Conversely, when the growth strain is included, ratcheting settles into a steady state after about 10 cycles. This result affirms the assertion made in Section 2 that a growth strain is needed to realize steady-state ratcheting. This steady-state response is the one that leads to the large overall displacements that govern cracking and failure in the top layer [Fig. 1(b)]. Repeating the calculations for a much larger substrate yield strength (800 MPa) changes the response (Fig. 8). Now, the behavior is strictly (linear) elastic, except

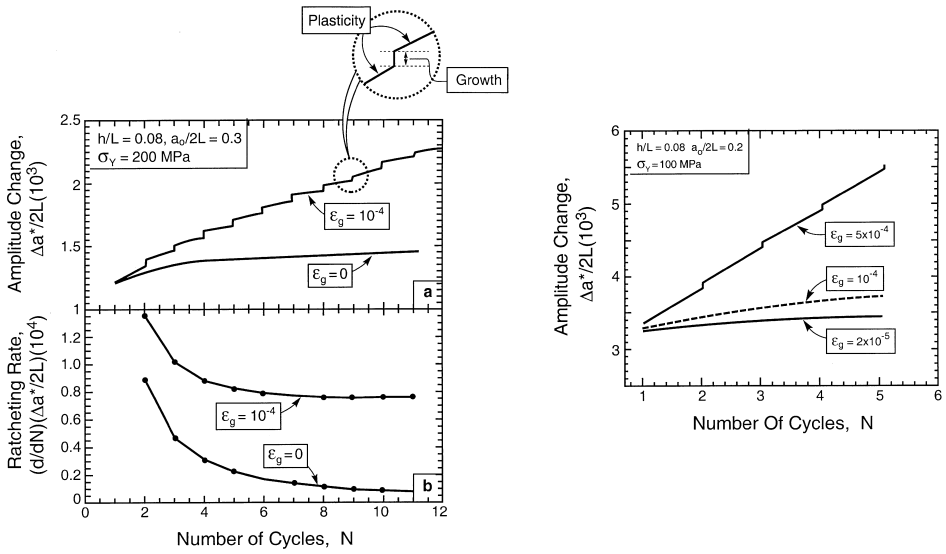

Fig. 7. (a) The effect of the growth strain, ε_g, on the amplitude change and ratcheting rate at ambient temperature for the parameter set indicated on the inset. (b) The influence of growth strain on the ratcheting rate.

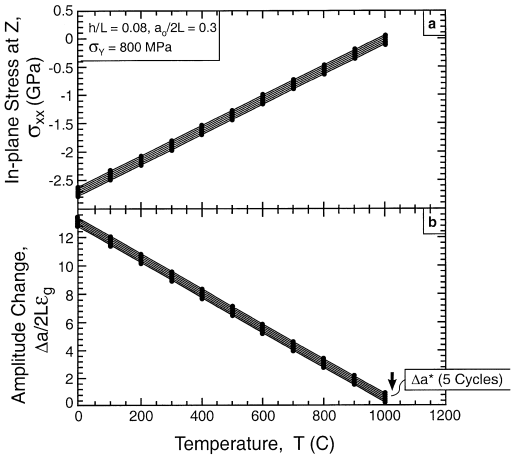

Fig. 8. Corresponding results to those in Fig. 4 for a higher yield strength substrate, $\sigma_Y = 800$ MPa.

for the addition of the growth strain at the end of each cycle.

The effect of varying the growth strain is shown on Fig. 7(c). As expected, the steady-state ratcheting rate, $d\Delta a^*/dN$, increases as ε_g increases. Within the small range studied, the scaling is not quite linear. That is, an increase in ε_g by a factor of five increases the ratcheting rate by a smaller factor (three to four). A subsequent study would be needed to examine the relevant scaling.

The Δa^* results obtained from many different calculations, all at a fixed growth strain ($\varepsilon_g = 10^{-4}$), can be summarized in the manner depicted on Fig. 9. This figure expresses the amplitude changes as a function and of the stress ratio, $\Sigma \equiv \sigma_0/\sigma_Y$. It distinguishes the contributions to the amplitude change per cycle from growth and cyclic plasticity. The former is invariant, while the latter increases as the stress ratio increases. For the undulations used in these calculations, the Δa_* from plasticity is zero when $\Sigma < 5$ corresponding to the elastic response shown on Fig. 8. When $5 \leqslant \Sigma \leqslant 9$, the plasticity component reduces with each cycle and becomes zero after about 10 cycles, reflecting shakedown. At $\Sigma > 9$, the plasticity component persists: indicative of the ratcheting shown in Fig. 4. These three domains are distinguished on the figure.

The effect of the initial undulation amplitude, $a_0/2L$, on the three domains, calculated using the same scheme, is presented on Fig. 10. As expected from earlier studies [3], the smaller the initial undulation, the higher the stress ratio, Σ, needed to activate ratcheting (rather than shakedown). The pertinence of these specific stress ratios is further addressed in Section 4.

3.4. Stresses in the film

The in-plane stresses that develop in the film as a consequence of thermal cycling are location sensitive. But after the first cycle, they remain largely invariant with subsequent cycling. These two effects are illustrated on Figs 11 and 12. The results in Fig. 11 refer to the σ_{xx} stresses in the film at the four sites (W, X, Y, Z) shown on Fig. 3. For clarity of presentation, only the first and fifth cycles are shown. The first feature to note is that the stresses are non-uniform through the film thickness, indicative of local bending. At the undulation peak (W, X), the stresses at the top of the film are tensile at the temperature maximum, but about zero at the bottom. This differential reflects a bending moment that tends to increase the undulation amplitude, consistent with the overall displacements. At the valleys (Y, Z), both sides of the film are in tension at the maximum in the temperature, indicative of a stretching enabled by the plastic deformation of the substrate at this site (Fig. 7). In addition, a bending deformation accounts for the larger tensile stress at

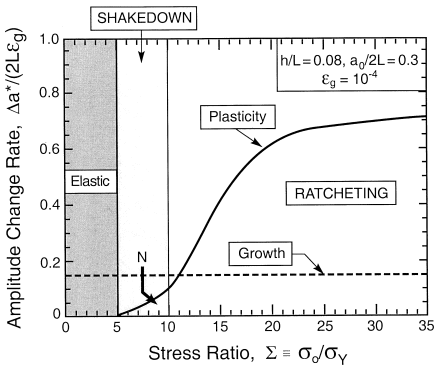

Fig. 9. A map of the three response domains using the amplitude change rate and stress ratio as coordinates. For TGO formed on superalloys, the misfit stress is almost invariant. The abscissa is thus affected largely by the yield strength of the substrate, in the sense that lower yield strength substrates are more prone to ratcheting.

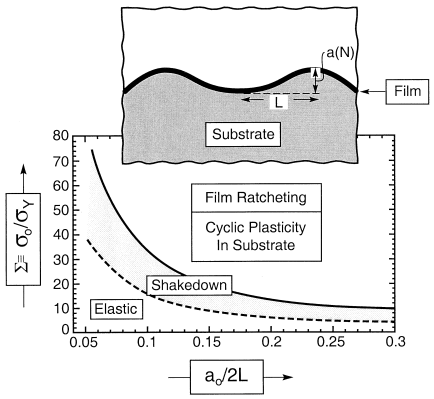

Fig. 10. The effect of initial undulation amplitude on the three domains shown on Fig. 9. The parameters used are those shown on the inset of Fig. 9.

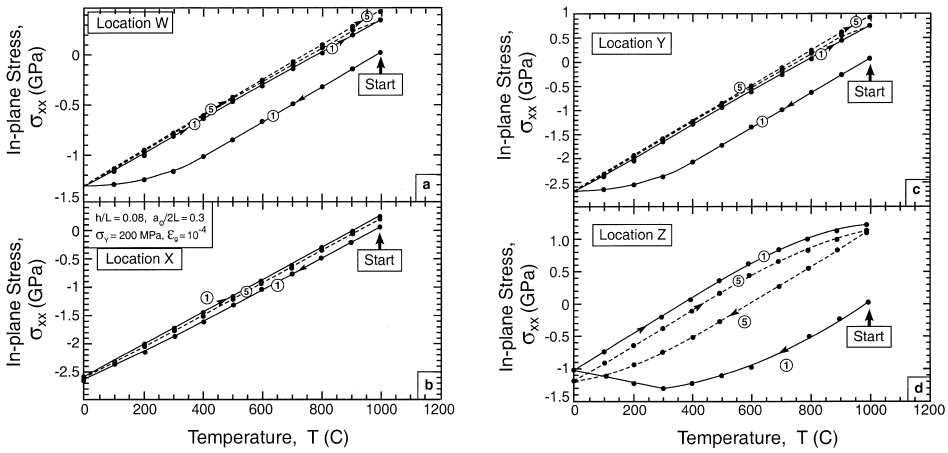

Fig. 11. In-plane stress in the first and fifth cycles at the four sites (W, X, Y, Z) shown on Fig. 3.

Z than at Y; again consistent with displacements that increase the undulation amplitude. These tensile stresses may induce film cracking [9].

The relative invariance of the stress levels with the number of cycles, when ratcheting occurs, is illustrated on Fig. 12. This contrasts with the trend in the displacements, because plasticity redistributes the stresses induced by the growth strain.

4. CONCLUDING COMMENTS

The results summarized on Fig. 10 provide general guidelines for anticipating the combination of circumstances that lead to ratcheting; particularly the effects of geometry, $a_0/2L$, and of the stress ratio, σ_0/σ_Y. Some corresponding effects of the growth strain, ε_g, have been illustrated in Fig. 7(a). The most basic result is that steady-state ratcheting requires a growth strain in each thermal cycle. Another key finding is that the undulations must exceed a critical relative amplitude, a_c/L, before they exhibit ratcheting. Moreover, this critical amplitude becomes smaller the lower the yield strength of the substrate material immediately adjacent to the film. Undulations smaller than a_c/L experience shakedown and remain geometrically stable. The growth strain also exerts a central influence on a_c. This is the least understood aspect of film growth upon oxidation [18]. New studies of this phenomenon are warranted.

For the particular case of aluminum oxide films growing on Ni-based materials, the stress ratio Σ merits some further discussion. With σ_0 being about 3 GPa [20] and the initial yield strength of the bond coat material being about 600 MPa, Fig. 10 indicates that the likelihood of ratcheting should be small, since a_c is large ($> 0.6L$). However, as the film thickens, the Al concentration in the material immediately beneath the film decreases [16], because it is consumed by the growing film. This depletion causes a phase change in the alloy that may reduce its yield strength immediately beneath the oxide film. There is a corresponding reduction in a_c because of the associated change in Σ. Experimental studies that explicitly address the critical amplitude are in progress. These assessments address changes in wavelength (not just amplitude) that may occur upon ratcheting, which have not been allowed in the present calculations.

The tensile stresses predicted to develop in the film are much larger than those that would arise in practice, because creep in the film at the higher temperatures would relax them appreciably [18]. To some extent, therefore, there is competition between creep and cracking of the film during the high temperature portion of the cycle. Moreover, stress relaxation by creep would affect the growth strain and must influence the ratcheting specifics. Introducing film creep in a meaningful manner constitutes the next key step in the understanding of ratcheting.

A durability model could clearly be built from the present results for Δa^* by relating this displacement to the crack opening in the TBC above the undulation [Fig. 1(b)]. The associated mechanics are addressed in another article.

Appendix D

PERGAMON

Progress in Materials Science 46 (2001) 249–271

Progress in Materials Science

www.elsevier.com/locate/pmatsci

Mechanics-based scaling laws for the durability of thermal barrier coatings

A.G. Evans [a,*], M.Y. He [b], J.W. Hutchinson [c]

[a] *Princeton Materials Institute, Princeton University, Princeton, NJ 08540, USA*
[b] *Materials Department, University of California at Santa Barbara, CA 91360, USA*
[c] *Division of Engineering and Applied Science, Harvard University, Cambridge, MA 02138, USA*

Abstract

The durability of thermal barrier systems is governed by a sequence of crack nucleation, propagation and coalescence events that accumulate prior to final failure by large scale buckling and spalling. This sequence is governed by the σ_{zz} stresses that develop normal to the substrate, around imperfections, as the thermally grown oxide (TGO) thickens. Their effect is manifest in the stress intensity factor, K, caused by the σ_{zz} stresses acting on cracks emanating from them. In turn, these events are governed by scaling laws, ascribed to non-dimensional groups governing σ_{zz} and K. In this article the basic scaling relations are identified and used to gain some understanding of the relative importance of the various mechanisms that arise for application scenarios with minimal thermal cycling. These mechanisms are based on stresses that develop because of TGO growth strains in combination with thermal expansion misfit. The results are used to identify a critical TGO thickness at failure and express it in terms of the governing material variables. The changes in behavior that arise upon extensive thermal cycling, in the presence of TGO ratcheting, are elaborated elsewhere.

Contents

* Corresponding author.
E-mail address: anevans@princeton.edu (A.G. Evans).

0079-6425/01/$ - see front matter
PII: S0079-6425(00)00007-4

1. Introduction

Thermal barrier coatings (TBCs) are widely used in turbines for propulsion and power generation [1–6]. They comprise thermally insulating materials having sufficient thickness and durability that they can sustain an appreciable temperature difference between the load bearing alloy and the surface. The benefit of these coatings results from their ability to sustain high thermal gradients in the presence of adequate back-side cooling. Lowering the temperature of the metal substrate prolongs the life of the component. Successful implementation has required comprehensive testing protocols, facilitated by engineering models [7–9]. Expanded application to more demanding scenarios requires that their basic thermo-mechanical characteristics be understood and quantified. This need motivates the analysis presented in this article. There are *four primary constituents* in a thermal protection system (Fig. 1). They comprise (i) the TBC itself, (ii) an aluminum containing bond coat (BC) between the substrate and the TBC, (iii) a thermally grown oxide (TGO), predominantly alumina, that forms between the TBC and the BC, and (iv) the superalloy substrate. The TBC is the insulator, the BC provides the oxidation protection and the alloy sustains the structural loads. The TGO is a reaction product. Each of these elements is dynamic and all interact to control the performance and durability. The thermal barrier coating is an insulating, ''strain tolerant'' oxide. Zirconia has emerged as the preferred material, stabilized into its cubic/tetragonal forms by the addition of yttria in solid solution. This material has low thermal conductivity with minimal temperature sensitivity [10]. Strain tolerance is designed into the material to avoid instantaneous delamination from the thermal expansion misfit with the substrate [1,4,6,7]. The deposition conditions are designed to create multi-scale porosity that provides the requisite strain tolerance and also reduces the thermal conductivity. The bond coat alloy is designed as a local Al reservoir, enabling α-alumina to form in preference to other oxides [11–13]. Alumina is the preferred thermally grown oxide because of its low oxygen diffusivity and superior adherence. Bond coats are in two categories.

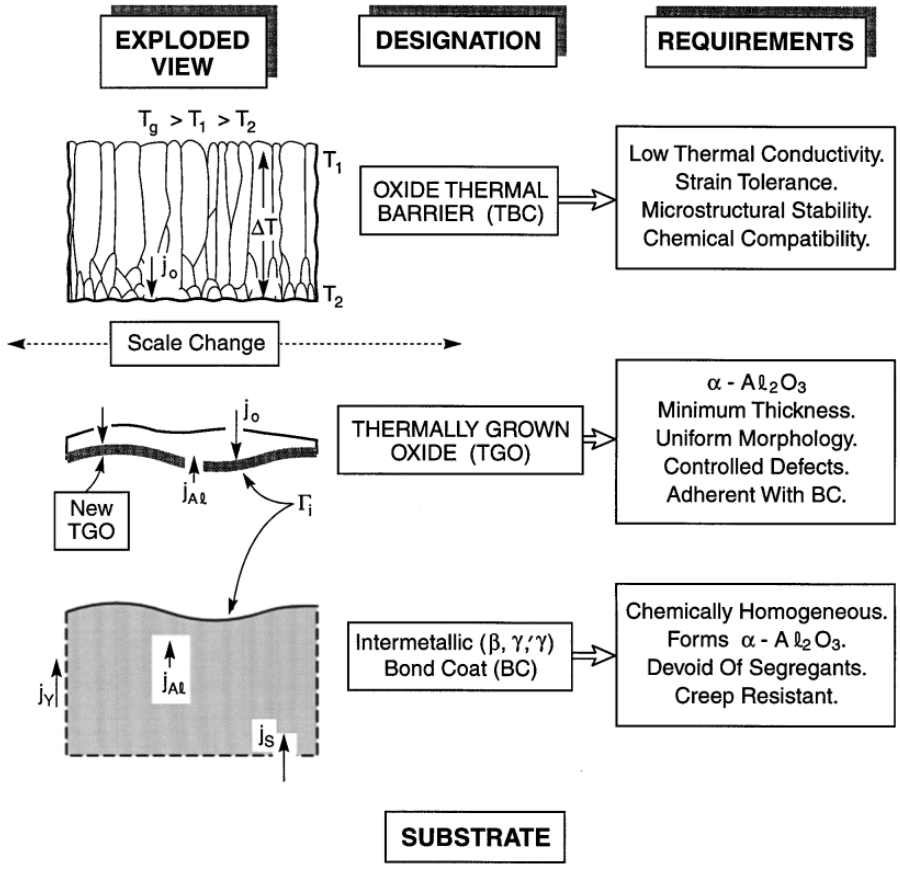

Fig. 1. An exploded view of the four major constituents of a thermal barrier system.

One is based on the NiCoCrAlY system. Such coatings are generally two phase (γ'-Ni_3Al with β-NiAl). The Y is added at low concentrations to improve the adhesion of the TGO, by acting as a solid state gettering site for S [14–16]. The second category consists of a Pt-aluminide. These coatings are typically single-phase-β, with Pt in solid solution [12]. The TGO layer, which forms predominantly at the highest temperature in the thermal cycle, develops extremely large residual compressions at ambient (3–6GPa) [17–19]. These arise primarily on cooling, because of its thermal expansion misfit with the substrate (Table 1). Smaller, yet significant, stresses also arise during TGO growth [12,18]. Though thin (about 10 μm), the strain misfit in the TGO motivates the failure mechanisms to be addressed in this article. In such cases, eventual failure is associated with the appearance of large-scale buckles (LSB), several mm in diameter [20,21]. Spalled areas may also appear at free edges [21].

The approach taken is to use basic failure-related observations to guide the development of mechanics-based scaling laws. Two general observations provide benchmarks. One finding is that failure of any specific TBC system is correlated with the thickness, h, of the thermally grown oxide [1,6,8,22]. There is also compelling evidence that failure is connected with the presence of imperfections between the

Table 1
Summary of material properties

1. *TBC (ZrO_2/Y_2O_3)*	
Thermal expansion coefficient, α_{tbc} (C^{-1} ppm)	11–13
Young's modulus, E_{tbc} (GPa)	0–100
Delamination toughness, Γ_{tbc} ($J\ m^{-2}$)	1–100
2. *TGO (α-Al_2O_3)*	
Young's modulus, E_o (GPa)	350–400
Growth stress, σ^g_{xx} (GPa)	0–1
Misfit compression, σ_o (GPa)	3–4
Mode I fracture toughness, Γ_o ($J\ m^{-2}$)	20
Thermal expansion coefficient, α_o (C^{-1} ppm)	8–9
3. *Interface (α-Al_2O_3/bond coat)*	
Mode 1 adhesion energy, Γ_1^o ($J\ m^{-2}$)	
Segregated	5–20
Clean	>100
4. *Bond coat*	
Young's modulus, E_s (GPa)	200
Yield strength (ambient temperature), σ_Y (MPa)	300–900
Thermal expansion coefficient, α_s (C^{-1} ppm)	13–16
5. *Substrate (Ni-alloy)*	
Thermal expansion coefficient, α_s (C^{-1} ppm)	13–16

TBC and the bond coat [23–26]. The most ubiquitous comprise undulations in the bond coat surface (Fig. 2). Stress development around such imperfections, as the TGO thickens, becomes a basic input to failure laws. Analysis of energy release rates for cracks emanating from these imperfections, followed by an assessment of their coalescence, completes this description.

With minimal thermal cycling, the sources of stress are those formed upon TGO growth, followed by the changes that happen because of thermal expansion misfit on cooling to ambient. Extensive thermal cycling introduces a different set of stresses, caused by phenomena such as ratcheting, which will be analyzed separately [27]. To address failure, the zones that experience tensile stress normal to the interface are most important, since these stresses are responsible for nucleating and propagating delaminations. Before attempting analyses that include the full geometric complexity of actual imperfections (Fig. 2), insights about the signs and relative magnitudes of the stresses and the energy release rates are obtained by analyzing spherical configurations subject to misfit strains. Subsequently, numerical results are obtained for configurations more similar to those found in actual TBCs.

2. Analytical assessments

The stresses induced by TGO growth differ from those caused by expansion misfit because of the differing nature of the associated "transformation" strains. Thermal

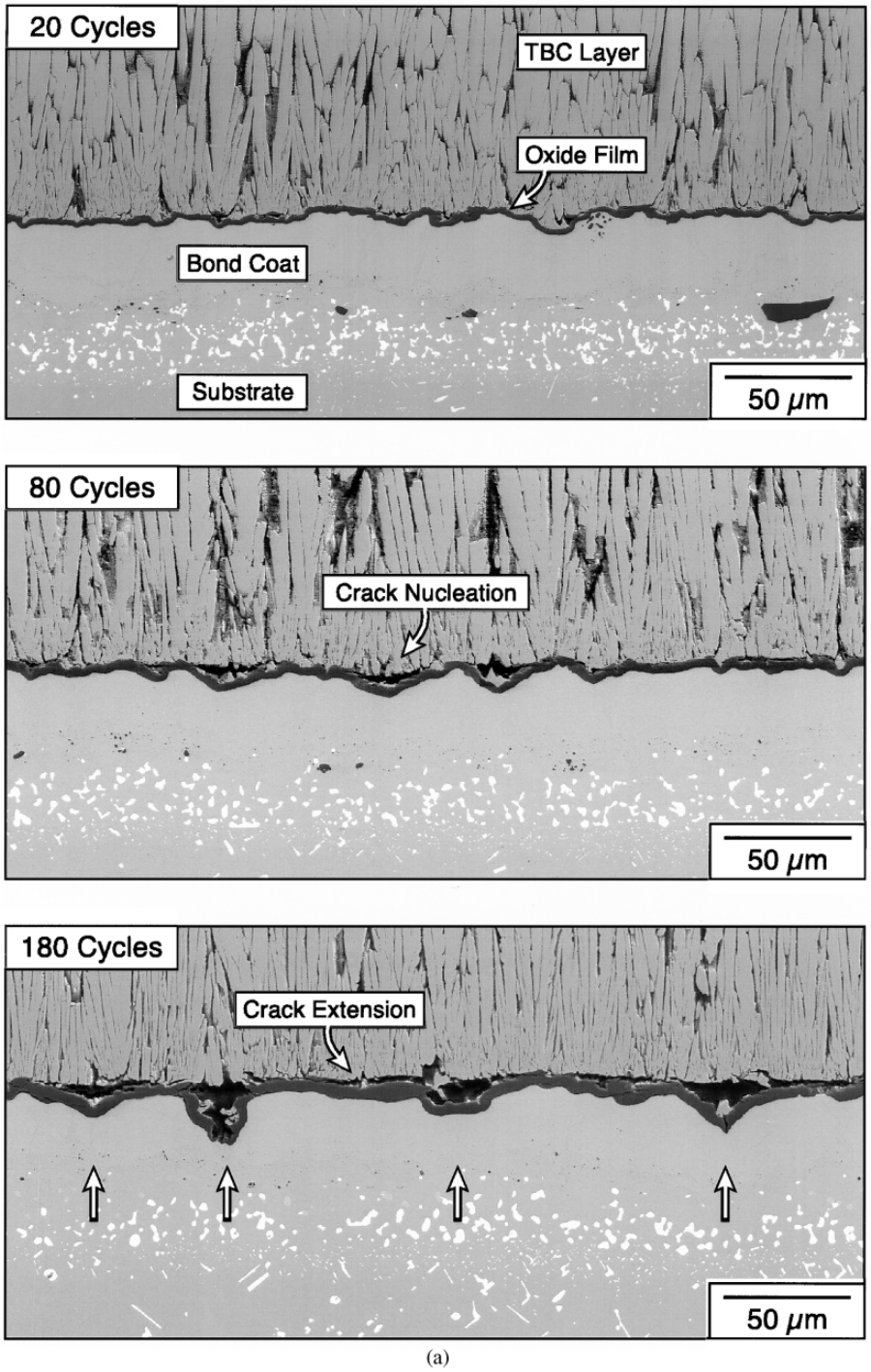

(a)

Fig. 2. Undulation imperfections found in typical thermal barrier systems. (a) A TBC made by electron beam physical vapor deposition (EB-PVD) on a Pt-aluminide bond coat. This sequence shows both the growth of the TGO as the system cycles and the growth of imperfections by ratcheting (courtesy D. Mumm). (b) A plasma sprayed TBC on a CoNiCrAlY bond coat. This sequence shows the growth of the TGO with exposure time and the evolution of cracks at imperfections. In the final image, the cracks have coalesced through the TGO (courtesy A. Rabiei).

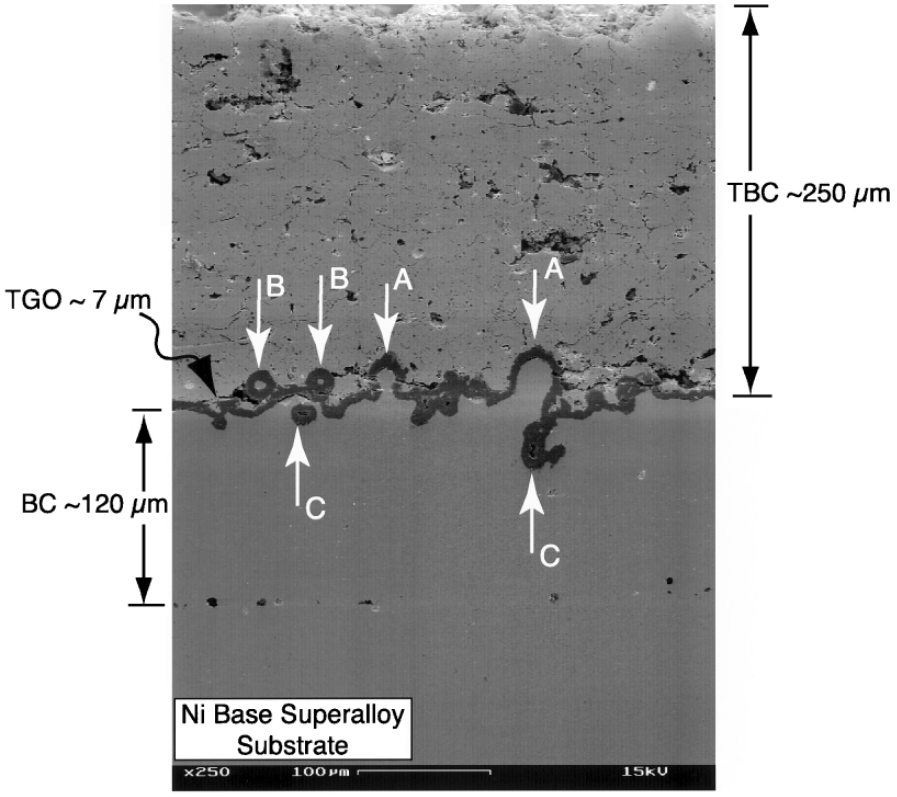

(b)

Fig. 2 (*continued*)

contraction is essentially isotropic with misfit strains of order 10^{-2} (Table 1). Conversely, the growth strains are anisotropic, partitioning differently normal and parallel to the interface [25,28,29]. The misfit is predominantly along the normal, because most of the new oxide forms at the TGO/bond coat interface (Fig. 3) [25]. While the strains are much larger than those caused by thermal expansion, the stresses need not be larger since they are partially redistributed by creep in the bond coat as well as the TGO itself.

Preliminary results for the stresses in the TBC, TGO and bond coat are estimated by considering imperfections having spherical symmetry (Fig. 4). There are two obvious limitations of this geometry. (i) The stress in the bond coat is hydrostatic and consequently, suppresses the yield and creep expected in more realistic configurations. (ii) The amelioration of the stresses enabled by the rigid body displacement of the TBC above an undulation is not allowed in the spherical model. The import of these deficiencies will be addressed in the second, numerical stage of the analysis, conducted for realistic imperfection morphologies. It will be demonstrated by such calculations that the stresses in the TGO and TBC near the apex of the imperfections are reasonably well-ordered in sign and magnitude by the analytical model. Solutions are first presented for a case wherein the three materials have the same elastic properties (Young's modulus, E, and Poisson's ratio, ν). Elastic mismatch can

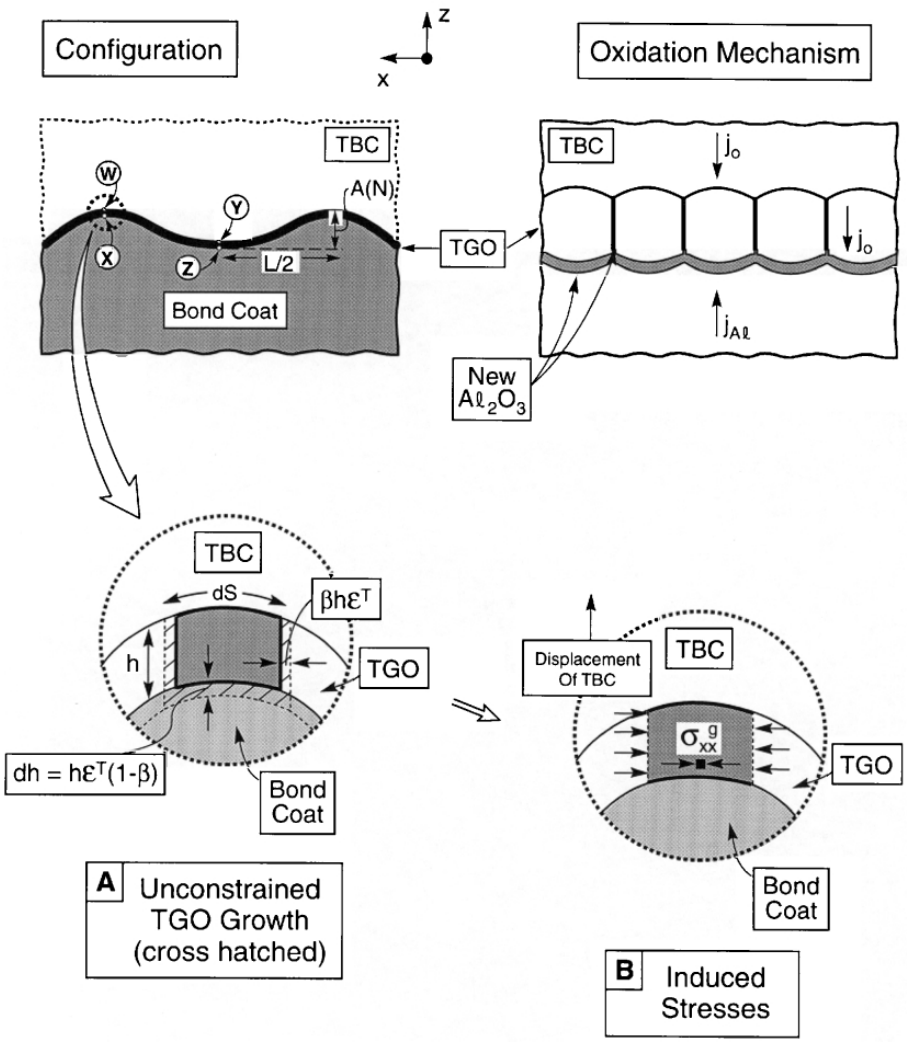

Fig. 3. Schematics of the configurations and the TGO growth mechanisms. The lower illustrations indicate phenomena that govern the growth stresses when anion-controlled.

also be taken into account, but the formulas become too lengthy to reveal trends. The effects of elastic mismatch are assessed later.

2.1. Thermal expansion misfit stresses

The elastic solutions for thermal expansion misfit in a tri-material system with spherical symmetry (Fig. 3) can be readily derived. The most straight forward approach employs the "Eshelby" protocol [30] of allowing the strains to occur unconstrained and imposing the tractions needed to assure displacement and traction continuity (Fig. 4**A**). The case of interest is one wherein the TGO (2) has the lowest thermal expansion coefficient, α_o, the substrate (3) the largest, α_s, and the TBC (1) the intermediate, α_{tbc}. The outer region (1) representing the TBC extends to

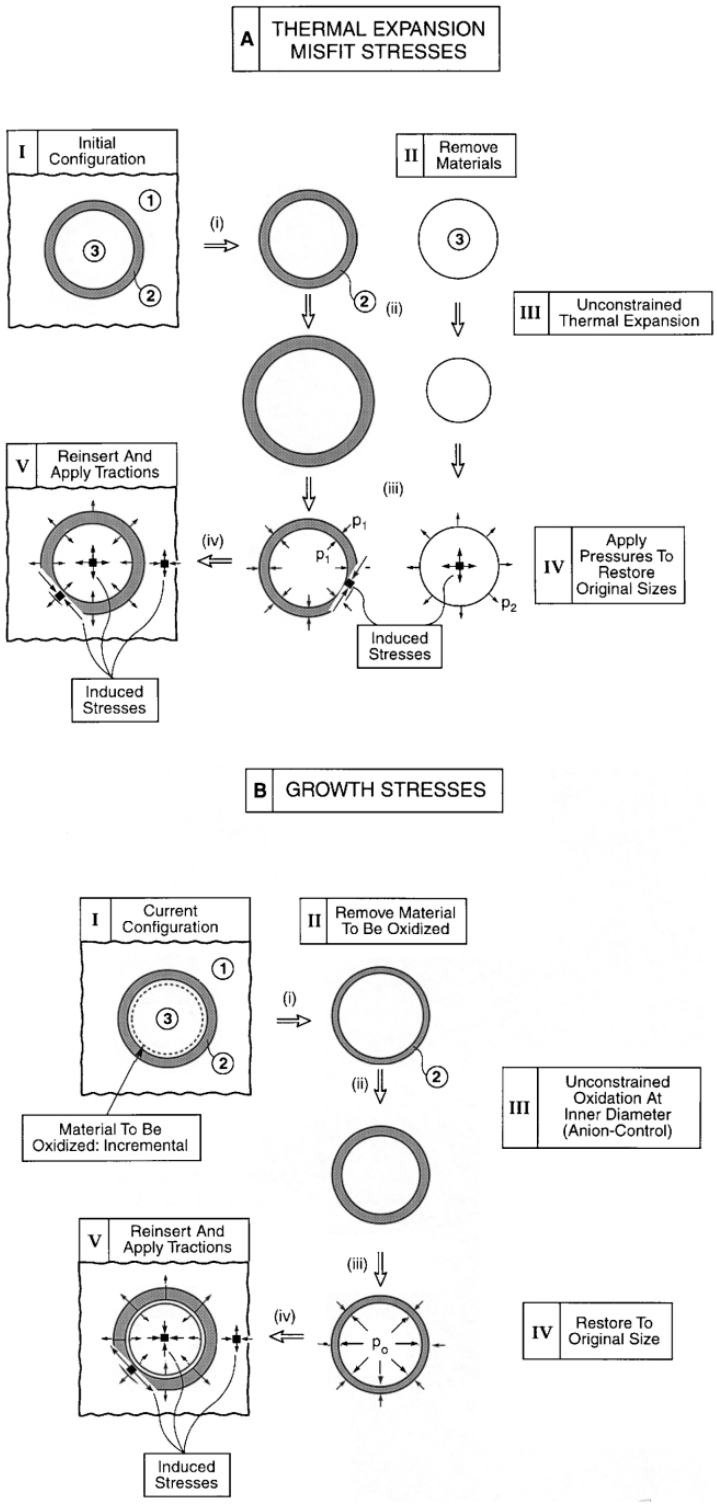

Fig. 4. The stresses that develop around spherical imperfections illustrated by using the "Eshelby" procedure [30]. (**A**) Thermal expansion misfit, (**B**) anion-controlled TGO growth. The three regions are as follows: (1) is the TBC, (2) is the TGO and (3) is a bond coat/substrate combination.

infinity. Throughout this section, the meridional stress, $\sigma_{\varphi\varphi}$, and the hoop stress, $\sigma_{\theta\theta}$, are equal by spherical symmetry. The stresses in the substrate/bond coat are:

$$\sigma_{rr} = \sigma_{\theta\theta} = \Lambda(\alpha_{tbc} - \alpha_s) \tag{1a}$$

where

$$\Lambda = 4\kappa\mu\Delta T/[\kappa + 4\mu/3], \quad \mu = E/[2(1+\nu)], \quad \kappa = E/[3(1-2\nu)]$$

and ΔT is the cooling range (negative in sign). Accordingly, the bond coat is in a state of hydrostatic tension, independent of α_o. The stresses in the TGO are:

$$\sigma_{rr} = \Lambda\left\{\alpha_{tbc} - \alpha_o - (\alpha_s - \alpha_o)[(R-h)/r]^3\right\}$$
$$\sigma_{\theta\theta} = \Lambda\left\{\alpha_{tbc} - \alpha_o + \frac{1}{2}(\alpha_s - \alpha_o)[(R-h)/r]^3\right\} \tag{1b}$$

where $2R$ is the diameter of the imperfection and h is the TGO thickness. Note that since, $\alpha_s > \alpha_{tbc} > \alpha_o$, the TGO is always in hoop compression and the interface between the substrate and the TGO is in radial tension. The stresses in the TBC are:

$$\sigma_{rr} = -2\sigma_{\theta\theta} = -\Lambda\left\{\alpha_o - \alpha_{tbc} + (\alpha_s - \alpha_o)(1 - h/R)^3\right\}(R/r)^3 \tag{1c}$$

In this case, the sign of the stresses depends on the relative TGO thickness, h/R. When the TGO is thin, the second term in the parenthesis dominates and the TBC is in radial compression. However, above a critical TGO thickness, radial tension develops. This thickness, h_*, is given by:

$$h_*/R = 1 - [(\alpha_{tbc} - \alpha_o)/(\alpha_s - \alpha_o)]^{1/3} \tag{2}$$

The hoop tension in the TBC and the radial tension at the interface have particular relevance, as discussed later.

Results for undulations in the TGO, absent the TBC, provide some ancillary insights. The stresses along the interface can be non-dimensionalized using [31]:

$$\sigma_{ij}/(\sigma_o A/L) = H_{ij}(h/L, A/h, x/L) \tag{3a}$$

where A and L are defined in Fig. 5 and σ_o is the misfit stress for a planar surface given by:

$$\sigma_o = E(\alpha_o - \alpha_s)\Delta T/(1-\nu) \tag{3b}$$

The functions H_{ij} have been computed with a finite element representation and are plotted in Fig. 5. Consistent with the results for the spherical imperfection, tensile stresses arise normal to the interface at the peaks in the undulations. These can be large enough to cause interface separation [32,33]. However, contrary to the solutions

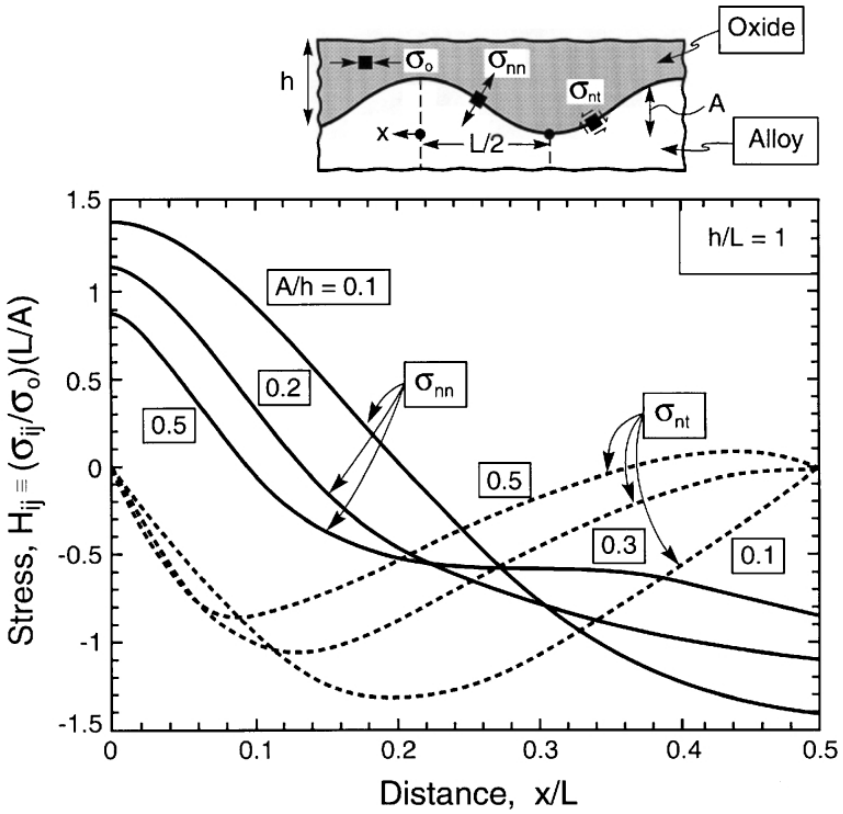

Fig. 5. Redistribution of thermal expansion misfit stress attributed to the presence of undulations. The stress σ_{nn} is that normal to the interface while σ_{nt} is the shear stress.

for the spherical geometry, shear stresses are induced in the bond coat at the sides of the imperfection that promote yielding and creep [31].

2.2. Oxide growth: intrinsic stresses

The stresses induced by TGO growth and thermal mismatch differ because the former occurs predominately at one of the interfaces (Figs. 3 and 4**B**) rather than uniformly throughout the TGO layer (Fig. 4**A**) [28,32]. For anion-control, growth is governed by inward diffusion of oxygen. It occurs at the interface where the bond coat is consumed (Fig. 3). For cation-control, the new oxide forms at the TGO/TBC interface, through the outward diffusion of Al (as well as Ni, Cr, etc.) [29]. The bond coat consumption still occurs at the inner interface. The former has been considered most relevant to α-alumina formation [11–16, 28]. The stresses within the TGO depend on the initial hoop stress component, $\sigma^i_{\theta\theta}$, generated at the instant of growth: an unknown quantity for most systems. The hoop stress distribution within the TGO will generally be different for the two growth processes.

The stresses due to growth of the TGO are determined upon neglecting creep and plasticity (see Section 2.3 for a discussion of the effect of creep in the spherical model). The calculation invokes small elastic strains and deformations. The stresses

for anion-control are obtained by an incremental process, wherein new TGO, thickness dh, is added at the TGO/bond coat interface. The ratio of new TGO volume to consumed bond coat volume is taken to be m. Thus, the net thickness of new material inserted is: $[(m-1)/m]\mathrm{d}h$. Each increment of new TGO is added at the current outer radius of the bond coat. Starting at $h=0$, the incremental expressions for the stresses are integrated to TGO thickness h. To be consistent with the small strain assumption, the analysis is limited to small values of h/R (e.g. no more than about 1/10), and the following results for the stresses have been expressed to lowest order in h/R. Within the bond coat,

$$\sigma_{rr} = \sigma_{\theta\theta} = -\frac{2E(m-1)}{3(1-\nu)m}\left(\frac{h}{R}\right) \tag{4a}$$

In the TBC, $r \geqslant R$,

$$\sigma_{rr} = -2\sigma_{\theta\theta} = -\frac{2E(m-1)}{3(1-\nu)m}\left(\frac{h}{R}\right)\left(\frac{R}{r}\right)^3 \tag{4b}$$

and within the TGO, $R-h \leqslant r \leqslant R$,

$$\sigma_{rr} = -\frac{2E(m-1)}{3(1-\nu)m}\frac{h}{R}$$
$$\sigma_{\theta\theta} = \sigma^{i}_{\theta\theta} + \frac{E(m-1)}{3(1-\nu)m}\left[\frac{r}{R} - \left(1-\frac{h}{R}\right)\right] \tag{4c}$$

For integration of the stress increments in the TGO, the only indeterminacy is the initial hoop stress at the growth interface, $\sigma^{i}_{\theta\theta}$, which can be prescribed arbitrarily. This initial value is included in the second of (4c), where its effect on the evolving hoop stress in the TGO becomes apparent. Otherwise, $\sigma^{i}_{\theta\theta}$ has no influence on the stresses in either the TBC or the bond coat. These results have the following features. The TBC is in radial compression and hoop tension, with radial compression in the TGO. These stresses increase as the TGO thickens. The hoop stress in the TGO is $\sigma^{i}_{\theta\theta}$ at the growth interface and $\sigma^{i}_{\theta\theta} + E(m-1)h/[3(1-\nu)mR]$ at the TGO/TBC interface. Thus, for example, if $\sigma^{i}_{\theta\theta} \cong 0$, the hoop stress throughout the TGO will be tensile. If $\sigma^{i}_{\theta\theta}$ is compressive, a tensile stress will develop at some stage in the outer portion of the TGO as it thickens.

The same steps can be carried out for cation-controlled growth wherein TGO growth occurs at the TGO/TBC interface and the bond coat is consumed at the inner TGO interface. Under the same small strain assumptions made above, the stresses in the bond coat and in the TBC remain the same, i.e. (4a) and (4b), respectively, and the radial stress in the TGO is still given by (4c). The only difference is in the distribution of the hoop stress within the TGO ($R-h < r < R$):

$$\sigma_{\theta\theta} = \sigma^{i}_{\theta\theta} - \frac{9E}{4(1-\nu)}\left(1-\frac{r}{R}\right), \tag{5}$$

Should $\sigma^{i}_{\theta\theta} \cong 0$, this stress will be compressive. Note that cation-controlled growth produces stress within the TGO even if there is no net volume change in the creation of the TGO ($m = 1$). This is a consequence of the transfer of material volume from the inner interface to the outer interface.

Subject to the simplifications used in the model, the stress magnitudes can now be compared. The growth stresses scale with $[Em/(m-1)](h/R)$, while the thermal stresses scale as $E\Delta\alpha\Delta T$. Evaluation for material properties representative of thermal barrier systems (Table 1), with $\Delta T = 1000^{\circ}$C and $h/R = 0.1$, indicates that TGO growth produces stresses on the order of several GPa in the TBC and tens of GPa in the TGO and bond coat. In practice, the low modulus of the TBC would partially alleviate these stresses. Thermal mismatch stresses are considerably less, on the order of several hundred MPa in the TBC and several GPa in the TGO and bond coat. The large stresses in the bond coat/substrate (region 3 in Fig. 4) are hydrostatic (a consequence of the spherical geometry), and will almost certainly relaxed by creep in the more realistic imperfection geometries discussed in Section 3. Moreover, the stresses in the TGO will be redistributed by internal creep. Nevertheless, the inference to be drawn from the above scaling is that the stresses induced by TGO growth predominate over those caused by expansion misfit. The tensile hoop stresses in the TBC are particularly relevant since they can lead to cracks spreading from the imperfection, as will be demonstrated in Section 2.4.

2.3. Role of TGO creep in redistributing stress in bond coat and TBC

A simple result based on the spherical model sheds considerable light on the extent which creep in the TGO (the most creep prone of the three materials [34–37]) is likely to produce stress redistribution in the TBC in the vicinity of the imperfection. Continue to ignore moduli differences among the three materials. Suppose the bond coat occupies the region, $r \leqslant R_s$; the TGO occupies $R_s \leqslant r \leqslant R$; and the TBC occupies $r \geqslant R$. Further, suppose creep occurs within the TGO such that the creep strain distribution is:

$$\varepsilon^{c}_{rr} = \varepsilon^{c}(r), \quad \varepsilon^{c}_{\theta\theta} = \varepsilon^{c}_{\varphi\varphi} = -\frac{1}{2}\varepsilon^{c}(r), \qquad (R_s \leqslant r \leqslant R) \tag{8}$$

The stress changes in the three regions, $\Delta\sigma_{ij}$, due to this creep can be obtained in closed form. In particular, the radial stress change acting on the TGO/TBC interface at $r = R$ is given by:

$$\Delta\sigma_{rr}(R) = 6\mu\left\{\int_{R_s}^{R}\left[r^{-1}\varepsilon^{c}(r) - R^{-3}r^{2}\left(\varepsilon^{c}(r) + \int_{R_s}^{r}\eta^{-1}\varepsilon^{c}(\eta)\mathrm{d}\eta\right)\right]\mathrm{d}r\right\} \tag{9}$$

For the case in which $\varepsilon^{c}(r) = \varepsilon^{c}$ is independent of r, (9) becomes:

$$\Delta\sigma_{rr}(R) = 2\mu\varepsilon^{c}\left[2\ln\left(\frac{R}{R_s}\right) - \frac{2}{3}\left(1 - \left(\frac{R_s}{R}\right)^{3}\right)\right] \tag{10}$$

Now let $R_s = R - h$ and expand (10) in small h/R to obtain:

$$\Delta\sigma_{rr}(R) = 2\mu\varepsilon^c\left(\frac{h}{R}\right)^2 + \ .....\tag{11}$$

By (11), creep affects the stresses in the TBC only to order $(h/R)^2$. While there is no reason to expect that the creep strain distribution through the TGO should be uniform: nevertheless, the above result strongly suggests that creep in the TGO will have minimal influence in relaxing the stresses in the TBC. (This conclusion must again be tempered by the limitations of the spherical imperfection model). Conversely, the deviatoric component of the stress in the TGO itself could relax, resulting in a reduction in the hoop stress (for compatibility reasons, the radial stress would be unaffected).

2.4. Cracking scenario

2.4.1. Crack patterns

The preceding distributions of tensile stress may be used to infer cracking patterns. These motivate the explicit fracture mechanics problems to be solved. They are validated by the solutions. The hoop tensions induced in the TBC as the TGO thickens would allow radial cracks to form (Fig. 6a). These are analyzed in Section 2.4.2. Such cracks would not be expected to penetrate back through the TGO, even though it is subject to hoop tension, because creep redistributes the concentrated stresses at the inner crack front (A in Fig. 6a). Subsequent cooling to ambient enhances the hoop tensions in the TBC (Fig. 4**B**), but diminishes the radial compressions normal to the interface between the TGO and the bond coat. Moreover, should the growth stresses be sufficiently relaxed by bond coat creep, then, at ambient, these stresses may be tensile. In either case, upon cooling, the radial crack in the TBC could extend from its inner front, through the TGO, and along the interface, to create a fully-connected radial crack (Fig. 6c). Solutions for such crack configurations are presented in Section 2.4.3. Since the formation of such a configuration requires that the crack penetrate the TGO, which is in hoop compression at ambient, it is surmised that this happens upon thermal cycling at temperatures wherein the TGO is brittle (below about 900C) yet the hoop stresses are still tensile (Fig. 6b).

2.4.2. Cracking in the TBC

Prior to cracking, the largest tensile hoop stresses in the TBC occur at temperature due to growth. From (4b), this stress is

$$\sigma_{\theta\theta} = \sigma^*\left(\frac{R}{r}\right)^3\tag{11a}$$

where

$$\sigma^* = \frac{E(m-1)}{3(1-\nu)m}\left(\frac{h}{R}\right)\tag{11b}$$

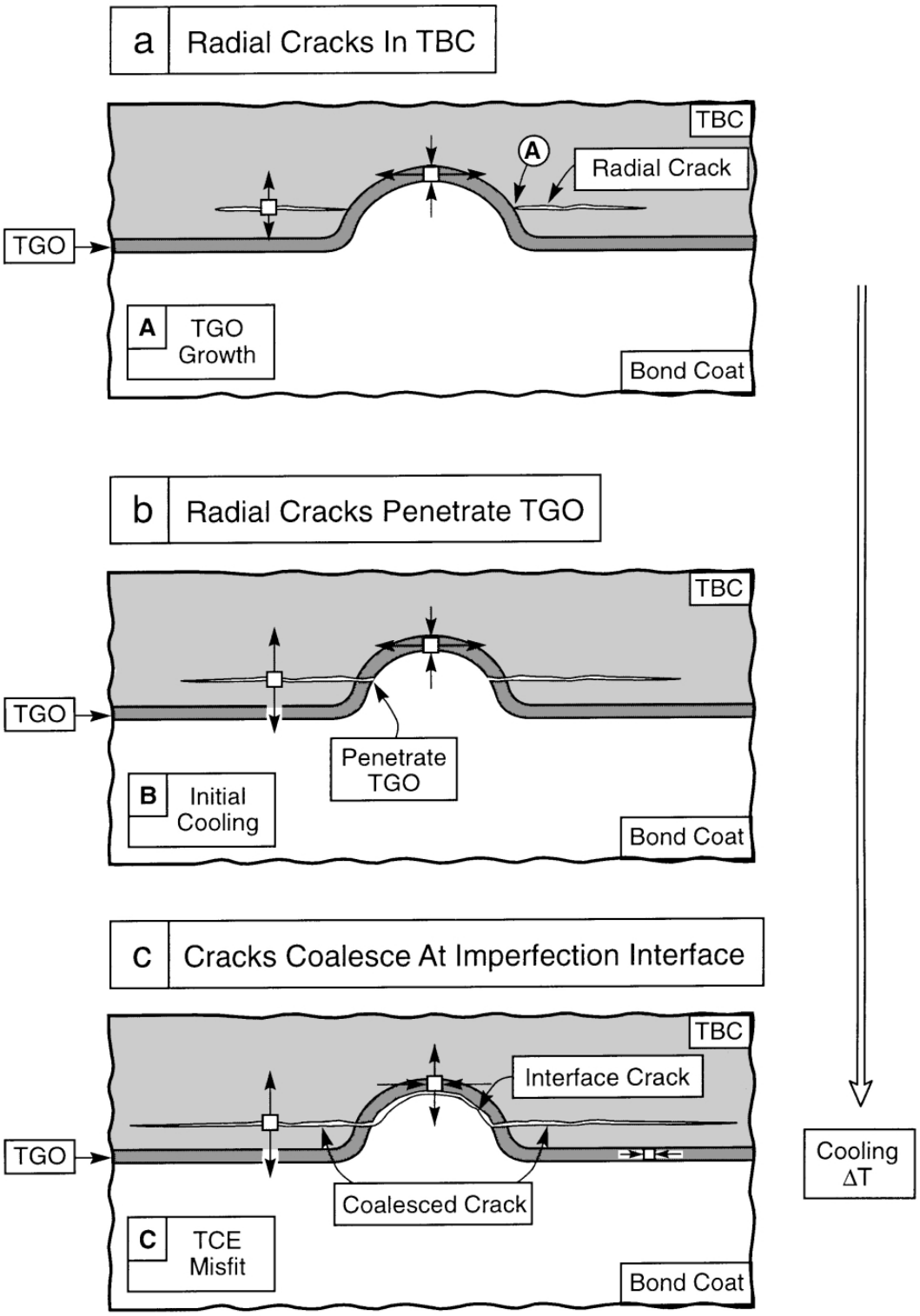

Fig. 6. Cracking patterns expected around imperfections as a result of the stress distribution (see Fig. 2b). The actual incidence of cracks depends on variables such as the TGO thickness, the imperfection diameter and the TBC toughness.

is the hoop stress in the TBC at the interface with the TGO. Shum and Huang [38] have presented results relevant to such a stress state for a configuration comprising an equatorial ring crack with inner radius R and outer radius a. The following are analytical expressions for the stress intensity factors at the inner and outer crack edges (which have been fitted to their numerical results) [38]:

$$\frac{K}{\sigma^*\sqrt{R}} = \sqrt{\frac{\pi}{2}\left(\frac{a}{R}-1\right)}\left(\frac{R}{a}\right)^{2.4} \qquad \text{(outer crack edge)} \tag{12a}$$

$$\frac{K}{\sigma^*\sqrt{R}} = \sqrt{\frac{\pi}{2}\left(\frac{a}{R}-1\right)}\left(\frac{R}{a}\right)^{0.55} \qquad \text{(inner crack edge)} \tag{12b}$$

These results are plotted in Fig. 7a. Note the very large stress intensity at the inner front. It is this intensity that motivates the crack to penetrate the TGO and coalesce along the interface (Fig. 6c) as the system thermally cycles. Eqs. (12a) and (12b) apply to the case of no elastic mismatch, but Shum and Huang [38] also present results for a full range of elastic mismatch between the inner spherical region, $r < R$, and the outer region, $r \geqslant R$. When applied to the present problem (Table 1), (12a) underestimates K by about 30%, with E in (11b) identified with the modulus of the TBC. As a representative example, consider a TBC with $E = 30$ GPa and $K_{\mathrm{Ic}}^{\mathrm{tbc}} = 0.5$ MPa $\sqrt{\mathrm{m}}$ [39–41] and an imperfection with $R = 20$ μm, $h/R = 1/10$ [41] and $m = 1.3$. If an equatorial crack were initiated at the imperfection, (12) predicts it would expand outward to a radius about three times R. Evidently, further increases in h/R (with greater exposure time) would cause the crack to continue expanding. Note from the plot in Fig. 7a that the same value of K is attained for a very small initiating crack, and thus there would appear to be only a very small barrier to the initiation of an equatorial crack in the TBC.

2.4.3. Cracking in the TBC and the TGO with debonding of the TGO/bond coat interface

It has just been demonstrated that the imperfection induces significant hoop tension in the TBC due to TGO growth, which can give rise to a substantial TBC crack at the growth temperature. Cyclic temperature variations may cause it to become fully connected and enlarge it further. A model for estimating the stress intensity factor at the outer edge of the fully cracked configuration is constructed as follows (neglecting elastic mismatch effects). The complete solution for a full circular crack, radius a, with faces subject to a uniform normal opening pressure p extending from the center out to radius R is given by Tada, Paris and Irwin [42]. The pressure p is identified by equating the opening displacement at the center of the crack with the wedge opening, $2(m-1)h/m$. The resulting stress intensity factor is [42]:

$$\frac{K}{\sigma^*\sqrt{R}} = \frac{3}{2(1+\nu)}\sqrt{\frac{\pi}{2}\frac{R}{a}}\left[1+\frac{(R/a)\cos^{-1}(R/a)}{1-\sqrt{1-(R/a)^2}}\right]^{-1} \tag{13}$$

This result is plotted in Fig. 7b for $\nu = 1/3$. Note that, for larger values of a/R, (13) asymptotes to:

$$\frac{K}{\sigma^* \sqrt{R}} = \frac{3}{2(1+\nu)\sqrt{\pi}} \left(\frac{R}{a}\right)^{3/2} \tag{14a}$$

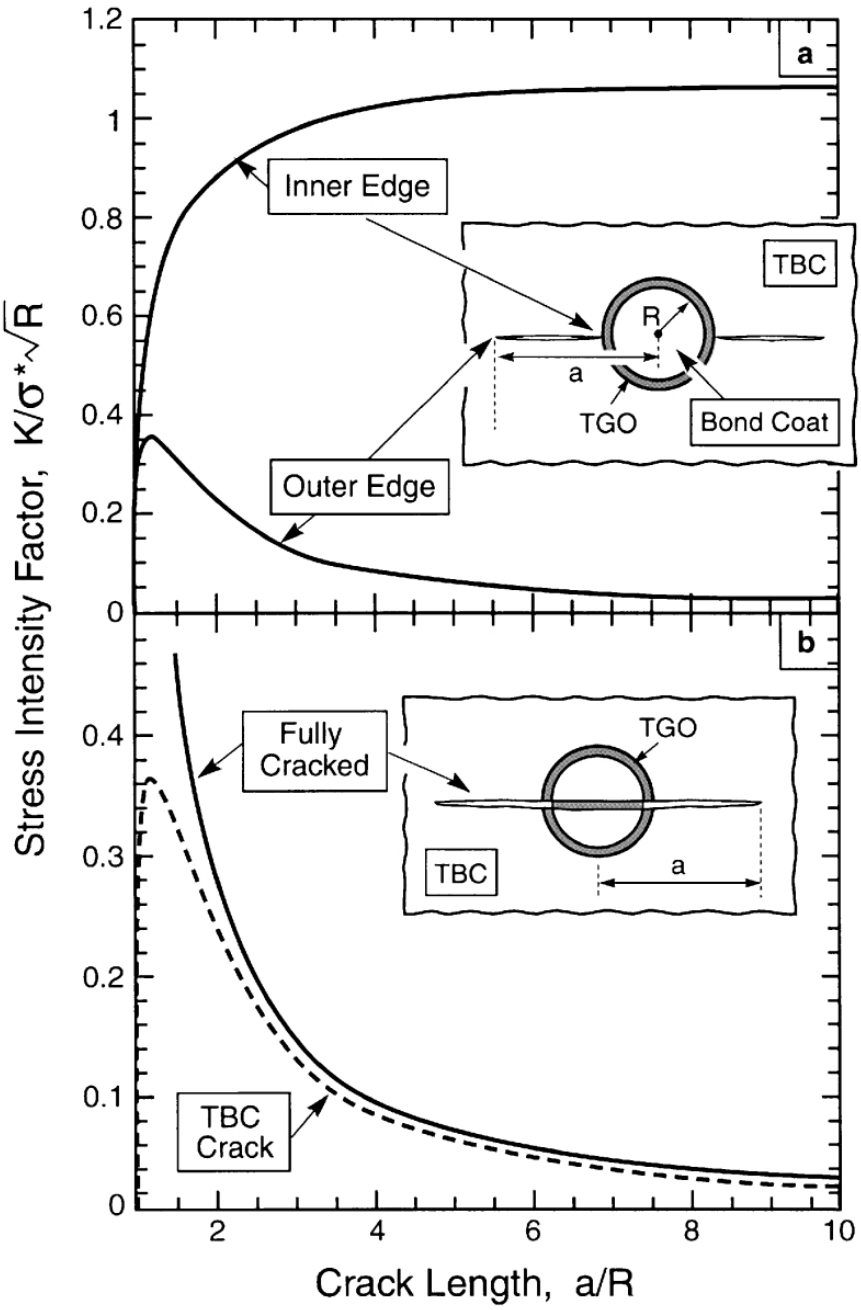

Fig. 7. Stress intensity factors calculated for the crack configurations depicted on the insets.

while (12a) asymptotes to

$$\frac{K}{\sigma^*\sqrt{R}} = \sqrt{\frac{\pi}{2}}\left(\frac{R}{a}\right)^{1.9} \tag{14b}$$

Over the range of a/R from 2 to 10 plotted, there is little difference between these results. Accordingly, the principal role of thermal cycling is to cause the inner front of the crack in the TBC (induced by the growth misfit) to penetrate back through the TGO, and along the interface, to form a fully-connected crack. In this configuration, the crack can coalesce with others to form a separation zone large enough to satisfy large scale buckling requirements, discussed next.

2.5.2. Coalescence

The mechanics of crack coalescence in residually stressed films are subject to nuances associated with remnant ligaments that arise because the energy release rates approach zero at convergence [43]: whereupon the ligaments can only be detached by applying a (small) transverse force [43]. With the simplifying assumption that such forces are always present (because of inertial effects or vibration), crack coalescence can be ascribed to a requirement that the crack diameter equal the spacing 2d between neighboring imperfections. With this simplification, (14a) can be re-expressed as a failure criterion. That is, fracture occurs at a critical TGO thickness, h_c, given by:

$$h_c = \frac{2\sqrt{\pi}(1-\nu^2)md^{3/2}K_{Ic}^{tbc}}{(m-1)RE_{tbc}} \tag{15}$$

Note the key role of imperfections, through their diameter $2R$, and the spacing, $2d$. Moreover, since h_c depends on time-at-temperature t ($h = \sqrt{D_{ox}t}$), then (15) can be re-expressed as a failure time. It is to be appreciated that D_o is a strong function of temperature and that K_{Ic}^{tbc} is sensitive to the TBC microstructure. Accordingly, this formula (15) can be used as the basis for durability models.

3. Numerical results

With the above assessment providing guidelines for the scaling as well as approximate magnitudes for the stresses and the TBC crack sizes, some selected numerical results have been obtained for imperfections having more realistic morphologies and for the explicit constituent properties indicated on Table 1. The imperfections are taken to have a cosine shape (Fig. 8) and the stresses are calculated with the finite element method using the ABAQUS code. It will be shown that the stresses induced by both thermal expansion misfit and growth have the same form as those anticipated by the analytical model, especially in the region around the apex of the imperfection.

3.1. Thermal expansion misfit

The stresses absent a TGO, upon cooling to ambient, are summarized on Fig. 8b and c (results for $h/L = 0$). Note that there are σ_{nn} tensile stresses at the interface around the undulation peaks, with a maximum at the apex. There are also σ_{zz} tensile stresses in the

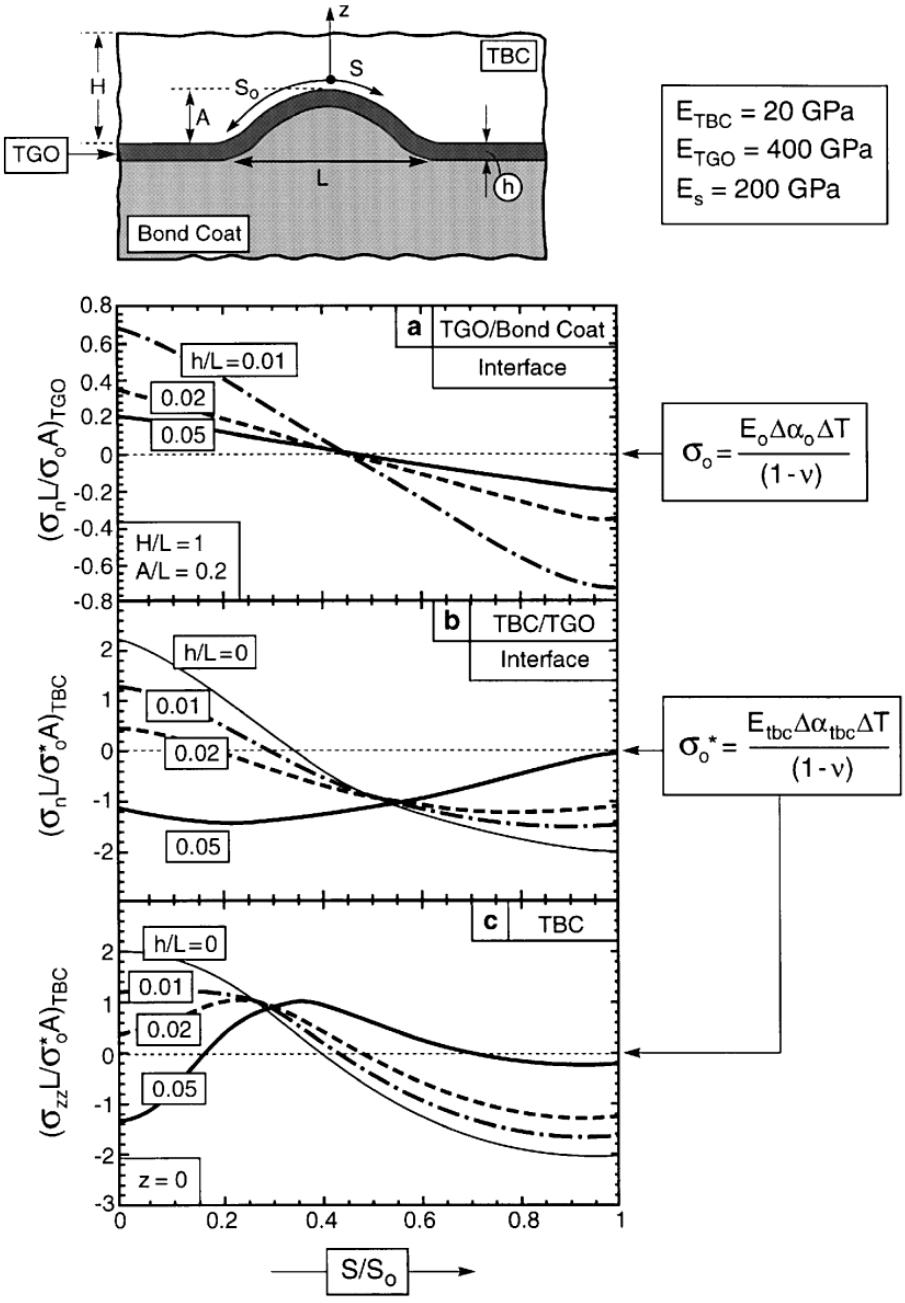

Fig. 8. The effect of TGO thickness, h/L, on the thermal expansion misfit stresses in the vicinity of a sinusoidal imperfection. (a) The normal stresses at the TGO/bond coat interface, normalized by σ_o. (b) The normal stresses at the TGO/TBC interface normalized by σ_*. (c) The σ_{zz} stress in the TBC normalized by σ_*.

TBC around the apex. The magnitudes are relatively small because of the compliance of the TBC.

The influence of the TGO on these stresses is crucial, since failure is known to be dependent on the TGO thickness. In order to separate the response on cooling from that during growth, the TGO has been introduced at the growth temperature and

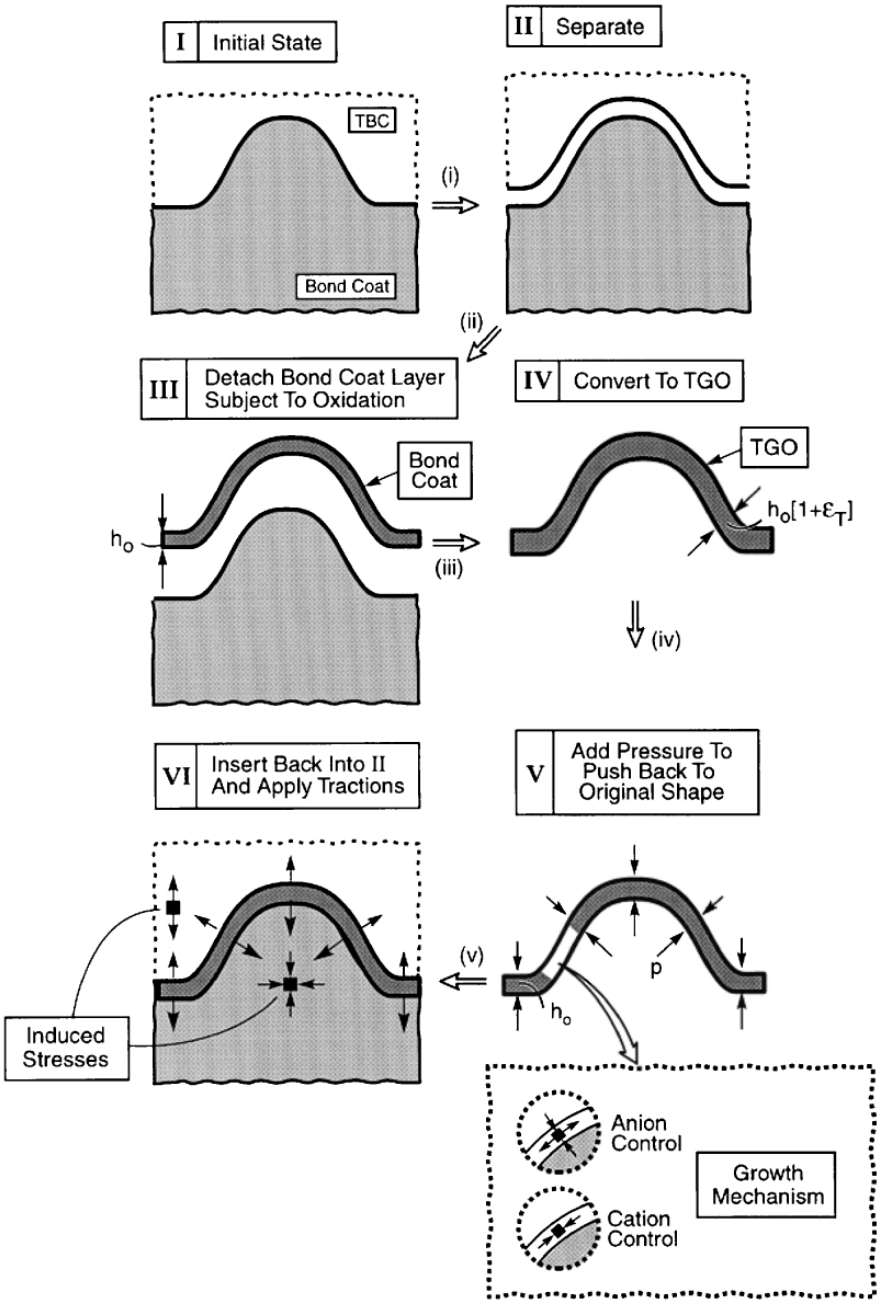

Fig. 9. A schematic of the Eshelby protocol used to calculate the growth stresses around an imperfection by using the finite element method.

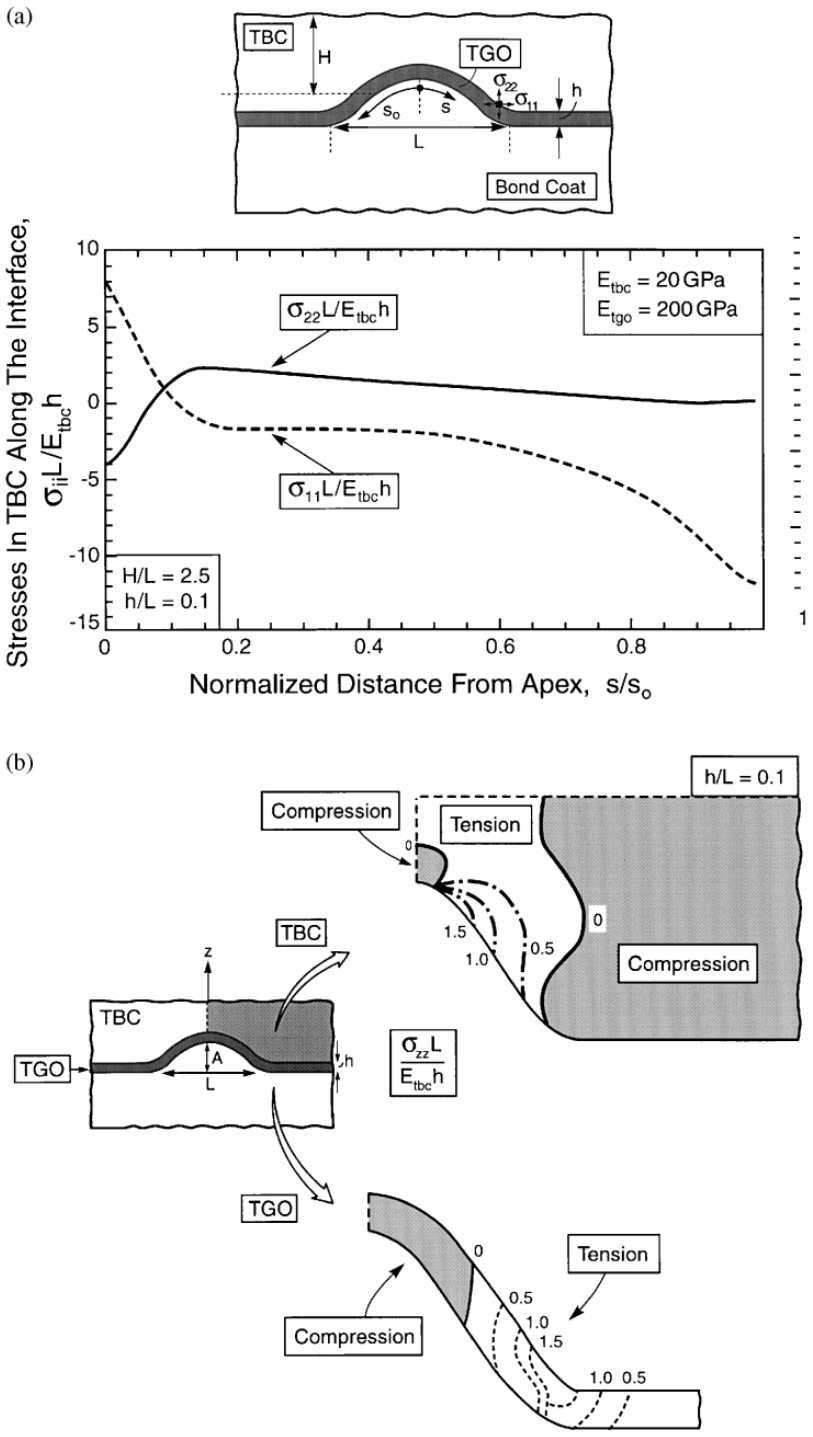

Fig. 10. Numerical results for the stress induced by anion-controlled TGO growth. (a) The σ_{zz} and σ_{xx} stress distributions along the TBC/TGO interface. (b) Contours of the σ_{zz} stresses in the TBC and TGO.

assumed to be stress-free. That is, growth stresses and strains are added-in later by superposition. The effect of the TGO on the σ_{zz} tensile stress distribution around the imperfections is shown on Figs. 9a–c (results for $h/L > 0$). The three main features of the stress near the apex are consistent with the analytical model.

(i) There is a tensile stress normal to the TGO/bond coat interface (Fig. 8a), but it decreases somewhat as the TGO thickens.
(ii) The stress at the TGO/TBC interface is initially tensile, but becomes compressive when the TGO thickness exceeds about $h/L = 0.03$ (Fig. 8b).
(iii) A zone of σ_{ZZ} tension develops in the TBC at the sides of the imperfection as the TGO thickens (Fig. 8c).

3.2. Growth stresses

The relative magnitudes of the stresses that develop during TGO growth are again determined by the Eshelby protocol (Fig. 9). For this purpose the following two problems are solved using the finite element method.

(i) Problem I. The interface between the TBC and bond coat is opened so that the new TGO can form in an unconstrained manner. Tractions, p, are calculated sufficient to push the TGO into the volume originally occupied by the bond coat before it was oxidized.
(ii) Problem II. The TGO is inserted back into the overall system to create the two new interfaces (TBC/TGO and TGO/bond coat), whereupon equal and opposite tractions, $-p$, are applied to regain equilibrium.

The final stress field is the sum of those induced in both steps. This process commences with a small initial thickness of TGO, the stresses are calculated and the process repeated multiple times to simulate the growth.

The results of one such calculation for anion-controlled TGO growth are summarized in Fig. 10a and b. Note that the σ_{ZZ} stresses have the same form as those assessed using the analytical model. Namely, the TBC just outside the TGO experiences tensile σ_{ZZ} stress over the full imperfection domain (Fig. 10a). The extent of the tensile zone is depicted on figure 10b. There is also σ_{ZZ} tension over a substantial portion of the TGO, along the sides of the imperfection (Fig. 10b). These σ_{ZZ} stresses allow radial cracks to form in the TBC as the TGO thickens (Fig. 6a).

4. Concluding remarks

Straightforward methods of analysis have been used to derive relationships that characterize the failure of TBCs. It is proposed that these relationships be used as scaling laws that predict trends with key variables and also rationalize experimental measurements. One of the basic findings is that (in accordance with practical experience) a critical TGO thickness, h_c, is needed to cause failure. Through the

present scaling laws, h_c can be related to underlying microstructural and morphological features present in the TBC system (15). This critical thickness can be related to the durability through the growth kinetics of the TGO. It remains to validate these predictions through a critical set of experimental measurements. Subject to validation, a future goal would be to use the scaling results to suggest directions for increasing the critical thickness and, thereby, enhancing durability.

It is reiterated that the scenario considered here is one involving minimal thermal cycling, whereupon ratcheting of the TGO is excluded as a major source of the σ_{zz} stress. When ratcheting conditions are created, the scaling laws change dramatically, as discussed elsewhere [27].

References

[1] Miller RA. J Am Ceram Soc 1984;67:517.
[2] Mariochocchi A, Bartz A, Wortman D. Thermal barrier coating workshop, NASA CP 3312, 1995. p. 79.
[3] Bose S, DeMasi-Marcin J. Thermal barrier coating workshop, NASA CP 3312, 1995. p. 63.
[4] DeMasi-Marcin JT, Gupta DK. Surf Coatings Technol 1994;68/69.
[5] Hillary R, editor. NRC Report. Coatings for high temperature structural materials, National Academy Press, 1996.
[6] Strangman TE. Thin Solid Films 1985;93–105:127.
[7] Meier SM, Gupta DK. Trans ASME 1993;116:250–7.
[8] Wright PK, Evans AG. Current Opinion in Solid State and Materials Science 1999;4:255–65.
[9] Wright PK. Mater Sci Eng 1998;A245:191–200.
[10] Kingery WD, Bowen HK, Uhlmann DR. Introduction to ceramics. Wiley and Sons, New York (1976): Nicholls JB, Lawson KJ, Rickerby DS, Morell P. AGARD Report R-823, April 1998.
[11] Golightly FA, Stott FH, Wood GC. Oxid Metals 1976;10:163.
[12] Stiger MJ, Yanar NM, Topping MG, Pettit FS, Meier GH. Z Metallk 1999;90:1069–78.
[13] Quadakkers WJ, Tyagi AK, Clemens D, Anton R, Singheiser L. In: Hampikian JM, Dahotre NB, editors. Elevated temperature coatings: science technology. Warrendale, PA: TMS, 1999. p. 119.
[14] Smeggil JG. Mater Sci Eng 1987;87:261–5.
[15] Smialek JL, Jayne DT, Schaeffer JC, Murphy WH. Thin Solid Films 1994;253:285–92.
[16] Smialek JL, Tubbs BK. Metall Mater Trans 1995;A26:427.
[17] Lipkin DM, Clarke DR. Oxid Metals 1996;45:267–80.
[18] Tolpygo VK, Clarke DR. Oxid Metals 1998;49:187–211.
[19] Christensen R, Lipkin DM, Clarke DR, Murphy K. Appl Phys Lett 1996;69:3754–6.
[20] Sergo V, Clarke DR. J Am Ceram Soc 1998;81:3237–42.
[21] Choi SR, Hutchinson JW, Evans AG. Mech Mater 1999;31:431–47.
[22] Meier SM, Nissley DM, Sheffler KD. Thermal barrier coating life prediction model development — phase II, NASA CR-18911, July 1991.
[23] He MY, Evans AG, Hutchinson JW. Mater Sci Eng 1998;A245:168–81.
[24] He MY, Evans AG, Hutchinson JW. Acta Mater 1997;45:3481–9.
[25] Tolpygo VK, Clarke DR. Acta Mater 1998;46:5153–66.
[26] Gell M, Vaidyanathan K, Barber B, Cheng J, Jordan E. Metall Mater Trans 1999;30A:427.
[27] He MY, Evans AG, Hutchinson JW. Acta Mater, 2000;48:2593–601.
[28] Rhines FN, Wolf JS. Metall Trans 1970;1:1701–10.
[29] Dove DB, Baldwin D. H Metall Trans 1974;5:1637–41.
[30] Eshelby JD, Proc R. Soc 1957;A241:376.
[31] Evans AG, He MY, Hutchinson JW. Acta Mater 1997;45:3543–54.
[32] Tolpygo VK, Clarke DR. Acta Mater 1998;46:5167–74.

[33] Tolpygo VK, Dryden J, Clarke DR. Acta Mater 1998;46:927–37.
[34] Cannon RM, Rhodes WH, Heuer AH. J Am Ceram Soc 1980;63:46.
[35] Heuer AH, Tighe NJ, Cannon RM. J Am Ceram Soc 1980;63:53.
[36] Cho J, Harmer MP, Chan HM, Rickman JM, Thompson AM. J Am Ceram Soc 1997;80:1013.
[37] Fang J, Thompson AM, Harmer MP, Chan HM. J Am Ceram Soc 1997;80:2005.
[38] Shum DKM, Huang YY. Eng Fract Mech 1990;37:107–17.
[39] Johnson CA, Ruud JA, Bruce R, Wortman D. Surf Coatings Technol 1998;108/109:80.
[40] Choi SR, Zhu D, Miller RA. Ceram Eng Sci 1998;19:293–301.
[41] Rabiei A, Evans AG. Metall Mater Trans, 2000;48:3963–76.
[42] Tada H, Paris PC, Irwin GR. Handbook for stress analysis of cracks, 2nd ed. Del Research, 1985 — to be reissued by the American Society of Mechanical Engineering.
[43] Evans AG, Hutchinson JW, He MY. Acta Mater 1999;47:1513–22.

Appendix E

PERGAMON

Progress in Materials Science 46 (2001) 505–553

Progress in Materials Science

www.elsevier.com/locate/pmatsci

Mechanisms controlling the durability of thermal barrier coatings

A.G. Evans [a,*], D.R. Mumm [a], J.W. Hutchinson [b], G.H. Meier [c], F.S. Pettit [c]

[a] *Materials Institute, Princeton University, Princeton, NJ 08540, USA*
[b] *Division of Engineering and Applied Sciences, Harvard University, Cambridge, MA 02138, USA*
[c] *Department of Materials Science and Engineering, University of Pittsburgh, Pittsburgh, PA 15261, USA*

Received 25 August 2000; accepted 10 October 2000

Abstract

The durability of thermal barrier coatings is governed by a sequence of crack nucleation, propagation and coalescence events that accumulate prior to final failure by large scale buckling and spalling. Because of differing manufacturing approaches and operating scenarios, several specific mechanisms are involved. These mechanisms have begun to be understood. This article reviews this understanding and presents relationships between the durability, the governing material properties and the salient morphological features. The failure is ultimately connected to the large residual compression in the thermally grown oxide through its roles in amplifying imperfections near the interface. This amplification induces an energy release rate at cracks emanating from the imperfections that eventually buckle and spall the TBC.

Contents

* Corresponding author. Tel.: +1-609-258-4762; fax: +1-609-258-1177.
E-mail address: anevans@princeton.edu (A.G. Evans).

0079-6425/01/$ - see front matter
PII: S0079-6425(00)00020-7

1. Background

1.1. The system

Thermal barrier coatings (TBCs) are widely used in turbines for propulsion and power generation [1–9]. They comprise thermally insulating materials having sufficient thickness and durability that they can sustain an appreciable temperature difference between the load bearing alloy and the coating surface. The benefit of these coatings results from their ability to sustain high thermal gradients in the presence of adequate back-side cooling. Lowering the temperature of the metal substrate prolongs the life of the component: whether from environmental attack, creep rupture, or fatigue. In addition, by reducing the thermal gradients in the metal, the coating diminishes the driving force for thermal fatigue. Both of these benefits can be traded off in design for greater component durability, or for reduced cooling air or for higher gas temperature/improved system efficiency. As a result, TBCs have been increasingly used in turbine engines. Successful implementation has required comprehensive testing protocols, facilitated by engineering models [9–12]. Expanded application to more demanding scenarios (Fig. 1) requires that their basic thermo-mechanical characteristics be understood and quantified. This need provides the opportunities and challenges discussed in this article.

There are *four primary constituents* in a thermal protection system (Fig. 2). They comprise (i) the TBC itself, (ii) the superalloy substrate, (iii) an aluminum containing bond coat (BC) between the substrate and the TBC, and (iv) a thermally grown oxide (TGO), predominantly alumina, that forms between the TBC and the BC. The TBC is the insulator, the TGO on the BC provides the oxidation protection and the alloy sustains the structural loads. The TGO is a reaction product. Each of these elements is dynamic and all interact to control the performance and durability.

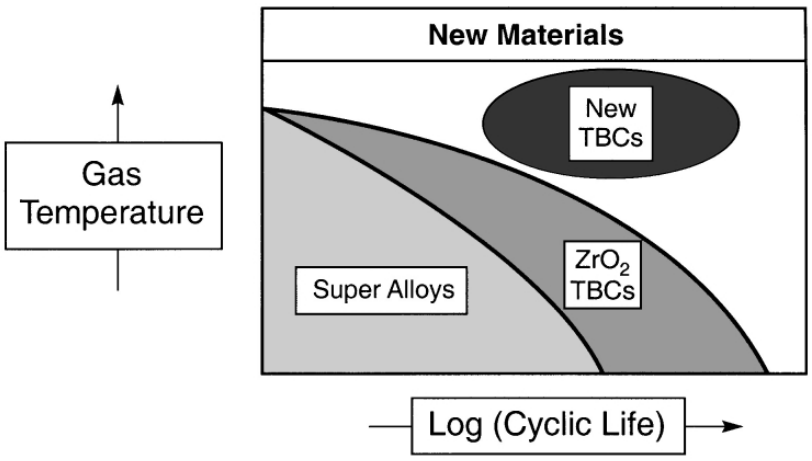

Fig. 1. Schematic indicating the operating domain for TBCs and the challenge for a new generation of materials.

The thermal barrier coating is a thermally insulating, "strain tolerant" oxide. Zirconia has emerged as the preferred material, stabilized into its cubic/tetragonal forms by the addition of yttria in solid solution. This material has low thermal conductivity ($\sim$1 W/m^2 K) with minimal temperature sensitivity (Fig. 3) [13,83]. The thermal resistance at lower temperatures corresponds to a phonon mean free path governed by structural vacancy scattering. Complex oxides having even lower conduction are being investigated, but there is no affirmation of their viability as TBCs. Strain tolerance is designed into the material to avoid instantaneous delamination from the thermal expansion misfit. Two methods are used to deposit strain-tolerant TBCs. Electron beam physical vapor deposition (EB-PVD) evaporates the oxide from an ingot and directs the vapor onto the preheated component [2,5,14]. The deposition conditions are designed to create a columnar grain structure with multiscale porosity (Fig. 2) that provides the strain tolerance and also reduces the thermal conductivity (to about 0.5 W/m K, Fig. 3). Air plasma spray (APS) deposition is a lower cost alternative [15–17]. The deposition is designed to incorporate intersplat porosity and a network of crack-like voids that again provides some strain tolerance, while lowering the thermal conductivity.

The thermally grown oxide has a major influence on TBC durability [8–12,18–20]. The bond coat alloy is designed as a local Al reservoir (Fig. 2), enabling α-alumina to form in preference to other oxides, as oxygen ingresses through the TBC (which is

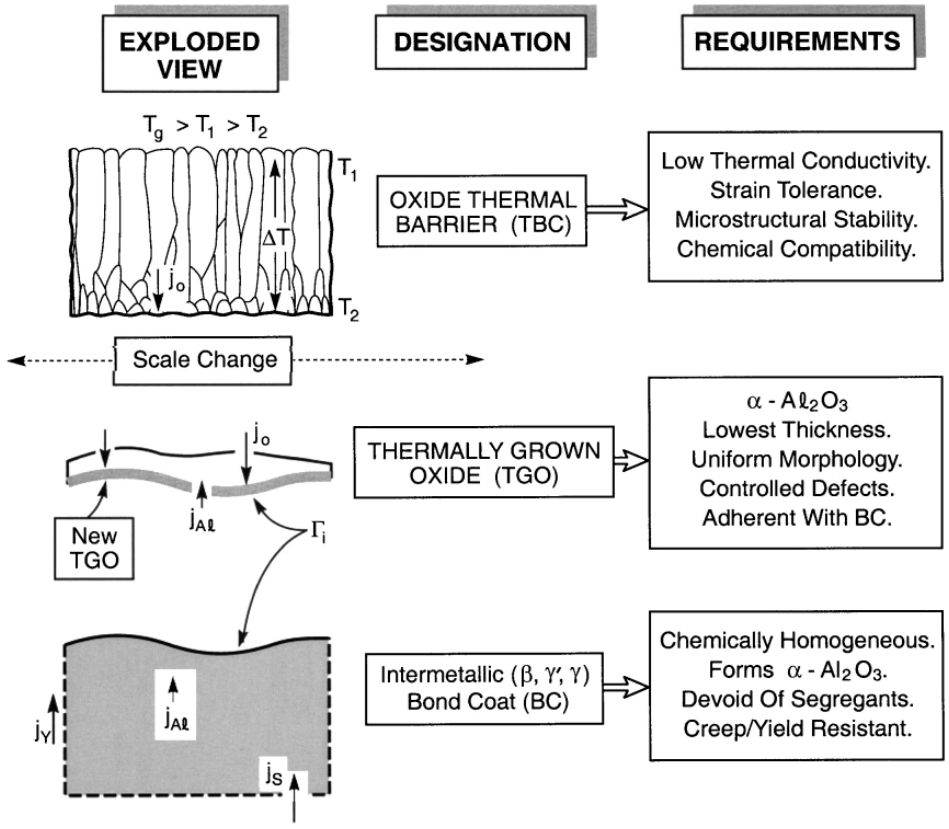

Fig. 2. The four major elements of a thermal barrier system: each element changes with exposure/cycling.

transparent to oxygen). Alumina is the preferred oxide because of its low oxygen diffusivity and superior adherence. This layer develops extremely large residual compressions (3–6 GPa, Fig. 4), as the system cools to ambient, primarily because of its thermal expansion misfit with the substrate (Fig. 5, Table 1) [21–27]. Stresses also arise during TGO growth [19,21]. They are much smaller (generally less than 1 GPa),

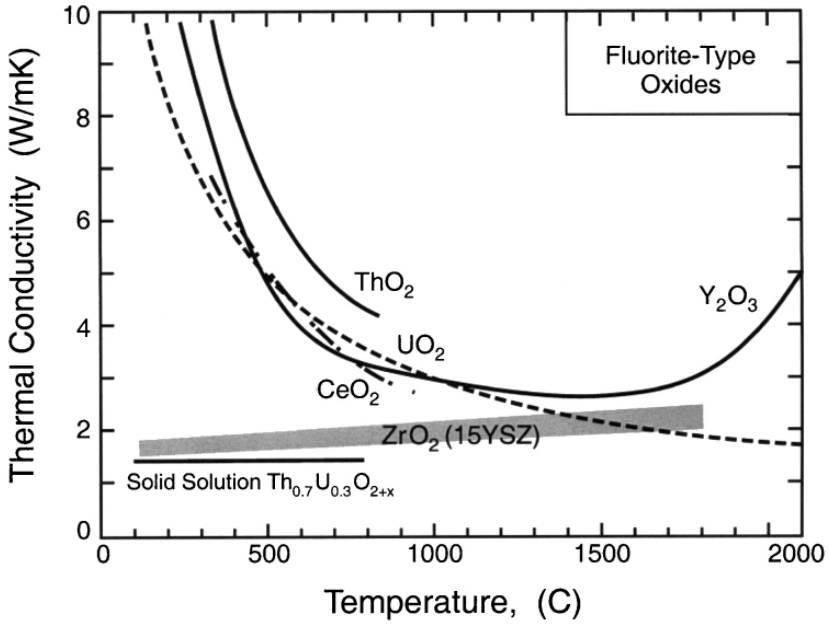

Fig. 3. The thermal conductivity of several insulating oxides illustrating the major role of solid solutions in affecting phonon transport.

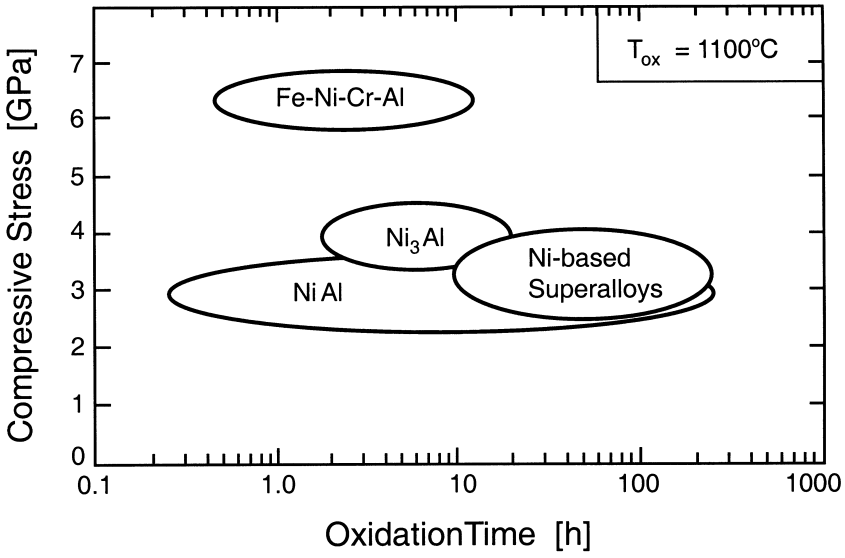

Fig. 4. Ambient residual compressions measured in the TGO developed on several alloy systems (after [21]).

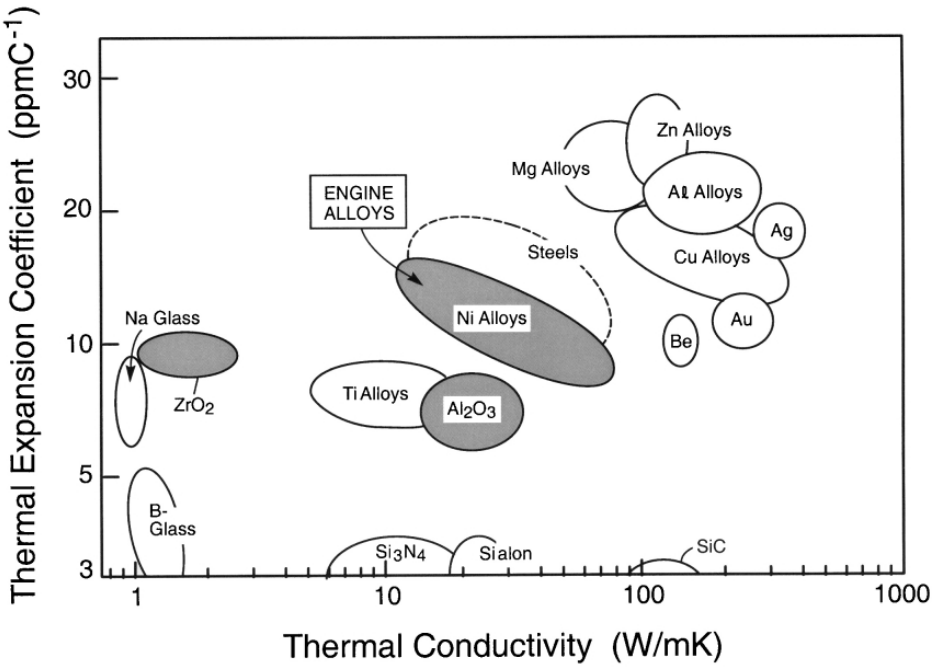

Fig. 5. Cross plot of the thermal expansion coefficient and thermal conductivity of the major material constituents in the TBC system.

Table 1
Summary of material properties

TGO (α-Al_2O_3)	
Young's modulus, E_o (GPa)	350–400
Growth stress, σ^g_{xx} (GPa)	0–1
Misfit compression, σ_0 (GPa)	3–4
Mode I fracture toughness, Γ_0 (J m^{-2})	20
Thermal expansion coefficient, α_o (C^{-1} ppm)	8–9
Bond coat	
Young's modulus, E_s (GPa)	200
Yield strength (ambient temperature) σ_Y (MPa)	300–900
Thermal expansion coefficient, α_s (C^{-1} ppm)	13–16
Interface (α-Al_2O_3/bond coat)	
Mode 1 adhesion energy, Γ^0_1 (J m^{-2})	
Segregated	5–20
Clean	>100
TBC (ZrO_2/Y_2O_3)	
Thermal expansion coefficient, α_{tbc} (C^{-1} ppm)	11–13
Young's modulus, E_{tbc} (GPa)	0–100
Delamination toughness Γ_{tbc} (J m^{-2})	1–100

but still important. Though thin (3–10 μm), the high energy density in the TGO motivates the failure mechanisms discussed in Section 3.

The bond coat is arguably the most crucial component of the TBC system. Its chemistry and microstructure influence durability through the structure and morphology of the TGO created as it oxidizes [19]. Moreover, system performance is linked to its creep and yield characteristics. Bond coats are in two categories. *One is based on the NiCoCrAlY system,* typically deposited by low-pressure plasma spraying (LPPS). It is usually two-phase [β-NiAl and either γ-Ni solid solution or γ′-Ni_3Al]. The γ/γ′ phases have various other elements in solution. The Y is added at low concentrations to improve the adhesion of the TGO, primarily by acting as a solid state gettering site for S [28–31], which diffuses up from the substrate. In some cases, small amounts of a Ni–Y intermetallic may also be present. *The second category consists of a Pt-modified diffusion aluminide*, fabricated by electroplating a thin layer of Pt onto the superalloy and then aluminizing by either pack cementation or chemical vapor deposition. These coatings are typically single-phase-β, with Pt in solid solution [19]. Their composition evolves during manufacture and in-service. Diffusion of Al into the substrate results in the formation of γ′ at β grain boundaries [19].

The interface between the TGO and bond coat is another critical element. It can be embrittled by segregation, particularly of S [28–31]. During thermal exposure, S from the alloy migrates to the interface. Dopant elements present in the BC getter much of this S and suppress (but not eliminate) the embrittlement. As already noted, bond coats based on NiCoCrAl contain Y for this purpose. The Pt–aluminide BCs do not contain elements which getter S. Nevertheless, they are durable and can have longer lives in cyclic oxidation than NiCoCrAlY systems [30]. While it has been proposed that the Pt mitigates the effects of S [31], there is no fundamental reason to expect this. A number of effects of Pt on the behavior of Pt-modified aluminides have been documented [32] but a complete understanding of the ''Pt effect'' is an important goal for future research.

A systems approach to TBC design and performance requires that several basic bifurcations be recognized and characterized. Three of the most important are addressed.

i. The NiCoCrAlY and Pt–aluminide bond coats result in distinct TGO characteristics as well as differing tendencies for plastic deformation. Accordingly, the failure mechanisms are often different.

ii. TBCs made by APS and EB-PVD are so disparate in their microstructure, morphology and thermo-physical properties that different failure mechanisms apply.

iii. The failure mechanisms may differ for the two predominant areas of application (propulsion and power generation), because of vastly different thermal histories. Systems used for propulsion and for power peaking experience multiple thermal cycles, whereas most power systems operate largely in an isothermal mode with few cycles. The frequency affects coating durability.

1.2. Failure phenomena

1.2.1. Generalities

Thermal barrier systems exhibit multiple failure mechanisms. Some of the most prevalent are indicated in Fig. 6. (i) In some cases, spinels form either between the

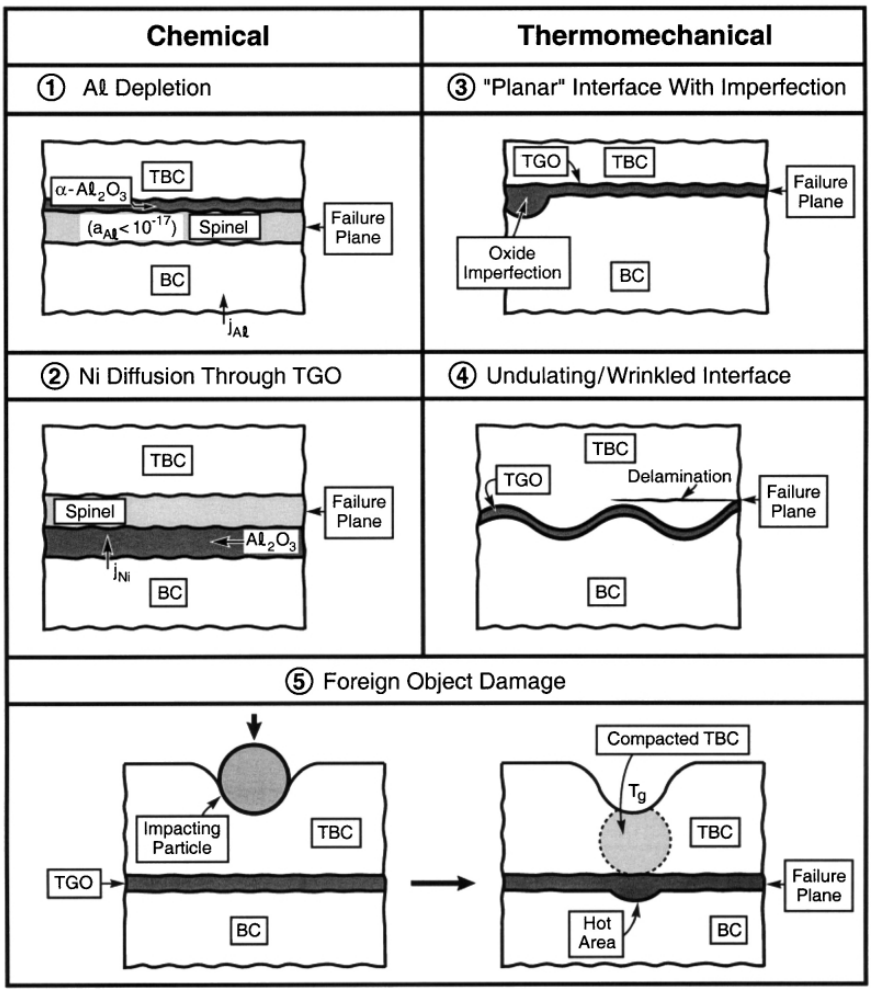

Fig. 6. Five of the major failure categories documented for TBC systems.

TGO and the bond coat or between the TGO and TBC [19]. When this happens, it is surmized (but not substantiated) that the ''brittleness'' of the spinel results in delamination. (ii) In other instances, regions of the component are subject to particle impact and foreign object damage (FOD) that locally compresses the TBC, resulting in hot spots in the underlying bond coat that contribute to failure [33]. Neither of these failure modes is addressed in this article. Instead, the emphasis is on the third category, (iii) wherein the energy density in the TGO and imperfections in its vicinity (Fig. 7) govern durability. This failure process occurs through a sequence of crack nucleation, propagation and coalescence events [8,24–27,34–38]. Prototypical sequences sketched in Fig. 8 will be elaborated in Section 3. These three elements, while analogous to the stages of cyclic failure in structural alloys [39], have the following special features: (a) Small cracks and separations *nucleate at imperfections* in (or near) the TGO. The tensile stresses that arise around these imperfections and the associated energy release rates govern the details. (b) Once nucleated, the *small*

cracks extend and coalesce, but the TBC may remain attached at remnant ligaments. (c) Failure happens when the ligaments are detached over a sufficient area that a separation becomes large enough to create either a large-scale buckle (designated LSB) or an edge delamination that eventually spalls from the substrate (see Fig. 20) [40].

1.2.2. Specific mechanisms

The specific ways in which the cracks nucleate and grow relate to the increase in the severity of the imperfections as the system is exposed and cycled. While this occurs in many ways, all are ultimately linked to the magnitude and scale of tensile σ_{zz} stresses that amplify as either the TGO thickens or the imperfections increase in size, or both. In turn, the stresses translate into stress intensity factors acting on

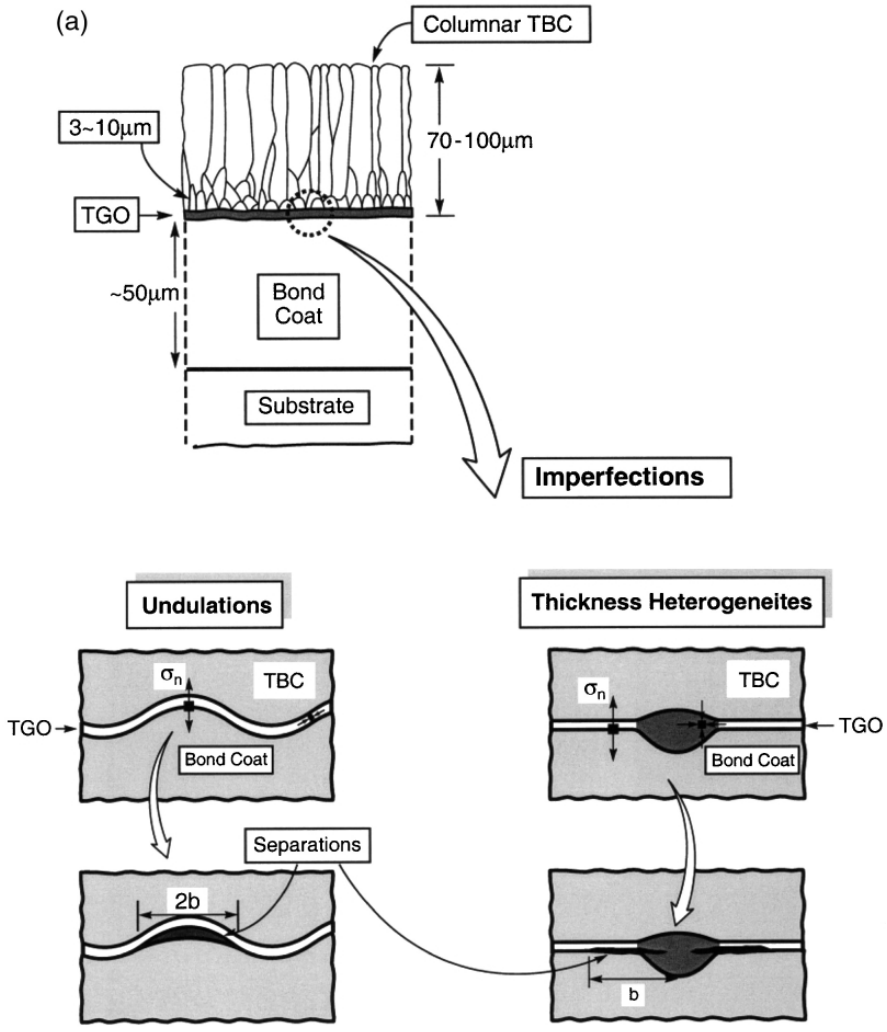

Fig. 7. (a) A schematic of two major categories of TGO imperfection that govern the TBC failure sequence; (b) a thickness imperfection in a TGO grown on a NiCoCrAlY bond coat; (c) an undulation imperfection that develops in a Pt–aluminide system upon thermal cycling.

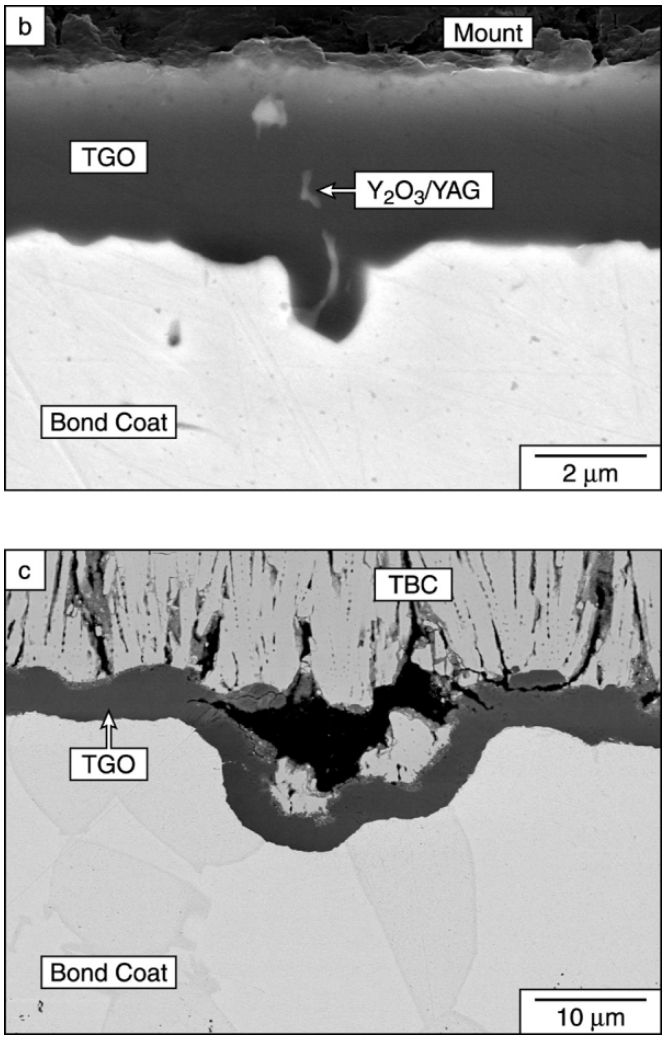

Fig. 7 (*continued*).

cracks that nucleate and propagate around the imperfections [41]. The examples presented in Fig. 8 illustrate the effects of increasing the TGO thickness and of enlarging the imperfection, respectively. Detailed analyses of these mechanisms are summarized in Section 3.

1.2.3. Related observations

After spalling of the TBC from the substrate, the exposed surfaces exhibit two broad morphological categories [19,42]. These observations must be consistent with the failure mechanisms.

i. One predominates for NiCoCrAlY bond coats with EB-PVD TBCs. In such systems, the exposed surface on the substrate side comprises predominantly bond coat with an imprinted TGO grain morphology [42] (Fig. 9a). The exposed surface on the TBC side consists of the TGO with a granular appearance that mirrors the imprint in the bond coat (Fig. 9b). Morphological imperfections in the TGO are

also in evidence. Most prominent are small (about 10 μm) polycrystalline oxide domains embedded in the bond coat [42]. They contain cleavage facets, indicating that they were mechanically detached from the TGO. There are corresponding features on the underside of the TGO.

ii. In other systems, especially those where the TBCs were deposited by the air plasma spray process, a substantial proportion of the delamination traverses the

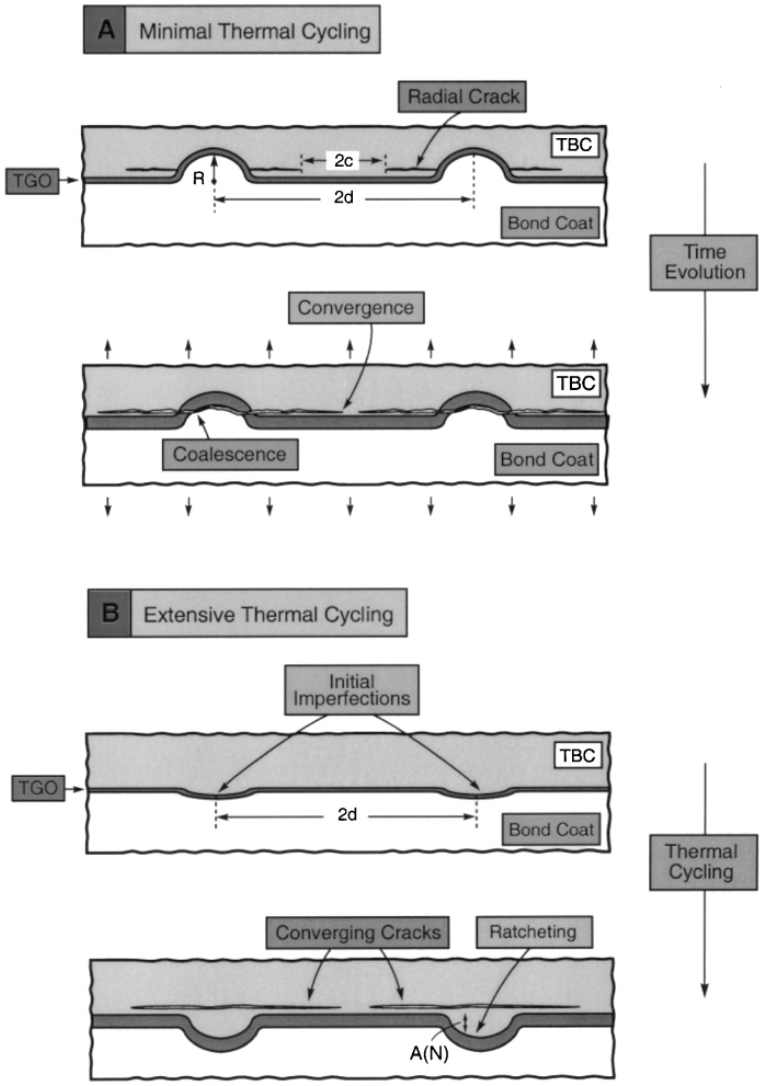

Fig. 8. Two examples of early and late stages of failure from imperfections: (a) schematic of a mode exhibited for scenarios subject to minimal thermal cycling showing how cracks can initiate in the TBC isothermally, due to the growth stresses, and then coalesce with an interface. Separation occurs upon cooling because of the thermal expansion misfit; (b) schematic of the growth of imperfections by ratcheting upon thermal cycling; (c) micrograph of an actual cross section of an APS TBC system highlighting the imperfections [44]. Cracks are in evidence near these imperfections; (d) cross-sections of an EB-PVD TBC on a Pt–aluminide bond coat showing the imperfections that enlarge by ratcheting and the cracks induced in the TBC [82].

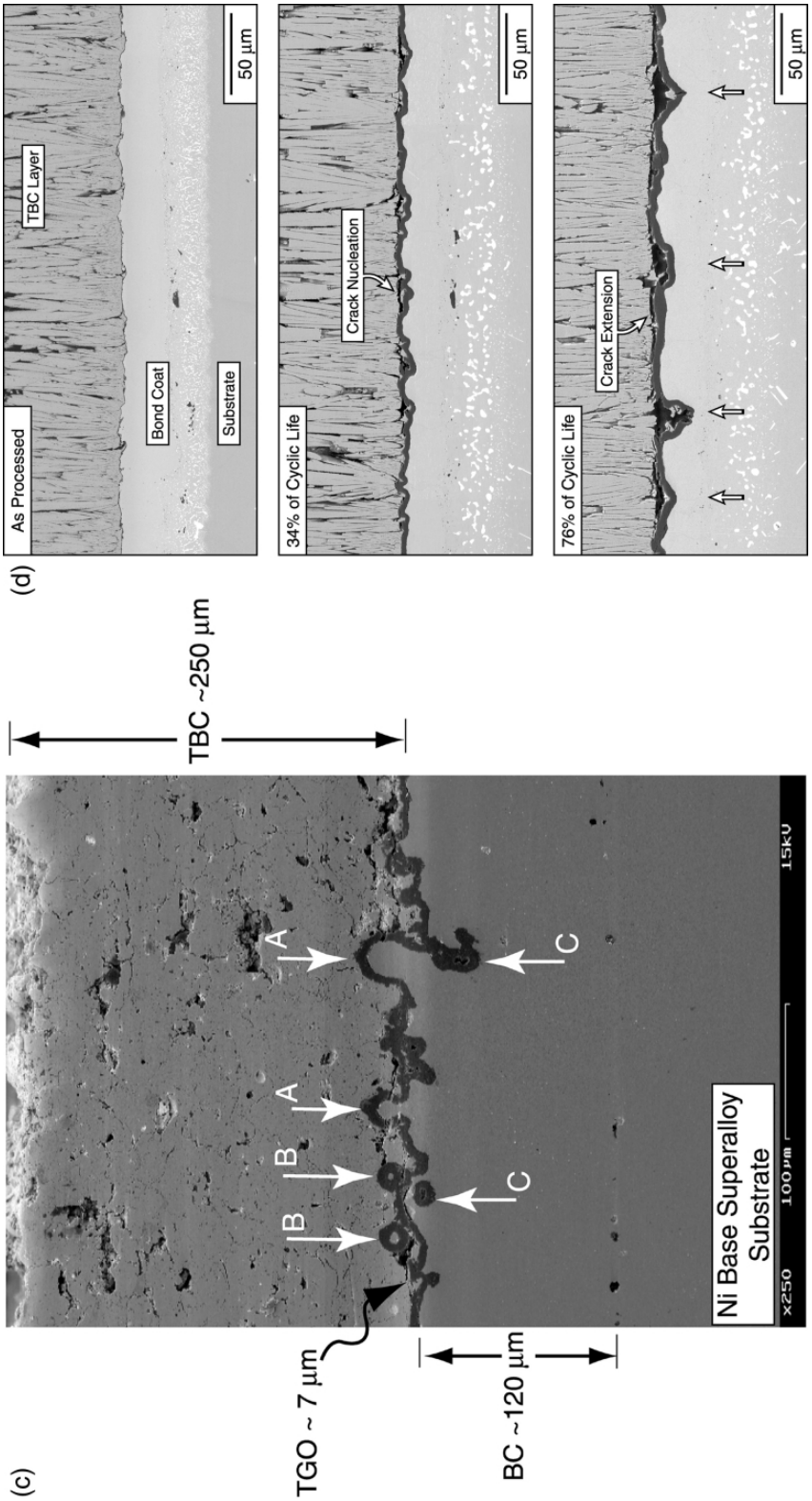

Fig. 8 (*continued*).

TBC itself, with local segments entering the TGO as well as the interface with the bond coat [44]. This mixed appearance diminishes the utility of such observations for interpreting failure mechanisms.

1.3. Overarching principles

Based on the above considerations and on detailed analyses to be elaborated below, the following three overarching principles govern the failure of TBC systems, as sketched in Fig. 10.

i. The TGO experiences large in-plane compressions, especially upon cooling. As with any compressed thin film, it attempts to alleviate the stress (and associated strain energy density) by lengthening itself, through out-of-plane displacements. This can happen by buckling as well as by visco-plastic deformation of the bond coat. These displacements induce tensile σ_{zz} stresses normal to the interface that motivate delamination mechanisms.

ii. When imperfections exist (or are developed) around the TGO, tensions are induced normal to the TGO/bond coat interface, as well as in the TBC, that nucleate and grow cracks in this vicinity. The coalescence of these cracks leads to failure.

iii. The TBC, despite its compliance, has sufficient stiffness to suppress small scale buckling (SSB) of the TGO. Accordingly, eventual failure often occurs by large scale buckling (LSB) [40], but only after a sufficiently large separation has developed near the interface, typically several mm in diameter. The durability of the TBC is governed by the time/cycles needed to develop such separations: through a nucleation, propagation and coalescence sequence, involving the energy density in the TGO, as well as the size and spacing of the prominent imperfections.

2. Thermally grown oxides

2.1. Growth phenomena

While the mechanisms of alumina formation prior to Al depletion are not quantitatively comprehended, especially in the presence of a TBC, the following four findings are pertinent.

i. The growth is essentially parabolic until spalling occurs:

$$h^2 = 2k_p t \tag{1}$$

where h is the thickness, t time and k_p the parabolic rate constant (Table 1). Accordingly, growth is diffusion (rather than interface) controlled. The alumina grows predominantly by inward diffusion of anions along the TGO grain boundaries but there is a contribution to k_p by outward diffusion of cations. This outward growth appears to be sensitive to cations dissolved in the alumina.

ii. In some cases, θ-alumina forms first, particularly on β-NiAl, and transforms to α-Al_2O_3 [45,46]. The θ-phase has an acicular morphology, indicative of growth by

outward diffusion of Al [47]. This morphology is retained upon transformation. The subsequent growth of α-Al_2O_3 appears to be unaffected by the prior transformation.

iii. In some case, the TGO formed on NiCoCrAlY bond coats entrains yttria [42]. The yttria in the TGO is related to the distribution of the Y in the bond coat. When yttria domains of sufficient size are incorporated into the TGO, it thickens more rapidly in these regions and produces thickness imperfections (see Fig. 7). Simultaneously, the yttria reacts with the surrounding alumina to form YAG.

iv. Present the TBC, the TGO may exhibit two distinct microstructural domains: a columnar zone (CZ) next to the BC and an equi-axed zone (EZ) next to the TBC [19]. The EZ found on MCrAlY coatings (which contain Fe), incorporates small (nm) oxide precipitates containing Fe and Cr cations [48], while that on Pt-aluminides comprises a mixture of zirconia and alumina [19].

2.1.1. Thermodynamics

The stability of oxide product phases that form on bond coat materials may be rationalized by constructing thermodynamic stability diagrams. Such a diagram for the Ni–Al–O system is presented in Fig. 11a [19]. This diagram describes the equilibria between the phases in this system (Al_2O_3, $NiAl_2O_4$, NiO and Ni–Al alloys), with the oxygen activity, a_O, as the ordinate and the aluminum activity, a_{Al} (interchangeable with a_{Ni}), as the abscissa. Fig. 11a can be constructed by formulating

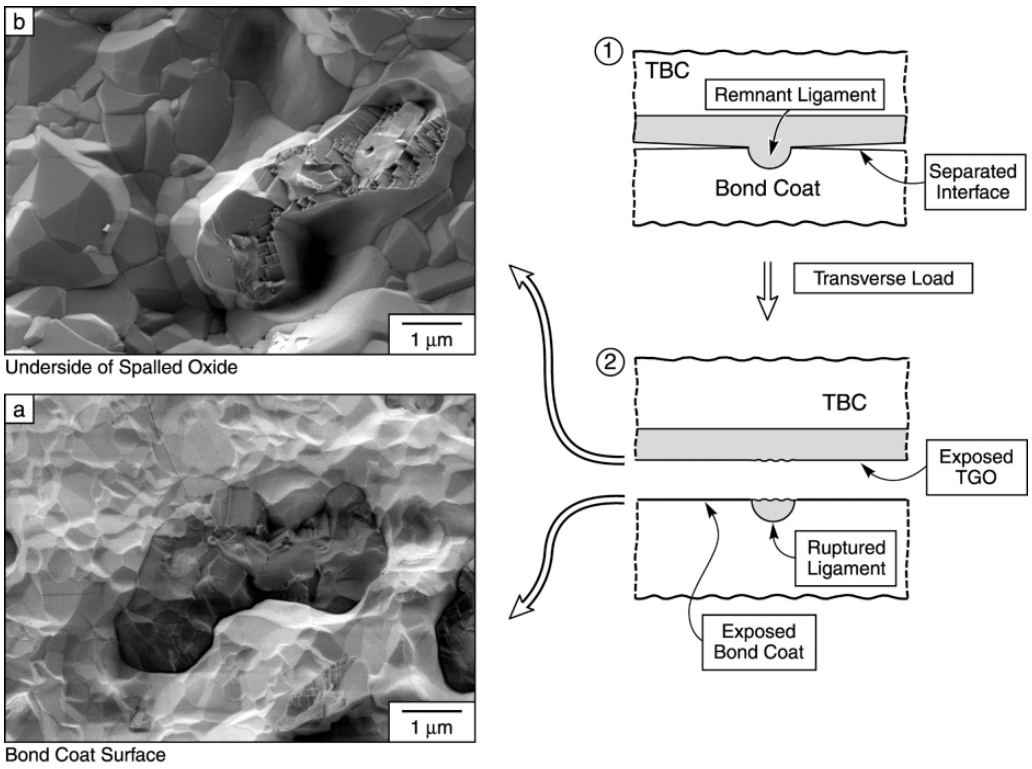

Fig. 9. SEM images of separated interface between a NiCoCrAlY bond coat and a TGO: (a) exposed bond coat; (b) matching surface of the TGO [42].

equilibrium reactions, provided that the standard free energies of formation are available and the activities are understood. The activity of Al in the alloy is related to X_{Al} through the activity coefficient γ_{Al}:

$$\gamma_{Al} = a_{Al}/X_{Al} \tag{2}$$

The activity of Ni is related to that for Al by the Gibbs–Duhem equation:

$$\log \gamma_{Ni} = -\int_{X_{Ni}=1}^{X_{Ni}} \left(\frac{X_{Al}}{X_{Ni}}\right) d\log \gamma_{Al} \tag{3}$$

Accordingly, in order to relate a_{Al} to compositions of the Ni–Al alloys, additional

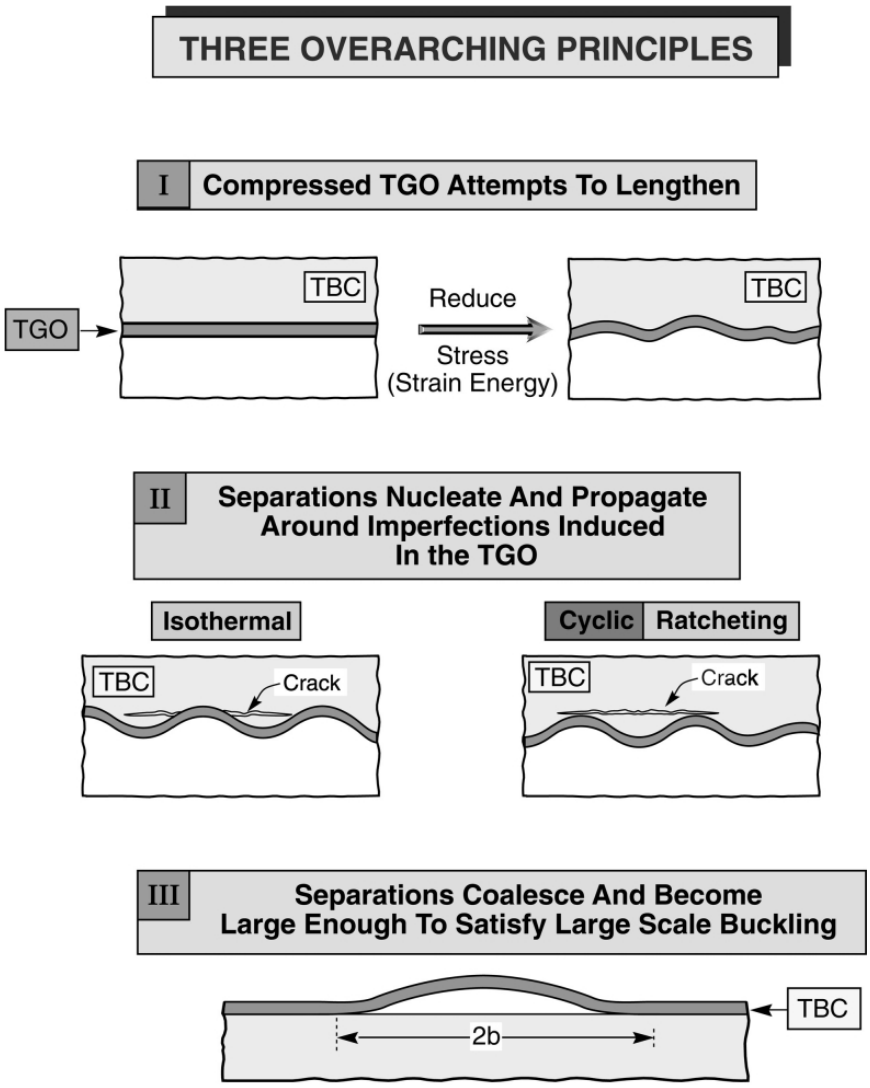

Fig. 10. Sketch illustrating the overarching principles governing TBC failure.

thermodynamic data are required [49] (Fig. 11b). Note that the activity of Al in the alloy is always much less than X_{Al}.

The important equilibria described in Fig. 11a are as follows:

- Line (1) represents Al_2O_3 in equilibrium with Ni–Al alloys through the reaction;

$$2Al(alloy) + 3O = Al_2O_3 \tag{4a}$$

- Line (2) refers to $NiAl_2O_4$ in equilibrium with the alloy via the reaction;

$$Ni(alloy) + 2Al(alloy) + 4O = NiAl_2O_4 \tag{4b}$$

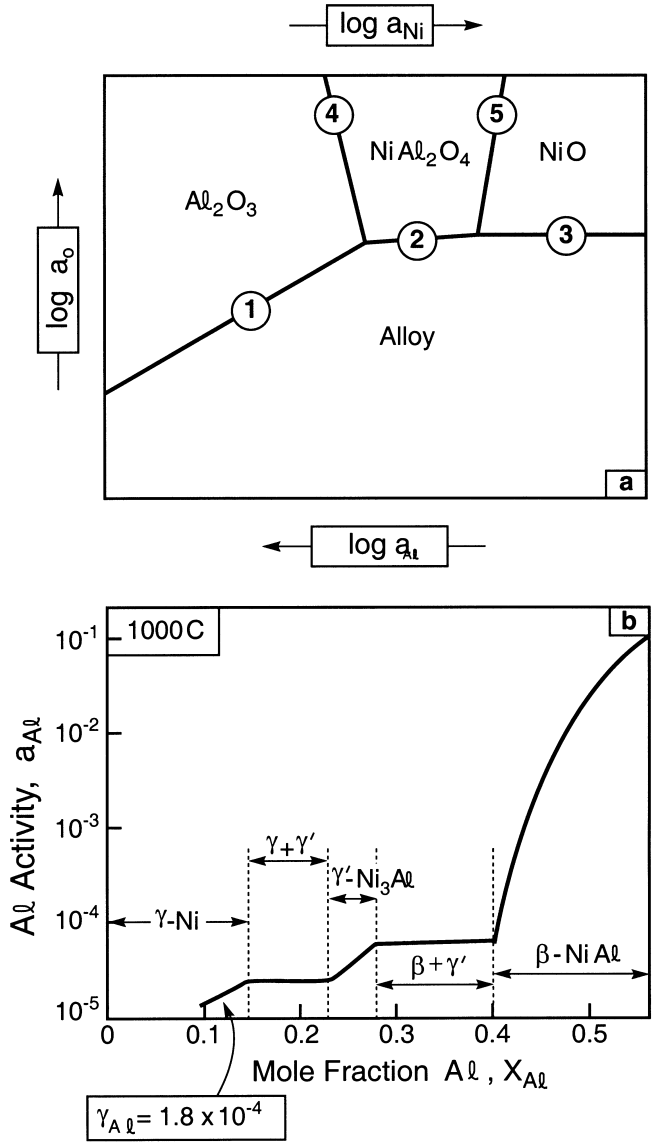

Fig. 11. (a) The thermodynamic stability diagram; (b) the activity coefficient for Al as a function of concentration for the Ni/Al binary [19].

- Line (3) involves NiO in equilibrium with the alloy;

$$\mathrm{Ni(alloy)} + \mathrm{O} = \mathrm{NiO} \tag{4c}$$

The junction of lines (1) and (2) defines a three-phase equilibrium through the reaction;

$$3\mathrm{Ni(alloy)} + 4\mathrm{Al_2O_3} = 3\mathrm{NiAl_2O_4} + 2\mathrm{Al(alloy)} \tag{4d}$$

and the junction of lines (2) and (3), the three phase equilibrium;

$$3\mathrm{Ni(alloy)} + \mathrm{NiAl_2O_4} = 4\mathrm{NiO} + 2\mathrm{Al(alloy)} \tag{4e}$$

The lines (4) and (5) involve two-phase equilibria that can be described through reactions (4d) and (4e), respectively, except that the activities of Al and Ni must be those in the oxide phases.

The stability diagram (Fig. 11a) indicates that at Al activities in the bond coat satisfying $a_{\mathrm{Al}} > 10^{-17}$, reaction (4a) dominates, resulting in $\mathrm{Al_2O_3}$ formation [19]: the thermodynamic situation most favorable for a durable TBC. Whenever $\mathrm{Al_2O_3}$ is stable, the oxygen activity at the interface is too low to form alternative oxides. Upon alumina growth, as the aluminum activity decreases, the oxygen activity at the interface increases along line (1) in Fig. 11a. When a_{O} reaches the intersection of lines (1) and (2), the $\mathrm{Al_2O_3}$ converts to $\mathrm{NiAl_2O_4}$ through reaction (4d). When this happens, the durability of the TBC may be compromised. [For practical bond coats, reaction (4c) never occurs].

Kinetic processes also play a significant role in phase evolution. The effects of kinetics could be included on the stability diagrams by indicating reaction paths, but these kinetics are currently incompletely understood. Two salient findings are as follows [19]:

i. Before a_{Al} in the bond coat decreases to a level that would cause spinel to form, the oxygen flux into the bond coat may exceed the Al flux toward the TGO, whereupon $\mathrm{Al_2O_3}$ precipitates form beneath the TGO in the bond coat.

ii. In some circumstances, as a_{O} at the interface increases, the solubilities of nickel and chromium (as well as Fe when present) in the $\mathrm{Al_2O_3}$ also increase. This condition can result in outward diffusion of cations, through the TGO. Upon encountering higher oxygen activities, these cations can form new oxide phases. For example, in regions between the TGO and the TBC, the thermodynamics and kinetics are such that spinel formation is allowed (Fig. 11a).

2.2. Stresses

The stresses in the TGO exert a central influence on TBC failure. Understanding these stresses is crucial to any model of the durability. There are two main sources of stress: one from the thermal expansion misfit upon cooling and the other from TGO growth [19,21–27,41,50,51]. Both stresses may be alleviated by TGO creep [52–54] and redistributed in the vicinity of imperfections [38,41]. Moreover, the stresses can be substantially modified by thermal cycling conditions that cause cyclic plasticity in the bond coat [37]. Sources of stress development, redistribution and relaxation are

addressed with emphases on the sign and magnitude in the vicinity of imperfections and on the consequences of thermal cycling. Ambient temperature measurements by X-ray diffraction [27] and laser piezo-spectroscopic techniques [21] indicate that thermal expansion misfit results in compressions that, on the average, range between 3 and 6 GPa (see Fig. 4). Direct measurement of the growth stresses by high temperature X-ray peak shift measurements [27,55] indicate that these stresses are also compressive and much smaller than the thermal stresses. They range from near zero for Ni-base alloys to about 1 GPa for FeCrAl(Y) alloys. Nevertheless, they may have an important role in TBC failure. In the vicinity of imperfections the stresses deviate from these average values. Upon thermal cycling, they can even change sign [37]. The specifics are assessed next.

2.2.1. Thermal expansion misfit stresses around imperfections

Imperfections cause the thermal expansion misfit stresses to redistribute. Normal tensions exist where the TGO is concave and vice versa (Fig. 12) [34]. Shear stresses exist at inclined sections. These stresses depend on the elastic mismatch and the ratio of the amplitude A, to the wavelength, L, of the oscillations. When the TGO is thin ($h/L \ll 1$), the stresses are given by [34]:

$$\sigma_{ij}/\sigma_0 = H_{ij}(\alpha_D)A/L \tag{5a}$$

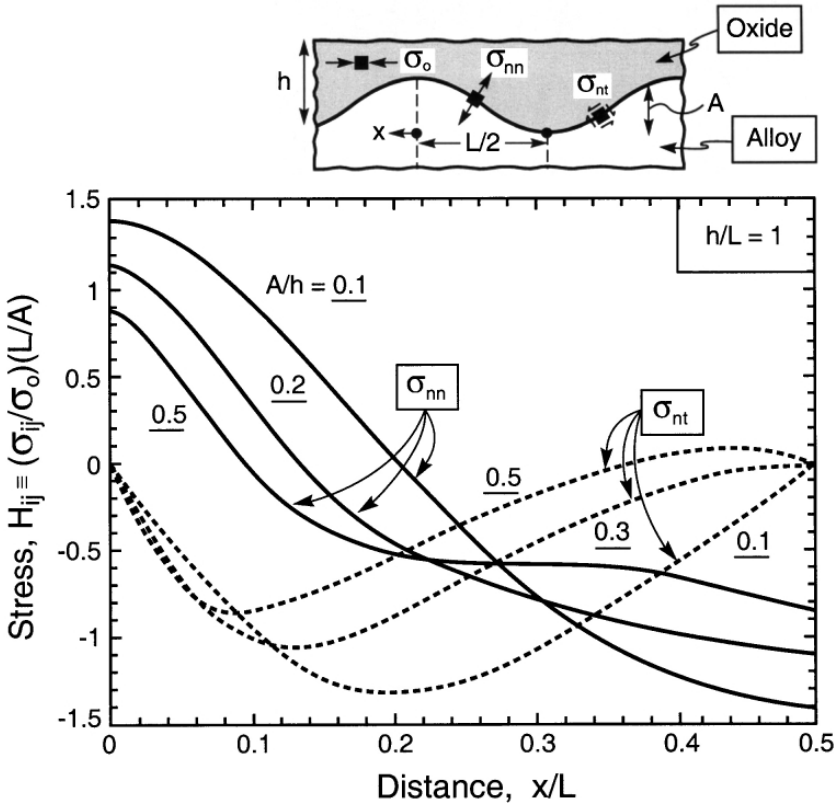

Fig. 12. Distribution of stresses at an undulating TGO interface [34].

where the misfit stress (the stress that would exist in a planar thin film) is [34]:

$$\sigma_0 = E_0 \Delta\alpha_0 \Delta T/(1-\upsilon), \tag{5b}$$

and α_D is the Dundurs' parameter, defined as [56]:

$$\alpha_D = \frac{\bar{E}_1 - \bar{E}_2}{\bar{E}_1 + \bar{E}_2} \tag{5c}$$

with $\bar{E}$ the plane strain Young's modulus and the subscripts 1 and 2 referring to the two adjoining materials. The functions H_{ij} are plotted in Fig. 12. As the TGO thickens, there are additional effects of h/L (Fig. 13).

2.2.2. Redistribution of misfit stresses by bond coat visco-plasticity

The misfit stresses are redistributed by creep or yielding of the bond coat during thermal cycling. Measurements and models characterizing the important effects are developmental [37]. Local misfit stresses around imperfections in the bond coat may become large enough to exceed its yield strength and, thereafter, to induce cyclic yielding. The response may be characterized through a Bree diagram [37,57,58] that identifies domains of elasticity, shakedown and cyclic plasticity (Fig. 14). The specifics are addressed in Section 3. Some elaboration is also given in Appendix E. The coordinates of this diagram are the undulation amplitude-to-wavelength ratio, A_0/L and the misfit stress, σ_0, relative to the bond coat yield strength σ_Y. When these coordinates reside in the elastic domain, yielding is prohibited and the stresses in the

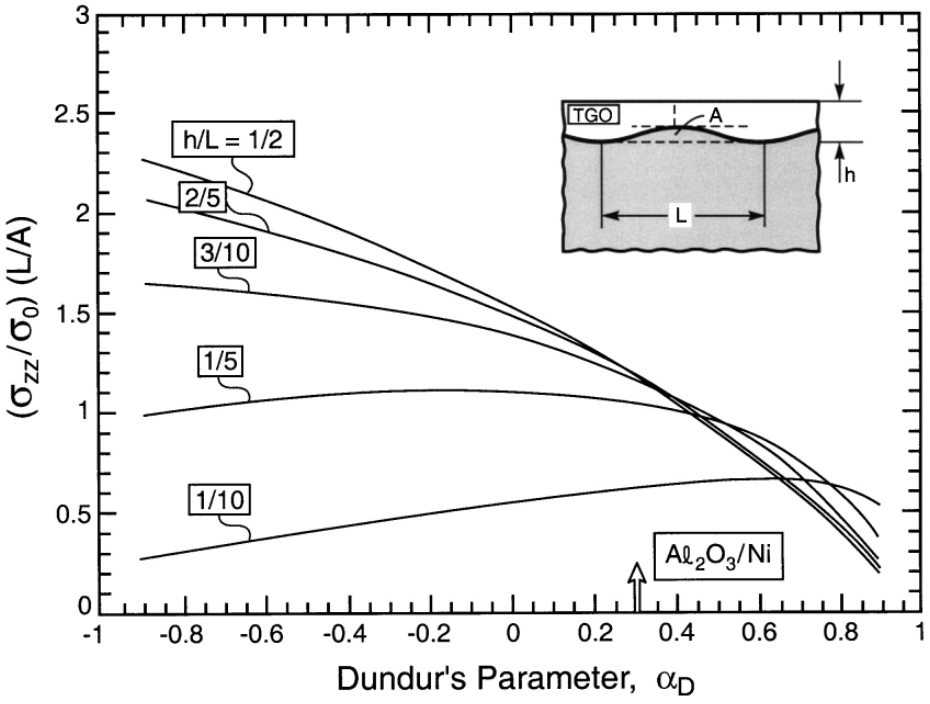

Fig. 13. The effect of elastic mismatch on the stress normal to the interface [34].

TGO are given by the above elasticity solutions. When the bond coat yield strength is exceeded, the stresses are redistributed such that the ambient compressive stress in the TGO is reduced (Fig. 15). Moreover, upon re-heating, regions of tensile stress may develop. These stresses tend to relax by creep (discussed below) but, in some cases, may cause the TGO to crack. In subsequent cycles, the stresses are "reset" by the plasticity that occurred in the first cycle [37]. The response thereafter depends on whether the system is within the "shakedown" or "cyclic plasticity" domain (Fig. 14). In the former, the system becomes elastic after a few cycles and, thereafter, the stresses vary linearly with temperature between the new limits established in the first cycle. Outside this range, the stresses are non-linear and exhibit hysteresis, with consequences for fatigue of the bond coat.

While further changes in the TGO stress may arise when growth strains are added to the thermal expansion misfit, the effect is relatively small, because of the equilibrating influence of bond coat yielding [37]. However, as discussed later, when ratcheting conditions are satisfied, the displacements of the TGO into the bond coat have a major effect on TBC failure.

2.2.3. Growth stresses

Oxidation is accompanied by growth strains and associated stresses [37,59,60]. The strain represents the overall volume increase upon converting the alloy to Al_2O_3. It comprises normal, m_{zz}, and in-plane, m_{xx}, components that depend on the growth mechanism and the induced stresses. In general it can be expressed in the form:

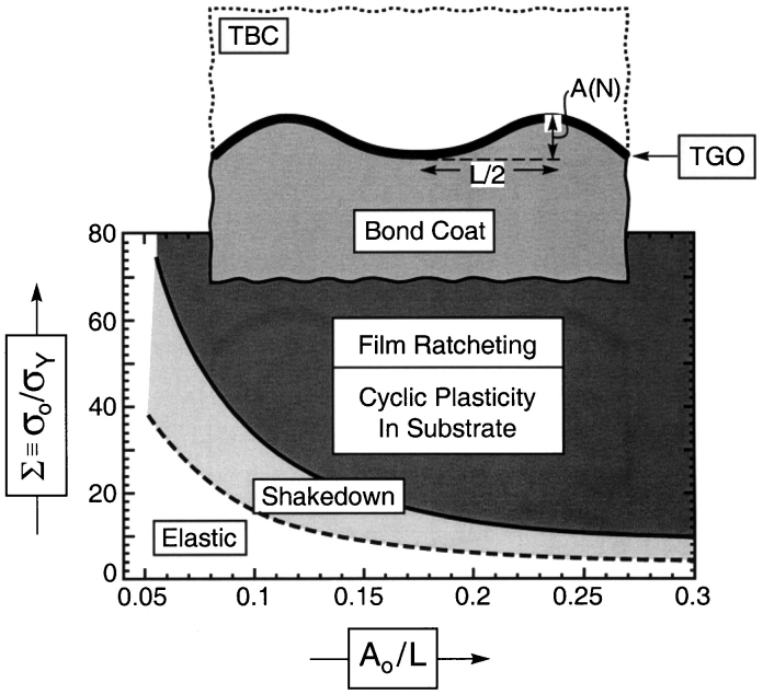

Fig. 14. Bree diagram for a TGO governing ratcheting and shakedown [37].

$$m_{zz}\left(\sigma_{xx}^{g}\right) + 2m_{xx}\left(\sigma_{xx}^{g}\right) = m \tag{6}$$

where σ_{xx}^{g} is the in-plane stress induced by the lateral growth strain. The fundamentals of the growth are incompletely understood. Formation of the new TGO at the interface with the bond coat results in m_{zz} thickening strains with a corresponding rigid body displacement [59,60]. Lateral strains are induced in proportion to that fraction, β, of the new Al_2O_3 that forms, internally, on grain boundaries normal to the interface (Fig. 16). These strains induce σ_{xx}^{g} compressions. When large enough, this stress suppresses internal TGO formation. This happens at a critical stress [59]:

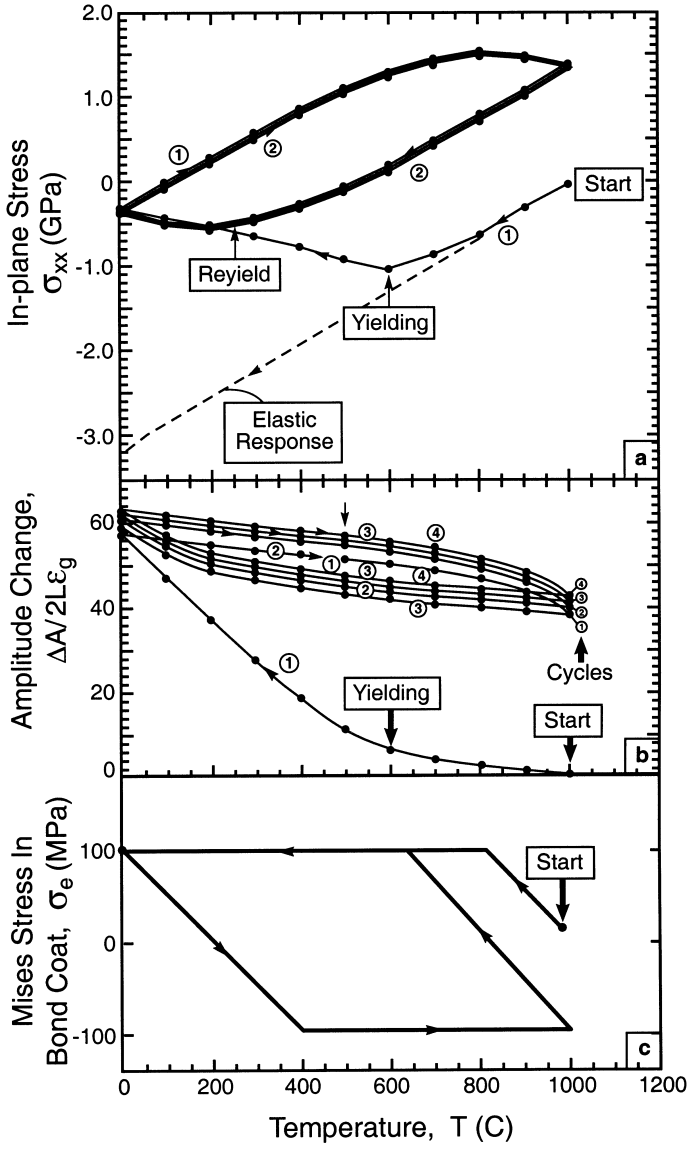

Fig. 15. The evolution of stresses and amplitudes when thermal cycling causes ratcheting: (a) stress in the TGO; (b) the change in the amplitude of the imperfection; (c) the Mises stress in the bond coat [37].

$$\sigma_* = -\left\{\frac{kT\ln[p^{g}_{O_2}/p^{eq}_{O_2}][1+1/(1+2(h/g))]}{24\Omega_{Al_2O_3}}\right\} \tag{7}$$

where g is the grain size of the TGO. Inserting typical values indicates a stress of order [59]: $\sigma_* \approx -3$ GPa. In all cases, the measured growth stresses are smaller than this, because the creep strength of the TGO is exceeded (discussed next). Ultimately, the stress levels are established by the creep characteristics.

Information about β and its effect on growth stresses can be gained from direct measurements on thick substrates [19,21,23,26,27,55], as well as from the extension of thin bond coat coupons as they oxidize [22]. On thick substrates, as the stress intensifies, creep

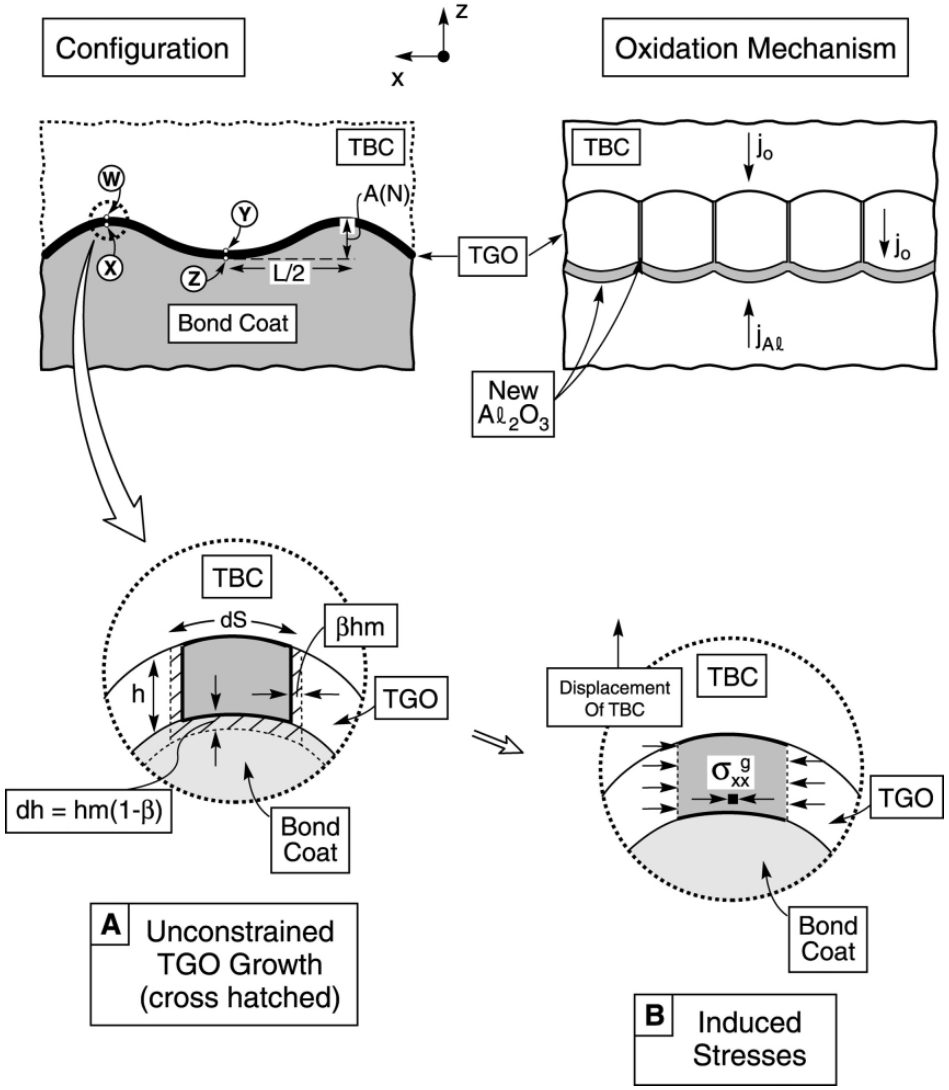

Fig. 16. Schematic indicating the TGO growth modes and its implications for the development of growth stresses.

relaxation ensues, and a dynamic equilibrium exists. This balance results in a "steady-state" growth stress, σ^{g}_{xx} (Appendix C). Within the creep formalism described below, the internal deposition fraction is implied to be of order $\beta \approx 0.1$. Similar values have been found from coupon tests [22]. It has not yet been possible to predict β from basic understanding of oxidation and creep. Note that for $\beta = 0$, the growth strains would be entirely normal to the interface such that, on a planar section, the stresses would be zero.

On non-planar segments of the interface, representative of imperfections, the growth stresses are quite different, because the growth normal to the interface cannot be entirely accommodated by rigid body displacement (Fig. 17) [41]. Moreover, the induced stresses differ for anion- and cation-controlled growth mechanisms. The former has been asserted to predominate for a TGO comprising α-Al_2O_3 [22,61–64]. An approximate

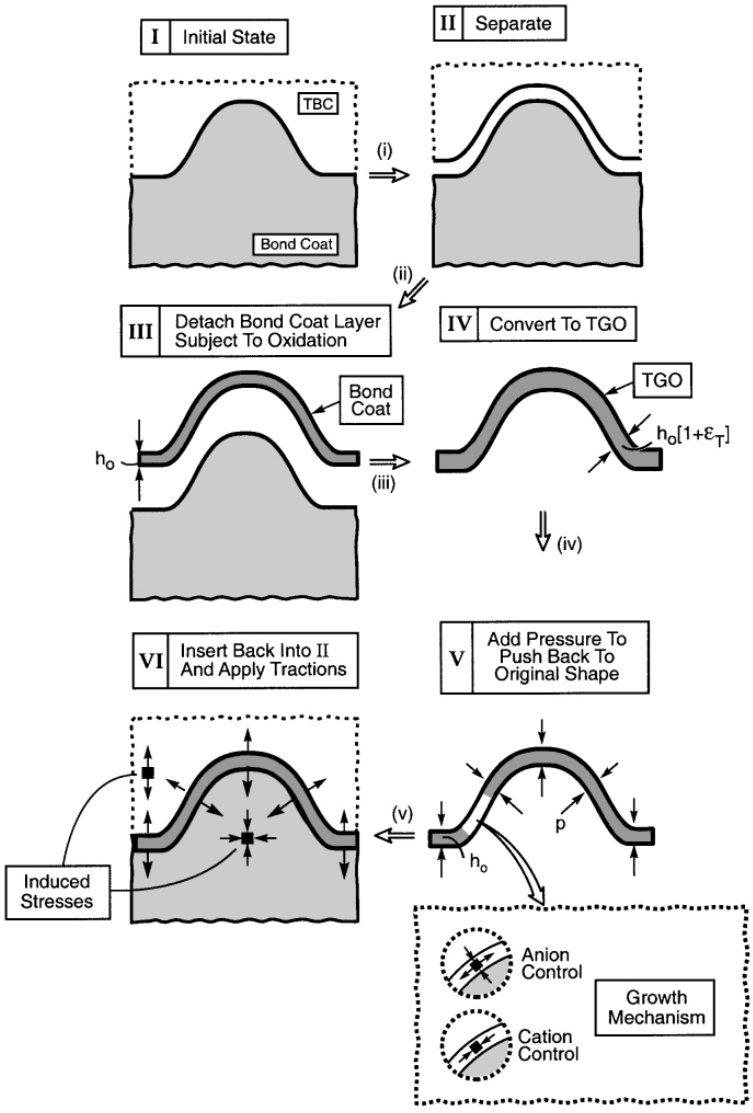

Fig. 17. An "Eshelby" sequence indicating the displacements and stresses that accompany TGO growth [41].

analytical model for a concave imperfection (Appendix B) [37] indicates that the TGO is in hoop tension and radial compression. These stresses have particular importance for cyclic failure mechanisms that involve ratcheting, as discussed in Section 3.

2.2.4. Creep relaxation

At the same temperatures that allow the TGO to thicken by oxidation it experiences creep, because grain boundary transport of anions and cations is involved in both phenomena. Experience with the creep of bulk polycrystalline α-alumina having equivalent grain size provides a frame of reference. When tested at the relatively low stresses amenable to measurement (about 50 MPa or lower), the bulk material deforms in accordance with the expression [65]:

$$\dot{\varepsilon}_c \equiv \dot{\varepsilon}_0(\sigma_*/\mu_0)^2 \tag{8}$$

with

$$\dot{\varepsilon}_0 \approx 100\left[\frac{D_b\delta_b\mu}{kT}\right]\left(\Omega_{Al_2O_3}^{2/3}/g^2\right)$$

where g is the grain size, μ the shear modulus, $\dot{\varepsilon}_0$ the reference strain-rate for creep (Table 2), $\Omega_{Al_2O_3}$ the molecular volume of alumina and σ_* a reference stress. The diffusivity, $D_b\delta_b$ is considered to be that for diffusion of Al^{3+} ions along the grain boundaries [52–54]. Additions of yttria at levels characteristic of those found in the TGO reduce $\dot{\varepsilon}_0$ (Table 2) [53,54]. While the mechanism responsible for creep in the TGO may differ (because the stress levels are much higher): nevertheless, first order estimates of creep-rates may be made using (8) (see Appendix C).

2.3. Adhesion

2.3.1. Metal/oxide interfaces

Clean metal/oxide interfaces devoid of reaction products are inherently tough and ductile: toughness exceeding 200 J m^{-2} (Fig. 18) [43,66]. The most vivid manifestation is crack blunting [66], which has been documented for interfaces between α-Al_2O_3 with Ni, Au, Cu, Al and Nb. Such high adhesion is realized even though the metals are polycrystalline and non-epitaxial (that is, despite the interfaces being either incoherent

Table 2
Summary of kinetic parameters

		Temperature (°C)		
		1100	1200	1300
Oxidation coefficient, k_p ($\times 10^{17}$ m^2/s)		3	12	81
Creep-rate coefficient, $\dot{\varepsilon}_0$ ($\times 10^{-7}$ s^{-1})	Pure	5	50	400
	Y-doped	0.25	5	50

or subject to a high density of misfit dislocations). However, broad toughness ranges have been cited. This variability arises because of interfacial contaminants or segregants. The effect is most clearly demonstrated by beginning with a clean interface and systematically infusing a contaminant, whereupon cracks propagate at toughness in the range 2–20 J m^{-2} [67,68] (Fig. 18). Beyond these basics, some interfaces are susceptible to stress corrosion in the presence of moisture: particularly Ni and Au [43]. Indeed, stress corrosion of the TGO/bond coat interface has been documented [24,69].

2.3.2. Mechanics

Two fundamentally important factors distinguish fracture at interfaces from that in homogeneous materials [56]:

i. The elastic property mismatch causes the energy release rate, G, and the mode mixity angle, ψ, to differ from that for homogeneous bodies subject to the same loading. These differences are fundamentally governed by the first Dundurs' parameter [56].

ii. Unlike isotropic solids, cracks may extend along interfaces even when the loading deviates from mode I (i.e. $\psi \neq 0$). Accordingly, the fracture toughness must be specified as a function of ψ. A useful phenomenological relation is [56]:

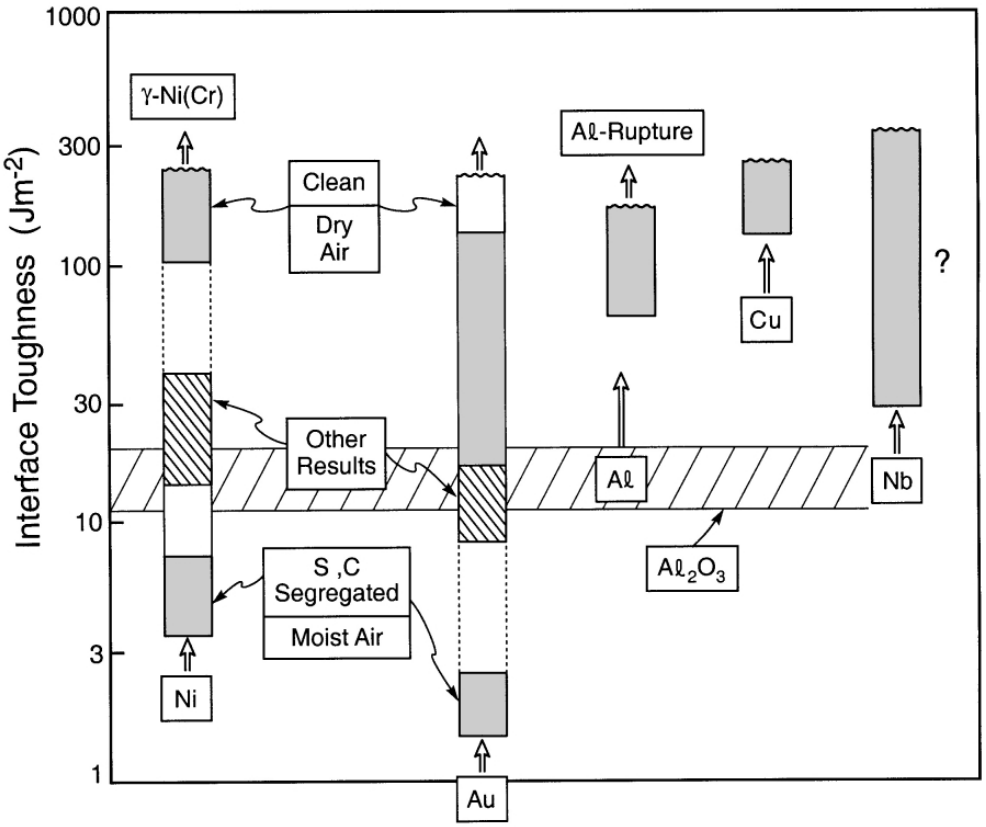

Fig. 18. Summary of experimental measurements of the mode I toughness between α-Al_2O_3 and several metals [43].

$$\Gamma_i = \Gamma_i^0 \tan^2[(1-\lambda)\psi] \tag{9}$$

where Γ_i^0 is the mode I toughness. The parameter λ is a mixity index defined such that there is a strong influence of mode II when λ is small. The effect is crucially important to the understanding of buckling, spalling and cracking [56,70]. Notably, as ψ increases (because of a relatively large shear loading), various responses reduce the displacements that transmit to the interface crack tip. These effects include friction at contacting crack wake asperities, as well as elongated plastic zones in the metal. The consequences include the stabilization of buckles and edge delaminations. One of the major challenges in characterizing interface adhesion is the determination of λ. This is especially true for the TGO/BC interface.

2.3.3. Test protocols

Interface toughnesses for films and coatings on ductile substrates are most readily determined by impression tests [42,71]. They can also be measured by inducing buckle propagation [70] (Appendix A). Impression methods use an indentor with

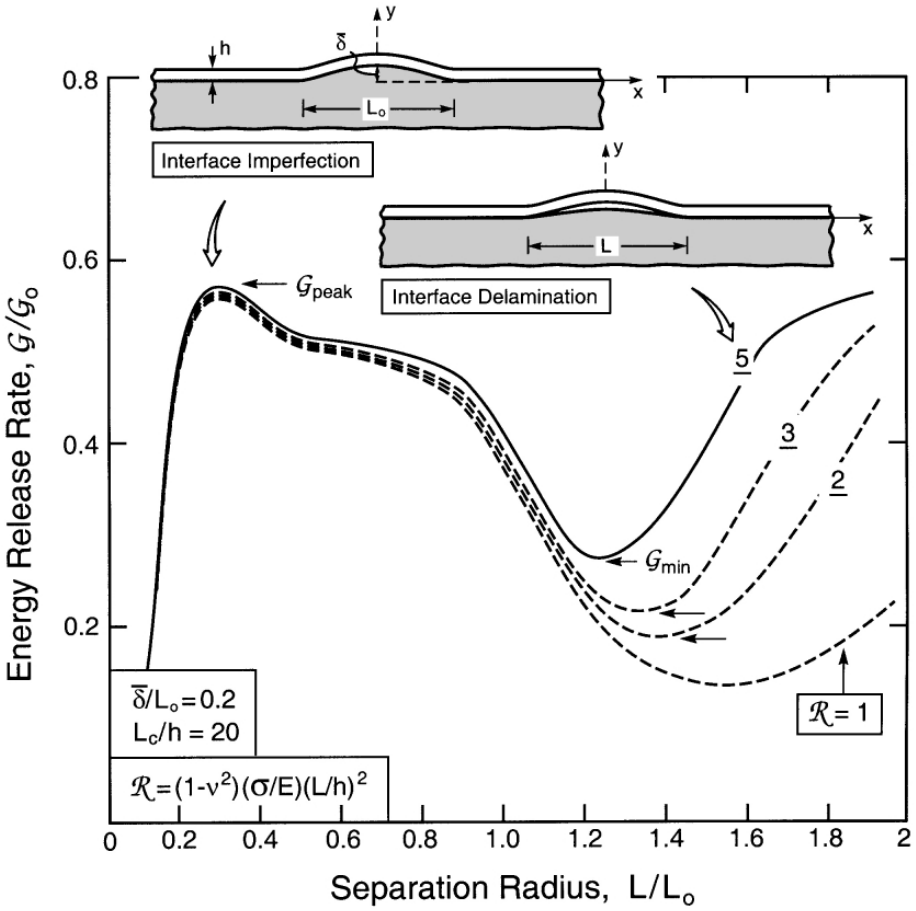

Fig. 19. The variation in energy release rate with separation size for a TGO, absent the TBC, in the vicinity of an imperfection [72].

prescribed geometry to plastically impress the substrate. The impression induces in-plane compressive strains along the surface that vary with distance from its center. These strains are transmitted up into the film. The strain energy density in the film (deriving from both the impression and the thermal expansion misfit) provides the energy release rate. In all cases, G initially decreases with distance from the impression, causing the delamination to develop stably as the impression depth increases.

2.3.4. Measurements

Direct measurements of the toughness of the interface between the TGO and bond coat have been recent and sparse [24,42,70]. Determinations made using the buckling method [24,70] have indicated that $\Gamma_i \approx 5$–10 J m^{-2}, with a mode mixity $\psi \approx 50^\circ$. Such low toughness is characteristic of embrittled Ni/Al_2O_3 interfaces [68] (Fig. 18). Wedge impression and edge delamination measurements performed with the TBC present have provided estimates of the mode II interface toughness: $\Gamma_{i\mathrm{II}} \approx 60$ J m^{-2} [42]. These higher values (relative to the buckling results) reflect the role of interface friction [λ in Eq. (9)].

2.4. Failure

TGO films eventually fail by small-scale, buckle-driven delamination [70] (SSB). Failure is motivated by the strain energy density in the TGO and resisted by the fracture toughness along the delamination plane, usually the interface. Should all of the strain energy be available for decohesion (which it is not), a lower bound for the thickness of the TGO that remains attached, $h_{\min}$, can be specified as [8]:

$$h_{\min} = E_0 \Gamma^0 / \sigma_0^2 (1 - \upsilon) \tag{10}$$

Actual failure phenomena involve a critical TGO thickness, h_c, related to the minimum by:

$$h_c = \xi h_{\min} \tag{11}$$

(with $\xi > 1$). The range expected for $h_{\min}$ is bound by choices made for Γ^0 and σ_0. It is between 70 nm and 1 μm [8], *appreciably smaller than the TGO thickness sustained in practice* (between 3 and 10 μm). The discrepancy arises because there is no mechanism capable of transmitting all of the strain energy into the delamination. Accordingly, mechanisms need to be postulated that transmit some of this energy into a release rate capable of growing a separation to a size large enough to cause SSB and spalling [40]. Imperfections in the TGO exert a major influence on this process [34–38].

In the presence of imperfections, particularly undulations of the surface (see Fig. 7), local tensile stresses are created normal to the interface, large enough and over sufficient spatial extent to cause the formation of well-defined separations. At this stage, the energy release rate G associated with the separation increases to a peak (Fig. 19) [72] and then decreases as it extends, causing it to be stable and self arresting. However, when the separation becomes large enough to satisfy buckling

requirements, opening of the crack occurs, substantially increasing G and resulting in a minimum (Fig. 19) [72]. *The minimum value represents a buckle propagation criticality*. It translates into a critical imperfection wavelength, L_c needed for SSB and ensuing failure [72]:

$$L_c \approx 5h_{min}\sqrt{E/\sigma_0} \tag{12}$$

The above results for h_c and L_c should be interpreted as follows. The combined inequalities, $h < h_c$ and $L < L_c$ represent a fail safe condition. That is, it can be assured that the TGO remains attached, even though separations may be present. However, when one inequality is not satisfied, there is a finite probability that the TGO will fail by SSB.

3. TBC failure mechanisms

Edge and buckle-driven delamination compete as mechanisms of final TBC failure. The failure map (Fig. 20) [40] represents the basic elements of this competition. In the upper right, the TBC has relatively high in-plane stiffness and limited strain tolerance, causing the residual stress in the TBC to be large and resulting in a high strain energy density. This energy density enhances that from the TGO and provides a strong driving force for edge delamination which, in turn, is resisted by the mode II toughness along the most brittle pathway (among the TBC, TGO or interface). In the lower left of the map, the low in-plane modulus of the TBC does not resist small scale buckling of the TGO, whereupon the system would fail under conditions similar to those for the TGO, absent the TBC. At the intermediate levels of in-plane modulus used in practice, SSB and edge delamination are suppressed, and the system resides in a "fail-safe" domain until degradation phenomena operating on either of these mechanisms envelop this domain. This failure map provides a conceptual framework for addressing durability. TBC systems operate within the following two principal domains:

i. When the TBC experiences thermo-mechanical loadings typical of those applicable to "power generation", with long high temperature exposures and minimal thermal cycling, the cracking patterns are dominated by a combination of the TGO growth stresses and those from the thermal expansion misfit.

ii. Loadings representative of aero-engines comprising extensive thermal cycling are more likely to be affected by strictly cyclic phenomena such as ratcheting, wherein cyclic displacements of the TGO into the bond coat set-up the delamination strains in the TBC.

3.1. TBC properties

3.1.1. Stress/strain relationships

Because of the porosity used to achieve strain tolerance, the thermo-physical properties of the TBC are non-linear and complex. They have yet to be adequately

characterized. Stress/strain curves measured on APS material [17] illustrate the predominant features (Fig. 21). The strains are anelastic/hysteretic, characteristic of those found for porous brittle solids and ceramic composites [73]. A generalized representation could be developed on the experience with these analogous materials, but has not yet been established. One useful approach is to express the tangent modulus E_T as a function of the in-plane pre-stress σ_0 [74] (Fig. 22). This representation leads to a "unified" relationship $E_T(\sigma_0)$ that can be used in design or life prediction. As yet, this relationship does not adequately account for either the hysteresis or the permanent strains.

While the use of a single-valued modulus for analyzing the performance of TBCs is clearly an oversimplification, without a fully-developed alternative, presently some judgement needs to be made about the appropriate value when a modulus is needed

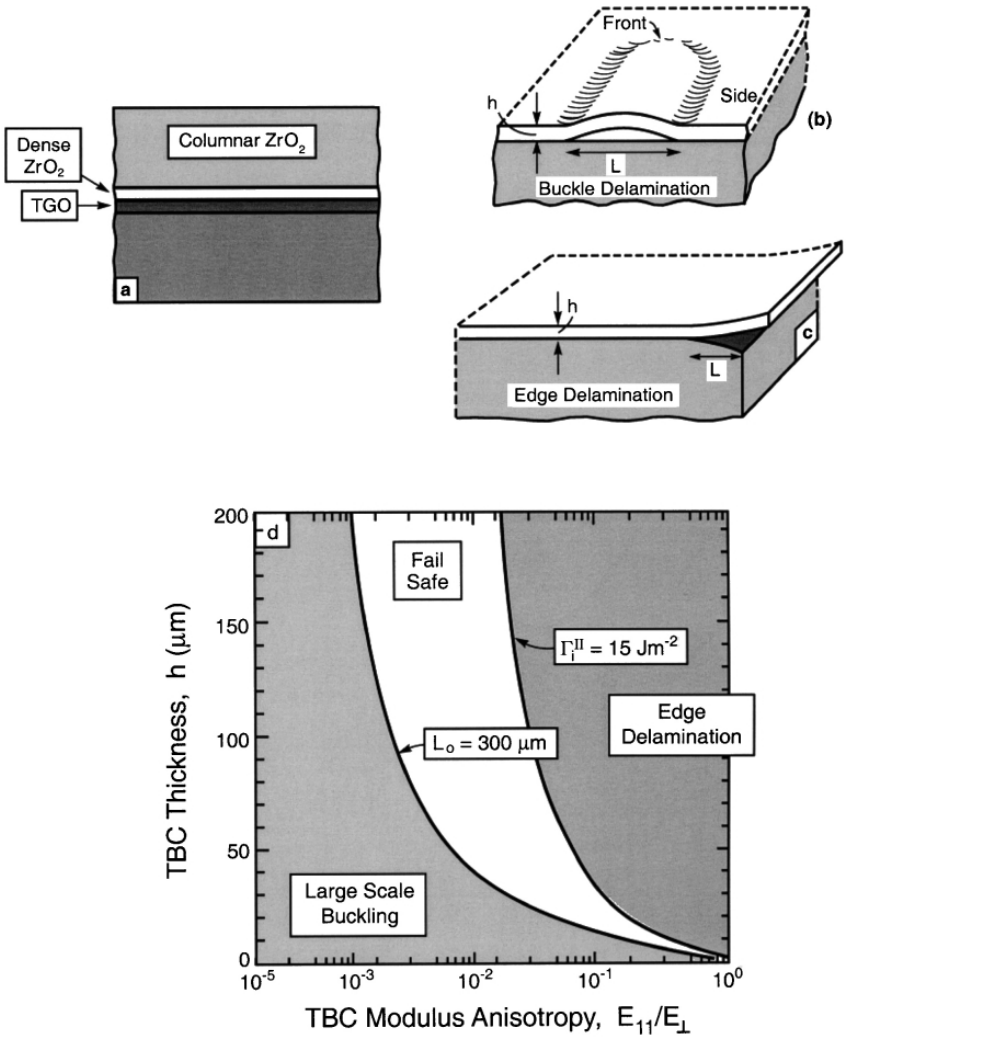

Fig. 20. TBC durability map indicating the domains for large scale buckling and edge delamination [40]. The intervening domain represents a "fail safe" condition. Over time and cycling this domain shrinks and is encompassed by one of the failure mechanisms.

as a parameter in durability models. *A substantial new study is needed to introduce anelastic phenomena in a manner that can be used effectively in a numerical model.*

3.1.2. Fracture resistance

The toughness of the TBC is anisotropic [17,75–78]. It is dependent on the deposition approach and strongly affected by the mode mixity, as well as being a function of crack length (because of short-crack and *R*-curve phenomena). It is also ill-defined, especially in the large crack limit, unless a full non-linear approach is used (such as either the *J*-integral or a large scale bridging algorithm). Given these complexities, plus the difficulty in testing actual coatings, the overall toughness domain is minimally encompassed. A framework for addressing the seemingly disparate measurements is sketched on Fig. 23a, with reference to cracks on delamination planes nominally parallel to the substrate. For short cracks (length in the range, $a \leqslant 100$ μm), the mode I toughness can be quite low. (Subject to the above proviso about the limitations of linear elastic fracture mechanics) the few measurements that have been made (all on APS materials) suggest toughness in the range: $0.1 \leqslant K_{\mathrm{Ic}}^{\mathrm{tbc}} \leqslant 1\ \mathrm{MPa}\sqrt{\mathrm{m}}$

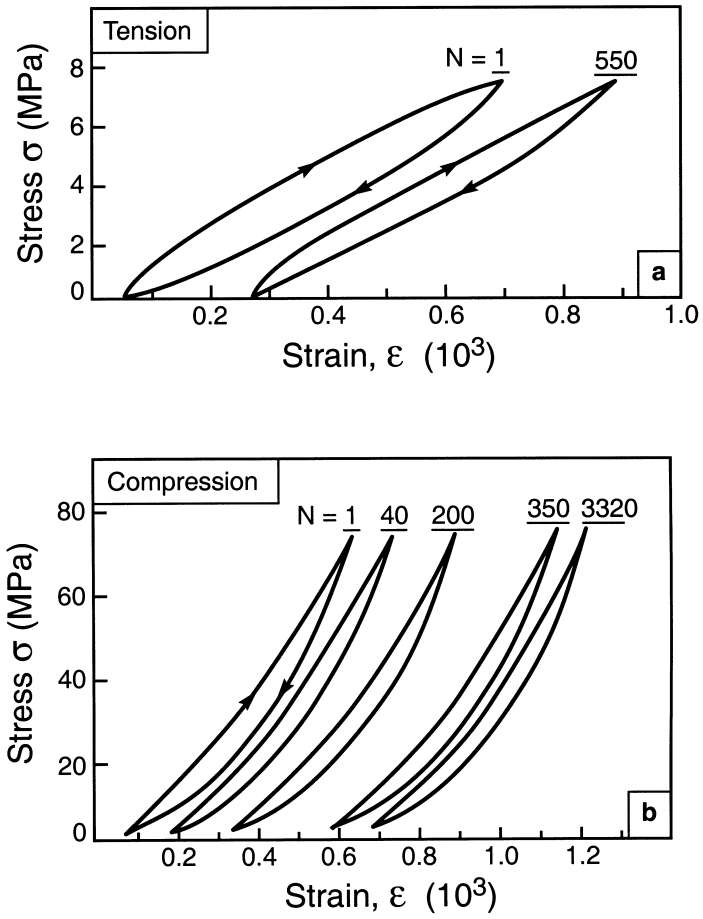

Fig. 21. The non-linear stress/strain characteristics of a TBC. These are derived from the results presented in reference [17].

[17,44]. Such values represent the fracture resistance of splat interfaces. Similar values might be expected for EB-PVD coatings because of the low toughness of t′-ZrO_2.

As the cracks extend, resistance curve behavior arises, particularly in mode II because of the strong influence of crack face friction [79]. For long cracks ($a \geqslant 1$ mm) in mode II, the toughness reaches: $K_{IIc}^{tbc} \approx 3$–$5\,MPa\sqrt{m}$ [75–78]. Friction arises in the presence of non-planarities along the crack plane. There are two interacting effects on the toughness. The undulations cause the TBC above the crack to displace upward as it propagates, resulting in elastic strains and associated strain energies that resist crack growth. Additionally, frictional dissipation occurs at the contacting asperities. The coupled effects are plotted in Fig. 23b. Beyond these influences, crack extension is resisted by intact ligaments and/or by microcracking.

3.2. The role of imperfections

Failures are associated with imperfections located at (or near) the TGO layer, especially those that induce tensile σ_{zz} stresses normal to the TBC surface, in the vicinity of the TGO. These stresses, in turn, initiate cracks along trajectories having lowest toughness [19,37]. Often, the important imperfections enlarge with exposure/cycling [37], thereby increasing the nucleation probability while also extending previously formed cracks.

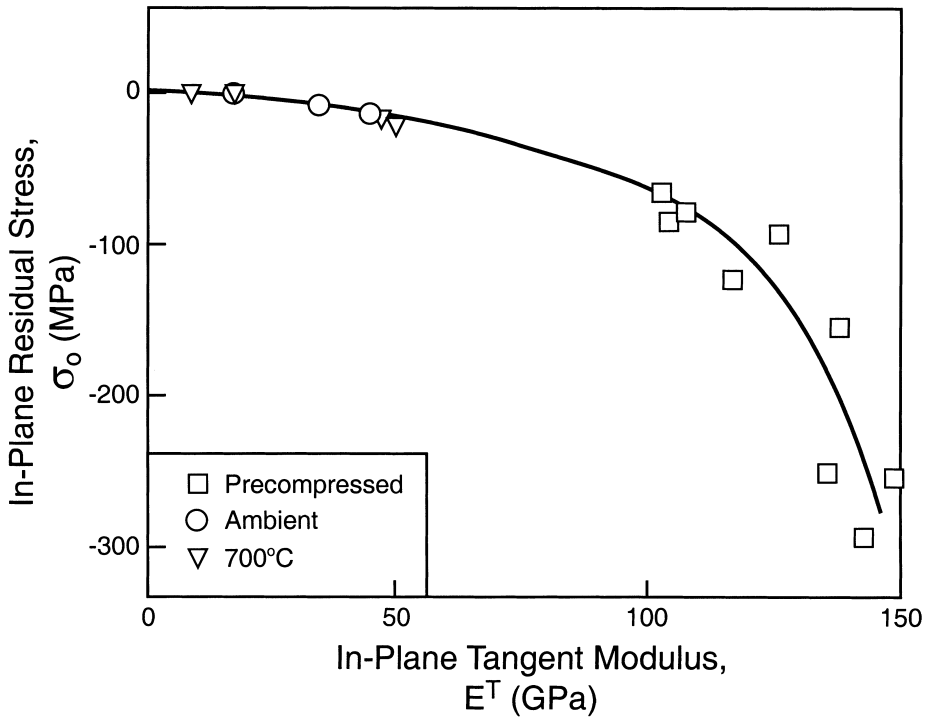

Fig. 22. Cross-plot of the (small strain) tangent modulus as a function of the pre-stress for TBCs [74].

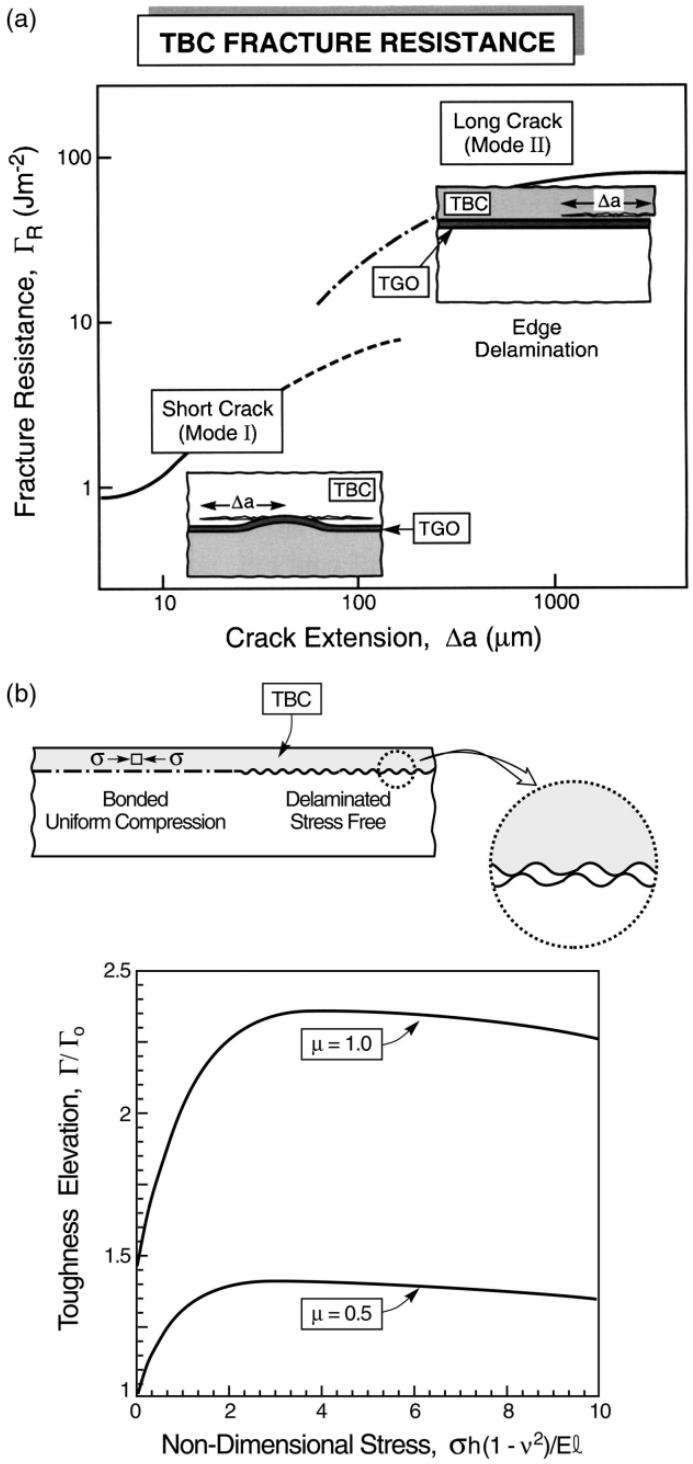

Fig. 23. (a) Schematic of the fracture toughness of TBCs. Short cracks in mode I have toughness in the range, $K_{IR} \approx 0.1 - 1\,\text{MPa}\sqrt{\text{m}}$, with a resistance that increases as the crack extends, because of the material non-linearity. Long cracks in mode II have toughness: $K_{IIR} \approx 5\,\text{MPa}\sqrt{\text{m}}$. This toughness includes contributions from crack face friction. (b) The effects of undulations and friction on the delamination toughness of compressed coatings [79].

There are three key technical challenges toward determining the role of imperfections in failure: (i) ascertaining the mechanisms that enlarge the imperfections, (ii) evaluating the energy release rates at cracks emanating from them and (iii) ascertaining their size and spatial distributions.

Undulations are pervasive imperfections. They emerge as failure origins for two reasons. Under predominantly isothermal conditions, the misfit from TGO growth results in appreciable stresses in the TBC around the imperfections [41]. With extensive thermal cycling, initial undulations in the TGO increase their amplitude upon thermal cycling [37]. This occurs by "ratcheting" of the TGO into the bond coat (Figs. 8 and 24). As the amplitude, A, increases, σ_{zz} stresses develop in the superposed TBC. These stresses ultimately lead to separations large enough to satisfy LSB and, thereafter, TBC failure. There are two main elements:

i. When the shear stresses induced in the bond coat upon cooling sufficiently exceed its yield strength, it flows plastically from the base to the peak of the prominent undulations, allowing the amplitude to increase. This process may continue for a few cycles, but then stabilizes [37].

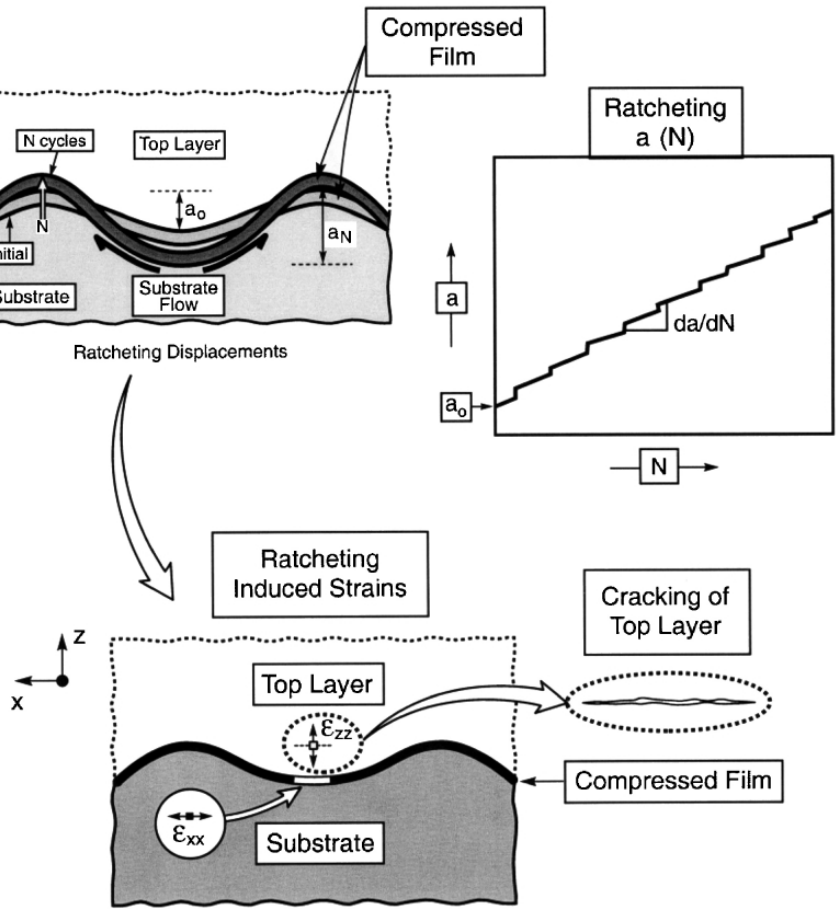

Fig. 24. Schematic indicating the ratcheting phenomenon and the steady-state growth in undulation amplitude that can arise when a critical size has been exceeded [37].

ii. For the undulation to continue to enlarge, the growth strain at high temperature "feeds" the process. In such cases, steady-state ratcheting becomes possible, whereby A increases with each thermal cycle [37] (Fig. 24). These cyclic phenomena are characterized through a modified Bree diagram (see Fig. 14), which shows that, for all intents and purposes, ratcheting initiates at undulations exceeding a critical aspect ratio, A_c/L, dependent on the bond coat yield strength and the TGO growth strain.

TGO thickness imperfections have been suggested as alternative failure nucleation sites [42]. They appear to become important when undulations are suppressed. They form and enlarge in regions where the O^{2-} diffusivity through the TGO is exceptionally large. This happens at locations where the TGO contains oxides other than α-Al_2O_3 having intrinsically lower resistance to O^{2-} diffusion. Examples comprise TGOs that entrain *Y* from the bond coat to form yttrium aluminates and become locally thick (see Figs. 7b and 9) [42]. Above a critical size, the tensile stresses around these imperfections are predicted to nucleate interfacial separations [72].

3.3. Stresses, cracking and failure

Imperfections are important because of the tensile stresses that develop around them as the TGO grows and the system thermally cycles. The principal focus is on the σ_{zz} stresses, because these are the stresses governing crack growth parallel to the interface, near the TGO. Moreover, σ_{zz} must increase systematically as the TGO thickens to account for its documented influence on TBC failure. In scenarios subject to minimal thermal cycling, σ_{zz} stresses in the TBC are dominated by TGO growth [41], augmented by expansion misfit (Appendix B). Extensive thermal cycling introduces other stresses by ratcheting of the TGO into the bond coat (Appendix E) [37]. The following analyses demonstrate how cracks nucleate and grow from imperfections and render expressions for the crack size. However, for failure to occur, many of these cracks must first coalesce. The practicalities of this are complicated by the residually-compressed remnant ligaments between cracks that experience a vanishing energy release rate at convergence. Ultimately, the detachment of these ligaments governs the onset of large scale buckling (LSB) [40] and failure in accordance with Fig. 20.

Progress is made by adopting the simplifying assumption that adequate transverse loadings are always present (because of inertial motions or vibration), whereupon crack coalescence can be ascribed to a requirement that the crack diameter equal the spacing 2d between neighboring imperfections.

Minimal thermal cycling scenarios, being immune to high cycle phenomena such as ratcheting, have durability governed largely by the stresses that arise upon TGO thickening. Within such scenarios, excursions to ambient are important. The overall cracking scenario is depicted in Figs. 25 and 26 [41,44].

Upon TGO growth around imperfections, the change in volume cannot be fully accommodated by rigid body displacements. The ensuing dilatation induces tangential tension in the surrounding TBC, with consequences for radial cracking (Appendix C). These stresses are unaffected by TGO creep [41].

Upon cooling, the compression normal to the TGO interface diminishes, because of thermal expansion misfit [41,80]. In fact, should the bond coat creep sufficiently during TGO growth, this stress becomes tensile at ambient and motivates interfacial separation. Furthermore, when the TGO exceeds a characteristic thickness, the tangential tensions within the TBC (caused by growth) are enhanced by the expansion misfit (Appendix B) [41,80].

Coalescence of the interface separations with the radial cracks in the TBC, through the TGO, creates a connected crack (Fig. 25c). Such delaminations have stress intensities [Appendix C (C1)] that result in a crack radius, a, given by [41]:

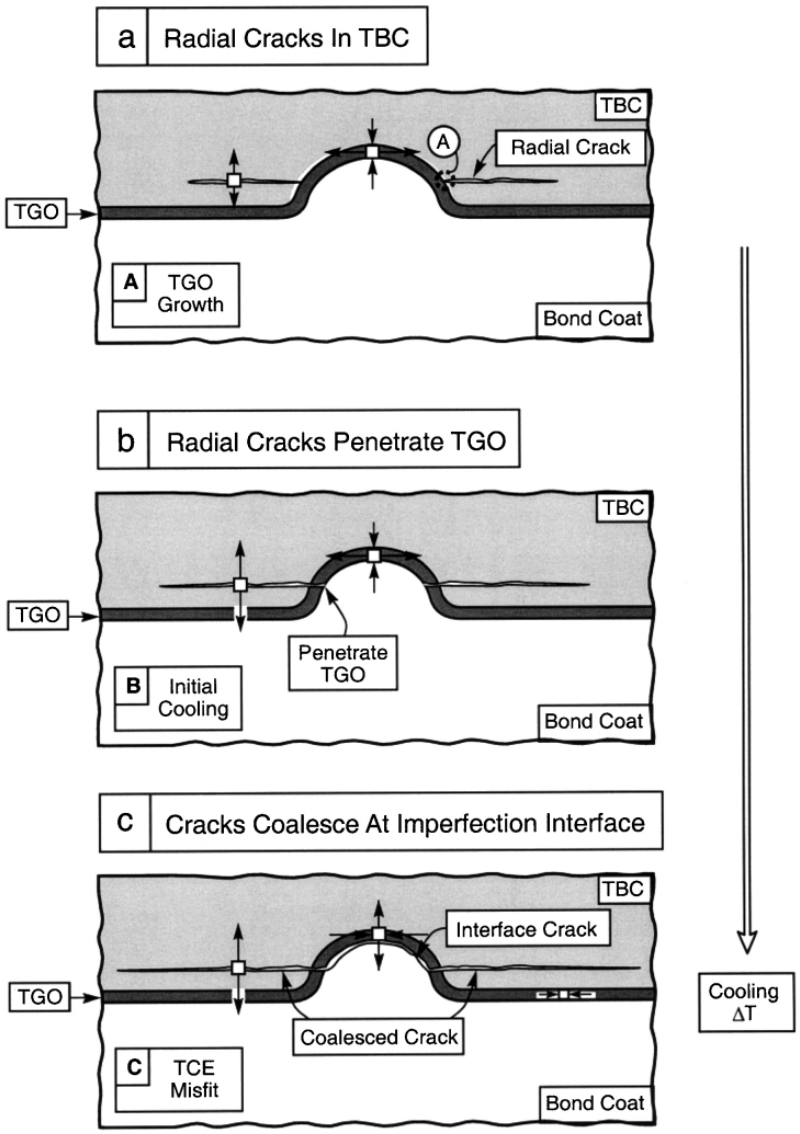

Fig. 25. Cracking sequence caused by growth misfit, followed by cooling to ambient. The radial crack in the TBC penetrates the TGO at its inner edge upon thermal cycling, because of the large stress intensity factor. Thereafter it coalesces along the interface [41,44].

$$a/R = \left[\frac{3\sigma^* \sqrt{R}}{2(1+\upsilon)\sqrt{\pi} K_{\mathrm{Ic}}^{\mathrm{tbc}}}\right] \tag{13}$$

where

$$\sigma^* = \frac{E(m-1)}{3(1-\nu)m}\left(\frac{h}{R}\right)$$

This result implies that the delaminations form preferentially at the larger imperfections. They are also larger for TBCs having low toughness. Note that, while the ultimate extent of these cracks is governed by growth strains, thermal expansion misfit (with cycling) is still an essential element. That is, only upon cooling are stresses induced that separate the interface and cause the cracking of the TGO: events that result in the continuous crack configuration represented by Fig. 25c.

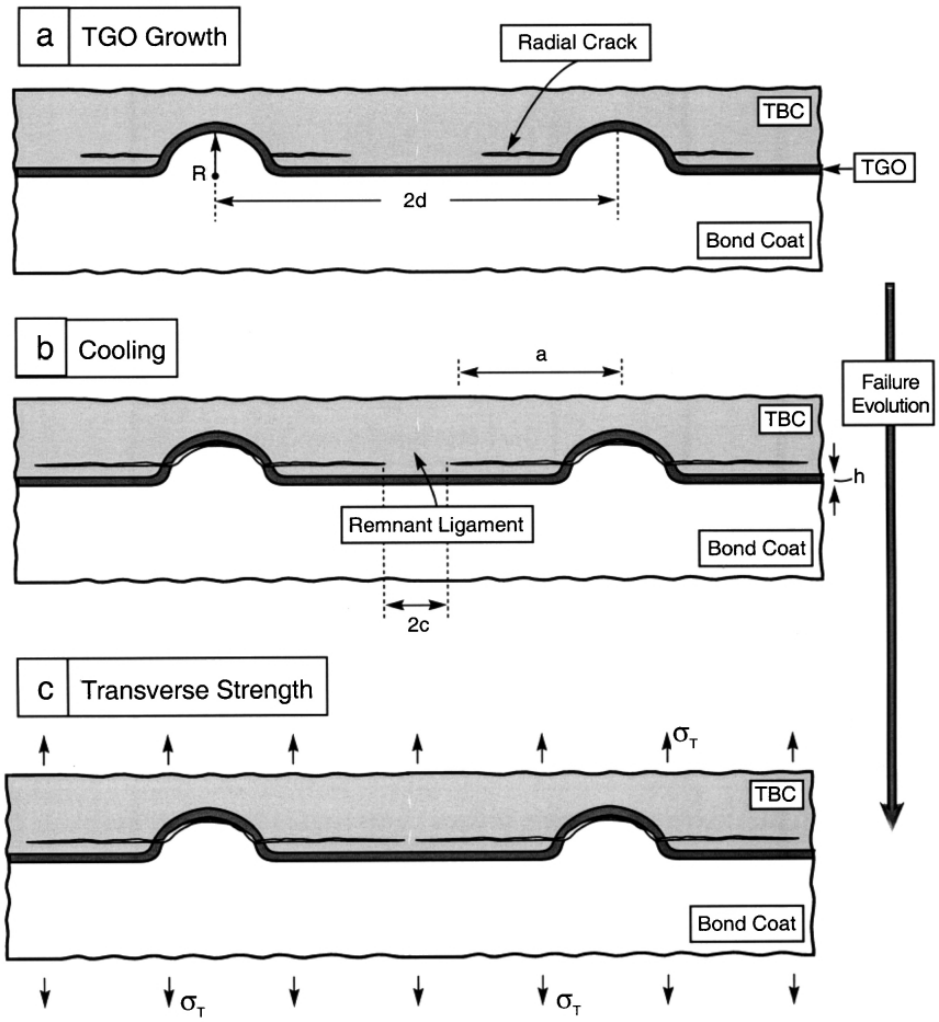

Fig. 26. Schematic of the coalescence of cracks emanating from neighboring imperfections.

Equating the crack diameter in (4) to the spacing between imperfections (Fig. 26) yields a critical TGO thickness, h_c, given by [41]:

$$h_c = \frac{2\sqrt{\pi}(1-\nu^2)md^{3/2}K_{Ic}^{tbc}}{(m-1)RE_{tbc}} \tag{14}$$

Note that the imperfections exert an important influence, through their diameter $2R$, and spacing $2d$. Moreover, since h_c depends on time-at-temperature [in accordance with (1)], then (14) can be re-expressed as a failure time:

$$t_f = h_c^2/2k_p \tag{15}$$

Recall that k_p is a strong function of temperature (Table 2) and that K_{Ic}^{tbc} is sensitive to the TBC microstructure. These later results [(14) and (15)] can be used as the basis for durability models.

Upon extensive thermal cycling combinations of thermal expansion misfit and growth strains in the presence of initial imperfections, cause the TGO to grow into the bond coat by a ratcheting mechanism [37,82] (Appendix E). This happens at interface imperfections that exceed a critical amplitude and penetrate preferentially into bond coat grains having a soft orientation. The consequence is that tensile stresses are induced in the superposed TBC. These are sufficiently large that cracks are readily initiated, causing the response to be governed by the ratcheting displacement, Δ_R. While a full model that relates Δ_R to the misfit strains and the material properties has yet to be devised, some insight can be gained from scaling arguments. If the ratcheting rate, $d\Delta_R/dN$, is specified, the cycles-to-failure has the dependence [Appendix E, (E2)]:

$$N_f \approx 2\sqrt{\pi}(1-\nu^2)d^{3/2}K_{Ic}^{tbc}/E(d\Delta_R/dN)L \tag{16}$$

where $2L$ is the imperfection wavelength. In turn, the ratcheting rate is expected to be roughly proportional to the growth strain, m, and dependent on the bond coat yield strength relative to the thermal expansion misfit stress, as well as the initial imperfection amplitude relative to the critical size.

4. Closure

Aspects of the performance and durability of thermal barrier systems have been clarified through studies of the material state at various fractions of life. All of this effort has been on commercially produced materials with "standard" compositions, microstructures and imperfection "states". This has lead to some understanding of the mechanisms that govern durability. In turn, the mechanistic understanding has been used to develop models of TBC life that contain the controlling material and topological parameters. That is, they reveal the interplay between the key material properties and imperfection topologies, expressed in terms of scaling laws.

As the measurements and observations have become more extensive, seemingly disparate findings all converge into patterns that suggest four simple principles:

i. Compressions in the TGO around interface imperfections, caused by growth and thermal expansion misfit, provide the underlying motivation.

ii. These misfits induce energy release rates at cracks emanating from the major imperfections large enough to exceed the delamination toughness of the TBC.

iii. The coalescence of these cracks results in a separation large enough to satisfy large scale buckling and spalling.

iv. In high cycle scenarios, the combined misfit (from growth and thermal contraction) enlarges the imperfections by a ratcheting mechanism, amplifying the energy release rates and accelerating failure.

The two major deficiencies in the present status concern: (a) the paucity of model validation and (b) as yet, a lack of effort on performance improvements guided by the implications of the models. Both require that materials and imperfections be systematically varied within a parameter space suggested by the models. In turn, this needs a capability for depositing the bond coat and the TBC with control of the surface/interface topology, microstructure and micro-chemistry. Until recently, such approaches and capabilities have not been within the grasp of the research community. Efforts of this type should provide an informed basis for designing superior TBC systems.

Appendix A. Small scale buckling

A1. Buckling maps

The buckling and buckle propagation stages of failure can be succinctly represented by a buckling map. The map is developed upon defining three non-dimensional indices, with three associated domains (Fig. A1). The indices comprise [56,70]:

i. An adhesion index:

$$\Sigma = \sigma_o \sqrt{\frac{(1-\nu)h}{E_0 \Gamma_i^0}} \tag{A1}$$

ii. A buckling index:

$$\Pi = (1-\nu^2)(\sigma_0/E_0)(b/h)^2 \tag{A2}$$

iii. The mode mixity index, λ [Eq. (9)].

The map assumes the pre-existence of an interface separation, size b_0. Modifications to the map that address nucleation are established later. The three domains associated with the buckling map (Fig. A1) are as follows.

- *Domain I.* Stable separations exist because the buckling condition is not satisfied.

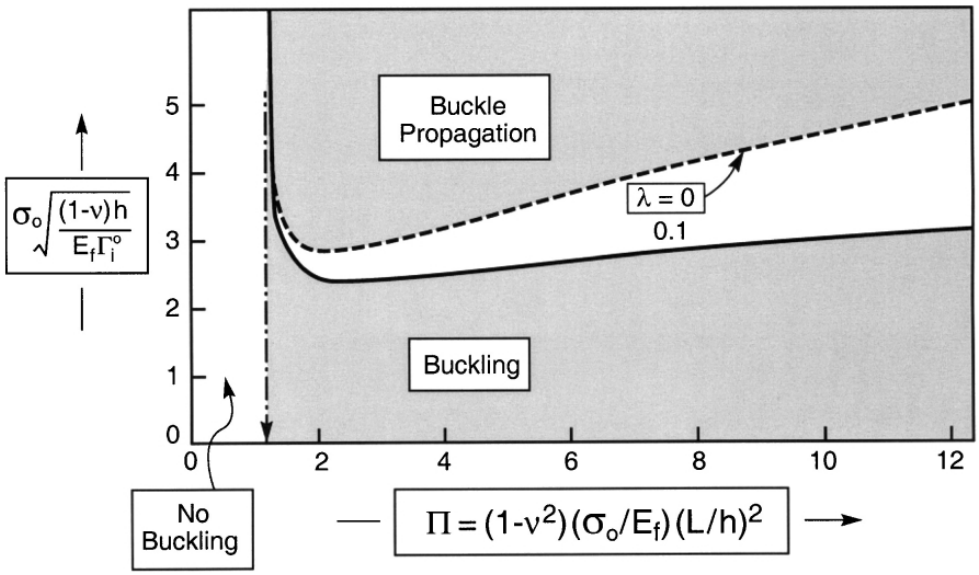

Fig. A1. (Small scale) buckling map relevant to the TGO, showing the buckle propagation domain (top right).

- *Domain II*. The buckling condition is satisfied, but the energy release rate is too low to cause propagation. The transition between I/II occurs at a critical buckling index, $\Pi_c \approx 1.22$. Accordingly, buckling happens at a TGO thickness, h_b, given by:

$$h_b = b_0[(1-\nu^2)\sigma_0/\Pi_c E_0]^{1/2} \tag{A3}$$

  For typical stresses ($\sigma_0 \approx 3$ GPa, Table 1), the critical buckling radius has magnitude: $b_0/h_b \approx 11$.

- *Domain III*. The energy release rate exceeds the interface fracture energy. The transition occurs when the adhesion index is in the range $\Sigma \approx 2-3$, dependent on Π and λ. Buckles propagate when Σ and Π reside along the region II/III transition line, at the relevant λ. At fixed λ, the buckle enlarges stably: that is, Π increases as Σ increases. This happens when either σ_0 or h increase and/or Γ_i^0 decreases upon segregation, fatigue, etc. The stability is enabled by the mode mixity effect on interface toughness, manifest in λ.

Superposing trajectories onto the map specifies conditions wherein the TGO buckles, as well as when the buckle abruptly propagates and arrests. One illustration is given in Fig. A2. It represents a simple thermo-mechanical loading. Following TGO growth at high temperature, to thickness h_0, cooling to ambient establishes a residual compression, σ_0. Then, present an interface separation, radius b_0, induced around a TGO defect, (A2) and (A3) give initial values of the coordinates Σ and Π,

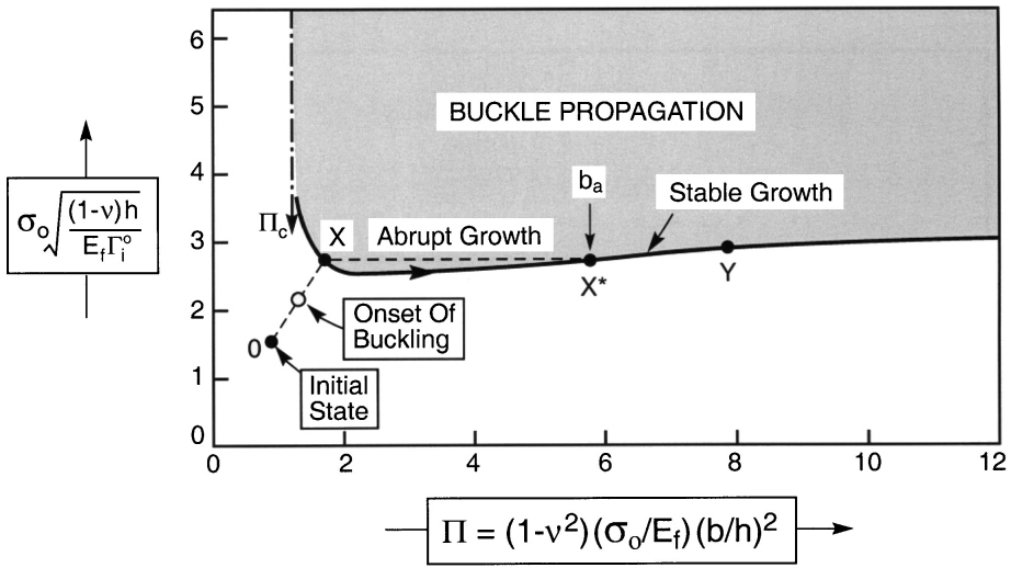

Fig. A2. Prototypical trajectory superposed on the buckling map due to cooling showing the onset of buckling, the initiation of buckle growth (at X) and buckle arrest (at X^*), followed by stable growth along X^*Y as the strain is further increased.

located at position O on Fig. A2. In this example, segregation levels are fixed such that Γ^0 is constant. Subsequent mechanical loading (say, because of bending) causes the compression in the TGO to increase. This stress elevation increases both Σ and Π proportionally [see (A2) and (A3)], resulting in a diagonal trajectory on the buckling map. When the stress elevation causes the trajectory to intersect the buckling transition at O', the TGO buckles, but remains stable if there are no further changes in stress. Additional stress elevation causes the trajectory to reach X. Now, at constant Σ (fixed stress) there will be an abrupt increase in buckle size, as Π jumps over to the region II/III transition, at X^*. Here the buckle arrests at radius, b_a, much enlarged relative to b_0. However, it remains stable at this size until either the stress increases again or Γ_i^0 decreases. Subsequent elevations in stress would cause the buckle to expand stably along X^*Y until either cracking or spalling conditions are satisfied. Because of the shallow trajectory of the region II/III transition, quite small changes in stress enable the final phase to proceed to completion.

A2. Role of imperfections

The influence of imperfections is illustrated by a trajectory superposed on a revised buckling map [70,72] (Fig. A3). Present an initial interface defect, as Σ increases, a critical level is reached (position A) at which a separation pops-in to a stable size, b_i (position B). When Σ further increases, the separation expands stably up to the maximum (point C). Here the separation buckles and abruptly expands to b_0 (point D). At this stage, the buckle may either spall or arrest, depending on conditions relative to the spall criterion. If it arrests, it can again expand stably as Σ increases, until spalling conditions are reached.

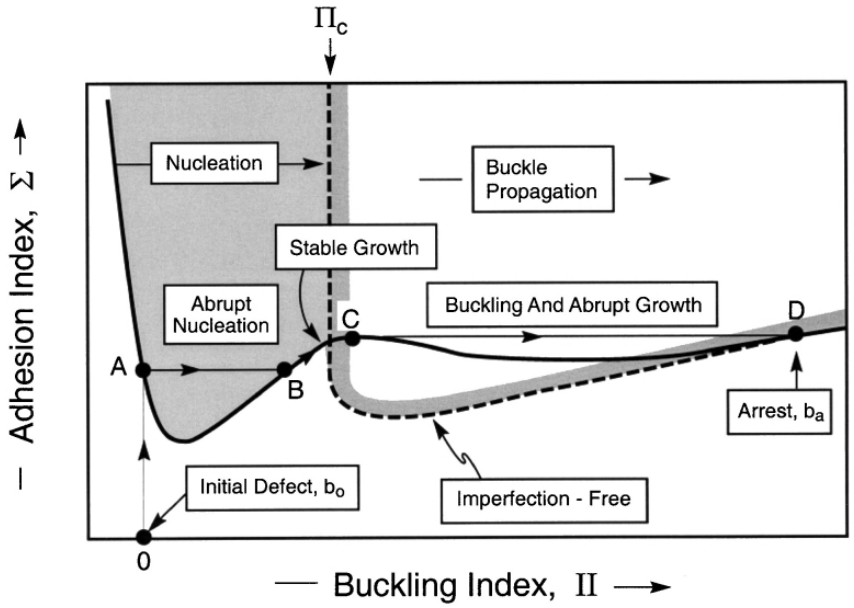

Fig. A3. The influence of imperfections in the TGO on the initiation of the buckling process [72].

Appendix B. Stresses

Preliminary results for the stresses in the TBC, TGO and bond coat are estimated by considering imperfections having spherical symmetry [41,79,80] (Fig. B1). While there are obvious limitations of this geometry, numerical results for more relevant configurations have revealed [41] that the stresses near the apex of the undulation are reasonably well ordered in sign and magnitude.

B1. Thermal expansion misfit

The elastic solutions for thermal expansion misfit in a tri-material system with spherical symmetry have been derived using the "Eshelby" protocol [41,80] (see Fig. 17). The case of interest is one wherein the TGO has the lowest thermal expansion coefficient, α_0, the substrate the largest, α_s, and the TBC the intermediate, α_{tbc}. The stresses in the substrate/bond coat are:

$$\sigma_{rr} = \sigma_{\theta\theta} = \Lambda(\alpha_{tbc} - \alpha_s) \tag{B1a}$$

where ΔT is the cooling range (negative in sign) and $\Lambda = 4\kappa\mu\Delta T[\kappa + 4\mu/3]$, $\mu = E[2(1+\nu)]$, $\kappa = E/[3(1-2\nu)]$. Accordingly, the bond coat is in a state of hydrostatic tension, independent of α_0. The stresses in the TGO are:

$$\sigma_{rr} = \Lambda\{\alpha_{tbc} - \alpha_0 - (\alpha_s - \alpha_0)[(R-h)/r]^3\}$$
$$\sigma_{\theta\theta} = \Lambda\{\alpha_{tbc} - \alpha_0 + \frac{1}{2}(\alpha_s - \alpha_0)[(R-h)/r]^3\} \tag{B1b}$$

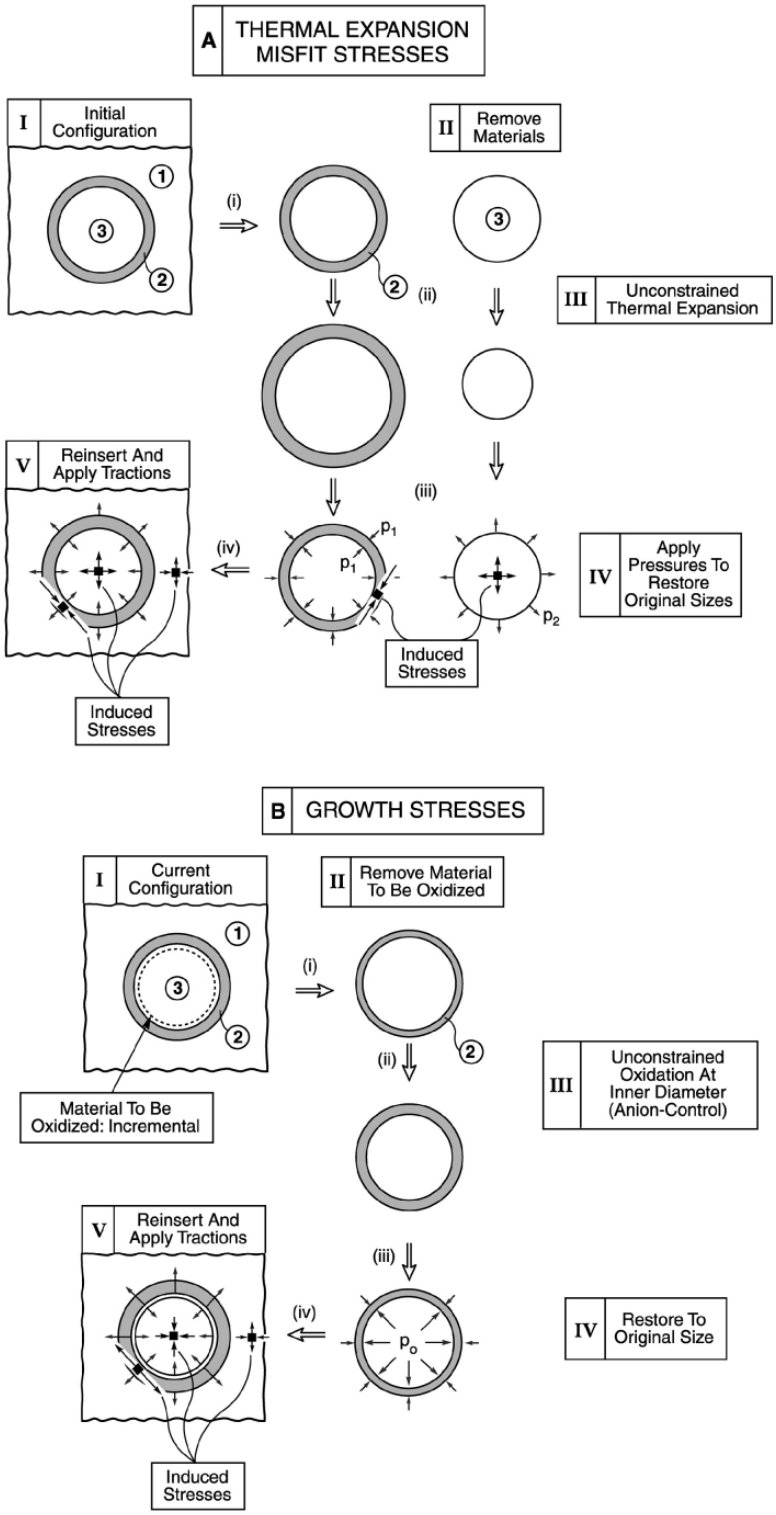

Fig. B1. The stresses that develop around spherical imperfections illustrated by using the ''Eshelby'' procedure. (A) Thermal expansion misfit, (B) anion-controlled TGO growth. The three regions are as follows: (1) the TBC, (2) the TGO and (3) the bond coat/substrate combinations.

where $2R$ is the diameter of the imperfection. Note that since, $\alpha_s > \alpha_{tbc} > \alpha_0$, the TGO is always in hoop compression and the interface between the substrate and the TGO is in radial tension. The stresses in the TBC are:

$$\sigma_{rr} = -2\sigma_{\theta\theta} = -\Lambda\{\alpha_0 - \alpha_{tbc} + (\alpha_s - \alpha_0)(1 - h/R)^3\}(R/r)^3 \tag{B1c}$$

In this case, the sign of the stresses depend on the relative TGO thickness, h/R. When the TGO is thin, the second term in the parentheses dominates and the TBC is in radial compression. Above a critical TGO thickness, radial tension develops. This thickness, h_*, is given by:

$$h_*/R = 1 - [(\alpha_{tbc} - \alpha_0)/(\alpha_s - \alpha_0)]^{1/3} \tag{B2}$$

B2. Oxide growth

The stresses induced by TGO growth differ because the misfit strain occurs predominately at one of the interfaces [41]. For anion-control, governed by inward diffusion of oxygen, the misfit occurs at the interface where the bond coat is consumed. For cation-control, the new oxide forms at the TGO/TBC interface, through the outward diffusion of Al (as well as Ni, Cr, etc.). To determine the stresses, the ratio of new TGO volume to consumed bond coat volume is taken to be m. For anion-control, the stresses within the bond coat are [41],

$$\sigma_{rr} = \sigma_{\theta\theta} = -\frac{2E(m-1)}{3(1-v)m}\left(\frac{h}{R}\right) \tag{B3a}$$

In the TBC, $r \geqslant R$,

$$\sigma_{rr} = -2\sigma_{\theta\theta} = -\frac{2E(m-1)}{3(1-v)m}\left(\frac{h}{R}\right)\left(\frac{R}{r}\right)^3 \tag{B3b}$$

and within the TGO, $R - h \leqslant r \leqslant R$,

$$\sigma_{rr} = -\frac{2E(m-1)}{3(1-v)m}\frac{h}{R}$$
$$\sigma_{\theta\theta} = \sigma^i_{\theta\theta} + \frac{E(m-1)}{3(1-v)m}\left[\frac{r}{R} - \left(1 - \frac{h}{R}\right)\right] \tag{B3c}$$

These results have the following features. The TBC is in radial compression and hoop tension. In the TGO, the radial stress is compressive, while the hoop stress is $\sigma^i_{\theta\theta}$ at the growth interface and $\sigma^i_{\theta\theta} + E(m-1)h/[3(1-v)mR]$ at the TGO/TBC interface.

For cation-control, the stresses in the bond coat and in the TBC as well as the radial stress in the TGO remain the same. The only difference is in the hoop stress within the TGO ($R - h < r < R$):

$$\sigma_{\theta\theta} = \sigma^{i}_{\theta\theta} - \frac{9E}{4(1-\nu)}\left(1 - \frac{r}{R}\right) \tag{B4}$$

Appendix C. Stress intensity factors

Radial cracks, radius, a, that form in the TBC as a consequence of the growth misfit have stress intensity factors, K, at the inner and outer crack edges given by [41,81]:

$$\frac{K}{\sigma^*\sqrt{R}} = \sqrt{\frac{\pi}{2}\left(\frac{a}{R} - 1\right)}\left(\frac{R}{a}\right)^{2.4} \text{(outer crack edge)} \tag{C1a}$$

$$\frac{K}{\sigma^*\sqrt{R}} = \sqrt{\frac{\pi}{2}\left(\frac{a}{R} - 1\right)}\left(\frac{R}{a}\right)^{0.55} \text{(inner crack edge)} \tag{C1b}$$

where

$$\sigma^* = \frac{E(m-1)}{3(1-\nu)m}\left(\frac{h}{R}\right)$$

These results are plotted in Fig. C1. Note the very large stress intensity at the inner front. It is this intensity that motivates the crack to penetrate the TGO and coalesce along the interface as the system thermally cycles. When this happens, the resulting stress intensity factor for the larger a/R of interest is [41]:

$$\frac{K}{\sigma^*\sqrt{R}} = \frac{3}{2(1+\nu)\sqrt{\pi}}\left(\frac{R}{a}\right)^{3/2} \tag{C2}$$

This is the result used in the text to predict cracking and failure.

Appendix D. TGO creep/growth dynamics

When a small fraction, β, of the newly formed TGO is manifest as a spatially uniform addition of matter to the vertical grain boundaries in the TGO (see Fig. 16), the in-plane displacement-rate $\dot{\delta}$ on a planar section is:

$$\dot{\delta} = \beta\dot{h}g/h. \tag{D1}$$

such that the in-plane extension-rate is:

$$\dot{\varepsilon}^{g}_{xx} \equiv \dot{\delta}/g = \beta\dot{h}/h \tag{D2}$$

With (1), the strain-rate becomes:

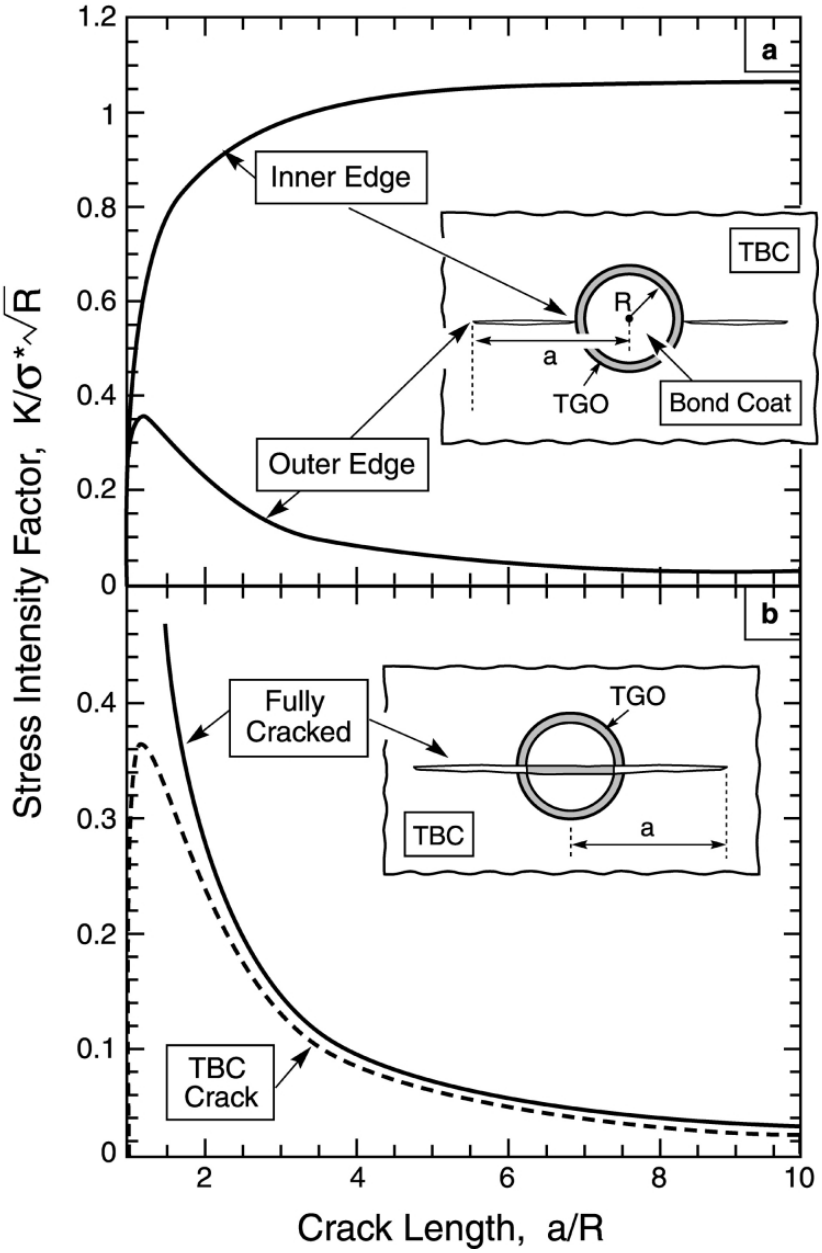

Fig. C1. Stress intensity factors calculated for the crack configurations depicted in the insets.

$$\dot{\varepsilon}^{g}_{xx} = 2\beta k_p / h^2 \tag{D3}$$

Upon equating the strain-rate in (D3) with that in (8), for growth/creep equilibrium (zero net strain-rate), the growth stress for an equi-axed TGO becomes:

$$\frac{\sigma_0}{\mu_0} = -\left(\frac{g}{h}\right)\sqrt{2\beta\,\Sigma}_* \tag{D4}$$

where

$$\Sigma_* = k_p/\dot{\varepsilon}_* \Omega_{Al_2O_3}^{2/3}$$

$$\dot{\varepsilon}_* = 100\left[\frac{D_b \delta_b \mu}{kT}\right]$$

Temperature and compositional effects are manifest in the non-dimensional kinetic ratio: Σ_* (Table 2). The tendency for σ_0 to decrease with increase in TGO thickness (D4) would be mediated by increases in grain size and would become invariant whenever $h \approx g$.

Appendix E. Ratcheting

Thin films on ductile substrates when residually compressed by a misfit stress are susceptible to various out-of-plane displacement instabilities. These displacements occur by distorting the substrate. Pre-existing undulations initiate the instability. Under some circumstances, the undulations increase in amplitude, with thermal cycling, by "ratcheting" [37]. When this happens, the increase in undulation amplitude induces out-of-plane tensile strains in the TBC. These strains cause cracks parallel to the interface which, in turn, induce failures.

Steady-state ratcheting arises when the growth and thermal expansion misfit combine in such a manner that the growth biases the strain by diminishing reverse yielding of the bond coat. That is, absent growth, cyclic yielding occurs as the TGO displaces around an average location established after the first few cycles: whereas, a growth strain causes the TGO to grow into the bond coat with each thermal cycle. The observations [82] and analyses [37] of this phenomenon suggest that two factors dictate the sites at which the ratcheting occurs. (i) Initial interface imperfections above a critical amplitude are needed to induce stresses in excess of the cyclic yield strength of the bond coat. (ii) Because of the extreme yield strength anisotropy of β-NiAl, some grains adjacent to the TGO exhibit a soft orientation in the sense that they are highly susceptible to plastic straining normal to the interface. This combination of orientation softness with interfacial imperfections dictates the ratcheting locations and, thereby, governs the TBC durability.

When undulations in the TGO ratchet in a steady-state manner with rate, $d\Delta_R/dN$, the stress intensity factor at a crack, radius a, in the TBC just above the interface with the TGO can be estimated as:

$$K \approx \frac{E(d\Delta_R/dN)}{2\sqrt{\pi}(1-\nu^2)\sqrt{L}}\left(\frac{L}{a}\right)^{3/2} N \tag{E1}$$

where $2L$ is the wavelength and N the number of thermal cycles. This formula is approximate since the elastic modulus mismatch is not taken into account.

Accordingly, with $2d$ as the spacing between neighboring undulations, the cycles to failure would be:

$$N_f \approx 2\sqrt{\pi}(1-\nu^2)d^{3/2}K_{Ic}^{tbc}/E(d\Delta_R/dN)L \quad \text{(E2)}$$

It remains to relate the ratcheting rate to the misfit strains and the physical properties of the system.

References

[1] Miller RA. J Amer Ceram Soc 1984;67:517.
[2] Mariochocchi A, Bartz A, Wortman D. Thermal barrier coating workshop. NASA CP 3312, 1995. p. 79.
[3] Bose S, DeMasi-Marcin J. Thermal barrier coating workshop. NASA CP 3312, 1995. p. 63.
[4] DeMasi-Marcin JT, Gupta DK. Surf Coatings Tech 1994;68/69:1–9.
[5] Hillery R, editor. NRC report. Coatings for high temperature structural materials. National Academy Press, 1996.
[6] Strangman TE. Thin Solid Films 1985;127:93–105.
[7] Meier SM, Gupta DK. Trans ASME 1993;116:250–7.
[8] Wright PK, Evans AG. Current Opinion in Solid State and Materials Science 1999;4:255–65.
[9] Wright PK. Mat Sci Eng 1998;A245:191–200.
[10] Cruse TA, Stewart SE, Ortiz M. J Eng Gas Turbines Power 1988;110:610.
[11] Bennett A, Toriz F, Thakker A. Surface and Coating Technology 1987;32:227–36.
[12] Meier SM, Nissley DM, Sheffler KD. Thermal barrier coating life prediction model development — phase II. NASA CR-18911, July 1991.
[13] Kingery WD, Bowen HK, Uhlmann DR. Introduction to ceramics. New York: Wiley and Sons, 1976
[14] Rigney DV, Viguie R, Wortman DJ, Skelly WW. Proc of the Workshop on Thermal Barrier Coatings, NASA-CP-3312. NASA Lewis Research Center, 1995. p. 135–50.
[15] DeMasi-Marcin JT, Sheffler KD, Bose S. ASME Paper 89-GT-132. New York: American Society of Mechanical Engineering, 1989.
[16] Lee EY, Sisson RD. In: Berndt CC, Sampath S. editors. Proc 7th National Thermal Spray Conference, Boston, MA, 20–24 June. Materials Park, OH: ASM International, 1994. p. 55–9.
[17] Choi SR, Zhu D, Miller RA. Ceramic Engineering and Science 1998;19:293–301.
[18] Golightly FA, Stott FH, Wood GC. Oxid Metals 1976;10:163.
[19] Stiger MJ, Yanar NM, Topping MG, Pettit FS, Meier GH. Z. Metallk 1999;90:1069–78.
[20] Quadakkers WJ, Tyagi AK, Clemens D, Anton R, Singheiser L. In: Hampikian JM, Dahotre NB, editors. Elevated temperature coatings: science and technology, Warrendale (PA): TMS, 1999. p. 119.
[21] Lipkin DM, Clarke DR. Oxid Metals 1996;45:267–80.
[22] Tolpygo VK, Clarke DR. Oxid Metals 1998;49:187–211.
[23] Mennicke C, Schumann E, Ulrich C, Ruehle M. Mater Sci Forum 1997;389:251–4.
[24] Sergo V, Clarke DR. J Amer Ceram Soc 1998;81:3237–42.
[25] Tolpygo VK, Clarke DR. Acta Mater 1998;46:5153–66.
[26] Christensen RJ, Tolpygo VK, Clarke DR. Acta Mater 1997;45:1761–6.
[27] Sarioglu C, Blachere JR, Pettit FS, Meier GH. In: Newcomb SB, Little JA, editors. London: Microscopy of oxidation 3. The Institute of Materials, 1997. p. 41.
[28] Smeggil JG. Mater Sci Engr 1987;87:261–5.
[29] Smialek JL, Jayne DT, Schaeffer JC, Murphy WH. Thin Solid Films 1994;253:285–92.
[30] Meier GH, Pettit FS. Report on AFOSR Contract F49620-981-0221. Univ. of Pittsburgh, 1 September, 1999.
[31] Haynes JA, Zhang Y, Lee WY, Pint BA, Wright IG, Cooley KM. In: Hampiklan JM, Dahotre NB,

editors. Elevated temperature coatings: science and technology. Warrendale (PA): TMS; 1999. p. 185.
[32] Schaeffer J, Kim GM, Meier GH, Pettit FS. In: Lang E, editors. The role of active elements in the oxidation behavior of high temperature metals and alloys. Elsevier, 1989. p. 231.
[33] Nicholls JR. Materials Science Forum 1997;935:251–4.
[34] He MY, Evans AG, Hutchinson JW. Mat Sci Eng 1998;A245:168–81.
[35] Gong X-Y, Clarke DR. Oxidation of Metals 1998;50(3/4):355–76.
[36] Gell M, Vaidyanathan K, Barber B, Cheng J, Jordan E. Met Mater Trans 1999;30A:427.
[37] He MY, Evans AG, Hutchinson JW. Acta Mater 2000;48:2593–601.
[38] Evans AG, Hutchinson JW, He MY. Acta Mater 1999;47:1513–22.
[39] Suresh S. Fatigue of materials. 2nd ed. Cambridge University Press, 1998.
[40] Choi SR, Hutchinson JW, Evans AG. Mechanics Materials 1999;31:431–47.
[41] Evans AG, He MY, Hutchinson JW. Progress in Materials Science 2001;46:249–71.
[42] Mumm DR, Evans AG. Acta Mater 2000;48:1815–27.
[43] Evans AG, Hutchinson JW, Wei YG. Acta Mater 1999;47:4093–113.
[44] Rabiei A, Evans, AG. Acta Mater 2000;48:3963–76.
[45] Clarke DR, Sergo V, He MY. In: Hampikian JM, Dahotre NB, editors. Elevated temperature coatings: science and technology. Warrendale (PA): TMS, 1999. p. 67.
[46] Mennicke C, Mumm DR, Clarke DR. Z Metallk 1999;90:1079–85.
[47] Graham MJ, Eldridge JI, Mitchell DF, Hussey RJ. Mater Sci For 1989;43:207.
[48] Ruehle M. Unpublished research.
[49] Steiner A, Komarek KL. TMS-AIME 1964;230:786–90.
[50] Rhines FN, Wolf JS. Met Trans 1970;1:1701–10.
[51] Dove DB, Baldwin DH. Met Trans 1974;5:1637–41.
[52] Cannon RM, Rhodes WH, Heuer AH. J Am Ceram Soc 1980;63:46.
[53] Cho J, Harmer MP, Chan HM, Rickman JM, Thompson AM. J Am Ceram Soc 1997;80:1013.
[54] Fang J, Thompson AM, Harmer MP, Chan HM. J Am Ceram Soc 1997;80:2005.
[55] Schumann E, Sarioglu C, Blachere JR, Pettit FS, Meier GH. Oxid Metals 2000;53:259.
[56] Hutchinson JW, Suo Z. Adv Appl Mech 1992;29:62–191.
[57] Bree J. J Strain Analysis 1968;3:122–7.
[58] Jansson S, Leckie FA. J Mech Phys Solids 1992;40:593–612.
[59] Cannon RM, Hou PY. In: McNallan M et al., editors. High temperature corrosion and materials chemistry. Electrochemistry Society Proc 1998;98/99:594.
[60] Evans AG, Cannon RM. Mater Sci Forum 1989;43:243.
[61] Hindam H, Whittle DP. Oxid Met 1982;18:245.
[62] Brumm MW, Grabke HJ. Corros Sci 1992;33:1677.
[63] Stott FH, Atkinson A. Materials at High Temperatures 1994;12:195.
[64] Huntz AM, Schutze M. Materials at High Temperatures 1994;12:151.
[65] Frost HJ, Ashby MF. Deformation mechanism maps. New York: Pergamon Press, 1982.
[66] Gaudette FA, Suresh S, Evans AG, Dehm G, Ruhle M. Acta Mater 1997;45:3503–14.
[67] Lipkin D, Clarke DR, Evans AG. Acta Mater 1998;46:4835–50.
[68] Gaudette FA, Suresh S, Evans AG. Met Mater Trans 2000;31A:1977–83.
[69] Janakiraman R, Meier GH, Pettit FS. Metall and Mater Trans A 1999;30A:2905.
[70] Wang JS, Evans AG. Acta mater 1999;47:699–710.
[71] Wang JS, Sugimura Y, Evans AG, Tredway WK. Thin Solid Films 1998;325:163–74.
[72] Hutchinson JW, He MY, Evans AG. Journal of Mech and Phys of Solids 2000;48:709–34.
[73] Levi CG, Yang JY, Dalgleish BJ, Zok FW, Evans AG. J Am Ceram Soc 1998;81:2077–86.
[74] Johnson CA, Ruud JA, Bruce R, Wortman D. Surf Coatings Tech 1998;108/109:80.
[75] Clyne TW, Gill SC. J Thermal Spray Tech 1996;5:401–18.
[76] Bartlett AH, DeMaschio R. J Am Ceram Soc 1995;78:1018–24.
[77] Tsui YC, Clyne TW. In: Berndt CC, editor. Thermal spray: practical solutions for engineering problems. ASM International, 1996. p. 275.
[78] McPherson R. Thin Solid Films 1981;83:297.

[79] Balint DS, Hutchinson JW. Unpublished research.
[80] Hsueh CH, Fuller ER Jr. Mat Sci and Engr 2000;A283:46–55.
[81] Shum DKM, Huang YY. Engr Fract Mech 1990;37:107–17.
[82] Mumm DR, Evans AG, Spitsberg IT. Acta Mater, in press.
[83] Nicholls JB, Lawson KJ, Rickerby DS, Morell P, AGARD REPORT R-823, April 1998.

Appendix F

PRECURSOR TO TBC FAILURE CAUSED BY CONSTRAINED PHASE TRANSFORMATION IN THE THERMALLY GROWN OXIDE

D. R. Clarke, V. Sergo and M-Y. He

Materials Department, College of Engineering
University of California, Santa Barbara, CA 93106-5050

Abstract

Failure of thermal barrier coatings by buckling and subsequent spalling requires that first there is a critical-sized flaw at the interface. Evidence is presented that the critical-sized flaw can be formed by the separation of the thermally grown oxide from the TBC as a consequence of the constrained phase transformation in the oxide. This may occur if the TBC is deposited prior to completion of the phase transformation in the alumina. A heuristic argument and associated finite element computations indicate that there exists a critical thickness of the thermally grown oxide above which interface separation will occur if the phase transformation in the oxide is incomplete before TBC deposition. The critical thickness criterion provides a basis for designing pre-treatment conditions prior to the deposition of the TBC. Luminescence characterization provides a means of quantitatively determining the extent of the phase transformations within the TGO.

Elevated Temperature Coatings:
Science and Technology III
Edited by J.M. Hampikian and N.B. Dahotre
The Minerals, Metals & Materials Society, 1999

Introduction

Failure of thermal barrier coatings usually refers to the spalling or separation of the thermal barrier coating (TBC) from the underlying alloy it is designed to protect. Over the years, a number of failure modes have been identified, ranging from spallation associated with aluminum depletion in the bond-coat to thermal cycling induced edge spalling. There is also substantial evidence that the life of a TBC prior to failure is associated with the oxidation of the bond-coat forming aluminum oxide at the bond-coat/TBC interface [1]. (Following convention, this oxide is referred to here as the thermally grown oxide, TGO). Recently, we have identified a new failure mode associated with moisture enhanced sub-critical crack growth along the TGO/bond-coat interface leading to spalling [2]. Post-failure observations indicated that not only did failure occur at the TGO/bond-coat interface but there was also evidence for a proposed precursor failure mechanism attributed to Strangman. He apparently suggested that longer TBC lives were likely to obtain if the phase transformation in the alumina TGO were completed prior to deposition of the TBC. In this contribution we explore the possibility that local separation of the TBC from the thermally grown oxide can occur as a result of the constrained volume change associated with phase transformations within the alumina TGO.

Failure by spalling of a compressively stressed film or coating generally occurs after buckling. Whilst the mechanics of spalling are still under intensive investigation, the mechanics of buckling is quite well developed [3-5]. One of the central results of this mechanics is that for buckling to occur requires a region along the interface to be already separated. For a typical thickness (~150-1000 μm) of a thermal barrier coating a debonded region several tens to hundreds of microns in size must form first. This leads to one of the major difficulties in predicting when buckling and spalling will occur, namely in understanding how such large regions of separation can arise or grow from smaller defects. One possibility is that this is associated with the oxidation process. Typical bond-coat alloys for TBCs are chosen to be strong alumina formers and aluminum oxide forms rapidly on the bond-coat even at intermediate temperatures and at low partial pressures of oxygen. As a result, alumina invariably forms during heat-up prior to TBC deposition as well as during any pre-deposition heat treatments, such as are applied to stabilize the bond-coat. Studies have shown that aluminum oxide first forms at low temperatures as an amorphous oxide and then subsequently transforms to the stable, high-temperature polymorph, alpha (α)-alumina. On several bond-coat alloys, including NiAl and platinum aluminide (NiPtAl), the amorphous alumina transforms first to gamma (γ) alumina, then to theta-(θ) alumina and finally to α-alumina [6]. Over a wide range of temperatures, the θ- and α- alumina can co-exist with the θ-alumina slowly transforming to α-alumina [6]. Indeed, as will be described below, α-alumina forms by a nucleation and growth process from the θ-alumina phase during oxidation [7]. As with other nucleation and growth processes, the time to complete the transformation depends on a variety of parameters including the composition of the bond-coat, the temperature, the surface roughness, the oxygen partial pressure and the presence of minor impurities.

If the thermal barrier coating is deposited on the bond-coated alloy before the phase transformation to α-alumina is complete, then the transformation is geometrically constrained. As a result stresses can be generated within the thermally grown oxide and across its interfaces with both the bond-coat and the TBC. As each of the phase transformations in alumina is accompanied by a decrease in volume, the stresses generated within the alumina TGO will be tensile and, under conditions to be analyzed, may be sufficient to cause interface separation. Such regions of separation may provide the critical interface defect required for the onset of spontaneous buckling on cooling. In this work we present evidence suggesting that such large

regions of separation can indeed occur as a result of phase transformations within the thermally grown aluminum oxide. From this we conclude that, as with other thin film residual stress problems [8], there exists a critical thickness of the untransformed thermally grown oxide above which interface separation can occur. The critical thickness, in turn, provides a criterion for avoiding this particular form of precursor to failure.

Observations

In this section we present two sets of observations. The first is that the θ- to α-alumina phase transformation can occur within the thermally grown oxide during typical pre-treatment and TBC deposition conditions. The second are observations indicating that separation of the TBC/TGO interface can also occur.

Evidence for the θ-to-α phase transformation within a growing alumina TGO comes from photostimulated luminescence observations [7]. The basis for these observations is that the luminescence, stimulated by a probing laser beam, from Cr^{3+} ions incorporated within the alumina TGO is characteristic of the phases present. Thus, the frequency of the principal luminescence lines can be used to identify both α- and θ- alumina phases [9,10]. Figure 1 presents the characteristic R1 and R2 lines from α- and θ-alumina. Under favorable circumstances, the luminescence signal can be used in mapping the distribution of the two polymorphs, much as characteristic X-rays can be used to map elemental distribution in a SEM. An example of this is shown in figure 2 taken from a platinum aluminide bond-coat after heating for one hour at 1100°C. In this particular case, islands of α-alumina have nucleated within the θ-alumina TGO and have grown to a size of ~ 8 μm. Observations, made over a range of oxidation times, indicate that the islands of α-alumina grow with time and eventually coalesce to form a continuous α-alumina TGO [7]. Although we have been unsuccessful in luminescence mapping through a TBC, presumably because of beam spreading and scattering within the TBC, our observations of the luminescence through TBCs after deposition often reveals that phase transformation within the TGO is incomplete. An example is shown in figure 3 in which the appearance of characteristics luminescence lines of both the α- and θ-alumina phases are indicated. We have made no attempt to quantify the proportions of the two phases with deposition conditions but it is evident that the phase transformation to α-alumina is not always complete prior to TBC deposition.

The evidence for local separation of the TBC/TGO interface is based on post-failure observations of TBCs [2]. When examined by scanning electron microscopy, we have observed that not only has failure occurred between the TBC and the TGO but also there are regions where there are no fracture markings on either the TBC or TGO failure surfaces. An example is shown in figure 4. This surprising lack of fracture markings can only be understood if the TBC/TGO interface were already separated prior to further oxidation and wholesale failure of the TBC. (It is emphasized that these are localized regions and do not extend over all the failure surface). An additional but related observation is that the TGO is itself cracked in a manner resembling classical "mud-cracking" of films under biaxial tension, a fracture mode usually described as tunneling cracking.

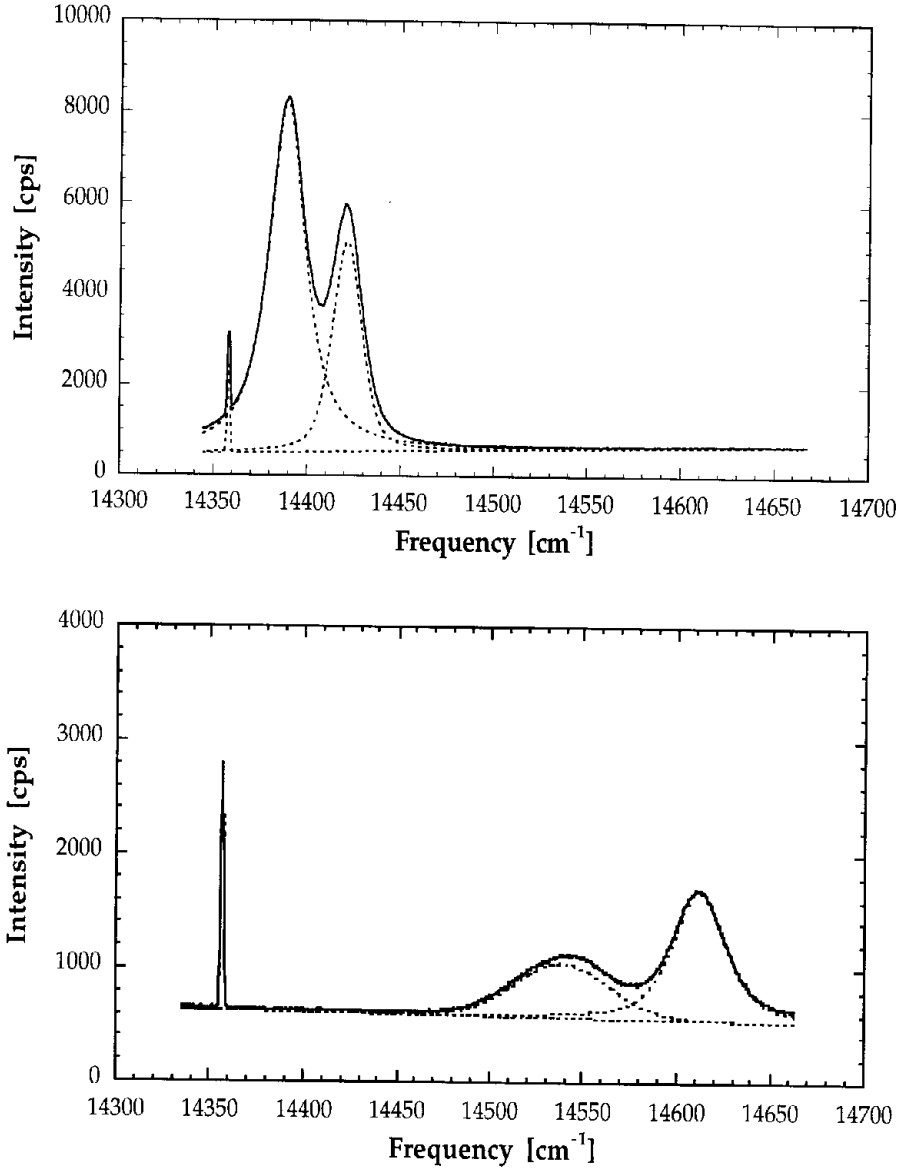

Figure 1. Characteristic photostimulated luminescence from α-alumina (top) and θ-alumina (bottom) phases.

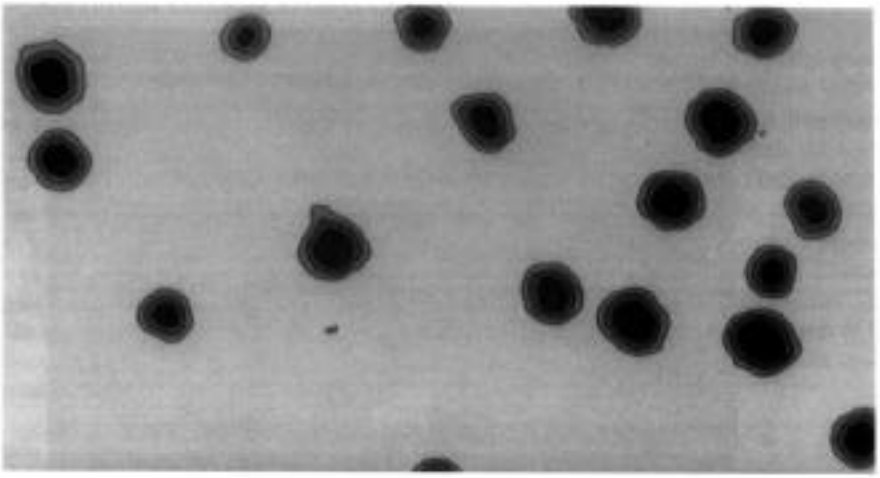

Figure 2. Image of alpha-alumina islands nucleated within a θ-alumina TGO formed by oxidation of NiAl for 1 hour at 1100°C. The image, presented as intensity contours, was obtained by mapping the intensity of the R-line photoluminescence from the α-alumina phase as a function of position across the bond-coat.

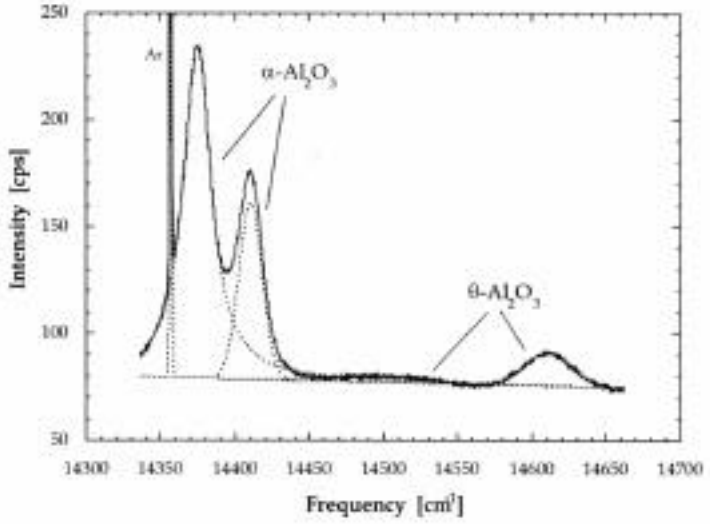

Figure 3. Luminescence spectrum through a 140 micron thick EB-PVD after deposition illustrating the presence of both α-alumina and θ-alumina within the TGO and hence incomplete phase transformation to α-alumina. (The photoluminescence yields from the two phases are not the same. Consequently, direct comparison of the relative intensities cannot be used to establish the volume fractions of the two phases.)

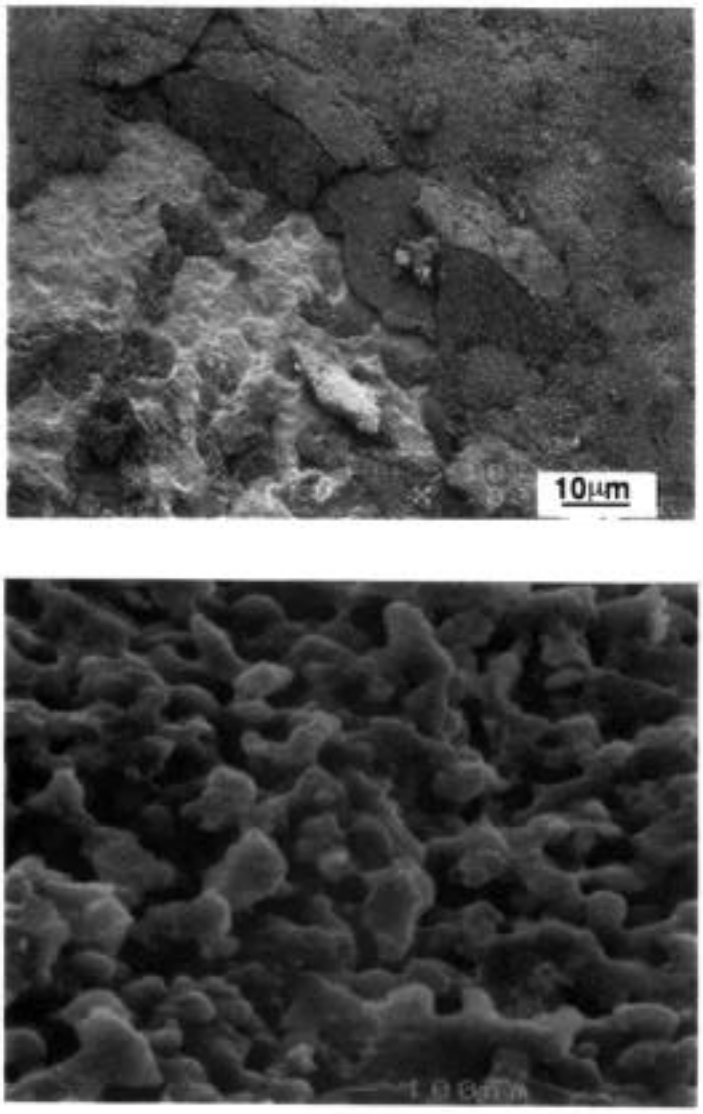

Figure 4. Low (top) and high magnification (bottom) images of the failure surface on the bond-coat side of a TBC. The low magnification image reveals both bare bond-coat (light regions) and thermally grown alumina. At higher magnification, the alumina surface exhibits the morphological characteristics of a free surface with no fracture markings.

Separation Resulting From A Constrained Phase Transformation

If the TBC is deposited prior to completion of the phase transformation in the thermally grown oxide to alpha-alumina, its transformation on subsequent high temperature exposure will be constrained by the TBC. If the transient alumina everywhere on the bond-coat transforms uniformly, then there will be a uniform densification, the TBC will be drawn towards the bond-coat and no stresses will be developed in the alumina or across the alumina/TBC interface. However, as suggested by the luminescence images, α-alumina usually forms by a nucleation and growth process in the transient alumina. If this process occurs but is incomplete prior to deposition of the TBC, then the subsequent transformation will be constrained, both laterally and vertically, with the result that stresses will be generated, including across the alumina/TBC interface. In the following the stresses are computed and the conditions for the separation of the interface presented. Both a heuristic argument for describing the separation conditions and a finite element computation are presented.

The situation is shown schematically in figure 5. A transient oxide of thickness, h, is assumed to have formed during thermal pre-treatment of the bond-coat and prior to TBC deposition. It is also assumed the nucleation of the α-alumina has occurred in places over the surface of the bond-coat to form islands that have grown through the thickness of the TGO. As a result, the partially transformed thermally grown aluminum oxide is sandwiched between the bond-coated alloy below and the thermal barrier coating above. For analytical simplicity and to obtain an estimate of the parameters involved, two further assumptions are made: that the spacing between α-islands is much greater than the thickness of the transient oxide, and that both the alloy and thermal barrier coating are assumed to be semi-infinite in extent and rigid. (These restrictions are lifted in the subsequent finite element computations described below). We now consider the stresses created when the remaining transient alumina subsequently transforms to α-alumina. Assuming that the contraction of the alumina is fully constrained, a state of hydrostatic stress is generated within the thermally grown oxide and a corresponding elastic strain energy is stored. The value of the hydrostatic stress, σ_h, is given by:

$$\sigma_h = \beta K \frac{\Delta V}{V}$$

where β is a geometric factor that depends on the shape of the transforming region, K is the bulk modulus and $\Delta V/V$ is the volume change accompanying the transformation. Assuming that the TBC and the underlying alloy are rigid, the elastic strain energy per unit volume in the alumina can be simply stated:

$$E_{elastic} = \beta K \left(\frac{\Delta V}{V} \right)^2$$

This elastic strain energy can be relaxed by interface separation, by tunneling cracking in the alumina or by both. Interface separation principally relieves the stress in the z-direction and would leave the oxide is biaxial tension, a stress state that could, in turn, be relieved by tunnel cracking. At this point, however, we consider interface separation only. (As a result only about one–third of the total elastic strain energy can be relieved.) Viewing the separation as the

nucleation and propagation of an interfacial crack, this will occur provided that there is a net decrease in overall energy. If the interfacial fracture energy is Γ per unit area, separation will be energetically favored provided that it is less than the elastic strain energy released per unit area, G:

$$G = \frac{hE}{Z}\left(\frac{\Delta V}{V}\right)^2 > \Gamma_c$$

Z is a number that incorporates both the Poisson ratio and the geometric factor. Thus, it can be seen that interface separation can occur when the thickness of the partially transformed oxide exceeds a critical thickness given by:

$$h_c = \frac{Z\Gamma_c}{E(\Delta V/V)^2} = \frac{Z\Gamma_c E}{\sigma_h^2}$$

This has the same form as many other thin film fracture problems [8]. Indeed, it has the same form as the critical thickness for tunneling cracking [11] but with a different numerical constant, Z_1:

$$h_c = \frac{\Gamma_c E}{Z_1 \sigma^2}$$

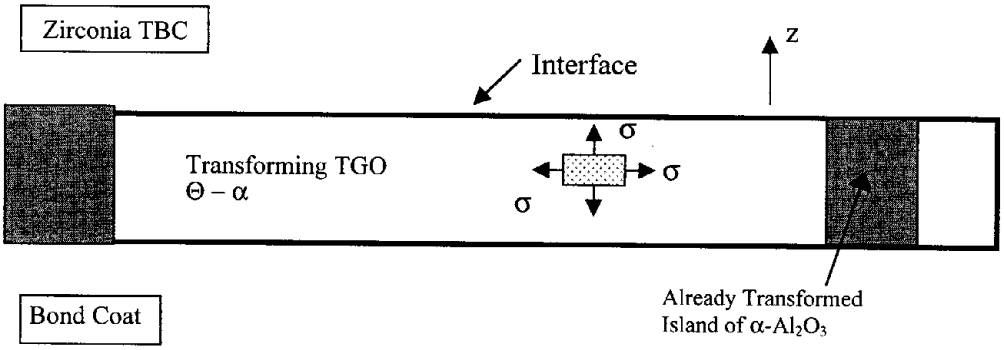

Figure 5. Schematic illustration of the stress state in a constrained alumina TGO undergoing a volumetric contraction associated with the Θ-α phase transformation.

The heuristic argument derived above for the energetics of interface separation is based on a number of rather restrictive assumptions, the most restrictive probably being that the TBC is assumed to be rigid. As a result, the elastic strain energy created by the constrained transformation is the maximum possible and hence the argument leads to a "worst-case" condition for interface separation. To incorporate both the finite modulus and thickness of the TBC, a series of finite element calculations of the strain energy release rate have also been performed. The results are shown in figure 6 for two different values of the elastic modulus of

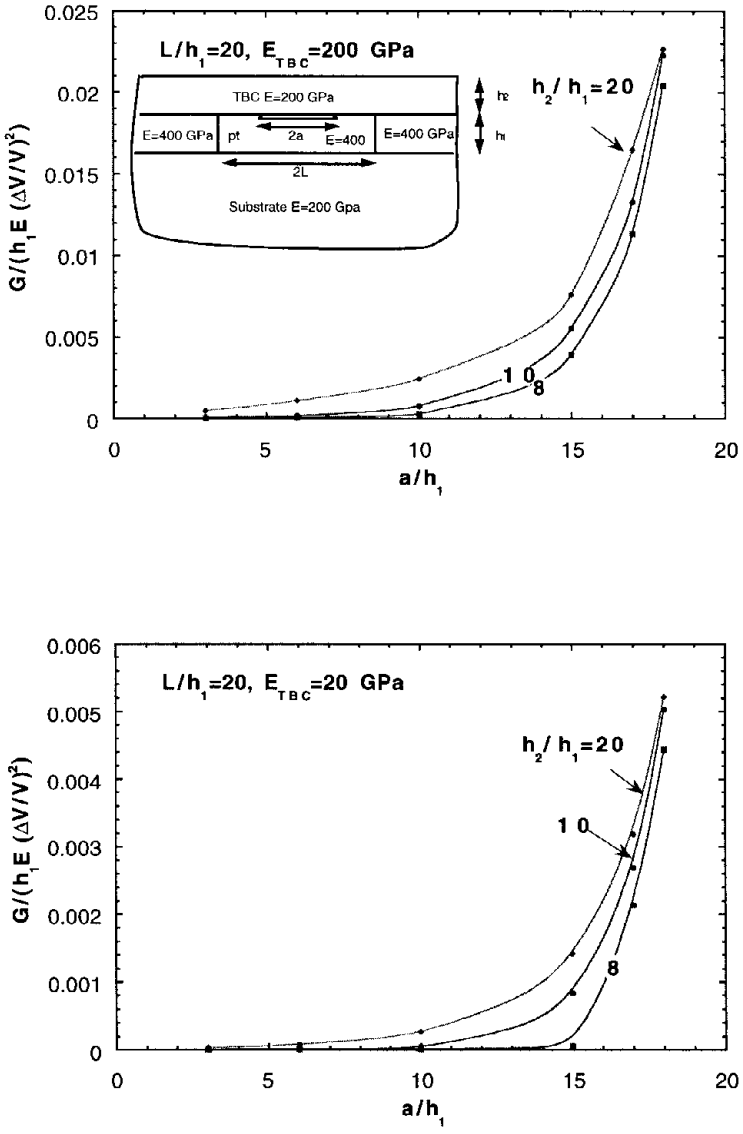

Figure 6. Normalized strain energy release rate for TBC/TGO separation as a function of interface flaw size for two TBCs with different elastic modulii. In the top graph the elastic modulus is that of dense zirconia whereas in the bottom graph the elastic modulus is taken to be 20 GPa, a value more typical of an EB-PVD coating.

the TBC. The upper figure corresponds to fully dense zirconia (E=200 GPa) and the lower to a low-density zirconia (E=20 GPa) typical of an electron-beam PVD coating with a columnar microstructure. In both graphs, the normalized strain energy release rate is plotted against the separation size (normalized by the TGO thickness) for different values of the TBC/TGO thickness ratio. The results are superficially very similar but the values of the strain energy release rate are notably different, being considerably larger for the stiffer TBC. A notable feature of both sets of curves is that above a thickness ratio of 20, the curves are almost indistinguishable, and hence are not plotted, indicating that the TBC is essentially rigid. Another notable feature is that below a thickness ratio of 8 the strain energy release rate is zero for all possible flaw sizes. Below this threshold value, it is energetically favorable for the TBC to flex in response to the volume change in the TGO rather than for interface separation to occur. This same competition between bending energy, constraint elastic energy and interface energy underlies the convex shape of the strain energy release rate curves for different TBC thicknesses: The incremental energy associated with bending the TBC slightly to accommodate a small flaw size is less than that associated with forming new interface area so is preferred until the flaw size is large. As the flaw increases in size or the TBC is thicker, the bending energy becomes proportionally larger and it is no longer favorable for bending to occur, rather the interface separates. Cracking perpendicular to the interfaces can also occur in order to relieve the biaxial stress. This is the tunneling mode of cracking and has already been analyzed [11].

Discussion and Conclusions

Based on the analysis presented here, there is a set of conditions that favor the separation of the TGO from the TBC if it is deposited prior to the completion of the phase transformations in the thermally grown oxide. This is important because, once formed, there is little likelihood that the interface separation will close up and heal. (Although the alumina scale will thicken with continued oxidation of the underlying bond-coat, its thickness is dictated by diffusion through the scale and this will be the same irrespective of position across the bond-coat once the scale is fully converted to α-alumina). Also, whilst our analysis does not specifically address the size of the interface separations it can be expected that they will be related to the spacing of the α-alumina islands formed at the nucleation stage of the transformation. As a result, the nucleation spacing will probably control whether the separations formed will be sufficiently large that they can act as the critical-sized flaws for subsequent buckling and spalling. The finite element calculations support the general heuristic argument that there exists a critical thickness of the TGO below which interface separation will not be favored energetically and can, hence, be avoided. The actual value depends in detail on the elastic modulus of the TBC and on the fracture resistance of the interface. However, to gain an appreciation of the magnitude of the thickness we can estimate the critical value from the volumetric change accompanying the θ-to-α transformation (4.7%), the bulk modulus of α-alumina (264 GPa), an assumed Young's modulus for the TBC (200 GPa) and an interface fracture resistance of $\sim$ 10 Jm^{-2}. With these values, the critical thickness above which the constrained phase transformation will lead to interface separation is $\sim$ 8 μm for a thick TBC if a flaw size of $\sim$ 30 μm already exists along the interface. These are both large values but if a weaker interface is formed, for instance as a result of contamination or segregation, with an interface fracture resistance of $\sim$1 Jm^{-2}, the corresponding critical thickness is only 0.8 μm and the flaw size is $\sim$ 4 μm. The form of the computed curves for the strain energy release rate has a number of other consequences. For instance, they suggest that if the transformation occurs during the TBC deposition, it is potentially least damaging if the transformation occurs whilst the TBC is still thin. Then, at least, the TBC can follow the shape of the transforming TGO. If the transformation does not

occur until later, it is too rigid and interface separation can occur if the oxide is above the critical thickness. Thus, again both the thickness of the TGO and the elastic modulus of the TBC play crucial roles.

On the basis of these calculations there appear to be two alternative means of assuring that interface separation of the sort discussed here does not occur. One is to practice a pre-treatment and deposition schedule in which less than the critical thickness of incompletely transformed alumina forms. Some surface alumina is generally thought to be desirable to promote adhesion of the depositing TBC to the bond-coat but, even if this is so, it probably need not be more than a few tens of nanometers. The alternative is to use a non-destructive, characterization means of ensuring that complete transformation to α-alumina occurs prior to TBC deposition. One possible method, as illustrated in section 2, is to utilize the photostimulated Cr^{3+} luminescence from the thermally grown aluminum oxide. It is equally applicable to examining phases on both flat and rough surfaces and, as also shown in section 2, is capable of being implemented in an imaging mode prior to TBC deposition to ascertain whether phase transformation is complete.

Acknowledgment

This work has been supported by the Advanced Gas Turbine Systems Research (AGSTR) program of the Department of Energy under grant 98-01-SR068 through the South Carolina Energy Research and Development Center.

References

1. R. A. Miller, " Oxidation Based Model For Thermal Barrier Coating Life", Journal of the American Ceramic Society, 67 (1984) 517-521

2. V. Sergo and D. R. Clarke, "Observation of Sub-Critical Spall Propagation of a Thermal Barrier Coating", Journal of the American Ceramic Society, in press.

3. A. G. Evans and J. W. Hutchinson, " On The Mechanics of Delamination and Spalling in Compressed Films", International Journal of Solids and Structures, 20 (1984) 455-466.

4. M. D. Thouless, J. W. Hutchinson and E. G. Liniger, "Plane Strain, Buckling Driven Delamination of Thin Films", Acta Metallurgica et Materialia, 40 (1992) 2639.

5. M. D. Thouless, " Combined Buckling and Cracking of Films", Journal of the American Ceramic Society, 76 (1993) 2936.

6. M. W. Brumm and H. J. Grabke, " The Oxidation Behavior of NiAl", Corrosion Science, 33 (1992) 1677-1690.

7. D. M. Lipkin D. R. Clarke, H. Schaffer and F. Adar, " Lateral Growth Kinetics of a-Alumina Accompanying The Formation of a Protective Scale on (111) NiAl During Oxidation at 1100°C", Applied Physics Letters, 70 (1997) 2550-2552.

8. J. W. Hutchinson and Z. Suo, " Mixed Mode Cracking in Layered Materials", Advances in Applied Mechanics, 29 (1992) 63-191.

9. D. M. Lipkin and D. R. Clarke, " Measurement of the Stress in Oxide Scales Formed by Oxidation of Aluminum-Containing Alloys", Oxidation of Metals, 45 (1996) 267-280.

10. Q. Wen, D. M. Lipkin and D. R. Clarke, " Luminescence Characterization of Chromium Containing Theta Alumina", Journal of the American Ceramic Society, in press.

11. D. K. Leung, M. Y. He and A. G. Evans, " The Cracking Resistance of Nanoscale Layers and Films", Journal of Materials Research, 10 (1995) 1693-1699.

Microstructural study of the theta-alpha transformation in alumina scales formed on nickel-aluminides

V.K. Tolpygo and D.R. Clarke
Materials Department, College of Engineering, University of California, Santa Barbara, CA 93106-5050, USA

Luminescence spectroscopy and scanning electron microscopy have been used to study the transformation from theta-Al_2O_3 to alpha-Al_2O_3 on the surface of platinum-modified nickel aluminide, (Ni,Pt)Al, bond coats on superalloys during initial stages of oxidation at 1,000-1,200°C. The transformation can proceed in a number of ways, depending on the surface roughness, leading to different microstructures of the stable alpha-alumina scale. The use of the luminescence method makes it possible to correlate microstructural features of the oxide with the local stress through piezospectroscopic shifts of both alpha- and theta-alumina optical spectra.

Keywords: alumina, nickel aluminide, luminescence spectroscopy, phase transformation, scanning electron microscopy

1. INTRODUCTION

High-temperature oxidation of nickel aluminides, in particular β-NiAl, has been extensively studied [1–8]. These materials form a protective α-Al_2O_3 scale during oxidation at temperatures around 1,200°C. At lower temperatures, the scale may contain metastable (transition) aluminas, and the transformation into the stable α phase has been the subject of various studies [4–6,9–11]. Among distinctive features of the metastable aluminas are their higher growth rate, in comparison with α-Al_2O_3, and morphology with needle- or whisker-type crystals on the surface [4,6,8–10]. This morphology is often considered evidence of the presence of the metastable phase in the scale.

Unlike β-NiAl, oxidation of platinum-modified nickel aluminides, (Ni,Pt)Al, has not been adequately explored. Only very limited information is available so far on the alumina morphology [12,13] and essentially no results have been reported on the phase transformations in the oxide scales. At the same time, this alloy has increasingly been used as a bond coat in thermal barrier coatings (TBC) [14], primarily due to its superior oxidation resistance. In the TBC systems, oxidation of the bond coat occurs beneath an outer zirconia layer. For this reason, the performance of the TBC largely depends on the morphology, growth rate, adherence and other characteristics of the alumina layer formed on the bond coat surface.

Typically, the aluminum content on the surface of a single-phase (Ni,Pt)Al coating is about 21 wt% (43 at.%) [14], which is sufficient to form a protective alumina scale during oxidation. However, similar to other nickel aluminides, in the early oxidation stages (Ni,Pt)Al can form metastable alumina phases, such as θ-Al_2O_3, which then transform to α-Al_2O_3. Our interest in studying the θ → α phase transformation was stimulated by the fact that TBCs are designed to keep the temperature of the metal surface below about 1,100°C. In this temperature range, transformation to the stable α-alumina may take quite a long time and may also be affected by a number of variables, for instance, roughness of the metal surface, as described in this paper. In addition, the morphology of the resulting α-Al_2O_3 scale is expected to depend on the morphology of its 'precursor', θ-Al_2O_3, and on the rate at which the transformation occurs. Hence, in addition to a purely scientific interest in studying the phase transformation, it may also have a practical significance by affecting the properties of the α-Al_2O_3 scale formed on oxidation.

Another purpose of the present work is to further explore the capabilities of the luminescence spectroscopy in studying alumina scales. In earlier contributions [7,15], this method was primarily used for measuring residual stresses in alumina. Further advances have recently been made with respect to θ-Al_2O_3 identification and recording two-dimensional images of α and θ luminescence, which show spatial distribution of both phases in the scale [11,16,17]. The results reported in this paper show that progress in understanding the θ → α phase transformation can be made by combining luminescence spectroscopy with SEM observations of growing alumina scales.

0964-3409/00/01/00035–12

2. MATERIALS AND EXPERIMENTAL PROCEDURE

Platinum-modified nickel aluminide, (Ni,Pt)Al, used in this study was supplied by Howmet Research Corporation (Whitehall, MI) in the form of 65–70 μm thick coatings made by chemical vapor deposition on the surface of Rene N5 coupons. The chemical composition of the coating surface, measured by EDX, is as follows (wt.%): Ni (bal.) – 22% Al – 25% Pt – 3.5% Co – 1.5% Cr. The coatings were subsequently prepared for different surface finishes ranging from 1 μm diamond polishing to 400-grit SiC abrasion. Oxidation was performed in air at 1,000-1,200°C. The surface morphology of the alumina scales was analyzed using optical and scanning electron microscopy (SEM). Alumina phases and their spatial distribution in oxide scales were studied using photo-stimulated luminescence spectroscopy (PSLS). All the relevant details of the PSLS measurements are presented in the following section whereas the experimental setup and interpretation of the luminescence spectra have been reported earlier [15,18].

3. CHARACTERIZATION OF ALUMINA SCALES USING PSLS

Photo-stimulated luminescence is a characteristic feature of alpha-alumina scales containing small amounts of substitutional Cr^{3+} ions. The luminescence spectrum of alpha-alumina consists of two major lines (R_1–R_2 doublet) and their position varies with stress (strain) in the oxide (see, for example, a brief review in [19]). Another pair of characteristic peaks, further on referred to as T_1–T_2 doublet, has been recently identified as Cr^{3+} luminescence in θ-Al_2O_3 [16]. The difference in frequencies of α and θ luminescence is presumably due to different Cr^{3+}-O^{2-} distances in the alpha and theta crystal structures [16]. Figure 1 shows examples of the luminescence spectra of α-Al_2O_3 and θ-Al_2O_3 recorded from the oxidized surface of Fe-Cr-Al and β-NiAl, respectively. Both doublets are shifted to smaller frequencies from their stress-free positions, shown by the dashed lines, as a result of 3.0–3.5 GPa residual compression in the oxide (piezospectroscopic shift). The relationship between stress and peak shift for α-alumina was established earlier [19]. Although no calibration of the stress-induced shift for θ-alumina is available at this time, its magnitude appears to be close to that for α-alumina.

The third spectrum in Figure 1 was obtained from the chromium-doped PVD alumina film annealed at 775°C which, according to previously reported X-ray data [20], is fully transformed from amorphous to gamma-alumina. Similar spectra have been obtained from chromium-doped sintered γ-Al_2O_3 ceramics [21]. The broad luminescence band, with a maximum around 14,470 cm^{-1} (691 nm), and the absence of characteristic peaks are probably caused by the fact that cations are distributed between octahedral and tetrahedral sites in the cubic spinel structure of γ-Al_2O_3. It should be noted that none of the (Ni,Pt)Al samples, studied so far, showed gamma-alumina spectra after oxidation at temperatures above 800°C, as opposed to θ-phase which is readily detected in the temperature range from 850 to 1,150°C. Nevertheless, the spectrum of γ-Al_2O_3 is presented in Figure 1 in order to emphasize that this phase can be identified by PSLS and distinguished from the metastable θ-phase.

The remarkably high sensitivity of the PSLS method to α-Al_2O_3 and θ-Al_2O_3 combined with relatively high spatial resolution of an optical microscope enables us to locate both phases on the oxidized surface in a volume as small as a few micrometers wide and less than 100 nm thick. Alternatively, spatially-averaged information can be obtained by scanning the optical probe over the surface during spectrum acquisition. The relative amount of α-Al_2O_3 and θ-Al_2O_3 in the scale can be qualitatively estimated by comparing the intensities of R and T lines (theta-alumina luminescence is 10–12 times weaker than alpha-alumina). Moreover, analysis of the frequency shift and shape of the peaks can be used for detecting different structural constituents in the scale under different residual stresses. Further improvements in this direction can be made using low-temperature PSLS. Decreasing temperature of the sample, for instance, to 77K substantially reduces thermal broadening of the characteristic peaks,

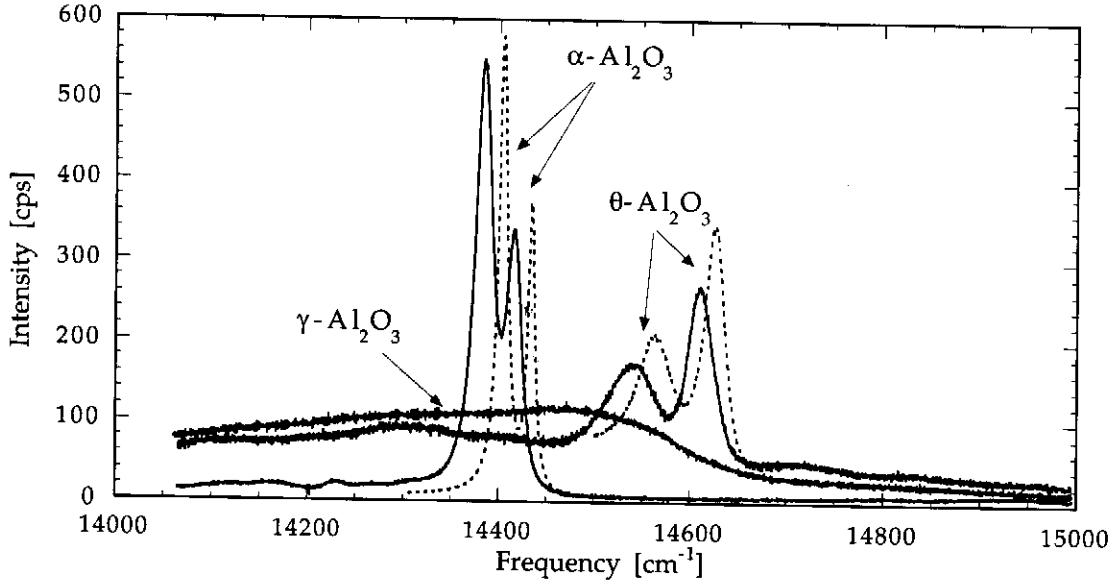

Figure 1 Cr^{3+} luminescence spectra from α, θ, and γ alumina. The dashed lines for α and θ correspond to the stress-free state while the solid lines demonstrate the stress-induced shift for both phases.

which provides the means for the individual contributions with higher and smaller shifts to be distinguished.

4. COMBINED SEM AND PSLS STUDIES OF α-$Al_2O_3 \rightarrow \theta$-$Al_2O_3$ TRANSFORMATION

In agreement with many previous studies of β-NiAl [4,7–10], oxidation of the platinum aluminide at temperatures about 1,000°C results in the formation of alumina scale composed of a continuous layer and blade-like crystals (whiskers). Figure 2(a,b) shows the alumina morphology after oxidation of a 1-μm polished surface for 1 h at 1,000°C. The oxide is entirely θ-Al_2O_3 as confirmed by the PSLS data in Figure 3 (spectrum after 1 h). With increasing oxidation time, alpha-alumina appears in the scale, and the luminescence spectrum demonstrates both α and θ lines (spectrum for 25 h in Figure 3) while the whiskers continue to grow [Figure 2(c)]. The majority of the luminescence spectra from the 'mixed' $\alpha+\theta$ scales contain both R- and T-lines, meaning that both phases, α-Al_2O_3 and θ-Al_2O_3, are present in the probed volume (about 3 μm in diameter). The relative amount of alpha-alumina increases with oxidation time. After 250 h, the scale contains only α-Al_2O_3 (top spectrum in Figure 3) but the surface morphology remains essentially the same as after 25 h.

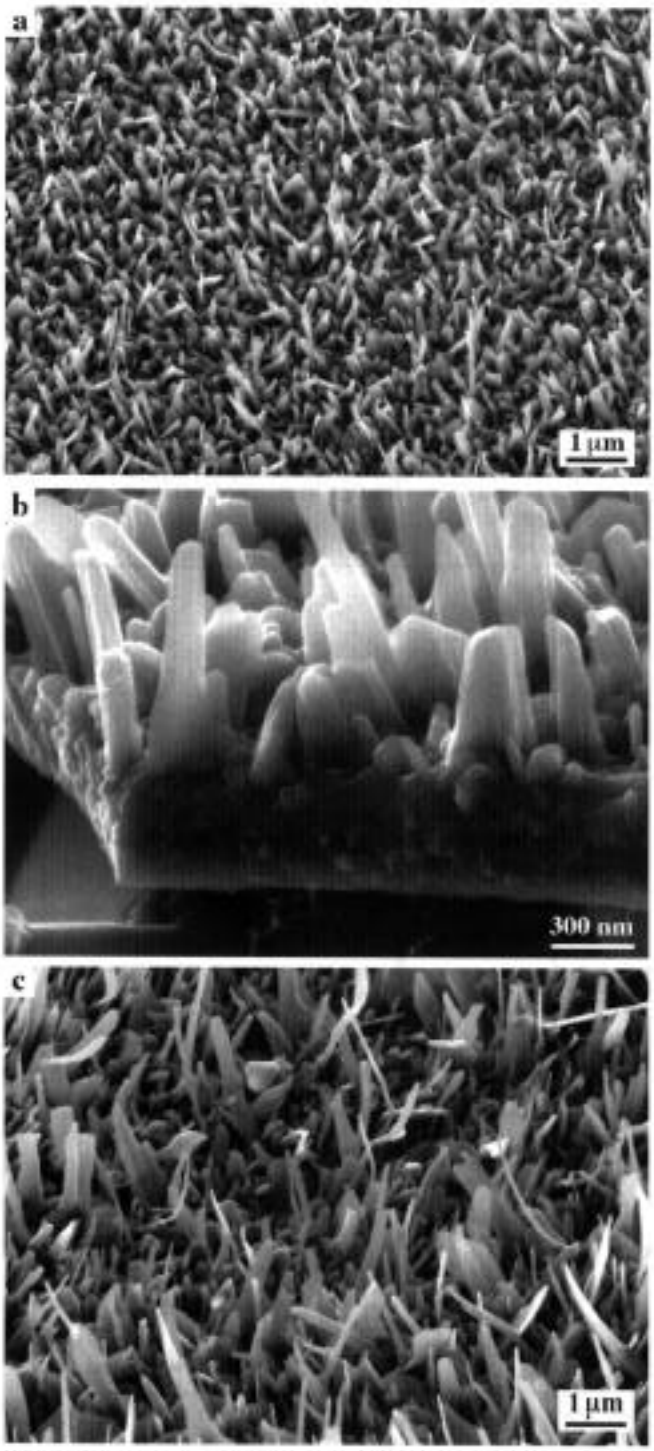

Figure 2 Alumina morphology developed during oxidation of 1-μm polished (Ni,Pt)Al at 1,000°C: (a) general view of θ-Al_2O_3 scale and fracture cross-section of the scale (b) after oxidation for 1 h showing 0.5-μm thick layer and 0.1–1.0 μm long whiskers; (c) general view of $\theta + \alpha$ scale after oxidation for 25 hr.

A strong asymmetry of the individual R and T peaks is a remarkable feature of all the luminescence spectra from the scales containing whiskers (Figure 4). It indicates that some portions of the oxide are under a smaller residual stress than the others. Deconvolution of the spectrum, as shown in Figures 4(b,c), makes it possible to distinguish between the components from low-stressed oxide (R_1^I, R_2^I and T_1^I, T_2^I at higher frequencies) and those under higher compression (R_1^{II}, R_2^{II} and T_1^{II}, T_2^{II} at smaller frequencies). Thus, each phase in the scale contains one (major) part under compression of about 3.0 GPa and another (minor) part under compression of about 0.6 GPa. Returning to the oxide morphology in Figure 2 it becomes clear that luminescence from the layer provides the lower-frequency peaks, while the whiskers, being less constrained by the underlying metal, give the peaks at higher frequencies. In these cases it should also be assured that the scale is intact, since any spalled alumina would give a similar stress-free signal.

A schematic illustration of the oxide cross-section and the distribution of the residual stress, imposed by metal constraint after cooling, is presented in Figure 5. Clearly, both stresses (minimum and maximum stresses in Figure 5) deduced from the frequency shifts represent the average values. In reality, there may be a substantial variation of stresses. For instance, the top portion of whiskers is essentially unconstrained whereas the part adjacent to the layer is under some in-plane compression (transition zone in Figure 5).

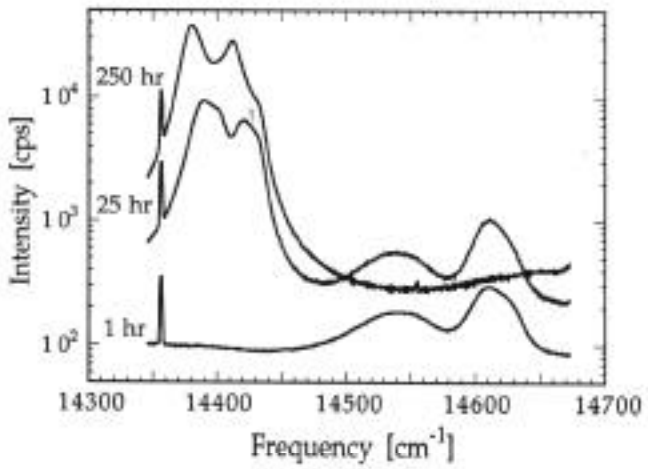

Figure 3 Typical luminescence spectra taken from different places of pure θ-Al_2O_3 scale (1 h), mixed $\theta + \alpha$ (25 h) and pure α-Al_2O_3 scale (250 h) after oxidation at 1,000°C. The sharp peak at 14357 cm^{-1} on these and all other spectra is a calibration line of the Ar lamp.

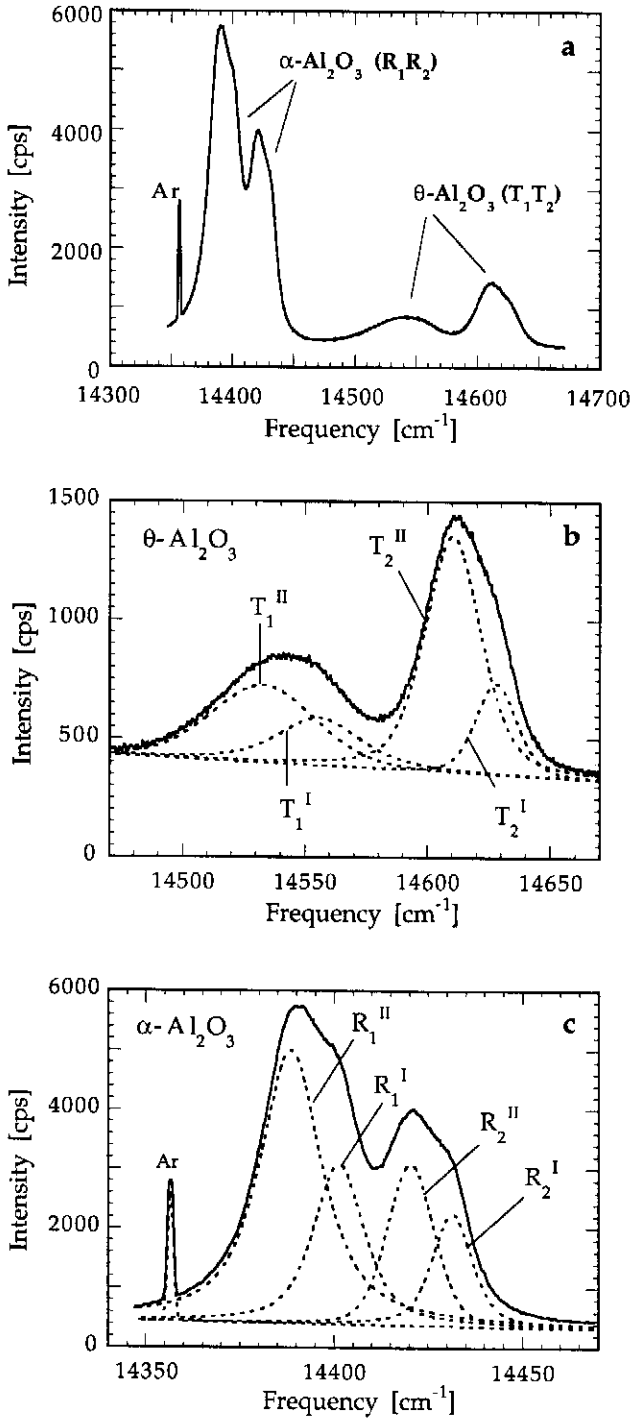

Figure 4 An example of the asymmetrical luminescence spectra with both α-Al_2O_3 and θ-Al_2O_3 at the same place in the scale on 1-μm polished (Ni,Pt)Al after 25 h oxidation at 1,000°C. Deconvolution of the spectrum, shown in (a), into lower- and higher-frequency doublets is given separately for θ-Al_2O_3 (b) and α-Al_2O_3 (c).

Another important feature is that the luminescence spectra from fully transformed α-scales (for example, spectrum for 250 h in Figure 3) remain asymmetrical, *i.e.*, all whiskers, originally developed as θ-Al_2O_3, eventually transform into whiskers of α-Al_2O_3. A better illustration of this result can be made using low-temperature PSLS data (Figure 6). Three luminescence spectra in Figure 6 were recorded at 77 K from three different places of a mixed α+θ scale. The low-temperature PSLS gives sharp peaks from the stress-free whiskers and compressed layer, so that the two components of each phase

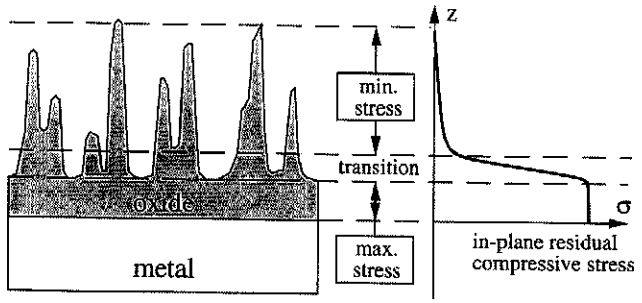

Figure 5 Schematic section of an oxide layer with whiskers and distribution of in-plane compression due to the metal constraint from a maximum value in the layer to a minimum value at the top of whiskers.

can clearly be distinguished. Both the fully transformed α region in Figure 6(b), as well as the θ region in Figure 6(a), exhibit splitting of the luminescence peaks due to different residual compression in the layer and whiskers. The third spectrum in Figure 6(c) corresponds to the region where the two phases coexist.

At the beginning of the $\theta \rightarrow \alpha$ transformation, small R_1–R_2 peaks from the first-formed grains of α-Al_2O_3 can be found in some places (Figure 7). The peak positions indicate conclusively that these grains are under high compression, for example, about –3.75 GPa in Figure 7. This, in turn, suggests that α grains nucleate in the oxide layer, presumably at the oxide-metal interface, in agree-

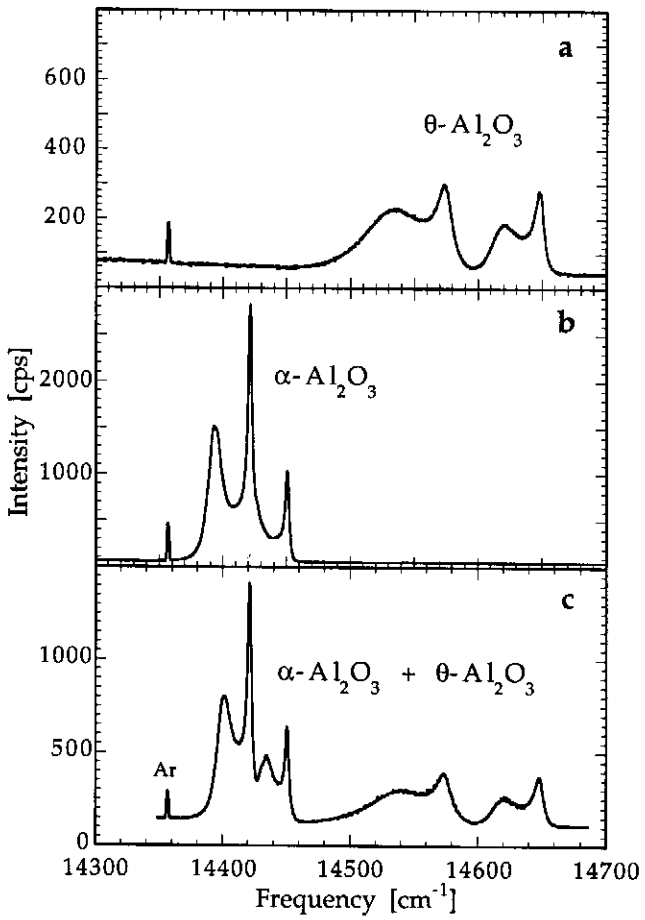

Figure 6 Examples of luminescence spectra recorded at 77 K from different regions of a mixed θ + α scale on 1-μm polished (Ni,Pt)Al after 1 h oxidation at 1,100°C. Splitting of R and T lines is much more distinct than at room temperature.

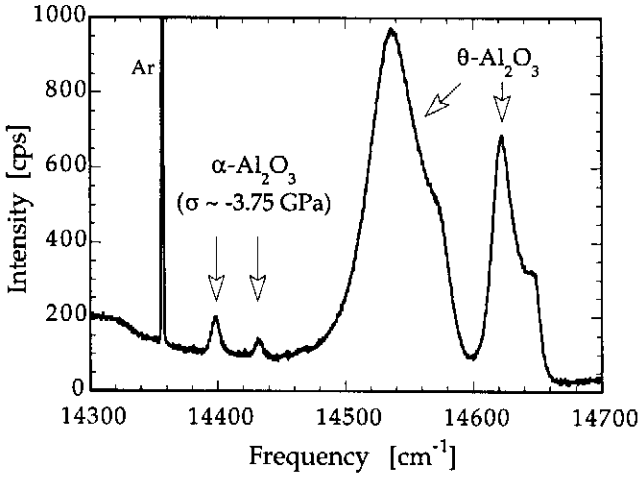

Figure 7 Luminescence spectrum recorded at 77 K from a small region of θ-Al_2O_3 scale, showing weak ruby lines at frequencies corresponding to about 3.75 GPa compression.

ment with TEM observations of α-Al_2O_3 nucleation [9], and not on the oxide surface.

As the transformation proceeds through the thickness of the oxide layer, it might be supposed that, closer to the end of the $\theta \rightarrow \alpha$ transformation, the last portions of θ-Al_2O_3 would be those at the top of whiskers. In such a case, PSLS should demonstrate a weak T_1–T_2 doublet from stress-free θ in addition to strong R_1–R_2 peaks. However, no such places were found in the scale. In all spectra recorded from an almost transformed α scale, the minor θ phase invariably exhibited split peaks [Figure 8(a)] indicating that the remaining small portions of θ-Al_2O_3 were still present both in the layer and in whiskers. Again, when the transformation is completed [Figure 8(b) and (c)], the splitting of the α signal confirms that both the layer and the whiskers consist of α-Al_2O_3 [the insert in Fig. 8(b) demonstrates that no θ is present]. The enlarged view of the split spectrum, shown in Figure 8(c), exhibits one sharp doublet corresponding to less than –0.1 GPa compression and another, major doublet corresponding to –4.2 GPa compression. The remaining part of the spectrum between these two doublets [dashed lines in Figure 8(c)], yields an average stress of about -1.4 GPa which, most probably, corresponds to some 'transition zone' at the bottom of whiskers (Figure 5).

The morphology of alpha-alumina, upon completion of the $\theta \rightarrow \alpha$ transformation, is shown in Figure 9. This scale was formed on a rough surface (400-grit finish) after oxidation for 1 h at 1,100°C. Similar to the scale on the polished surface at 1,000°C (Figure 2), the oxide consists of a continuous layer and whiskers, however it is entirely α-Al_2O_3, as evidenced by the PSLS results in Figure 8(b). An interesting feature of this morphology is the presence of α-whiskers of different length, from less than 100 nm to 1–2 μm. Since cation diffusion is believed to be much faster in θ than in α-Al_2O_3 [4,6], the whiskers grow as long as they are θ-Al_2O_3 and there is a θ-layer underneath. When the oxide transforms to alpha alumina, the whiskers stop growing, therefore the places which transformed earlier have shorter whiskers than those transformed later. (Certainly, there is also a distribution of the whisker size and shape due to their different crystallographic orientation). Another closely related feature is the variation of the oxide thickness. Since the growth rate of θ-Al_2O_3 is about an order of magnitude

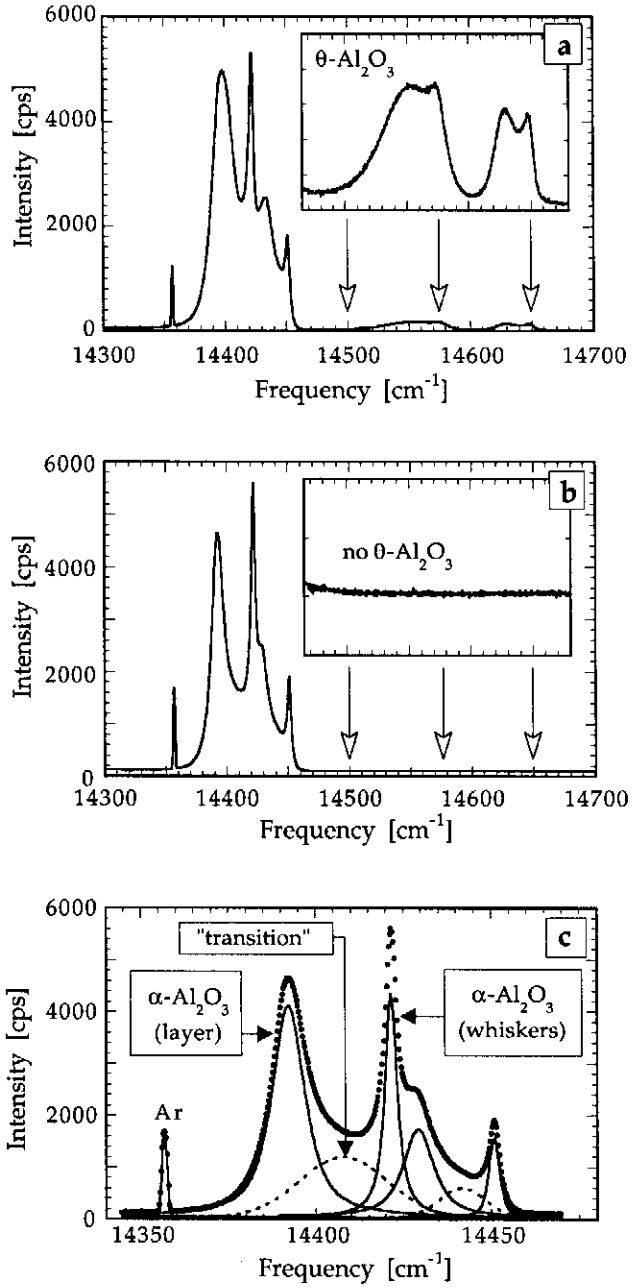

Figure 8 (a) Spectrum at 77 K from mainly α scale formed on the surface with 400-grit finish after 15 min oxidation at 1,100°C. The insert in (a) shows splitting of θ luminescence from the 'last' portions of θ-Al_2O_3; (b) spectrum from purely α scale on the same sample after oxidation for 1 h, showing no θ; (c) deconvolution of the ruby spectrum in (b) into three doublets. The spectrum in (b) was recorded from the oxide shown in Fig. 9.

higher than α-Al_2O_3 [4,6], the oxide layer is expected to be thinner in places which transformed earlier, and it should be thicker in places which remained θ-Al_2O_3 for a longer time. The micrograph in Figure 10 shows that the thickness of α-scale may vary substantially even over neighboring areas on the surface.

It is important to emphasize that oxide whiskers, once formed on the surface of the theta-scale, remain on the surface of the alpha-scale [Figures 11(a) and (b)]. Their shape becomes smoother with time as a result of surface diffusion and, possibly, evaporation at high oxidation temperatures. Nevertheless, asymmetry of the R-peaks, caused by the presence of stress-free whiskers, persists for times as long as 980 hr at 1,100°C [Figure 11(c)].

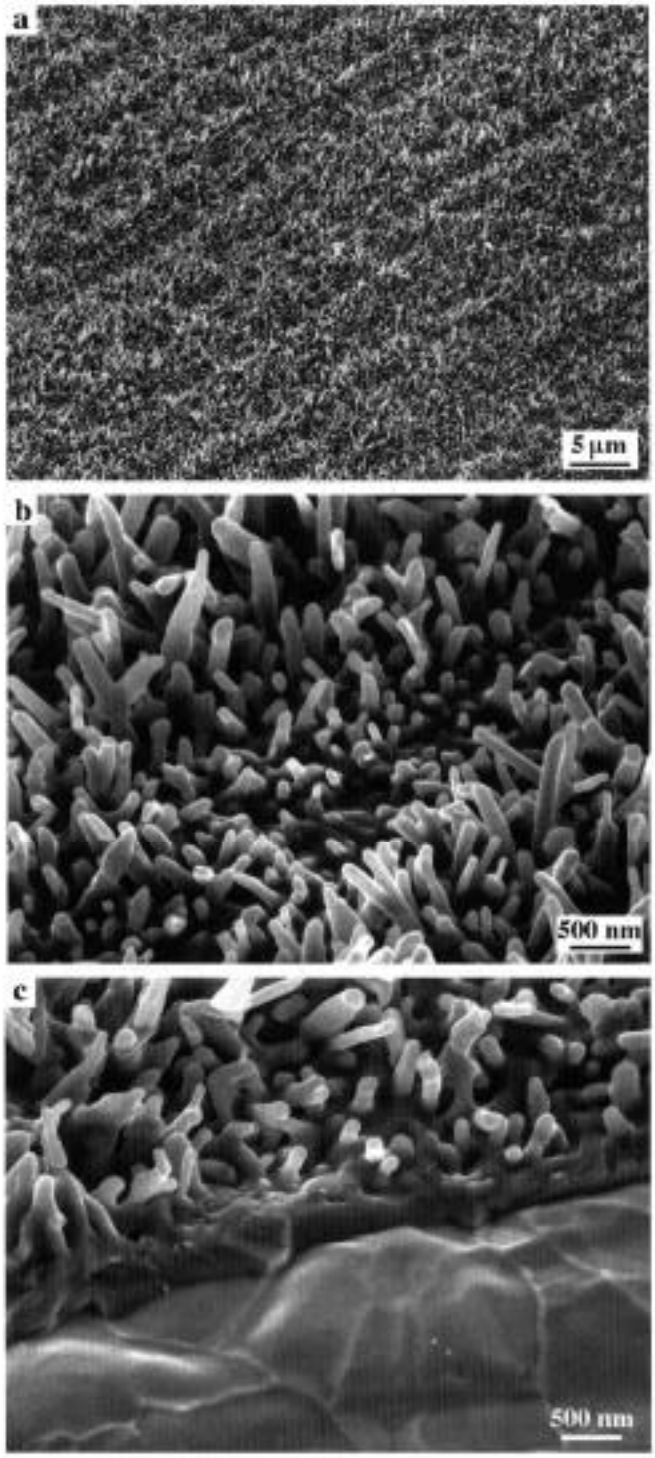

Figure 9 α-Al_2O_3 morphology formed on the abraded (400-grit SiC) surface after oxidation for 1 hr at 1100°C: (a) general view showing abrasion markings; (b) higher magnification image with short whiskers along a scratch and longer whiskers from both sides of the scratch; (c) fracture section of the α scale and exposed metal surface.

The PSLS results together with the microstructural observations presented above demonstrate that θ-Al_2O_3 forms first on the surface of (Ni,Pt)Al during oxidation at 1,000–1,100°C. The initial θ scale is composed of a continuous layer and outward growing whiskers. During oxidation, the θ layer transforms into an α layer and, concurrently, θ whiskers transform into α whiskers. These results are in agreement with previous TEM observations of alpha alumina whiskers on iron aluminides after oxidation at 1,000°C [22].

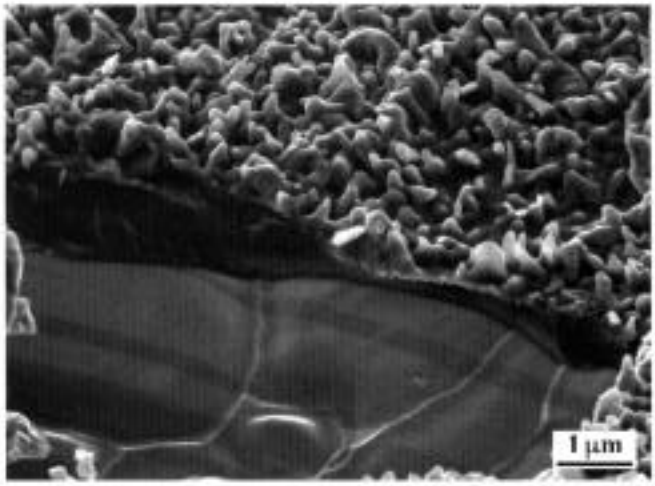

Figure 10 Small area of spalled α scale after 25 h oxidation at 1,100°C of 1-μm polished sample. Thickness of the oxide layer varies in different areas. The exposed metal surface exhibit large (3–5 μm wide) imprints of alumina grains.

The luminescence spectra from different areas of a mixed $\alpha+\theta$ scale show that both phases may coexist. Besides, analysis of the shape of R- and T-lines in these cases indicates that the two-phase zone *is not* composed of an alpha-layer with theta-whiskers. These results seemingly contradict a simple model in which α-Al_2O_3 islands nucleate in the metastable θ matrix and grow laterally until impingement [4,7,11]. Obviously, when the distance between neighboring α-Al_2O_3 nuclei is smaller than the probe size, the luminescence spectrum will contain overlapping α and θ signals from closely spaced α and θ regions. It was, therefore, important to analyze the cases when individual α nuclei are large enough and can be clearly resolved.

The micrographs in Figure 12 show the morphology of a partially transformed $\alpha+\theta$ scale formed on a 1-μm polished surface after oxidation at 1,120°C for 15 min. At this temperature, isolated islands of α-Al_2O_3 are much larger than at 1,100°C and can readily be probed by PSLS. There is also a clear contrast in both SEM [Figures 12(a) and (b)] and optical [Figure 12(c)] images due to the difference in surface microstructure. The central region of each island is rather smooth, while their periphery and the surrounding θ matrix are covered with small whiskers. As suggested above, this difference results from a gradual advancement of the transformation front from the nucleation center: whiskers did not develop in the center of islands which transformed earlier. Radial tears (cracks) in the α-islands [Figure 12(b)] form because of a large volume shrinkage associated with the $\theta \rightarrow \alpha$ transformation in the scale [7].

Figure 13(a) shows typical profiles of the luminescence intensity of α-Al_2O_3 and θ-Al_2O_3 across the alpha-alumina island shown in Figure 12(b). The intensity is taken as the integrated area of all peaks for each phase regardless of their stress-induced shifts. Similar profiles after longer oxidation time are shown in Figure 13(b). These results provide the following information about the phase transformation.

The central part of each island is completely transformed into α-Al_2O_3 including the oxide which forms on a freshly exposed metal surface inside the tears. On the other hand, no alpha-alumina is present beyond the radius of about 20 μm (after 15 min) or 25 μm (after 1 h).

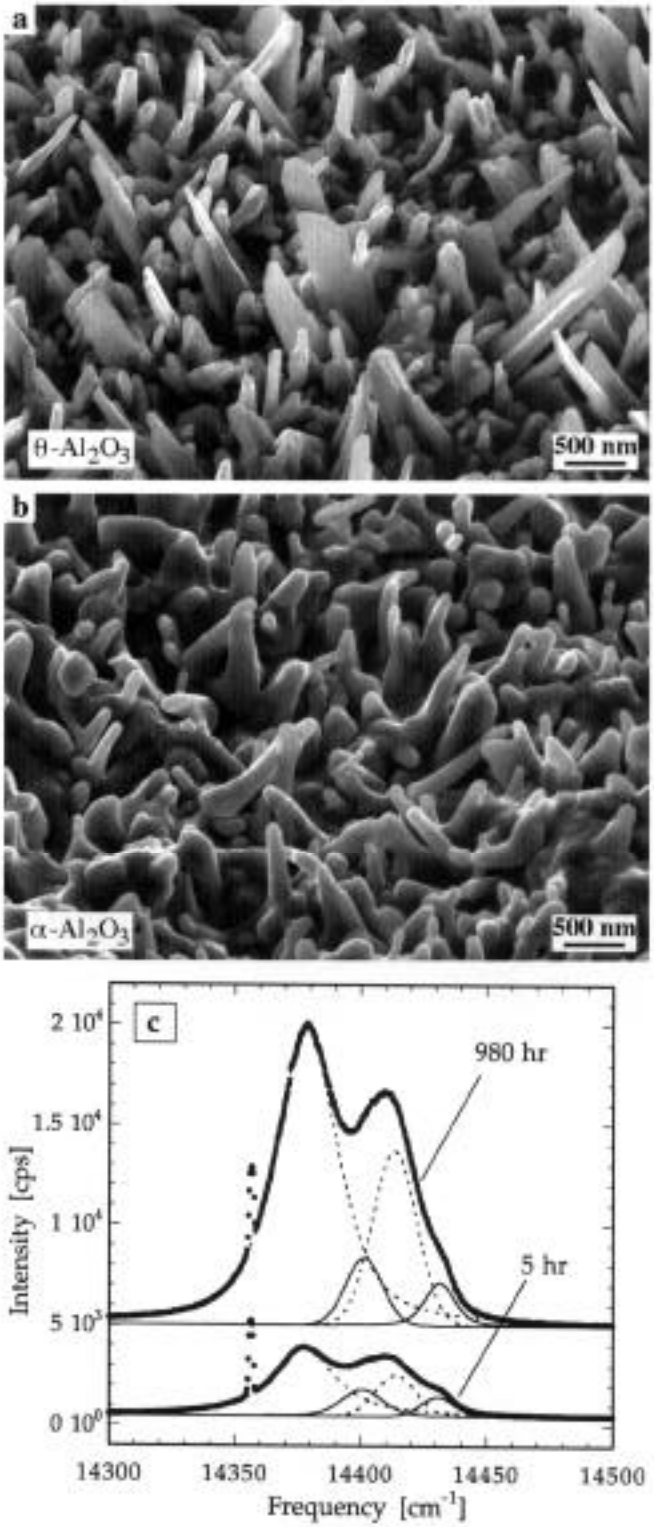

Figure 11 Surface morphology of θ scale on 1-μm polished sample after 0.5 h at 1,100°C (a) and α scale on the same sample after 980 h at 1,100°C (b). Two asymmetrical luminescence spectra shown in (c) indicate the contribution of the low-stress signal from α whiskers.

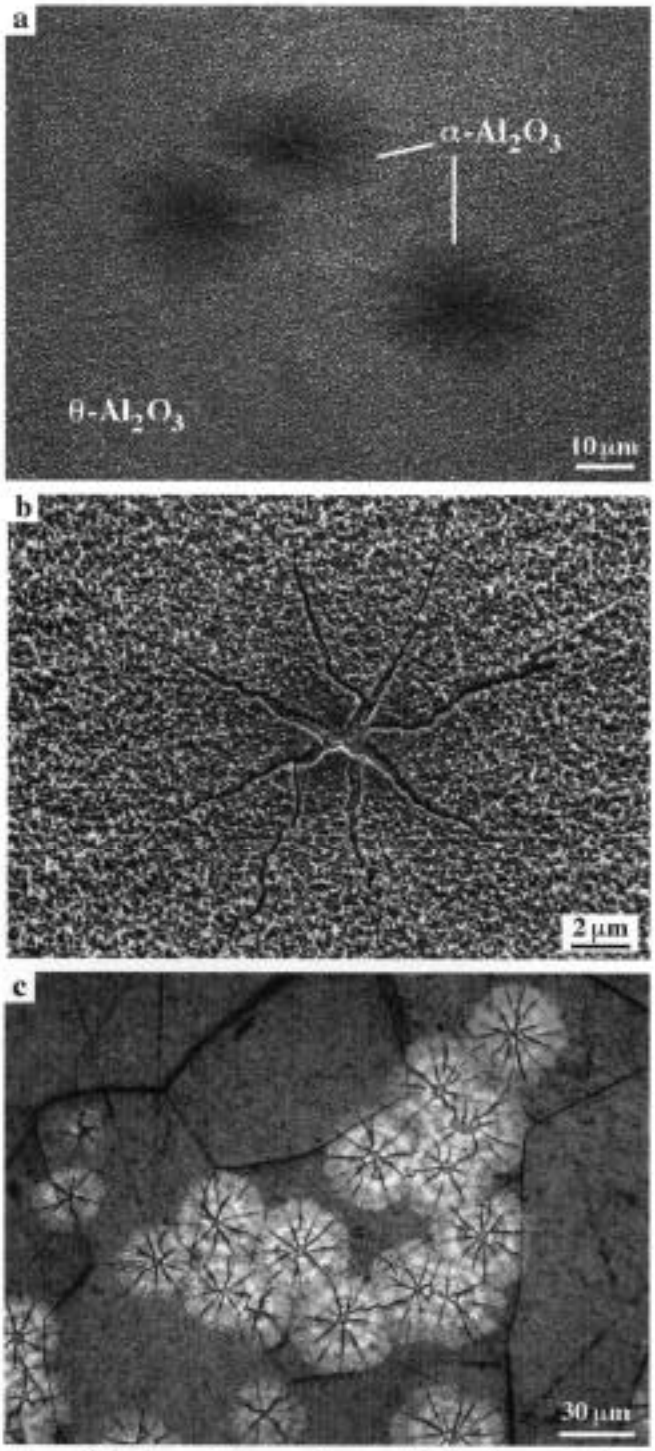

Figure 12 Oxide morphology on 1-μm polished surface after 15 min oxidation at 1,120°C: (a) general view of θ-Al_2O_3 scale with circular α-Al_2O_3 islands; (b) tensile cracks (tears) in the center of α-Al_2O_3 island and small whiskers at the periphery; (c) optical image demonstrating a distinct contrast between α-Al_2O_3 islands and θ-Al_2O_3 matrix.

The alpha luminescence intensity is the smallest at the center of each island and increases toward its periphery. Since the intensity is proportional to the oxide thickness, it means that the islands are thinner in their central part. This, in turn, shows that early transformation produces a thinner alpha layer, whereas, as the front moves away, the theta layer becomes thicker and transforms into a thicker alpha layer at the perimeter of the islands. The presence of circular interference fringes on the optical images [Figures 12(c) and 14(d)] confirms that the oxide thickness varies with distance from the center. A two-phase α+θ zone, which is more than 10 μm wide after 15 min, indicates the area at the periphery of each α-island where the two phases coexist. The variation of α and θ intensities across this area (Figure 13) means that the relative amount of alpha gradually decreases with increasing distance from the center. Most probably, it results from a non-uniform advancement of the transformation front.

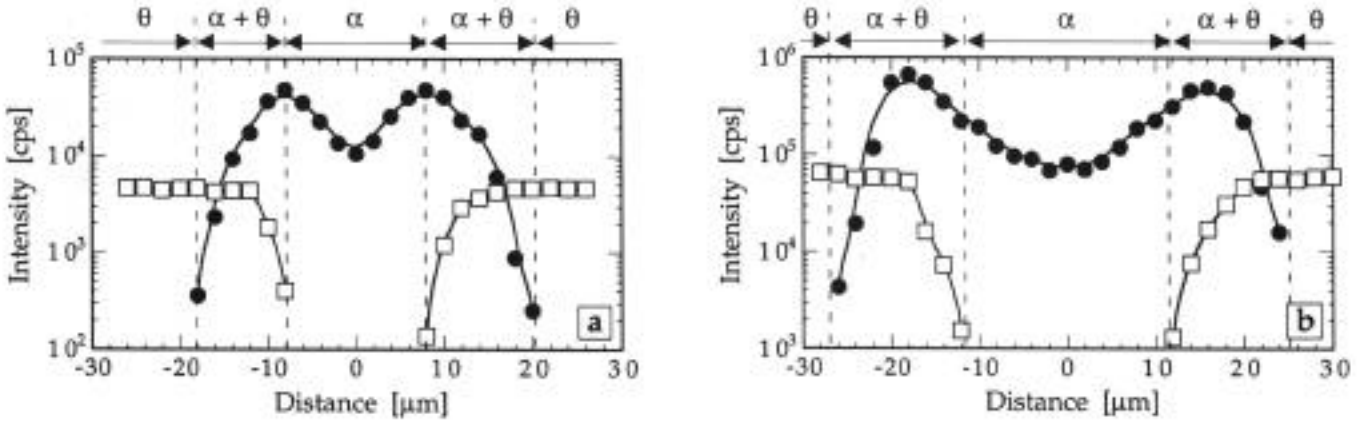

Figure 13 Profiles of the luminescence intensity across α-Al_2O_3 islands, shown in Figure 12, after oxidation at 1,120°C for 15 min (a) and 1 hr (b). Open squares - θ-Al_2O_3; solid circles - α-Al_2O_3.

After longer oxidation, θ-Al_2O_3 eventually disappears as a result of both the lateral growth of existing α-islands and formation of new alpha-nuclei [Figure 14(a)]. The latter process is accompanied by the development of 'secondary' tears in the scale [Figure 14(c)]. These new alpha-regions can be identified by PSLS and distinguished from the 'primary' α-islands because the oxide, transformed at the later stages, retains the surface morphology typical to that of theta-alumina. This also explains the optical contrast between the primary α-islands and the oxide transformed later [Figure 14(d)]. Further widening of the tears, seen in Figure 14(b), occurs as a result of the growth of small α-Al_2O_3 grains. Eventually, these grains form outward protrusions (ridges) which were reported earlier in oxidation studies of β-NiAl [1,2,4–8]. It should be clarified, however, that the formation and growth of the ridges occurs long after the $\theta \rightarrow \alpha$ transformation is complete (Figure 15).

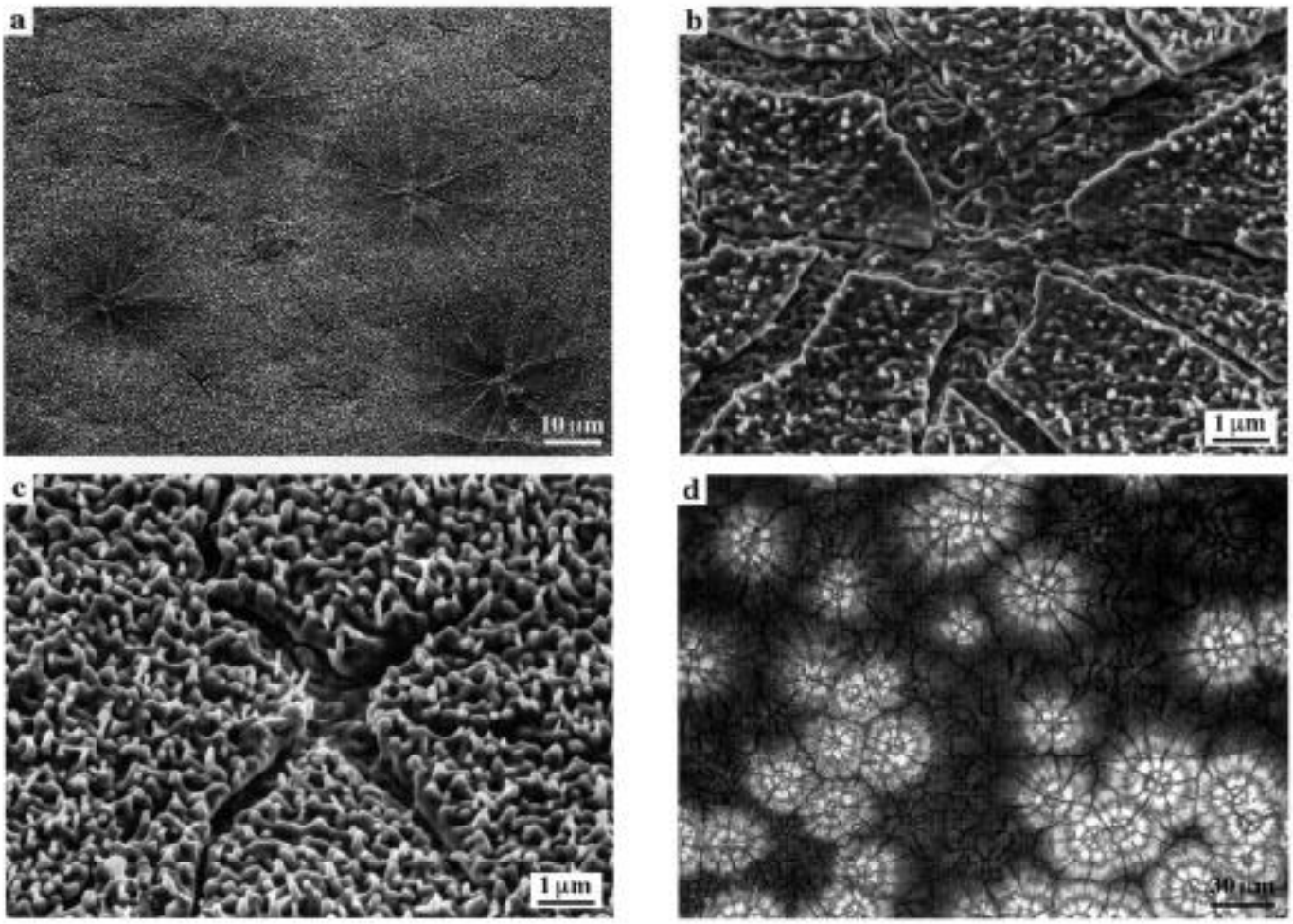

Figure 14 Oxide morphology on 1-μm polished surface after 10 h oxidation at 1,120°C: (a) general view of pure α-Al_2O_3 scale where the circular islands are still visible; (b) the tears in the center of islands become wider; (c) 'secondary' tears in the α-Al_2O_3 scale between the 'primary' islands; (d) optical image of the α-Al_2O_3 scale shown in (a).

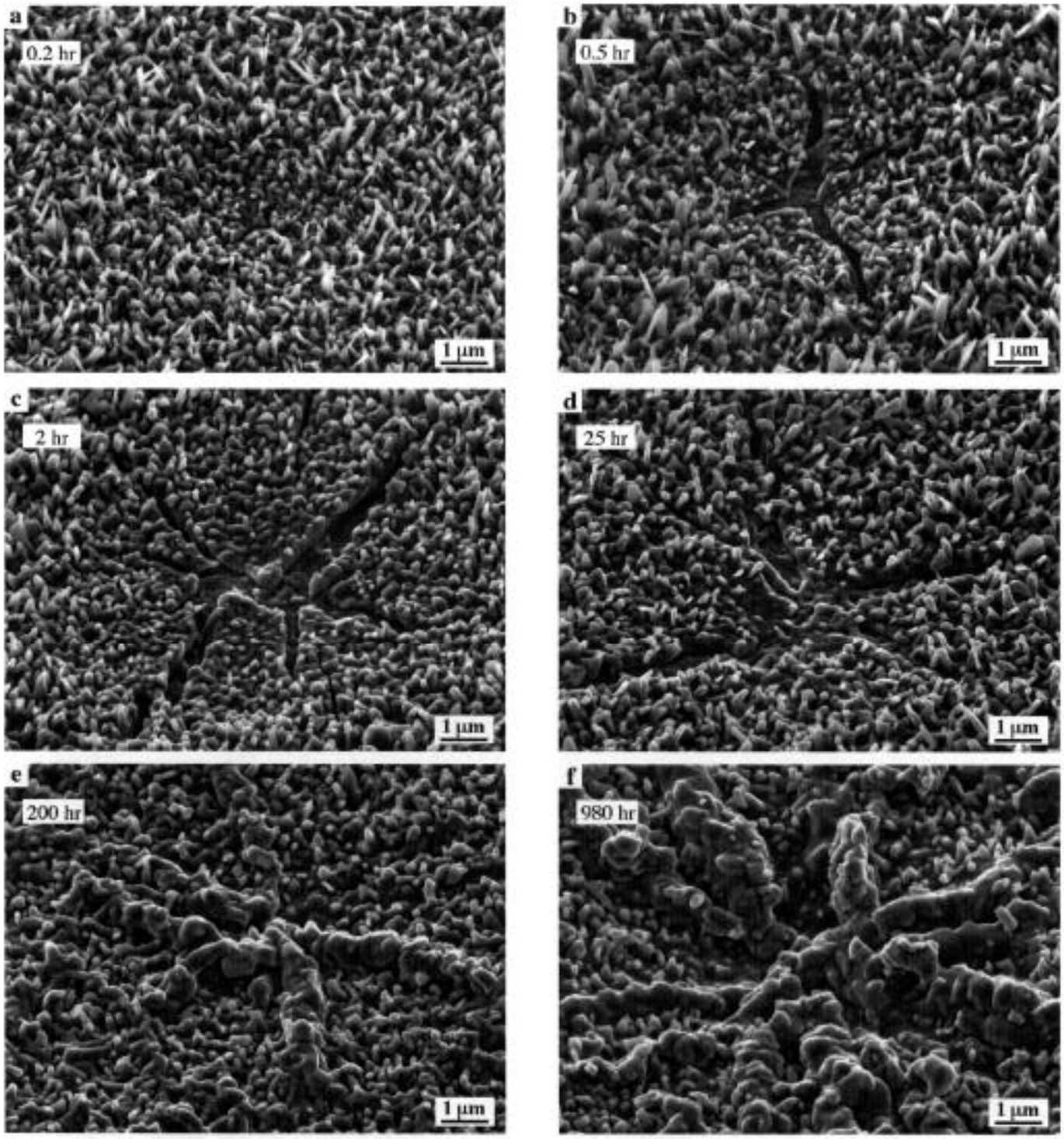

Figure 15 Evolution of the oxide morphology on the polished (1-μm) surface of (Ni,Pt)Al during oxidation at 1,100°C: (a) a small area of α-Al_2O_3 in θ matrix after 12 min; (b) further opening of radial tears and whisker growth; (c) the scale is entirely α-Al_2O_3 after 2 h; (d)–(f) the tears become filled with a conglomerate of small alpha grains and develop into radial ridges which continue to grow outwards.

5. THE EFFECT OF SURFACE ROUGHNESS AND OXIDATION TEMPERATURE.

Analysis of the oxide morphology in the previous section suggests that the structure of α-Al_2O_3 scale depends on the way the $\theta \rightarrow \alpha$ transformation occurs. In particular, two factors appear to be of importance: density of α nuclei in the θ scale and their growth rate. It was established [4,6] that the transformation is accelerated at higher temperatures and takes much longer at lower temperatures. Oxidation temperature apparently determines the growth rate of individual α-Al_2O_3 nuclei (certainly, there may also be an incubation period before the first nuclei appear, especially, at lower temperatures). It is reasonable to assume that the growth rate of α grains in a θ matrix is some constant for a given temperature. In this case, the overall transformation rate should be proportional to the density of α-nuclei.

Observations of the alumina scale morphology after different surface finishes show that scratches and other microscopic defects on the metal surface provide places for the nucleation of α-Al_2O_3. One of the examples of this phenomenon was presented in Figure 9(b), where the variation of the length of whiskers indicated that

α-Al_2O_3 appeared first along a scratch mark and then propagated sideways. With a higher density of alpha-nuclei on a rough surface, an earlier impingement of growing α grains will produce a continuous α layer earlier than on a smooth surface. For example, the transformation is 3–5 times faster on the surface after 400-grit SiC than after 1-μm polishing at all temperatures studied. Moreover, the grain size of the resulting α-Al_2O_3 scale can be also affected, as illustrated in Figure 16. During oxidation at 1,200°C, the $\theta \rightarrow \alpha$ transformation is complete after a few minutes, as confirmed by PSLS data. It was, in fact, difficult to determine whether the metastable oxide indeed formed initially at such a high temperature, or it appeared only during heating. Nevertheless, on a smoother surface with 800-grit finish [Figure 16(a)], the grains of α-alumina are several times larger than with 400-grit finish [Figure 16(b)]. During further oxidation the grain size essentially does not change, as seen in Figure 16(c). The grain boundary ridges, formed at the boundaries between adjacent α-Al_2O_3 grains, become coarser with oxidation time. Notably, the thickness of α grains remains very small, for example, below 1 μm after 50 hr at 1,200°C, while the grain boundaries form deep protrusions [Figure 16(d)].

Another example of the effect of surface finish on the scale morphology is presented in Figure 17. The optical micrographs show the oxide formed during oxidation at 1,000°C for 250 h after 1-μm polishing [Figure 17(a)] and 400-grit SiC grinding [Figure 17(b)]. Tears in the oxide are clearly seen on the polished sample but not on the abraded sample. Both oxides are fully transformed to α-Al_2O_3, however the transformation takes place in about 30 h on the rough surface and more than 100 h on the polished surface. The major difference between these two samples is the density of alpha-alumina nuclei. The α-Al_2O_3 scale on the rough surface exhibits alternating regions with short and long whiskers [Figure 17(d)]. Shorter whiskers show the places where α-Al_2O_3 nucleated in the θ-scale. On the polished surface [Figure 17(c)], these places are much further apart, therefore θ-Al_2O_3 remains longer. For the same reason whiskers are longer at 1,000°C [Figure 17(c,d)] than at 1,100°C (Figures 9,11), reflecting the time-span during which they remained θ-Al_2O_3.

6. CONCLUDING REMARKS

Summarizing the observations made in this work, it appears that oxidation temperature is only one of the factors which affects the phase transformation and the morphology of α-Al_2O_3 scales on the (Ni,Pt)Al alloy. The $\theta \rightarrow \alpha$ transformation can be 'delayed' on a smooth, polished surface, or it can be 'accelerated' on a rough surface. Apparently, the population density of alpha nuclei in θ-Al_2O_3 scale plays a role. Although θ-Al_2O_3 eventually transforms into stable α-Al_2O_3, the resulting

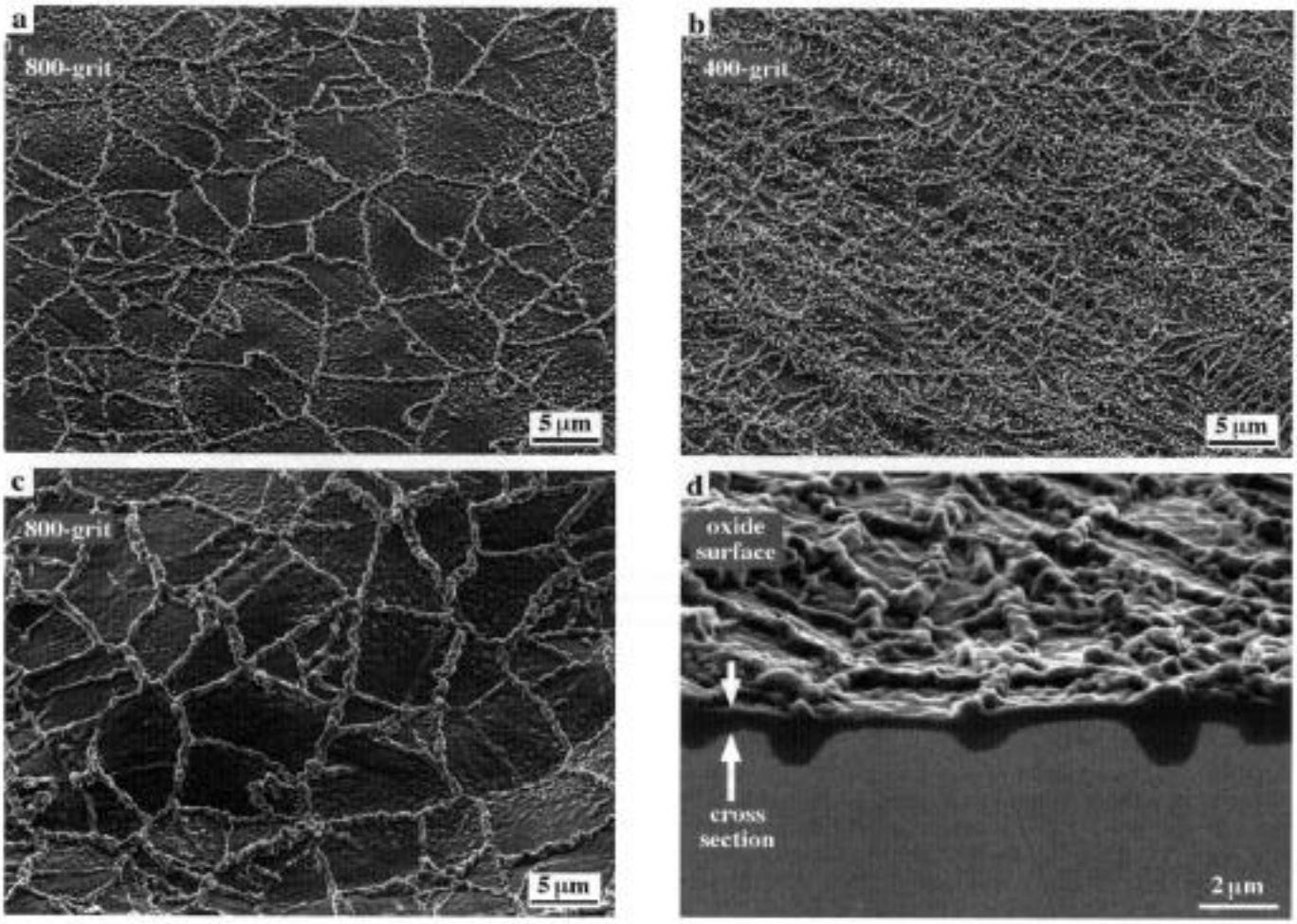

Figure 16 An example of the effect of surface roughness on the α-Al_2O_3 morphology formed at 1,200°C: (a) - 800-grit surface finish, 1 h; (b) 400-grit surface finish, 1 h; (c and) 800-grit surface finish, 50 h. The polished cross section in (d) demonstrate thin α grains and thicker grain boundary regions with outer ridges and inner protrusions.

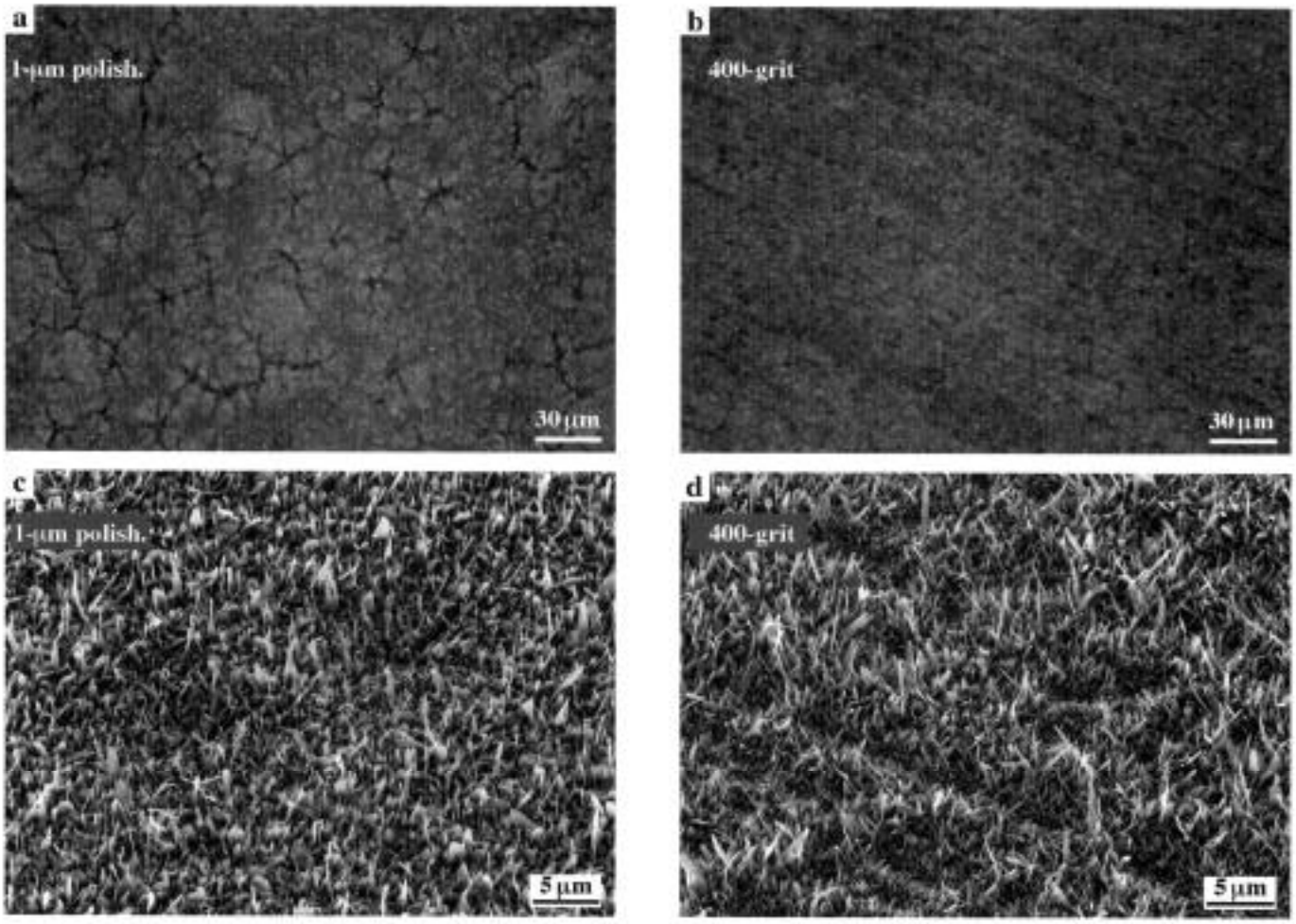

Figure 17 Optical (a,b) and SEM (c,d) images of alumina scale formed on 1-μm polished (a) and (c) and 400-grit abraded surface (b) and (d) during oxidation at 1000°C: the scale is α-Al_2O_3 after 250 h on both samples (a,b), whereas after 50 hr the scale is mixed $\alpha+\theta$ on the polished sample (c) and purely α-Al_2O_3 on the abraded sample (d).

oxide morphology (and, possibly, its protective properties) depends on the transient oxidation behavior.

The results show that luminescence spectroscopy can be successfully used for a detailed analysis of the phase transformation in alumina scales. The PSLS method provides a means to identify metastable theta-alumina and follow the evolution of the $\theta \rightarrow \alpha$ transformation. One of the questions remaining to be answered is to what extent the phase transformation affects performance of protective alumina scales. Finally, although this study has been performed on one specific alloy, the results are believed to be applicable to other aluminides which form metastable alumina phases.

ACKNOWLEDGMENTS

The authors are grateful to Mr. K.S. Murphy at Howmet Research Corporation for providing samples for this study and to the DOE-AGTSR for financial support.

REFERENCES

[1] Smialek, J.L. Oxide morphology and spalling model for NiAl. *Met. Trans.* **9A**(3), 309-320 (1978).
[2] Hindam, H.M. and Smeltzer, W.W. Growth and microstructure of α-Al_2O_3 on β-NiAl. *J. Electrochem. Soc.* **127**(7), 1630-1635 (1980).
[3] Young, E.W.A. and de Wit, J.H.W. The use of a ^{18}O tracer and Rutherford backscattering spectrometry to study the oxidation mechanism of NiAl. *Solid State Ionics* **16**, 39-46 (1985).
[4] Rybicki, G.C. and Smialek J.L. Effect of the θ-α-Al_2O_3 transformation on the oxidation behavior of β-NiAl+Zr. *Oxid. Met.* **31**(3/4), 275-304 (1989).
[5] Doychak, J. and Rühle, M. TEM studies of oxidized NiAl and Ni_3Al cross sections. *Oxid. Met.* **31**(5/6), 431-452 (1989).
[6] Brumm, M.W. and Grabke, H.J. The oxidation behavior of NiAl – I. Phase transformations in the alumina scale during oxidation of NiAl and NiAl-Cr alloys. *Corros. Sci.* **33**(11), 1677-1690 (1992).
[7] Lipkin, D.M., Clarke, D.R., Hollatz, M., Bobeth, M. and Pompe, W. Stress development in alumina scales formed upon oxidation of (111) NiAl single crystals. *Corros. Sci.* **39**(2), 231-242 (1997).
[8] Pint, B.A., Treska, M. and Hobbs, L.W. The effect of various oxide dispersions on the phase composition and morphology of Al_2O_3 scales grown on β-NiAl. *Oxid. Met.* **47**(1/2), 1-20 (1997).
[9] Yang, J.C., Schumann, E., Levin, I. and Rühle, M. Transient oxidation of NiAl. *Acta Materialia* **46**(6), 2195-201 (1998).
[10] Doychak, J., Smialek, J.L. and Mitchell, T.E. Transient oxidation of single-crystal β-NiAl. *Met. Trans.* **20A**(3), 499-518 (1989).
[11] Lipkin, D.M., Schaffer, H., Adar, F., and Clarke, D.R. Lateral growth kinetics of α-alumina accompanying the formation of a protective scale on (111) NiAl during oxidation at 1100°C. *Appl. Phys. Lett.* **70**(19), 2550-2552 (1997).
[12] van Manen, P.A., Leibbrandt, G.W.R., Klumpes, R. and de Wit, J.H.W. The oxidation mechanism of $Pt_{20}Ni_{50}Al_{30}$. *Journal de Physique IV*, **3**(C9), 123-131 (1993).
[13] Haynes, J.A., Zhang, Y., Lee, W.Y., Pint, B.A., Wright, I.G. and Cooley, K.M. Effects of platinum additions and sulfur impurities on the microstructure and scale adhesion behavior of single-phase CVD aluminide bond coatings. In: *Elevated Temperature Coatings: Science and Technology III*. Ed. J.M. Hampikian and N.B. Dahotre, The Minerals, Metals & Materials Society, pp.185-196 (1999).

[14] Warnes, B.M., Punola, D.C. Clean diffusion coatings by chemical vapor deposition. *Surf. Coat. Technol.* **94-95**(1-3), 1-6 (1997).
[15] Lipkin, D.M. and Clarke, D.R. Measurements of the stress in oxide scales formed by oxidation of alumina-forming alloys. *Oxid. Met.* **45**(3/4), 267-280 (1996).
[16] Wen, Q., Lipkin, D.M., and Clarke, D.R. Luminescence characterization of chromium-containing θ-alumina. *J. Am. Ceram. Soc.* **81**(12), 3345-3348 (1998).
[17] Atkinson, A., Clarke, D.R., and Webb, S.J. Mapping residual stress using optical microprobe in alumina films formed by thermal oxidation of NiAl. *Mater. Sci. Technol.* **14**(6), 531-534 (1998).
[18] Ma, Q. and Clarke, D.R. Stress measurement in single-crystal and polycrystalline ceramics using their optical fluorescence. *J. Am. Ceram. Soc.* **76**(6), 1433-1440 (1993).
[19] He, J. and Clarke, D.R. Determination of the piezospectroscopic coefficients for chromium-doped sapphire. *J. Am. Seram. Soc.* **78**(5), 1347-1355 (1995).
[20] Simpson, T.W., Wen, Q., Yu, N., and Clarke, D.R. Kinetics of the amorphous→γ→α transformations in aluminum oxide: effect of crystallographic orientation. *J. Am. Ceram. Soc.* **81**(1), 61-66 (1998).
[21] Feofilov, S.P., Kaplyanskii, A.A., Kutsenko, A.B., Vasilevskaya, T.N. and Zakharchenya, R.I. Sol-gel technology grown monolithic highly porous aluminum oxide with chromium and rare earth ions and size-resonant terahertz acoustic vibrations of nanocrystalline particles. *Materials Science Forum* **239-241**, 687-690 (1997).
[22] Alexander, K.B., Prüssner, K., Hou, P.Y. and Tortorelli, P.F. Microstructure of alumina scales and coatings on zirconium-containing iron aluminide alloys. In: *Microscopy of Oxidation 3*. Eds. S.B. Newcomb and J.A. Little, The Insitiute of Materials, pp.246-255 (1997).

PERGAMON

Appendix H

Acta mater. Vol. 47, No. 4, pp. 1297–1305, 1999

Printed in Great Britain
1359-6454/99 $19.00 + 0.00

PII: S1359-6454(98)00407-8

SPALLING FAILURE OF A THERMAL BARRIER COATING ASSOCIATED WITH ALUMINUM DEPLETION IN THE BOND-COAT

E. A. G. SHILLINGTON and D. R. CLARKE†

Materials Department, College of Engineering, University of California, Santa Barbara, CA 93106-5050, U.S.A.

(Received 16 June 1998; accepted 23 November 1998)

Abstract—A plasma-sprayed thermal barrier coating is observed to spall after oxidation at 1121°C from a CoNiCrAlY bond-coated superalloy at the interface between the thermally grown oxide (TGO) and the zirconia thermal barrier coating (TBC). Phase characterization by photostimulated luminescence and X-ray diffraction, as well as microstructural characterization by scanning electron microscopy, indicates that the spalling is associated with the conversion of the initially formed α-alumina thermally grown oxide to α-chromia and a (CoNi)(CrAl) spinel. It is proposed that the phase conversion occurs after the alumina TGO has cracked on thermal cycling and the underlying bond-coat alloy is depleted of aluminum with concurrent enrichment of the oxide by Cr, Co and Ni. The observations suggest that monitoring the luminescence intensity as a function of oxidation time might form the basis of a nondestructive tool for detecting the onset of failure based on the disappearance of α-alumina. © *1999 Acta Metallurgica Inc. Published by Elsevier Science Ltd. All rights reserved.*

1. INTRODUCTION

Although thermal barrier coatings (TBCs) are already being widely used in a variety of gas turbine and diesel engine applications, greater benefits are expected to accrue with TBCs that can be used in critical applications, namely those in which a loss of the coating would expose the underlying metal to a temperature in excess of its design specifications. This requires an increase in the reliability of the coatings particularly with regard to failure by spalling since the TBCs are usually under biaxial compression, as a result of the smaller coefficient of thermal expansion of most TBCs compared with the underlying metal.

Considerable increases in the reliability of TBCs have come from improvements in the processes used for deposition, in large part because of improvements in coating consistency. However, one of the difficulties in choosing a combination of alloy/bond-coat/TBC for improved reliability is that the mechanisms by which TBCs spall have not been fully identified. There is an additional complication in that there is circumstantial evidence to suggest that different failure mechanisms pertain in the failure of TBCs deposited by electron beam evaporation and plasma-spraying. This is further complicated by the fact that plasma-sprayed coated materials tend to be used at lower temperatures than those deposited by electron beam evaporation. In this work we present experimental observations suggesting that one failure mode is associated with a compositional change in the thermally grown oxide from alumina to a mixture of chromia and spinel, and that this is, in turn, associated with depletion of Al from the bond-coat and concurrent enrichment of Co, Ni and Cr in the oxide. Failure of alumina scales on overlay oxidation coatings has previously been associated with aluminum depletion effects [1–3] and it has recently been implicated in the failure of TBCs on a MCrAlY bond-coat [4].

The coated system investigated in this work was an IN939 superalloy with a MCrAlY (CT102) bond-coat of nominal composition 38Co–32Ni–21Cr–8Al–0.8Y (wt%) and a plasma-sprayed thermal barrier coating of nominal composition ZrO_2–9% Y_2O_3. For purposes of evaluating the dependence of the thickness of the TBC coating on the residual stress, the TBC had been polished at an angle of 1:100 to produce a gradient in TBC thickness across the sample as well as to expose the bond-coat on one side. The sample is shown in the optical micrograph of Fig. 1, with the exposed bond-coat at the left-hand side. (The vertical bands correspond to different thicknesses of the TBC and the dark, circular dot is a hole drilled in the specimen so as to suspend it in the furnace during oxidation.)

†To whom all correspondence should be addressed.

2. RESIDUAL STRESS EVOLUTION ON OXIDATION

The specimen was oxidized in air at 1121°C for successively longer periods of time (1, 2, 4, 8, 16, 32 h). After each oxidation the sample was cooled to room temperature and the photostimulated Cr^{3+} fluorescence (luminescence) spectrum recorded. The luminescence was studied as both a probe for the presence of α-alumina and the piezospectroscopic measurement of residual stress in the oxide formed at the interface between the TBC and the bond-coat alloy. The experimental procedure and the data analysis have been described previously [5–8]. The nominal compressive stress was determined from the observed frequency using the phenomenological equation:

$$\Delta\nu_{\text{stress}} = \Pi_{ij}\sigma^{c}_{ij} = \Pi_{ij}a_{ki}a_{lj}\sigma_{kl} \tag{1}$$

where Π_{ij} is the ijth component of the piezospectroscopic tensor and σ^{c}_{ij} the stress state in the crystallographic basis of the host crystal. (The Einstein summation convention is assumed.) In a general coordinate system, the stress state, σ_{ij}, is related to σ^{c}_{ij} by the transformation matrix, a_{ij}. Because the off-diagonal terms of the piezospectroscopic tensor are nearly zero for alumina [9], equation (1) may be substantially reduced:

$$\Delta\nu_{\text{stress}} = \Pi_{ii}\sigma_{jj} - [\Pi_a(a_{i2}a_{j2} + a_{i3}a_{j3}) + \Pi_m(a_{i1}a_{j1} + a_{i3}a_{j3}) + \Pi_c(a_{i1}a_{j1} + a_{i2}a_{j2})]\sigma_{ij} \tag{2}$$

where the subscripts a, m and c refer to the respective crystallographic directions in the corundum structure. For an untextured polycrystalline material, provided the volume probed by the exciting laser beam is large compared to the grain size, the piezospectroscopic shift can be shown to depend only on the hydrostatic component of the stress:

$$\overline{\Delta\nu} = \frac{1}{3}\Pi_{ii}\sigma_{jj} \tag{3}$$

where equation (3) is obtained by averaging equation (2) over all spatial orientations. For oxide scales having no crystallographic texture, the stresses can be assumed to be equi-biaxial, such that $\sigma_{xx} = \sigma_{yy} = \bar{\sigma}$ and $\sigma_{zz} = 0$. In this limit, equation (3) reduces to

$$\overline{\Delta\nu} = \frac{2}{3}\Pi_{ii}\bar{\sigma} \tag{4}$$

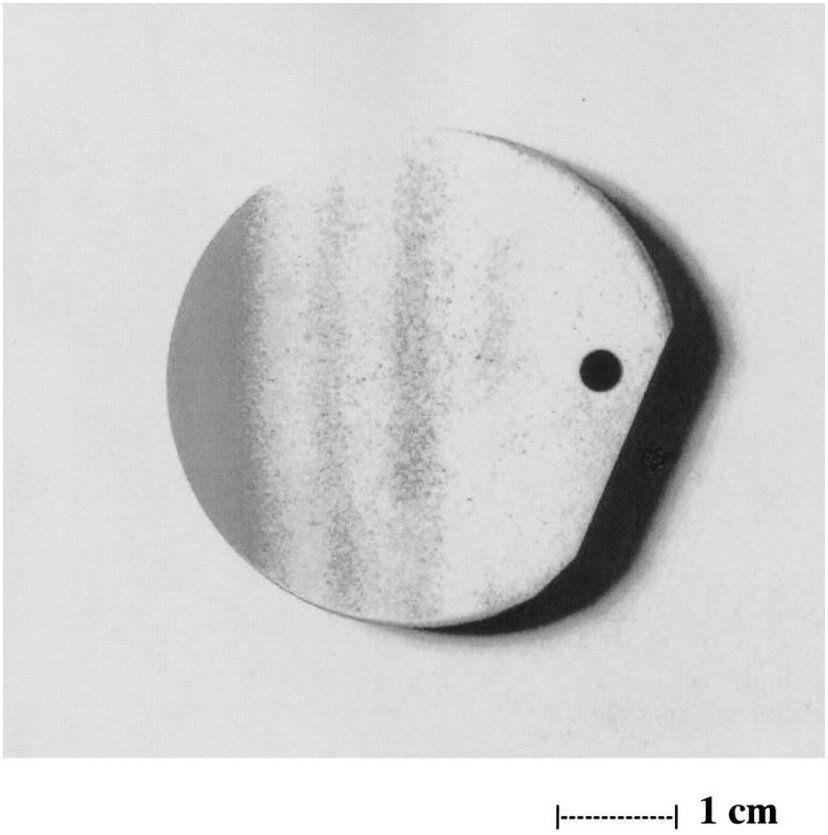

Fig. 1. Optical micrograph of the plasma-sprayed TBC after taper polishing the TBC so that the bond-coat is exposed at the left-hand side. (The hole is used to suspend the sample in the oxidation furnace.)

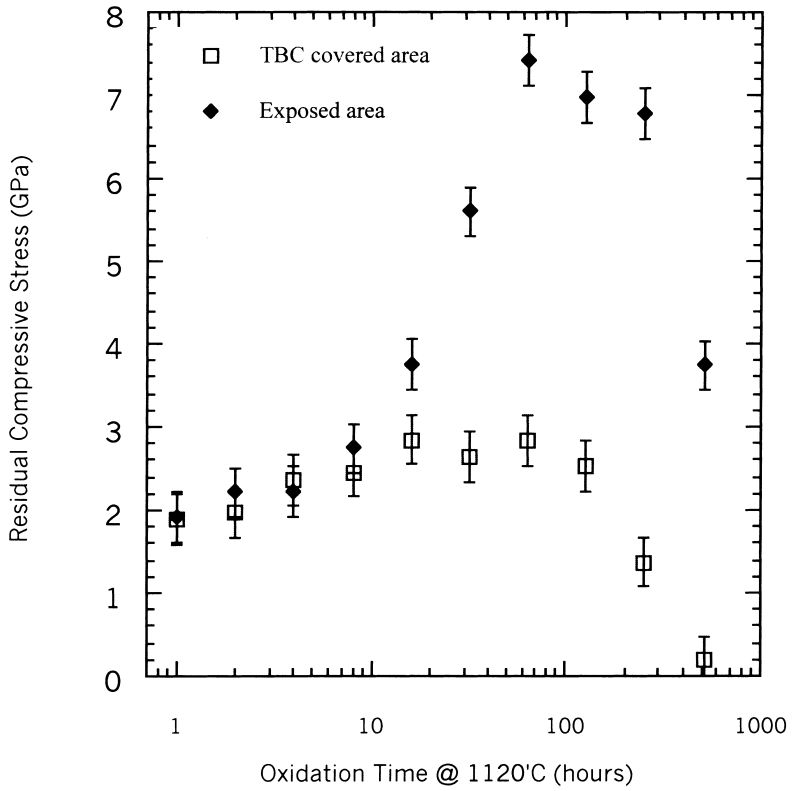

Fig. 2. The nominal biaxial compressive residual stress in the thermally grown alumina as a function of oxidation time at 1121°C. The stresses were calculated from the measured frequency shift of the R2 fluorescence line using equation (4) in the text.

where $\bar{\sigma}$ is the net effect of the growth stresses established at the oxidation temperature and the thermal expansion mismatch stress arising upon cooling. The experimentally measured value of Π_{ii} is 7.60 cm^{-1}/GPa for both of the ruby lines [9]. The term, nominal compressive stress, is used since the relationship of equation (1) assumes that the oxide is formed on a flat surface. When the surface is not flat, the determination of the residual stress state from the observed frequency shift requires a detailed and quantitative knowledge of the surface roughness [10]. (The same proviso of course, pertains to the interpretation of residual stress from X-ray diffraction measurements [10].)

Not normally considered is that changes in chromium concentration in the α-alumina also cause a shift in the characteristic luminescence lines. According to Kaplyanskii *et al.* [11], the frequency shift varies linearly with chromium concentration, c_m, as $\Delta\nu = 0.99c_m$, so increasing chromium concentration has the same effect as decreasing hydrostatic stress.

Since the bond-coat was exposed in polishing the wedge, both thermally grown oxide on the bare bond-coat as well as under the TBC could be probed after each oxidation exposure. The evolution of the nominal compressive stress in the thermally grown oxide is shown in Fig. 2. (Note, the oxidation time is plotted on a logarithmic scale.) The stress under the TBC builds up slowly with time for the first 10 h and then remains almost constant at about 2.5 GPa up to about 128 h. In this respect it behaves in a similar manner to the stress evolution on the same bond-coat under an EB-PVD coating. In contrast, the compressive stress in the thermally grown oxide on the polished bond-coat surface continued to increase up to a maximum of about 7.5 GPa. The higher value of the nominal stress on the polished bond-coat than under the TBC is attributed to the fact that the bond-coat is rough under the TBC and so it is not in a state of biaxial compression as it is on the polished surface. As a result, there are out-of-plane stresses in the thermally grown oxide and so the simple relation of equation (4) cannot strictly be used. Nevertheless, for comparison purposes, as is done in this work, it is used. (The effect of sinusoidal roughness is to decrease the observed frequency shift [10] but without quantitative knowledge of the detailed geometry of the roughness of the coating, the actual stress in the alumina cannot be determined.)

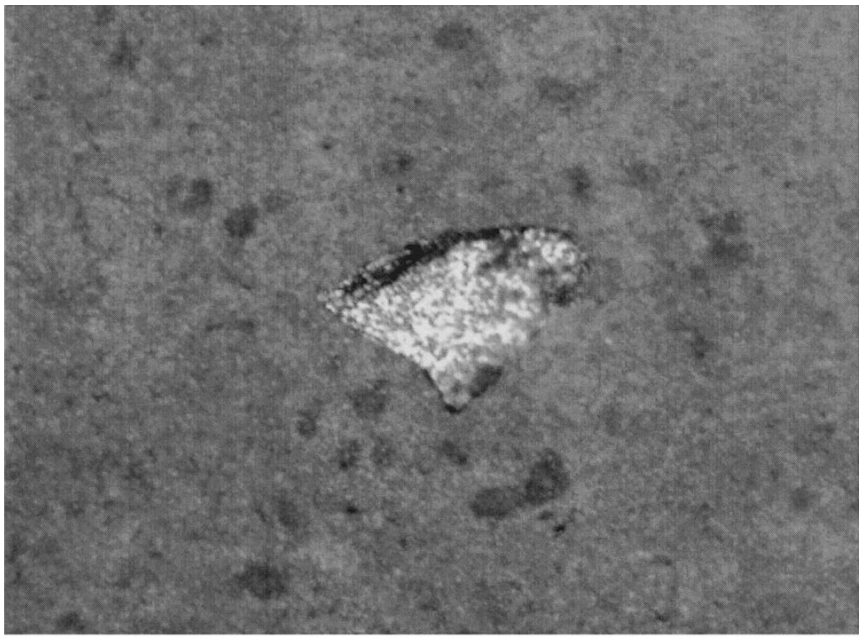

Fig. 3. An example of the occasional localized spalling noted after oxidation. The spalling in these cases occurs at the interface with the bare bond-coat as indicated by the specular optical reflection from these regions and the absence of any luminescence.

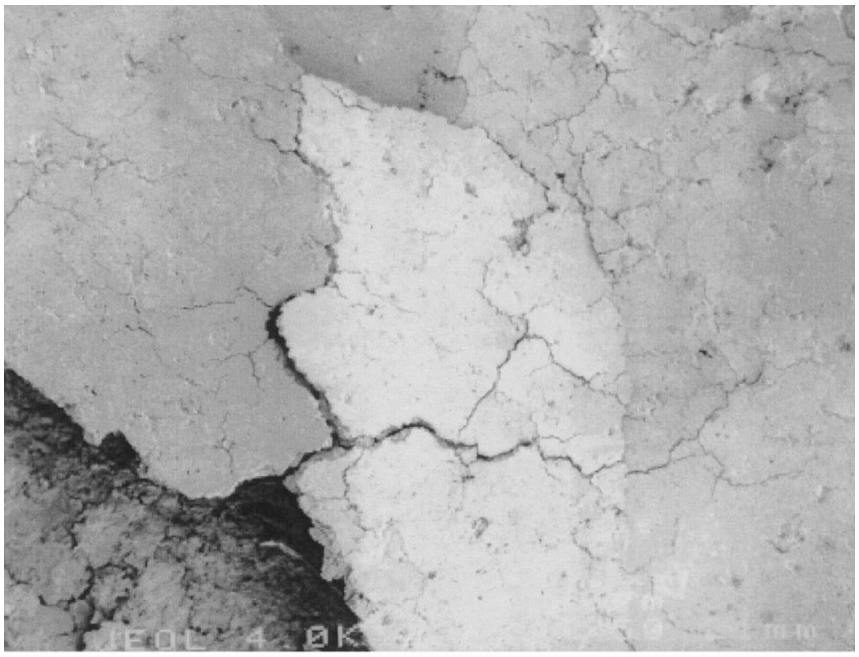

Fig. 4. The surface of the small region of still adhering TBC after the majority of the TBC had spalled away. Extensive cracking and buckling of the TBC is apparent. Scanning electron micrograph.

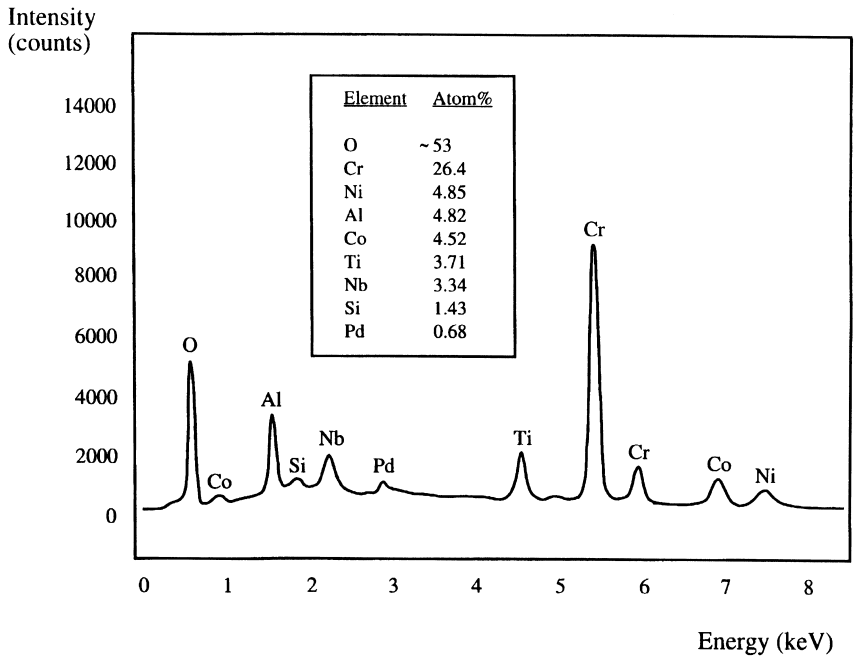

Fig. 5. Energy dispersive X-ray spectrum recorded from the bond-coat surface exposed by spalling.

Then, with subsequent oxidation after 128 h the frequency shift, and hence the nominal compressive stress, began to decrease in magnitude on both the polished bond-coat surface and under the thermal barrier coating, as shown by the data in Fig. 2. In addition, small isolated spalls, such as shown in the photomicrograph of Fig. 3, also began to occur after 128 h with the spalling occurring at the bond-coat/TGO interface exposing the bare metal. Finally, after a total of 512 h oxidation at 1121°C, most of the TBC spalled, in one piece, from the bond-coat on cooling. The spalled piece was preserved for analysis as was the bond-coat surface exposed by the spalling.

3. POST-SPALLING CHARACTERIZATION

Although most of the TBC had spalled away, a small region remained adhered to the specimen. The intensity of the fluorescence was very low, almost two orders of magnitude smaller than that from the coating after 128 h. In addition, the nominal compressive stress determined from the luminescence frequency was almost zero (Fig. 2). Examination of both the bond-coat surface exposed by the spalling and the underside of the spalled TBC revealed that fluorescence was only obtained from small isolated patches, a few microns across, suggesting that little α-alumina remained on either the bond-coat or the TBC surfaces.

The adhered piece of the TBC and the bond-coat surface exposed by the spalling were examined using scanning electron microscopy. As shown in Fig. 4, the adhered TBC was extensively cracked and appeared to have buckled. Scanning microscopy of the exposed bond-coat surface was not useful in identifying the nature of the surface but EDAX analysis of the surface revealed a high concentration of Cr and only comparatively low concentrations of Al, Co, Ni, Ti and Nb (Fig. 5). X-ray diffraction analysis of the surface, Fig. 6, revealed a much more complex picture indicating mainly Cr_2O_3 and a spinel phase, possibly a (Co,Ni)(Cr,Al) spinel, as well as the presence of weaker peaks of Al_2O_3 and zirconia and rutile. The X-ray diffraction analysis identification of chromia, spinel and the other phases was thus consistent with there being little detectable fluorescence from α-Al_2O_3 over most of the surface. Interestingly, the lattice parameters, determined from the X-ray diffraction peaks, of both the α-Cr_2O_3 and the remaining α-Al_2O_3 corresponded to that of the bulk, unstrained oxides.

4. PHASE EVOLUTION IN THE THERMALLY GROWN OXIDE

In order to elucidate the changes in the thermally grown oxide during oxidation a series of experiments were performed to characterize the phases and their spatial distribution at different oxidation times. Pieces of the same bond-coated alloy were oxidized for different times (64, 128, 256, 384, 512 and 640 h) at 1121°C and the plasma-sprayed coating was then pried from the samples to facilitate X-ray diffraction of the oxide. They were then cross-

Appendix I

PERGAMON

Acta mater. 48 (2000) 3283–3293

Acta MATERIALIA

www.elsevier.com/locate/actamat

SURFACE RUMPLING OF A (Ni, Pt)Al BOND COAT INDUCED BY CYCLIC OXIDATION

V. K. TOLPYGO and D. R. CLARKE†

Materials Department, College of Engineering, University of California, Santa Barbara, CA 93106-5050, USA

(Received 11 May 2000; accepted 22 May 2000)

Abstract—The surface of an initially flat, platinum-modified nickel aluminide bond coat formed on a single crystal superalloy is shown to progressively roughen (''rumple'') with thermal cycling in air. Far less surface roughening occurs after isothermal oxidation or after the same number of thermal cycles but with a shorter high-temperature exposure in each cycle. Mechanisms of the observed rumpling and the implications of the bond coat surface evolution leading to the failure of thermal barrier coatings are discussed. It is concluded that local volume changes in the bond coat, caused by aluminum depletion and subsequent decomposition of the β-(Ni, Pt)Al phase, are responsible for the observed rumpling. © *2000 Published by Elsevier Science Ltd on behalf of Acta Metallurgica Inc.*

Keywords: Coating; Oxidation; TBC

1. INTRODUCTION

Interface and surface roughening is an important phenomenon because it is one possible way in which an oxide film under biaxial compression on an initially flat surface can distort and develop localized tensile stresses perpendicular to the interface at the convex portions of the surface [1–3]. In the absence of such roughening there are no tensile stresses acting across the interface and hence no internal force that can serve to separate the film. Consequently, roughening is a necessary pre-requisite for the failure of compressed oxide films growing on initially flat surfaces. (The one exception is when a flat film can buckle and spall but this requires a pre-existing, critically sized flaw to be at the interface, a condition not usually met in thermally grown oxide scales.)

The roughening of an oxide film is also of contemporary importance since it appears that the failure of thermal barrier coatings (TBCs) can initiate from roughening of the interface between the thermally grown oxide and the bond coat with thermal cycling. Failure in this class of materials is especially intriguing since the TBCs are so thick (typically 100–200 μm), that although they eventually fail by buckling and spalling, the critical flaw needed for buckling is several millimeters in size [4]. No interface defects of this size are normally observed, therefore failure must first occur in many smaller regions that further link up and form the flaw large enough for buckling. The initiation of the localized damage and the mechanisms by which they link up in the TBC-coated materials remain unresolved. The work presented here is a contribution towards understanding the initiation process based on the roughening of the bond coat during cyclic oxidation.

Roughening, sometimes termed ''rumpling'' or ''scalloping'', has previously been observed during cyclic oxidation of both aluminide [5–8] and MCrAlY [7] coatings on nickel-based superalloys. Apart from mechanical straining under an external load, this type of coating degradation has been variously attributed to coating–substrate thermal expansion mismatch [5, 7] or to repeated oxide cracking and spallation [6, 8]. The former explanation would suggest that roughening can be avoided in the coatings with matching expansion coefficients and furthermore that it is not an oxidation-related phenomenon. The other explanation would imply that the oxide behavior is a key factor and therefore the coating–substrate interaction is of secondary importance. Neither of these explanations has been experimentally tested.

In this work we report a series of observations of bond coat rumpling under different experimental conditions designed to elucidate and test various possible mechanisms of this intriguing and potentially harmful process. The observations also set the stage for future studies of the effect of bond coat rumpling in initiating TBC failure.

† To whom all correspondence should be addressed.

1359-6454/00/$20.00 © 2000 Published by Elsevier Science Ltd on behalf of Acta Metallurgica Inc.
PII: S1359-6454(00)00156-7

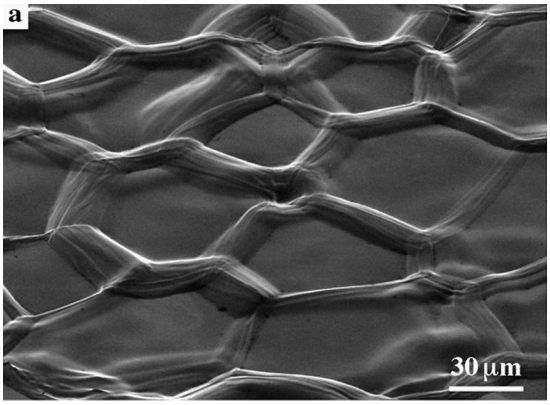

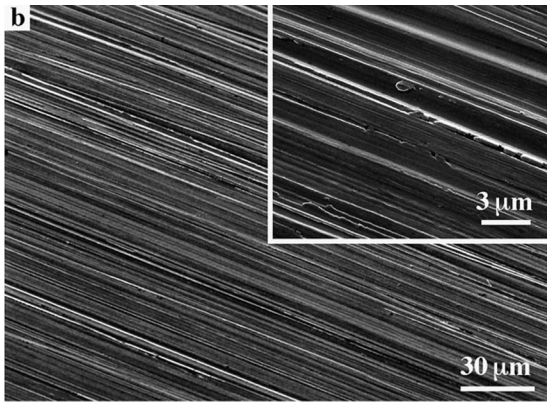

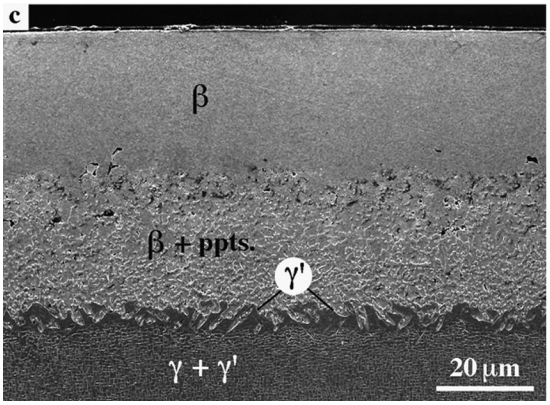

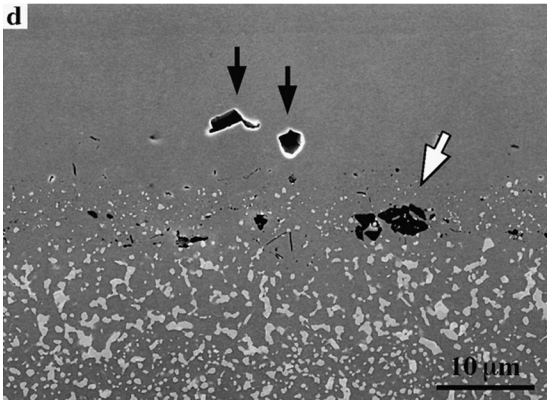

Fig. 1. (*Caption opposite*).

2. EXPERIMENTAL DETAILS

The samples investigated were cut from bond-coated discs of René N5 single crystal superalloy prepared and provided by Howmet Corporation (Whitehall, MI). The platinum aluminide coating was deposited by platinum electroplating followed by a low activity CVD aluminizing [9]. The majority of samples were polished using 400-grit SiC paper to produce a macroscopically flat surface and to remove the ridges formed during the aluminizing process along grain boundaries of the bond coat. It has been established previously that this surface finishing promotes the formation of α-alumina scale almost immediately at the beginning of oxidation at temperatures above 1100°C [10]. In several experiments, no surface polishing was used and the as-aluminized samples with grain-boundary ridges were oxidized.

Isothermal and cyclic oxidation experiments were performed at 1150 and 1200°C in air. The hold time at high temperature during cycling was 1 h and the time at room temperature between cycles was about 10 min. The samples were periodically removed from the temperature cycling rig for examination. An additional set of cyclic oxidation experiments was carried out with a short (6 min) high-temperature exposure in each cycle. The rate of heating and cooling in all experiments was about 200°C/min.

The samples were examined by both optical and scanning electron microscopy (SEM) and the residual stress in the oxide film was assessed using photostimulated luminescence spectroscopy [11, 12]. The frequency shift of the R_2 characteristic line of Cr^{3+} luminescence in α-Al_2O_3 relative to its stress-free position was converted into an effective biaxial compressive stress in alumina. Although the conversion is not strictly valid for a non-planar film [2], it was nevertheless used for comparison between different samples, since the frequency shift is proportional to the elastic strain energy density. The distribution of elements through the bond coat thickness was determined by energy dispersive X-ray spectroscopy (EDX) after cross sectioning. The surface roughness of the bond coat was qualitatively estimated from SEM and optical microscopy images.

Fig. 1. Microstructure of the (Ni, Pt)Al bond coat surface and cross sections prior to oxidation: (a) grain-boundary ridges on the bond coat surface after aluminizing; (b) surface roughness with amplitude about 1 μm due to scratches formed by polishing with 400-grit SiC (the inset shows an enlarged view of the surface); (c) cross section of the bond coat showing the outer β-(Ni, Pt)Al layer and the inner multi-phase layer of the β-phase with refractory-rich particles; (d) unetched cross section showing small pores (indicated by the black arrows) and entrapped alumina particles (white arrow) in the mid-section of the bond coat.

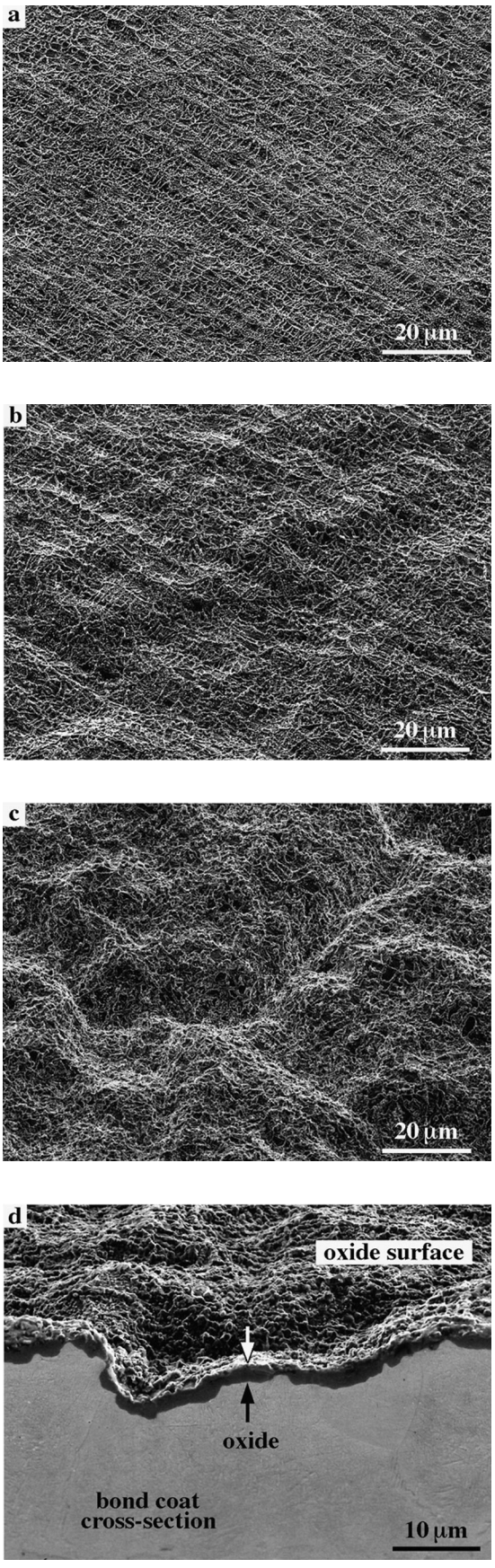

Fig. 2. (*Caption opposite*).

3. RESULTS AND OBSERVATIONS

3.1. Initial structure of the bond coat

In the as-aluminized condition, the bond coat surface exhibits large grains of platinum-modified nickel aluminide (β-NiAl) outlined by grain-boundary ridges, as shown in Fig. 1(a). This morphology is well characterized and typical of outwardly growing aluminide coatings [13, 14]. The height of the ridges is about 3–4 μm and the size of the grains in the bond coat is between 20 and 100 μm.

The roughness of the bond coat surface polished with 400-grit SiC and the microstructure of the coating cross section prior to oxidation are shown in Figs 1(b)–(d). After polishing a few micrometers from the surface, the thickness of the outer single-phase β-(Ni, Pt)Al layer is about 30 μm. The concentration of the major elements on the coating surface is as follows (at.%): 45% Ni–44% Al–6% Pt–3.5% Co–1.5% Cr. The inner multi-phase layer of the coating is also about 30 μm thick and consists of the β-phase matrix (containing Pt, Cr and Co), and inclusions rich in refractory metals (Ta, W, Mo). Small alumina particles, which were trapped at the alloy surface prior to Pt plating, are located below the boundary between the layers, as indicated in Fig. 1(d). Finally, a thin discontinuous layer of γ'-Ni_3Al separates the bond coat and the superalloy. A few small pores (possibly the result of initial porosity in the Pt layer) can be found in the outer β-(Ni, Pt)Al layer, as shown in Fig. 1(d). The surface roughness, having an amplitude of about 1 μm, created by polishing is clearly seen in Fig. 1(b).

3.2. Surface roughening during cyclic oxidation

Oxidation in air at 1150–1200°C leads to the formation of a continuous α-alumina film on the bond coat surface. After a few hours of oxidation, the initial roughness associated with polishing scratches remains visible on the surface [Fig. 2(a)] but then it becomes increasingly indistinguishable as the oxide thickens. Concurrently, another type of surface roughness, the rumpling, becomes apparent as shown in the sequence of micrographs in Figs 2(a)–(c). This sequence illustrates the evolution of the bond coat during the course of cyclic oxidation at 1200°C. Surface undulations with a wavelength of the order of 30–50 μm gradually develop and their amplitude increases with oxidation time.

Observations of the alumina scale between oxidation cycles confirm that it remained intact and

Fig. 2. Rumpling of the bond coat surface polished with 400-grit during cycling in air at 1200°C (one-hour cycles): (a) 1 cycle; (b) 10 cycles; (c), (d) 50 cycles. The SEM micrographs in (a)–(c) are taken at the same magnification and the same sample tilt so that the extent of rumpling can be compared directly. The micrograph in (d) shows the polished section together with the oxide surface and reveals a small variation in oxide thickness.

did not spall (within the time interval studied). This invalidates the possibility that the surface depressions appear as a result of repeated spalling and re-oxidation. After 50 one-hour cycles at 1200°C the oxide is about 2 μm thick, far smaller than the amplitude of surface undulations (up to 10–15 μm). The cross section micrograph in Fig. 2(d) clearly shows that the rumpling is not related to oxide thickness variation nor is a result of oxide buckling above the metal surface. Similarly, no deep crack-like protrusions, which would indicate local oxygen ingress through cracks or fissures in alumina, were seen. Thus, it appears that the rumpling during cyclic oxidation is produced by concurrent deformation of the bond coat together with the adherent oxide scale.

3.3. Residual stress in alumina scales

One of the possible explanations of the surface roughening during oxidation is that it may occur due to relaxation of the growth stresses in the oxide. Indeed, a compressive stress in the scale in the direction parallel to the surface (the growth stress) may induce plastic deformation of the bond coat surface at high temperature driven by the reduction in elastic energy in the oxide. Besides, upon cooling from the oxidation temperature, the oxide stress increases because of the thermal expansion mismatch between the oxide and the superalloy, which would provide an additional strain energy driving force for deformation. It was, therefore, essential not only to measure the stress in the alumina but also to find the conditions under which the growth stress could be varied. Then, the extent of rumpling could be compared for different oxide stresses.

Obviously, the thermal mismatch stress is a constant value for a given metal–oxide system and interface geometry. However, the growth stress in the α-Al_2O_3 scale on (Ni, Pt)Al coating was found to vary over a wide range depending on the alumina scale morphology. For example, the scale with small grains usually exhibits lower residual stress than the scale with large plate-like grains on the same substrate and under the same oxidation conditions. In turn, the morphology of the scale, growing on β-(Ni, Pt)Al, can be influenced by surface finishing prior to oxidation [10].

A clear illustration of the variation in stress that can occur in alumina scales is presented in Fig. 3. The residual stress, at room temperature, was measured in the course of cyclic oxidation at 1200°C (1 h cycles) on two similar samples. The average stress values were obtained by scanning an optical probe over the sample surface in order to offset local stress variations in the rumpled oxide. Both samples were polished prior to oxidation: sample 1 with 800-grit and sample 2 with 400-grit SiC. This seemingly minor difference in polishing grit size has a large effect on the α-Al_2O_3 morphology. The surface after finer polishing provides fewer places for α-alumina nucleation. On the other hand, no metastable aluminas form in the scale at 1200°C (apart from during a short heating period). Since the grain size of α-Al_2O_3 in the direction parallel to the surface is mainly determined by the distance between individual α-nuclei, it is much larger on the smoother sample (sample 1) than on sample 2, as shown in Figs 4(a) and (b). On these micrographs the oxide grains are clearly seen as they are outlined by distinct grain-boundary ridges [10].

The residual stress data in Fig. 3 demonstrate that the oxide stress is almost 50% higher on the surface polished with 800-grit. However, the surface rumpling produced by cyclic oxidation is not any larger. On the contrary, the SEM images in Figs 4(c) and (d) demonstrate even less rumpling of the surface with higher stress in the oxide. Quantitative analysis of the surface evolution will be needed to establish this point unequivocally but the effect is quite noticeable. Another important result is that the difference between the residual stress values on these two samples persists from the very beginning of oxidation, when the surface is essentially flat. This indicates that the in-plane growth stress in the oxide is much higher on the 800-grit polished sample and smaller, if not zero, on the 400-grit polished sample. Thus, it appears that the rumpling of the bond coat surface occurs irrespective of the stress in the oxide at the oxidation temperature.

3.4. Effect of initial surface morphology

The rumpling developed, during cycling, on the polished surface appears to be associated with the grain structure of the β-(Ni, Pt)Al layer, so that the largest depressions are seemingly arranged along grain boundaries of the bond coat [Figs 4(c) and

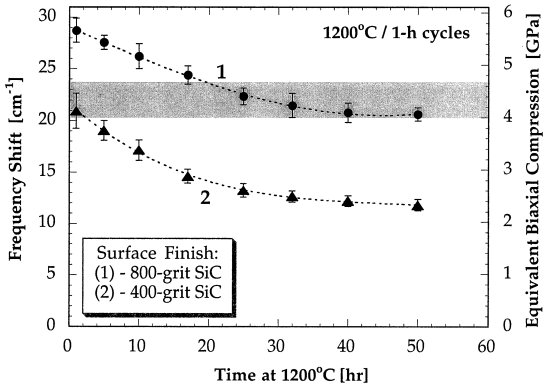

Fig. 3. Frequency shift of Cr^{3+} luminescence and equivalent biaxial residual room-temperature stress in α-Al_2O_3 scales formed on two samples in the course of cyclic oxidation at 1200°C. Surface finishing prior to oxidation: 800-grit (sample 1) and 400-grit (sample 2). The calculated thermal mismatch stress is indicated by the shaded area at 4.0–4.6 GPa.

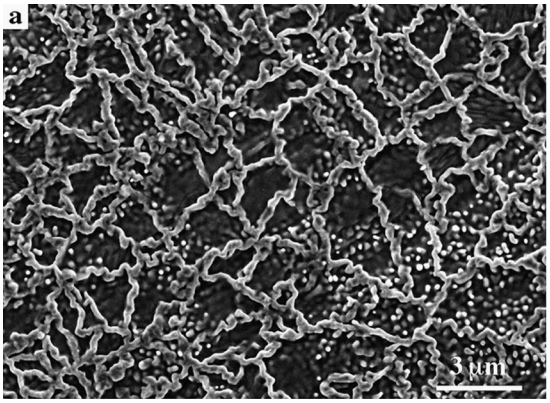

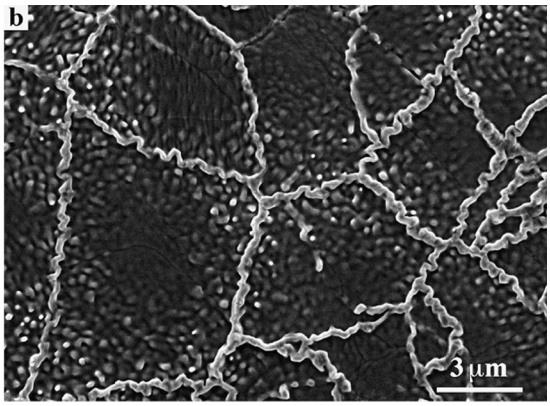

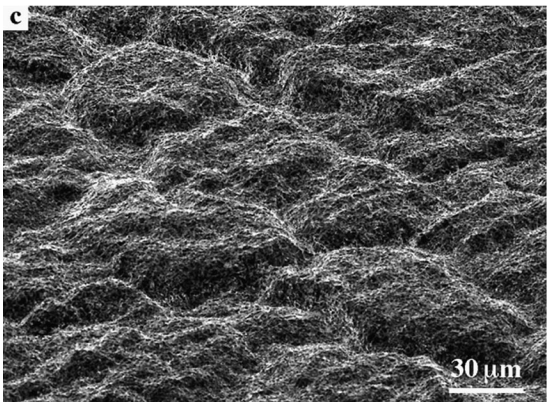

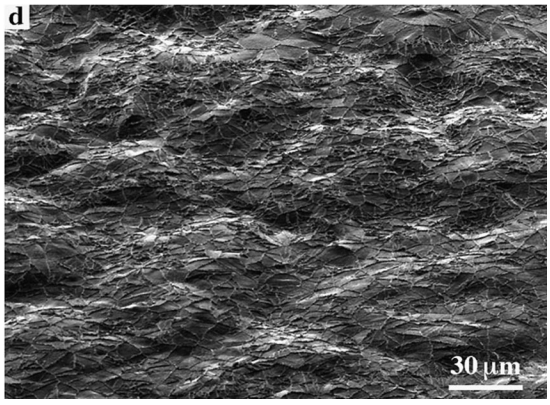

Fig. 4. (*Caption opposite*).

(d)]. In addition, smaller perturbations form on the surface of the grains. On the as-aluminized surface, where ridges were already present along the grain boundaries, the rumpling is markedly different. Instead of forming the grooves, the ridges apparently increase their height with thermal cycling (Fig. 5).

A small difference in alumina growth rate between the ridge areas and the surface of bond coat grains is mainly caused by the difference in alumina grain size. This effect is probably of minor importance since in both cases the oxide thickness does not exceed 2 μm after 50 h at 1200°C. The micrograph of the bond coat cross section in Figs 5(b) and (c) clearly shows that the rumpling is not related to variation of the oxide thickness. Also, as in the case of the polished samples, no cracking of the scale occurs in the course of 50 one-hour cycles at 1200°C.

We note that the increase in roughness of the as-aluminized surface may be described by either the ridge growing upwards (relative to some macroscopic reference plane) or, alternatively, the flat regions between the ridges moving down (again, relative to the reference plane). Although the resulting surface configuration may be the same, the two processes are essentially different. The growth of the ridges implies that there may be a flow of metal from the grain interior *toward* the grain boundaries. At the same time, on the polished surface (Figs 2 and 4), the grain boundaries deepen, which would mean that the metal flow is directed *out of* the boundaries. There is no reason to believe that the bond coat behavior depends that much on the surface configuration. Therefore, the more likely process is the flat valley deepening which, in turn, suggests that the coating volume decreases for some reason during oxidation. If the coating shrinks, then existing depressions on the as-aluminized surface (the valleys) may deepen whereas, when the coating is polished, depressions may form along the grain boundaries. The possible reason for the volume decrease in the bond coat will be considered in the following sections.

3.5. *Influence of the oxidation regime*

Generally, the thermal expansion coefficients of the bond coat and the superalloy are different. Since the superalloy is much thicker, any temperature change produces a mismatch strain and, possibly, plastic deformation in the bond coat. Plastic

Fig. 4. Morphology of the α-Al_2O_3 scale formed at 1200°C on the (Ni, Pt)Al bond coat surface with different surface finishing prior to oxidation: 400-grit (a, c) or 800-grit (b, d). The size of the oxide grains, outlined by grain-boundary ridges, is clearly seen after 1 h oxidation (a, b); the surface rumpling is shown after 50 one-hour cycles (c, d) (60° tilt).

deformation under compression during heating or cooling (depending on the ratio between the expansion coefficients) may result in surface rumpling. In this case, the extent of rumpling will increase with the number of cycles and, most importantly, the effect produced by thermal cycling should not depend on the cycle length. The following experiments were performed in order to test these arguments.

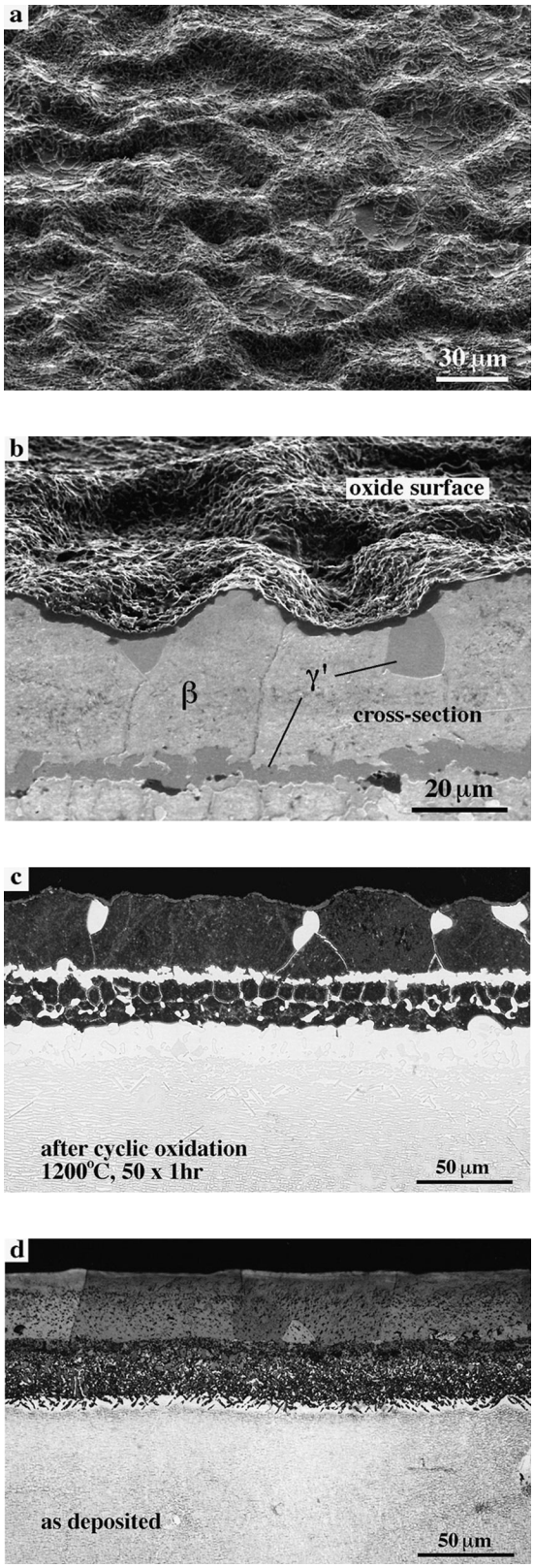

Fig. 5. (*Caption opposite*).

The morphology of the bond coat surface after 100 one-hour oxidation cycles at 1150°C is presented in Fig. 6(a). As in the experiments described above, this rather short oxidation time was used to ensure that the oxide remains intact and no spallation of the alumina scale occurs. For comparison, Fig. 6(b) shows the surface of another sample with the same surface finish after 100 cycles at 1150°C but with only 6 min high-temperature exposure in each cycle. Other cycling parameters, heating and cooling rates and hold time at room temperature, were identical for both samples. The surface rumpling is obviously much less pronounced after the 0.1 h cycles (about 10 h total time at 1150°C) than after the same number of 1 h cycles (100 h oxidation time). Thus, it appears that it is the oxidation time, rather than the number of cycles *per se*, that determines rumpling. This suggests that the evolution of the bond coat surface takes place at temperature and not during heating or cooling.

If this last conclusion is correct then isothermal oxidation should be expected to produce surface rumpling similar to cyclic oxidation with the same total time at high temperature. However, this is also not the case. As the micrograph in Fig. 6(c) shows, very little rumpling occurs after isothermal oxidation for 100 h at 1150°C.

Together, these observations present a puzzling dilemma. On the one hand, the rumpling is much smaller after short cycles than after the same number of one-hour cycles, implying that the time at high temperature is crucial. On the other hand, isothermal oxidation also produces only a minor rumpling, indicating that the temperature changes are of primary importance. These seemingly contradictory results suggest that there may be an intrinsic difference in the bond coat behavior during isothermal and cyclic oxidation. In the search for this difference the bond coat microstructure was studied in greater detail.

3.6. Microstructural evolution of the bond coat

Apart from the surface rumpling, the oxide morphology is generally the same after both iso-

Fig. 5. Microstructure of the as-aluminized bond coat after 50 one-hour cycles at 1200°C: (a) surface rumpling [cf. Fig. 1(a)]; (b) cross section showing a rather uniform oxide layer and strong surface undulations (γ'-phase is revealed by etching); (c), (d) optical micrographs showing etched cross section before and after cyclic oxidation. Dark areas on the optical images correspond to the β-phase whereas the γ'-phase in the coating appears white.

thermal and cyclic oxidation. However, the bond coat structure exhibits remarkable differences as seen in Fig. 7. The micrographs in Figs 7(a)–(c) (the left-hand column) show the cross section of the bond coat after 100 one-hour cycles at 1150°C. Aluminum depletion due to oxidation and inter-diffusion produces a continuous layer of γ'-phase in the β-(Ni, Pt)Al near the interface between the outer and inner layers of the bond coat. The β-phase, with about 32 at.% Al, is present both above and below the γ'-layer and measurements of the aluminum distribution across the bond coat thickness exhibit a relative minimum at this location. The same intermediate layer of γ'-Ni_3Al is also seen in Fig. 5(c) appearing as a bright band in the coating cross section. Small amounts of γ'-phase are formed along the grain boundaries in the outer β-layer. Some part of the β-phase is also transformed into γ' at the bond coat–superalloy interface.

Examination of the bond coat cross section after isothermal oxidation for 100 h at 1150°C reveals no intermediate layer of γ'-phase [Figs 7(d)–(f)]. However, the most striking feature is the formation of large cavities inside the bond coat. The size of these cavities may be as large as 10–20 μm in the direction parallel to the surface and they are mainly located near the interface which had formerly separated the outer and inner layers of the bond coat. As with the sample after cyclic oxidation, β-(Ni, Pt)Al remains the major phase in the coating, although the distribution of the γ'-phase in the outer layer is somewhat different.

Thus, unlike isothermal oxidation, during which the internal cavities form and the surface rumpling is small, cyclic oxidation produces rumpling but the bond coat remains dense. These differences in the coating microstructure suggest that surface rumpling and cavity formation may, in fact, be two different manifestations of the same, as yet, unidentified diffusion process.

4. DISCUSSIONS AND IMPLICATIONS

4.1. Assessment of the existing models

The observations presented above allow us to discount a number of explanations previously advanced for bond coat rumpling on thermal cycling. These are discussed first.

In several previous publications the phenomenon of bond coat rumpling was attributed to local failure of the protective scale, repeated spallation and re-oxidation on thermal cycling [6, 8]. Such a process would, indeed, lead to non-uniform oxidation and produce oxide thickness variations and depressions on the bond coat surface. In the present work, however, the total oxidation time was sufficiently short so that no oxide spallation or cracking was observed. So, although local failure of the oxide during cycling would enhance the existing roughness of the bond coat surface, it is not responsible for the rumpling described in this work.

Another explanation, based on the plastic deformation of the bond coat due to the thermal expansion mismatch with the underlying superalloy [5, 7], is not consistent with the significant difference in rumpling between short and long oxidation cycles (Section 3.5). Some other mechanisms proposed earlier, such as sub-surface melting, roughening under an external load or thermal gradients through

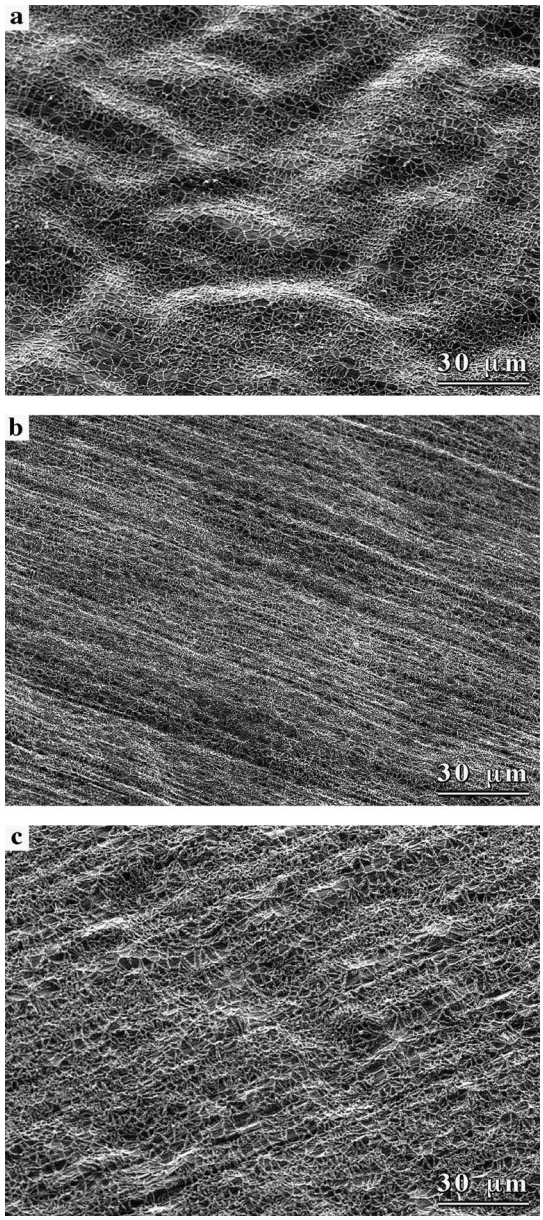

Fig. 6. Surface rumpling on three identical samples after oxidation at 1150°C with different oxidation regimes: (a) 100 one-hour cycles; (b) 100 short (6 min) cycles; (c) 100 h isothermal oxidation. All samples were polished with 400-grit SiC prior to oxidation.

the coating thickness are not applicable to the present experimental conditions.

A similar type of surface evolution during oxidation, often termed "wrinkling", but on a smaller length scale, also cannot account for the observed rumpling. Wrinkling occurs at the oxidation temperature and is driven by the in-plane compressive strain in the oxide during its growth [15], whereas rumpling takes place mainly during thermal cycling. Furthermore, the magnitude of the growth stress in the oxide apparently has no effect on rumpling, as demonstrated in Section 3.3. Recently, an analysis has been presented [16] which describes rumpling as a thermal "ratcheting" phenomenon associated with the elastic/plastic mismatch between the bond coat and the growing oxide. This analysis, however, implies that rumpling should be inherent in all metal–oxide systems that develop compressive stress in the oxide and not only in the bond coats on superalloys, which is apparently not the case. Also, it should be emphasized that any model relying on the mechanical interaction between the oxide and the bond coat as a driving force for rumpling is inconsistent with prior experience: nickel aluminide coatings rumple whereas bulk samples of the nickel aluminide do not. (Presumably this would also be true for the platinum-modified aluminide, but bulk samples are unavailable.)

A comparison between the roughness development on the polished surface (Figs 2 and 4) and on

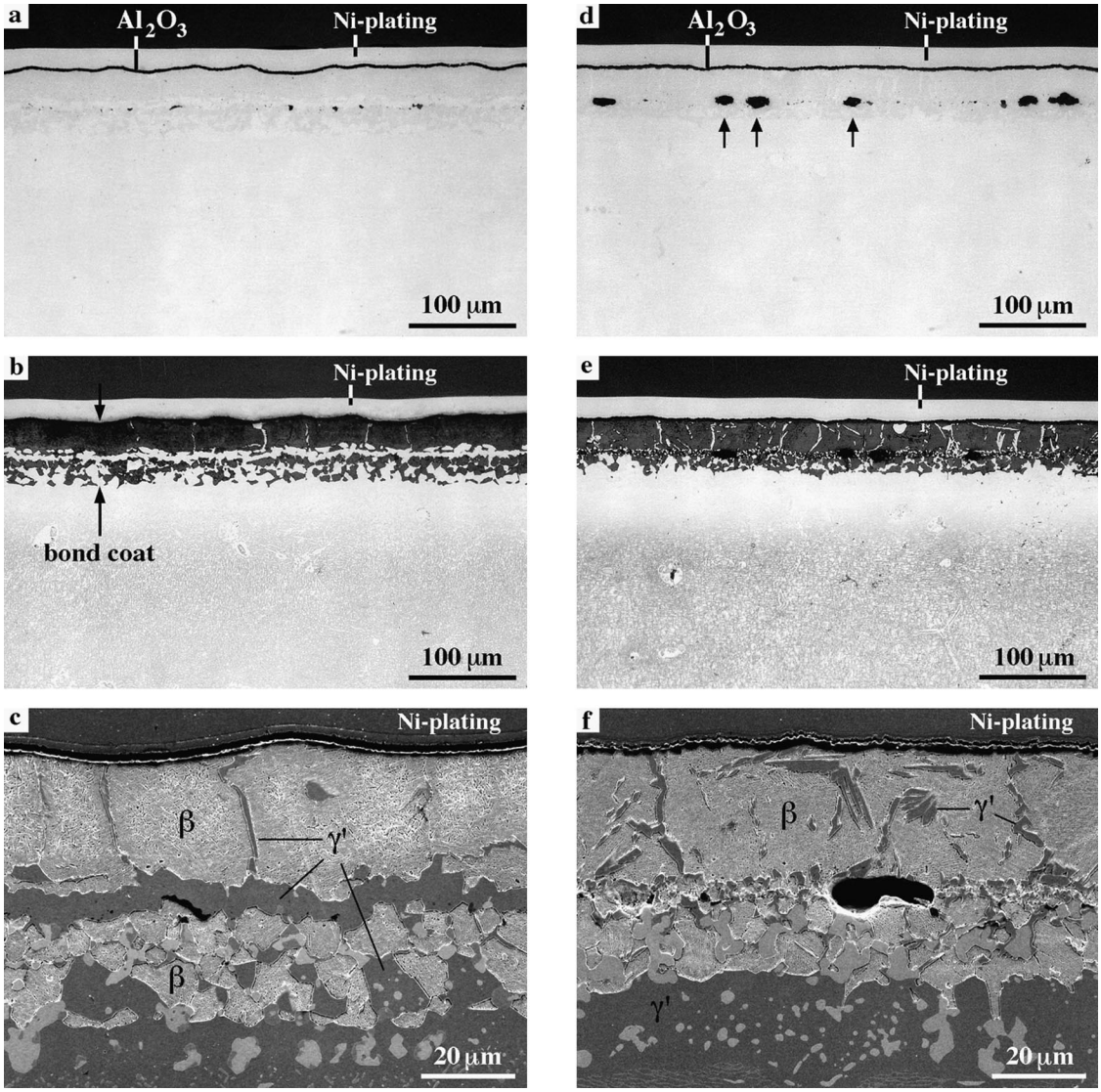

Fig. 7. Bond coat cross section after 100 one-hour cycles (a)–(c) and 100 h isothermal oxidation (d)–(f) at 1150°C. The optical images of the unetched cross section in (a) and (d) show the difference in bond coat rumpling and internal cavities (indicated by the arrows). In the etched cross sections in (b) and (e) the β-phase in the coating appears dark. The higher magnification SEM micrographs in (c) and (f) reveal the distribution of γ'-phase and the porosity in the bond coat after isothermal oxidation. Both samples were polished with 400-grit SiC prior to oxidation.

the as-aluminized surface with grain-boundary ridges (Fig. 5) further limits our search of the underlying mechanism. For example, an approach based on plastic or diffusional metal flow parallel to the surface would hardly explain why, in one case, the boundaries form grooves, whereas the ridges along the boundaries increase in the other.

Hence, a mechanism is needed which describes how a macroscopically flat surface of the bond coat on a superalloy rumples during cyclic oxidation. One possibility (which is briefly described below) is that the rumpling occurs as a result of the decomposition of the β-NiAl phase and precipitation of the γ'-Ni_3Al phase accompanied by a volume reduction in the bond coat. The key feature is that the process is driven by aluminum depletion and that the net volume decrease can be accommodated by the development of surface depressions and by the formation of internal cavities. It is, however, not clear why the former occurs on thermal cycling and the latter occurs during isothermal exposure. These will be explored in future work, although it is noted that thermal cycling will invariably drive plastic deformation in the bond coat (due to its thermal expansion mismatch with the superalloy) that could close up porosity.

4.2. Surface rumpling driven by aluminum depletion during oxidation

Obviously, rumpling of the bond coat surface during oxidation involves two concurrent processes: deformation of the oxide and deformation of the metal. Based on the results presented in this contribution and the above discussion, it appears that rumpling is associated with the metal deformation and that the oxide deforms in compliance with the metal surface.

The major change in the bond coat microstructure during oxidation is the formation of the γ'-Ni_3Al phase. This is attributed to aluminum depletion caused by the formation of Al_2O_3 on the surface and by inward Al diffusion into the superalloy. The reaction describing the decomposition of the β-phase during oxidation (for simplicity the presence of other elements in the bond coat is ignored) can be expressed as

$$3\mathrm{NiAl} + \frac{3}{2}\mathrm{O_2} \rightarrow \mathrm{Ni_3Al} + \mathrm{Al_2O_3}.$$

Using the molar masses and densities of the solid phases (5.9 g/cm^3 for β-NiAl, 7.5 g/cm^3 for γ'-Ni_3Al and 3.9 g/cm^3 for Al_2O_3), the molar volume of each phase, $V(\beta)$, $V(\gamma')$ and $V(\mathrm{ox})$, can be found. Comparing the volumes of the metallic phases, Ni_3Al and NiAl, it follows that the decomposition of the β-phase leads to a considerable decrease of the bond coat volume:

$$V(\gamma') = 0.62V(\beta).$$

Since the coating is constrained laterally by the underlying substrate, the volume decrease is equivalent to the reduction of the coating thickness

$$h(\gamma') = 0.62h(\beta).$$

If only a portion of the β-phase is transformed (as in the present experiments), the volume decrease can be related to the volume of the oxide formed according to

$$\Delta V = V(\beta) - V(\gamma') = 0.63V(\mathrm{ox}).$$

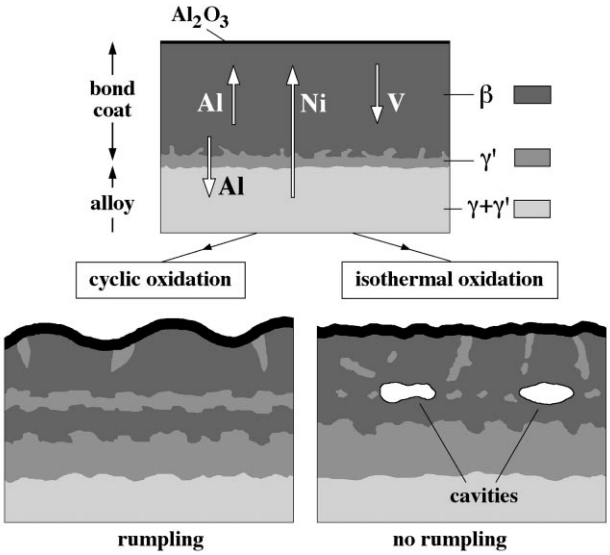

Fig. 8. Schematic illustration of the major diffusion fluxes, Ni, Al and vacancy (V) during bond coat oxidation and microstructure evolution leading to rumpling or cavity formation.

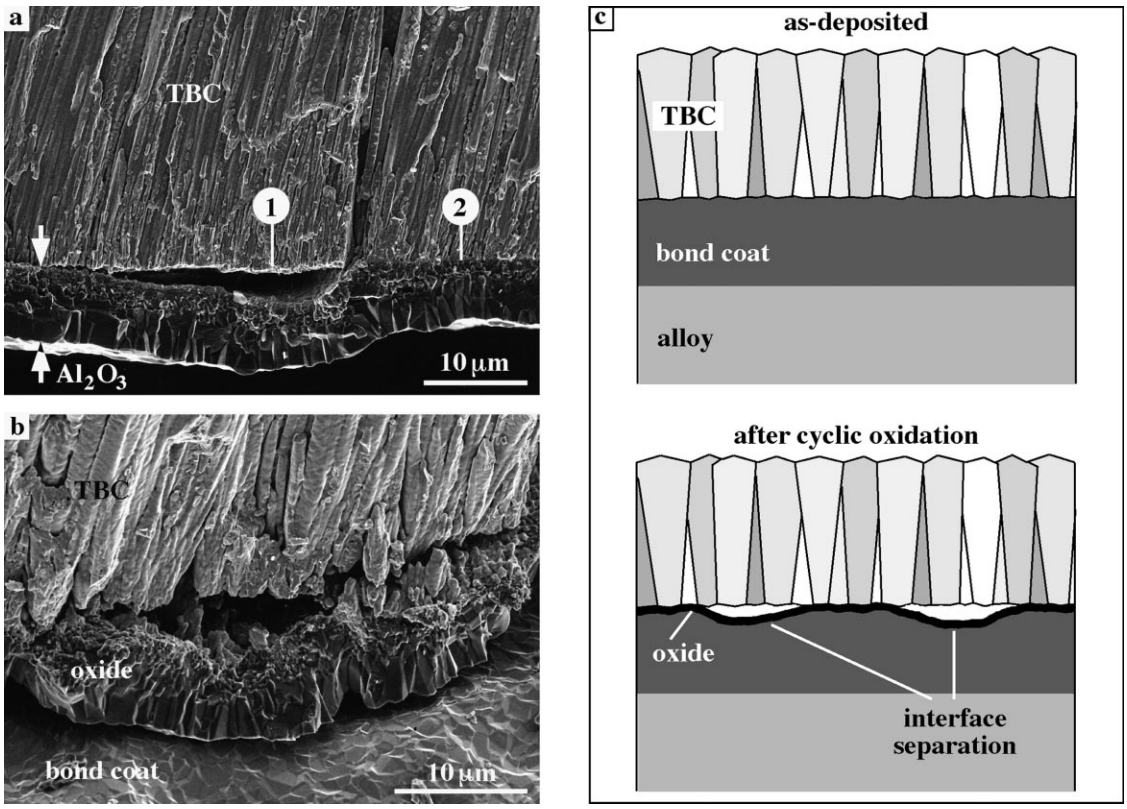

Fig. 9. (a), (b) Examples of the separation observed at the interface between an EB-PVD TBC and the thermally grown alumina after cyclic oxidation at 1150°C. (c) Schematic illustration of the interface separation as a result of distortion of the bond coat surface together with the scale during cyclic oxidation.

Correspondingly, the same ratio applies for the thicknesses

$$\Delta h = h(\beta) - h(\gamma') = 0.63h(\text{ox}).$$

Obviously, the reduction of the bond coat volume (thickness) associated with aluminum depletion does not necessarily lead to surface distortions. If the decomposition of the β-NiAl phase takes place uniformly over the whole surface under the growing oxide, the Ni_3Al phase will appear as a uniform layer under the scale and the surface will not distort but merely move inwards. However, if the $\beta \rightarrow \gamma'$ transformation occurs locally or at a different time in different places, then the volume reduction will also be localized. This may cause the bond coat surface to distort from its original shape or cavities to form inside the bond coat. Indeed, analysis of the coating microstructure (Figs 5 and 7) shows that the γ'-phase originally forms in different locations in the bond coat, not as a uniform sub-scale layer.

The concept of the Al depletion-driven volume reduction as a motivation for surface rumpling is not in conflict with the observations that the grain boundaries may either elevate or lower depending on the initial surface geometry. Rumpling of the metal surface requires plastic deformation of the oxide layer since they remain in contact. Therefore, when the oxide is initially flat (on the polished sample), it can distort into grooves in any place following undulations of the metal surface. However, when the oxide has already been formed on the convex surface of the existing ridges (on the as-aluminized sample), this configuration will tend to remain rather than flatten. With subsequent cycling, volume reduction will be accommodated by the valleys deepening between the existing ridges.

This simple qualitative description does not include inter-diffusion between the bond coat and the superalloy during oxidation. Although the effect of the diffusion processes on the coating integrity and surface configuration requires detailed study, one specific feature of the diffusion fluxes should be mentioned. Three major fluxes through the bond coat thickness occur during oxidation, as shown schematically in Fig. 8. The growth of the Al_2O_3 scale on the surface requires outward diffusion of aluminum. However, nickel also diffuses in the same direction from the superalloy and, concurrently, aluminum diffuses inward into the superalloy. This remarkable feature of Ni and Al diffusion fluxes in coatings, in contrast to "normal" diffusion couples, leads to another possible cause of volume reduction. In the outer part of the bond coat both Ni and Al diffuse toward the surface, therefore there should be a compensating vacancy flux in the opposite direction. The result is expected to be

either the formation of Kirkendall porosity or, if the pores collapse, a decrease of the coating volume. It is possible that the pores tend to collapse during cycling because of thermal stresses in the bond coat, whereas they coalesce into large cavities at constant temperature.

Voids or pores in the diffusion zone have frequently been observed in β/γ Ni–Cr–Al diffusion couples [17, 18]. Besides, the formation of cavities, presumably as a result of the Kirkendall effect during inter-diffusion, has been reported in simple aluminide coatings [19]. This process, however, has not hitherto been related to the possibility of coating surface distortions when cavities close up on thermal cycling.

Lastly, volume reduction associated with Al depletion can also be expected to cause "rumpling" in MCrAlY coatings. As-deposited MCrAlY bond coats typically consist of a mixture of β- and γ-phases. Because of the higher chromium content in the coating (about 20 at.%), the phase which precipitates from β-NiAl upon aluminum depletion is the solid solution γ-Ni(Cr, Al), rather than γ'-Ni_3Al. Since the density of γ is even higher than that of γ', the volume reduction upon aluminum depletion should, correspondingly, be even larger than in the nickel aluminide coatings.

4.3. *Effect of bond coat rumpling on TBC failure*

Although the observations reported in this contribution have been made on the bond-coated materials, they have a number of implications regarding the failure of thermal barrier coatings. The bottom surface of the TBC is expected to conform to the shape of the bond coat upon deposition. If the bond coat behavior is the same with and without TBC, then surface rumpling during cyclic oxidation would create a geometrical incompatibility with the TBC and lead to separation at the TBC–alumina interface. Apparently, the stiffness of the ceramic top coat should constrain the formation of convex regions on the metal surface. However, the concave regions may develop as the bond coat, together with the oxide, pull away from the TBC. In this case, local separations will open up at the TBC–oxide interface, as shown in Figs 9(a) and (b). Note that in these examples the TBC failure has occurred at the oxide–metal interface, however the separations first formed at the TBC–oxide interface. The schematic illustration in Fig. 9(c) shows the formation of these separations under seemingly intact TBC.

The most important consequence of this process is that the local separations will gradually accumulate on thermal cycling, link together and eventually form the critical sized flaw required for TBC buckling [4]. The most likely areas of separation are those between the ridges (on the as-aluminized surface) or along the grain boundaries (on the polished surface). Importantly, the separation does not require any failure of the thermally grown oxide. On the contrary, the oxide is expected to fail (because of excessive roughness of the oxide–metal interface) when there is no constraint from the top TBC layer. If, however, the TBC–oxide interface is strong enough to suppress separation, the volume reduction will lead to the formation of cavities in the bond coat, instead of rumpling. Indeed, this type of coating degradation is observed in the TBC-coated materials, as reported elsewhere [20].

Quantitative measurements of rumpling are clearly needed to provide a more critical assessment of its role in TBC-coated materials but the circumstantial evidence suggests that one mode of TBC failure is associated with roughening of the bond coat [20].

Acknowledgements—The authors are grateful to K. S. Murphy and J. S. Smith of Howmet Corporation (Whitehall, MI) for providing the bond-coated superalloy samples used in this work. The research was supported by the Advanced Gas Turbine Systems Research (AGTSR) program through the Department of Energy.

REFERENCES

1. Evans, A. G., Crumley, G. B. and Demaray, R. E., *Oxid. Metals*, 1983, **20**, 193.
2. Gong, X.-Y. and Clarke, D. R., *Oxid. Metals*, 1998, **50**, 355.
3. Evans, A. G., He, M. Y. and Hutchinson, J. W., *Acta mater.*, 1997, **45**, 3543.
4. Hutchinson, J. W., He, M. Y. and Evans, A. G., *J. Mech. Phys. Solids*, 2000, **48**, 709.
5. Deb, P., Boone, D. H. and Manley, T. F., *J. Vac. Sci. Technol.*, 1987, **A5**, 3366.
6. Holmes, J. W. and McClintock, F. A., *Metall. Trans.*, 1990, **21A**, 1209.
7. Pennefather, R. C. and Boone, D. H., *Surf. Coat. Technol.*, 1995, **76–77**, 47.
8. Zhang, Y. H., Withers, P. J., Fox, M. D. and Knowles, D. M., *Mater. Sci. Technol.*, 1999, **15**, 1031.
9. Warnes, B. M. and Punola, D. C., *Surf. Coat. Technol.*, 1997, **94–95**, 1.
10. Tolpygo, V. K. and Clarke, D. R., *Mater. High Temp.*, 2000, **17**, 59.
11. Ma, Q. and Clarke, D. R., *J. Am. Ceram. Soc.*, 1993, **76**, 1433.
12. Lipkin, D. M. and Clarke, D. R., *Oxid. Metals*, 1996, **45**, 267.
13. Sivakumar, R. and Seigle, L. L., *Metall. Trans.*, 1976, **7A**, 1073.
14. Zhang, Y., Lee, W. Y., Haynes, J. A., Wright, I. G., Pint, B. A., Cooley, K. M. and Liaw, P. K., *Metall. Mater. Trans.*, 1999, **30A**, 2679.
15. Tolpygo, V. K. and Clarke, D. R., *Acta mater.*, 1998, **46**, 5153.
16. He, M. Y., Evans, A. G. and Hutchinson, J. W., *Acta mater.*, 2000, **48**, 2593.
17. Nesbitt, J. A. and Heckel, R. W., *Metall. Trans.*, 1987, **18A**, 2087.
18. Merchant, S. M., Notis, M. R. and Goldstein, J. I., *Metall. Trans.*, 1990, **21A**, 1901.
19. Boone, D. H., Crane, D. A. and Whittle, D. P., *Thin Solid Films*, 1981, **84**, 39.
20. Tolpygo, V. K. and Clarke, D. R., to be published.

journal

Appendix J

J. Am. Ceram. Soc., **83** [5] 1165–70 (2000)

Piezospectroscopic Analysis of Interface Debonding in Thermal Barrier Coatings

Xiao Peng and David R. Clarke*

Materials Department, College of Engineering, University of California, Santa Barbara, California 93160–5050

One of the principal modes by which electron-beam-evaporated thermal barrier coatings fail is via the nucleation of local regions of debonding, which grow and link together until reaching a critically sized flaw for spontaneous buckling and spalling. This progressive-failure mode is used as a basis for analyzing the changes that can occur in photostimulated luminescence spectra that have been recorded from the thermally grown oxide. This process also provides a basis for the quantitative determination of the extent of local damage prior to spalling from an analysis of the shape of the luminescence spectra.

I. Introduction

As with many other engineering materials, it would be highly desirable to have a nondestructive method of monitoring the damage evolution in thermal barrier coatings (TBCs) that leads to their eventual failure. Such a method could be used both as the basis of an inspection tool and as input for the development of quantitative models for predicting life-to-failure. One monitoring method that seems to have considerable promise is piezospectroscopy[1] (in particular, piezospectroscopy that uses the photostimulated luminescence ("fluorescence") from Cr^{3+} ions incorporated into the thermally grown oxide (TGO) that is formed at the interface between the zirconia TBC and the bond coat[2,3]). The luminescence is a particularly strong signal, and it can be detected through rather thick thermal barrier coatings, including both electron-beam-deposited thermal barrier coatings (EB-PVD TBCs), as shown in Fig. 1, and plasma-sprayed thermal barrier coatings (PS-TBCs). In addition, as the luminescence is photostimulated, its spatial distribution can be investigated using an optical probe. As presently implemented, the luminescence measurements have been made at room temperature after the TBC-coated materials have been cooled, following high-temperature exposure.[3,4] As a result, the luminescence shift is due to the combined thermal expansion mismatch stresses that are produced on cooling and the intrinsic stresses that are associated with the growth of the oxide.[2,5,6]

In previous work, the frequency shift of the most-intense luminescence lines (R1 and R2) has been used to investigate the evolution of the residual stress in the TGOs, relative to high-temperature exposure in air, on a variety of bond coats and oxidation-resistant alloys.[2–6] Contrary to some expectations, the residual stress in the TGO does not steadily increase as the exposure time or temperature increases; instead, it is almost independent of oxidation time after a transient period. The origin of the transient period is not completely understood; however, in some alloys, the transient period is associated with the kinetics of the transformation from metastable aluminas in the TGO to the stable, α-alumina phase.[6,7] (The Cr^{3+} luminescence spectrum also provides a means of identifying the presence of θ-alumina in the TGO and distinguishing it from α-alumina.[8]) The accumulated data that have been obtained indicate that the magnitude of the residual stress in the steady-state regime do not correlate with the lifetimes to failure, although there is some evidence that the residual stress decreases just prior to failure. However, there are other attributes of the luminescence spectrum that may provide a more reliable indication of the presence of damage. In this work, we consider the effect of localized damage in the TGO on two of the principal attributes, namely the shape and broadening of the luminescence spectrum.

The motivation for considering these parameters in particular is twofold. The first motivation is that there is substantial microstructural evidence to indicate that the failure of EB-PVD TBCs commonly occurs at the TGO/bond-coat interface.[9–11] Failure at this interface seems to be prevalent, although the features that are responsible for initiating failure vary substantially from one bond-coat material to another (and possibly from one manufacturer to another). The second motivation is that we frequently have observed that the shape of the R1 and R2 doublets changes with high-temperature exposure and thermal cycling. Unfortunately, the shape changes are not systematic, so it is unlikely that they are due to changes that are deterministic in nature.

Although the microstructural evidence is not unambiguous, it is consistent with a progressive form of failure mode. This mode is characterized by the nucleation of subcritical interface separations

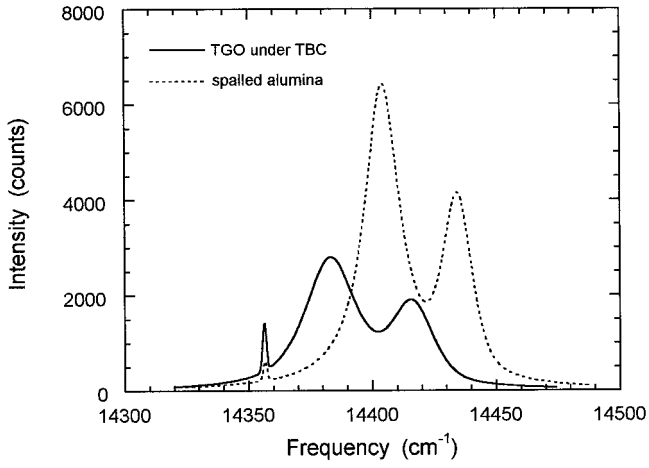

Fig. 1. Photostimulated R-line luminescence from a spalled piece of alumina (dotted line) and the alumina TGO in an EB-PVD TBC sample after one-cycle oxidation at 1200°C (solid line); the lower intensity of the spectrum from the TBC sample is a result of absorption and scattering within the TBC coating. Sharp line at ~14 355 cm^{-1} is an Ar emission line used to calibrate the frequency.

J. E. Ritter Jr.—contributing editor

Manuscript No. 189261. Received June 25, 1999; approved October 15, 1999.
Supported through the DOE-AGTSR Program. Author XP acknowledges partial support from the Chinese Academy of Sciences.
*Member, American Ceramic Society.

that occur at several randomly located sites on the interface. These grow in size with thermal cycling and/or oxidation time, linking together to form a critically sized flaw. After such a flaw has formed, the TBC can buckle spontaneously at the flaw; then, the buckle can grow to a second critical size and finally spall away from the alloy. After the TBC has buckled or spalled, it generally is visible optically, for instance, via direct visual inspection or using a boroscope. However, prior to buckling, there are no superficial indications of how far damage may have progressed or, indeed, whether it has even nucleated. Nevertheless, the progressive-failure mode provides a conceptual framework for establishing a mechanism-based methodology for monitoring progressive failure using piezospectroscopy. This procedure is the basis for the model that is described in the following section. In section III, microscopy observations of a severely (yet still only partially) debonded TBC sample are presented, together with luminescence spectra that have been obtained from the same sample. The observations are, in our experience, very unusual, because the debonded regions under the TBC can be observed directly via optical microscopy in this particular case. Nevertheless, these regions provide an unusual opportunity to relate the details of the luminescence spectra to the observed damage and are interpreted based on the model that has been presented here.

II. Piezospectroscopic Model

In this section, we start by describing the luminescence from a homogeneously stressed material and then consider the features of the luminescence spectra that occur in the general case, in which there are spatial variations in stress within a probed volume of a film. Following this general description, specialized equations are used to describe the spectral features that can be expected from the idealized stress distribution that is associated with the progressive-debonding failure concept.

Our starting point is the piezospectroscopic relationship. For a homogeneously strained body, the luminescence lines are systematically shifted, according to the following relation:

$$\nu = \nu(\sigma) \tag{1}$$

Over a wide range of stresses, but still small in comparison to the elastic modulus, a homogeneous stress (σ_{ij}) causes a linear shift in frequency ($\Delta\nu$) of the lines from their stress-free frequency:

$$\Delta\nu = \Pi_{ij}\sigma_{ij} \tag{2}$$

where Π_{ij} is a first-order phenomenological tensor whose values have been determined experimentally.[12] (Repeated index notation is used here.) The luminescence lines that are recorded from an unstressed alumina material have a mixed Gaussian–Lorentzian line shape, as a result of thermal broadening and various instrumental factors. As a result, the measured line shape ($\Phi(\nu)$) can be represented by

$$\Phi(\nu) = (1 - M)I_{\max}\exp\left[-\left(\frac{\nu - \nu_m}{w}\right)^2(4\ln 2)\right] + M\left[\frac{I_{\max}}{1 + 4\left(\frac{\nu - \nu_m}{w}\right)^2}\right] \tag{3}$$

where the first term is the Gaussian component and the second term is the Lorentzian component. M is the relative proportion of Lorentzian character, ν_m the frequency at the maximum intensity ($I_{\max}$), and w the full width at half maximum. Therefore, for a homogeneously strained body, the luminescence line is unchanged in shape and merely shifted by a constant frequency $\Delta\nu$.

For an *inhomogeneously* strained material, the shape of the luminescence peaks is different. This difference is illustrated by the comparison in Fig. 1 between the relatively sharp luminescence from a piece of unstressed alumina that has spalled from a bond coat and the considerably broader luminescence from the intact alumina TGO beneath a TBC. The physical basis for analyzing the change in the shape of the luminescence spectra is that the photon emission from each Cr^{3+} ion is independent of the other Cr^{3+} ions. Consequentially, each ion acts as an independent strain sensor, so the overall luminescence from a probed region is the sum of the photons that are emitted by the individual Cr^{3+} ions. If there is a variation in strain within the probed volume, then the individual ions within the probed volume will luminesce at different frequencies and cause an apparent peak broadening of the overall spectrum (see Fig. 2). As a result, the peak broadening is generally proportional to the variation in stress within the probed volume. A general treatment that relates spectral shapes to spatial property distributions recently has been presented by Lipkin and Clarke.[13] According to this analysis, the effect of an arbitrary, continuous stress distribution, as a function of position r within the probed region ($\sigma_{ij}(r)$), can be related to the measured peak shape ($I(\nu)$) by the relation

$$I(\nu, r_0) \propto \int_{-\infty}^{+\infty} \Phi[\nu - \nu_0(\sigma(r))]B(r - r_0)\,dr \tag{4}$$

where $B(r - r_0)$ represents the spatial variation in intensity of the optical probe and r_0 is the position of the center of the optical probe.

In principle, Eq. (4) can be inverted and the stress distribution within the probed volume determined from the shape of the luminescence spectrum. To the authors' knowledge, this process has not been attempted yet, nor is there any assurance that a unique solution for the stress distribution can be obtained by any inversion process.

To proceed, we consider the spectral features that would result from a progressive-debonding failure model. Two stages in the progressive failure of the TGO are shown schematically in Fig. 3. In the first stage, isolated regions have debonded at the TGO/bond-coat interface, with fully bonded material between them (Fig. 3(a)). In the second, later stage (Fig. 3(b)), two such debonded regions have linked together by fracturing through the TGO and then along the TGO/TBC interface. For pedagogical purposes, we assume that the size of each of these debonded regions is large in comparison to the thickness of the TGO, which means that we can assume that the stress in the TGO is essentially independent of position within the individual regions A, B, and C. We also assume that the stress is highest in region A, lowest in region B, and intermediate in region C. The justification for this latter assumption is based on the differences in the thermal expansion coefficient of typical bond-coat metals, polycrystalline alumina, and polycrystalline zirconia.

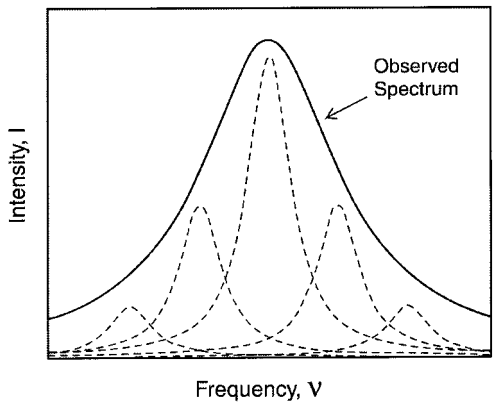

Fig. 2. Illustration of the peak broadening that results from the luminescence from individual Cr^{3+} ions in differently strained local environments within a probed volume.

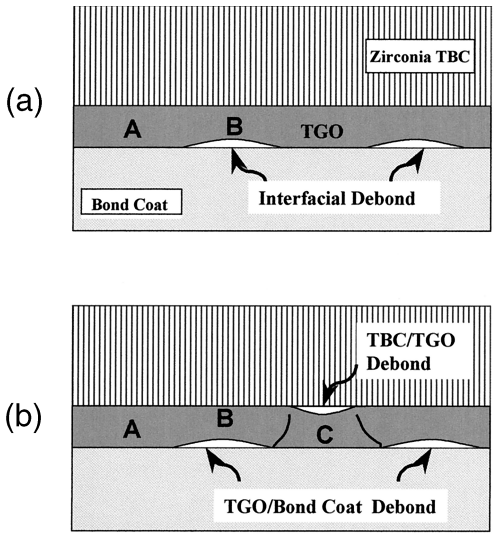

Fig. 3. Idealization of the interface debonding forming a progressive failure ((a) isolated debonding at the TGO/bond-coat interface and (b) TGO/bond-coat debonds linked by fracture through the TGO and interfacial separation along the TGO/TBC interface. The size of the debonds is assumed to be much larger than the TGO thickness. (Figure not drawn to scale.)

If a sufficiently small optical beam is used, regions A, B, and C can be probed individually, with the result that the luminescence spectra from the three regions would be as shown schematically in Fig. 4. Thus, in moving the optical probe over the region in Fig. 3(a), the spectrum would correspond to the highly stressed regions (region A), the intermediately stressed regions (region B), or a combination of the two. Similarly, in Fig. 3(b), a small probe may detect one of the three differently stressed regions or a combination of them. More generally, the probe would be much larger than the individual regions and encompass all three. Then, the overall spectrum would be given by the integral over the probed volume of the luminescence from each individual region *i*:

$$I(\nu) \propto h \int_{-r_p}^{+r_p} \sum_i W_i \Phi(\nu(\sigma_i))\, B(r)\, dr \qquad (5)$$

where r_p is the probe radius and W_i represents the relative area of region *i* (where *i*, for instance, is A, B, and C). The thickness (h) of the TGO is assumed, for simplicity, to be constant everywhere, which is not an unreasonable assumption, because the oxide thickness varies parabolically with oxidation time.

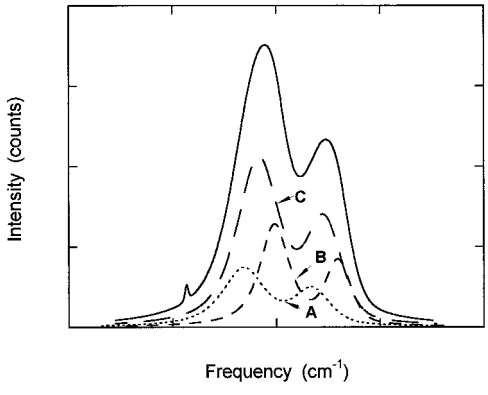

Fig. 4. Synthesis of a R-line spectrum from three individual R-line spectra, each from a region of different residual stress, such as regions A, B, and C in the idealization shown in Fig. 3.

This form of the luminescence intensity (Eq. (5)) suggests that the luminescence peak can be fitted with several individual spectra, each corresponding to the area fraction of differently stressed regions within the probed volume and the average stress in those regions superimposed. The procedure for fitting a spectral peak with a combination of peaks is a standard feature of many commercial software packages for spectral analysis, such as the GRAMs package that has been used in our work. Of the numerical algorithms that have been developed for spectral peak fitting, we have used one that is based on the Levenberg–Marquardt nonlinear peak method.[14]

III. Observations

Quite fortuitously, we have observed a particularly severe form of TBC failure that provides an opportunity to use some of the general ideas presented above and illustrate the spectral analysis. The sample was a CMSX-4 superalloy, with a platinum aluminide bond coat, that had been coated with a 100-μm-thick EB-PVD zirconia coating at the University of California, Santa Barbara.[15] The sample had three through-thickness holes, which were introduced as part of an ongoing investigation into the effect of holes on the residual stress in the TGO. After exposure to air at 1200°C for 32 h, luminescence spectra were recorded, through the TBC, from several places on the sample. Then, the sample was subjected to a series of thermal cycles. The zirconia TBC spalled from most of the sample abruptly on cooling after the 50th thermal cycle. The sample appearance after spalling is shown in the low-magnification micrograph in Fig. 5.

Figure 5 shows that the TBC has spalled from the center of the semicircular sample, which left the TBC around the semicircular periphery. The lighting that has been used to photograph the sample shows that both intact and debonded regions of the interface are visible through the TBC. The debonded regions under the TBC, such as region "D," appear somewhat lighter than the intact regions, such as region "E." In the spalled area, failure seems to have occurred from several separate regions, such as region "F." These brighter regions are bare bond-coated metal that is surrounded by alumina (region "G"), which appear darker in this image. These two regions are shown at higher magnification in the scanning electron microscopy (SEM) micrographs in Fig. 6. The alumina was identified using its R-line luminescence and energy-dispersive X-ray (EDAX) analysis. Although the individual failure

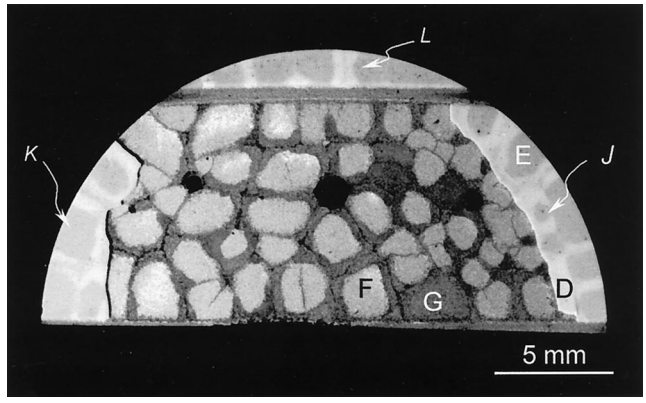

Fig. 5. Optical image of a severely spalled TBC half-circular disk sample under strong vertical illumination; the TBC remains attached at the periphery of the sample. Regions of interfacial debonding beneath the TBC can be observed by their slightly lighter contrast. On the spalled surface, bare bond-coat regions appear bright, whereas intact TGO attached to the bond coat appears darker. The letters refer to specific areas mentioned in the text. (The three black circles aligned horizontally in the middle of the micrograph are holes in the sample, whereas the horizontal stripe in the upper third of the micrograph is an impression in the TBC caused by the wire used to hold the sample during TBC coating.)

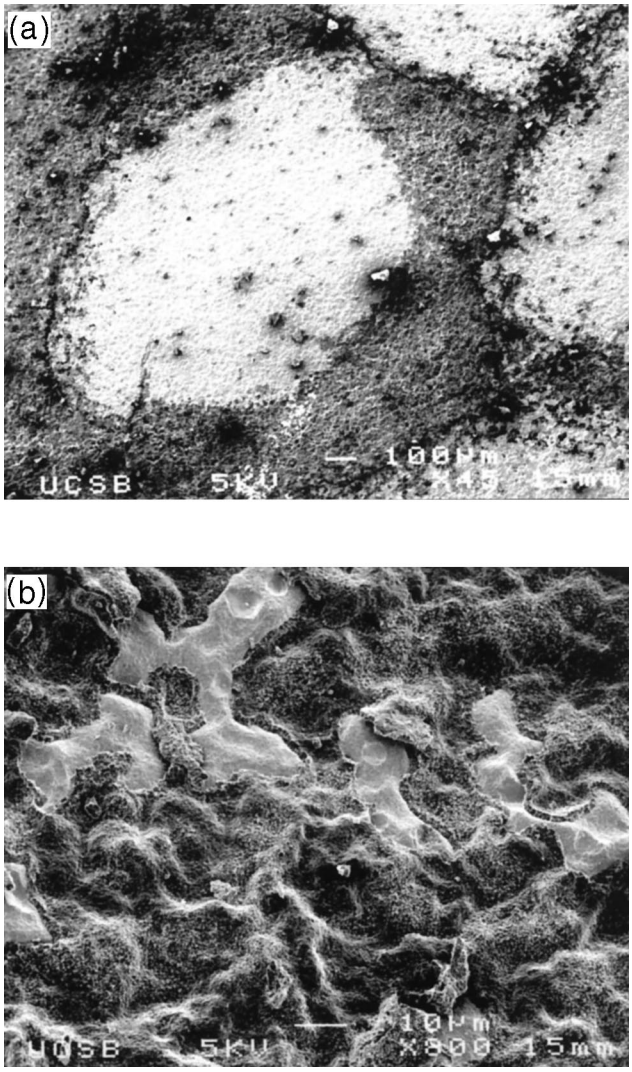

Fig. 6. SEM micrographs of (a) the bare bond coat and (b) the surrounding alumina TGO attached to the bond coat; this latter area corresponds to region "G" in the optical micrograph shown in Fig. 5.

origins from which spalling initiated could not be identified by either SEM or optical microscopy, the through-thickness holes clearly were not failure origins.

Luminescence spectra were obtained from a variety of positions on the sample;[†] spalled, isolated pieces of the TGO and the TBC with an attached piece of TGO also were used. A comparison of the R-line spectra is shown in Fig. 7. The sources of these spectra included the following: (i) the intact TGO that was attached to both the bond coat and the TBC (spectrum "E"), (ii) the TGO that was attached to the bond coat (spectrum "G"), (iii) the TGO that was attached to an isolated, spalled piece of TBC (spectrum "H"), (iv) the TGO that was present in the debonded region but measured through the TBC (spectrum "D"), and (v) a spalled piece of the TGO that was detached from both the TBC and the alloy (spectrum "I"). Clear differences in the spectra are evident and are quantified in terms of the frequency shift and broadening. These findings are summarized in Table I. The individual spectra plots D, E, G, and H provide the basis for analysis of the spectra from the damaged regions.

Spectra also were obtained through the TBC, using several different illumination procedures. Some spectra were obtained by stepping the optical probe along a line across a debonded region, whereas others were obtained by illuminating an area that was large, in comparison to the size of the debonded regions. Three examples of spectra that were obtained in the latter manner are shown in Fig. 8 and will be used as the basis for analysis in the following section.

IV. Analysis and Discussion

The observations presented in the previous section provide an opportunity to illustrate the piezospectroscopy methodology for assessing the degree of damage quantitatively, in terms of a progressive-failure model. The individual spectra that were obtained from the TGO that was attached to the bond coat (spectrum D), the TGO that was attached to an isolated piece of spalled TBC (spectrum H), and the intact TGO that was attached to both the bond coat and the TBC (spectrum E) are assumed to represent the spectra that would be obtained from positions C, B, and A, respectively, in the model schematics in Fig. 3. Then, these spectra

[†]The luminescence spectra were obtained using an optical microprobe, as described in the work of Lipkin and Clarke,[2] in which a laser beam could be focused to different diameters to probe features that were identified in the optical microscope portion of the microprobe.

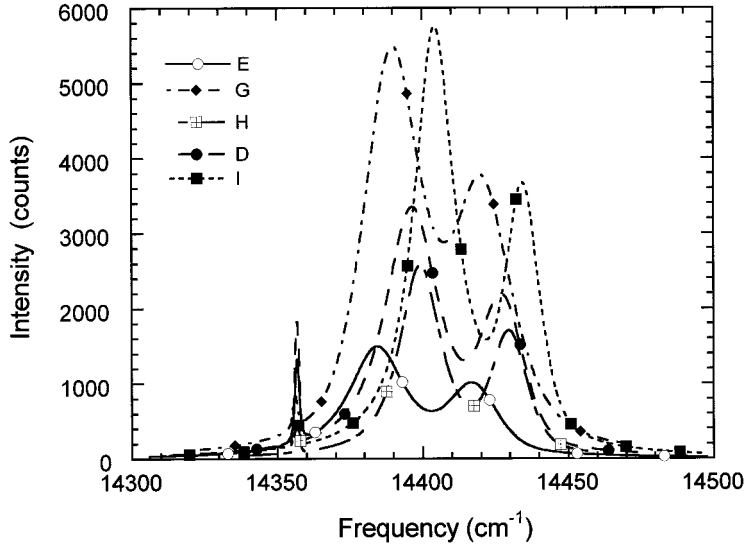

Fig. 7. Comparison of R-line spectra from intact TGO (spectrum "E"), TGO attached to the bond coat (spectrum "G"), TGO attached to TBC (spectrum "H"), and TGO in the debonded region but through TBC (spectrum "D").

Table I. Characteristics of Unit Spectra

Spectra from Fig. 5	R2 frequency shift (cm^{-1})	Residual stress (GPa)	FWHM† of R2 line (cm^{-1})
E	17.90 ± 0.25	−3.53 ± 0.05	21.70 ± 0.77
G	14.23 ± 1.24	−2.80 ± 0.24	21.65 ± 0.80
H	4.99 ± 0.21	−0.98 ± 0.04	14.70 ± 0.13
D	8.07 ± 0.70	−1.59 ± 0.14	17.6 ± 0.66
I	0.0	0.0	13.5 ± 0.12

†Full width at half maximum.

are used as the unit spectra to fit and reconstruct the spectra that are recorded through the TBC from the damaged regions.

The spectra shown in Fig. 8 were used to illustrate the analysis procedure. They were recorded, through the TBC, from large (~10 mm^2) regions in the vicinity of the areas labeled "J," "K," and "L" in Fig. 5. All three spectra evidently are broadened considerably from the spectra that is recorded from the intact regions of the TBC and are not simple Gaussian–Lorentzian peaks. Assuming that the spectra were the result of the superposition of the luminescence from regions at different stages in the progressive failure, the spectra were fit to be a combination of the three unit spectra (spectra D, E, and H). The fitting was performed using the Levenberg–Marquardt nonlinear peak method in the GRAMs software by forcing the spectra to be linear combinations of the unit spectra with fixed peak positions but variable relative intensities. Then, the relative intensities of the unit spectra that produced the best fit to the observed spectra in Fig. 8 were assumed to correspond to the fractional areas of the damaged and undamaged regions that are shown schematically in Fig. 3. These data are listed in Table II. In relating the results of this spectral analysis to the fractional areas of damage, it is assumed that any variations in optical scattering from the differing interfaces are already considered in recording the unit spectra.

These examples illustrate that quantitative information about damage in the TGO that is formed beneath a TBC can be deduced via detailed analysis of the luminescence spectra, using a specific damage-mechanism model. Although the analysis is based on a series of assumptions, which can lead to the calculated proportion of the debonded regions being erroneous, it nevertheless can be used to study the evolution of the relative proportion of damage systematically, for instance, with thermal cycling or thermal exposure. Such tests are presently underway. However, it is important to emphasize that many practical precautions must be taken in recording the luminescence spectra, to minimize extrinsic errors. Thus, the unit spectra used here were all recorded through the TBC, so that the scattering and absorption within the TBC were constant from one spectrum to another. Similarly, all the spectra were obtained at low levels of laser power, so that effects that were due to local heating and thermal dissipation could be assumed to be the same.

V. Summary

A mechanism-based methodology is presented for analyzing the changes in shape of photostimulated luminescence spectra that have been recorded from the thermally grown oxide, which can occur as a result of the development of localized interface debonding. This methodology provides a basis for determining damage nondestructively from changes in the shape of the luminescence spectra. Damage is assumed to occur via a progressive form of failure in which individual regions of damage are nucleated at the interface, which grow and link together until failure occurs. The spectral-analysis methodology is applied to determine the area fractions of damage for a severely spalled thermal barrier coating (TBC) where the local regions of debonding under the TBC were visible.

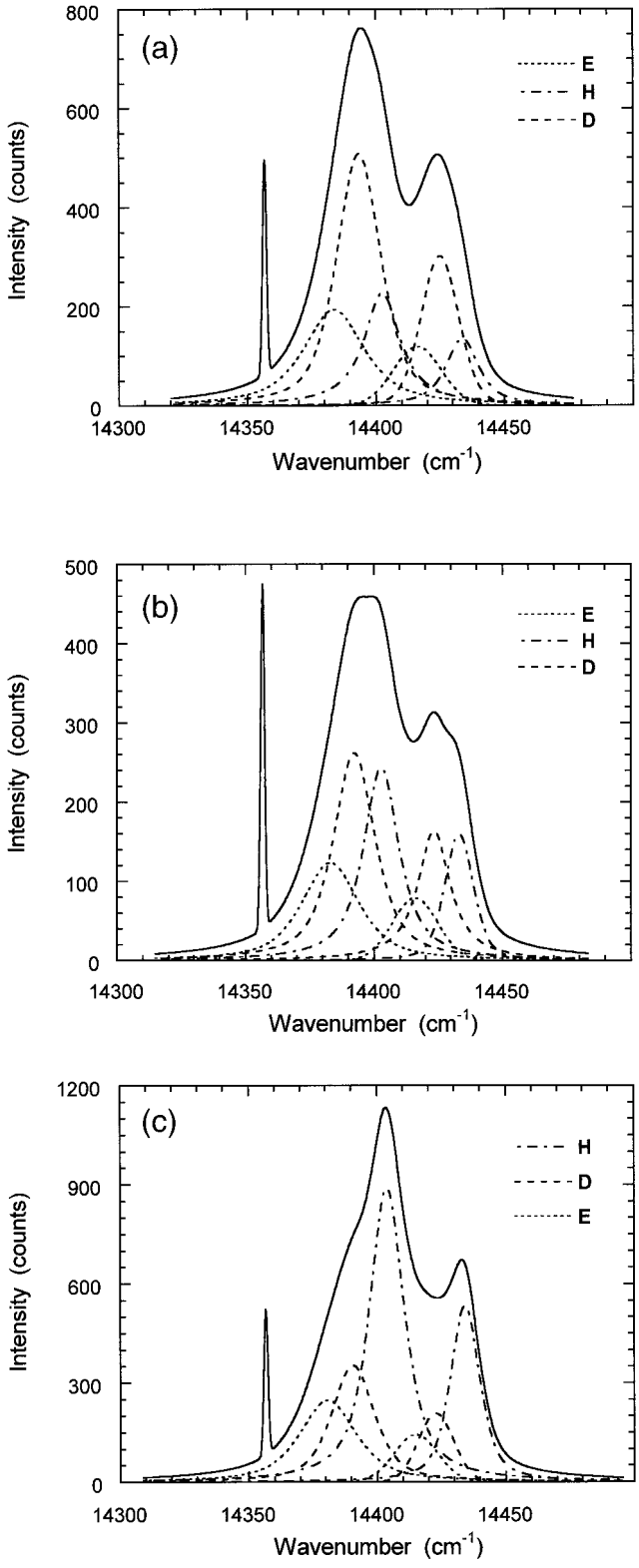

Fig. 8. Comparison of the spectra obtained by moving the probe over the TBC surface over (a) region J, (b) region K, and (c) region L in Fig. 5. Deconvolutions of the individual spectra into unit spectra H, D, and E from Fig. 7 are shown, and the sharp line at ~14 355 cm^{-1} is an Ar emission line used to calibrate the frequency.

Acknowledgments

The authors are grateful to S. Terry and J. Litty for providing the TBC-coated sample. Professor Carlos Levi and Dr. Vladimir Tolpygo are acknowledged for discussions throughout.

Table II. Area Fractions of Damaged and Undamaged Regions Determined by Spectral Analysis

Location in Fig. 5	Area fraction		
	Intact interface	TGO only attached to the TBC	TGO only attached to the bond coat
J	0.235	0.551	0.214
K	0.241	0.336	0.423
L	0.264	0.226	0.510

References

[1]Q. Ma and D. R. Clarke, "Stress Measurement in Single-Crystal and Polycrystalline Ceramics Using Their Optical Fluorescence," *J. Am. Ceram. Soc.*, **76** [6] 1433–40 (1993).

[2]D. M. Lipkin and D. R. Clarke, "Measurement of the Stress in Oxide Scales Formed by Oxidation of Aluminum Containing Alloys," *Oxid. Met.*, **45**, 267–80 (1996).

[3]R. Christensen, D. M. Lipkin, D. R. Clarke, and K. Murphy, "Non-destructive Evaluation of Oxidation Stresses through Thermal Barrier Coatings Using Cr^{3+} Piezospectroscopy," *Appl. Phys. Lett.*, **69**, 3754–56 (1996).

[4]D. R. Clarke, R. Christensen, and V. K. Tolpygo, "The Evolution of Oxidation Stresses in Zirconia Thermal Barrier Coated Superalloys Leading to Spalling Failure," *Surf. Coat. Technol.*, **94–95**, 89–93 (1997).

[5]V. K. Tolpygo, J. Dryden, and D. R. Clarke, "Determination of the Growth Stresses Generated during Oxidation of Fe-22Cr-4.8Al-0.3Y Alloy," *Acta Mater.*, **46** [3] 927–37 (1998).

[6]D. M. Lipkin, D. R. Clarke, M. Hollatz, M. Bobeth, and W. Pompe, "Stress Development in Alumina Scales Formed Upon Oxidation of (111) NiAl Single Crystals," *Corros. Sci.*, **39** [2] 231–42 (1997).

[7]D. M. Lipkin, D. R. Clarke, H. Schaffer, and F. Adar, "Lateral Growth Kinetics of α-Alumina Accompanying the Formation of a Protective Scale on (111) NiAl during Oxidation at 1100°C," *Appl. Phys. Lett.*, **70**, 2550–52 (1997).

[8]Q. Wen, D. M. Lipkin, and D. R. Clarke, "Luminescence Characterization of Chromium Containing θ-Alumina," *J. Am. Ceram. Soc.*, **81** [12] 3345–48 (1998).

[9]S. M. Meier and D. K. Gupta, "The Evolution of Thermal Barrier Coatings in Gas Turbine Engine Applications," *Trans. ASME* (1993).

[10]J. Wang and A. G. Evans, "Effects of Strain Cycling on Buckling, Cracking and Spalling of a Thermally Grown Alumina on a Nickel-Based Bond-coat," *Acta Mater.*, **47** [2] 699–10 (1999).

[11]V. Sergo and D. R. Clarke, "Observation of Sub-critical Spall Propagation of a Thermal Barrier Coating," *J. Am. Ceram. Soc.*, **81** [12] 3237–42 (1998).

[12]J. He and D. R. Clarke, "Determination of the Piezospectroscopic Coefficients for Chromium-Doped Sapphire," *J. Am. Ceram. Soc.*, **78** [6] 1347–53 (1995).

[13]D. M. Lipkin and D. R. Clarke, "Sample-Probe Interactions in Spectroscopy: Sampling Microscopic Property Gradients," *J. Appl. Phys.*, **77**, 1855–63 (1995).

[14]D. W. Marquardt, "An Algorithm for Least-Squares Estimation of Non-Linear Parameters," *J. Soc. Ind. Appl. Math.*, **11**, 431–41 (1963).

[15]J. Litty, S. Terry, and C. Levi; unpublished work. □

EVOLUTION OF POROSITY AND TEXTURE IN THERMAL BARRIER COATINGS GROWN BY EB-PVD

Scott G. Terry, Jennifer R. Litty and Carlos G. Levi

Materials Department., University of California
Santa Barbara, CA, 93106-5050

Abstract

The pattern and distribution of porosity in the columnar microstructure of thermal barrier coatings (TBCs) grown by electron-beam physical vapor deposition (EB-PVD) are key factors in determining the coating compliance, and consequently its resistance to spallation, as well as its thermal conductivity, and hence the requisite thickness for a given degree of insulation. The present study aims to advance the understanding of the evolution of porosity during EB-PVD growth, as well as its relationship with the concurrent evolution of crystallographic texture. TBCs with the conventional 7 wt.% yttria partially-stabilized zirconia composition were deposited on stationary substrates at temperatures of 900°C (~0.40T_M) and 1100°C (~0.46T_M). The substrates were shaped to explore deposition under normal and oblique (45°) vapor incidence in order to provide insight on the shadowing mechanisms responsible for the formation of porosity. It was shown that the characteristics of the porosity can change dramatically with both vapor incidence angle (VIA) and deposition temperature. The column growth direction was found to be ⟨101⟩ for both normal and oblique incidences at 1100°C, but changed from ⟨111⟩ to predominantly ⟨101⟩ for deposition at 900°C. The role of substrate manipulation during deposition is discussed in the context of these findings.

Elevated Temperature Coatings:
Science and Technology III
Edited by J.M. Hampikian and N.B. Dahotre
The Minerals, Metals and Materials Society, 1999, pp. 13-26.

Introduction

Thermal barrier coatings (TBCs) have emerged as arguably the most critical materials issue for the next generation of gas turbine technology [1]. The addition of TBCs to turbine airfoils is estimated to have the potential for increasing their temperature capability by as much as ~150°C, a performance improvement equivalent to that produced by the last 20 years of alloy development and cooling engineering [2]. Notwithstanding a record of nearly three decades of service in gas turbines, full realization of the TBC potential remains hindered by concerns about their reliability and a lagging science base that can guide their optimization.

In addition to the obvious requirements of refractoriness and low thermal conductivity, TBCs must have "strain tolerance", i.e. high resistance to spalling under thermal cycling [3]. The latter is not a property of the thermal barrier alone but rather of the complete material system, as the stresses that drive spalling arise primarily from the mismatch in coefficients of thermal expansion (CTE) between the substrate, the TBC, and the thermally grown oxide (TGO) which forms between the TBC and the underlying "bond coat" (BC) [2]. From this perspective, the ideal TBC should have a high in-plane compliance in order to minimize its contribution to the residual stresses in the coating. (The stresses are then dominated by the TGO/substrate mismatch, whereupon TBC life could be conceptually related to the attainment of a critical TGO thickness, in qualitative agreement with practical observations.) This argument has been used to explain why columnar TBCs produced by electron-beam physical vapor deposition (EB-PVD) are generally more durable than those produced by plasma spray (PS) [3].

Current TBCs are nearly universally based on ZrO_2 partially stabilized with ~7wt.%Y_2O_3 (YPSZ) [4]. The coatings tend to exhibit significantly lower thermal conductivity and higher compliance in comparison with the monolithic oxide alone, revealing important contributions from the microstructure. Perhaps the most critical feature in this regard is the porosity and its associated parameters, i.e. concentration, morphology, size scale and spatial distribution. For example, both EB-PVD and PS coatings can be viewed as containing relatively large voids of high aspect ratio. However, the ribbon-like voids in the former are aligned normal to the plane of the coating, separating the columnar grains and yielding superior compliance [3], whereas the disk-like voids in the latter occur between the splats, parallel to the plane of the coating and promoting superior insulating efficiency [2]. Recent work has further suggested that the graded microstructure inherent in EB-PVD TBCs, where the coating density (and consequently the in-plane modulus) decrease with distance away from the substrate [3], could have major implications in the mode of failure and the strain tolerance of the TBC [5]. EB-PVD coatings also contain a much finer scale of porosity within the columns [6] which can have, in principle, a greater effect on the thermal conductivity of the coating than the intercolumnar voids.

Notwithstanding the obvious importance of porosity to the thermal, mechanical, and even chemical performance of the TBCs, surprisingly little research has focused on quantifying its relationship with the fundamental coating properties, or on establishing and quantifying its dependence on processing conditions. An effort in the latter direction has been initiated by the authors for coatings produced by EB-PVD. This paper reports on the effects of temperature and vapor incidence angle (VIA) on the evolution of intercolumnar porosity in TBCs, as well as on the related evolution of crystallographic texture.

A key issue to be examined is the apparent inconsistency between the purported microstructure and compliance goals for the TBCs, and the temperatures normally used in their deposition. In the context of the conventional "structure map" (Figure 1), TBCs are rather unique because they aim to combine the well aligned columnar structure of Zone 2 with the substantial porosity

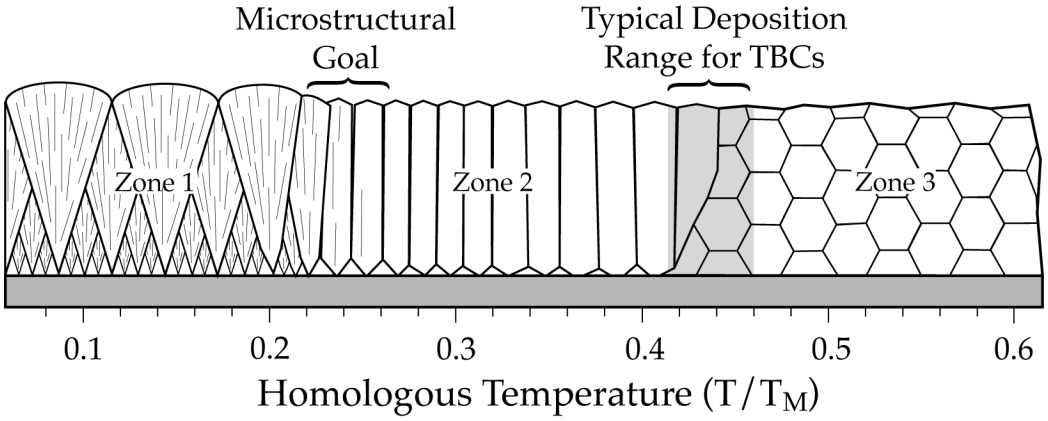

Figure 1. Schematic structure map, adapted from Reference [7]. The transition temperatures between zones were reported as ~380°C (1-2) and ~1000°C (2-3) for YPSZ deposited at 20-40nm/s.

characteristic of Zone 1. This would place the desirable microstructure at the transition between Zones 1 and 2, which for ZrO_2 is reported at ~380°C (~0.22T_M) [7]. However, TBC deposition is usually performed above ~1000°C (~0.42T_M) [8], which is the reported temperature for the Zone 2-3 transition [7]. The high deposition temperatures are apparently selected to promote strong bonding with the underlying BC [8], and indirectly as a means to enhance the stability of the coating against sintering during service. Porous columnar TBCs with desirable compliance are nonetheless obtained under these high temperatures, at variance with zone structure models which would predict the microstructure to be dense and probably equiaxed (T/T_M ~0.5). Boone et al. [9] first noted that intercolumnar gaps evolved in normally dense metallic films when the substrate was rotated during coating, an observation that led to the "segmented" microstructure concept for strain tolerant TBCs [3]. Schulz et al. [10] ascribed the effect to "shadowing" and later proposed a modification of the structure map to account for the effects of rotation [11]. At this point, however, there is only a superficial understanding of the relevant mechanisms in the TBC literature.

Because the intercolumnar pores evolve with the aligned columnar structure, elucidating the origin of the former also implies understanding the mechanisms that give rise to the latter. Much of the literature on thin films views the columnar structure as a result of the evolution of pipelike voids produced by a combination of insufficient surface diffusion and atomic-scale shadowing. Columnar growth, however, is more often the consequence of "evolutionary selection" [12] wherein grains (within a random polycrystalline array) having their preferred growth directions oriented in the direction of the vapor flux gradually occlude less favorably oriented neighbors. The result is a film with an out-of-plane fiber texture consistent with the preferred growth direction. The literature, however, reports not one but several crystallographic textures in YPSZ TBCs, notably ⟨100⟩ [6, 13-16] but also ⟨113⟩ [17-19] and ⟨111⟩ [19, 20]. The multiplicity of textures has been ascribed to variations in the processing conditions but clear relationships have not been established and some disagreement exists among different studies.

The strategy adopted to shed additional light on these issues involves establishing first a baseline for microstructure evolution in the absence of rotation. Particular attention has been placed on accurately measuring and controlling the substrate temperature during deposition, a critical parameter which is often uncertain in previous studies. The microscopic aspects of shadowing have been explored by deposition on stationary substrates oriented at different angles relative to the vapor flux.

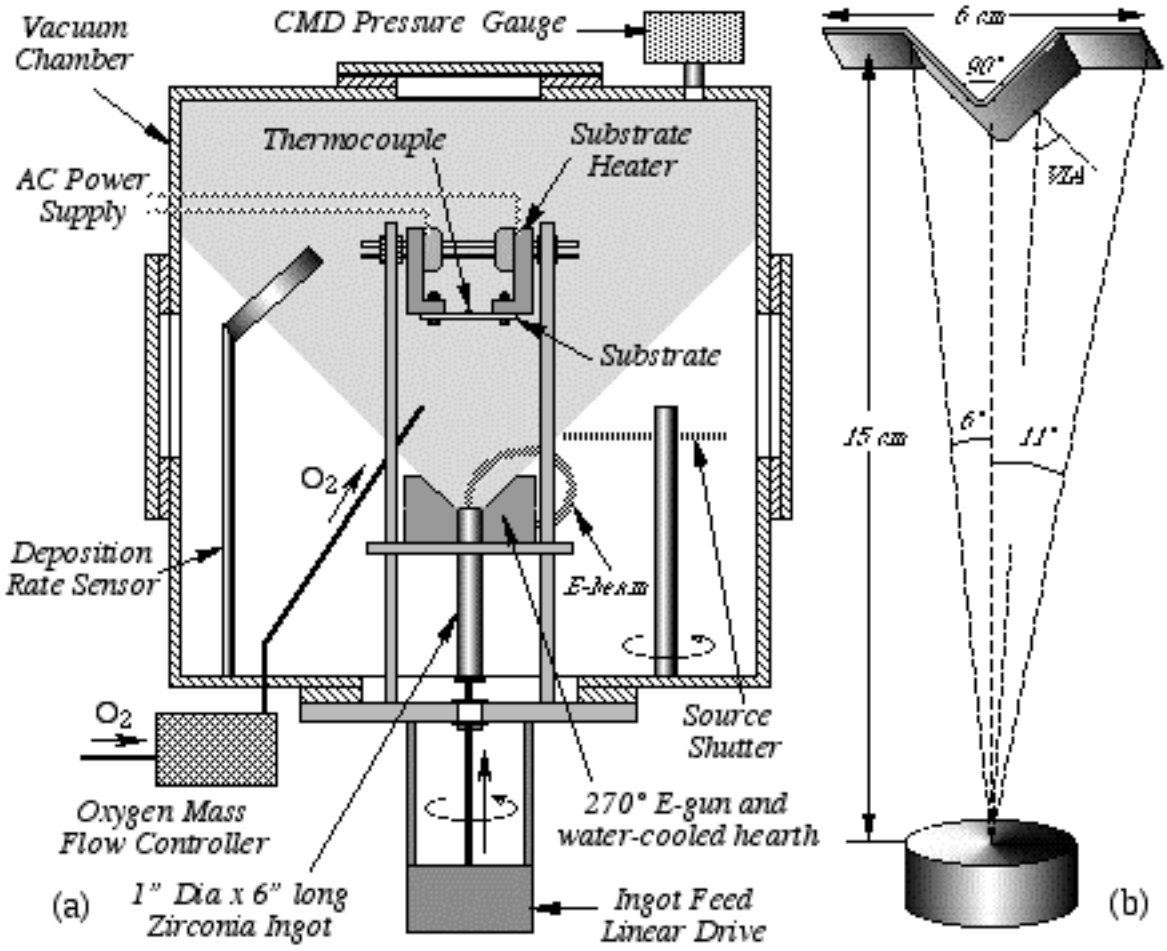

Figure 2. Schematic of the UCSB EB-PVD system as used for the experiments in this paper (a) and detail of the "V" specimens used to study oblique deposition (b).

Experimental Procedures

All deposition experiments were performed in house using the electron-beam PVD system schematically depicted in Figure 2(a). The system consists of a cubic vacuum chamber, 60 cm on the side, with a 10 kW, 270° electron gun and a water-cooled copper hearth modified to accept a continuously fed ceramic ingot 25 mm in diameter. The gun is driven by a 10kV, 14kW power supply (AIRCO/Temescal CV-14). The deposition rate is monitored using a quartz-crystal sensor (Leybold-Inficon CrystalSix), shuttered intermittently so it can operate effectively at high rates over long periods of time, whose signal is fed into a close-loop controller for the e-gun (Leybold-Inficon IC/5). Separate controls are available for the beam sweep pattern and rate (AIRCO VWS-1090). An electronic mass flow control system (MKS 1159A) meters a preset flow of oxygen into the chamber during deposition. Total chamber pressure is regulated via a feedback-controlled variable conductance exhaust valve using a capacitance manometer sensor.

The deposition rate in the present set-up is limited by the maximum total pressure that the 270° gun can tolerate (~10^{-4} torr) before it turns itself off automatically to prevent rapid filament degradation. As the system is evacuated to 10^{-6} torr prior to evaporation, the total pressure is essentially comprised of the evaporated ceramic plus the excess oxygen fed into the chamber (at ~20 sccm) to promote stoichiometric deposition. At present, deposition rates for stoichiometric films are limited to ~2 μm/min (referred to a stationary substrate under normal incidence), which is significantly lower than current industrial practice but in the range used to develop the structure map of Figure 1. The deposition rate can be readily increased up to ~4 μm/min with the same

oxygen feed rate and without exceeding the operating pressure limit, but the resulting coatings tend to be oxygen deficient (manifested by a grayish color). System modifications are underway to extend the feasible range up to ~20 μm/min.

The ceramic ingots used in this investigation were 25 mm dia. x 150 mm long with nominal composition ZrO_2-7wt.%Y_2O_3 (Trans-Tech, Adamston, MD). Major impurities reported are (in weight percent) 1.35HfO_2, 0.08TiO_2, 0.02SiO_2, with ≤0.01 each of CaO, MgO, Al_2O_3, Fe_2O_3, Na_2O, U and Th. The ingot density is 3.77Mg/m^3, equivalent to a porosity content of ~38%.

The substrates were rectangular strips 70 x 10 x 1 mm cut from Fecralloy® sheet, nominally Fe-22Cr-4.8Al-0.3Si-0.3Y (in wt.%). [1] The sheet was vacuum annealed for 17 hours at 1100°C and then mechanically sheared into strips, which were subsequently polished to a final media size of 3 μm. Some of these strips were hot formed into a "V" shape (cf. Figure 2b), using a bending press, and then hand polished with 3 μm diamond paste to remove the oxide generated during the forming operation. Flat and bent substrates were oxidized in air for 12 hours at 1100°C to form a stable α-Al_2O_3 layer about 1.5 μm thick prior to deposition of the TBC. The substrates were then mounted on a stage (Figure 2a) and resistively heated to the desired deposition temperature using 20V AC power. For the present experiments, the temperature was monitored using a Type K thermocouple spot-welded to the substrate, and controlled within ±10°C of the desired value.

The deposition experiments performed for this study are summarized in Table I. The substrate temperatures are equivalent to ~0.4 and 0.46T_M in the homologous scale, representing approximately the bounds of the range typical of current industrial practice. The flat specimens provide a baseline for normal deposition (0° VIA), whereas the "V" specimens are intended to explore the effect of high vapor incidence angles (~45°VIA) on the TBC microstructure. The tip and "wing" sections of the "V" (Figure 2b) receive approximately normal fluxes and provide a useful comparison with the microstructures found in the flat substrates. The processing conditions were selected to give approximately the same rate of coating deposition normal to the substrate plane in all cases (~20 nm/s or 1.2 μm/min). This implied the use of higher vapor fluxes for the "V" specimens, by a factor of $\cos(VIA)^{-1}$ (Table I), and hence faster evaporation rates.

The coatings were characterized primarily by X-ray diffractometry (XRD) and scanning electron microscopy (SEM). Observations were made on both polished cross sections and growth surfaces, as well as fracture surfaces of some samples generated by notching the substrate with a diamond saw and breaking the specimen in bending. Cross sections were prepared by cutting sections of the coating and substrate with a low speed diamond saw, placing two pieces in a "sandwich" configuration with the coating in the center, impregnating the assemblage with epoxy resin, and polishing using conventional metallographic techniques. Polishing media was diamond paste with colloidal silica for the finishing step.

Table I. Deposition conditions for TBCs studied in this investigation.

Nominal VIA	Substrate Temp. (°C)	Thickness (μm)	Deposition time (min)	Average Rate (μm/min)	Rate Normal to Vapor Flux
0°	1100	120	96	1.3	1.3
0°	900	110	88	1.3	1.3
45°	1100	65	56	1.2	1.6
45°	900	61	62	1.0	1.4

[1] Material supplied by Goodfellow, Berwyn, PA. The actual Y content is typically ~0.05 wt.%.

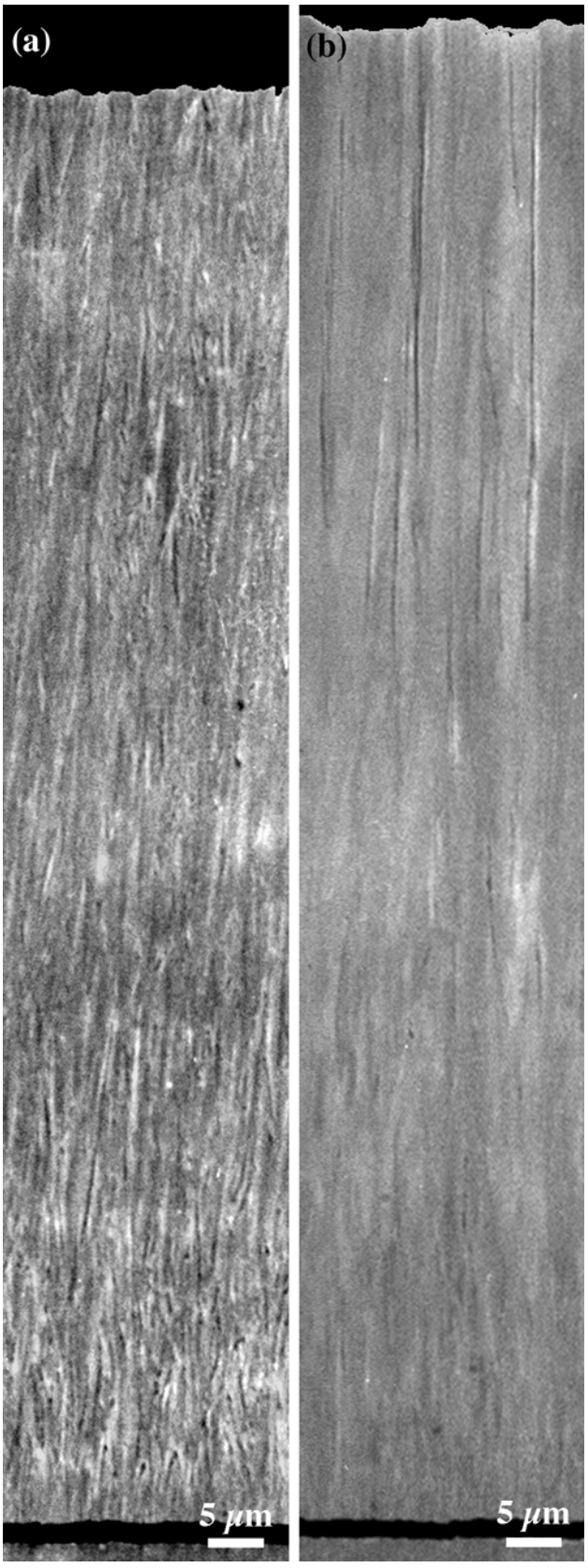

Figure 3. SEM cross sectional views of YPSZ coatings deposited under normal incidence (nominal VIA 0°). (a) 900°C, (b) 1100·C. The dark phase near the bottom is the TGO formed during the oxidation treatment prior to deposition.

Results and Discussion

General views of the microstructure of the coatings are shown in Figures 3 to 5. A comparison of Figures 3 and 4 reveals that the coatings produced under nominally normal incidence (flat substrates located directly above the source and normal to the ingot axis) appear much denser than those produced under oblique fluxes ("V" specimens) at equivalent temperatures. The structure is fully columnar in all cases, although this is more difficult to discern in the 0° coatings because of a lack of clearly developed intercolumnar gaps. Nevertheless, closer examination shows that there is indeed a non-negligible amount of high-aspect-ratio porosity aligned in the growth direction in these 0° specimens. These pores may extend over significant fractions of the thickness, but often show contact points and in some cases appear to be composed of arrays of very small circular voids. What is particularly significant is that these 0° coatings depart from the structure map, even though they were deposited at rates comparable to those used by Movchan and Demchishin [7], at temperatures in the upper end of Zone 2 (cf. Figure 1), and without any rotation that could promote shadowing. A possible scenario to account for the evolution of this porosity will be discussed later.

The cross sectional views in Figure 4 reveal the dramatic effect of the vapor incidence angle in developing the intercolumnar gaps, *even in the absence of substrate rotation*. The effect is most striking at the higher temperature, cf, Figs. 3(b) and 4(b), where the individual columns become distinctly defined and separated by wide gaps as the flux changes from normal to oblique. The intercolumnar gaps originate very close to the substrate and the evolutionary selection process is clearly reflected in the coarsening of their spacing with increasing thickness.

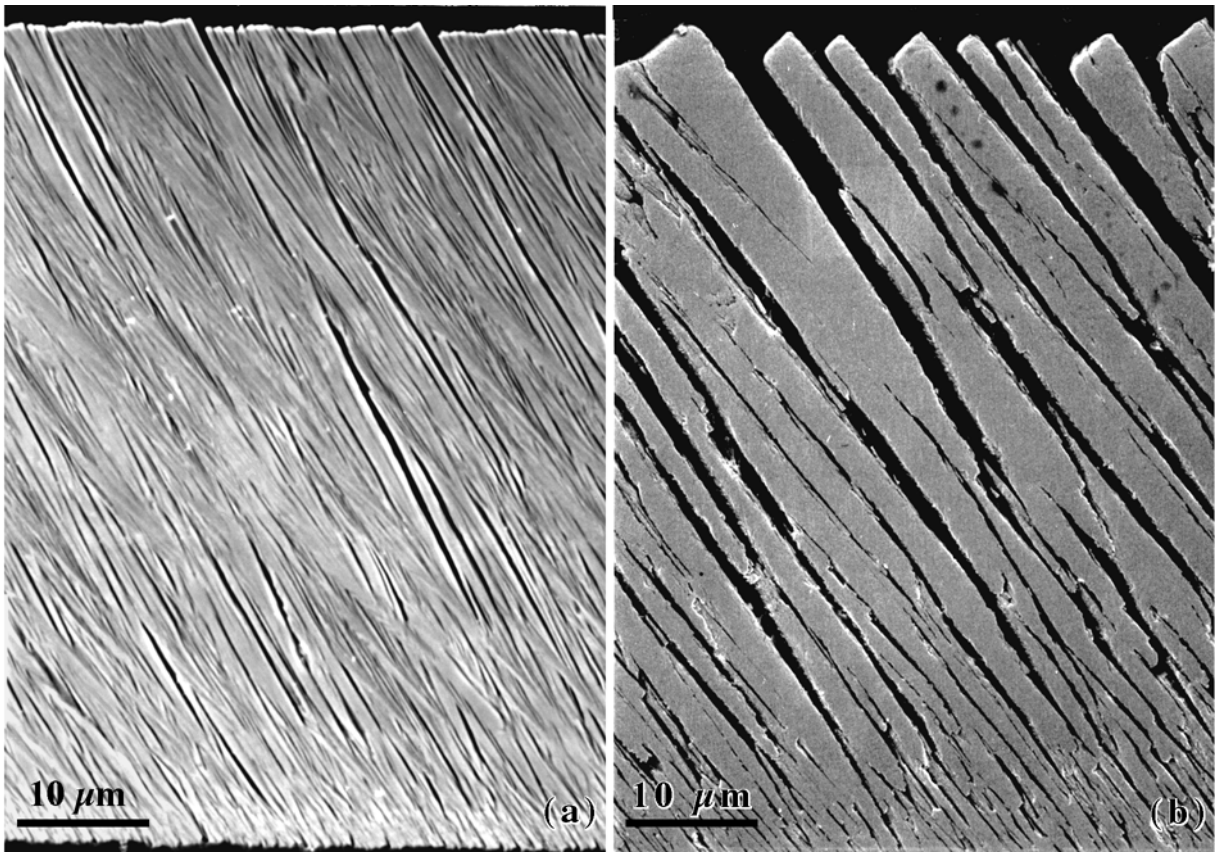

Figure 4. SEM cross sectional views of coatings deposited under oblique vapor incidence (nominal VIA 45°). (a) 900°C, (b) 1100·C. The column orientation angle is ~31° in (a) and ~36° in (b). The scale of the micrographs is the same as in Figure 3 but the total thickness of the coatings is somewhat lower, as indicated in Table 1.

The coating grown under oblique incidence at the lower temperature, Figure 4(a), also contains well defined elongated voids that initiate near the substrate, but the column definition is less distinct suggesting that the columns themselves may have long intragranular gaps. The different microstructural scale between Figures 4(a) and (b) is qualitatively consistent with the refinement of the porosity that would be expected from the effect of the lower temperature on surface diffusion. A correspondingly higher porosity content should also be anticipated for the lower temperature, but this is not immediately evident from the micrographs and needs to be ascertained by more quantitative measurements.

The shadowing phenomena responsible for the evolution of this elongated porosity is revealed by the micrographs in Figure 5, showing details of the column tips on the top surface of the coatings corresponding to Figures 3 and 4. It is first noted that there is no significant evidence of open gaps intercepting the surface under normal incidence, Figs. 5(a) and (b), in agreement with the nearly dense appearance of the cross sections in Figure 3. In contrast, the growth surfaces in Figs. 5(c) and (d) show well developed voids on the side of the columns where a "shadow" would be produced by the interplay between the column tip and the vapor flux. Closer examination reveals that the downstream profile of these voids closely replicates the shape of the edge of the tip. It is also evident from Figs. 5(c) and (d) that the finer scale of the columnar pores observed at the lower deposition temperature, Figure 4(a), is a direct consequence of the finer scale of the crystallographic tips casting the shadows that give origin to them. The link between porosity and texture is also reflected in these observations, as the type and configuration of the facets that form the tip is directly related to the growth direction of the columns.

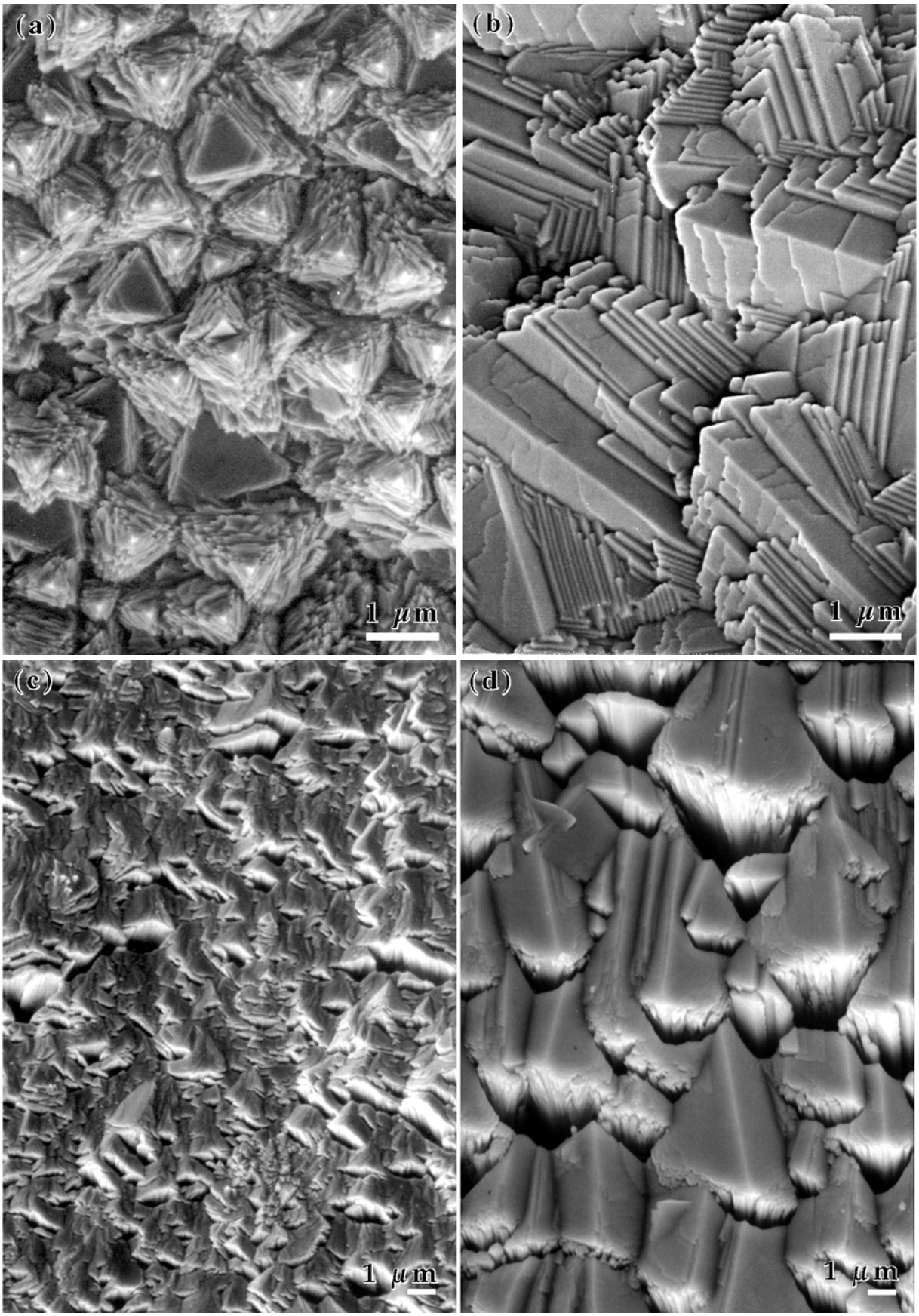

Figure 5. SEM views of the top (growth) surfaces for the specimens in Figures 3 and 4: (a) 900°C, VIA 0°; (b) 1100°C, VIA 0°; (c) 900°C, VIA 45°; (d) 1100°C, VIA 45°. The vapor flux in (c) and (d) descended from top to bottom at an angle of ~45° from the plane of the image. Note the clear connection between the voids and the "shadows" cast by the column tips as they interact with the vapor flux.

Texture Evolution

Examination of Figure 5 from a crystallographic perspective reveals that the tips evolving from deposition at the higher temperature have the appearance of "rooftops" with well developed facets. Figure 5(b) suggests that these dominant facets grow by ledge propagation and should correspond to the slowest growing planes for ZrO_2, with the preferred growth direction defined by the arrangement of these facets [21]. A Periodic Bond Chain (PBC) analysis for the fluorite structure [22] predicted that the dominant facets should be of the {111} type. Neglecting the slight tetragonality of the t' phase in these coatings [19], it can be readily shown that ⟨001⟩, ⟨111⟩, and ⟨101⟩ growth directions for the columns can be defined by tips consisting of {111} facets arranged as, respectively, a four sided pyramid, a three sided pyramid, and a two-sided "rooftop". Pole figure analysis of the 1100°C specimens has shown the column axes to be consistently of the ⟨101⟩ type for both 0° and 45° VIA [23]. The angle between the bounding facets is ~110°, suggesting that they are of the{111} type in agreement with the PBC argument. The columns of the 0° coating do not appear to have any preferred orientation in-plane but develop a secondary alignment mode as the VIA changes to 45°. This is manifested by an alignment of the "rooftops" in Figure 5(d), compared with a more random distribution in Figure 5(b).

The 900°C coatings show a rather different behavior of the column tips. Pole figure analysis reveals that the 0° coating has a preferred ⟨111⟩ orientation [23], consistent with the triangular shape of the pyramidal tips in Figure 5(a). It is noted, however, that the bounding sides of the tips are not well developed facets and in some cases the pyramids are truncated, showing a flat triangular facet normal to the growth direction. This suggests that the active growth planes may not be at an angle to the column axis, as in the 1100°C coating, but rather parallel to the substrate, as is often the case for epitaxial growth. The pyramids might then be interpreted as a mesoscopic form of "island growth" [21], which could explain why the sides are not flat as ledge propagation would not normally occur on them. The details of the mechanism and the underlying reasons for this behavior remain the subject of current work.

The effects of an oblique VIA on the column texture is also different at the two temperatures. While no change in the growth axis is observed at 1100°C, pole figure analysis reveals that the columns exhibit a mix of two orientations at 900°C, namely a dominant ⟨101⟩ and a secondary ⟨111⟩. Comparison of Figures 5(a) and (c) also reveals that the tip facets change from pyramidal to a "rooftop" shape, showing similarities with the higher temperature tips, cf. Figure 5(d), but with facets which are generally less well developed. One might hypothesize from these observations that the ⟨111⟩ mode of column growth is relatively unstable, perhaps because it relies on one dominant facet perpendicular to the growth axis. A substantially oblique VIA appears to activate an alternate set of facets which leads to ⟨101⟩ growth. The transition, however, is not well understood and requires further investigation.

The present TBCs also show differences in texture with previous reports in the literature. The ⟨101⟩ texture prevailing in three of the four coatings is not commonly observed, and when noted in other studies it was concluded to be not a true fiber texture but an apparent out-of-plane orientation resulting from the growth of ⟨001⟩ textured columns at ~45° from the film plane [19]. It is also evident that under some conditions changes in VIA may indeed change the crystallographic axis of the columns, as suggested by some authors [16], but also that the column axis may remain invariant with changes in VIA, as indicated by others, e.g. [19]. In any event, if the columns do grow with well defined crystallographic axis and the column orientations relative to the substrate may be changed arbitrarily by changes in VIA, there is no obvious reason why the coatings should exhibit any specific out-of-plane orientation and textures reported in that frame of reference are not particularly relevant.

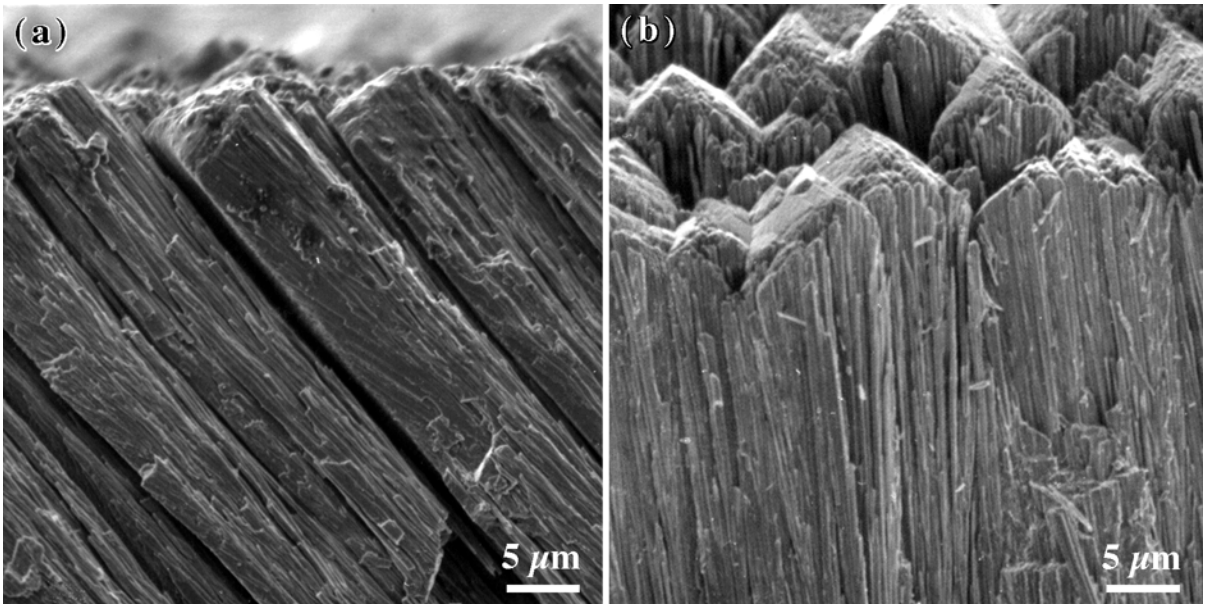

Figure 6. SEM images showing details of the columns near the growth surface in the 1100°C coating deposited at 45° VIA. The views correspond to the edges of fracture surfaces normal to the coating plane. (a) View normal to the plane of incidence; and (b) view along to the plane of incidence in a direction approximately perpendicular to the axes of the columns.

The Role of Rotation

It is noted from Figures 5(c) and (d) that the distribution of intercolumnar porosity induced by an oblique VIA on a non-rotating substrate is anisotropic. Figure 6(a) shows that open gaps between columns are clearly evident along the plane of incidence (POI, defined by the direction of vapor incidence and the normal to the substrate). In contrast, a view along to this plane and normal to the column axes, Fig. 6(b), reveals a much lower density of intercolumnar gaps. One would then anticipate that the in-plane compliance of such coating might be much higher in the former direction than in the latter. Moreover, the scale of the intercolumnar gaps in Figure 4 is probably much larger than needed for compliance, especially for the coating deposited at 1100°C, and might be detrimental to the resistance of the coating to erosion and/or chemical attack.

The role of rotation emerges now more clearly in the context of these issues. Rotating the substrate along an axis perpendicular to the POI would shift the column axis back to normal to the plane of the coating, but the sunrise-sunset effect would produce shadows on both sides of the column during deposition, which would lead to the formation of intercolumnar gaps narrower than those produced by a fixed VIA. On the other hand, rotation about a single axis may not alleviate significantly the anisotropy of the film, as shadowing effects parallel to the rotation axis would be less pronounced than along the POI. Minimization of this anisotropy requires oblique vapor incidence in at least two non co-planar directions, such as might be produced by simultaneous rotation and cyclic tilting of the substrate. Substrate rotation and tilting are then important not so much as means to produce shadowing, which can be achieved simply by oblique vapor incidence on a stationary substrate, but primarily as a way of *controlling the pattern of shadowing around the columns*. The present findings also suggest that substrate rotation could also modify the selection of active facets and hence the column texture, in agreement with observations reported by Shultz et al. [24]. In current technology, however, the pattern of manipulation of the substrate in the vapor plume is defined predominantly by the requirements of conformal coverage and coating thickness distribution, with much less attention given to its potential role in controlling the microstructure and local properties of the TBC.

Other Manifestations of Shadowing

Closer examination of the intercolumnar gaps in Figure 4(b) reveals finer scales of "columnar growth" taking place within these regions, as illustrated in Figure 7. On the downstream side of the gap there is evidence of "feathering", consisting of submicron size "cells" growing off the column side in a direction approximately parallel to the vapor flux. This form of growth is absent on the other side of the gap, which shows branching rod-like features parallel to the column axis. The fine cells are a manifestation of the fact that the VIA does not have a single value but represents the mean of a cone of vapor directions emanating from different points in the source. The tip edge blocks the majority of the flux and produces a shadow, but there is a small fraction of vapor that can penetrate the gap and impinge on the column side at a locally high VIA, yielding nano-scale "columns" that produce the feather-like appearance. The deposition is still line-of-sight as no growth occurs on the opposite side, which is completely shadowed by the tip edge. One may hypothesize that the nano-scale columnar growth mode is a consequence of finer scale shadowing produced by surface features on the side of the main column. However, futher work is needed to elucidate the nature of these features and the details of their interplay with the vapor flux.

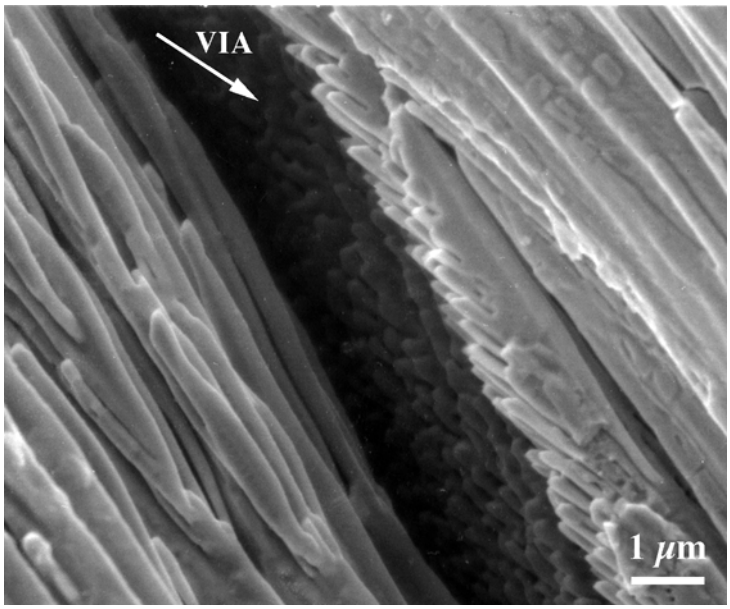

Figure 7. Details of the intercolumnar gap in a coating grown at 1100°C with 45° VIA. The image was taken from a fracture surface along the plane of incidence.

The existence of a distribution of VIAs is likely to be also the cause for the small amounts of columnar porosity noted in Figure 3. One can readily estimate for the conditions of the present experiments that a flat substrate under nominally normal incidence (average VIA = 0°) actually has a range of VIA from ~0±5° for a point directly above the center of the source, to ~10±5° for the ends of the substrate (cf. Figure 2b). This appears to give rise to sufficient shadowing to induce the formation of porosity, even at temperatures on the order of $0.46T_M$.

Concluding Remarks

The present investigation has provided new insight on how shadowing mechanisms operate to generate the intercolumnar porosity which is essential to the strain tolerant performance of EB-PVD TBCs, and on the connection between porosity and texture evolution. It has also been shown that substantial changes in the structure of the coating may occur even within the range of processing temperatures typical of industrial practice, with potentially important implications for TBC performance. These findings provide an improved foundation on which to build a better understanding of the effects of substrate manipulation during deposition.

Acknowledgments

This research was sponsored by the Collaborative UC-Los Alamos Research program under grant CULAR-9830. Additional support for S.G. Terry through the NSF Fellowship program and for J.R. Litty under DOE/AGTSR contract 98-01-SR068 are gratefully acknowledged.

References

1. National Research Council, Coatings for High-Temperature Structural Materials: Trends and Opportunities, (Washington, D.C.: National Academy Press, 1996).
2. R.L. Jones, "Thermal Barrier Coatings,"in Metallurgical and Ceramic Protective Coatings, ed. K.H. Stern, (London, UK: Chapman & Hall, 1996) 194-235.
3. T.E. Strangman, "Thermal Barrier Coatings for Turbine Airfoils," Thin Solid Films, 127 (1985) 93-95.
4. S. Stecura, "Optimization of the NiCrAl-Y/ZrO_2-Y_2O_3 thermal barrier system," NASA Tech. Memo. 86905 (Cleveland, OH, NASA, 1985).
5. S.R. Choi and J.W. Hutchinson, "Delamination of Multilayer Thermal Barrier Coatings," submitted to Mechanics of Materials (1988).
6. O. Unal, T.E. Mitchell, and A.H. Heuer, "Microstructures of Y_2O_3- Stabilized ZrO_2 Electron Beam-Physical Vapor Deposition Coatings on Ni-base Superalloys," J. Am. Ceram. Soc., 77 (4) (1994) 984-992.
7. B.A. Movchan and A.V. Demchishin, "Study of the Structure and Properties of Thick Vacuum Condensates of Nickel, Titanium, Tungsten, Aluminum Oxide and Zirconium Dioxide," Fiz. Metal. Metalloved., 28 (4) (1969) 83-90.
8. D.V. Rigney et al., "PVD Thermal Barrier Coating Applications and Process Development for Aircraft Engines," NASA Conf. Pub. 3312 (1995) 135.
9. D.H. Boone, T.E. Strangman, and L.W. Wilson, "Some Effects of Structure and Composition on the Properties of Electron Beam Vapor Deposited Coatings for Gas Turbine Superalloys," J. Vac. Sci. Technol., 11 (4) (1974) 641-646.
10. U. Schulz, K. Fritscher, M. Peters, "EB-PVD Y_2O_3- and CeO_2/Y_2O_3-stabilized zirconia thermal barrier coatings—crystal habit and phase composition,"Surface and Coatings Tech. 82 (1996) 259-269.
11. U. Schulz et al, "Thermocyclic Behavior of Microstructurally Modified EB-PVD Thermal Barrier Coatings," Mater. Sci. Forum, 251-254 (1997) 957-964.
12. A. Van der Drift, "Evolutionary Selection, A Principle Governing Growth Orientation in Vapour-Deposited Layers," Philips Res. Rep., 22, (1967), 267-288.
13. A.S. James, K.S. Fancey, and A. Matthews, "Thermionically Assisted R.F. Plasma Assisted Physical Vapour Deposition of Stabilized Zirconia Thermal Barrier Coatings," Surf. Coat. Technol., 32 (1987) 377-387.
14. A.S. James and A. Matthews, "Thermal Stability of Partially-Ytrria-Stabilized Zirconia Thermal Barrier Coatings Deposited by r.f. Plasma-assisted Physical Vapor Deposition," Surf. Coat. Technol., 41 (3) (1990) 305-313.
15. U. Schulz and K. Fritscher, "Behavior of Subsurface-modified EB-PVD Porcessed Thermal Barrier Coatings on Cyclic Tests," in Ceramic Coatings, ed. K. Kokini, (New York, NY: ASME, 1993) 163-172.
16. U. Schulz, H. Oettel, and W. Bunk, "Texture fo EB-PVD Thermal Barrier Coatings Under Variable Deposition Conditions," *Z. Metallkd.*, **87**, (1996), pp. 488-492
17. E.Y. Lee, R.R. Beiderman, and R.D. Sisson, Jr., "The Microstructural Characterization of Plasma Sprayed and Physical Vapor Deposited Partially Stabilized Zirconia TBCs," in Plasma Surface Engineering, ed. E. Bronzeit, (Oberursel: DGM, 1989) 365-373.
18. L. Lelait, S. Alperine, and C. Diot, "Microstructural Investigations of EBPVD Thermal Barrier Coatings," Journal de Physique IV, Colloque C9, (1993) 645-654.
19. Y.H. Sohn, R.R. Biederman, and R.D. Sisson, Jr., "Microstructural Development in Physical Vapour-Deposited Partially Stabilized Zirconia Thermal Barrier Coatings," Thin Solid Films, 250, (1994), pp. 1-7
20. F. Jamarani et al., "Compositionally Graded Thermal Barrier Coatings for High Temperature Aero Gas Turbine Components," Surf. Coat. Technol., 54-55 (1992) 58-63.
21. W.A. Tiller, The Science of Crystallization (Cambridge, UK: Cambridge Univ. Press, 1991).
22. P. Hartman, "On the Crystal Habit of Fluorite," in: Mineral Genesis, eds. I. Aleksiev and T.G. Padonova, (Sofia, Bulgaria: Bulg. Acad. Sci., 1974), 111-116.
23. S.G. Terry, J.R. Litty and C.G. Levi, unpublished work.
24. U. Schulz et al., "Ein Mantel für die Turbinenschaufel," DLR-Nachrichten, 73 (1993) 27-31.

Development of Laser Fluorescence as a Non-Destructive Inspection Technique for Thermal Barrier Coatings

March 1, 2001 to August 31, 2001

Eric Jordan and Maurice Gell	Principal Investigators School of Engineering University of Connecticut Storrs, CT 06269-3136
David R. Clarke	Principal Investigator Materials Department, College of Engineering University of California – Santa Barbara Santa Barbara, CA 93106-5050
Yong Ho Sohn	Post-Doctoral Fellow
K. Vaidyanathan, L. Xie, J.H. Kim, S, Sridharan	Graduate Student Researchers

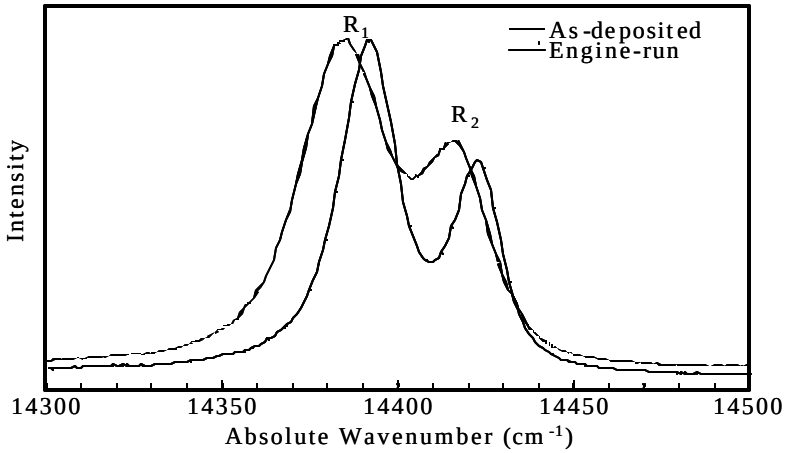

Cr^{3+} Photoluminescence spectra acquired from TBC coated turbine blades before and after the engine run.

School of Engineering
University of Connecticut
Storrs, CT 06269-3136

March 15, 2001

AGTSR Subcontract # 99-01-SR073

Clemson University Research Foundation
South Carolina Energy Research and Development Center
Clemson, South Carolina, 29634-5181

This report was prepared with the support of the US Department of Energy
Morgantown Energy Technology Center, Contract DE-FE21-92MC29061

Table of Contents

Table of Figures

EXECUTIVE SUMMARY

Thermal barrier coatings (TBCs), consisting of ZrO_2-7~8wt.%Y_2O_3 (YSZ) ceramic coatings, metallic bond coats and superalloy substrates, offer thermal/environmental protection for hot components in gas turbine engines. Failure of TBCs, in general, occurs by the spallation of YSZ coatings near the interface between YSZ coatings and bond coats where the thermally grown oxides (TGO) grow during high temperature exposure. Thus, it is necessary to develop a non-destructive inspection technique for the assessment of structural integrity of TBC, especially at the interfaces involving TGO. The Cr^{3+} photoluminescence spectroscopy (also known as laser fluorescence) enables one to measure, non-destructively, the average stress within TGO by examining the Cr^{3+} photoluminescence signals originating from Cr^{3+} impurities in the TGO, which predominantly consist of α-Al_2O_3. The objective of this program is to develop and establish the laser fluorescence technique as a non-destructive inspection technique for thermal barrier coatings (TBCs).

For Type B TBCs, 1-hour thermal cycling at 1121°C was completed in the previous reporting period. Average lifetime around 400 cycles was obtained. Fluorescence data was also used to predict remaining life to within 5% but only neural network methods were capable of this accuracy.

For type A samples, 1-hour thermal cycling at 1121°C were completed in the previous reporting period for Type A TBCs. The lifetime of Type A TBCs ranges from 665 to 745 cycles. It was also demonstrated that using either direct regression method or neural networks failure life of individual samples could be predicted within 5% using the nondestructively measured stresses. In the present reporting period the 24-hour thermal

cyclic tests at 1121°C tests were completed. Based on results to date it is apparent that the lives in hours (not cycles) under 24 hour cycling ranged from 768 to 1032 hours, substantially longer than lives in the 1 hour cycle test. This clearly indicates the damaging effects of cycling vs. time at temperature alone. It is also the case that the rate of decease in residual stress in the TBO with cycles is slower (in terms of time) than in the 1-hour cycle tests. This leads to the conclusion that the relationship between fluorescence data and remaining life is temperature history specific in general. Only the drop in stress seen in the last %5 of life seems to be relatively history independent. Regression method were successful in estimating he remaining life to within 7% of the total life achieving a standard deviation of error of predicted life less then 1/3 of the inherent standard deviation for the lives themselves. Useful engineering predictions are thus shown to be possible for the 24 hour cycle as was shown for the 1 hour cycle. The prediction method however requires knowledge of cycle time. All predictions were made at roughly mid life. It appears that all samples show sudden drop near the end of life and a method independent of cycle type may be possible but only for prediction quite near in a percentage sense the end of part life. This possibility will be studied in the next reporting period.

Extensive work was done to understand the failure mechanisms for Type A samples and these mechanisms were model these mechanisms quantitatively. Specifically the mechanism for non grit blasted versions of the Type A samples were studied and it was shown that the life controlling event is the debonding of the TGO at the top of surface ridges present at the grain boundaries and that this debonding occurs at a nearly constant tensile normal stress of 300 MPa. Fracture mechanics is used to show

that such debonding if it occurs near a free edge, it is sufficient to cause wide spread debonding. Original fracture solutions to the relevant interface fracture problem were developed motivated and partially funded by this project. In addition new fracture mechanics solutions were developed for the propagation of a debond crack on a ridge and on a spherical asperity. These new fracture mechanics results show that such ridge top cracks will propagate over most or the entire asperity ounce they are initiated given the strain energy known to be present in the TGO. The strain energy is known due to PLPS stress measurements and thickness measurements done in the current program. It is beginning to appear that the quantitative explanation of failure in this system is reasonably general for samples with grain boundary ridges and as such the failure concept and associated fracture mechanics solutions will be useful for a significant number of cases involving samples similar to type A.

Testing was started at a lower temperature of 1100 °C and a higher temperature of 1151°C. The results expected from these additional tests will provide the necessary database to get a complete view of how PLPS might function as an NDI method and provide some of the necessary data to calibrate such a system.

I. INTRODUCTION

Thermal barrier coatings (TBCs) have been used extensively for thermal protection of hot components in gas turbine engines for more than 25 years . In general, a TBC for a high temperature superalloy consists of yttria stabilized zirconia (YSZ; ZrO_2-7~8wt.%Y_2O_3) ceramic, metallic bond coat and a thermally grown oxide (TGO) that forms between the bond coat and the ceramic. Failure of the TBC has been observed to occur by the spallation of the YSZ at or near TGO. Thus, it is desirable to develop a non-destructive inspection technique for the assessment of structural integrity of TBCs. In this regard, the Cr^{3+} photoluminescence piezo-spectroscopy (CPLPS, also known as laser fluorescence) has demonstrated promising results for measuring the average stress within TGO by examining the Cr^{3+} photoluminescence signals originating from Cr^{3+} impurities in the α-Al_2O_3 TGO. The Cr^{3+} photoluminescence of TGO may be considered an in-situ sensor located at or near the plane of spallation that can be activated using laser light.

The overall objective of this program is to establish CPLPS as a non-destructive inspection (NDI) technique for thermal barrier coatings (TBCs) in gas turbine engines. This objective will be fulfilled through accomplishing the following goals:

Identify the optimal criteria for assessing TBC life from the several parameters found in Cr^{3+} photoluminescence piezo-spectroscopy measurement during high temperature cyclic oxidation tests for TBC specimens.

Develop an understanding for the evolution of stress in TGOs and the associated failure mechanisms during high temperature cyclic oxidation of TBC specimens.

Demonstrate the measurement of stress in the TGO by laser fluorescence on actual engine parts in a laboratory setting.

Demonstrate the measurement of stress in the TGO by laser fluorescence on actual engine parts through boroscope access sites.

The University of Connecticut, University of California – Santa Barbara, and industrial NDI experts will work cooperatively with Renishaw Inc. to develop a portable laser fluorescence instrument for practical applications (e.g., gas turbine engines in industrial settings).

In order to achieve these goals, the University of Connecticut has assembled a strong, knowledgeable team with a wealth of gas turbine engine, thermal barrier coatings, and NDI experience to conduct this program. The team, presented in Figure 1, consists of investigators at the University of Connecticut and the University of California - Santa Barbara, ATS engine developers and industrial review board members (ABB, Allied Signal Engines, GE Power systems, Pratt & Whitney, Rolls Royce – Allison Engines, Siemens – Westinghouse Power Generation and Solar Turbines), coating suppliers (Howmet International) and the laser fluorescence instrument manufacturer (Renishaw, Inc.). Figure 2 presents the schedule for the program.

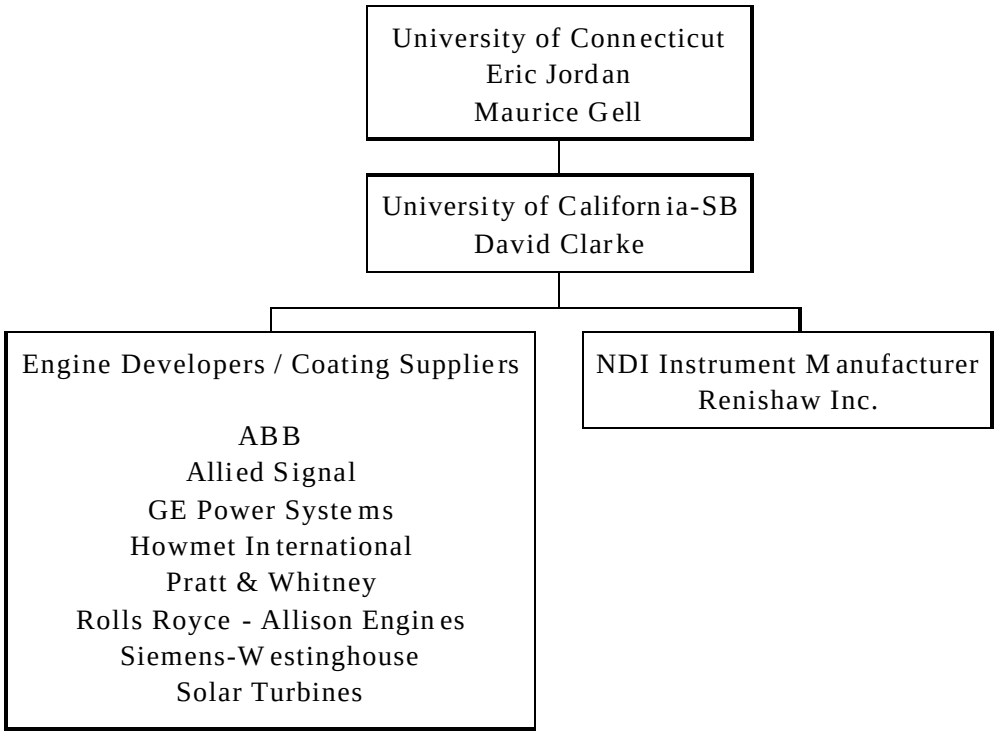

Figure 1: A partnership of universities and industries organized for the development of laser fluorescence as a NDI technique for TBC's.

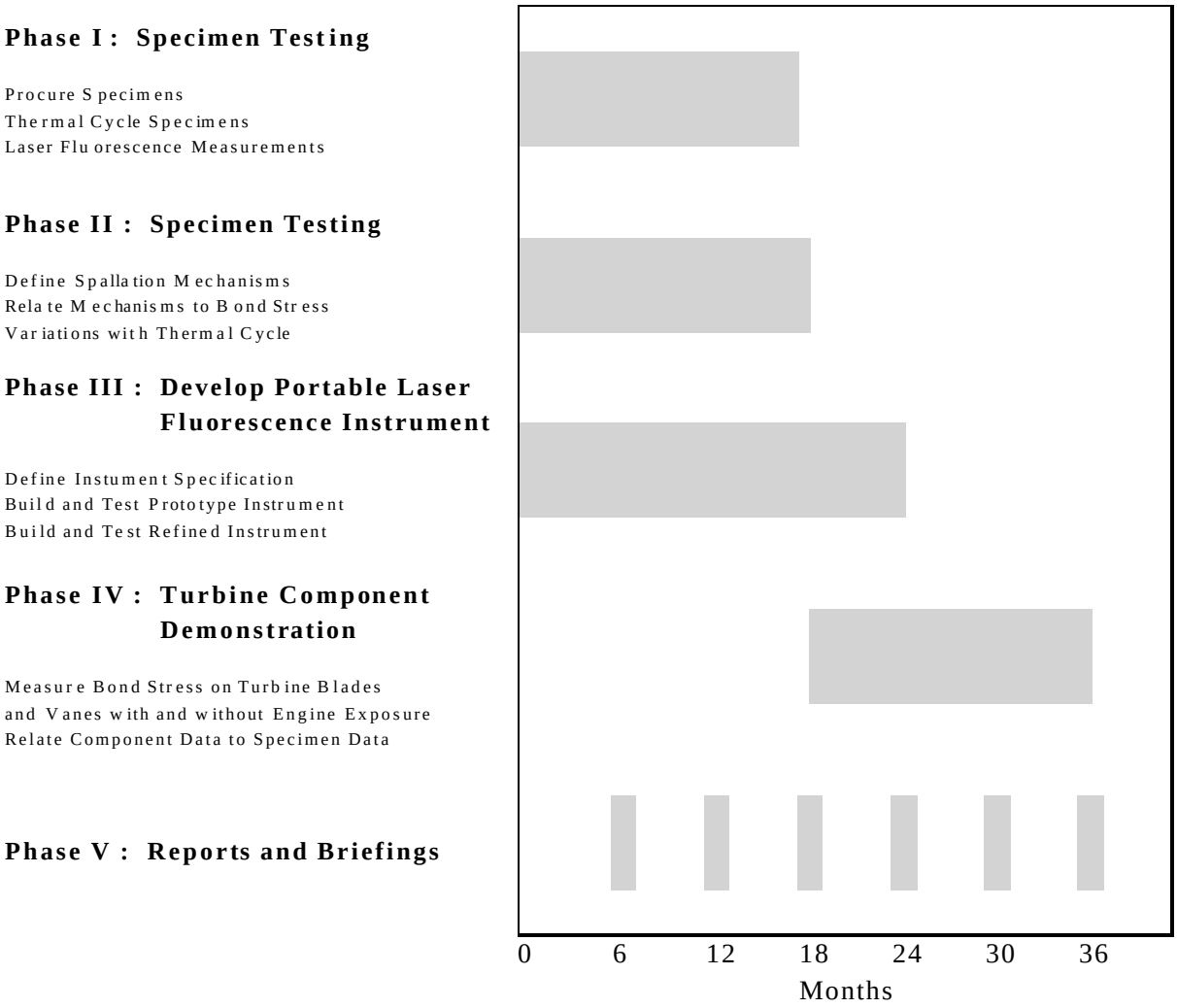

Figure 2: Program schedule for the development of laser flourescence as a NDI technique for TBC's.

II. DESCRIPTION AND DELIVERY OF TBC Systems

Three TBC systems identified in Table 1 as Type A, B and C were selected for the development of laser fluorescence as a NDI technique. The program partners supply 100 disk samples of each TBC system (25.4 mm in diameter and 3.2 mm in thickness as schematically show in Figure 3). To date Type B and A specimens have been delivered to the University of Connecticut, while the TBC systems C has had production difficulties and was delivered near the start of this reporting period. A schematic of the TBCs investigated in this program is shown in Figure 3.

Table 1: Thermal barrier coatings (TBCs) selected for the development of laser fluorescence as a NDI technique.

TBC System	Ceramic Coating	Deposition Method	Bond Coat	Deposition Method	Superalloy Substrate
A	ZrO_2-7wt.%Y_2O_3	EB-PVD	(Ni,Pt)Al	CVD	Rene'N5
B	ZrO_2-7wt.%Y_2O_3	EB-PVD	MCrAlY	VPS	IN-738
C	ZrO_2-8wt.%Y_2O_3	APS*	MCrAlY	VPS	GTD-111

* Note: Dense vertically cracked (DVC) coatings.

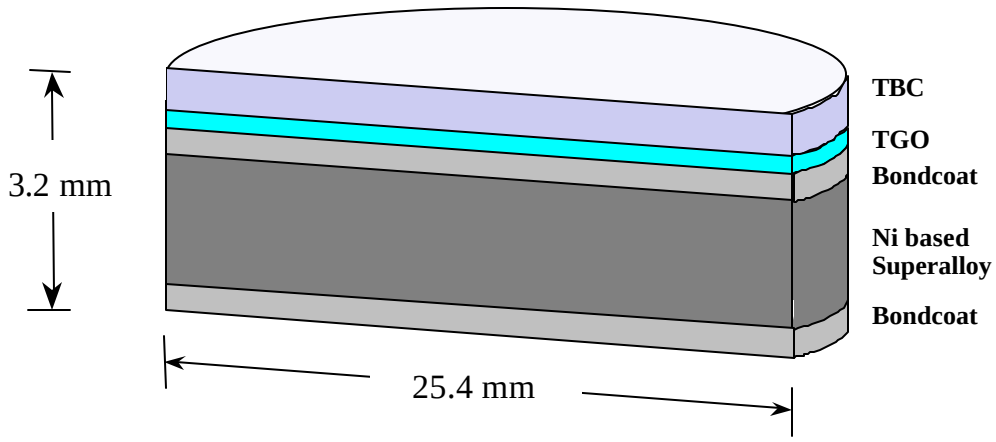

Figure 3: The specimen geometry and layered structure for TBCs investigated in this program.

III. Evaluation of Type A TBCs: 1121 C; 24-Hour Cycle

III.1 Spallation Life and Macro-Failure Mode

The 24-hour cyclic testing of the Type A TBCs started in the previous reporting period has now been completed. The failure mechanisms of these samples are currently being investigated. The Spallation lives of these samples varied over a range of 33 to 55 24-hour cycles as shown in Figure 4. The stress measurements were carried out on all 16 specimens and the evolution of the TGO stress has been studied as a function of the number of cycles and as a function of the total hot time. The samples cycled over the 24-hour testing period have longer Spallation lives as compared to those cycled over the 1-hour period. This indicates that the 1-hour cycling is more damaging than the 24-hour cycling.

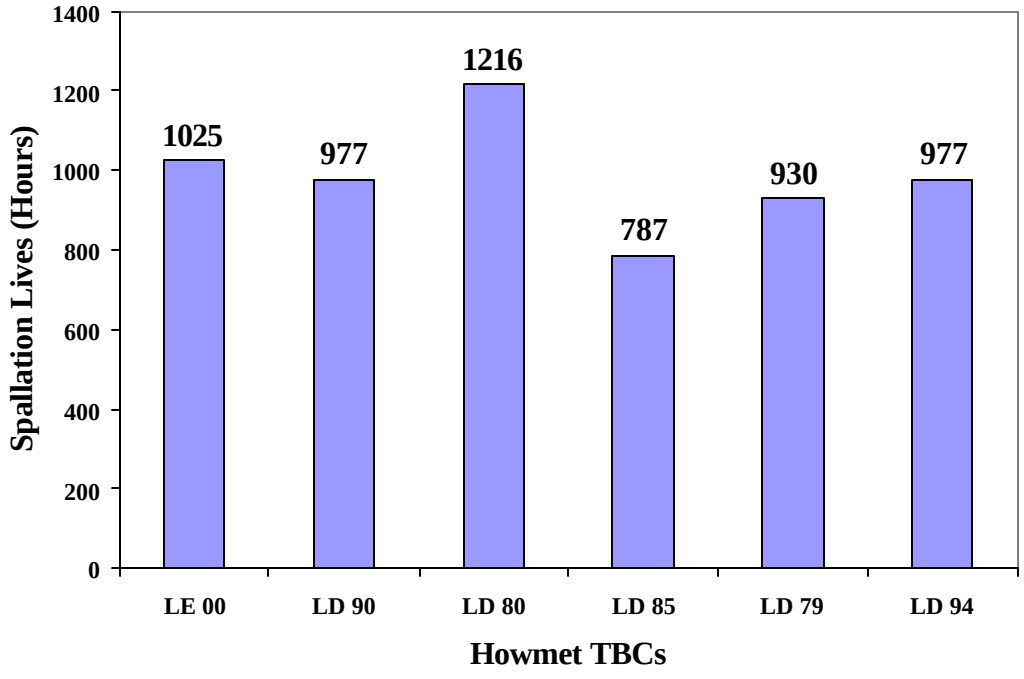

(a)

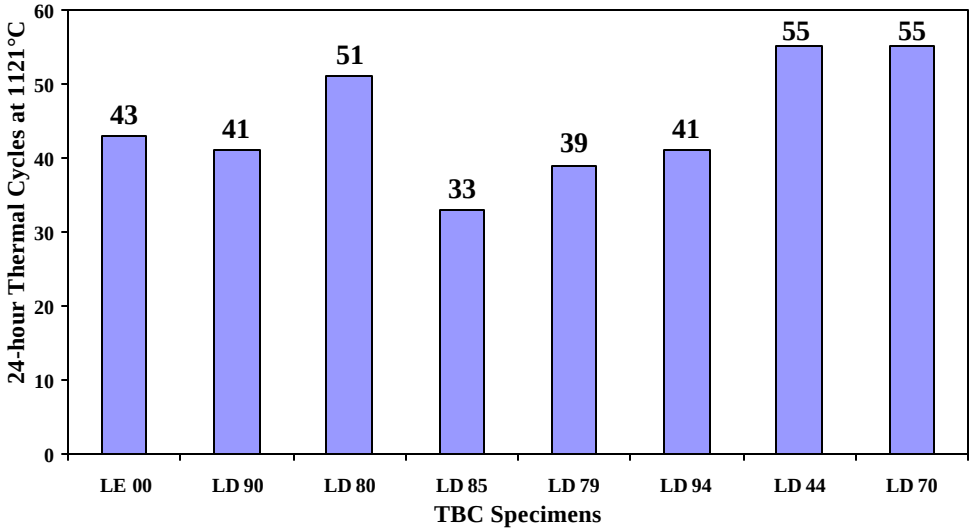

(b)

Figure 4: Spallation lives under the 24-hour Thermal Cycling Tests at 1121°C- (a) Hours & (b) Cycles.

III. 2 Laser Fluorescence

The trends in stress and other stress related attributes have been studied and they look qualitatively similar to the 1-hour cycling results, though the rate of change of the measured values is slower in terms of elapsed time than in the 1-hour tests. The TGO stress is seen to increase sharply during the first eight cycles and then begins to drop off gradually until failure, as shown in Figure 5 However, there is a conspicuous decrease in the stress immediately prior to failure. This has been observed in all the specimens cycled so far. This could be used as an indicator of the impending failure. A plot of the TGO stress as function of the life fraction for a few samples clearly describes this as shown in Figure 6. No bimodal peaks were present in this data. The macro photos of the failed samples also indicate that the failure mode is distinctly different from that of the samples

cycled over the 1-hour period, as shown in Figure 7. The change of peak width and relative intensity of R_1 and R_2 peak with thermal cycling was also analyzed. The shape of the fluorescence line, represented by the half-width at half maximum (HWHM), reflects the through-thickness stress distribution, while the ratio of the integrated intensities under the respective R-lines is sensitive to the orientation of the crystal lattice with respect to the polarization vector of the laser. The small change of peak widths during thermal cycling, as shown in Figure 8, means that the through thickness stress distribution did not change much during cycling. However, compared to the typical peak widths of stress free alpha-alumina, it is obvious that there is a stress gradient in the TGO layer. An interesting result is the linear relationship between the peak width and compressive stress, as shown in Figure 9, which may indicate that there is certain manner of stress distribution in the TGO layer. The ordinate of Figure 10 is the ratio of the sum of integrated area of peak R1 and R_2 to the integrated area of R_2. The difference between that of the sample and the untextured α-alumina disk is obvious, which means the TGO in TBCs is textured.

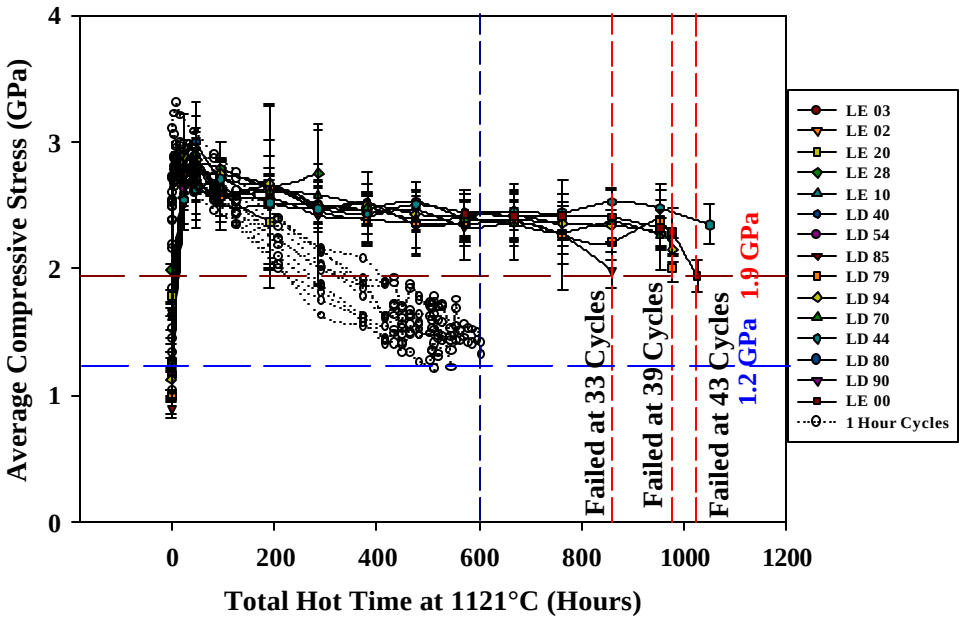

Figure 5: Evolution of TGO Stress during 24-hour thermal cycling at 1121°C.

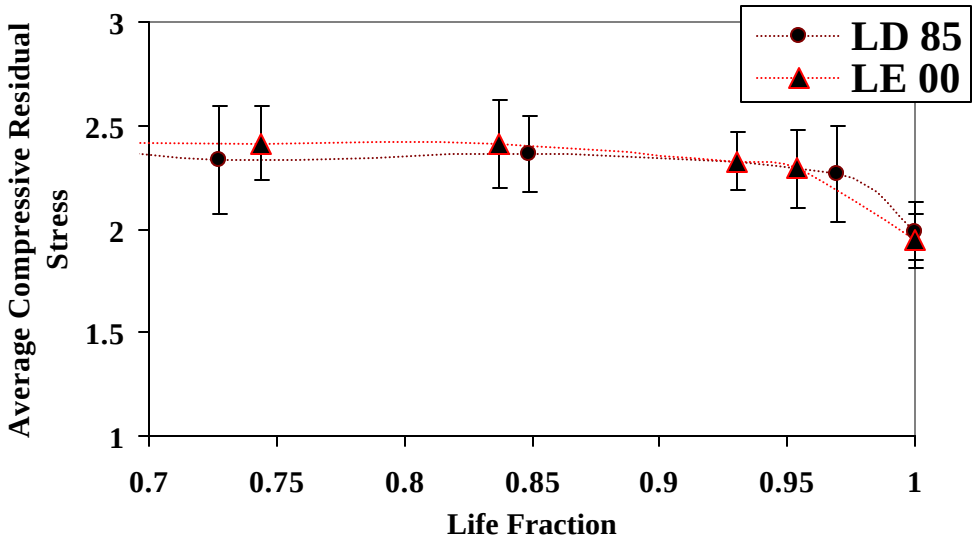

(a)

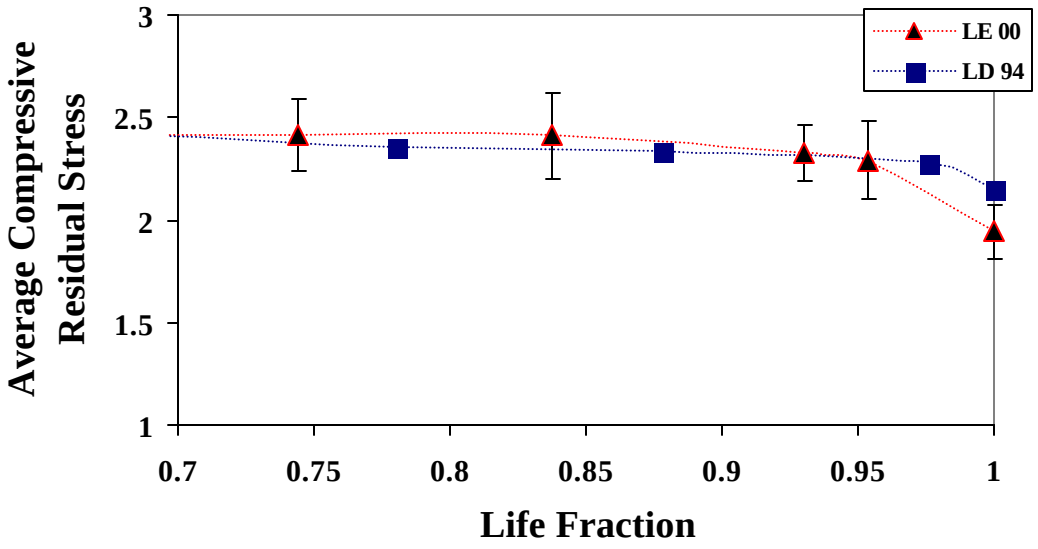

(b)

Figure 6 (a) & (b): Photoluminescence Piezospectroscopy for Failure Prediction in TBCs

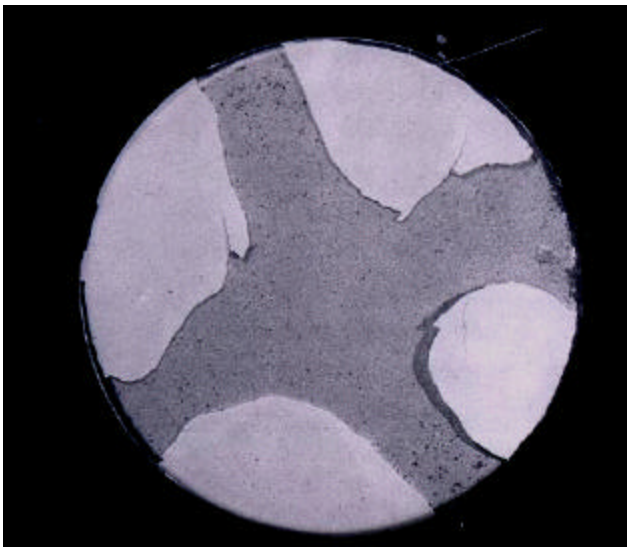

(a)

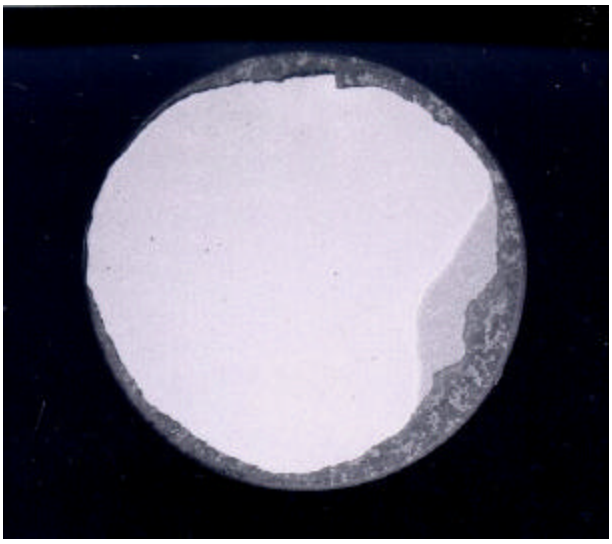

(b)

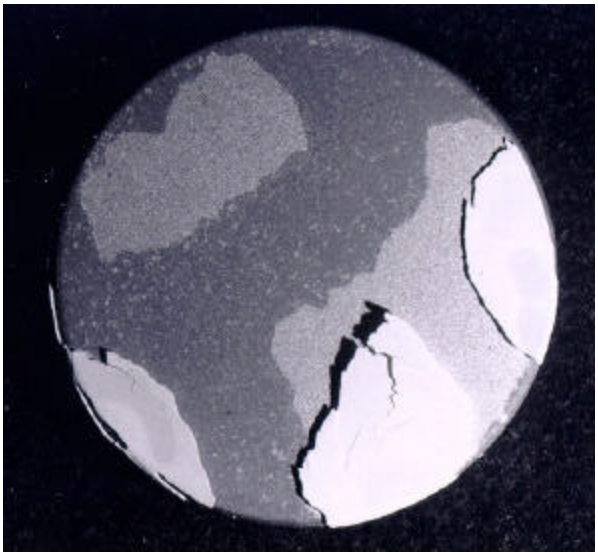

(c)

(d)

Figure 7: Macro Photos of; (a) LD 79-failed after 39 Cycles; (b) LD 94-failed after 39 Cycles; (c) LD 90-failed after 41 Cycles; (d) LD 85-failed after 33 Cycles.

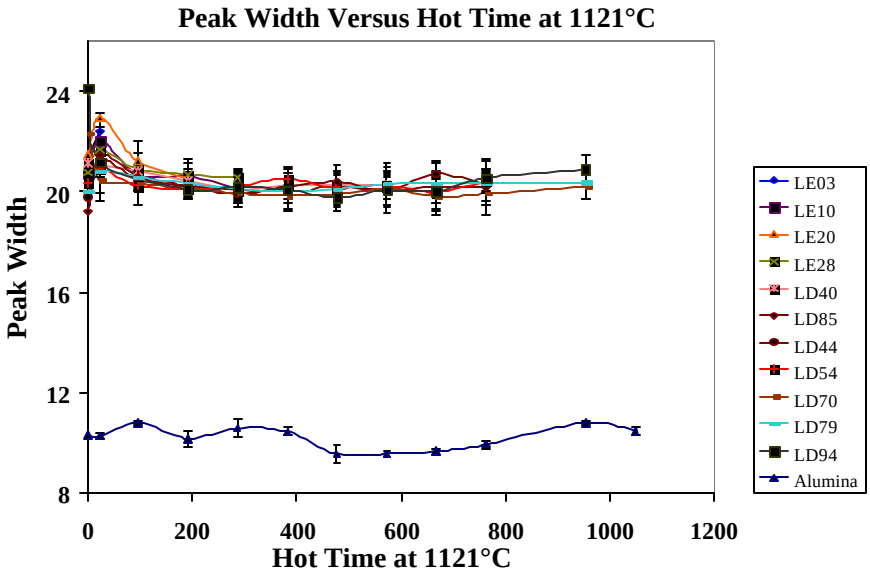

(a)

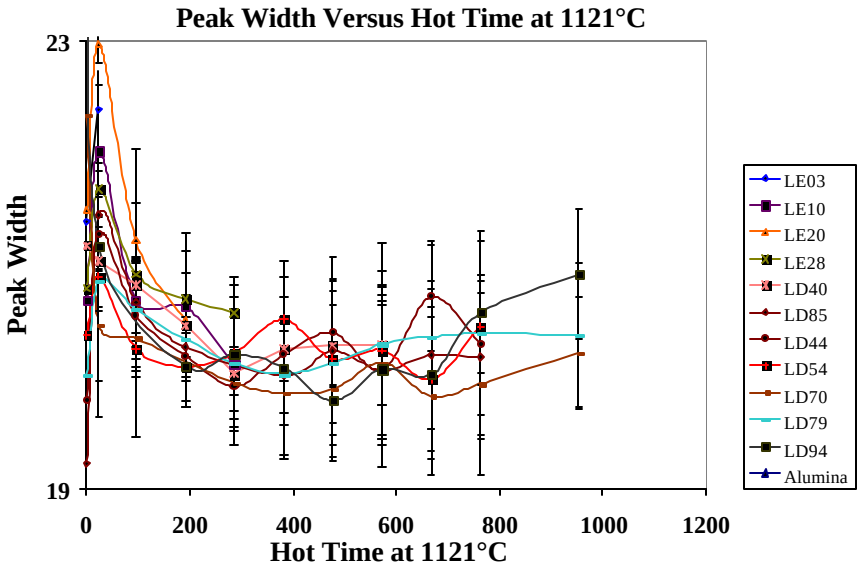

(b)

Figure 8: (a) & (b): Change of R2 Peak Width with Total Hot Time at 1121°C.

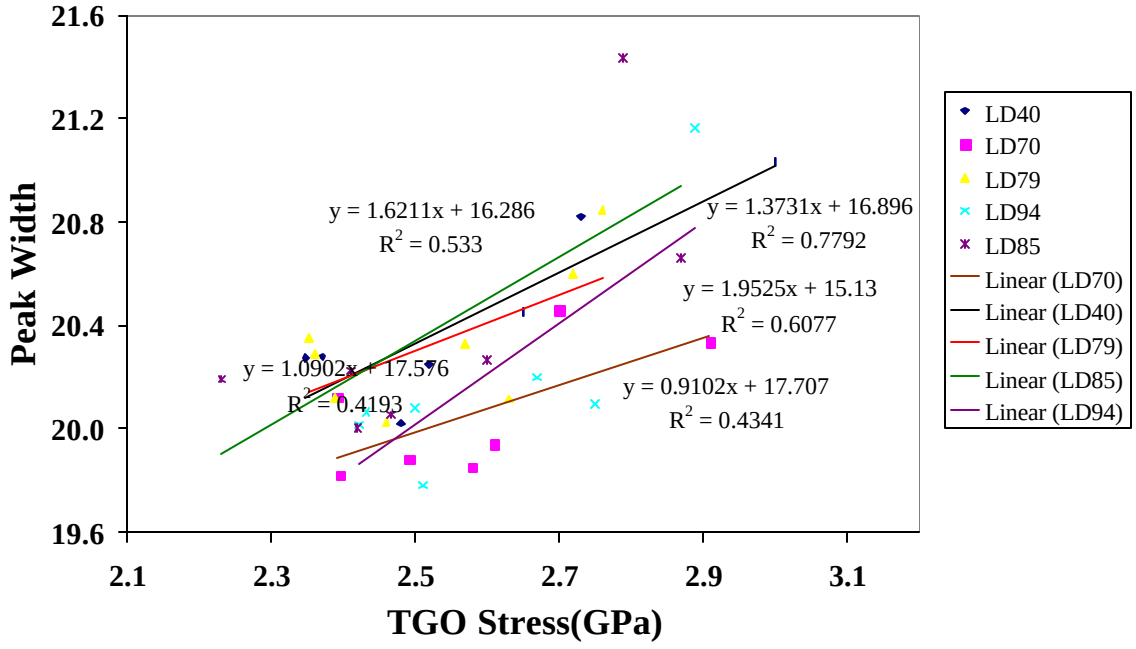

Figure 9: Change of R2 Peak Width with TGO Stress.

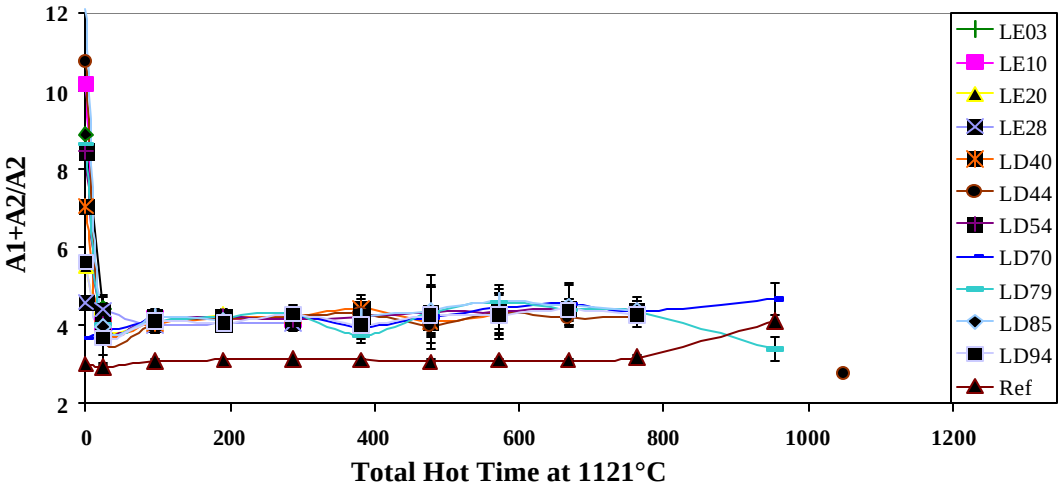

Figure 10: Change of Peak Intensity Ratios with Total Hot Time at 1121°C.

III. 3 Micro structural Characterization

SEM studies are currently being carried out on the failed samples. The preliminary results are presented here in Figure 11, Figure 12, Figure 13, Figure 14, Figure 15. These indicate that the failure has predominantly taken place at the TGO to Bond Coat interface. The high magnification micrographs also indicate the presence of smooth pores and cavities. The role of these pores and cavities in the failure mechanism of the samples is currently under investigation. The TGO growth has also been studied as function of cycles, as shown in Figure 16.

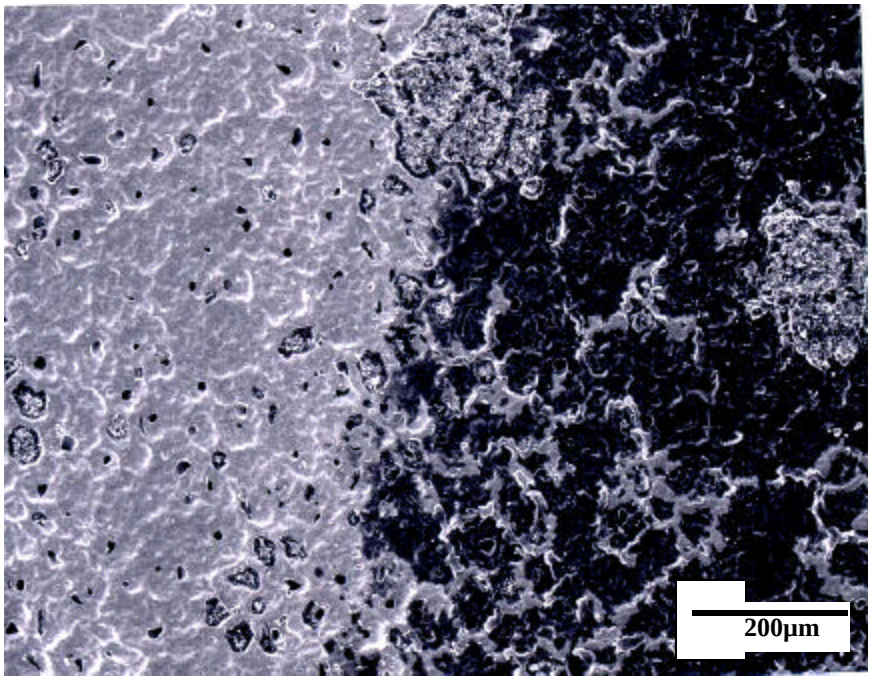

(a)

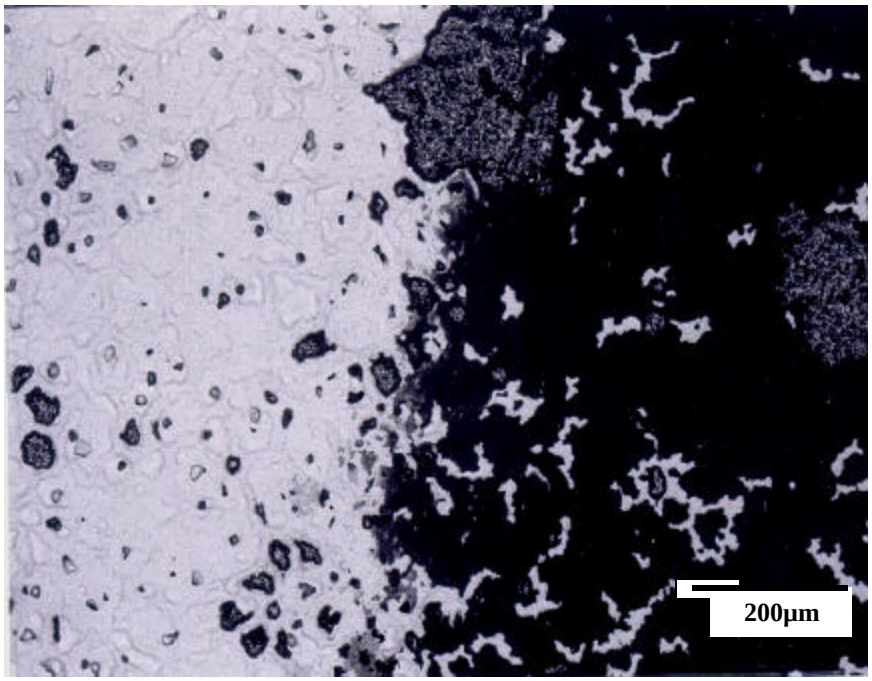

(b)

Figure 11: (a) Secondary Electron & (b) Back Scattered Electron Images of the Spallation Surface of LD 90-failed after 41 Cycles.

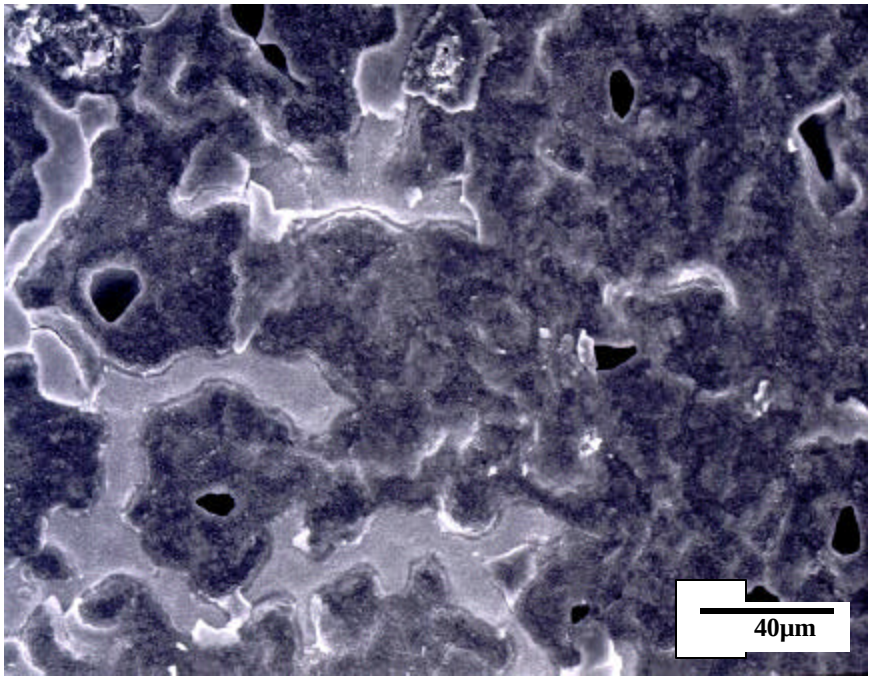

(a)

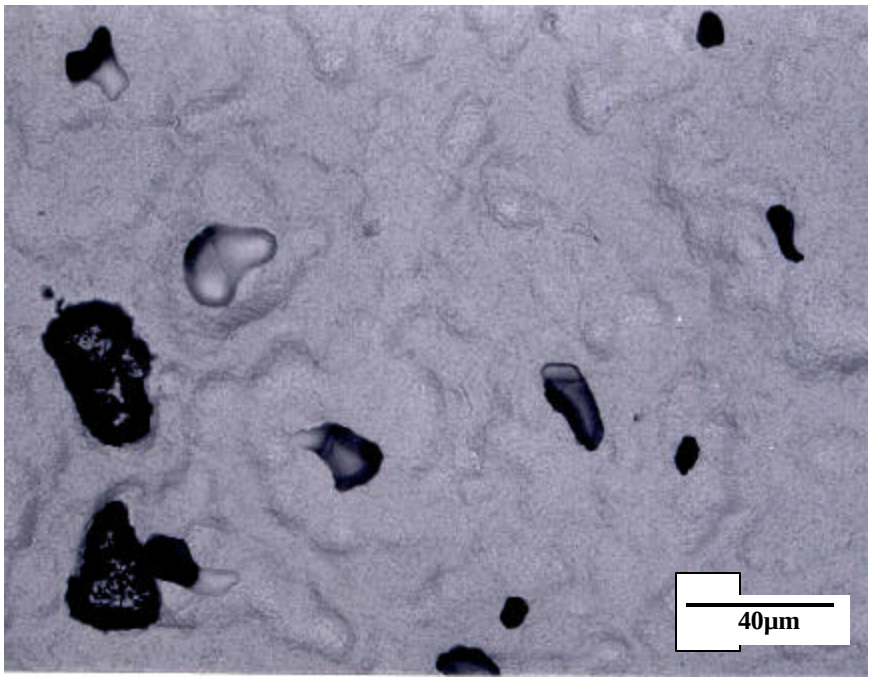

(b)

Figure 12: (a) Secondary Electron & (b) Back Scattered Electron Images of the Spallation Surface of LD 90-failed after 41 Cycles.

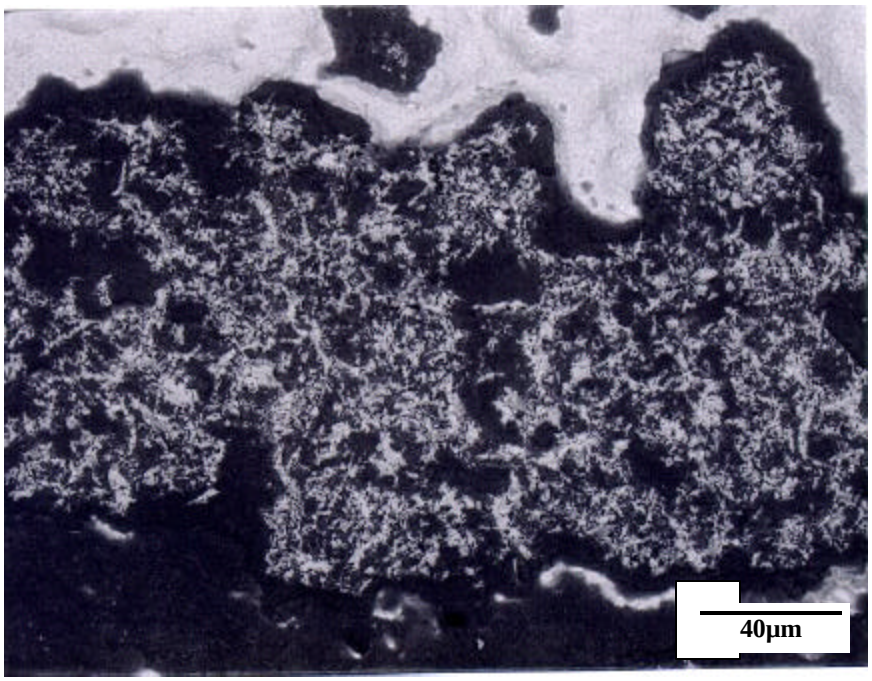

(a)

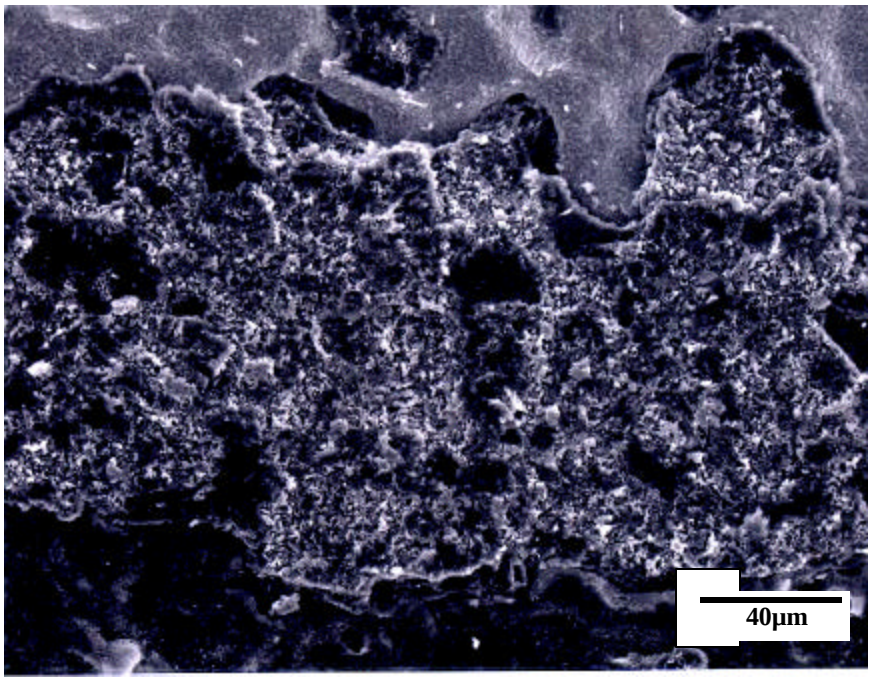

(b)

Figure 13: Secondary Electron & (b) Back Scattered Electron Images of the Spallation Surface of LD 90-failed after 41 Cycles.

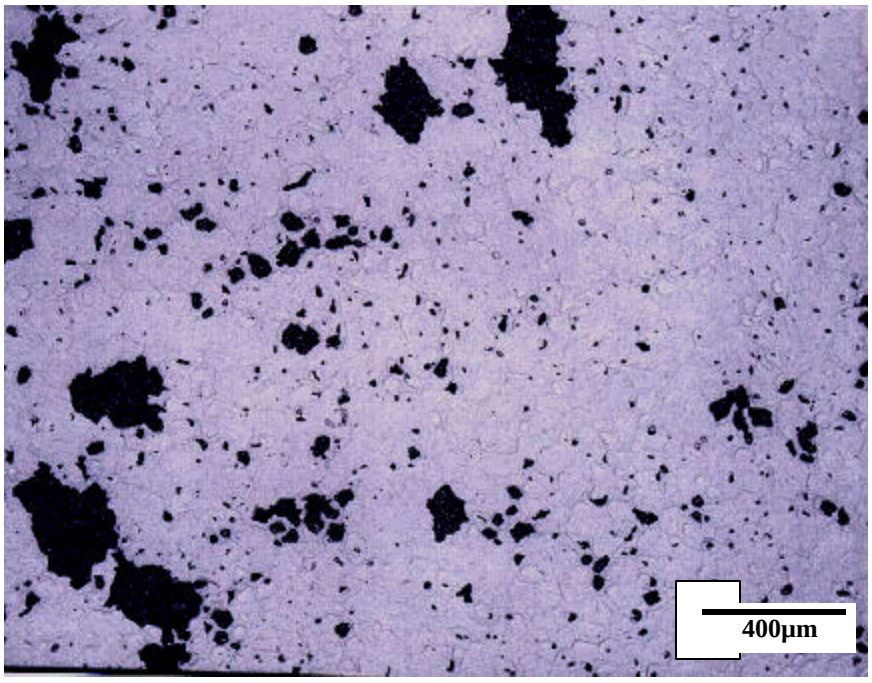

(a)

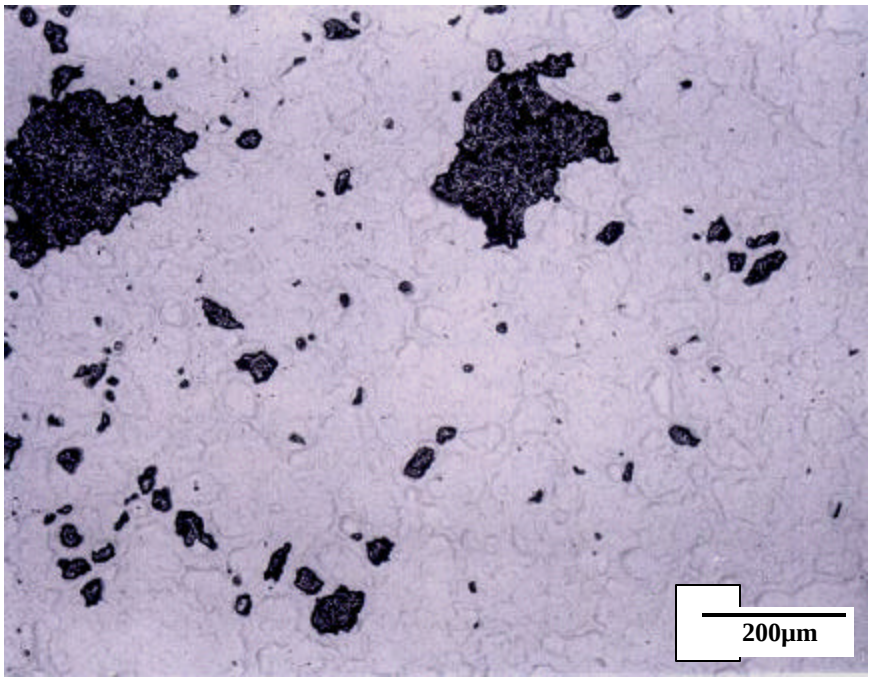

(b)

Figure 14: (a) Secondary Electron & (b) Back Scattered Electron Images of the Spallation Surface of LD 85-failed after 33 Cycles.

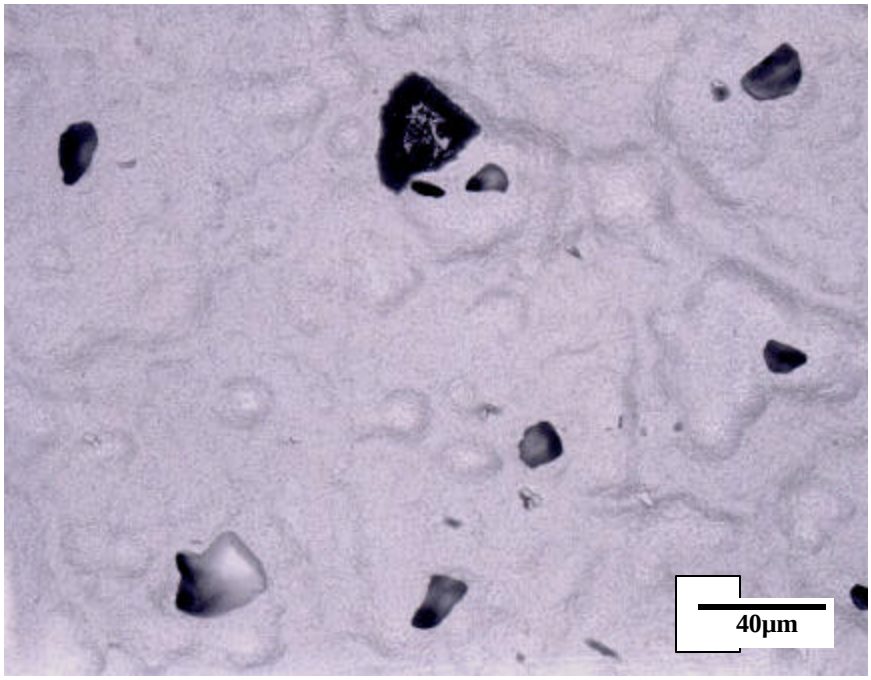

(a)

Figure 15: (a) Secondary Electron & (b) Back Scattered Electron Images of the Spallation Surface of LD 85-failed after 33 Cycles.

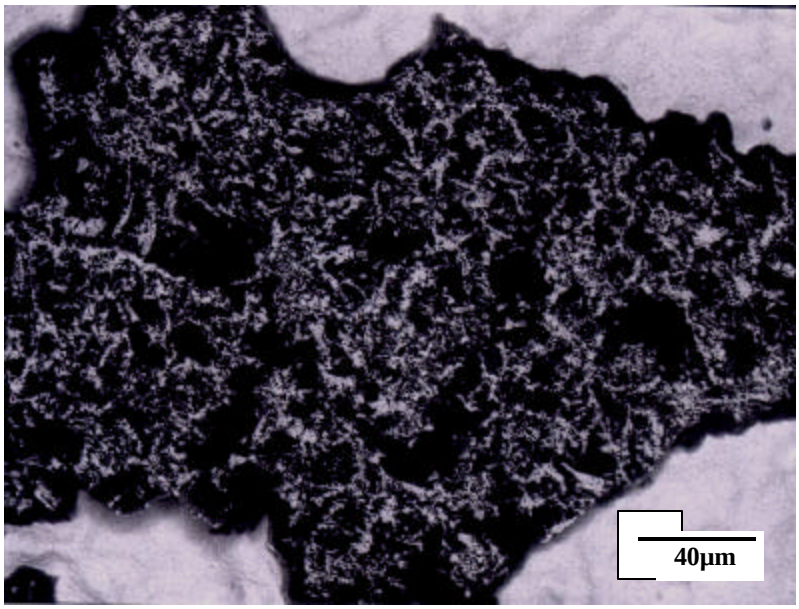

(b)

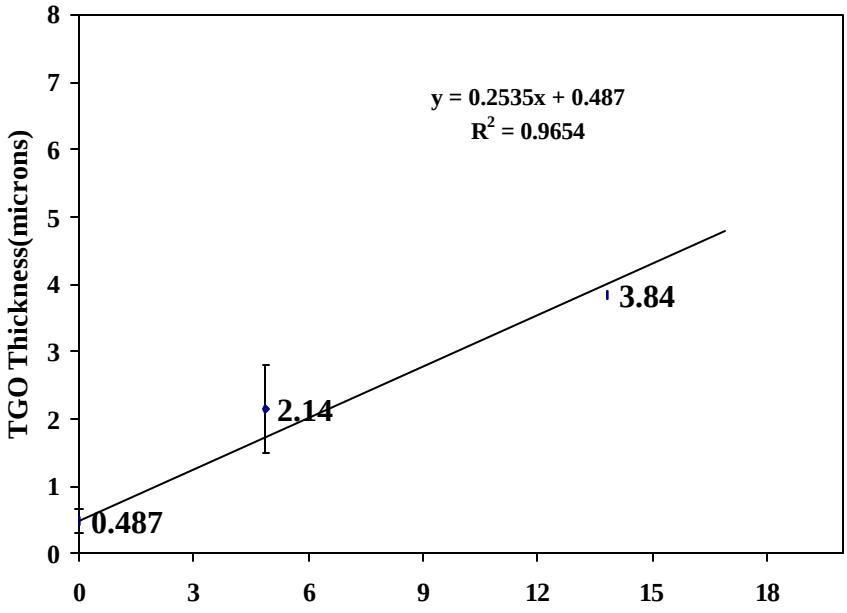

Figure 16: Parabolic Growth Rate of TGO Thickness.

III. 4 Failure Mechanism Discussion

The 24-hour cycle failure surfaces and those for the same system with 1-hour cycles are generally similar and more over are similar to the surfaces seen on a highly similar system studied in part in our previous AGTSR grand and under the present one including the completion of the thesis write up completed in this reporting period. Here we will present the detailed failure mechanism analysis of a system identical to the samples in system A except that these samples were not grit blasted and those of system A were grit blasted. The relevance is that we are currently expecting to explain the failure of system A by the same general approach given below for the system that is nearly identical to system A.

III.5.0 Quantitative Discussion of Failure Mechanisms in Un-grit Blasted Type A Samples

TBC specimens identical to system A except these samples were not grit blasted was also tested and the mechanism of failure was studied and modeled quantitatively. These samples were coated to industry specifications were tested under 1 hour thermal cycling conditions at a peak temperature of 1121°C, until eventual spallation failure. The results indicate a 10-fold variation in spallation lives, ranging from 190 cycles to 1917 cycles. It is hence important to understand the underlying mechanisms responsible for such a wide variation, which would prove useful for coating manufacturers, in producing more durable and consistently performing TBCs It was found that the presence of native morphological features in the form of bond coat grain boundary ridges at the TGO/bond coat interface played a definitive role in damage initiation.

The failure of the thermal barrier coating system investigated in this study is always located at or near the TGO layer. This is attributed to the high strain energy associated with the TGO layer, in spite of the fact that it is thin relative to the 7YSZ layer. This can be verified through simple calculations using nominal dimensions for the TGO and 7YSZ TBC. The TBC system studied, comprises four different layers: a 125 μm thick strain-tolerant 7YSZ EB-PVD ceramic coating, a 75 μm thick single phase β-(Ni,Pt)Al bond coat, a creep-resistant René N5 superalloy substrate and a thermally grown oxide (TGO) that grows to an average thickness of 5 μm in service, between the ceramic and the bond coat. As the specimens are rapidly cooled from 1121°C, compressive stresses are generated in the TGO layer due to a difference in thermal coefficient of expansion between the TGO and the underlying bond coat. Since the TGO layer is very thin relative to the substrate, the stress state of the TGO layer can be assumed biaxial and the stress component, σ_o can be calculated from the following expression [Timoshenko and Goodier; 1971]:

$$\sigma_o = \frac{E_{TGO}}{(1-\nu_{TGO})} \cdot (\alpha_{TGO} - \alpha_{BC}) \cdot \Delta T \qquad (5.1)$$

where E_{TGO} is the Young's modulus of the TGO layer, ν_{TGO} is its Poisson's ratio, α_{TGO} and α_{BC} are respectively the coefficient of thermal expansion for TGO and bond coat.

Table 2. 1: Room temperature properties of various layers of the TBC system.

	Symbol	**TBC (YSZ)**	**Bond Coat (Ni,Pt)Al**	**TGO (a -Al_2O_3)**
Young's Modulus	E (GPa)	0-100[a] 44[b]	200[a, c]	400
CTE	α (ppm/°C)	11-13[a]	13-16[a] 13.6[c]	8-9[a] 8[c]
Poisson's Ratio	ν	0.23[c]	0.30[c]	0.23[c]
Residual Compression	σ_o	40 MPa[b]	-	3.5 GPa[c]

a Mumm and Evans; 2000
b Vasinota and Beuth; 2000
c Cheng *et al*; 1998

Based on the material properties listed in Table 2, the value obtained for σ_o is 3.2 GPa. This value corresponds well with that of measurements made by photoluminescence piezospectroscopy (PLPS), which indicates a range of stress values, from 3.2 GPa to 3.8 GPa) Figure 17.

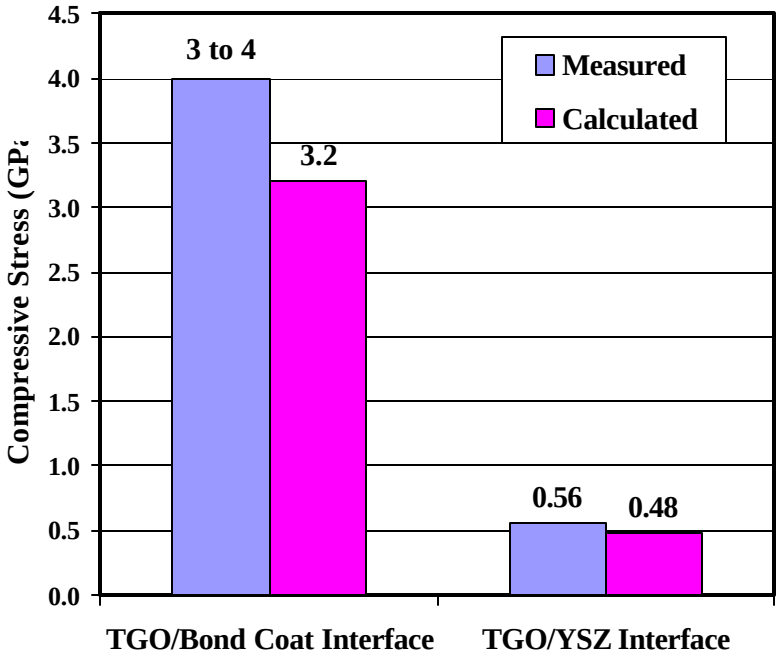

Figure 17: Comparison between calculated stresses and measured stresses using PLPS technique for TGO layer.

The stored elastic energy per unit area of the layers can be now calculated from knowing the compressive stress in the layer, σ_o, and its thickness, h, through the following expression [Suo; 1995]:

$$U_E = \frac{(1-\nu)\cdot h\cdot \sigma_o^2}{E} \quad (5.2)$$

It can be seen from equation 2, which the total elastic energy is function of square of the magnitude of the compressive stress and varies linearly with the thickness of the TGO. Substituting appropriate material properties listed in, Table 2 for TBC and TGO, the elastic strain energy associated with the YSZ layer of nominal thickness of 125 µm and the TGO layer of nominal thickness of 5 µm are 2 J/m² and 152 J/m² respectively. This clearly indicates that the TGO layer is the high energy density domain where failure will be concentrated.

III.5.1 Damage Initiation

The stresses in the TGO exert a strong influence on TBC failure. The failure in the TBC system studied is dominated by the presence of native morphological features in the form of bond coat grain boundary ridges at the TGO/bond coat interface. The tensile stress normal to the interface found at the TGO/bond coat interface, at the top of these bond coat ridges increase with increasing TGO thickness and is responsible for debonding at this interface [Suo; 1995, Clarke and Pompe; 1999]. It will be hypothesized that this debonding is the life-controlling event. The appearance of the fracture is profoundly affected by development of cavities in the bond coat due to a ratcheting process driven by bond coat cyclic plasticity. This damage lowers the interface toughness, however, the main consequence of cavity formation is the redirecting of the crack path during final spallation to include more separation at the TBC to TGO interface. For the sake of clarity, the two mechanisms that are responsible for damage initiation and progression and hence the appearance of the final spallation surfaces will be described first.

III.5.2 Damage Mechanism I

The description of this mechanism is given as a sequence of events:

1. The bond coat surface has a geometric network of ridges that are associated with grain boundaries.
2. The TGO layer thickens with thermal cycles and grows uniformly according to parabolic rate laws.
3. The TGO grows stress free at peak temperature and, upon cooling to room temperature, the TGO is in compression in direction parallel to the interface due to

the mismatch in coefficient of thermal expansion (CTE). However, based on simple force balance, the normal stress at the TGO/bond coat interface along the crest of the ridges is tensile normal to the interface and compressive parallel to the interface, at room temperature (Figure 18(a)). The tensile stress increases with increasing oxide thickness.

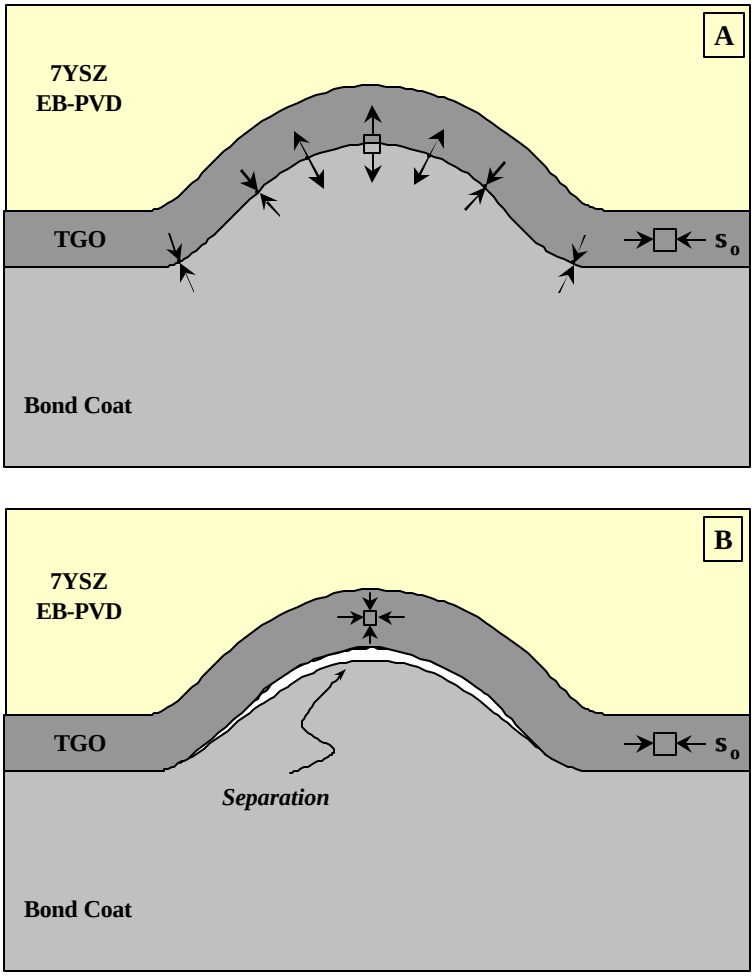

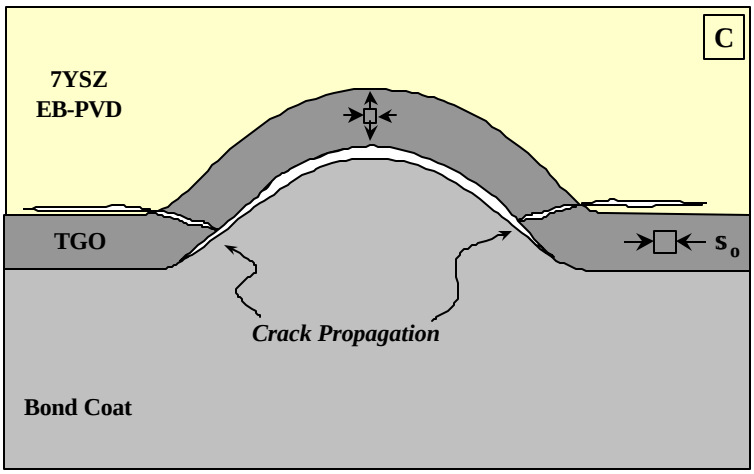

Figure 18: Damage initiation mechanism I for specimens with bond coat ridges.

The cracking occurs in the TGO during cooling down to ambient temperature. (a) upon cooling tensile stresses are generated at the asperity tips of bond coat ridges (b) when the critical normal tensile stresses are reached, debonding at TGO/bond coat interface is promoted (c) the crack propagates further along the TGO/7YSZ interface leading to formation of wing cracks.

This can be illustrated using a simple Laplace-Young formula (a more general analytical approach is adopted in Appendix I):

$$\sigma_N = -\left(\frac{1}{R_1} + \frac{1}{R_2}\right) \cdot h_{TGO} \cdot \sigma_o \quad (5.3)$$

where, σ_N, is the normal tensile stress at the TGO/bond coat interface, R_1 and R_2 are principal radii of curvature of the bond coat ridge, h_{TGO} is the thickness of the TGO layer and σ_o is the compressive stress in the TGO layer. In the present context, the surface of the bond coat ridges can be modeled as a cylinder, in which

case the equation (5.3) can be reduced as follows:

$$\sigma_N = -\left(\frac{h_{TGO}}{R}\right)\cdot \sigma_o \qquad (5.4)$$

Thus, it can be seen that for a given radius of curvature, the tensile stress at the TGO/bond coat interface increases with increasing oxide thickness.

4. After thermal cycling, when the TGO reaches a critical thickness, preferential debonding along the TGO/bond coat interface occurs along the crest of the ridges, upon cooling to room temperature (Figure 18 (b)).
5. In the case of ridge debonding, we believe that a single ideally situated ridge debond event can produce a crack of sufficient size to result in unstable crack propagation parallel to free edge of the specimen. Upon reaching a critical length, which is 3 - 5 mm, the crack propagation switches to buckling which rapidly spalls the majority of the coating. Thus, the life-limiting event is the widespread development of debonding at the TGO/bond coat interface along the crest of the ridges. We will subsequently show that the physical evidence and fracture mechanics calculations are consistent with these hypotheses.

III 5.4 Damage Mechanism II

For this mechanism, an initial imperfection that is oriented into the bond coat is necessary .This mechanism is aided by cyclic plasticity of the bond coat and the related response of the TGO layer, which involves lengthening through cracking or creep. Hence, extensive thermal cycling is necessary.

1. The majority of the bond coat ridges are asymmetric and have a steep side and a

smooth side associated with them

2. When the specimen is cooled after the first cycle, the TGO layer is in in-plane compression everywhere. For a perfectly flat bond coat surface the stress in the bondcoat is zero everywhere except near the free edge. However, along the sides of the ridges, the TGO will develop out-of-plane compressive stresses and at the top of the ridges develop out-of-plane tensile stresses. Once the TGO becomes thick enough, large compressive stresses are generated in the bond coat that leads to formation of a plastic zone (Figure 19 (a)).
3. During the heating cycle, the stress in the TGO becomes less compressive. However, the compressive plastic strains in the bond coat induce in-plane tensile strains in the TGO layer due to misfit caused by plastic deformation (Figure 19 (b)) [Cheng *et al*; 1998, Ambrico *et al*; 2001].
4. If the TGO responds to the tensile stresses by lengthening, which may happen if TGO develops cracks normal to the interface or elongates due to creep, a permanent change occurs to the length of the TGO. When the oxide is sufficiently thin, in-plane tensile stresses are not enough to induce a change in the TGO layer, the plastic zone will cycle between tension and compression and no enlargement will occur ((Figure 19 (c)) [Cheng *et al*; 1998, Ambrico *et al*; 2001].
5. When the TGO lengthens for the first time, the process repeats during every successive heating cycle leading to progressive elongation of the TGO to form into a cavity [Ambrico *et al*; 2001].
6. Also, large in-plane tensile stresses are generated, at room temperature, near the tip of the cavity and at peak temperature along the shoulders of the cavity. This

respectively leads to TGO cracking, perpendicular to the interface, at the tip and along the shoulders as observed [Cheng *et al*; 1998].

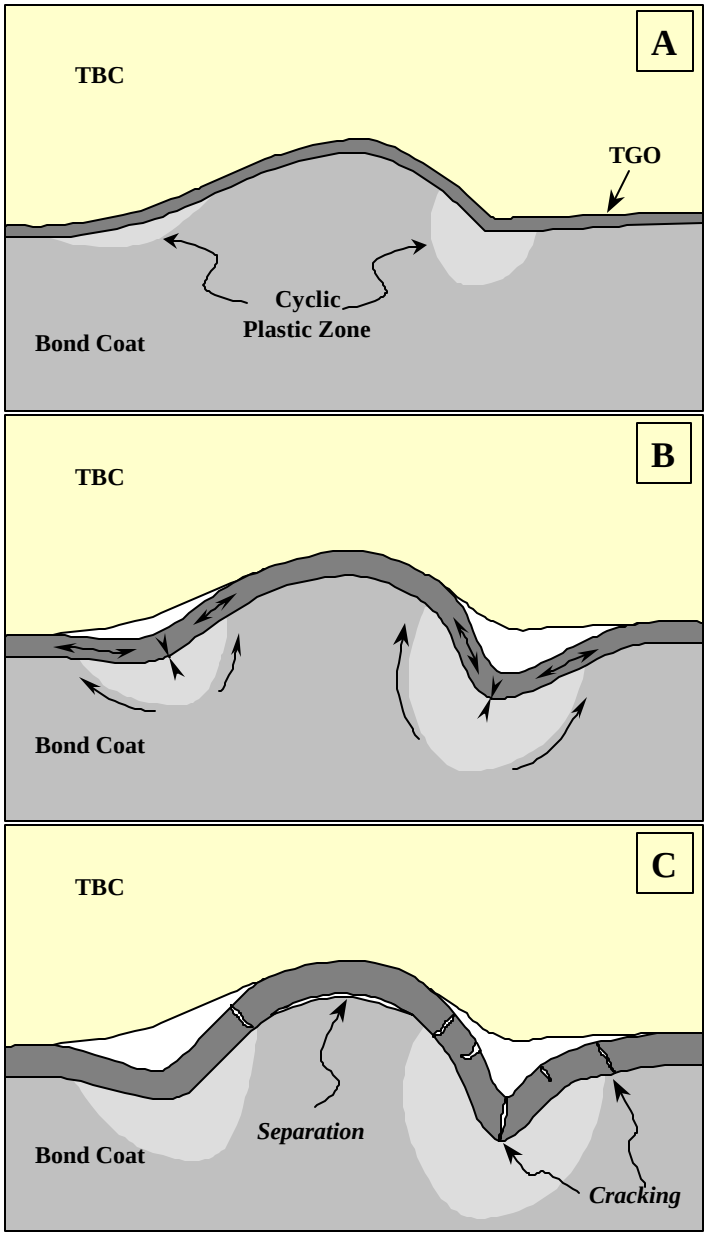

Figure 19: Damage initiation mechanism II for specimens with bond coat ridges.

Ratcheting mechanism of TGO leading to cavity formation (a) with TGO growth large compressive stresses are generated in the bond coat leading to formation of a plastic zone

(b) after a critical TGO thickness, large tensile stresses are generated in the TGO leading to permanent change in TGO by lengthening (c) The process repeats until tensile cracks are generated at the shoulders of the cavity at peak temperature and along the tip of cavity at room temperature (Cheng *et al*; 1998, Ambrico *et al*; 2001).

III 5.4 Fracture Propagation along the Interfaces

Due to the ten-fold variation in spallation lives, the specimens will be discussed in three categories, short-life specimens, intermediate-life specimens and long-life specimens. The observed spallation surfaces of all the specimens can be rationalized based on the two mechanisms described above. The observations from intermediate-life specimens will be treated first, following which the other two extreme scenarios will be discussed.

III 5.4A Intermediate-Life Specimens (739-1227 Cycles)

Both damage initiation mechanisms I and II are simultaneously operative for specimens that had spallation lives in this regime. The final fracture propagates both along the TGO/bond coat and TGO/7YSZ interfaces. Area fraction analysis of the spallation surface indicates that the fracture has occurred at the TGO/bond coat interface to about 50 % of the entire area of the specimens. Also, the TGO layer that formed into cavities, along the sides of the bond coat ridges through mechanism II, amounts to 8-10 % of the total spallation area. It is important to note that formation of these cavities is responsible for the fracture path switching between the TGO/bond coat and TGO/7YSZ interfaces. In other words, the cavity formation that occurs preferentially along the sides of the bond coat ridges, leads to preexisting separations at the TGO/7YSZ interface. The cavity formation however does not alter the convex geometry of the bond coat ridges. The TGO

that grows on the bond coat ridges is susceptible to debonding from the bond coat surface from increased tensile stresses as described in mechanism I. When the final fracture propagates, the TGO that is already separated from the 7YSZ due to cavity formation remains adhered to the bond coat and the crack switches between the TGO/bond coat and TGO/7YSZ interfaces upon encountering a bond coat ridge. The supportive evidence for the proposed path for crack propagation is that the TGO found on the spallation surfaces is always contained within the bond coat grains. Also, debonding always occurs at the TGO/bond coat interface along the bond coat ridges. The critical event precipitating failure is the TGO/bond coat separation near the free edge of the specimen by mechanism I.

III 5.4B Short-Life Specimens (190-670 Cycles)

The dominant mechanism that is operative in this set of specimens is mechanism I. The final spallation occurs in these specimens before mechanism II becomes operative. The main reason for this behavior is attributed to a high bond coat ridge aspect ratio. In other words, higher ridge aspect ratio implies smaller radius of curvature as shown by a schematic in Figure 20.

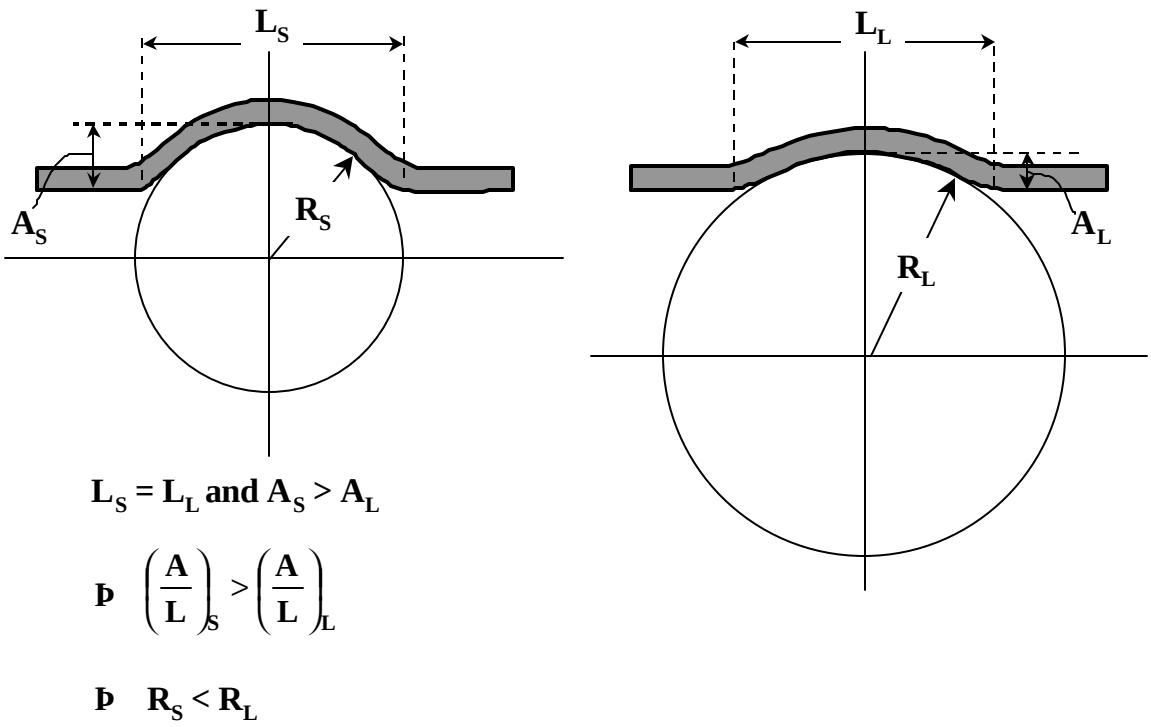

Figure 20: Schematic showing the relationship between the aspect ratio of bond ridges and its associated radius of curvature.

The ridge aspect ratio of the short-life specimens (S) is higher than long-life specimens (L). The bond coat ridge width is chosen to be the same for both cases for illustration purposes. It can be seen from equation 5.4 that smaller radius of curvature leads to higher tensile stress. The spallation surface indicates that the TGO was confined to the intra-granular portion of bond coat grains, suggesting formation of wing cracks that propagated preferentially along the TGO/bond coat interface over the ridges and at the TGO/7YSZ interface along the intra-granular regions. As seen in the intermediate-life specimens, spallation has occurred at both TGO/bond coat and TGO/7YSZ interfaces. Area fraction analysis indicates that debonding at the TGO/bond interface occurred at 70 % of the total area for specimen AG53 (190 cycles) and 50 % of the total area for specimen AG48 (670 cycles). Bond coat cavities were formed along the ridges and accounted for about 4 and

6% of the total area respectively at 190 cycles and 670 cycles. This is despite the fact that these two specimens had relatively larger area fraction of bond coat ridges, due to smaller bond coat grain size. In essence, smaller bond coat grains tend to have taller ridges and hence fail sooner due to mechanism I.

III 5.4C Long-Life Specimens (1754-1917 Cycles)

Similar to the short-life specimens, the dominant mechanism responsible for the observed spallation surface in this set of specimens is mechanism-I. Even though the specimens have experienced extensive thermal cycling, the cavity formation was suppressed due to smaller aspect ratio of bond coat ridges. The majority of the spallation occurred at the TGO/bond coat interface as indicated by area fraction analysis, 80 % for specimen AE43 (1754 cycles) and 100 % for specimen AD56 (1917 cycles). Bond coat cavities that were formed accounted for about 6 % of the area for specimen AE43 (1754 cycles) and no cavities were formed for specimen AD56 (1917 cycles). These observations are consistent with the fact that, in the absence of cavity formation along the grain boundaries, the spallation predominantly occurs at the TGO/bond coat interface.

To summarize, the failure of the TBCs studied is dominated by the presence of bond coat ridges. Damage initiation due to mechanism-I is operative for all the specimens examined and is especially dominant for both the short-life and long-life specimens. The difference in spallation lives is entirely due to difference in aspect ratio of ridges: the higher the aspect ratio the shorter the life of the specimen. Additional evidence for this will be presented in the section describing the fracture mechanics aspects of failure. Damage initiation due to mechanism II is mainly responsible for cavity formation and is

dominant for specimens with intermediate lives. To this end, area fraction analysis suggests that the extent of cavity formation is a function of starting geometry and aspect ratio of ridges, wherein an optimum combination of these two factors exists for maximum cavity formation. This also suggests that the aspect ratio of the bond coat ridges of intermediate-life specimens is in between the values of short-life and long-life specimens in order to allow both mechanisms-I and II to operate simultaneously. The final failure is initiated near the free-edge of the specimen due to debonding at the TGO/bond coat interface resulting from mechanism I.

III 5.5.0 Failure Mechanisms

The primary driving force for final spallation is the release of elastic strain energy of TGO due to debonding at the TGO/bond coat interface. As indicated before, the elastic strain energy associated with the 7YSZ layer is insignificant compared to the strain energy associated with the TGO layer. Hence, for all the cases, debonding at the TGO/bond coat interface is necessary for final spallation. Based on the observations, the following sequence of events is proposed. Formation of an interface crack of critical size at the TGO/bond coat near the free-edge of the specimens. Edge-delamination and interface crack growth that eventually leads to spallation buckling.

III 5.5.1 Macroscopic Observations

It was possible to maintain close observation of the macro-level aspects of final spallation for specimens cycled at the University of Connecticut. Based on the observations, a qualitative description is summarized in Figure **21**.

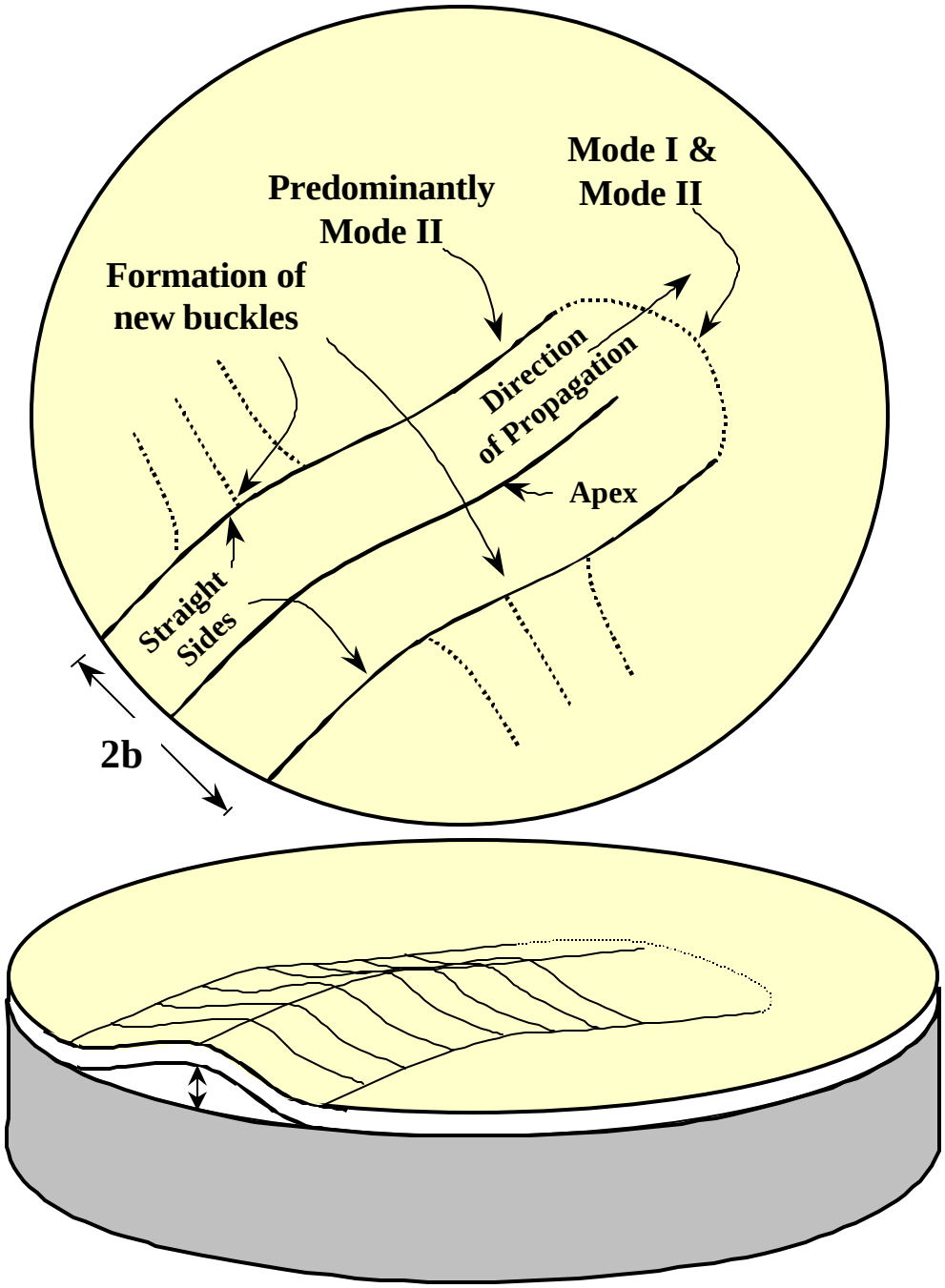

Figure 21: Schematic of spallation initiation at the free edge of the 7YSZ EB-PVD TBCs.

Prior to spallation, extensive edge spallation was seen along the free-edge of the disk coupon specimens. Typically, a 3-5 mm wide buckle originated from the free edge of the

specimen and traversed across the entire surface of the specimen. Subsequent to the buckling, the TBC layer cracked at the apex and along the straight edges, leading to the formation of a new edge along the sides of the buckle. Onset of another buckle occurs from this newly formed edge almost in a direction normal to the previous direction. Thus, the spallation propagates across the entire specimen surface until all of the TBC is spalled.

The initiation of delamination from the free-edge can be rationalized as follows: Given a perfectly smooth TGO/bond coat interface, the entire TGO layer is under a compressive stress that is equi-biaxial in nature. There are no shear stresses in the TGO layer except at the very circumference of the layer, which holds the entire film in compression [Evans *et al*; 1983]. Hence, the TGO layer along the free edge is susceptible to delamination almost entirely in a mode II (pure shear) fashion, where the TGO has no constraint for relieving the stored strain energy. This hypothesis is supported by experimental evidence, wherein line scans of TGO stress done using PLPS technique, diametrically across the disk coupon specimens, indicate damage along the circumference of the 7YSZ TBC layer. In addition, all failures are edge connected. The next step is to investigate what other factors might lead the separation to exceed the critical dimensions that would favor large-scale buckling (LSB).

III 5.6 Fracture Mechanics Model

Based on the observations, thus far, damage initiation mechanism I is predominantly responsible for debonding at the TGO/bond coat interface. As mentioned before, only this type of debonding is capable of releasing the stored strain energy in the TGO. It is

hence hypothesized that the debonding that occurs at the TGO/bond coat interface over a bond coat ridge that is ideally located parallel to the free-edge of the specimen is primarily responsible for the failure of the specimen. A schematic of such a configuration is shown in.Figure 22

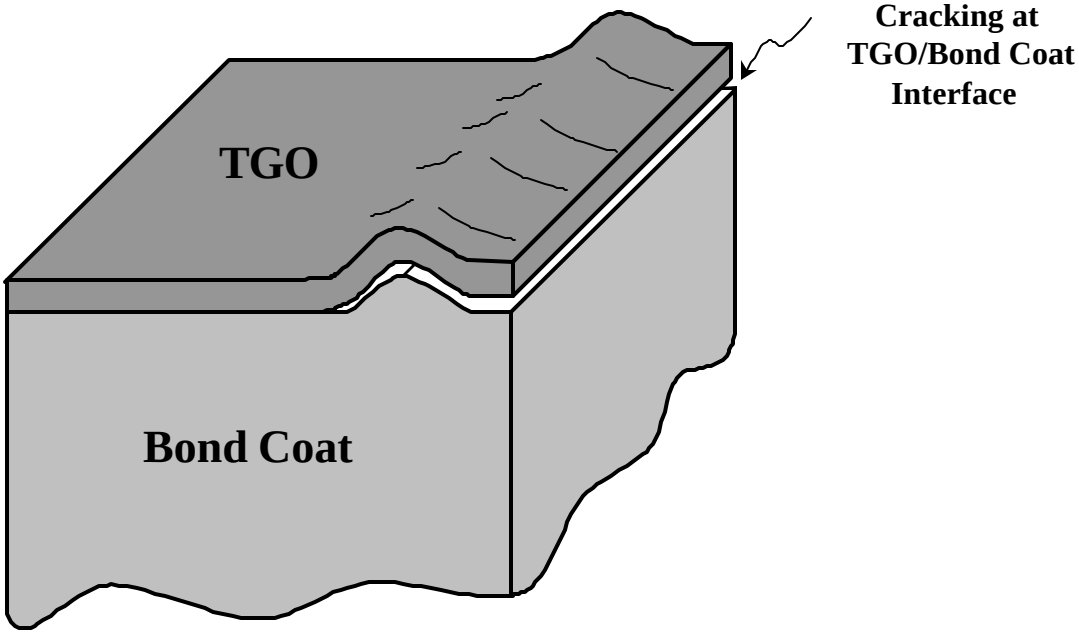

Figure 22: An ideally positioned bond coat ridge, parallel to the free-edge of the specimen.

The debonding that occurs at the ridge top, along TGO/bond coat interface, provides the interfacial crack necessary for fracture propagation.

The following sections will examine this scenario through ideal crack-geometries and the crack driving force that results from those geometries. It is worth mentioning that the non-destructive measurement of TGO stress as a function of thermal exposure by PLPS technique makes this analysis possible.

For an interface crack propagating from the edge, the energy release rate G_o approaches a steady state value. Under such circumstances, the crack releases the elastic energy in the

TGO layer, and is subjected to a plane strain condition in the direction parallel to crack front [Choi *et al*; 1999]. The expression for G_o is given by:

$$G_o = \frac{(1-\nu_{TGO}^2)\cdot h_{TGO}\cdot \sigma_o^2}{2\cdot E_{TGO}} \quad (5.5)$$

where, ν is the Poisson's ratio, h is the layer thickness and E is the young's modulus of the TGO layer. Figure 23 shows the calculated strain energy density as a function of cycles based on the measured mean TGO stress (PLPS technique) and measured mean TGO thickness (microscopy).

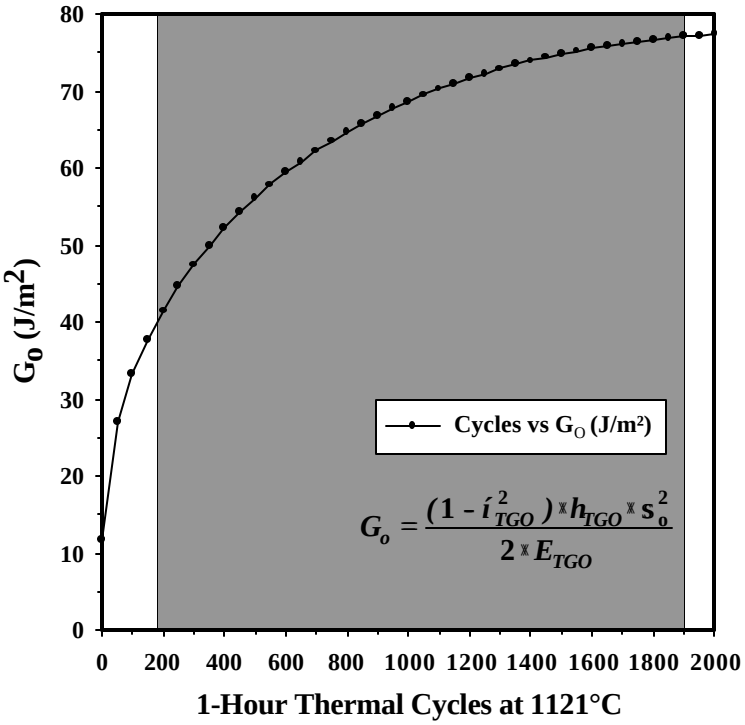

Figure 23: Stored strain energy calculated from measured TGO stress values and TGO thickness for specimens with bond coat ridges. The shaded region indicates the range of interest: 190 cycles to 1917 cycles

For the spallation lives ranging from 190 cycles to 1917 cycles, the thickness of the TGO increases from 2.6 μm to 6.8 μm, the TGO compressive stress decreases from 3.6 to 3.1

GPa and hence the corresponding elastic strain energy, G_o, of the TGO increases from 42 J/m^2 to 77 J/m^2.

Thus, the life limiting event in this scenario would be to create a debonding at the TGO/bond coat interface, along the crest of the ridges as shown in **Figure 28**. For debonding to occur through mechanism I, a threshold value for tensile normal stress must exist at the asperity tips of bond coat ridges. To this end, the normal stress at the TGO/bond coat interface was calculated from the analytical solution provided by Gong and Clarke (1998) for both short-life and long-life specimens (The procedure adopted for measuring the radius of curvature of the bond coat ridges and for calculating the normal stress is listed in Appendix I). The normal stress thus computed for two extreme situations, the shortest-life and the longest-life specimens are plotted as a function of thermal cycles in Figure **24**.

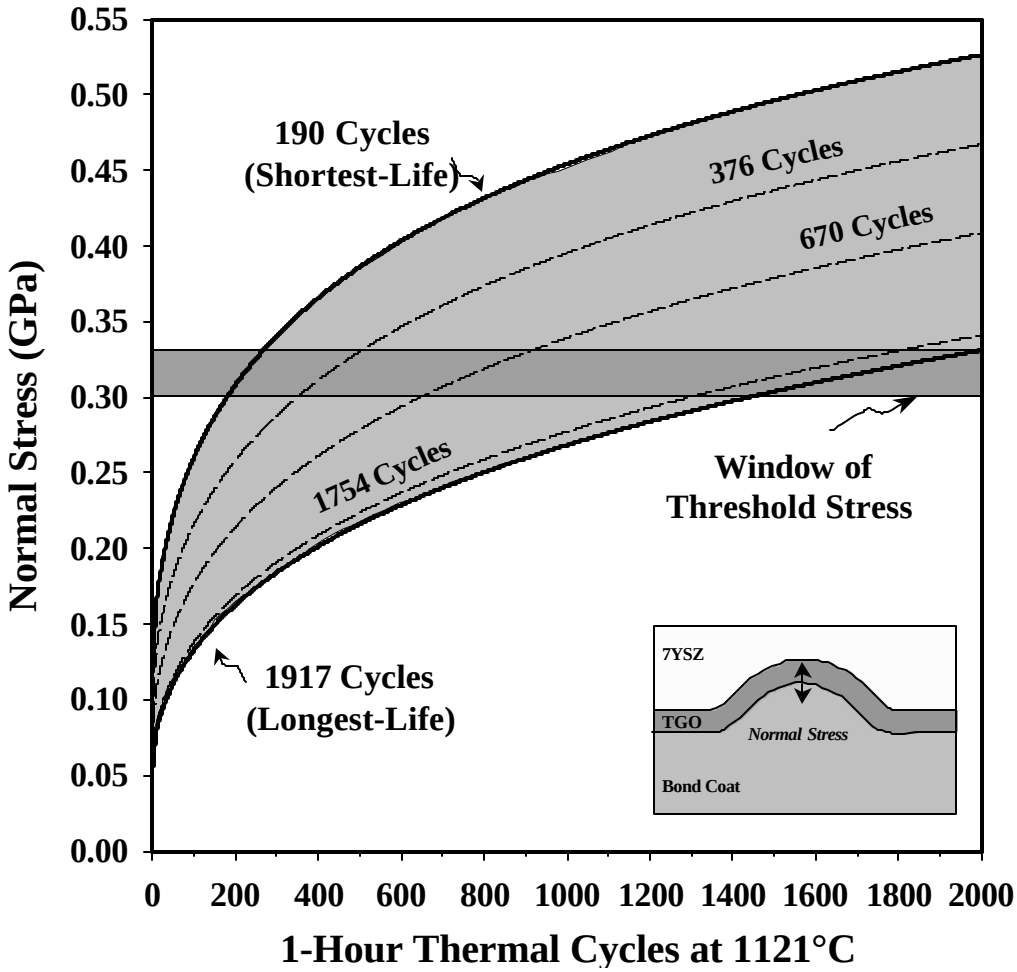

Figure 24: Range of normal stresses for specimens with bond coat ridges. A window of threshold stress exists, within which the debonding at the TGO/bond coat interface is favored.

Note that the normal stress rises faster for the shortest-life specimen in comparison to the longest-life specimen. Also, the magnitude of tensile stress for the specimen that failed at 190 cycles (0.30 GPa) is about twice the value (0.15 GPa) of the longest-life specimen after the same number of cycles, where failure did not occur. It is interesting to note that the normal stress values for the specimen that failed earliest at 190 cycles are equal to those for the longest life specimen that failed at 1917 cycles as shown in Figure 25.

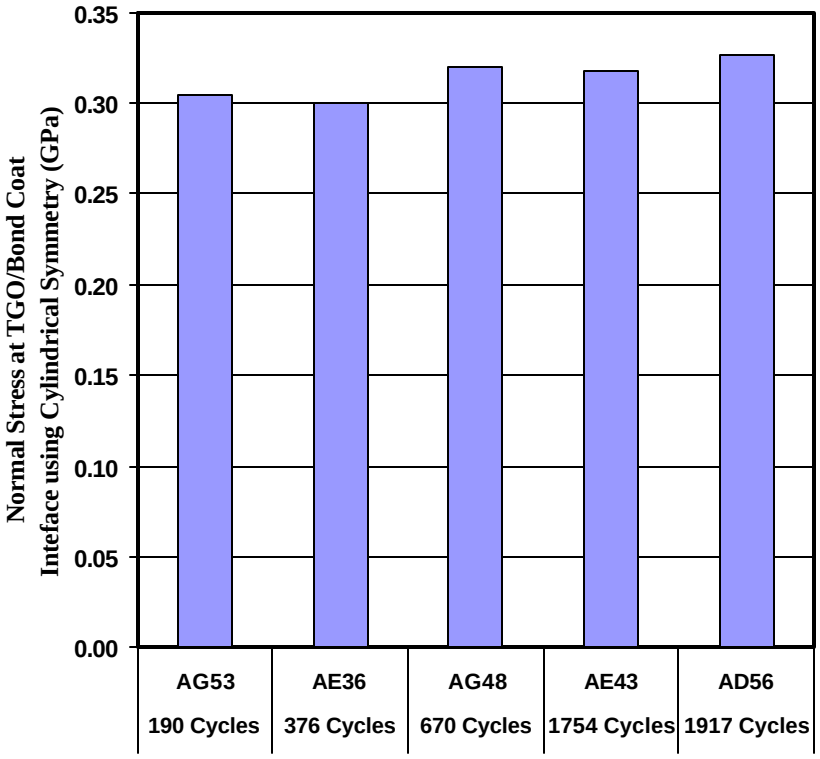

Figure 25: Calculated normal stress at failure, at the TGO/bond coat interface at the crest of bond coat ridges using analytical solutions for cylindrical symmetry form Gong and Clarke (1997).

Thus, a critical normal stress value of about 0.3 GPa promotes delamination at the TGO/bond coat interface. Most importantly, due to parabolic thickening of TGO layer, the critical stress is reached after a large number of cycles for the long-life specimens, as the TGO grows at a much lower rate as number of thermal cycle increases. For the failure scenario proposed it is assumes that when the ridge crest TGO separates from the bond coat the resulting crack is of such a size and shape that it results in a strain energy release rate larger that the interface toughness and results in a catastrophic unstable fracture. . In

the next several paragraphs we will show that such an unstable fracture is credible in light of our measured TGO stress and thickness and based on fracture mechanics.

The separation of the ridge top is not nearly large enough to result in buckling spallation at an interior location [Thouless, M. D., Hutchinson, J. W. and Liniger, W. G. (1992)]. Instead we propose that the critical separation is that for a ridge top separation parallel to and next to a free edge. In doing this we will somewhat arbitrarily assume a flaw size and show subsequently that an even smaller flaw would also have been consistent with the failure observed. Specifically we will assume that a debonded grain boundary 150 microns long located at the free edge is produced when the crest of the ridges separate and that the flaw width perpendicular to the free edge is 15 microns and that the TGO thickness is 5 microns which is typical for separations occurring near the mean sample life. The general configuration is shown in Figure 26[Ambrico, J M. and Begley,(2002) M. R.]

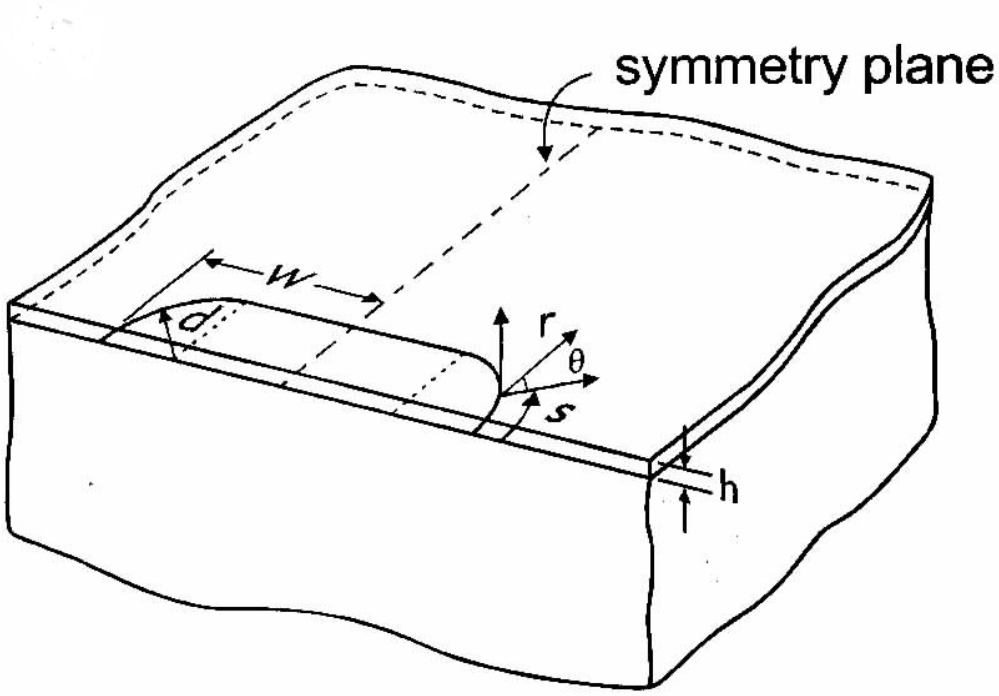

Figure 26: Fracture Mechanics Showing that Ridge Debonding Produces Total Debonding

The strain energy release rate and mode mixity for such edge flaws has been found from a parametric finite element written up separately [Ambrico, J M. and Begley,(2002) M. R.] elsewhere. The solution assumes that the Dander's parameter beta is nearly zero for simplicity. Selected results from that study are represented here in Figure 27. For the assumed edge flaw the relevant non-dimensional geometric parameters are d/W= 0.2, W/h=15 and d/h= 3. For this case the normalized strain energy at the symmetry plane is 0.75. We use this value as reasonably approximation to the strain energy release rate for inward growth due to the fact that for the geometry under consideration the crack front is mostly made up of the straight edge section parallel to the free edge. The mixity angle at the symmetry plane is 52 degrees.

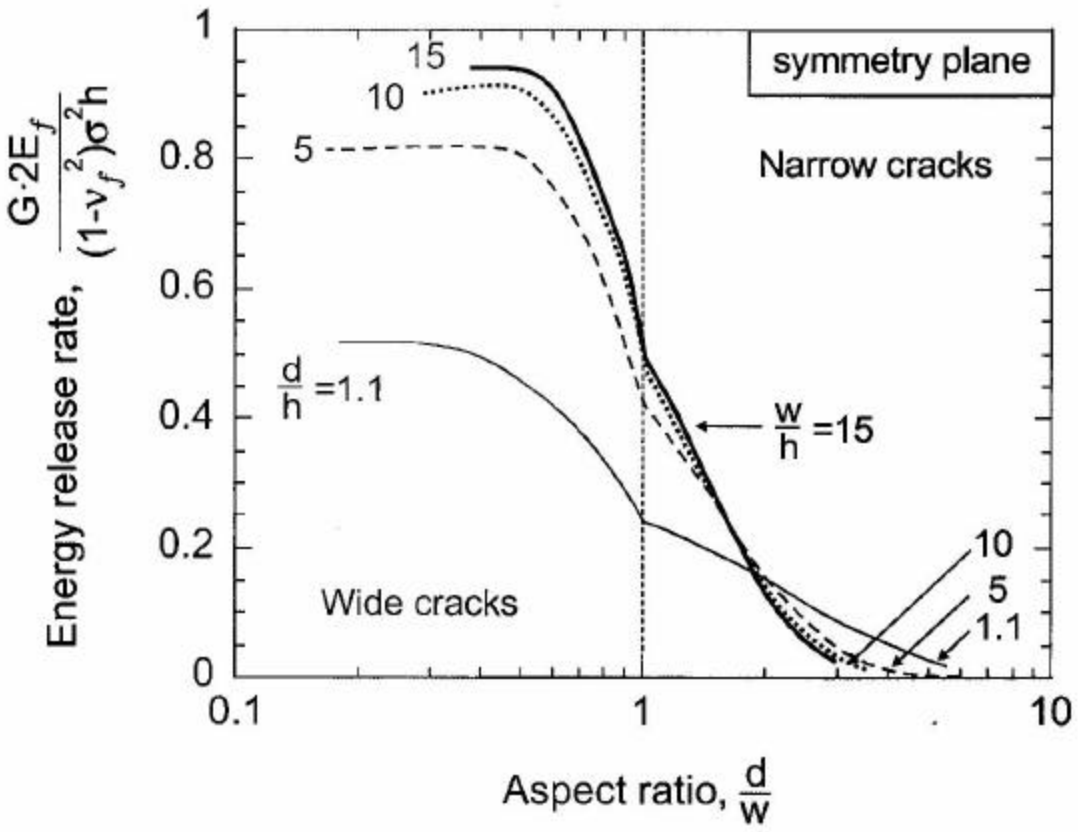

Figure 27

The crack might in alternative grow along the free edge increasing the dimension W. The question of whether or not unstable fracture occurs can be resolved without a decisive answer to which growth direction is preferred. This is true because as will be shown next the crack could grow inward accounting for sensible mixity effects. The crack would only grow latterly if such growth was easier than inward growth and hence the conclusion that growth would occur would be even more true if lateral growth were preferred. The interface toughness has been measured by Mumm et al using wedge indentation for the oxide bond coat interface of a system similar to the present and a value of 55 J/m^2 was obtained for a load conditions that was essentially mode II. To estimate the behavior in the present case it is necessary to estimate the mode I toughness that corresponds to a

Mode Ii toughness of 55 J/m2. This has been done by Clarke and also by Evans and a value of 5 J/m^2 is obtained. If one assumes the mixity behavior of this system is similar to that of an epoxy glass system a tough of about 8 is estimated. The lowest value of G0 at failure is 46 J/m^2 which yields based on Ambrico a value of applied G of more than 34 J/m^2 compared to the estimated toughness for the phase angle of 52 degrees which is expected to be near the pure mode I value of 5-8 J/m^2 leads to an expectation of unstable fracture at the interface and the answer is strong enough to withstand altering some of the assumptions made over a wide range and still the same conclusion would be reached. It thus is credible in light of fracture mechanics that instable fracture would occur when the ridge tops debond near the free edge.

III 5.6 Finite Element Fracture Mechanics Analysis of Ridge Top Debonding

The failure scenario just described requires that the ridges debond due to the presence of an initial flaw of some kind. At present there exists no fully realistic solution for the strain energy release rate for crack at cylindrical ridges or the corresponding cracks at spherical asperities as is relevant to plasma sprayed system. As part of the current effort the necessary solutions were generated using finite element approaches.

It has been determined here that bond coat asperities play a prominent role in the initiation of TBC spallation. The asperities that are responsible for the initiation process are the grain boundary ridges normally present in chemical vapor deposited Pt-Al bond coats. Other anomalies are the result of bond coat modification such as grit blasting and splat boundaries associated with plasma sprayed bond coats. It is believed that the large out of plane tensile stress inherent at the crest of these ridges is the primary driving force

responsible for initiating crack propagation. It is evident that TGO to bond coat separation predominantly takes place at the peaks of these asperities seen from ESEM micrographs showing TGO spallation at the crest of grain boundary ridges for a Type A sample tested using 1 hour cycles at 1121°C is show in Figure 28. From this observation it has be hypothesized that removal of bond coat ridges may be beneficial. Recent experimental evidence has shown that in the absence of grain boundary ridges a 4*x* life improvement is possible [Gell et al (1999)]. The implication of this finding has motivated us to determine the strain energy release rate associated with curved interfaces, in order better understand spallation of TBC's.

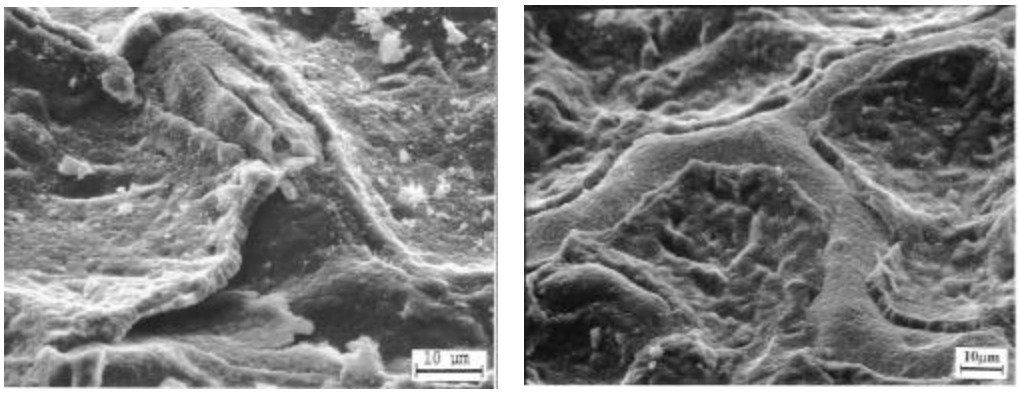

Figure 28: ESEM micrographs showing TGO spallation predominantly occurring along grain boundary ridges.

Model Idealization and (VCCT)

The present models shown Figure 29 consist of a cylindrical idealization of a grain boundary ridge and a spherical idealization of a general type asperity that may occur due to bond coat grit blasting and or plasma spray process. Both models will be analyzed using finite element virtual crack closure technique (VCCT) and the energy release rates associated with both modes I and mode II crack propagation will be evaluated. **Rybicki** and Kanninen **[**Rybicki, E.F. and Kanninen, M.F.(1977)**]** first proposed this technique in

1976 and it is based on Irwin's claim that the energy released as a crack extends an amount Δa is equal to the amount of work required to close the crack and is formally stated in polar coordinates as follows:

$$G = \lim_{\Delta c \to 0} \frac{1}{2\Delta a} \int_0^{\Delta a} \acute{o}_y(\Delta c - r, 0)\bar{v}(r, \pi)dr$$
$$+ \lim_{\Delta c \to 0} \frac{1}{2\Delta a} \int_0^{\Delta a} \tau_{xy}(\Delta c - r, 0)\bar{u}(r, \pi)dr \quad (1)$$

The energy release rates associated with mode I and mode II deformations are related to the first and second integrals respectively.

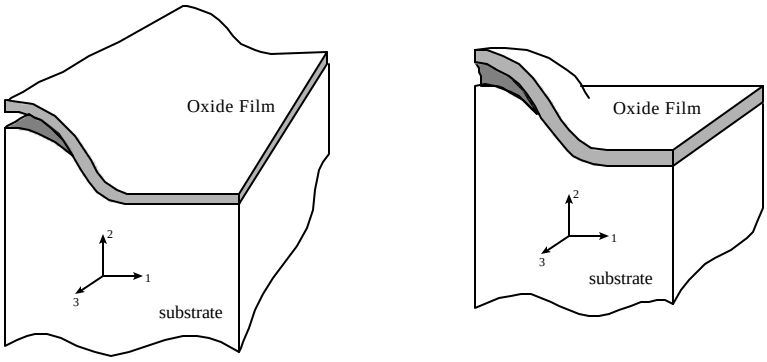

Figure 29: Cylindrical idealization of grain boundary ridge (left). Spherical asperity idealization associated with plasma sprayed systems (right).

Energy release rates calculated in terms of finite element analysis are as follows Figure 30 shows a typical finite element crack closure depic tion and the energy release rate associated with mode I can be computed as:

$$G_I = \frac{1}{2} \times \frac{1}{\ddot{A}a \times b} F_Y \times \ddot{A}Y \qquad (2a)$$

similarly for mode II

$$G_{II} = \frac{1}{2} \times \frac{1}{\Delta a \times b} F_x \times \Delta X \qquad (2b)$$

where F_X and F_Y are the forces required to close the crack, Δa is the length of the element, b is the thickness which differs depending on the model, ΔY and ΔX are mode I and mode II opening displacement respectively. For purposes of calculating the above quantities for the spherical and cylindrical cases it is a simple matter of vector rotation to get the normal and tangential components of F_x, F_y, ΔX and ΔY to the interface.

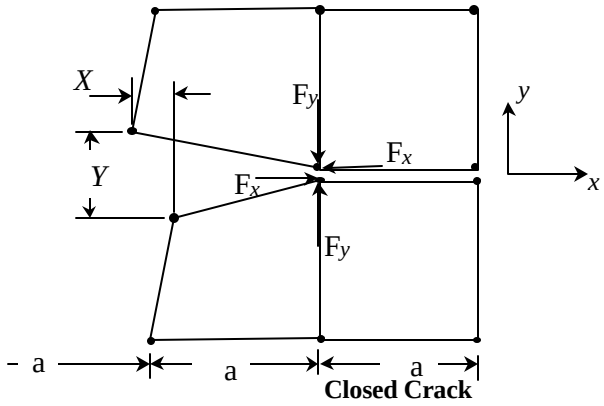

Figure 30: Finite Element depiction of the 4 tip elements needed to determine relevant forces and displacements in VCCT.

While Rybicki and Kanninen have demonstrated that VCCT works reliably for flat interfaces in non-bimaterial systems we have to show that the method can be used to strain energy release rates the bimaterial case where material properties differ. This is demonstrated using a closed form solution to the bimaterial fracture specimen that Liechti and Chai have developed [Liechti, K.M. and Chai, Y.S.(1992)]. The specimen includes two infinite half spaces with dissimilar properties bonded at the interface with a semi-infinite through crack. The bottom of the specimen is held rigidly while the top is held in a grip that can impose both a horizontal and or vertical displacement facilitating the

ability to vary relative amounts of mode mixity. The closed form solution can be found in [Hutchinson, J.W. and Suo, Z.(1992)]. Table 1 shows that VCCT accurately predicts stress intensity factors for bimaterial interfaces where the bimaterial constant β is essentially zero.

Table 2

Constant Strain, = 0.0005							
U	**V**	K_{I}exact	K_{I}FEM	K_{II}exact	K_{II}FEM	exact	FEM
1.00E-05	1.00E-05	16.90E+6	16.7E+6	6.78E+6	6.9E+6	21.8	22.4
2.00E-05	1.00E-05	17.86E+6	17.7E+6	15.30E+6	15.5E+6	40.4	41.2
3.00E-05	1.00E-05	18.79E+6	18.5E+6	23.80E+6	24.1E+6	51.6	52.5

Material combinations in which $\beta \neq 0$ produces an oscillatory stress singularity complicating interpretation of stress intensity factors. The choice of $\beta = 0$ is regarded as a reasonable choice given the materials involved. In particular when $\beta = 0$ stress field surrounding the crack tip are analogous to those in homogeneous material and will produce essentially uncoupled results whereby the phase angle ψ and the strain energy release rate G is then directly calculable by the following equations:

$$\psi = \tan^{-1}\left(\frac{K_{II}}{K_{I}}\right) \qquad (3)$$

$$G = \frac{K_{I}^{2}}{E^{*}} + \frac{K_{II}^{2}}{E^{*}} \qquad (4)$$

Where the bimaterial elastic constant E* in plain strain is computed by:

$$\frac{1}{E^*} = \frac{1}{2}\left(\frac{1-\nu_{ox}}{E_{ox}} + \frac{1-\nu_{sub}}{E_{sub}}\right) \quad (5)$$

The bimaterial constant is calculated by:

$$\beta = \frac{1}{2}\frac{\mu_{ox}(1-2\nu_{sub}) - \mu_{sub}(1-2\nu_{ox})}{\mu_{ox}(1-2\nu_{sub}) + \mu_{sub}(1-2\nu_{ox})} \quad (6)$$

Where E_{ox}, ν_{ox}, and μ_{ox} are the Young's modulus, Poisson's ratio, and shear modulus of the oxide film respectively and similarly for the substrate. A convergence study has revealed that the crack tip element length may be as large as 5% of total crack length and strain energy release rate computed from equations 2a and 2b is within 2% of that procured from finite element code.

Finite Element Model

The goal is to calculate the energy release rate for cracks emanating from the crest of idealized cylindrical and spherical asperities associated with bond coat surfaces. The stresses typically involved in TBC failures are the result of thermal cycling. Since it is assumed that the oxide forms stress free at the peak temperature and the only loading considered in this analysis is that produced by thermal expansion mismatch between the TGO and bond coat during cool down.

The two preliminary models considered here consist of a bond coat substrate and a TGO layer previously shown in.Figure **29**. The addition of a ceramic topcoat is of secondary

importance due to its significantly lower elastic modulus and will be ignored for now. The actual material properties used in the models are:

	E		
OX	380GPa	0.17	8.40E-06
SUB	200Gpa	0.35	1.36E-05

For the cylindrical model, plain strain four node constant strain elements were used. In order to simulate the oxide as a thin film the following boundary constraints and material properties are used: Rollers where applied along the bottom to suppress bending and the end symmetry planes were constrained by rollers to prevent horizontal motion. It should be noted that for the cylindrical case end rollers produce a period boundary condition. The thermal expansion coefficient of the substrate was selected as 0.0 and while the oxide is the difference between oxide and the substrate. These boundary conditions have produced the desired equi-biaxial stress state S_o associated with the thin film analogy within 3% of the expected value by equation 7. The spherical model is identical except that element type was changed to axi-symmetric and the boundary conditions no longer produce a periodic geometry however the equi-biaxial stress state remains.

$$S_o = \frac{E_{ox}(\alpha_{sub} - \alpha_{ox})(\Delta T)}{(1-\nu_{xo})} \qquad (7)$$

Since the analysis is entirely elastic and the strain energy release rates will be normalized by equation 8 the units of model dimensions are relative.

$$G_o = \frac{(1-\nu^2_{ox}) \cdot h_{ox} \cdot S_o^2}{2 \cdot E_{ox}} \qquad (8)$$

The tip element length i.e. Δa was varied from 0.5 to 0.005 and the strain energy release rate values obtained by equations 2a and 2b are in good agreement with values acquired from finite element code for $\Delta a \leq 0.1$. The geometry used in these preliminary finite element models are shown in.Figure **31**. Both models incorporate an interface radius r_i = 10, transition radius r_t = 4 and an oxide thickness h = 1. The total length of the entire model is $3r_i$ and the thickness of the flat region is $r_i/3$. These dimensions are more than

sufficient to suppress any influence that the boundary constraints may have on values obtained for the strain energy release rates. The crack length a/2 = r_i ***q*** ranges from initial length of 1.122 to a final length of 7.812 just prior to reaching the transition radius where ***q*** has been incremented in 6.429° intervals.

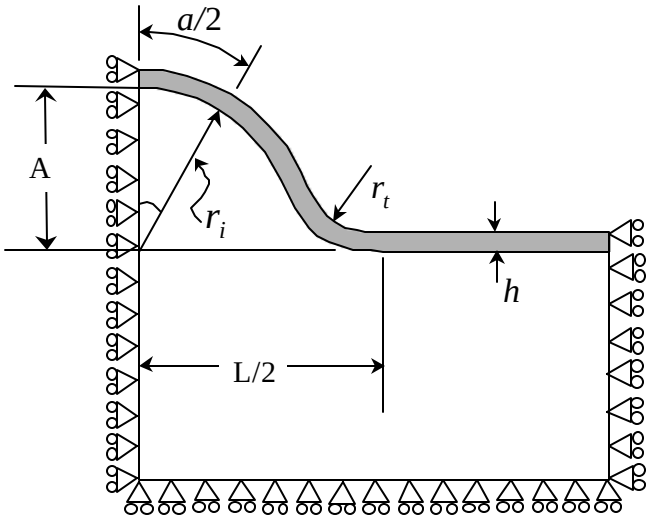

Figure 31: Geometry used in finite element computations. The cylindrical case is modeled in plane strain. In the spherical case axi-symmetric elements are used.

Results

The results presented here will demonstrate key features associated with mode I and mode II deformation obtained for the two geometries considered. The energy release rates for both the cylindrical and spherical models are plotted together in.Figure **32**. The strain energy release rates in both cases rise steeply until about 19° at which they begin to taper off. In the cylindrical case the total strain energy release rate reaches an extreme value where both mode I and mode II attain the same value at about 26°. Then total strain energy release rate steadily tapers off to the extreme mode II value as mode I tends to zero as seen by comparing Figure 32 and Figure 33. However, in the spherical case the

extreme value of the total energy release rate does not occur when both mode I and mode II attain the same value but rather total strain energy release rate tends to a steady state value at about 36° as mode I deceases at approximately the same rate as mode II increases from that point on as seen in **Figure 34**. The interesting differences between the two models is: The mode I driving force in the spherical case remains dominate all the way up to about 48° just prior the start of the transition radius, implying that spherical asperities would be potentially more detrimental. This may help to explain the significantly shorter life expectancy associated with plasma sprayed TBC systems. Also, the total energy release rate for the spherical case essentially remains constant for $\theta \geq 33°$ implying that mode II is a significant contributor in the failure process. An attempt to explain influence of mode mixity is presented in the next section.

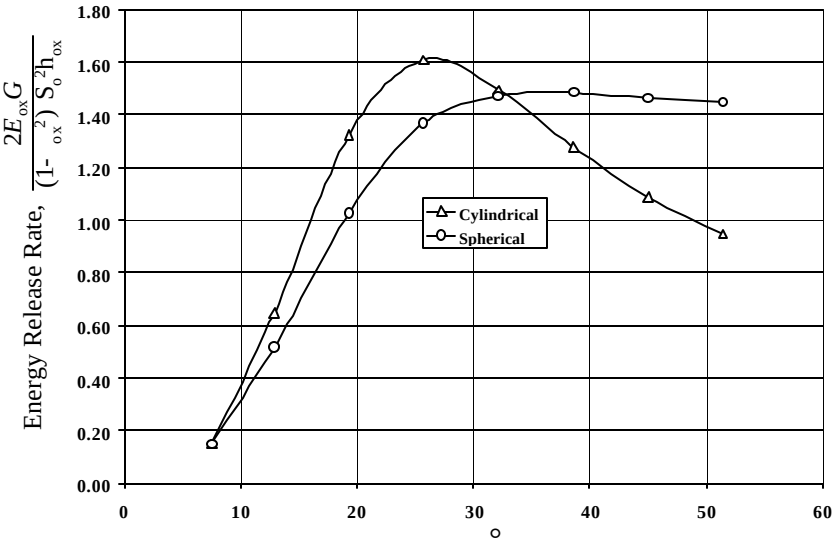

Figure 32: Normalized energy release rates for both the cylindrical and spherical models.

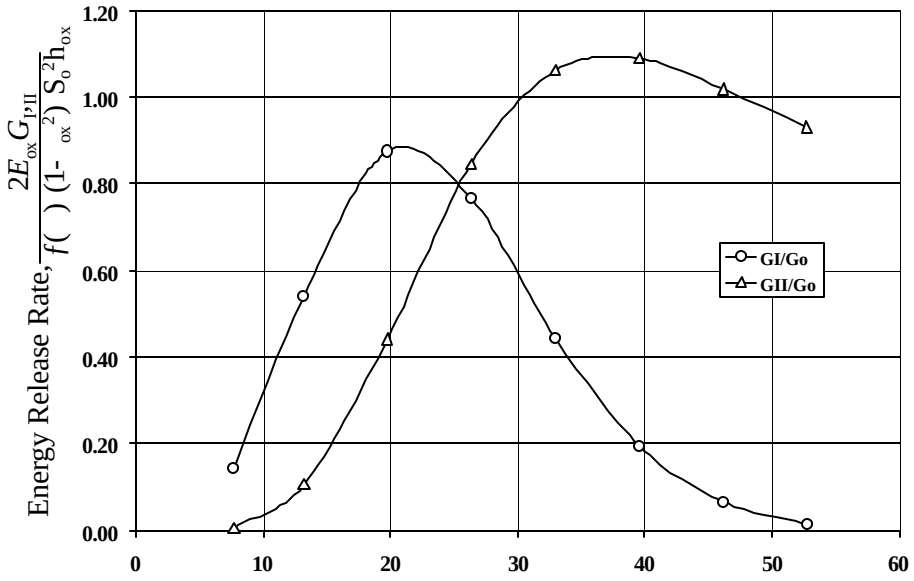

Figure 33: Normalized mode I and mode II energy release rates for the cylindrical model.

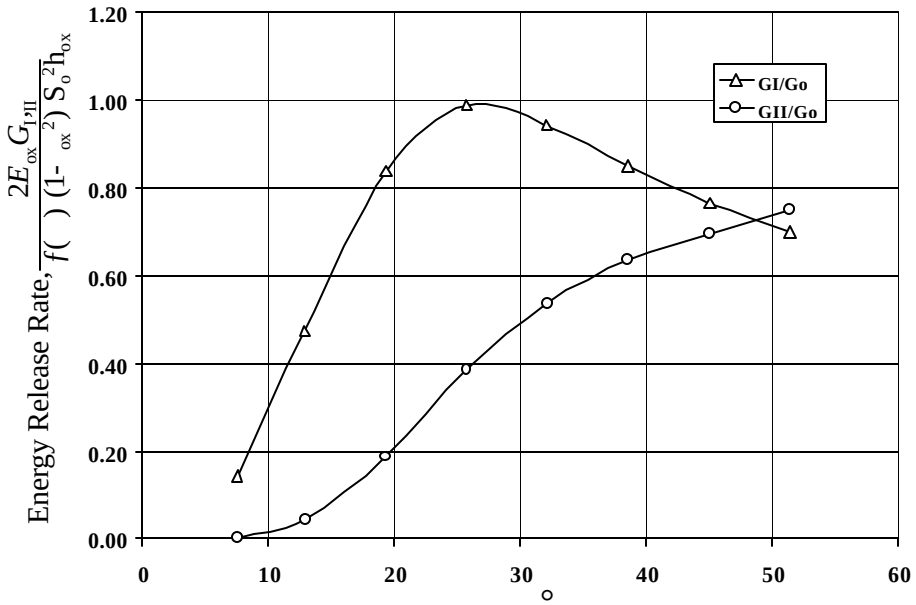

Figure 34: Normalized mode I and mode II energy release rates for the spherical model.

Phase Influence

It well know that mode mixity has a profound effect on toughness [Jensen, H.M., Hutchinson, J.W., and Kim, K.S.(1990)] however, the reference material property in most theories is the mode I toughness. In order to facilitate how phase dependence may influence the crack propagation a simple one-parameter family of mixed mode fracture criteria for both cases will be presented. Where the mixed mode toughness function is:

$$\Gamma(\phi) = G_I^c(1+(\lambda-1)\cdot\sin^2\phi)^{-1} \qquad (9)$$

Where G^c_I is the critical energy release rate associated with mode I and the parameter λ adjusts the influence of mode II on toughness e.g. in the case that $\lambda = 0$ crack propagation is only influenced by mode I deformation and for $\lambda = 1$ both modes of deformation are contributing equally to crack propagation. Since G^c_I is not known accurately for the system at hand a more general way illustrating the influence of mode II to toughness is done by plotting the total energy relates rate normalized by toughness function and replacing G^c_I by G_o as shown in.Figure **35** and Figure **36**. In this manner if G^c_I is known r any material combination critical flaw size and crack arrest can be determined form for this geometry.

The aspect ratio used by in this section to characterize asperities is A/L and in this model is approximately equal to 0.3 with h/r_i equal to 0.1 comparable to A/L = 0.17 and h/r_i = 0.086 reported for short life specimens. The parametric finite element done thus far is reasonably similar to this. If for example, the mode I toughness of the TGO to bond coat interface is 10 J/m^2 and with G_o equal to 42 J/m^2 for short life specimens of this section. It can be seen from Figure 36 the critical flaw size required to promote crack propagation in the cylindrical case occurs for $\theta \approx 9°$ regardless of λ. Crack arrest assuming that only mode I deformations are of primary concern correlates to $\theta \approx 33°$ and crack propagation

would continues at least until the transition radius for all $\lambda > 0.25$. The initial flaw size in the spherical case also occurs for $\theta \approx 9°$ and will propagate the transition radius regardless of λ see Figure 36.

Concluding Remarks

The Virtual Crack Clouse Technique provided significant insight in determining the strain energy release rate driven by the large tensile stresses associated with irregular surface topography. While the models presented herein do not encompass all the geometrical features reported by Vaidyanathan VCCT has provided a means in determining a critical flaw size associated with similar geometries. A complete parametric study encompassing a wide range of aspect ratios including varying h/r_i will provide qualitative means in determining the surface topography required to optimize the life of thermal barrier coatings. The present results are consistent with the fact that ridges debond over most or all of their width ounce the critical conditions is reached and further suggest that the critical initial flaw size is roughly 9 degrees of arc.

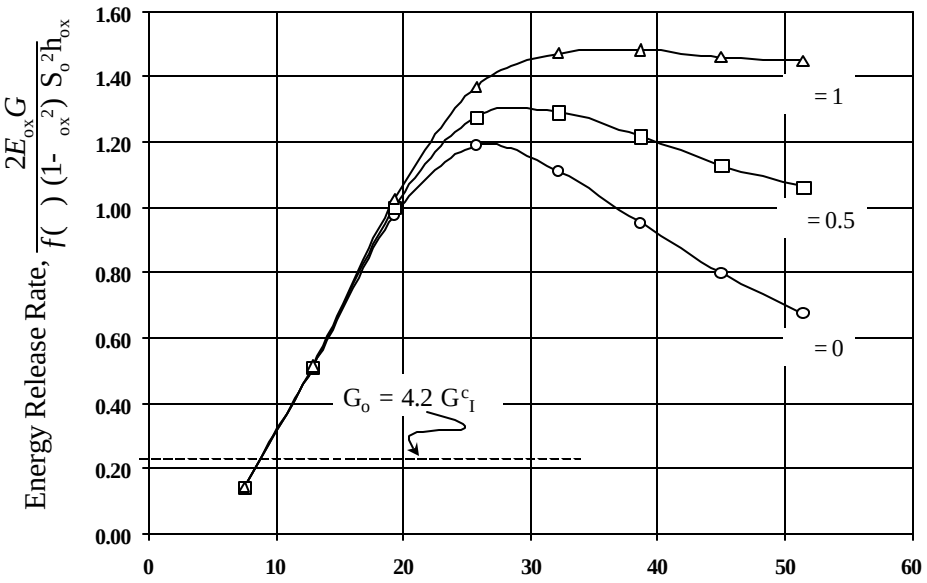

Figure 35: Local Energy release rate for the cylindrical case normalized by the one-parameter mode dependant toughness.

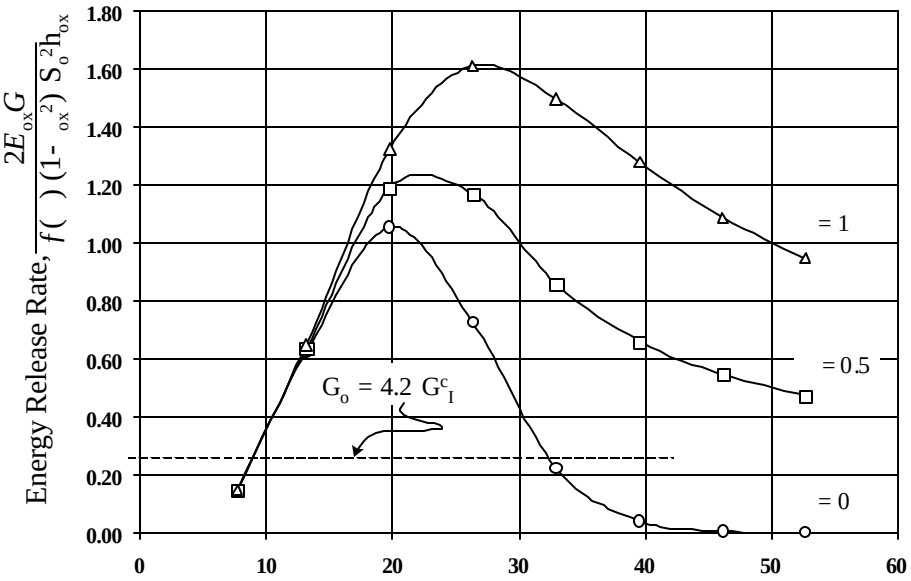

Figure 36: Local Energy release rate for the spherical case normalized by the one-parameter mode dependant toughness.

To conclude, the bond coat ridge aspect ratio and the bond coat grain size play an important role in determining the lives of these TBCs. There is an indication of variation in bond coat ridge heights and bond coat grain size of the specimens obtained from different batches. The short-life specimen AG53 (190 cycles) had the smallest grain size of 40 µm and the long-life specimen AD56 (1917 cycles) had the largest grain size of 65 µm. In addition, the aspect ratio of bond coat ridges of the short-life specimen (0.16) was twice the aspect ratio of the long-life specimen (0.08). Analysis has been presented that show that ridge top separation will cause total spallation for the cases studied and new

fracture solutions have been generated that show that ridges and other asperities tend to debond over most or all of their area ounce separation starts.

The variation in bond coat grain size and ridge height is a result of bond coat processing variations. To this end, the current method adopted by coating manufacturers to reduce the variation is accomplished by reducing the size of the imperfections is by grit-blasting the bond coat surface prior to ceramic deposition. Even though this procedure leads to consistent spallation lives, the mean life (660 cycles) of the specimens is about a one third of the life as seen in case of specimen AD56 (1917 cycles) that had no grit-blasting process [AGTSR Semi-annual report; 2000]. Thus, the implication of the results is that by identifying the key bond coat process parameters responsible for formation of ridges, the size of the ridges can be controlled, thereby leading to coatings that are more durable.

III.7 PLPL Based Remaining Life Prediction for 24 Hour Cycles at 1121 °C

For this data set, we have five samples. For each sample, we have stresses and the standard deviation of the stresses vs. cycles (Hours). The stress was curve fit using various polynomial functions, and it was deemed that a linear polynomial was the most appropriate (Figure 1).

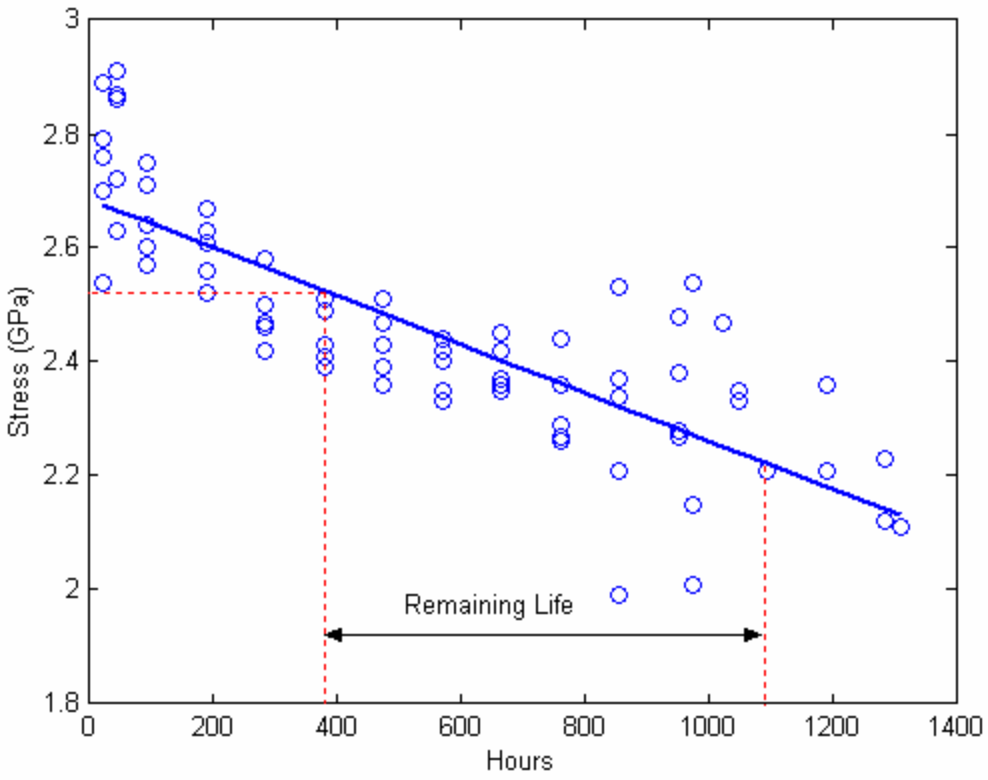

Figure 37 Linear prediction model for data set I

A stress threshold was selected, for example ***S***=2.5247. Then the corresponding number of cycles was found from the master curve in this example ***NS***=381.33. We assume the average life of all the samples as the actual life ***N***=1086.8. So we can calculate the remaining life corresponding to this stress threshold ***NR***=705.47. We will use this as remaining life for each sample.

Now data was selected for the individual sample up to this cycle ***NS***. Then fit each individual data with linear curve using only data up to that point (***NS***). Get the coefficients of each curve. Calculate the number of cycles for each sample corresponding to the stress threshold. To the number of cycles corresponding to the stress threshold we

add the remaining life expected based on the mean behavior of all samples to get the prediction life for each sample. Our results are shown in table 1. Other stress thresholds may be selected for use in remaining life predictions if desired.

Table 3 Results of Linear Regression Prediction

Sample	Hours (S=2.5247)	Remaining Life	Actual Life	Prediction Life
LD 85	243.58	705.47	858	949.05
LD 79	249.56	705.47	977.17	955.03
LD 94	334.18	705.47	977.17	1039.65
LD 70	335.37	705.47	1310.83	1040.84
LD 70	199.50	705.47	1310.83	904.97
Average			1086.8	977.91
Standard Deviation			210.22	60.10

In this case the standard deviation of the error was less than 7% of the expected life making such predictions of potential engineering use. More significantly the standard deviation for the predicted life is more than 3X smaller than the inherent deviation showing real predictive capabilities.

Finally, we also tried the quadratic prediction model. The dilemma of using this model is that there are two values corresponding to one stress threshold. What we did is to use the slope of the quadratic prediction model instead of itself. The results show that the standard deviation of the error was about 13% of the expected life and hence this was inferior to the linear regression.

IV. Evaluation of Type B TBCs: 1121 °C; 24-hour Cycle

IV.1 Polished Sample Preparation and Testing

After observing the role played by surface defects it was decided to reduce the defect size by polishing the bondcoat and then applying the TBC and then rerun the cyclic furnace test. In this way the role of defects can be shown and an improved TBC systems is expected to result. The sample was polished from the as received condition which was grit blasted down to 1 micron diamond as show in Figure 38. After polishing and before coating, a light grit blast was unfortunately done. However, the resulting sample as shown in Figure 38 was much smoother with respect to large-scale features.

Figure 38: Optical micrographs showing the procedure of smoothing

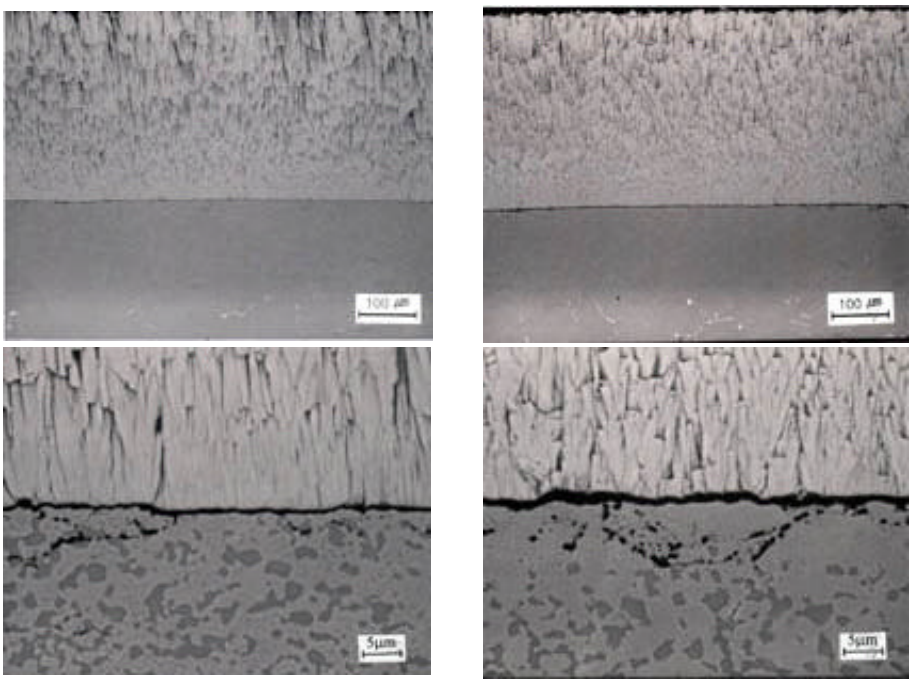

As-grit blasted

1 cycle

Figure 39: Cross-sectional backscatter electron micrographs of Grit-blasted TBCs

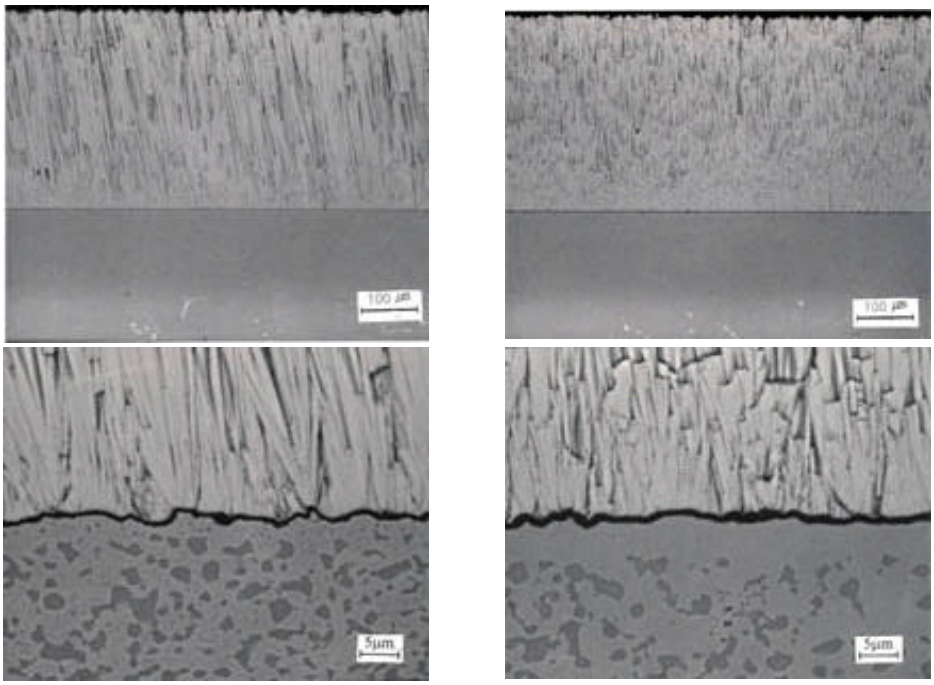

As-smoothed 1 cycle

Figure 40: Cross-sectional backscatter electron micrographs of smoothed TBCs

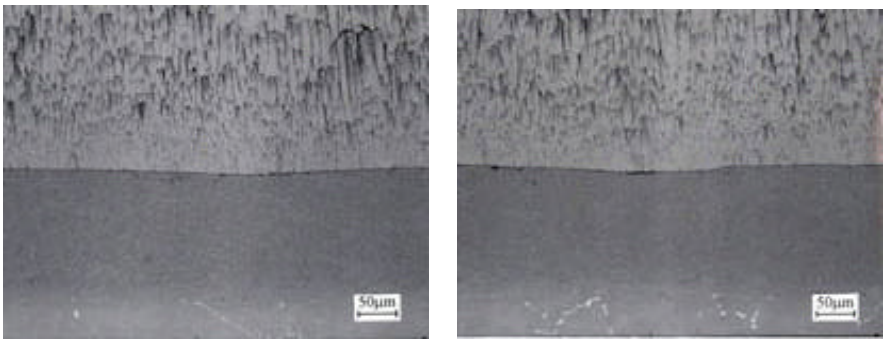

As-grit blasted

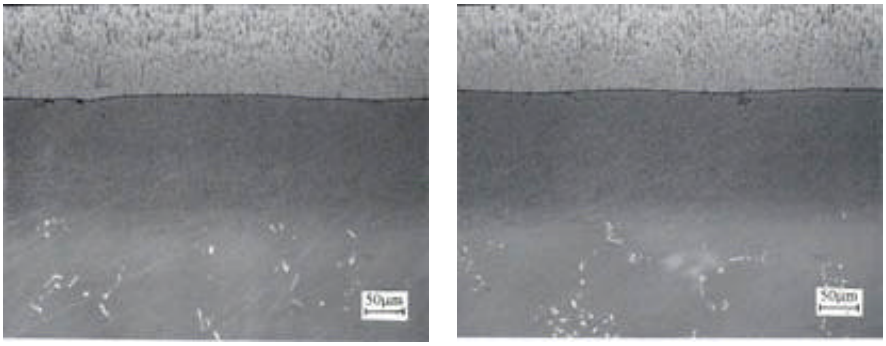

1 cycle

Figure 41: Cross-sectional backscatter electron micrographs of grit blasted TBCs

In the previous reporting period, the samples with and with out polishing had been subjected to 63 1-hour cycles. Because of the greater thickness of the samples, they were placed in the furnace laying flat on the insulating holder. This resulted in a profound change in cyclic life. The grit blasted samples failed in as few as 63 cycles indicating that their thermal conditions are not comparable to all earlier tests. This is being quantified by thermocouple measurement. Piezospectroscopic measurement was done on the grit blasted and polished samples and the results shown below Figure 42,

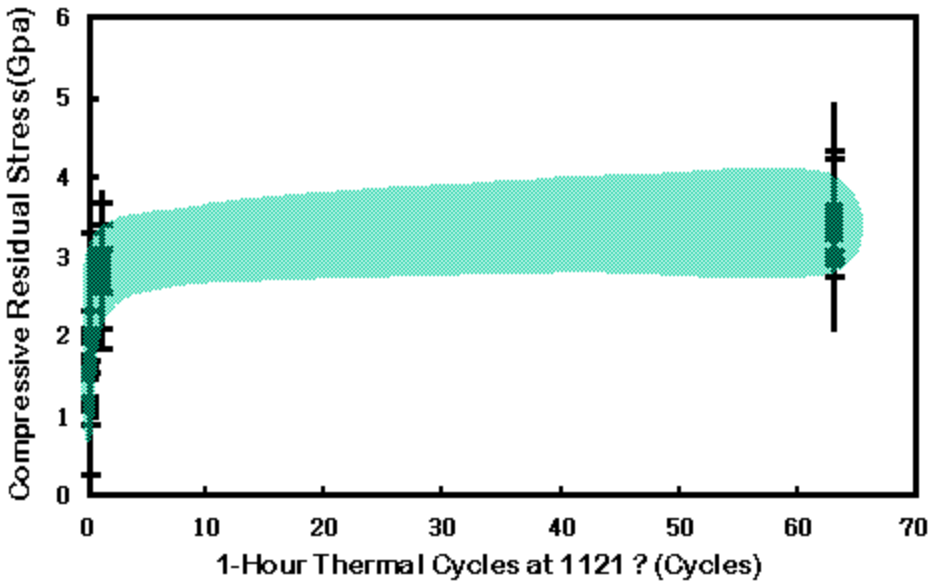

Figure 43, Figure 44 and Figure 45 show that the two types of samples behave in a very similar manner.

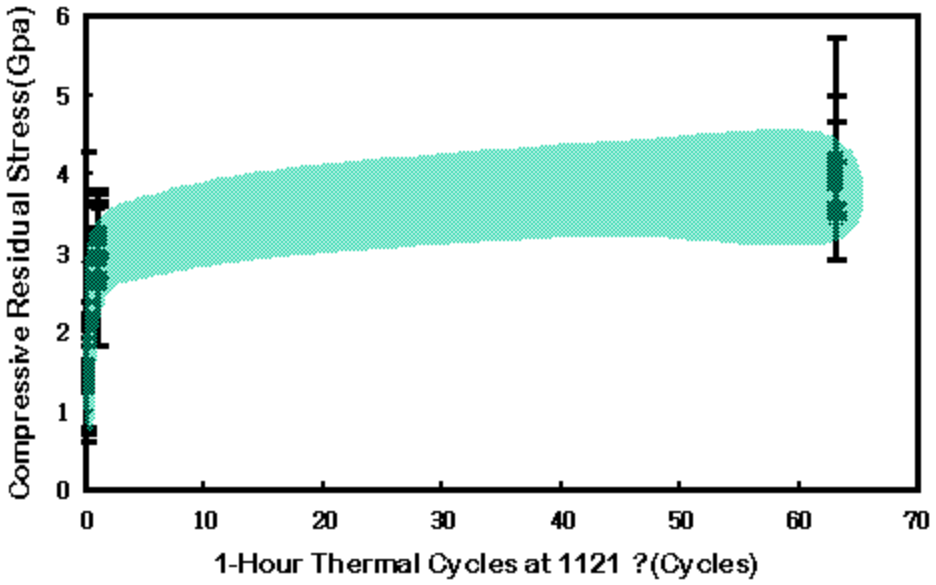

Figure 42: Evolution of TGO stress with 1-hour thermal cycling at 1121 on the YSZ/MCrAlY coated top surface of the Smoothed Type B TBCs.

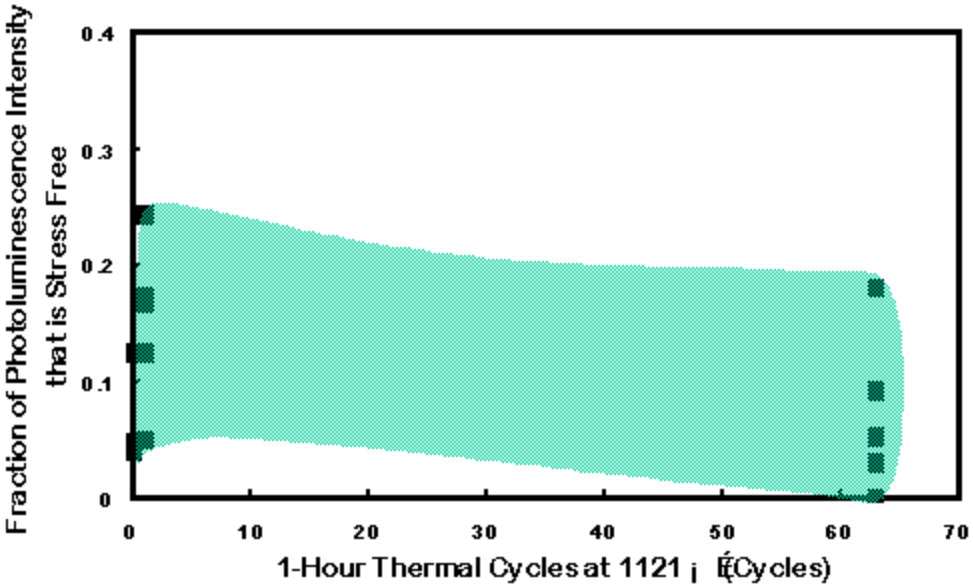

Figure 45: Evolution of fraction of stress-free photoluminescence peaks on the YSZ/MCrAlY coated top surface of smoothed TBCs as a function of 1-hour thermal cycle at 1121°C

In this reporting period, these tests have been completed and we will next quantify the difference in thermal conditions found in these tests compared to all other tests.

IV. 2. Spallation Life and Macro Failure Mode

The work for the 24-hour cycling period is currently being carried on to completion. The macro photos of the failed samples are shown in Figure 46.

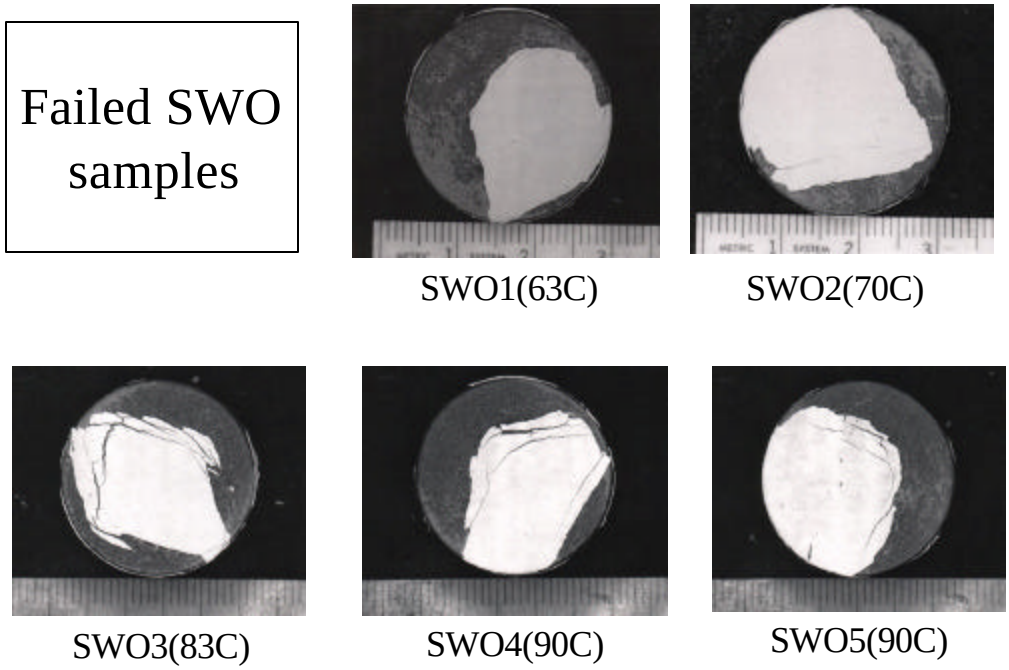

Figure 46: Macro photos of samples failed during 24-hour cycles at 1121°C

IV. 3. Laser Fluorescence

The stress measurements have been made on the grit blasted and the polished samples. The TGO stress evolution is shown in Figure 47.

Figure 47: Evolution of TGO Stress for: (a) the grit blasted and (b) the polished samples during 24-hour cycling at 1121°C.

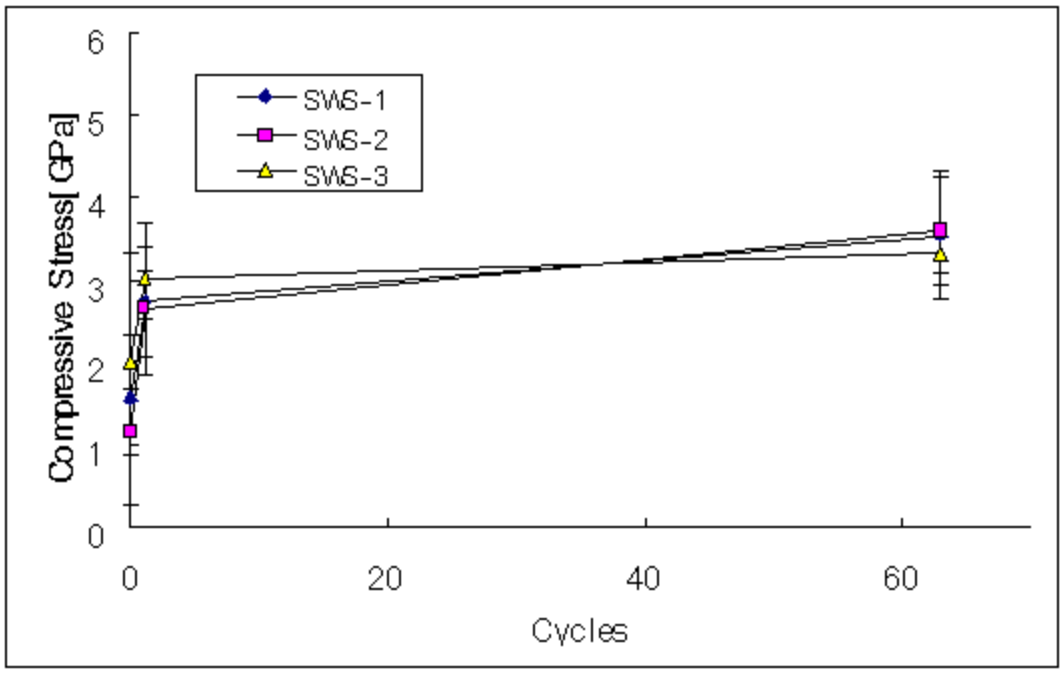

(a)

Compressive Stress of SWO Samples

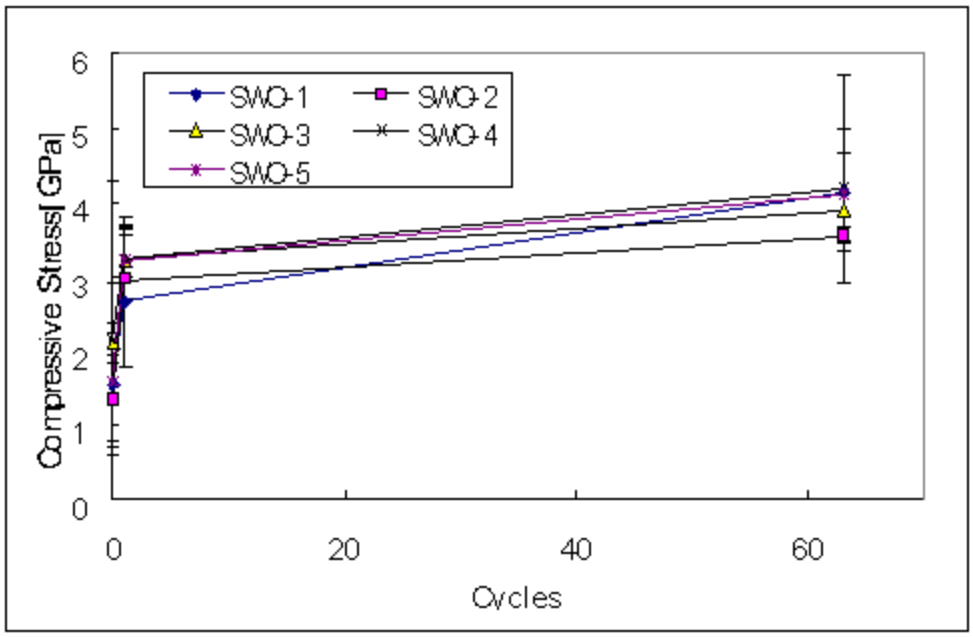

(b)

IV. 4. Micro structural Characterization

The TGO growth evolution has been studied as a function of 24-hour cycles in order to determine the TGO Parabolic growth rate as shown in Figure 48.

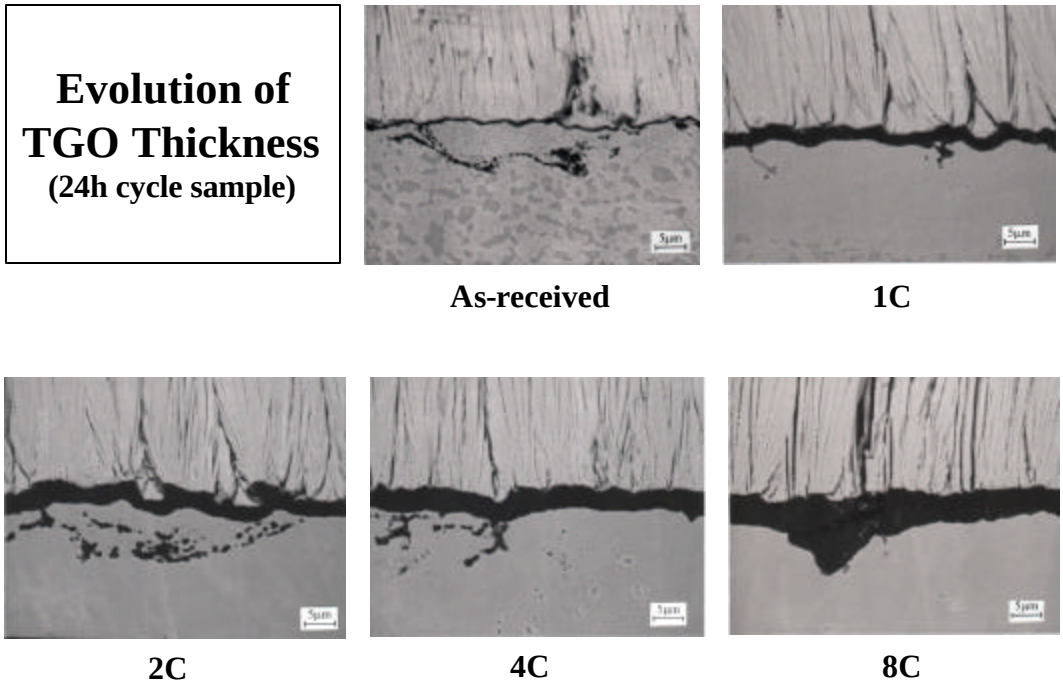

(a)

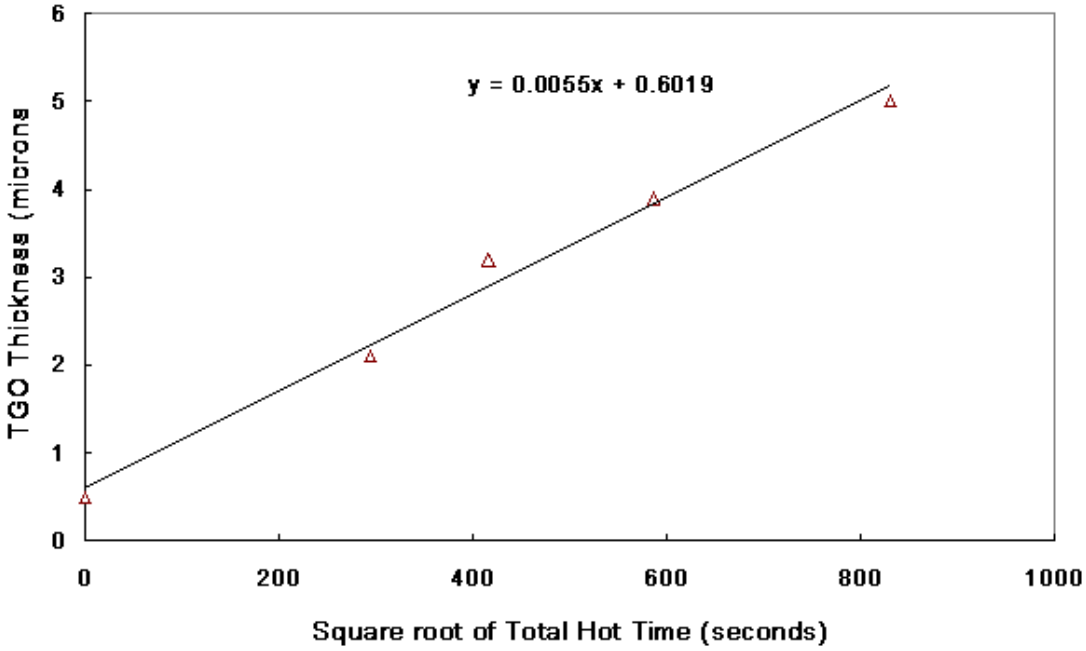

(b)

Figure 48 (a) & (b): Evolution of TGO thickness as a function of 24-hour cycles at 1121 C.

$K_p=5.5x10^{-3}$ m/sec$^{1/2}$

V Evaluation of Type C TBCs: 1121 C; 1-hour Cycle

A new batch of the Type C specimens has been selected for 1-hour thermal cycling tests at 1121°C.

V. 1. Spallation Life and Macro-Failure Mode

Four samples have been cycled to failure during this reporting period. The macro photos of these four failed samples have been shown in Figure 49. The average Spallation life based on these four samples is 325 Cycles.

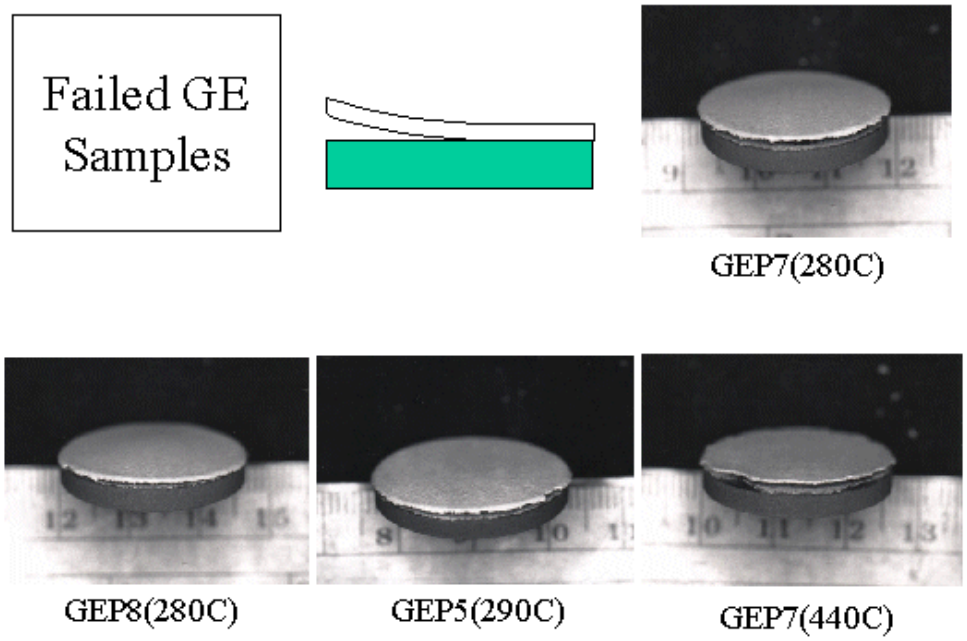

Figure 49: Macro photos of samples failed during 1-hour thermal cycling tests at 1121°C.

V 2 Laser Fluorescence

The laser measurements could not be made on the Type C specimens due to the large thickness of the TBC on these specimens. Taper polishing was done in order to determine the critical thickness of the TBC that gave a reasonable laser peizospectroscopy signal.

The normalized intensity obtained from the taper polished specimens has been plotted as a function of the YSZ thickness, as shown in.Figure 50 and

Figure51

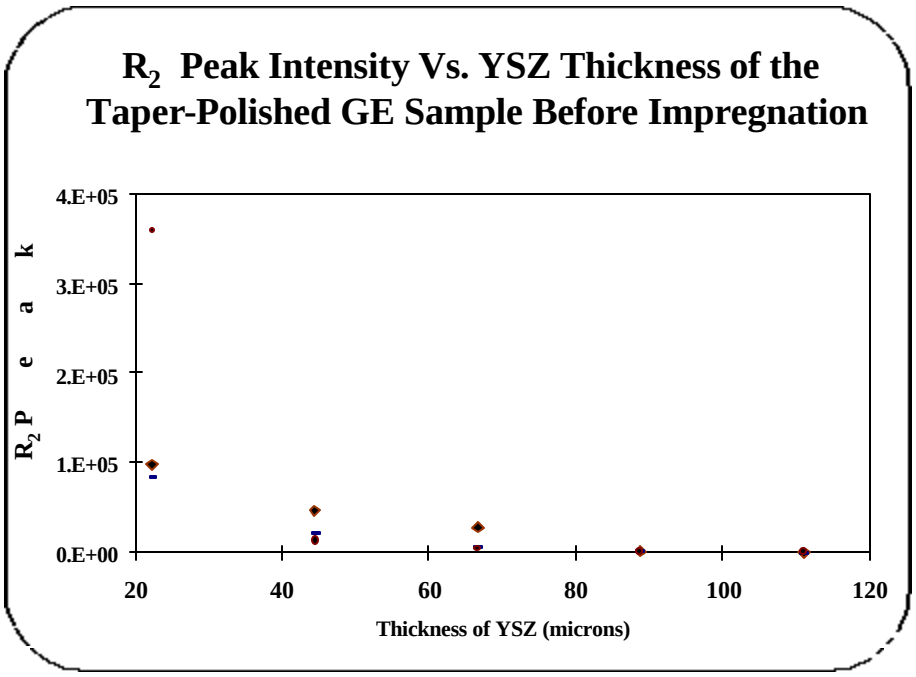

Figure 50**: R2 Peak Intensity vs. YSZ Thickness of the Taper-Polished Sample before Impregnation.**

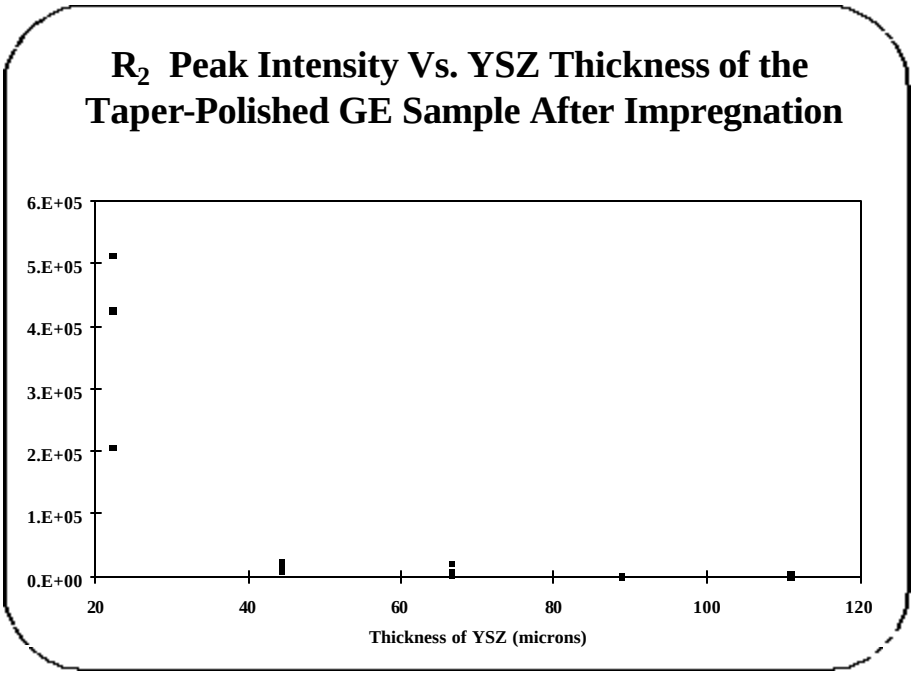

Figure 51: R2 Peak Intensity vs. YSZ Thickness of the Taper-Polished Sample after Impregnation

V 3 Micro structural Characterization

The morphology of the top surface of these samples has been studied in the as-coated condition, as shown in Figure 52. The SEM studies have been done on the samples in cross-section and are to be studied as a function of the one–hour cycles. This is shown in Figure 53.

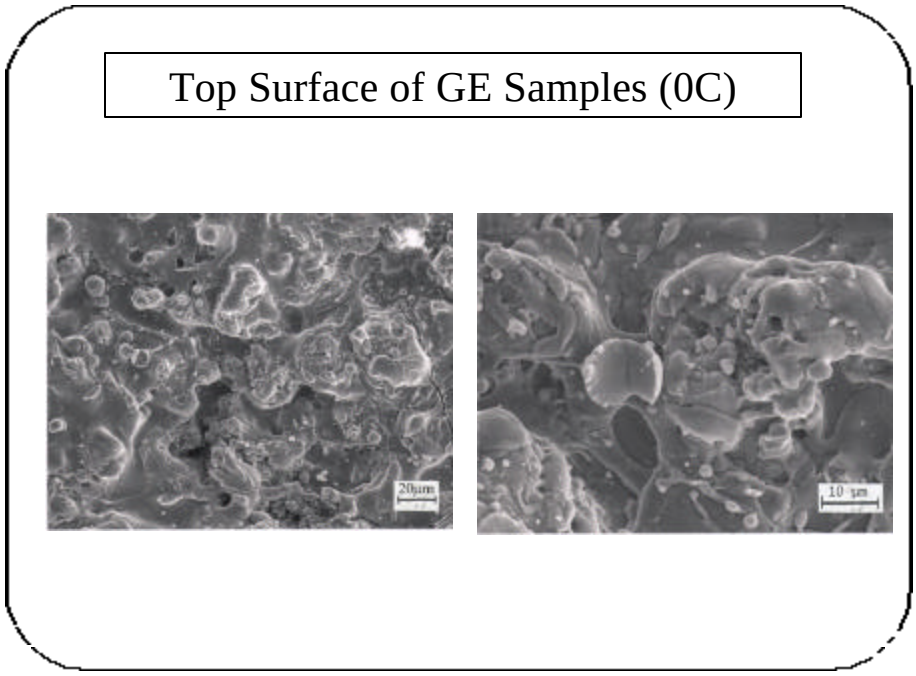

Figure 52: Back Scattered Electron Micrographs showing the Top Surface of the as-coated sample

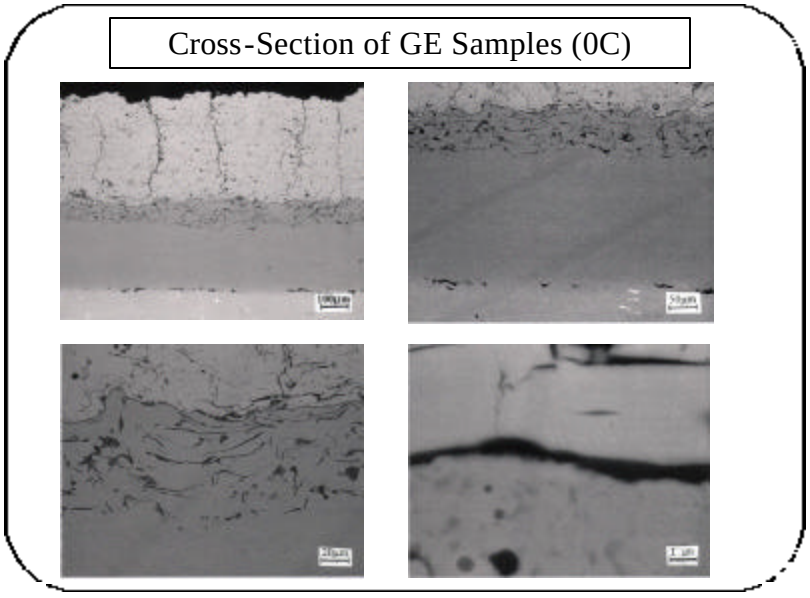

Figure 53: Back Scattered Electron Micrographs showing the cross-section of the as-coated sample

VI Low and High Temperature Thermal Cycling Tests

A new series of high and low temperature 1-hour cycling tests have been started to evaluate the failure life and determine the failure mechanism of Type A and Type B TBCs. A similar test is also being conducted on the GE specimens. These low and high temperature tests can be used to study the effect of the cycling time & temperature on the failure life and the failure mechanism of all three TBC systems. The high temperature tests are being conducted at 1151°C and the low temperature tests are being carried on at 1100°C. Laser fluorescence measurements and micro structural characterization are to be carried out on all these samples after a selected number of thermal cycles. Besides, a few samples of each type have also been cycled to failure in order to determine the average life of these samples. The 1-hour test consists of 10-minute heat up.40-minutes at the target temperature and 10-minute cooling down. For the low temperature tests, 16 Type A samples, 11 Type B samples and 15 Type C samples have been selected. For the high temperature tests, 15 Type A, 11 Type B and 15 Type C samples have been selected. More results on these tests will be available during the next reporting period.

VII. References

Ambrico, J M. and Begley(2002), M. R. ," The Role of Flaw Geometry in Thin Film Delamination From Two- Dimensional Interface Flaws Located Along Free Edges," Under Review 2002.

Ambrico, J. M. (2001) Begley, M. R., and Jordan, E. H., “Stress and shape evolution of irregularities in oxide films on elastic-plastic substrates due to thermal cycling and film growth,” *Acta Materialia*, **49**, pp. 1577-88.

Cheng, J. (1998), Jordan, E. H., Barber, B., and Gell, M., “Thermal/residual stress in a thermal barrier coating system,” *Acta Materialia,* **46**[16], 5839.

Choi, S. R. (1999), Hutchinson, J. W. and Evans, A. G., "Delamination of multilayer thermal barrier coatings," Mechanics of Materials, **31**, pp 431-447.

Clarke, D. R. (1999), and Pompe, W., "Critical radius for interface separation of a compressively stressed film from a rough surface," *Acta Materialia*, **47**[6], 1749-1756.

Evans, A. G. (1983), Crumley, G. B., and Demaray, R. E., "On the mechanical behavior of brittle coatings and layers," *Oxidation of metals*, **20**[5/6], pp. 193- 216.

Gell, M., Vaidyanathan, K., Barber, B., Cheng, J., and Jordan, E.H.(1999), "Mechanism of Spallation in Platinum Aluminide/Electron Beam Vapor Deposited Thermal Barrier Coatings", Metallurgical and Materials Transactions A, Vol. 30A,Feb., pp. 427-436.

Hutchinson, J. W. and Suo,(1992) Z. Advances in Applied Mechanics, 29, 63- 191.

Jensen, H.M., Hutchinson, J.W., and Kim, K.S.(1990) Decohesion of a Cut Prestressed Film on a Substrate. International Journal of solids and Structures. 1990; vol.26 pp.1099-1114

Liechti, K.M. and Chai,(1992) Y.S. "Asymmetrical Shielding in Interfacial Fracture Under In-Plane Shear". *ASME Journal of Applied Mechanics*, vol. 59 pp. 295-304

Mumm, D. R. (2001), Evans, A. G., and Spitsberg, I. T., "Characterization of a Cyclic Displacement Instability for a Thermally Grown Oxide in Thermal Barrier Coating System," Submitted to *Acta Materialia*, 2001

Rybicki, E.F. and Kanninen, M.F.(1977) "A Finite Element Calculation of Stress Intensity Factors by a Modified Crack Closure Integral". *Engineering Fracture Mechanics* 1977;9:931-8

Sergo, V. (1998), Clarke, D. R., "Observation of sub-critical spall propagation of a thermal barrier coating," *J. Am. Ceram. Soc.*, **81** [12], pp. 3237-42.

Suo, Z. (1995), "Wrinkling of the oxide scale on an aluminum-containing alloy at high temperatures," *J. Mech. Phys. Solids*, **43**[6], pp. 829-846.

Thouless, M. D., Hutchinson, J. W. and Liniger, W. G. (1992), Plane-strain, Buckling - dirven Delamination of Thin Films: Model Expeiments and Mode II fracture, *Acta Materialia*, Vol. 40 No 10, pp. 2639-2649.

Timoshenko, S. P. (1971) and Goodier, J. N., *Theory of elasticity*, McGraw-Hill, New York.

Vaidyanathan, K.K.(2001)"Failure Mechanisms of Platinum Aluminide Bond Coat / Electron Beam–Physical Vapor Deposited Thermal Barrier Coatings". PhD Thesis, Institute of Material Science, University of Connecticut, Storrs, 2001.